PROCEEDINGS

20TH INTERNATIONAL SYMPOSIUM ON SPACE TERAHERTZ TECHNOLOGY

ISSTT 2009

April 20 – 22, 2009
Charlottesville, Virginia USA

Proceedings of the

20TH INTERNATIONAL SYMPOSIUM ON SPACE TERAHERTZ TECHNOLOGY

Omni Hotel
Charlottesville, VA, USA
April 20-22, 2009

Edited by Eric Bryerton, Anthony Kerr, and Arthur Lichtenberger

Preface

The 20th International Symposium on Space THz Technology (ISSTT2009) was held from April 20 to 22, 2009, in Charlottesville, Virginia. It was attended by over 160 scientists and engineers from 14 countries. 35 were students working in the field of Terahertz technology.

The Symposium organizers from the National Radio Astronomy Observatory (NRAO), the University of Virginia, and Virginia Diodes, Inc. (VDI) want to thanks all participants and authors for making this symposium a scientifically interesting and very enjoyable event.

There were a total of 88 presented papers, 49 as fifteen minute oral presentations and 39 as posters. In addition, there were 6 invited plenary talks from distinguished THz researchers. These proceedings contain all papers submitted by May 26, 2009. The accepted abstract was used in cases where a full paper was not submitted.

Invited/Plenary Speakers (no abstract or paper included):

Al Wooten (NRAO), "*ALMA Status and Science Opportunities*"
Adrian Russell (NRAO), "*ALMA – The Push for the High Site*"
Mark Rosker (DARPA), "*The DARPA Terahertz Electronics Program*"
Susumu Komiyama (University of Tokyo), "*Ultra-High Sensitive Detectors in the Terahertz Region*"
Jürgen Stutzki (Universität zu Köln), "*SOFIA: A Far-Infrared Astronomy Platform for the next Two Decades*"
Jeffrey Hesler (Virginia Diodes, Inc.), "*Broadband Multiplier Development for ALMA, and its Implications for General THz Measurements*"

The organizers would like to thank the Scientific Organizing Committee for review of the technical program and the Local Organizing Committee for taking care of the local arrangements and initial abstract sorting and review. Special thanks are due to Gene Runion, Josh Malone, and Dale Nordstrom for the fantastic A/V work they did for the entire conference, with additional thanks to Gene for taking photographs, some of which are included later in this preface.

The symposium organizers would like to thank the National Radio Astronomy Observatory (NRAO), University of Virginia (UVA), and Virginia Diodes, Inc. (VDI) for sponsoring this event.

ISSTT 2009 Organizational Information

Local Organizing Committee:

Scott Barker, UVA
Eric Bryerton, NRAO, Co-Chair
Laurie Clark, NRAO, Event Planner Extraordinaire
Tom Crowe, VDI
Jeffrey Hesler, VDI
Anthony Kerr, NRAO
Arthur Lichtenberger, UVA, Co-Chair
Kamaljeet Saini, NRAO
Robert Weikle, UVA, Co-Chair

Scientific Organizing Committee

Scott Barker, UVA, USA
Eric Bryerton, NRAO, USA (Co-Chair)
Victor Belitsky, Chalmers, Sweden
Raymond Blundell, Harvard Smithsonian, USA
Tom Crowe, VDI, USA
Brian Ellison, Rutherford Appleton Laboratory, UK
Gregory Goltsman, Moscow State Pedagogical Univ., Russia
Jeffrey Hesler, VDI, USA
Karl Jacobs, KOSMA, Germany
Alexandre Karpov, CalTech, USA
Anthony Kerr, NRAO, USA
Bernard Lazareff, IRAM, France
Arthur Lichtenberger, UVA, USA (Co-Chair)
Alain Maestrini, The Observatoire de Paris, France
Imran Mehdi, JPL, USA
Antti Raisanen, Helsinki University of Technology, Finland
Kamaljeet Saini, NRAO, USA
Yutaro Sekimoto, NAOJ, Japan
Sheng-Cai Shi, Purple Mountain Observatory, China
Jan Stake, Chalmers, Sweden
Christopher Walker, University of Arizona, USA
Robert Weikle, UVA, USA (Co-Chair)
Wolfgang Wild, SRON, The Netherlands
Jonas Zmuidzinas, CalTech, USA

ISSTT 2009 Registered Participants

Last Name	First Name	Affiliation	Email
Ahlberg	Mikael	Swedish Space Corporation	mikael.ahlberg@ssc.se
Albanna	Sarmad	Univeristy of Arizona College of Optical Science & Steward Observatory	salbanna@as.arizona.edu
Arsenovic	Alex	University of Virginia	aia8v@virginia.edu
Barker	Scott	University of Virginia	barker@virginia.edu
Barkhof	Jan	Kapteyn Astronomical Institute	j.barkhof@sron.nl
Baryshev	Andrey	Netherlands Institute for Space Research	a.m.baryshev@sron.nl
Bauwens	Matt	University of Virginia	mfb8b@virginia.edu
Belitsky	Victor	GARD, Chalmers University of Technology	victor.belitsky@chalmers.se
Benoit	Bob	University of Virginia	rrb4m@virginia.edu
Billade	Bhushan	Chalmers University of Technology	bhushan.billade@chalmers.se
Blundell	Raymond	Smithsonian Astrophysical Observatory	rblundell@cfa.harvard.edu
Boussaha	Faouzi	LERMA - Paris Observatory	faouzi.boussaha@obspm.fr
Bryerton	Eric	NRAO	ebryerto@nrao.edu
Carrion	Enrique	University of Massachusetts	enrique.carrion1@gmail.com
Chattopadhyay	Goutam	JPL/Caltech	goutam@jpl.nasa.gov
Chen	Lihan	University of Virginia	1c4kh@virginia.edu
Chen	Ming-Tang	Academica Sinica	mchen@asiaa.sinica.edu.tw
Clark	Laurie	NRAO	lclark@nrao.edu
Crowe	Tom	Virginia Diodes, Inc.	tomvdi@earthlink.net
Cyberey	Mike	University of Virginia	mcyberey@ieee.org
Czakon	Nicole	California Institute of Technology	czakon@caltech.edu
Datesman	Aaron	Argonne National Laboratory	datesman@anl.gov
De Amici	Giovanni	Northrop-Grumman	giovanni.deamici@ngc.com
Denisov	Alexander	SRC "Iceberg"	denisov@ukrpack.net
Dieleman	Pieter	SRON	p.dieleman@sron.nl
Donovan	Jason	University of Massachusetts - Amherst	jasondonovan@gmail.com
East	Jack	University of Michigan	jeast@eecs.umich.edu
Edgar	Mick	Caltech	mick@submm.caltech.edu
Ellison	Brian	STFC Rutherford Appleton Lab.	brian.ellison@stfc.ac.uk
Emrich	Anders	OmniSystems	ae@omnisys.se
Erickson	Neal	University of Massachusetts	neal@astro.umass.edu
Fisher	Rick	NRAO	rfisher@nrao.edu
Fourie	Peet	European Southern Observatory	alma_admin@eso.org
Gao	Jian-Rong	SRON/TU Delft	j.r.gao@tudelft.nl
Gerecht	Eyal	NIST	ferecht@nist.gov
Giordano	Jose Luis	University of Talca	JLGiordano@hotmail.com
Goltsman	Gregory	Moscow State Pedagogical University	goltsman00@mail.ru
Gong	Songbin	University of Virginia	sg2ju@virginia.edu
Gonzalez	Alvaro	California Institute of Technology	algongar@gmail.com
Grajal	Jesus	Technical University of Madrid	jesus@gmr.ssr.upm.es
Grammer	Wes	NRAO	wgrammer@nrao.edu
Grimes	Paul	Oxford University Astrophysics	p.grimes1@physics.ox.ac.uk
Groppi	Chris	University of Arizona	cgroppi@as.arizona.edu
Haupt	Christoph	European Southern Observatory	alma_admin@eso.org

Hawasli	Sami	University of Virginia	shh6b@virginia.edu
Hedden	Abigail	Center for Astrophysics	ahedden@cfa.harvard.edu
Hekman	Peter	European Southern Observatory	alma_admin@eso.org
Herald	Bert	University of Virginia	dlh7t@virginia.edu
Hesler	Jeffrey	Virginia Diodes, Inc.	hesler@virginiadiodes.com
Hesper	Ronald	Kapteyn Astronomical Institute	r.hesper@sron.nl
Huebers	Heinz-Wilhelm	German Aerospace Center (DLR)	heinz-wilhelm.huebers@dlr.de
Huelsmann	Axel	Fraunhofer IAF	axel.huelsmann@iaf.fraunhofer.de
Huggard	Peter	STFC Rutherford Appleton Lab.	peter.huggard@stfc.ac.uk
Hunter	Todd R.	NRAO	thunter@nrao.edu
Jackson	Brian	SRON / NOVA	b.d.jackson@sron.nl
Jiang	Ling	University of Tokyo	ljiang@taurus.phys.s.u-tokyo.ac.jp
Jung	Cecile	Observatoire de Paris	cecile.jung@obspm.fr
Justen	Matthias	KOSMA, University of Cologne	justen@ph1.uni-koeln.de
Karasik	Boris	NASA Jet Propulsion Laboratory	boris.s.karasik@jpl.nasa.gov
Karpov	Alexandre	California Institute of Technology	karpov@submm.caltech.edu
Kent	Brian	NRAO	bkent@nrao.edu
Kerr	Tony	NRAO	akerr@nrao.edu
Khosropanah	Pourya	SRON	p.khosropanah@sron.nl
Klapwijk	Teun	Delft University of Technology	t.m.klapwijkt@tudelft.nl
Klein	Bernd	Max-Planck-Institut für Radioastronomie	bklein@MPIfR-Bonn.MPG.de
Komiyama	Susumu	University of Tokyo	skomiyama@thz.c.u-tokyo.ac.jp
Kooi	Jacob	California Institute of Technology	kooi@submm.caltech.edu
Lauria	Gene	Raytheon	glauria@raytheon.com
Lazareff	Bernard	IRAM	lazareff@iram.fr
Lee	Choonsup	Jet Propulsion Laboratory	choonsup.lee@jpl.nasa.gov
Lee	Mark	Sandia National Laboratories	mlee1@sandia.gov
Leech	Jamie	University of Oxford	jxl@astro.ox.ac.uk
Li	Chao-Te	ASIAA	ctli@asiaa.sinica.edu.tw
Lichtenberger	Art	University of Virginia/NRAO	lichtenberger@virginia.edu
Lin	Huilin	University of Virginia	hl9b@virginia.edu
Lin	Sophie	(None)	
Liu	Lei	University of Virginia	118j@virginia.edu
Lo	Fred K.Y.	NRAO	flo@nrao.edu
Lobanov	Yury	Harvard-Smithsonian Center for Astrophysics	ylobanov@cfa.harvard.edu
Lopez-Fernandez	Isaac	Observatorio Astronomico Nacional	isaac@oan.es
Maestrini	Alain	Observatoire de Paris	alain.maestrini@obspm.fr
Maier	Doris	IRAM	maier@iram.fr
Malone	Josh	NRAO	jmalone@nrao.edu
Mattauch	Robert	Virginia Commonwealth University	rjmattau@vcu.edu
Matthews	Roy	University of Virginia	roy.matthews.iv@gmail.com
Mayo	Mary	NRAO	mmayo@nrao.edu
Mehdi	Imran	Jet Propulsion Laboratory	imran.mehdi@jpl.nasa.gov
Meledin	Denis	Chalmers University of Technology	denis.meledin@chalmers.se
Mena	Fausto	Universidad de Chile	pmena@ing.uchile.cl
Mencia-Oliva	Beatriz	Universidad Politecnica de Madrid	bmencia@gmr.ssr.upm.es
Miao	Wei	Observatoire de Paris	wei.miao@obspm.fr
Michael	Ernest	Universidad de Chile	emichael@ing.uchile.cl

Miller	Dave	California Institute of Technology	davem@submm.caltech.edu
Monje	Raquel	Caltech	raquel@caltech.edu
Morgan	Matt	NRAO	matt.morgan@nrao.edu
Mori	Tetsuo	Infrared Limited	tmori@infrared.co.jp.
Murk	Axel	University of Bern	murk@iap.unibe.ch
Muthee	Martin	University of Massachusetts	magachi@gmail.com
Narayanan	Gopal	University of Massachusetts - Amherst	gopal@astro.umass.edu
Noguchi	Takashi	National Astronomical Observatory of Japan	takashi.noguchi@nao.ac.jp
Nordstrom	Dale	NRAO	dnordstr@nrao.edu
Noroozian	Omid	California Institute of Technology	omid@caltech.edu
Pan	S. -K.	NRAO	span2@nrao.edu
Patrick	Kevin	Raytheon	kwpatr@raytheon.com
Patt	Ferdinand	European Southern Observatory	alma_admin@eso.org
Payne	John	NRAO	jpayne@nrao.edu
Pearson	John	Jet Propulsion Laboratory	john.c.pearson@jpl.nasa.gov
Pejcinovic	Branimir	Portland State University	brano@ece.pdx.edu
Percy	Becca	University of Virginia	rrp4d@virginia.edu
Pospieszalski	Marian	NRAO	mpospies@nrao.edu
Puetz	Patrick	KOSMA, University of Cologne	puetz@ph1.uni-koeln.de
Reck	Theodore	University of Virginia	tjr3r@virginia.edu
Reyes	Nicolas	Universidad de Chile	nireyes@das.uchile.cl
Rieland	George	University of Arizona, Steward Observatory - ARO	benson@e-mail.arizona.edu
Risacher	Christophe	SRON - Groningen	c.risacher@sron.nl
Rodriguez	Mike	NRAO	mrodrigu@nrao.edu
Roesch	Markus	IRAM	roesch@iram.fr
Rosker	Mark	DARPA	Mark.Rosker@darpa.mil
Runion	Gene	NRAO	grunion@nrao.edu
Russell	Adrian	NRAO	arussell@nrao.edu
Saini	K.	NRAO	ksaini@nrao.edu
Schlecht	Erich	Jet Propulsion Laboratory	erich.t.schlecht@jpl.nasa.gov
Sekimoto	Yutaro	National Astronomical Observatory of Japan	sekimoto.yutaro@nao.ac.jp
Shi	Sheng-Cai	Purple Mountain Observatory, China	scshi@mail.pmo.ac.cn
Shillue	William	NRAO	bshillue@nrao.edu
Siles	Jose V.	Technical University of Madrid	jovi@gmr.ssr.upm.es
Sklavounos	Angelique	University of Virginia	ahs3v@virginia.edu
Sobakinskaya	Ekaterina	Institute for Physics of Microstructures RAS	katja@ipm.sci-nnov.ru
Sobis	Peter	Omnisystems	ps@omnisys.se
Srikanth	S.	NRAO	ssrikant@nrao.edu
Stake	Jan	Chalmers University of Technology	jan.stake@chalmers.se
Stanec	James	University of Virginia	jrs6tj@virginia.edu
Strandberg	Magnus	Chalmers University of Technology	magnus.strandberg@chalmers.se
Stronko	Greg	University of Virginia	gss7m@virginia.edu
Stutzki	Jürgen	Universität zu Köln	stutzki@ph1.uni-koeln.de
Surek	Jack	NIST	jsurek@boulder.nist.gov
Tan	Boon Kok	Oxford	tanbk@astro.ox.ac.uk
Tan	Gie Han	ESO	ghtan@eso.org
Thacker	Skip	NRAO	sthacker@nrao.edu

Thomas	Bertrand	NASA-Jet Propulsion Laboratory	bertrand.c.thomas@jpl.nasa.gov
Tong	Edward	Harvard-Smithsonian Center for Astrophysics	etong@cfa.harvard.edu
Treuttel	Jeanne	Observatoire de Paris	jeanne.treuttel@obspm.fr
Uzawa	Yoshinori	National Astronomical Observatory of Japan	y.uzawa@nao.ac.jp
Vaks	Vladimir	Institute for Physics of Microstructures RAS	vax@ipm.sci-nnov.ru
Vaselaar	Dustin	NRAO	dvaselaa@nrao.edu
Walker	Chris	University of Arizona	cwalker@as.arizona.edu
Wang	Jie	University of Virginia	jw4cr@virginia.edu
Wang	Ming-Jye	ASIAA, Taiwan	mingjye@asiaa.sinica.edu.tw
Wanke	Mike	Sandia National Laboratories	mcwanke@sandia.gov
Watts	Galen	NRAO	gwatts@nrao.edu
Webber	John	NRAO	jwebber@nrao.edu
Weikle	Bobby	University of Virginia	rmw5w@virginia.edu
White	Steve	NRAO	swhite@nrao.edu
Wild	Wolfgang	ESO	wwild@eso.org
Wollack	Edward	NASA Goddard Space Flight Center	edward.j.wollack@nasa.gov
Wootten	Al	NRAO	awootten@nrao.edu
Wu	Guoguang	University of Virginia	gw9d@virginia.edu
Wu	Peiheng	University of Nanjing	phwu@nju.edu.cn
Wylde	Richard	Thomas Keating Ltd / St. Andrews University	r.wylde@terahertz.co.uk
Xu	Haiyong	University of Virginia	hx4g@virginia.edu
Yagoubov	Pavel	European Southern Observatory	pyagoubo@eso.org
Yassin	Ghassan	University of Oxford	g.yassin1@physics.ox.ac.uk
Yngvesson	Sigfrid	University of Massachusetts - Amherst	yngvesson@ecs.umass.edu
Zhang	Jian	University of Virginia	jz4n@virginia.edu
Zoltowski	Steve	Infrared Laboratories, Inc.	lwhite@irlabs.com

Sunday, April 19: Check-In and Icebreaker Reception

Co-chair Art Lichtenberger and Event Planner Extraordinaire Laurie Clark prepare for check-in.

Co-chair Art Lichtenberger signing conference T-shirts.

Bob Mattauch enjoying good drink and conversation at the icebreaker reception.

Co-chair Eric Bryerton getting complements from the NRAO director, Fred Lo, on a job well done.

Icebreaker reception attendees were entertained by a lovely string quartet from Charlottesville High School.

Marian Pospieszalski and Art Lichtenberger enjoying a cold beer and greeting each other at the icebreaker.

Monday, April 20: Oral Sessions

ALMA North American Project Manager Adrian Russell kicking off the afternoon with his plenary talk, "ALMA – The Push for the High Site, a Status Report".

Co-chairs Eric Bryerton and Art Lichtenberger paying very close attention to speaker.

Jacob Kooi wide awake on Monday morning, watching intently.

Alexandre Karpov pauses during his presentation to smile for the camera

Master sound engineer Josh Malone pushing all the right buttons.

The audience watches one of the 49 oral presentations.

Monday, April 20: NRAO Technology Center Open House

Bus bringing guests to the NRAO Technology Center, passing by the dogwoods in bloom.

NRAO chemist Gerry Petencin talking plating and electroforming with Giovanni De Amici.

Marian Pospieszalski conveying his amplifier knowledge to the next generation.

John Webber, Director of NRAO's Central Development Laboraty, talks about the ALMA correlator.

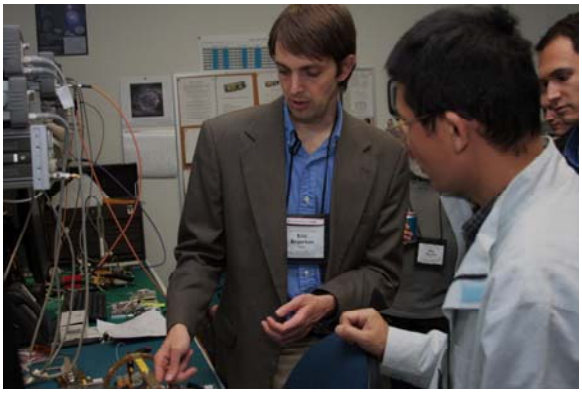

Eric Bryerton explaining the inner workings of the ALMA local oscillators.

Admiring the master workmanship of a NRAO low-noise amplifier.

Monday, April 20: VDI Sponsored Poster Reception

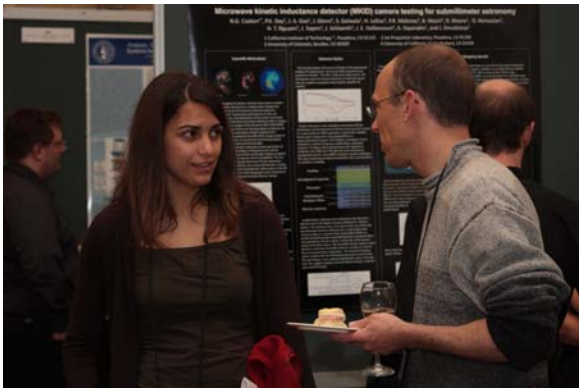

Raquel Monje and Axel Murk talk things over at the poster reception.

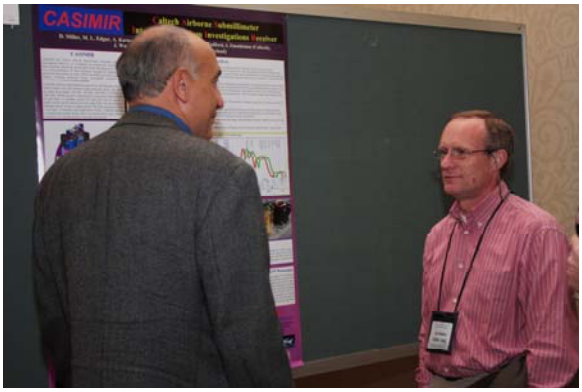

Alexandre Karpov tells Nick Whyborn all about the CASIMIR receiver.

Alain Maestrini and Brian Ellsion discussing plans for the 2010 ISSTT in Oxford.

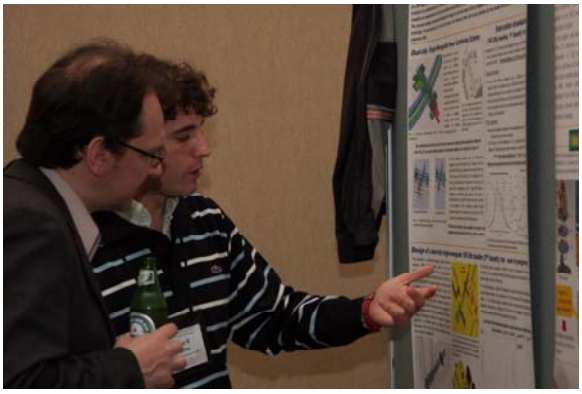

Jose Siles presenting his work on dual-chip single-waveguide power combining for frequency multipliers.

Jian-Rong Gao making a point about QCLs to Michael Wanke.

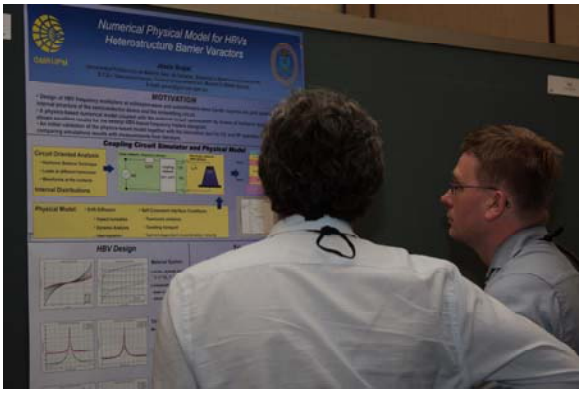

Checking out one of the 39 posters on display during the poster reception.

Tuesday, April 21: Oral Sessions

DARPA program manager Mark Rosker giving his plenary talk on “The DARPA Terahertz Electronics Program”.

Susumu Komiyama from the University of Tokyo, Japan, giving his plenary talk on “Ultra-High Sensitive Detectors in the Terahertz Region”.

Andrey Baryshev spreading the word about Millimetron.

ISSTT steering committee members Ray Blundell and Wolfgang Wild admiring the ISSTT2009 abstract book.

Tuesday, April 21: Conference Dinner at Ash Lawn-Highland

Ash Lawn-Highland, the former home of President James Monroe, is an historic house and 535-acre working farm.

Ed Wollack and Richard Wylde discussing something quite profound.

Doris Maier enjoying a glass of wine before dinner.

NRAO administrative assistant Mary Mayo strolling the grounds.

Enjoying dinner and conversation at the Ash Lawn-Highland pavillion.

Wednesday, April 22: Oral Sessions

Plenary speaker, Jürgen Stutzki from the Universität zu Köln, speaks about SOFIA.

Plenary speaker, Jeffrey Hesler from Virginia Diodes, Inc., speaks about broadband frequency multiplier development.

NRAO librarian, Lance Utley, demonstrating the Online Space THz Proceedings Archive.

Tom Crowe rises to question the speaker.

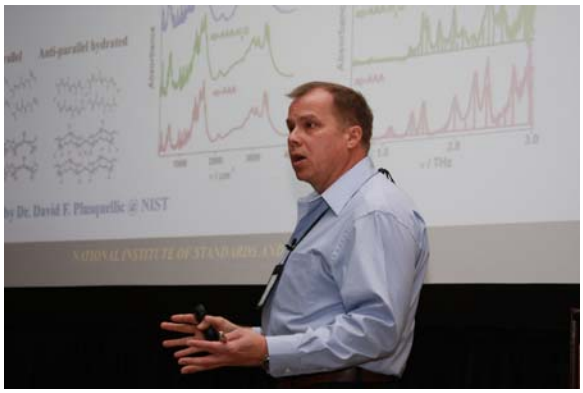

Jack Surek presenting his work on a mobile THz spectroscopic system.

Sarmad Albanna and Chris Groppi enjoying the last moments of the conference.

ISSTT 2010 Preliminary Information
Oxford / Rutherford Appleton Lab (RAL), UK
March 23 – 25, 2010
http://www.physics.ox.ac.uk/stt2010/

Local Organizing Committee:

Brian Ellison, RAL
Ghassan Yassin, Oxford
Peter Huggard, RAL
David Matheson, RAL
Jamie Leech, Oxford
Paul Grimes, Oxford

ISSTT 2011 Preliminary Information
Tucson, AZ, USA
April 26-28, 2011

Local Organizing Committee:

Chris Walker, U. Arizona
Christian d'Aubigny (TeraVision, Inc.)
Chris Groppi (Arizona State Univ.)
Craig Kulesa (U. Arizona)
Delmar Barker (Raytheon Inc.)
Gene Lauria (Raytheon, Inc.)
Hao Xin (U. Arizona)
Jerry Moloney (U. Arizona)
William Owens (Raytheon Inc.)

Table of Contents

ORAL SESSIONS

M1: ALMA Cartridges (Wolfgang Wild, Chair)

M2: SIS Receivers (Jacob Kooi, Chair)

M3: THz Sources (Imran Mehdi, Chair)

M4: QCLs (Brian Ellison, Chair)

T1: First Light THz Instruments (Anthony Kerr, Chair)

T2: Direct Detectors (Brian Jackson, Chair)

T3: THz Systems (Patrick Pütz, Chair)

T4: Components and Novel Applications (Thomas Crowe, Chair)

W1: Schottky Mixers and Detectors (Heinz-Wilhelm Hübers, Chair)

W2: HEB Mixers and Receivers (Boris Karasik, Chair)

W3: Receivers and Backends (Victor Belitsky, Chair)

W4: Testing and Measurements (Bertrand Thomas, Chair)

POSTER SESSIONS

P1: Sources

P2: Waveguides, Antennas, and Quasi-Optics

P3: Novel Devices and Measurements

P4: Schottky Diodes

P5: SIS Mixers

P6: Physics and Measurements of SIS Devices

P7: HEB and Direct Detectors

P8: Receivers and Backends

Session M1

ALMA Cartridges

Chair: Wolfgang Wild

Monday, April 20
9:20 – 10:20

Prototype ALMA Band 5 Cartridge: Design and Performance

V. Belitsky, I. Lapkin, B. Billade, E. Sundin, A. Pavolotsky, D. Meledin, V. Desmaris, M. Strandberg, R. Finger, O. Nyström, M. Fredrixon, S.-E. Ferm, H. Rashid, D. Henke

***Abstract*— The Atacama Large Millimeter/submillimeter Array (ALMA), an international astronomy facility, is a partnership of East Asia, Europe and North America in cooperation with the Republic of Chile and aims to build an interferometer radio telescope consisting of more than 60 antennas. The instrument is under construction at the Llano de Chajnantor, about 50 km east of San Pedro de Atacama, Chile. This work presents a part of ALMA frontend, the development, design and performance of one of the frequency channels of the ALMA receiver, the Band 5 prototype cartridge for 163 – 211 GHz frequency band.**

***Index Terms* — ALMA receiver cartridge, optics, cryogenics, 2SB SIS mixer.**

I. INTRODUCTION

THE ALMA Band 5 is an EC Framework Program 6 (FP6) infrastructure enhancement project aiming at the development and design of a prototype receiver cartridge fulfilling specifications of ALMA Band 5. After the prototype cartridge is accepted, the project consideres to supply 6 production cartridges for the ALMA Project for integration into the ALMA frontend receiver. Group for Advanced Receiver Development, OSO, Chalmers University, is responsible for cold cartridge assembly (CCA). CCLRC Rutherford Appleton Laboratory, UK, are our partners in the ALMA Band 5 project and responsible for development of the Band 5 warm cartridge assembly (WCA) and the local oscillator (LO) sources.

The Band 5 cartridge is a dual - polarization receiver with the polarization separation performed via orthomode transducer (OMT) [1]. The receiver is based on sideband rejection quadrature layout (2SB) and employs modular design with SIS DSB waveguide mixers, covering 163-211 GHz with 4 - 8 GHz intermediate frequency (IF) band.

The ALMA Band 5 cartridge is the lowest frequency channel of the ALMA frontend that utilizes *all - cold optics* and thus has the largest mirrors amongst the other ALMA bands with cold optics. The Band 5 optics mirrors together with its support structure leave very little room for placing the receiver components, such as the corrugated horn, OMT, the mixers for both polarizations and the IF system and thus calling for specific technical and design solutions for the layout of the cartridge.

II. OPTICS DESIGN

Band 5 mirrors and corrugated horn formal parameters are based on the design proposed by M. Carter, et al. [2] and has been analyzed by M. Whale, *et al.* [3] through physical optics simulations to ensure no unwanted cross-polarization components added and overall efficiency is within specs.

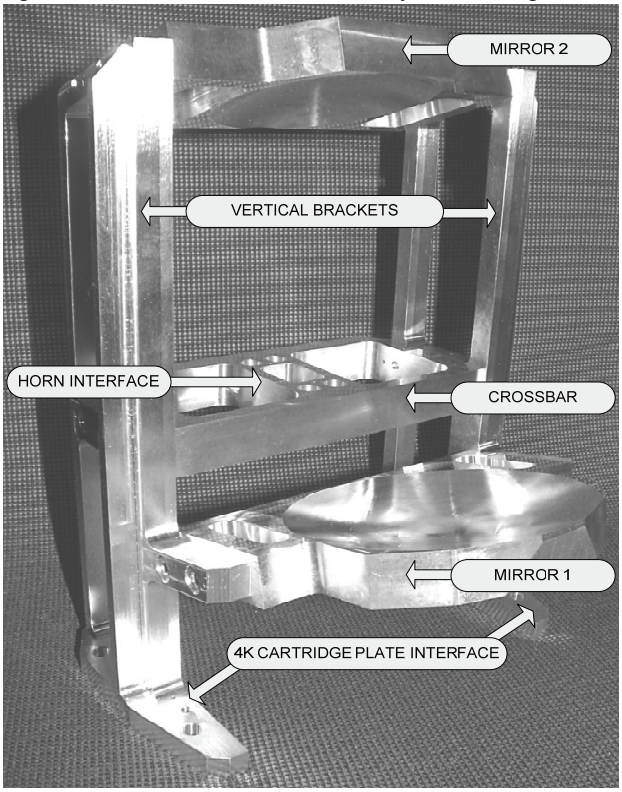

Fig. 1. Band 5 optics integrated. The two mirrors are supported by two vertical brackets with the crossbar providing reference plane, cooling and support for the mixer assembly integrated around the OMT. Additional vertical support bracket (not shown) provides supplementary cooling and adds stiffness to the main support brackets.

Manuscript received on April 20, 2009. This work was supported by EC Framework Program 6 (FP6) in its part of infrastructure enhancement under contract 515906.

V. Belitsky (e-mail Victor.Belitsky@chalmers.se), I. Lapkin, B. Billade, E. Sundin, A. Pavolotsky, D. Meledin, M. Strandberg, , O. Nyström, V. Desmaris, M. Fredrixon, S.-E. Ferm are with the Group for Advanced Receiver Development (GARD), Department of Radio and Space Science and Onsala Space Observatory, Chalmers University of Technology, SE 412 96, Gothenburg, Sweden

D. Henke is currently with the NRC Herzberg Institute of Astrophysics, (NRC-HIA), 5071 West Saanich Road, Victoria, British Columbia, Canada V9E 2E7

R. Finger is with Departamento de Astronomía, Universidad de Chile, Casilla 36-D, Santiago, Chile.

In order to make the cold optics structure stiff and yet easier to manufacture, the Band 5 optical support was designed integrated out off several parts rather than machined as a single piece. The optics mounted on the 4K plate of the cartridge includes the support brackets, two at the sides and one central, the crossbar for mixer assembly interfacing and two mirrors, all made off aluminum alloy, Fig. 1.

The corrugated horn is directly attached to the crossbar connecting the vertical optics support brackets and providing a mechanical interface to the mixer assembly. The corrugated horn has 94 corrugations (Fig. 2) and has been designed using an optimization procedure that simultaneously aims to the best Gaussian fit of the main lobe while minimizing the side-lobs below -30 dB level, Fig 2.

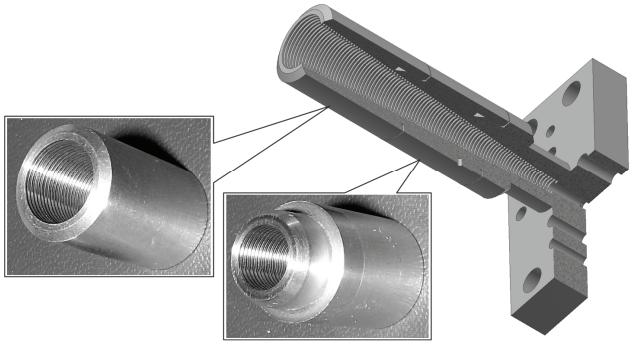

Fig. 2. ALMA Band 5 corrugated horn. The horn is made of aluminum and consists of 3 parts connected via press-fit joints. The split was made to facilitate machining.

III. Mixer Assembly

As discussed in the introductory part, the cold mirrors of the ALMA Band 5 cartridge with the specified mirror rim size of five beam waists ($5w_o$) are large, as compared to other ALMA bands, because of it relatively low operating frequencies. The space available for placing the mixer assembly is next to the Mirror 1 (M1), Fig. 1. In order to fit this room, the polarizations should be split by an OMT and directed towards opposite sides in parallel behind M1.

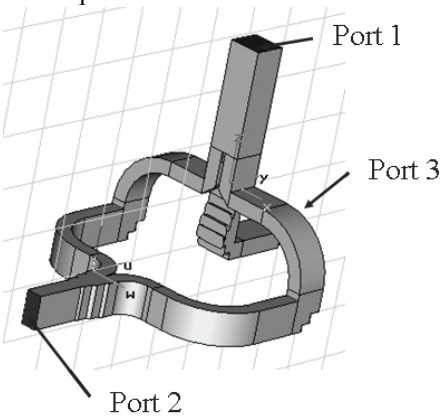

Fig. 3. Band 5 cartridge OMT [1] with input via square waveguide (port 1) and outputs (port 2 and 3) at the opposite sides to facilitate compact mixer assembly design. In order to use the same 2SB mixers for both polarizations we have added 90-degree waveguide twist.

The OMT for the Band 5 cartridge uses the core design of ALMA Band 4 [1] with redesigned output of one polarization; a 90-degree waveguide bend is added to place the OMT outputs at the opposite sides, Fig. 3. The measured OMT insertion loss at room temperature is less than 0.4 dB for both S12 and S13 over the entire RF band.

In order to fit the receiver components into the cartridge, we had to revise the originally proposed design for the Band 5 mixer as a scaled version of APEX Band 1 2SB SIS mixer [4] in favor of a more compact design. For the Band 5 mixer, we use MMIC style design of the SIS mixer with integrated on-chip LO injection and SIS junction capacitance integrated tuning circuitry. The mixer chip however has one DSB mixer [5, 6] in contrast to [4]. In order to use the same configuration 2SB mixer for both polarizations, we have added a 90-degree waveguide twist, Fig. 4.

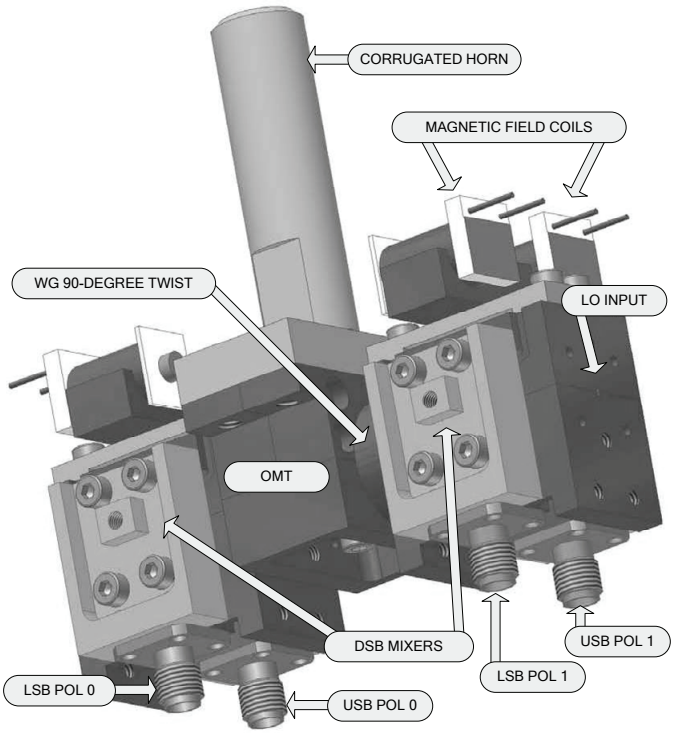

Fig. 4. Band 5 mixer assembly. The assembly comprises the OMT, two 2SB mixers and corresponding IF chains (not shown) with the corrugated feed horn attached to OMT input port 1 (Fig.3).

The mixer block has end-piece configuration with SIS mixer substrate having mirrored layout for different polarizations and being placed facing the RF and LO signals in the waveguides, with the IF outputs are directed towards the cartridge 300 K flange. Such design allows us to use the space between the mirror and the optics support brackets for placing the mixer assembly, all integrated around the OMT. Consequently, we use a specially designed IF hybrid to align the IF chains with the 2SB mixer IF outputs. Fig. 4 shows the mixer assembly, comprising, the OMT, two 2SB mixers and the IF chain integrated with the corrugated feed horn.

The result of this design is that the IF system streamlined along the vertical axis of the cartridge; it uses all the space between the 4 K and 15 K stages. This relatively long IF chain is exposed to potentially harmful mechanical stress as a result of thermal contraction. The mechanical stress caused by thermal contraction of different materials was largely removed by introducing a titanium intermediate piece in the IF support

bracket, an approach similar to the one used by ALMA Band 9 to secure tightening of the screws. The titanium contraction coefficient is the least as compared to aluminum and copper. In order to remove the stress, a simple equation should be solved equalizing thermal contraction of the aluminum optics supporting brackets with the combined contraction of the copper and titanium parts of the IF supporting bracket that provides rigid support for the IF chain.

The cold IF amplifiers [7] are 3 - stage HEMT amplifiers with the first stage using InP HRL HEMT provided by ESO for ALMA Band 5 project and the two other stages using GaAs HEMT transistor MGFC 4419G with amplifier performance presented in Fig. 5. The amplifiers have been redesigned in order to facilitate integration of Band 5 cartridge IF chain.

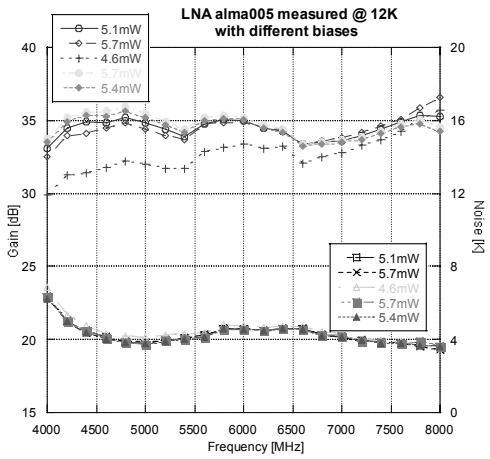

Fig. 5. Band 5 IF amplifier performance: gain (left axis) and noise (right axis) at different bias voltages @12 K ambient temperature. Typical power dissipation of the amplifier is below 7 mW.

The IF hybrid, the amplifiers with CTH1365K25 type PAMTech isolators, all use matched SMA contacts allowing direct connection of the IF components to each other and the corresponding 2SB mixers, Fig. 6.

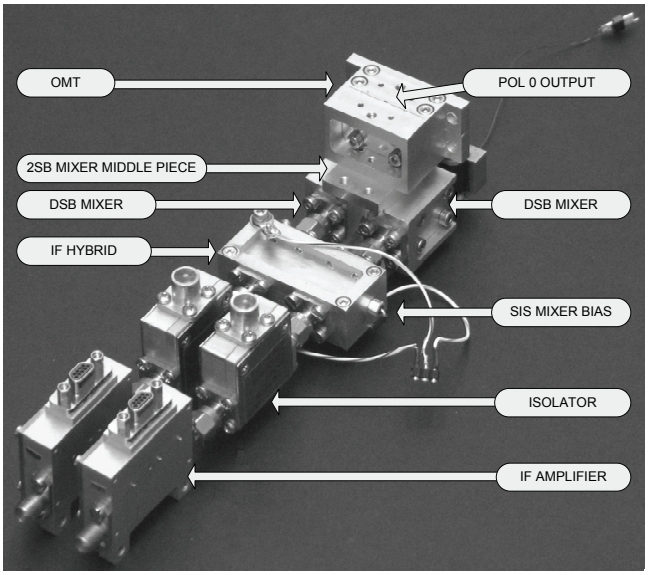

Fig. 6. Picture of the Band 5 cartridge mixer assembly for one polarization. The assembly comprises OMT, 2SB mixer, custom-made IF hybrid with integrated SIS mixer bias-Ts, isolators [8], and IF amplifiers.

IV. Integrated LO Assembly

LO sources for Band 5 are developed by Rutherford Appleton Laboratory, UK. The suggested LO source layout comprises active tripler followed by a power amplifier and with final stage times two multiplier. This translates the required LO frequency band 171 – 203 GHz into input frequency band of 28.5 – 33.83 GHz. This relatively low input frequencies for the LO source allow us to use off-shelf vacuum bulk-head feed through K-type connector to avoid complexity of employing a custom-made waveguide LO interface between the WCA and CCA. However, this requires accommodation of the two LO sources inside the cartridge on 300 K plate at the vacuum side and installing an additional DC connector to bias active multipliers and power amplifiers. Fig. 7 shows the planned layout for integration of the LO sources on the 300 K plate of the Band 5 receiver cartridge.

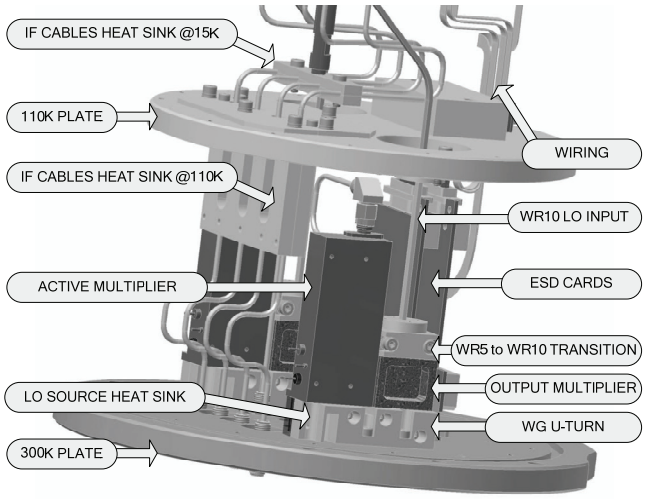

Fig. 7. Band 5 cartridge integrated LO sources. The sources are combined in U-shape to improve cooling and extend the distance of the LO output to the 110 K plate. That reduces thermal load @110 K via LO output waveguide.

V. Cartridge Cabling and Wiring

The Band 5 receiver cartridge uses standard ALMA DC interface connector with ESD cards directly attached to it at the vacuum side at 300 K plate, Fig 7, 8. The wiring inside the cartridge is done using cryowires with 12 twisted pairs integrated into a loom [9]. Heat sinks for every temperature level are done similar to the design presented in [10]. The IF cables are shaped to relief stress caused by thermal contraction and to allow minimize the thermal load due to thermal conduction through the cables and wires and power dissipation, for wires. For more details, please see poster and report M. Strandberg *et al.* [11].

ESD cards employ protection circuitries similar to those used by ALMA Band 3. We have chosen to use dedicated wire bus for SIS mixer DC bias only and separate wire buses for DC biasing of IF amplifiers for each polarization; the forth wire bus carries magnetic field coil currents, defluxer and temperature sensor connections. This is done to reduce EMI for SIS DC bias and HEMTs. Necessary cross-connections are done between the two ESD cards.

Finally, Fig. 8 displays a 3D model of the entire ALMA Band 5 cold cartridge assembly with removed fiberglass

spacers between the temperature plates, for better visibility of the cartridge design and internal components.

Currently, ALMA the Band 5 receiver cartridge is in the final integration stage and we expect an extensive test program to be started shortly. The cartridge tests include room temperature optics characterization, based on Agilent vector network analyzer with frequency extension for direct vector measurements in the band 160 – 220 GHz. The cartridge test cryostat [12] has been integrated with Y-factor measurement system, sideband rejection characterization setup and cartridge cold beam measurement hardware similar to [13]. In order to eliminate effects of atmospheric water on the measured data, the measurement equipment is enclosed into a plastic cabinet purged with dry Nitrogen.

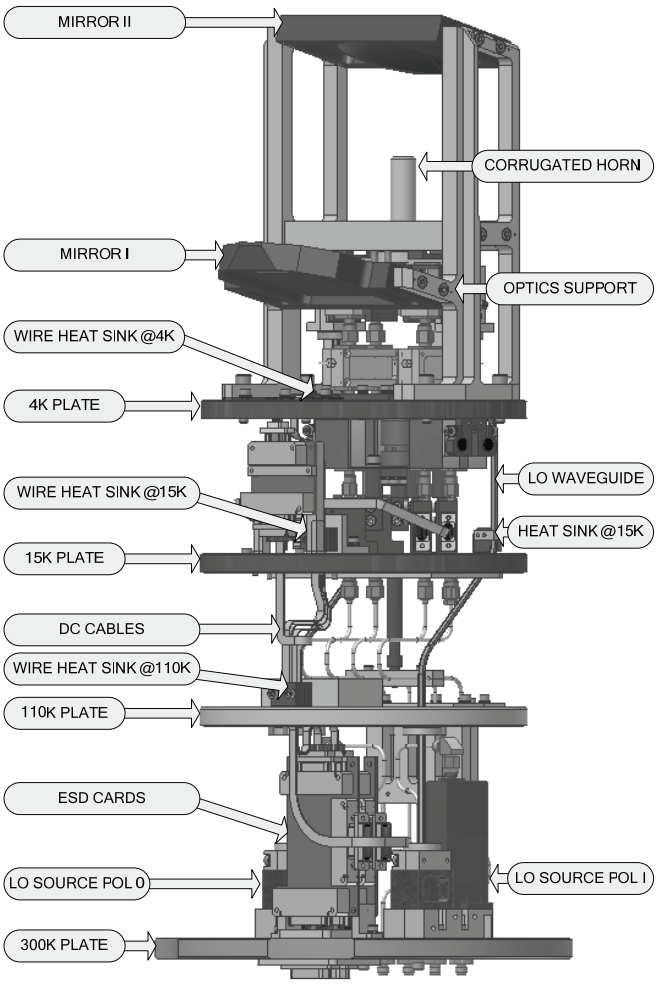

Fig. 8. Band 5 receiver cartridge cold assembly 3D model. The fiberglass spacer between the cartridge plates have been removed for better visibility of the details and inner components.

VI. Conclusion

We presented details on the design of ALMA Band 5 prototype receiver cartridge and some data on performance of its components. Detailed information on 2SB mixer design and its performance is presented in [6]. We successfully solved problems of integration of the dual polarization 2SB receiver into the cartridge whereas keeping required cold mirror rim size of the $5\omega_o$. We expect extensive test program of the prototype Band 5 receiver cartridge to be started shortly.

Acknowledgment

Authors acknowledge Dr. S. Asayama, NAOJ, and Dr. J. Kooi, Caltech, for their spirit of collaboration and direct contribution to Band 5 OMT and 2SB RF hybrid respectively. We would like to thank Prof. N. Trappe and Dr. M. Whale for their contribution on the optics analysis. We would like to thank Dr. B. Lazareff and ALMA Band 7 team for generous sharing information, advises and assistance with software for cartridge tests. We would like to thank Dr. B. Jackson, Dr. R. Hesper and entire Band 9 team for sharing information and hardware, advises and assistance. We would like to acknowledge Dr. G. H. Tan, ESO, for his insight in the Band 5 project, help in obtaining ALMA hardware, assistance and guidance in getting necessary information on ALMA project. We would like to thank our partners in the project Prof. B. Ellison and RAL team for their creative contribution on the LO side.

References

[1] Band 5 OMT is slightly modified design suggested by Dr. S. Asayama for Band 5 and based on the ALMA Band 4 cartridge OMT.

[2] M. Carter, *et al.*, "ALMA Front-end Optics Design Report", FEND-40.02.00.00-035-B-REP, available from ALMA Project documentation server.

[3] M. Whale, N. Trappe, I. Lapkin, V. Belitsky, "Physical Optics Analysis of the ALMA Band 5 Front End Optics", *Proceedings of the 19th International Symposium on Space Terahertz Technology*, pp. 368 – 372, Groningen, April 28-30, 2008.

[4] V. Vassilev, D. Henke, I. Lapkin, O. Nyström, R. Monje, A. Pavolotsky, V. Belitsky, "Design and Characterization of a 211-275 GHz Sideband Separating Mixer for the APEX Telescope", *IEEE Microwave and Wireless Components Letters*, pp.55-60, Vol. 18, Number 1, January 2008.

[5] B. Billade, I. Lapkin, R. Monje, A. Pavolotsky, V. Vassilev, J. Kooi, and V. Belitsky, "ALMA Band 5 (163-211 GHz) Sideband Separating Mixer Design", *Proceedings of the 19th International Symposium on Space Terahertz Technology*, pp. 250-252, Groningen, April 28-30, 2008..

[6] B. Billade, I. Lapkin, A. Pavolotsky, J. Kooi, and V. Belitsky, "ALMA Band 5 (163-211 GHz) Sideband Separating Mixer", *to be presented at the 20th International Symposium on Space Terahertz Technology*, Charlottesville, April 20-23, 2009.

[7] E. Sundin, "Development of Cryogenic Low Noise 4 – 8 GHz HEMT Amplifier and its Advanced Characterization," *Thesis for Licentiate in Electrical Engineering, Technical report No. 2006:9L, Chalmers University of Technology, 2006*.

[8] Isolator CTH1365K25, PAMTECH Inc., 4053 Calle Tesoro, Camarillo, CA, USA.

[9] ICE Oxford Ltd., Unit 3, Ferry Mills, Osney Mead, Oxford, OX2 0ES, UK.

[10] D. Koller, J. Effland, A. R. Kerr, K. Crady and F. Johnson, "Miniature, Modular Heat Sinks for ALMA Cryostats", *ALMA MEMO #437*, 2002. Available: http://www.alma.nrao.edu/memos/html-memos/abstracts/abs437.html .

[11] M. Strandberg, I. Lapkin, V. Belitsky, A. Pavolotsky and S.-E. Ferm, "Analysis, Simulation and Design of Cryogenic Systems for ALMA Band 5 Prototype Cartridge", *to be presented at the 20th International Symposium on Space Terahertz Technology*, Charlottesville, April 20-23, 2009.

[12] Y. Sekimoto, T. Kamba, S. Yokogawa, M. Sugimoto, T. Okuda, R. Kandori, K. Tatematsu, K. Muraoka, A. Ueda, T. Nishino, N. Okada, T. Fukuda, K. Kaneko, H. Ogawa, K. Kimura, K. Noda, K. Narasaki, and K. Suzuki, "Cartridge Test Cryostats for ALMA Front End", *ALMA MEMO #455*, 2003. Available: http://www.alma.nrao.edu/memos/html-memos/abstracts/abs455.html.

[13] O. Nyström, I. Lapkin, V. Desmaris, D. Dochev, S.-E. Ferm, M. Fredrixon, D. Henke, D. Meledin, R. Monje, M. Strandberg, E. Sundin, V. Vassilev, and V. Belitsky, "Optics Design and Verification for the APEX **S**wedish **He**terodyne **F**acility **I**nstrument (SHeFI)", to be published in *Int. Journal Infrared and Millimeter Waves*, 2009.

M1B

Evaluation of ALMA Band 8 S/N01 Cartridge

Y. Sekimoto[1,2*], Y. Iizuka[1], T. Ito[1], K. Kumagai[1], N. Satou[1], M. Kamikura[1,2], Y. Serizawa[1,2], N. Naruse[1,2], Y. Niizeki[1], Y. Fujimoto[1], and W. L. Shan[3]

1 Advanced Technology Center, National Astronomical Observatory of Japan, National Institutes of Natural Sciences

2 Department of Astronomy, University of Tokyo,

3 Purple Mountain Observatory, Chinese Academy of Sciences

* Contact: sekimoto.yutaro@nao.ac.jp

***Abstract*— ALMA Band 8 (385 – 500 GHz) is one of frequency bands which cover atmospheric windows on the Atacama desert in the northern Chile. We have developed a cartridge-type receiver which receives two orthogonal polarizations and down-converts the sideband separated signals to intermediate frequencies (IF) between 4 and 8 GHz. A waveguide polarization splitter or ortho-mode transducer (OMT) has been developed, which enables the cryogenic optics quite simple. It achieved low loss of ~0.4 dB at 4 K and polarization isolation of -25 dB in 385 – 500 GHz [1]. A sideband separating mixer consists of two DSB Nb-based SIS mixers and waveguide quadrature coupler [2].**

The receiver noise temperature was less than 8 hf/k or 196 K in SSB and the image rejection ratio of > 10 dB in the 90 % of ALMA Band 8 frequency. Gain compression of this receiver was measured. The amplitude and phase stabilities were confirmed to comply the ALMA specifications. The co-polar and cross polar beam patterns of this receiver were measured in five frequencies [3]. Test results of S/N 01 cartridge will be presented.

[1] M. Kamikura et al. in preparation
[2] M. Kamikura et al. 2006 IJIRMW 27, 37
[3] M. Naruse et al. 2008 Exp. Astronomy

Series Production of State-of-the-Art 602-720 GHz SIS Receivers for Band 9 of ALMA

B. D. Jackson, R. Hesper, J. Adema, J. Barkhof, A. M. Baryshev,
T. Zijlstra, S. Zhu, and T. M. Klapwijk

***Abstract*—The Atacama Large Millimeter/Sub-millimeter Array (ALMA) requires the development and production of 73 state-of-the-art receivers for the 602-720 GHz range – the ALMA Band 9 cartridges. Development and "pre-production" of the first 8 cartridges was completed between 2003 and 2008, resulting in a cartridge design that meets the project's challenging requirements. The cartridge design remains essentially unchanged for production, while the production and test processes developed during pre-production have been fine-tuned to address the biggest new challenge for this phase – ramping up production to a rate of ~ 2 cartridges per month over 2009-2012.**

***Index Terms*—submillimeter wave receivers, radio astronomy, superconductor-insulator-superconductor mixers.**

I. INTRODUCTION

THE Atacama Large Millimeter / Sub-millimeter Array project is a collaboration between Europe, North America, Asia, and Chile, to build an aperture synthesis telescope consisting of at least 66 antennas at 5000 m altitude in Chile [1]. When complete, ALMA will observe in 10 frequency bands between 30 and 950 GHz, with maximum baselines of up to 14 km, offering unprecedented sensitivity and spatial resolution at millimeter and sub-millimeter wavelengths. As the highest frequency band in the baseline project, the 602-720 GHz Band 9 receivers will provide the observatory's highest spatial resolutions and probe higher temperature scales to complement observations in the lower-frequency bands in the baseline project (between 84 and 500 GHz).

The Band 9 cartridge design [2] combines a compact focal-plane optics assembly; fixed-tuned superconductor-insulator-superconductor (SIS) mixers with state-of-the-art sensitivities across the 602-720 GHz signal frequency range; a wide-band, low-noise 4-12 GHz IF chain; and an electronically tunable solid-state local oscillator (developed at NRAO). Given the large number of receivers that ALMA requires (73 cartridges, including spares), two essential elements of the design are that the implementation of these critical elements takes advantage of the capabilities of commercial sub-contractors wherever possible, and that cartridge assembly remains as clean and simple as possible.

The Band 9 cartridge design was validated by producing eight "pre-production" units between 2005 and 2007 – effectively one prototype, followed by a series of seven identical units that incorporated lessons learned from the prototype. While ongoing development may yet offer improved performance in the future (for example, by implementing next-generation Band 9 mixers incorporating AlN SIS junctions), at this time, it is critical to ALMA that cartridge production meets the aggressive schedule required by plans for higher-level system integration and testing. With this in mind, production of the next 65 Band 9 cartridges started in late 2007. Following a start-up phase in 2008, during which additional assembly and test capacity was added and cartridge components were sub-contracted, assembly and testing of the production cartridges has started, and is ramping up towards the required delivery rate of roughly 2 per month.

This paper describes the development and production of the Band 9 cartridges, including conclusions from development and pre-production and plans for production. These plans have been developed to address the unique challenge of the ALMA project – in particular, the need to produce 73 receivers, all with excellent performance and high reliability, in a short period of time, and with a reasonable amount of effort.

II. CARTRIDGE TECHNICAL REQUIREMENTS AND DESIGN

The Band 9 cartridge is a double side-band, dual-polarization SIS receiver with state-of-the-art performance, including low noise, high optical efficiency, wide IF and RF bandwidth, and high output power and phase stability. The mechanical design of the cartridge is driven by the design of the blank cartridge body (a cylinder 17 cm in diameter and 28 cm tall, with plates at each of the temperature levels: 300, 110, 15, and 4 K) and the available 20 cm of space above the 4 K plate. Table 1 summarizes the main technical requirements placed upon the Band 9 cartridge.

Manuscript received 20 April 2009. This work was financed by the European Organisation for Astronomical Research in the Southern Hemisphere under contract number 16173/ESO/07/14997/YWE.

B. D. Jackson and A. M. Baryshev are with the SRON Netherlands Institute for Space Research, Landleven 12, 9747 AD Groningen, The Netherlands (corresponding author phone: +31-50-363-8935; fax: +31-50-363-4033; e-mail: B.D.Jackson@sron.nl).

B. D. Jackson, R. Hesper, J. Adema, J. Barkhof, and A. M. Baryshev are with Netherlands Research School for Astronomy (NOVA), Niels Bohrweg 2, 2333 CA Leiden, The Netherlands.

R. Hesper, J. Adema, J. Barkhof, and A. M. Baryshev are with the Kapteyn Astronomical Institute, University of Groningen, Landleven 12, 9747 AD Groningen, The Netherlands.

T. Zijlstra, S. Zhu, and T. M. Klapwijk are with the Kavli Institute of Nanoscience, Faculty of Applied Sciences, Delft University of Technology, Lorentzweg 1, 2628 CJ Delft, The Netherlands.

TABLE 1 PRIMARY TECHNICAL REQUIREMENTS

Property	Required Performance
mixer configuration	linearly polarized, double side-band
RF bandwidth	614-708 GHz (LO range) 602-720 GHz (signal rnage)
IF bandwidth	4-12 GHz
total power receiver noise	< 169 K over 80% of the LO range < 250 K over 100% of the LO range
total power output power	-32 dBm < P_{out} < -22 dBm
output power variations	< 7 dB p-p over 4-12 GHz IF band < 5 dB p-p within 2 GHz sub-bands of the IF band
output power Allen variance	< 4 x 10^{-7} for 0.05-100 s delay < 3 x 10^{-6} for 300 s delay
signal path phase stability	7.1 fs for 20-300 s delay
aperture efficiency	80% for an ideal / unblocked telescope
polarization efficiency	> 97.5%
beam squint	polarization beam co-alignment better than 10% of FWHM
strength and stiffness	lowest eigenfrequency > 70 Hz, survival of "minimum integrity test" random vibration test plus aircraft and road transport
lifetime	15 years
mean time between failure	20 years

Fig. 1 contains an image of the cryogenic portion of the cartridge design that was developed to meet these requirements. The core components of this design are low-noise, broadband SIS mixers [3]; a low-noise 4-12 GHz IF chain including a cryogenic isolator [4] and low-noise amplifier [5], plus a 2nd stage room-temperature amplifier; a cold optics assembly [6] including polarization splitting grid, LO injection beamsplitters, and LO and signal path mirrors; and a tunable solid-state local oscillator (from NRAO) [7] based upon a high-power mm-wave (68-79 GHz) power amplifier [8] and a cryogenic frequency multiplier [9]. The warm components of the cartridge (bias module, warm IF amplifiers, and room-temperature LO components) are not shown.

Additional details regarding the cartridge design can be found in [2].

III. CARTRIDGE DEVELOPMENT CYCLE

The development and production of the Band 9 cartridges followed the same basic sequence as the other ALMA cartridges. Initial efforts (to 2003) addressed critical components (esp. the Band 9 mixers) and the conceptual design of the cartridge. The development and pre-production phase followed between 2003 and 2008, and resulted in both the preliminary and detailed design, plus the the first 8 Band 9 cartridges. Cartridge manufacturing, assembly, and test procedures were also developed and verified during this phase. Finally, based upon the detailed design and procedures developed in pre-production, the project's production phase will yield the remaining 65 cartridges needed to complete the ALMA array between 2009 and 2012.

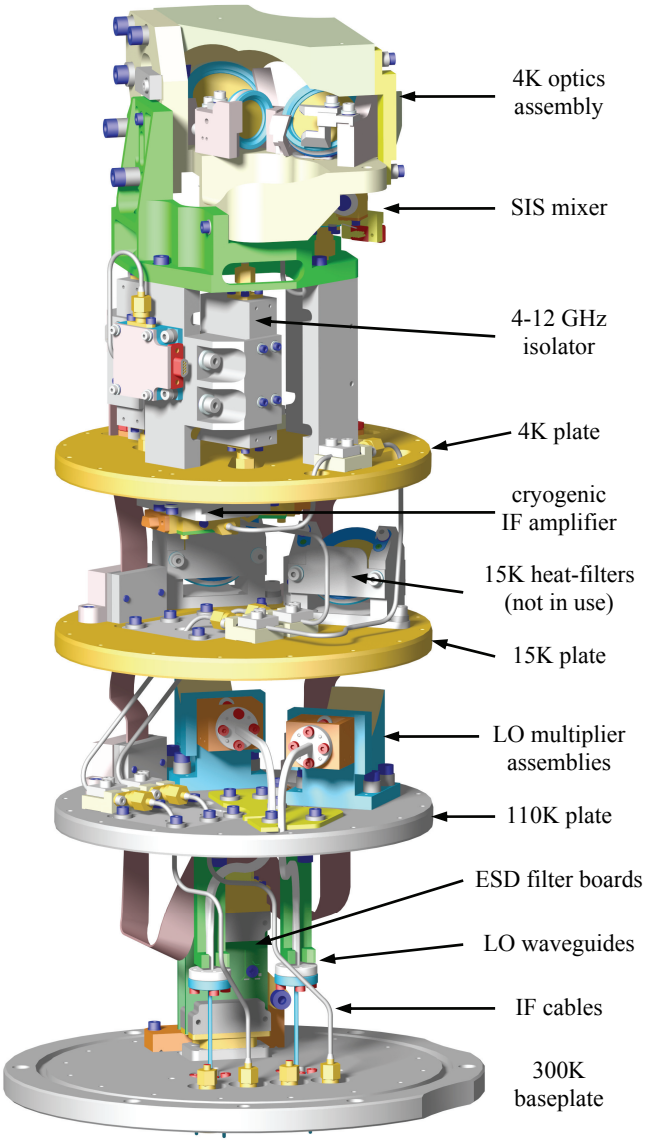

Fig. 1 – The cryogenic portion of the ALMA Band 9 cartridge. The fibre-glass cylinders that separate the temperature levels are not shown. Also not shown is the warm electronics assembly, including bias module and warm LO components (from NRAO) and warm IF amplifiers. From [2]

IV. CONCLUSIONS OF THE DEVELOPMENT AND PRE-PRODUCTION PHASE

During development and pre-production, the detailed cartridge design was verified by producing and testing eight cartridges – one deliverable prototype plus a series of seven built based upon lessons learned from the prototype. The series of seven are largely identical, and were produced as a test case for larger scale production, allowing the production and test procedures to be evaluated and fine-tuned.

A. Cartridge Performance and Design

The pre-production cartridges offer state-of-the-art performance – see Fig. 2 for noise temperature test results of a typical pre-production cartridge. The cartridges' total power DSB receiver noise temperatures reach their minima in the center of the band below 100 K, remain < 150 K in the upper

portion of the band, and drop somewhat more sharply towards the lower frequency end of the band (remaining within the 250 K requirement).

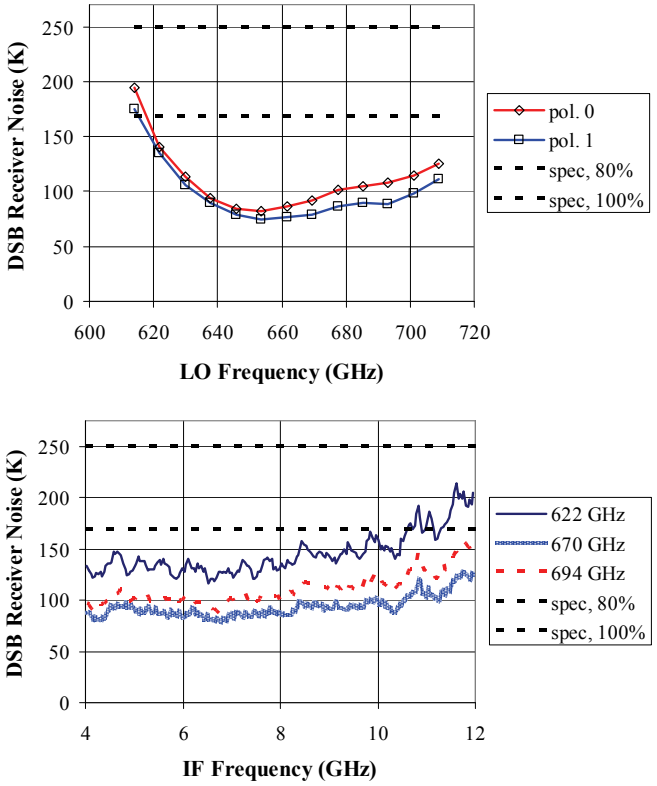

Fig. 2. DSB noise performance of cartridge #1 (a typical cartridge). (top) Total power noise temperature as a function of LO frequency. (bottom) Noise temperature as a function of IF frequency for three LO frequencies. In both plots, the dashed horizontal lines indicate the total power noise temperature required over 80% and 100% of the 614-708 GHz LO frequency range.

Acceptance testing of the pre-production cartridges covered all major requirements, including 2-dimensional near-field scans of the cartridge's beam-pattern, polarization efficiency, output power stability and phase drift measurements, gain compression for a 100°C input load, and output power flatness. Polarization efficiency and output power variations within 2 GHz sub-bands of the 4-12 GHz IF band were critical in the pre-production cartridges. With regards to the output power variations within 2 GHz sub-bands of the 4-12 GHz IF band, the measured peak-to-peak variations of up to 5 dB (and typically 3 dB) are low given the broad 4-12 GHz IF band and the state-of-the-art performance of individual IF components (in particular, the mixer's IF output coupling circuit, 4-12 GHz cryogenic isolators, and low-noise amplifiers).

B. *Manufacturing and Assembly*

In addition to verifying the cartridge design and performance, the second major goal of pre-production was to establish and validate manufacturing, assembly, and test procedures in advance of production. In this respect, this phase was a success – following the assembly and test of the first (prototype) cartridge, a broad redesign was implemented with the primary goal of easing manufacturing and assembly. This revised design was used for cartridges #2-8, with only minor modifications thereafter.

With only a few exceptions (such as the absorbing coatings used as beamdumps in the 4 K optics assembly, and the SIS junctions), component manufacturing was sub-contracted in pre-production – for all critical components, one or more sub-contractors were identified and evaluated. Because of the attention paid to ease-of-assembly during the design phase, the cartridge assembly effort was minimized once the second half of the pre-production series was reached. In fact, the work to inspect and clean parts and prepare sub-assemblies, dominated the assembly effort – assembly of the cartridge structure and integration of the optics and mixers is relatively straightforward. Ultimately, even though the time-consuming preparatory work of inspection, cleaning, and sub-assembly was performed as part of assembly, a throughput of 1 per month was achieved. Fig. 3 shows a photograph of production cartridges #3-8 prior to their deliveries to the project.

Fig. 3. Six Band 9 pre-production cartridges (#3-8) assembled, tested, and awaiting acceptance and delivery to the ALMA project in Aug. 2007.

C. *Acceptance Testing and Delivery*

Cartridge acceptance testing during pre-production showed similar experience – tests of the first cartridges took longer, as test procedures were developed and fine-tuned. However, once the 2nd half of the pre-production phase was reached, a test throughput of one per 3-4 weeks was realized. This was largely thanks to the development of a test system that allows both the semi-automated execution of mixer bias optimization and magnet tuning, plus unattended execution of time consuming tests such as near-field beam scans and output power and phase stability testing. Ref. [10] describes this semi-automated test system in more detail.

V. Production Plans and Status

A. *Production Phase Requirements*

Moving into the project's production phase, the technical requirements have remained largely unchanged. New requirements on aperture efficiency and the co-alignment of the cartridge's two polarization beams were introduced, the

cross-polarization requirement has been confirmed, and a number of other requirements have been clarified. However, the core technical requirements, including sensitivity and RF and IF bandwidth, have not changed.

With only minimal changes in the technical requirements, the biggest change is in the increased scope of the production effort – in place of eight cartridges in 1 year, the production phase requires 65 cartridges in 4.5 years, including an eventual delivery rate of about 2 per months. This increased scope has required revised procedures and processes when compared with the earlier development and pre-production phase.

B. Component Procurement

The cartridge design was developed with the goal of sub-contracting as much manufacturing as possible to commercial suppliers – as reported above; this was already accomplished in pre-production. In this respect, the biggest change going into production is in the size of the orders – with the larger orders for production come additional formalities in the contracting process, and thus much longer lead-times. Because of these long lead-times, it was essential to freeze the design for production early, and the design for the production phase was frozen in late 2007, allowing procurement to start in mid-to-late 2007.

Orders for the full production quantities were placed between late 2007 and mid-2008. As a result, where single-batch production was most efficient (including mechanical parts and off-the-shelf components), full production quantities have already been inspected, cleaned, and placed in storage. For components that are produced in smaller batches, the goal is to receive components half a year or more before they are needed, to minimize risks to the cartridge deliveries. This was not feasible for the first production component deliveries, but every effort is being made to reach this goal by mid-2009. Particular attention is paid to components that are critical to cartridge performance and reliability, including corrugated mixer horns, SIS junction mounts, 4 K mirror blocks, polarizing grids, 4-12 GHz isolators, cryogenic semi-rigid cables, and LO waveguides and horns.

Three critical cold cartridge components come from ALMA partners (cryogenic amplifiers from CAY, Spain; cold LO multipliers from NRAO and VDI, USA; and the blank cartridge bodies from RAL, UK). The warm LO assembly and cartridge bias modules also come from NRAO.

C. Cartridge Test System Expansion and Upgrade

Provided that components are available well before they are needed for assembly, the critical item in the production project schedule is cartridge testing (including trouble-shooting, if needed).

Although cartridge acceptance testing is extensive (most performance requirements are verified on all cartridges), the semi-automated Band 9 cartridge test system [10] allows this to be done efficiently. Taking into account the time required for cartridge bias optimization and performance testing, plus the inevitable need to repeat some tests and rework some cartridges, a throughput of one cartridge per three weeks is realistic. Thus, two test systems are needed to keep up with the required production rate of up to two cartridges per month. Built around a single-cartridge test cryostat developed at NAOJ [11] and using the same cryo-cooler as in the ALMA cryostat [12], the 2nd cartridge test system (see Fig. 4) was built in 2007 and 2008.

Fig. 4. Two cartridge test cryostats (from NAOJ, Japan). With a test throughput of 1 cartridge per 3 weeks, a 2nd test system was built in 2007-2008 to allow a delivery rate of 2 cartridges per month to be realized.

D. Manufacturing and Assembly

As discussed above, assembly typically required one month per cartridge in pre-production. However, a significant contributor to this rate was the time required to inspect and prepare parts and sub-assemblies, as assembly proceeded one cartridge at a time. For production, these preparatory activities have been removed from the assembly process, and are being performed in large batches in advance, allowing work to be more efficiently organized. In this approach, final assembly of the cartridge structure and its integration with the mixers and optics is feasible at the required rate of 2 cartridges per month, even with an increased level of inspection of incoming parts.

E. Optics and Mixer Testing

Plans for mixer testing in production do not deviate significantly from the approach followed during pre-production. Making use of a small liquid helium dewar that can be cycled 2-3 times per day, pre-selection of candidate mixers is done by Fourier Transform spectrometer tests of their direct detection responses. Potentially good mixers are then heterodyne tested in a two-mixer test dewar. The quick cycling times of both dewars, combined with test software that allows two mixers to be heterodyne tested in one day, allow sufficiently quick testing to meet the project's requirements.

The 4 K optics assemblies are receiving additional attention during the production phase. As in pre-production, room-temperature near-field beam-pattern measurements of all assemblies are used to verify that the cartridge's optical requirements are met. For production, these RF measurements

are preceded by mechanical inspections of all 4 K mirror blocks by their manufacturer to verify that the manufacturing tolerances are achieved – these inspections were introduced to help ensure that the required co-alignment of the cartridge's two polarization beams is achieved. Verified optics assemblies are placed into storage as assemblies (minus the mixers).

F. Cartridge Testing and Delivery

The cartridge test program for production is largely based upon that used in pre-production, with some fine-tuning to improve test accuracy and/or to address requirements that were revised since for production. With two cartridge test systems operating in parallel, if reworking or retesting of a cartridge is required, work on the following units can proceed, allowing cartridge deliveries to continue.

VI. Ongoing Developments

Although the production of cartridges meeting the project's requirements is the clear top priority at this phase of the project, ongoing development continues with the goal of improving Band 9 cartridge performance in both the near and longer term.

In the near-term, efforts continue towards the application of AlN SIS junction technology [13-15]. When compared with the baseline AlO_x SIS junctions AlN junctions offer good junction qualities for much higher junction current-densities. Because the fixed-tuned bandwidth of AlO_x SIS junctions in Band 9 is largely limited by the *RC* product of the SIS junction's tunnel barrier, the potential to use much higher current-density junctions (with correspondingly lower values of *RC*) offers a substantial increase in the fixed-tuned bandwidth of the Band 9 mixers. Ref. [15] describes the evaluation of prototype AlN mixers in a Band 9 cartridge during 2007-2008. Since that demonstration, work has continued to optimize AlN mixer performance in Band 9 [16]. Although development is not yet complete, implementing AlN SIS junctions in the Band 9 cartridge requires only a change of the junction chip in the mixer – this potentially allows a design change to be implemented mid-way through production, without significantly affecting the production process.

In the longer term, development of a side-band separating mixer for ALMA Band 9 continues. A side-band separating configuration offers the potential for substantial improvements in receiver sensitivity by eliminating the noise contribution of the atmosphere in the image side-band, in particular for line observations. See [17] for more information.

Acknowledgment

The staff of the NOVA Band 9 group at the University of Groningen and SRON (M. Bekema, M. van den Bemt, G. Gerlofsma, M. de Haan, R. de Haan, R. Jager, A. Koops, J. Koops van het Jagt, P. Mena, J. Panman, and C. Pieters) are acknowledged for their continuing efforts to produce and test the Band 9 cartridges. W. Boland and E. van Dishoeck (NOVA), F. Helmich (SRON), and G. H. Tan (ESO) are acknowledged for their ongoing support of the Band 9 effort. W. Wild (ESO) and Th. de Graauw (JAO) are acknowledged for their ongoing contributions, and particularly those in the project's earlier phases.

References

[1] www.almaobservatory.org,

[2] R. Hesper *et al.*, "Design and development of a 600-720 GHz receiver cartridge for ALMA Band 9," *16th Int. Symp. On Space THz Technology*, ISSTT 2005, Chalmers University of Technology, Göteborg, Sweden, May 2-4, 2005.

[3] A. Baryshev, E. Lauria, R. Hesper, T. Zijlstra, W. Wild, "Fixed-tuned waveguide 0.6 THz SIS mixer with wide band IF," in: R. Blundell and E. Tong (Eds.), *Proc. 13th Int. Symp. on Space THz Technology*, Harvard University, Harvard, MA, Mar. 26-28, 2002, pp. 1-10.

[4] Passive Microwave Technology, Incorporated, 4053 Calle Tesoro, Suite A, Camarillo, CA 93012, USA.

[5] I. López-Fernández, J. D. Gallego, C. Diez, A. Barcia, "Development of Cryogenic IF Low Noise 4-12 GHz Amplifiers for ALMA Radio Astronomy Receivers", 2006 IEEE MTT-S Int. Microwave Symp. Dig., pp. 1907-1910, 2006.

[6] M. Candotti *et al.*, "Quasi-Optical Verification of the Band 9 ALMA Front-End," *16th Int. Symposium on Space THz Technology – ISSTT 2005*, Chalmers University of Technology, Göteborg, Sweden, May 2-4, 2005; and A. Baryshev, R. Hesper, K. Wielinga, G. Gerlofsma, and M. Carter, "Design and verification of ALMA Band 9 receiver optics," in: G. Narayanan (Ed.), *Proc. of the 15th Int. Symp. on Space THz Technology*, Univ. of Massachusetts, Amherst, MA, April 27-29, 2004, pp. 433-440.

[7] E. Bryerton, M. Morgan, D. Thacker, and K. Saini, "Maximizing signal-to-noise ratio in local oscillator chains for sideband-separating single-ended mixers," *18th Intl. Symp. on Space Terahertz Technology*, Pasadena, CA, March 2007.

[8] M. Morgan *et al.*, "A millimeter-wave diode-MMIC chipset for local oscillator generation in the ALMA telescope," IEEE MTT-S Intl. Microwave Symposium, Long Beach, CA, June 2005; and M. Morgan *et al.*, "Wideband medium power amplifiers using a short gate-length GaAs MMIC process," IEEE MTT-S Intl. Microwave Symposium, Boston, MA, June 2009.

[9] Virginia Diodes, Inc., 979 Second Street, S.E., Suite 309, Charlottesville, VA 22902-6172, USA; www.virginiadiodes.com.

[10] J. Barkhof, B.D. Jackson, A.M. Baryshev, and R. Hesper, "Automated test system for the ALMA band 9 cartridges," these proceedings.

[11] Y. Sekimoto *et al.*, "Cartridge Test Cryostats for ALMA Front End," ALMA memo 455, 2003.

[12] A. Orlowska, M. Harman, and B. Ellison, "Receiver Cryogenic System," Ch. 6 in: J. Baars (Ed.), ALMA Construction Project Book Version 5.50, 2002.

[13] T. Shiota, T. Imamura, and S. Hasuo, "Nb Josephson junction with an AlNx barrier made by plasma nitridation," *Appl. Phys. Lett.*, vol. 61, 1228 (1992).

[14] J. W. Kooi *et al.*, "A 275-425-GHz tunerless waveguide receiver base don AlN-barrier SIS technology," *IEEE Trans. Microwave Theory and Techn.*, vol. 55, 2086 (2007).

[15] C.F.J. Lodewijk *et al.*., Bandwidth of Nb/AlN/Nb SIS mixers suitable for frequencies around 700 GHz, in: *Proc. 19th International Symposium on Space THz Technology* (Ed. W. Wild), Groningen, The Netherlands, 28-30 April 2008, pp. 86-89.

[16] S. Zhu *et al.*, "Magnetic field dependence of the microwave properties of proximity effect Nb/Al bilayers close to the gap-frequency," these proceedings.

[17] R. Hesper, A.M. Baryshev, G. Gerlofsma, and T. Zijlstra, "A sideband-separating mixer upgrade for ALMA band 9," these proceedings.

M1D

Development of the 787-950 GHz ALMA Band 10 Cartridge

Y. Uzawa[1*], T. Kojima1[1, 2], M. Kroug[1], M. Takeda[3], M. Candotti[1], Y. Fujii[1], W.-L. Shan[4], K. Kaneko[1], S. Shitov[1], and M.-J. Wang[5]

1 National Astronomical Observatory of Japan, Tokyo 181-8588, Japan*
2 Osaka Prefecture University, Osaka 599-8531, Japan
3 National Institute of Information and Communications Technologies, Kobe 651-2492, Japan
4 Purple Mountain Observatory, Nanjing 210008, China
5 Academia Sinica Institute of Astronomy & Astrophysics, Taipei 10617, Taiwan
* Contact: y.uzawa@nao.ac.jp, phone +81-422-34-3807

***Abstract*—We are developing the Atacama Large Millimeter/Submillimeter Array (ALMA) Band 10 (787-950 GHz) receiver cartridge. The incoming beam from the 12-m antenna is reflected by a pair of two ellipsoidal mirrors placed in the cartridge, and then split into two orthogonal polarizations by a free-standing wire-grid. Each beam enters a corrugated feed horn attached to a double-side-band (DSB) mixer block. The mixer uses a full-height waveguide and an NbTiN- or NbN-based superconductor-insulator-superconductor (SIS) mixer chip. We are testing the following three types of mixer chips: 1) Nb SIS junctions + NbTiN/SiO2/Al tuning circuits on a quartz substrate, 2) Nb SIS junctions + NbN/SiO2/Al tuning circuits on an MgO substrate, and 3) NbN SIS junctions + NbN or NbTiN tuning circuits on an MgO substrate. The IF system uses a 4-12-GHz cooled low-noise InP-based MMIC amplifier developed by Caltech. So far, the type 1) has shown the best performance. At LO frequencies from 800 to 940 GHz, the mixer noise temperatures measured by using the standard Y-factor method were below 240 K at an operating physical temperature of 4 K. The lowest noise temperature, 169 K, was obtained at the center frequency of the band 10, as designed. These well-developed technologies will be implemented in the band 10 cartridge to achieve the ALMA specifications.**

Session M2

SIS Receivers

Chair: Jacob Kooi

Monday, April 20
10:55 – 12:10

230 GHz sideband-separating mixer array

Doris Maier

***Abstract*—Since 2001 the HEterodyne Receiver Array , HERA, is installed at IRAM's 30m telescope in Spain. It consists of two arrays with 3x3 pixels for two orthogonal polarizations. The receiver is equipped with SSB backshort mixers covering an RF frequency range from 218 to 267 GHz with an IF band of 3.5 to 4.5 GHz.**

In the near future IRAM will replace this receiver by a new dual-polarization multi-beam receiver with 7x7 pixels. The receiver will be equipped with sideband-separating mixers covering an RF frequency range from 200 to 280 GHz with an IF band from 4 to 12 GHz. The RF quadrature couplers as well as the LO couplers will be realized as branchguide couplers and be integrated with the mixer blocks into one E-plane split-block. The DSB mixers will use Nb junction technology and the IF couplers will be custom made for the use at cryogenic temperatures. This paper presents the concept of the new array as well as the designs of the DSB mixers and the different couplers.

***Index Terms*—2SB mixer array, multi-beam receiver, SIS mixer**

I. INTRODUCTION

IN 2001 IRAM installed the **HE**terodyne **R**eceiver **A**rray, HERA, at its 30m telescope in Spain [1]. In the beginning the receiver was equipped with 3x3 pixels for one polarization. In 2004 the second unit of 3x3 pixels for the second polarization followed. Since then it has been operating successfully and delivered routinely many interesting astronomical results.

The receiver is equipped with SSB mixers tuned with backshorts. They cover an RF frequency range of 218 GHz to 267 GHz with an IF band of 1 GHz [2].

Since the installation of HERA, mixer development progressed further. Nowadays, mixers delivering both sidebands with larger RF bands and instantaneous bandwidths of 8 GHz are available [3]. Furthermore, the noise performances of recently developed mixers are better than those of the HERA mixers.

Therefore IRAM started the work on a new multibeam receiver called **S**uper **HE**terodyne **R**eceiver **A**rray, SHERA, which will make use of these new developments. SHERA will be equipped with sideband-separating mixers. The mixer design covers RF frequencies from 200 to 280 GHz and the IF band of the mixers is 4 to 12 GHz. Due to the currently limited capacities of the backends, only one sideband per pixel and an IF band of only 4-8 GHz will be exploited in the beginning. But as soon as the necessary backends are available the receiver can be easily upgraded.

Manuscript received 20 April 2009.

II. SIDEBAND-SEPARATING MIXER ARRAY

The new multibeam-receiver will be composed of respectively two 7x7 pixels units as shown in Figure 1 for each of the two orthogonal polarizations. Each range of 7 pixels is composed of a 3 and a 4 pixels unit. The 3, respectively 4 pixels have one common LO input. The flanges for the LO inputs of the 3 pixels units can be seen in Figure 1 on the right-hand side. The 4 pixels units are fed with LO power from the left. The feedhorns for the signal input are mounted on the flanges on the front of the units and the IF signals are coming out on the back.

The size of such a 7x7 mixer array is 175x175x30 mm^3, which means that one pixel (without feedhorn) fits into a cube of 25x25x30 mm^3.

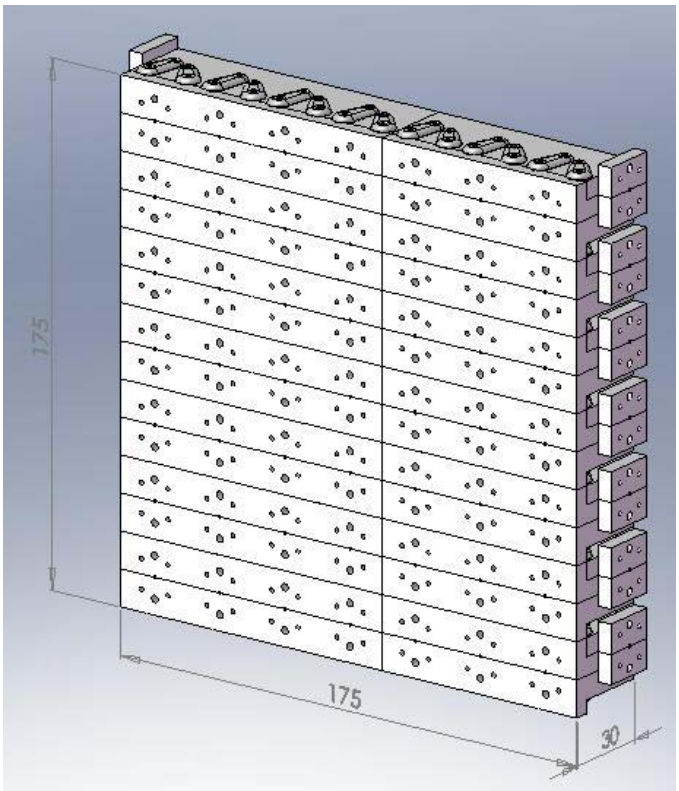

Figure 1: 7x7 pixels unit for one polarization.

D. Maier is with the Institut de Radio Astronomie Millimétrique, Grenoble, France (phone: +33 4 76 82 49 16; fax: +33 4 76 51 59 38; e-mail: maier@iram.fr).

III. 3 AND 4 PIXELS UNITS

The whole 7x7 pixels array is subdivided into 3 and 4 pixels units. A picture of a 3 pixels unit is shown in Figure 2.

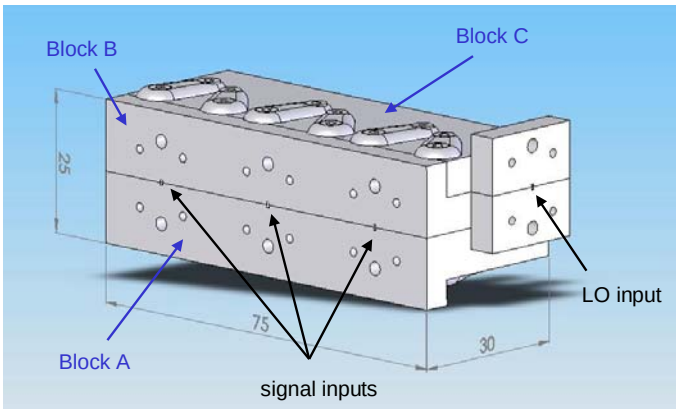

Figure 2: 3 pixels unit consisting of three E-plane split blocks.

The sub-units consist of three E-plane split blocks, called A, B, and C. Blocks A and B form the 2SB mixers with RF input and IF output. Figure 3 shows a top view of block A. The signals are coming in from the top of the figure and are going to the 2SB mixers. The IF outputs of the mixers are connected to the SSMA connectors situated at the back of the block.

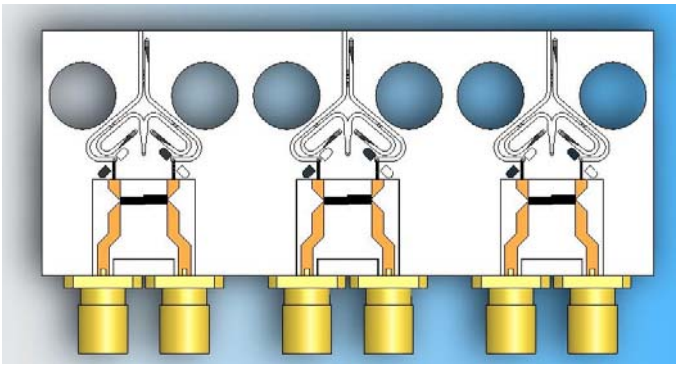

Figure 3: Top view of block A of a 3 pixels unit.

The LO input is situated in the plane between blocks B and C (see Figure 4). Branchguide couplers are used to couple a fraction of the signal to each of the first pixels. The last pixel receives the residual LO power. The couplers are designed in such a way that each pixel receives the same amount of LO power taking into account the losses in the waveguides between the pixels. The LO signals then go through block B and are coupled to the 2SB mixers.

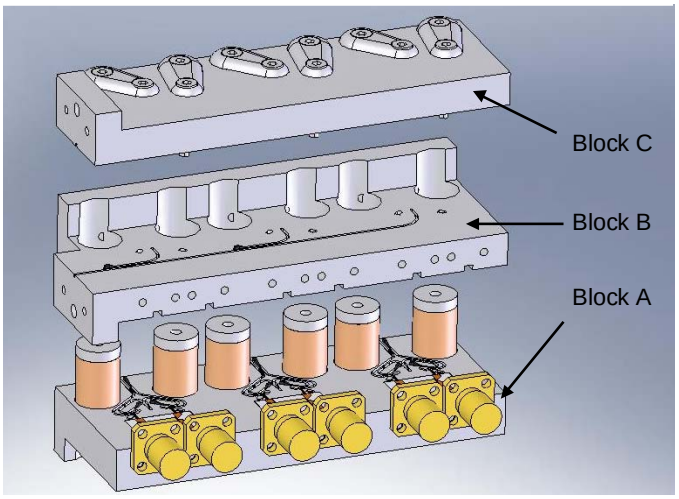

Figure 4: One three pixels unit is composed of three E-plane split blocks.

IV. 2SB MIXER

Figure 5 shows one pixel of the mixer array. The signal comes in on the left-hand side and is split by the 90º hybrid coupler in two. The LO signal comes in from above. It is split in two and coupled to the signal by the LO couplers which is then coupled to the mixer chip. On the right-hand-side the IF output of the mixers is connected to an in-plane 90º IF coupler. Magnetic coils are placed in the holes indicated in Figure 5 and pole pieces are placed in the vicinity of the mixer chips, in order to suppress the Josephson currents in the junctions.

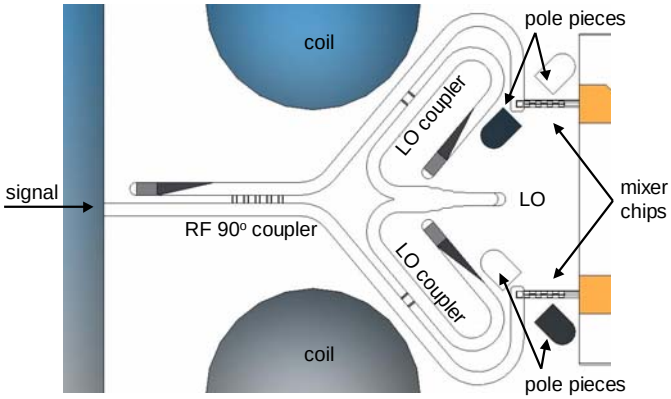

Figure 5: View of the sideband-separating mixer (for details see text).

A. LO input

Since the LO input is located in a plane parallel to the 2SB mixers, we need not only a splitter, but also two H-plane bends in order to feed the LO signal to the two DSB mixers of each pixel. Both components have been designed as described in [4] and optimized using CST Microwave Studio [5]. Design and simulated performances are shown in Figure 6 and Figure 7.

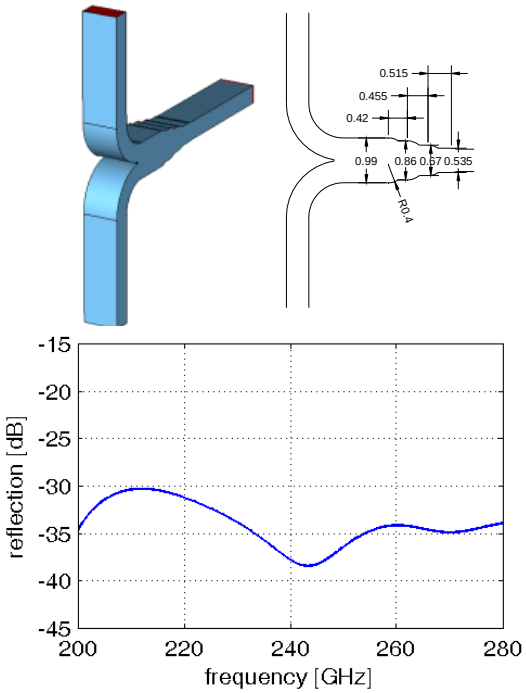

Figure 6: Design and simulated performance of the Y-splitter.

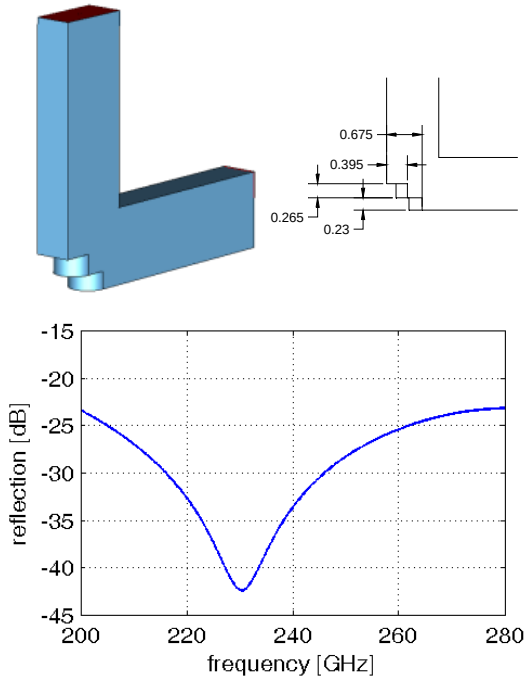

Figure 7: Design and simulated performance of the H-plane bend.

B. RF couplers

The RF couplers of the sideband-separating mixers are realized as branchguide couplers [6]. The 90º hybrid coupler uses five slots, whereas the LO couplers are made with only 2 slots. The designs have been optimized with CST Microwave Studio. Dimensions and theoretical performances of the couplers are shown in Figure 8 and Figure 9.

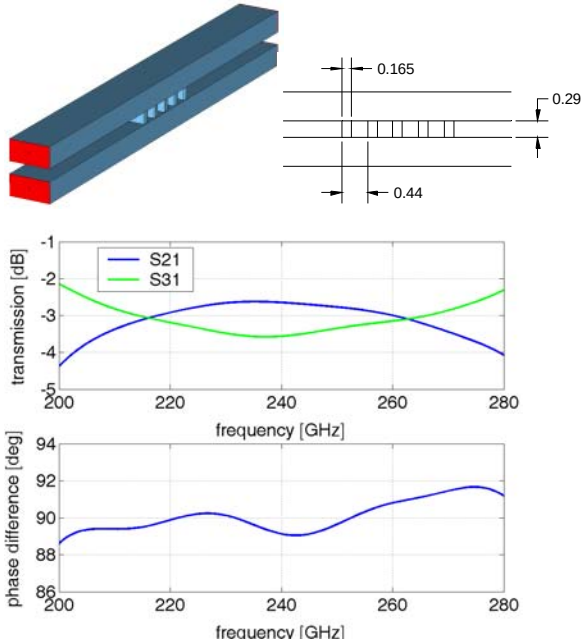

Figure 8: Design and simulated performance of the 90º hybrid coupler.

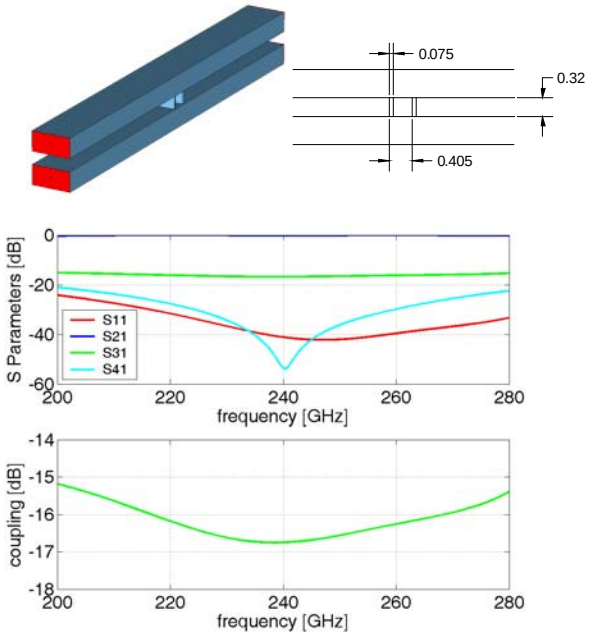

Figure 9: Design and simulated performance of the LO coupler.

C. DSB mixer

The design of the DSB mixer is quite similar to our previous designs [7]–[9]. The mixing element is a superconductor-insulator-superconductor (SIS) tunnel junction, which is deposited together with a superconducting circuit onto a quartz substrate. This circuit comprises the waveguide-probe providing a full-height waveguide to suspended microstrip transition, the RF choke and the actual tuning circuit, whose role is the compensation of the junction's capacitance and matching to the antenna impedance. Figure 10 shows the layout of one individual mixer chip with a size of 0.26 x 2.4 x 0.08 mm^3. These devices are fabricated by IRAM's SIS group. The Nb-Al/ALO_x-Nb tunnel junction has an area of 1 μm^2 and is made by e-beam lithography [10], [11].

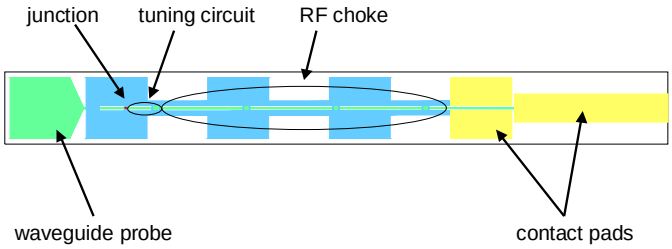

Figure 10: Layout of the mixer chip.

The mixer chip is placed in a channel perpendicular to the waveguide axis and stretches only partly across the waveguide as can be seen in Figure 11. The full-height waveguide to microstrip transition is provided by an antenna structure that has been optimized using CST Microwave Studio [5].

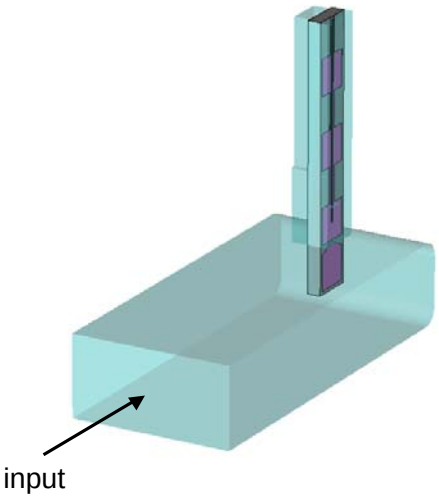

Figure 11: Full-height waveguide to microstrip transition.

The resulting antenna impedance is shown in Figure 12 for frequencies between 200 and 280 GHz. It is slightly capacitive, but its real part is quite constant over the whole frequency range.

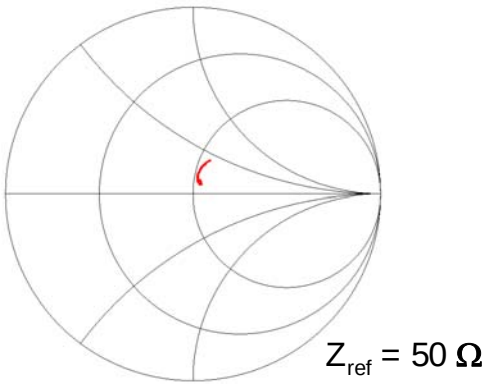

Figure 12: Antenna impedances for frequencies between 200 and 280 GHz.

In order to tune out the junction's capacitance, a superconducting tuning circuit has been developed and optimized using Sonnet [12] and ADS [13]. Figure 13 shows a picture of this circuit. Its equivalent circuit is shown in Figure 14.

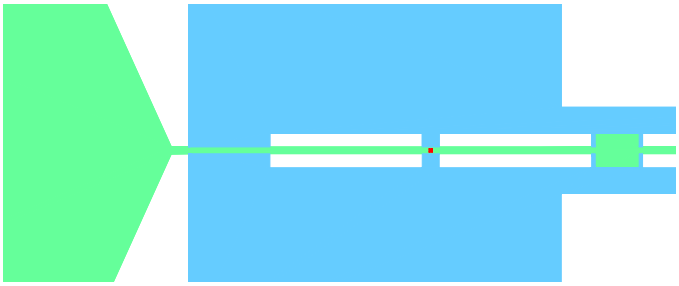

Figure 13: Picture of the tuning circuit.

The compensation of the junction's capacitance is achieved with a coplanar waveguide followed by a capacitance serving as a parallel inductance connected to a virtual ground. The whole structure is then matched to the antenna impedance with the help of a λ/4 transformer realized as a series of microstrips and coplanar waveguide.

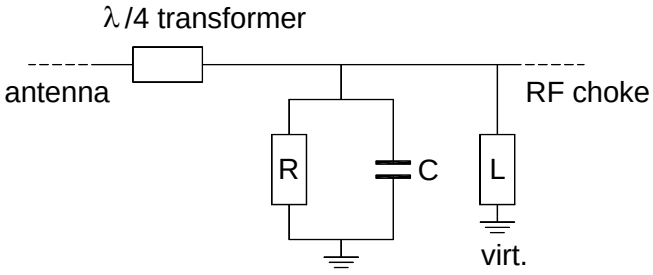

Figure 14: Equivalent circuit of the tuning structure.

The thus achieved embedding impedance of the junction is shown in the Smith chart of Figure 15 for frequencies between 200 and 280 GHz. It is quite close to the junction's RF impedance, so that the coupling to the junction is better than 97% as can be seen in the plot in Figure 16.

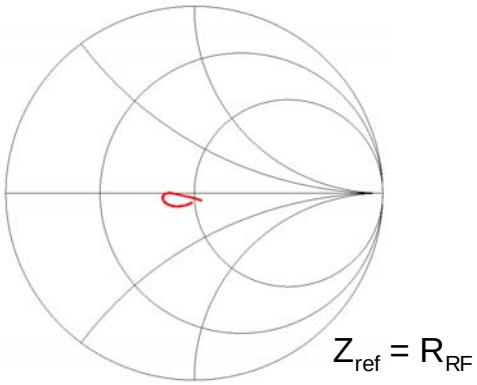

Figure 15: Embedding impedance of the junction for frequencies between 200 and 280 GHz.. The Smith chart is normalized to the junction's RF impedance.

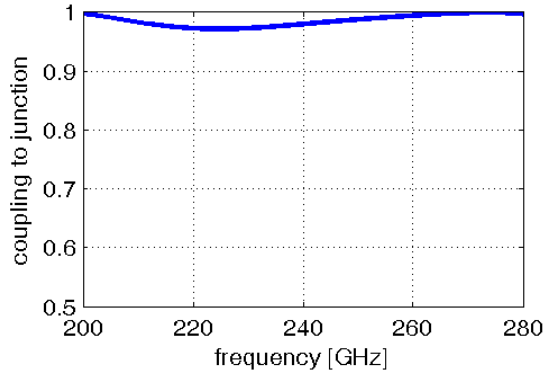

Figure 16: Fraction of power coupled to the junction.

D. IF coupler

Up to now we used commercially available IF 90º couplers for our sideband-separating mixers [7], [9]. But this is no longer possible, if we want to reduce the size of one pixel to fit into about (25 mm)^3. Therefore the IF coupler will be custom made. It will be realized as Lange coupler [14]. This allows the integration of the coupler into the combined RF coupler/mixer block. This type of coupler has already been used in 2SB mixers [15].

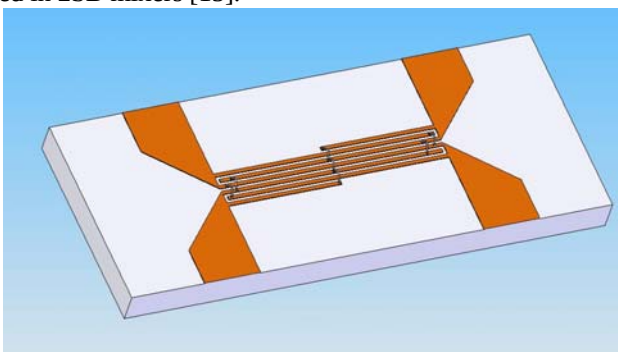

Figure 17: Lange coupler.

We intend to use a Rogers 4003 substrate with 1.524 mm dielectric thickness [16]. Figure 18 shows the simulated performance achievable with such a substrate for the 4-8 GHz band.

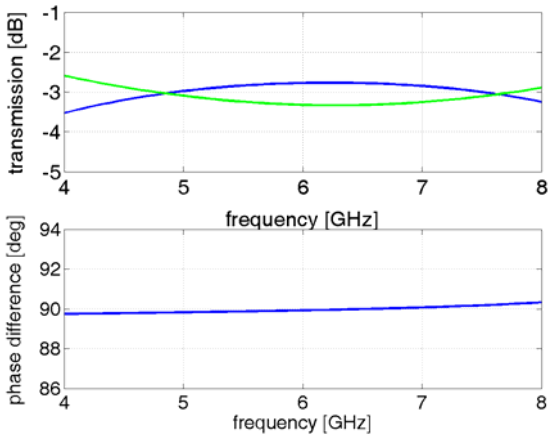

Figure 18: Simulated performance of a Lange coupler with a Rogers 4003 substrate with 1.524 mm dielectric thickness.

V. Outlook

Before realization of the new mixer array, the different components will be tested individually or in sub-units. First the mixer design will be verified by DSB mixer tests in simple DSB mixer blocks and the design of the IF coupler will be optimized. In the next step one pixel, i.e. one sideband-separating mixer, will be made and characterized. And finally, a 3 pixels unit will be made and tested.

References

[1] K.F. Schuster, C. Boucher, W. Brunswig, M. Carter, J.-Y. Chenu, B. Fouilleux, A. Greve, D. John, B. Lazareff, S. Navarro, A. Perrigouard, J.-L. Pollet, A. Sievers, C. Thum, and H. Wiesemeyer, "A 230 GHz heterodyne receiver array for the 30 m telescope," Astronomy & Astrophysics, vol. 423, pp. 1171-1177, 2004

[2] A. Karpov, J. Blondel, M. Carter, D. Billon-Pierron, and K.H. Gundlach, "A multibeam SIS mixer module for a focal plane array receiver," Int. J. Infrared and MM Waves, vol. 19, pp. 1175-1190, 1998

[3] A.R. Kerr, S.-K. Pan, E.F. Lauria, A.W. Lichtenberger, J. Zhang, M.W. Pospieszalski, N. Horner, G.A. Ediss, J.E. Effland, and R.L.Groves, "The ALMA Band 6 (211-275 GHz) Sideband-Separating SIS Mixer-Preamplifier," ALMA Memo 498, 2004

[4] A.R. Kerr, "Elements for E-Plane Split-Block Waveguide Circuits," ALMA Memo 381, 2001

[5] CST Microwave Studio, Bad Nauheimer Str. 19, D-64289 Darmstadt, Germany

[6] S. Claude, C.T. Cunningham, A.R. Kerr, and S.-K. Pan, "Design of a Sideband-Separating Balanced SIS Mixer Based on Waveguide Hybrids," ALMA Memo 316, 2000

[7] D. Maier, A. Barbier, B. Lazareff, and K.F. Schuster, "The ALMA Band 7 Mixer," in *Proc. 16th ISSTT*, Göteborg, Sweden, 2005, pp. 428-431

[8] D. Maier, S. Devoluy, M. Schicke, and K.F. Schuster, "230 GHz SSB SIS Mixer for Band 3 of the New Generation Receivers for the Plateau de Bure Interferometer," in *Proc. 16th ISSTT*, Göteborg, Sweden, 2005, pp. 33-36

[9] D. Maier, D. Billon-Pierron, J. Reverdy, J. Reverdy, and M. Schicke, "100 GHz Sideband-Separating Mixer with Wide IF Band," *in Proc. 18th ISSTT*, Pasadena, USA, 2007, pp. 260-263

[10] I. Péron, P. Pasturel, and K.F. Schuster, "Fabrication of SIS junctions for space borne submillimeter wave mixers using negative resist e-beam lithography," IEEE Trans. on Applied Superconductivity, vol. 11, pp. 377-380, 2001

[11] N. Krebs, A. Barbier, D. Billon-Pierron, S. Halleguen, M. Schicke, and K.F. Schuster, "Fabrication of Sub-Micrometer SIS Junctions for Radio Astronomy," IEEE Trans. on Applied Superconductivity, vol. 17, pp. 191-193, 2007

[12] Sonnet Software, 100 Elwood Davis Road, North Syracuse, NY 13212

[13] Advanced Design System, Agilent Eesof EDA

[14] J. Lange, "Intergitated Stripline Quadrature Hybrid," IEEE Trans. MTT, vol. 20, pp. 1150-1151, 1969

[15] V. Vassilev, D. Henke, I. Lapkin, O. Nystrom, R. Monje, A. Pavolotsky, and V. Belitsky, "Design and Characterization of a 211-275 GHz Sideband-Separating Mixer for the APEX telescope," IEEE Microwave and Wireless Components Letters, vol. 18, pp.58-60, 2008

[16] Rogers Corporation, www.rogerscorp.com

ALMA Band 5 (163-211 GHz) Sideband Separation Mixer

Bhushan Billade, Victor Belitsky, Alexey Pavolotsky, Igor Lapkin, Jacob Kooi

***Abstract*— We present the design of ALMA Band 5 sideband separation SIS mixer and experimental results for the double side band mixer and first measurement results 2SB mixer. In this mixer, the LO injection circuitry is integrated on the mixer substrate using a directional coupler, combining microstrip lines with slot-line branches in the ground plane. The isolated port of the LO coupler is terminated by wideband floating elliptical termination. The mixer employs two SIS junctions with junction area of 3 μm^2 each, in the twin junction configuration, followed by a quarter wave transformer to match the RF probe. 2SB mixer uses two identical but mirrored chips, whereas each DSB mixer has the same end-piece configuration. The 2S mixer has modular design such that DSB mixers are measured independently and then integrated into 2SB simply by placing around the middle piece.**

Measurements of the DSB mixer show noise temperature of around 40K over the entire band. 2SB mixer is not fully characterized yet, however, preliminary measurement indicates SSB (un-corrected) noise temperature of 80K.

***Index Terms*— Millimeter wave mixers, Superconductor-insulator-superconductor mixers, Millimeter wave receivers, Thin film circuits.**

I. INTRODUCTION

THE Atacama Large Millimetre/sumillimeter Array (ALMA) is a radio interferometer under construction by an international consortia consisting of European countries (ESO), USA, Canada, and Japan. With its more than 60 antennas and reconfigurable baseline up to 10 Km, ALMA will be the most sensitive radio telescope at mm/submm wavelengths.

The work presented here concerns development of one of the bands of ALMA project, ALMA Band 5. ALMA Band 5 will be a dual polarization sideband separating heterodyne receiver covering 163-211 GHz with 4 - 8 GHz IF. For each polarization, Band 5 receiver employs sideband rejection quadrature layout (2SB) based on SIS mixers [3]. The major challenge with Band 5 mixer design is that, there is a very limited space inside the cartridge. Amongst the other ALMA bands, Band 5 is the lowest frequency band, which uses all cold optics. The optics dimensions put strong constrains on the sizes of all the receiver components and demands a very compact design. Furthermore, the arrangement of the components in the cartridge is such that we have to direct the IF output of the mixers pointing down along the cartridge axis. In such a configuration, the mixer design with a spilt block technique becomes too big to fit inside the cartridge. We have found that the only possible solution is to use a mixer block configuration with waveguide back piece [2]. This design allows very compact design of the mixer block and also IF output pointing in desirable direction. Furthermore, to avoid extra cables and hence RF losses, all the components in the chain are directly attached to each other with SMA connectors. This design requires a custom made IF hybrid in order to fit the distance between the SMA connectors of the 2SB mixer IF outputs.

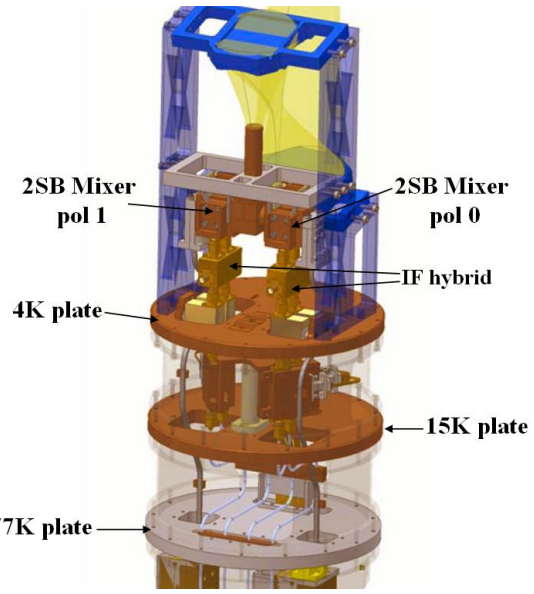

Fig. 1. ALMA Band 5 cartridge layout.

Since there is limited cooling capacity at 4K stage, we can only allow 36mW of heat produced at 4K stage, which does not allow us to integrate the DC bias circuitry into the mixer. In our design, the DC biasing to the mixer is done using a bias box placed on 15K plate. The IF hybrid connected to the combined IF/DC output of the 2SB mixer have an integrated bias-T, and the DC biasing is thus achieved through the output SMA connector of the mixer (Fig. 1).

Manuscript received on April 20, 2009. This work was supported by EC Framework Program 6 (FP6) in its part of infrastructure enhancement under contract 515906.

Bhushan Billade, Victor Belitsky, Alexey Pavolotsky and Igor Lapkin are with the Group of Advanced Receiver Development (GARD) at Chalmers University of Technology, Gothenburg, Sweden. (phone: 46-31-772 1851; fax: 46-31-772 1801; e-mail: bhushan.billade@chalmers.se).

Jacob Kooi is with the California Institute of Technology, Pasadena, USA.

II. Mixer Design

A. Mixer Chip Design

The chip is fabricated on a 90 µm thick crystalline Z-cut quartz substrate with dimensions 310 µm wide and 2640 µm long. The mixer chip contains along with the SIS junctions most of the DSB components integrated on the same substrate: the chip comprise of an E-plane probes, waveguide-to-microstrip transition, for both the LO and RF, an RF choke at the end of the probe provides virtual ground for the RF/LO signals. We use the same probe with impedance of around 40 Ω for both the LO and RF.

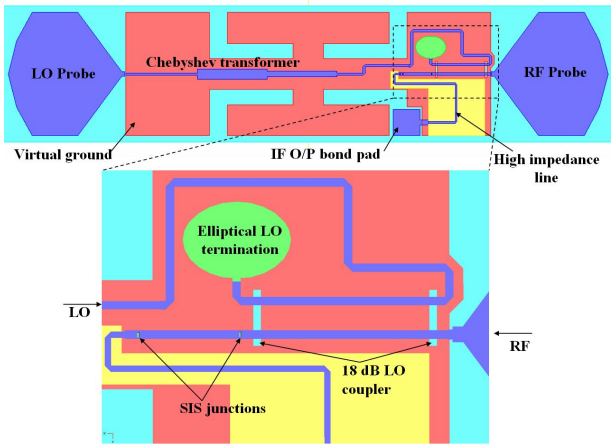

Fig. 2. Mixer chip layout on quartz substrate, containing LO and RF probe, RF choke structure, and IF bond pad. A zoomed vied of 18dB LO coupler, elliptical termination and SIS junction.

The RF probe is followed by a LO coupler and two SIS junctions in the twin configuration, and the IF is extracted between the RF and LO waveguides using a high impedance line (Fig. 2). The LO probe is followed by a three stage Chebyshev transformer to match the probe impedance to the LO coupler input, and the reflected signal at the isolated port of LO coupler is terminated using wideband floating elliptical resistive termination [1]. The elliptical termination has the sheet resistance (12 Ω), the same as that of the impedance of the LO coupler input.

The shape of the E-plane probe is optimized for a broad band performance using Agilent Electromagnetic Design System (EMDS), a full 3D EM solver. Probe's real impedance is 42Ω with ± 4% variation across the entire RF band and imaginary impedance of the probe varies between +j5 Ω to –i2 Ω. A hammer type RF choke provides a virtual ground for the RF/LO signal applied between the end of the probe and the choke, which excites microstrip mode between the top conductor layer (LO/RF) and the bottom ground (choke) layer. The thickness of the silicon dioxide layer used for the micro strip line is 350 nanometres. In order to achieve broad band performance from the mixer we use two SIS junctions in twin junction configuration [3, 4] with junctions of size 3 µm² each and RnA product of 30. The transmission line length between the two junctions is optimized such that the imaginary part of the twin junction configuration is tuned out. In this configuration the LO coupler serves two purposes: first, it couples the LO signal to RF with weak - 18 dB coupling and, secondly, it transforms the probe impedance from 40 Ω to the input impedance of the twin junction circuitry.

B. Mixer Block Design

The mixer block consists of two parts, a mixer back piece and a middle piece. In the mixer back piece, the mixer chip is glued to the block using wax, a 50 to 15 Ω IF transformer produced on 500µm thick alumina substrate, the IF signal from the mixer chip is extracted using a bond wire with a single layer capacitor employed at the IF side to compensate for the inductance of the bond wire and the mixer circuitry in order to achieve good IF matching.

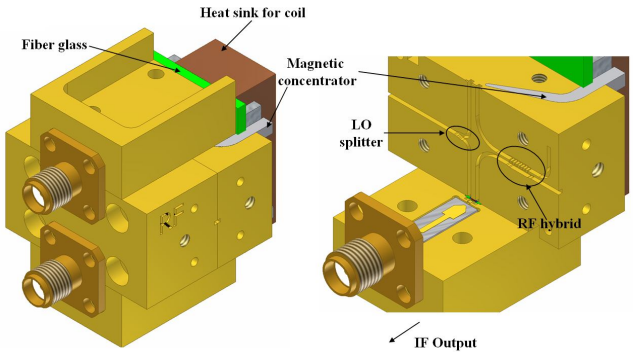

Fig. 3. 2SB Mixer block with two mixer back piece and a middle piece.

The two mixer back pieces should be used in the 2SB configuration and are exactly identical to facilitate production, however the mixer chips used have mirrored layout. The middle piece consists of a 90^0 RF hybrid and an in phase LO splitter. In order to suppress the Josephson current, the middle piece also holds magnetic concentrators, and the magnetic coils sit in a copper heat sink. This assembly is connected to the middle piece, using a fibre glass in between, to avoid heat leak from the coils to the mixer block.

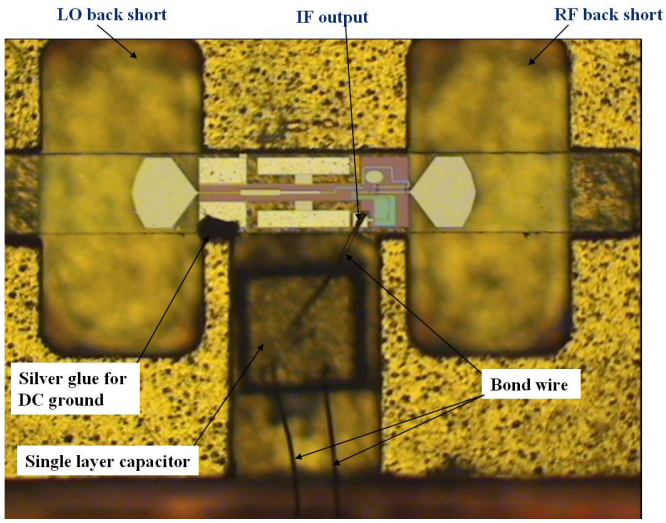

Fig. 4. Mixer back piece with mixer chip.

Fig. 4 shows the picture of the mixer back piece with the chip mounted. In this configuration the mixer chip is installed perpendicular to the direction of E-field in the waveguide. The quartz substrate, used for the chip, extends into the full height for both LO and RF waveguides and even further; this enables a better thermal contact with the mixer block.

III. DSB Measurement Results

Fig. 5, shows the first experimental results of the DSB mixer, the noise measurements were performed with standard Y factor measurement technique using a hot (293K) and cold (LN2 77K) load placed in front of the test cryostat window. In Fig. 5, we show the noise measurement performed over the entire IF bandwidth with respect to a particular LO frequency. It could be seen from the plot that the noise performance is flat over the IF band for all LO frequencies, except there are peaks at IF for LO frequencies 188 and 192 GHz, and at 197 GHz the Y factor drops abruptly, rising the noise temperature to 170K.

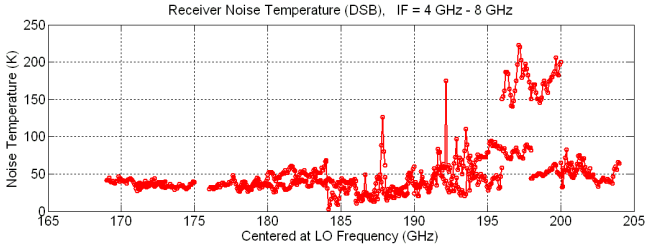

Fig. 5. An un-averaged noise measurement results of DSB mixer.

Fig. 6 displays the noise measurements averaged over the entire bandwidth, measurements shows results with around 35K noise across the band.

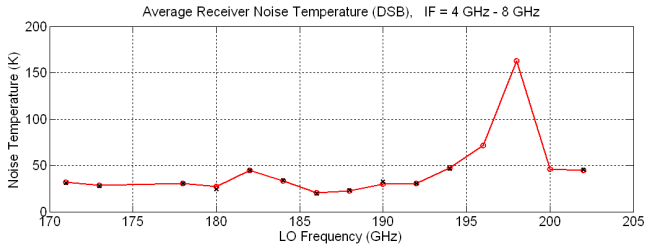

Fig. 6. Noise measurements averaged over the entire IF bandwidth.

After analysis, we realized that the increase in the noise temperature at around 197 GHz is associated with resonance in the mixer back piece. Fig. 7 shows the design of the mixer back piece and the position of the mixer chip. As discussed above, in order to provide better thermal contact between the mixer chip and the block, the mixer chip extends outside the wave guide.

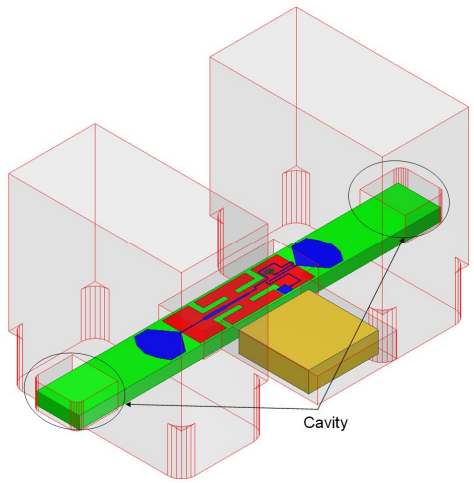

Fig. 7. The original mixer back piece design with deeper substrate channel.

The cavity created above the chip at the two ends causes resonance at around 197 GHz. Since the whole structure is electrically large and thus very complicated to simulate as the whole; we could not see this resonance effect in our simulations, while simulating each component separately. This resonance will also change the behavior of the RF chock structure. Fig. 8 shows the modified mixer back piece, where the top cover height is reduced about the chip, at the two ends. This should move the resonance frequency of the cavity outside the RF band. Fig. 9, shows the noise temperature measurements repeated after reducing the height of the cavity about the chip.

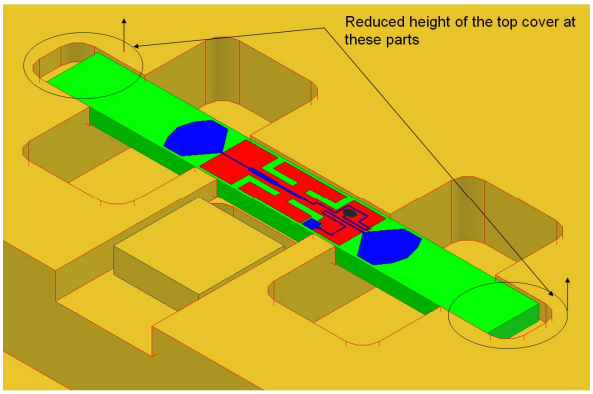

Fig. 8. Modified mixer block with reduced substrate channel height cures "resonances".

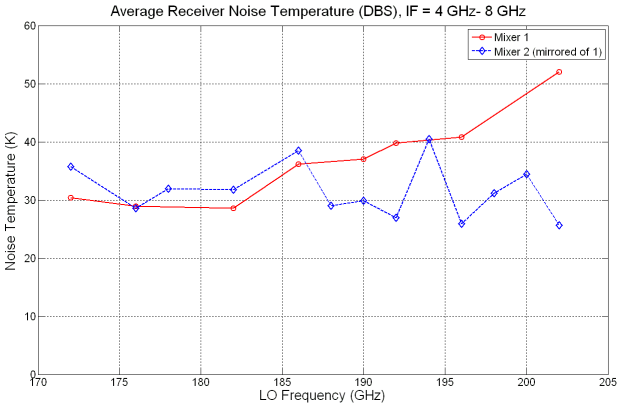

Fig. 9. DSB Noise measurement of two chips used in first 2SB test.

Evidently, the noise peak at 197 GHz is gone and the noise temperature for both the mixers, which are used further for SB measurements, is close to 40K.

IV. IF Hybrid Design

For the reasons discussed in earlier sections and [3], ALMA band 5 design requires a custom made IF hybrid. Since we can not put the SIS bias circuitry at 4K plate, an SIS DC bias-T circuitry is also integrated into the IF hybrid. In order to minimize the RF losses and eliminate series resistance in the SIS junction DC bias circuitry, we use all Niobium superconducting IF hybrid employing Lange-coupler. The pitch between the input SMA connector is pre-defined by the distance between the two output SMA connectors of the 2SB mixer block. The IF hybrid has been fabricated at the in-house facility and uses a 500µm thick Alumina substrate. In order to

avoid possible substrate mode, we use separate substrate of alumina for the Lange coupler itself and for connecting lines: one for the Lange coupler, two for 50 Ohm connecting lines and two for bias-Ts. The interconnection between the different substrates is done using bond wires. Fig. 10, shows the layout of the IF hybrid. DC biasing of the mixer use EMI protection filter bulkhead connectors.

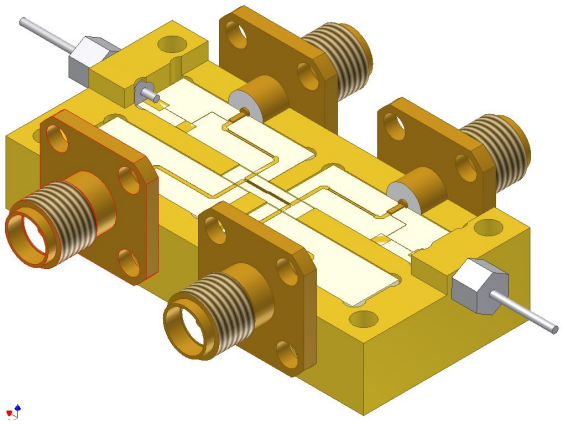

Fig. 10. IF Hybrid with integrated DC bias-Ts.

V. Single Sideband Measurement

Fig. 11 shows the measurement setup used for 2SB mixer measurements. Mixer output is connected directly to the IF hybrid, followed by an isolator. The noise measurements were performed by Y factor technique while the side band rejection measurements were made by placing a pilot signal at RF employing a comb-generator.

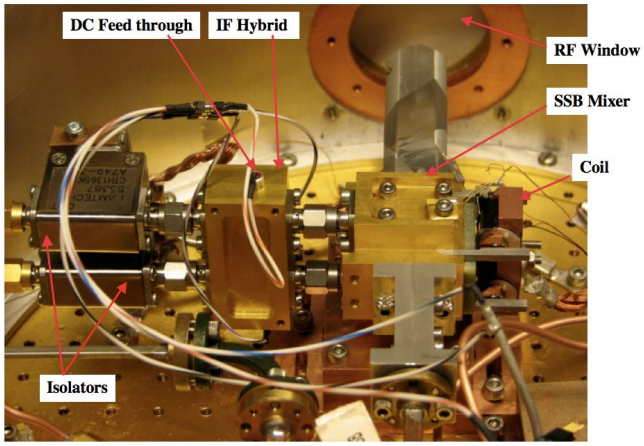

Fig. 11. Single sideband measurement setup.

In Fig. 12, the current voltage characteristics (IVCs) of the two mixers are presented after the suppression of super current and used in the 2SB measurements. Both the mixers have very symmetric and identical IV characteristics. However, it is noticeable difference in the noise performance of the mixers, especially at the higher frequencies of the RF band. While performing measurements of the 2SB configuration, we have noticed that the mixers susceptibility to the LO pumping is different despite the high similarity of the IVCs. We are investigating a possible reason for such behavior, which clearly causes degradation of the 2SB noise temperature as compared to the expected from DSB mixer tests.

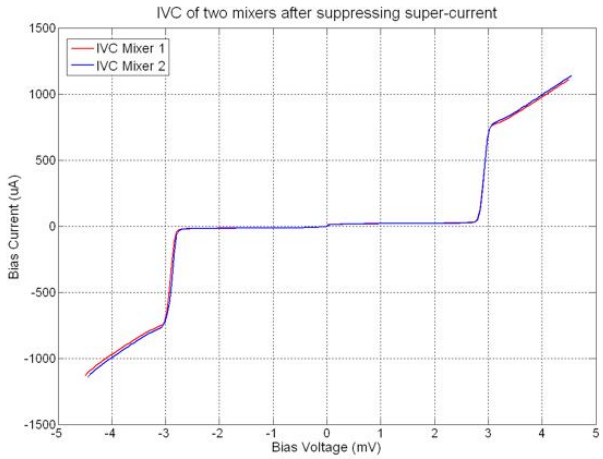

Fig. 12. IVC of two mixers used in 2SB mixer is highly identical that should provide required symmetry of the quardrature layout.

Fig. 13 shows the first noise measurement results of the single sideband mixer. The 2SB noise temperature is between 85K and 170K. This is far more than what we expected from DSB measurements. However, this is the first 2SB noise measurement and analysis of the results is in process.

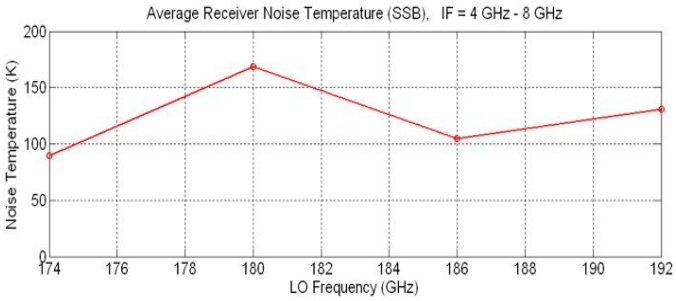

Fig. 13. SSB Noise temperature measurement

VI. Conclusions

In this paper, we present the design of ALMA Band-5 (163-211 GHz) mixer, measurement results of DSB mixer and first measurement results of the 2SB mixer. The mixer design uses on - chip LO injection circuitry employing a -18 dB microstrip – slot-line directional coupler and a high performance elliptical termination for the isolated port of the LO coupler. The DSB measurement of ALMA Band 5 mixer shows promising results with 35K to 40K noise temperature, across the band. The SSB measurements show noise temperature between 85K and 170K.

Acknowledgment

Authors would like to thank Dr. D. Meledin and D. Dochev for their help and useful discussion and Dr. V. Desmaris for his advice in designing and for the fabrication of the IF hybrid. We would like to thank our machining expert, Sven-Erik Ferm, for his useful tips and comments on designing the mixer block. Authors would like acknowledge Doug Henke, Dr. R. Monje and Dr. V. Vessilev for useful discussion and their help during the design of the mixer.

REFERENCES

[1] R. R. Monje, Vessen V. Vassilev, Alexey Pavolotsky and Victor Belitsky, "High Quality Microstrip Termination for MMIC and Millimeter-Wave Applications", *IEEE MTT-S International Microwave Symposium*, ISSN: 01490-645X, pages 1827-1830, Long Beach, California, June 12-17, 2005.

[2] Raquel Monje, Victor Belitsky, Christophe Risacher, Vessen Vassilev and Alexey Pavolotsky, "SIS Mixer for 385-500 GHz with on chip LO injection", *Proceedings of 18th International Symposium on Space Terahertz Technology*, March 2007.

[3] V. Belitsky, I. Lapkin, B. Billade, E. Sundin, A. Pavolotsky, D. Meledin, M. Strandberg, R. Finger1, O. Nyström, D. Henke, V. Desmaris, M. Fredrixon, S.-E. Ferm. "Prototype ALMA Band 5 Cartridge, Design and Performance", to be published in the *Proceedings of the 20th International Symposium on Space Terahertz Technology*, Charlottesville, 20-22 April 2009.

[4] Belitsky V. , Tarasov M.A., "SIS Junction Reactance Complete Compensation", *IEEE Trans. on Magnetic*, 1991, MAG- 27, v. 2, pt. 4, pp. 2638-2641.

[5] V. Belitsky V., S.W. Jacobsson, L.V. Filippenko, S.A. Kovtonjuk, V.P. Koshelets, E.L. Kollberg, "0.5 THz SIS Receiver with Twin Junctions Tuning Circuit., " *Proc. 4th Space Terahertz Technology Conference*, p.538, March 30 - April 1, 1993, Los Angeles, USA.

[6] John Tucker and Marc Feldman, "Quantum detection at millimeter wavelengths", *Review of Modern Physics*, vol. 57, No. 4, Oct 1985.

[7] V. Belitsky, C. Risacher, M. Pantaleev, V. Vassilev, "Model Study of Superconducting Microstrip Line at Millimeter and Sub-Millimeter Waves", *Int. Journal of Infrared and Millimeter Waves*, Vol.27, No. 6, pp. 809-834, June 2006, ISSN 0105-9271, Springer.

[8] J. Kooi, G. Chattopadhyay, S. Withington, F. Rice, J. Zmuidzinas, C. Walker, and G. Yassin, "A full height waveguide to thin film micro-strip transition with exceptional RF bandwidth and coupling efficiency", *Int. Journal of Infrared and Millimeter Waves*, Vol. 24, no. 3, 2003.

[9] A. R. Kerr, "Surface impedance of superconductors and normal conductors in EM simulators", MMA memo no. 245, Jan 1999. Available: http://www.alma.nrao.edu/memos/.

Development of SIS Mixers for SMA 400-520 GHz Band

Chao-Te Li, Tse-Jun Chen, Tong-Liang Ni, Wei-Chun Lu, Chuang-Ping Chiu, Chong-Wen Chen, Yung-Chin Chang, Ming-Jye Wang and Sheng-Cai Shi

***Abstract*—SIS junction mixers were developed for SMA 400-520 GHz band. The results show receiver noise temperature around 100 K across the band, with noise contribution from RF loss and IF estimated to be around 50 K and 20K, respectively. Two schemes were used to tune out junction's parasitic capacitance. When a parallel inductor is employed, the input impedance is close to R_n, which facilitates impedance matching between the junction and the waveguide probe. Waveguide probes were designed to achieve a low feed-point impedance to match to the junction resistance. Optimum embedding impedances for lower receiver noise temperature were investigated. Performances of two schemes and composition of receiver noise were also discussed.**

***Index Terms*—integrated tuning circuit, SIS junction mixer, SMA, waveguide probe**

I. Introduction

The Sub-millimeter Array (SMA)[1,2], constructed by Smithsonian Astrophysical Observatory (SAO) and Institute of Astronomy and Astrophysics, Academia Sinica (ASIAA) is a radio interferometer of eight 6-m antennas. Receivers with superconducting-insulator-superconducting (SIS) mixers are being used for observations through major submillimeter atmospheric windows from 180 GHz to 900 GHz. This paper describes the development of SIS mixers for one target frequency band (400-520 GHz). The emphasis of this work is to compare mixer designs with two different tuning schemes and explore the optimum embedding impedance for lower receiver noise temperature. We adopted the single-junction design, considering low LO power available at high frequencies.

II. Waveguide Probe Design

To be consistent throughout the array operations, we adopted SAO's mixer block design. A detailed drawing of the center portion of the mixer block is shown in Fig. 1. The reduced height waveguide section (0.55 x 0.138 mm) has a fixed back-short, measuring 0.17 mm in depth. The fused quartz mixer chip, measuring 0.250 x 0.050 x 2.276 mm, is clamped between the horn section and the back piece of the block in a suspended microstrip configuration. The thickness of the substrate is reduced from 0.060 mm to 0.050 mm to avoid higher order modes of propagation along the microstrip transmission lines seen during simulations.

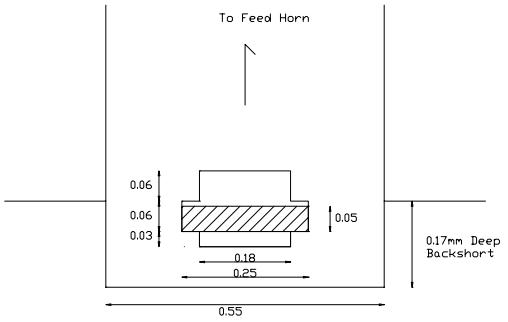

Fig. 1. Sectional view of the mixer block center portion. The quartz substrate is hatched. The cross section of the suspended microstrip and the fixed back-short of the block are shown. All dimensions are in mm.

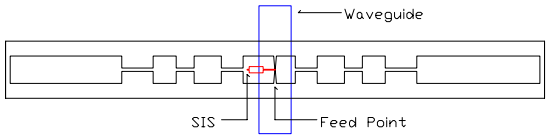

Fig. 2. Top view of the mixer chip sitting in a channel along the E-plane of the waveguide.

A bow-tie probe[3] was used with its feed point located at the center of the waveguide. The RF chokes following the low-impedance sections of the probe present an open at RF to the probe. The feed-point impedance can be reduced by shortening the lengths of probe's low-impedance sections. However, to accommodate the circuit consisting of the SIS junction, the tuning circuit, and impedance transformers, one side of the probe is extended as shown in Fig. 2. The shape of the probe also has some effect. In general, a broader probe (large θ in Fig. 5) yields a lower feed-point impedance. This configuration, along with the RF chokes, creates a feed-point impedance of about 26 Ω – j 23 Ω at 460 GHz, shown as the blue trace in Fig. 3. The waveguide probe was simulated using

C. T. Li, T. J. Chen, T. L. Ni, W. C. Lu, C. P. Chiu, C. W. Chen, Y. C. Chang and M. J. Wang are with the Institute of Astronomy and Astrophysics, Academia Sinica, Taipei, 10617 Taiwan (phone: 886-2-3365-2200; fax: 886-2-2367-7849; e-mail: ctli@asiaa.sinica.edu.tw).

S. C. Shi is with the Purple Mountain Observatory, Chinese Academy of Sciences, Nanjing, 210008 China (e-mail: scshi@mail.pmo.ac.cn).

a 3-D EM field simulator (HFSS). During simulations, the back-short depth was reduced to rotate the impedance locus onto the real axis of the Smith chart, shown as the red trace in Fig. 3.

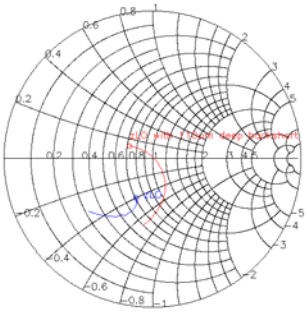

Fig. 3. Locus of the waveguide probe feed point impedance (in blue), and that with a reduced back-short (in red) from 400 GHz to 520 GHz. Circles mark where the impedances are at 400 GHz.

III. Tuning Circuits

There are two different schemes to tune out the junction's capacitance, as shown in Fig. 4, along with their corresponding optimum source resistance. End-loaded stubs were widely used as series inductors. This topology also lends itself to distributed junction designs. However, after the junction's capacitance is tuned out, the resistance converted by the series inductor is $R' = R/(\omega RC)^2$, much lower than R when $(\omega RC)^2 >> 1$. It usually requires 2 quarter-wavelength impedance transformers to bring the input impedance up to the level of few tens of ohms to match the feed-point impedance, as shown in Fig. 5. On the other hand, with a parallel inductor, the input impedance of the tuned junction is R, which is on the order of the junction normal state resistance R_n. Thereby only one or none impedance transformer is needed. This facilitates the impedance matching between the junction and the waveguide probe. Hopefully the bandwidth of the design would not be affected by that of transformers.

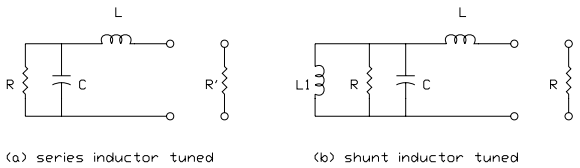

Fig. 4. Equivalent circuits of (a) a series inductor end-loaded with a junction, and (b) a parallel-inductor-tuned junction, where C represents the junction capacitance, R is the junction resistance, and $R' = R / (\omega RC)^2$.

For our designs, the end-loaded configuration corresponds to Fig. 1 (b) in [4] with $\omega RC \sim 4$ and $\omega L/R \sim 0.3$. The parallel-inductor-tuned case can be referred to Fig. 1 (c) in [4] with L = 0. From the analysis[4], despite the difference in input impedances, both configurations have similar bandwidths when terminated with their respective optimum source resistance. To increase the bandwidth, it would be necessary to reduce the value of ωRC or adopt a multi-junction design.

Fig. 6 shows how the input impedances at LO frequencies Z_{inLO} evolve after each section of transmission lines for our end-loaded design. Z_{inLO} is calculated via the complex current response of the junction at each LO frequency. The value could be quite different from the input impedance at RF, Z_{in}, which is derived from inversion of junction's admittance matrix. Simulation is done using the 5-port approximation to the quantum mixer theory[5] and an analytical model for thin-film superconducting microstrip lines[6]. The design comprises Nb/Al-AlO_x/Nb tunnel junctions integrated with Nb/SiO_2/Nb microstrip tuning circuits. The junction is characterized by a normal state resistance R_n of 19.5 Ω, J_c of 10 kA/cm^2, a junction area of 1 μm^2, and a junction capacitance of 90 fF. The simulated single-side-band (SSB) T_{RX} is shown in Fig. 7, along with the LO coupling and 4 times quantum noise limit.

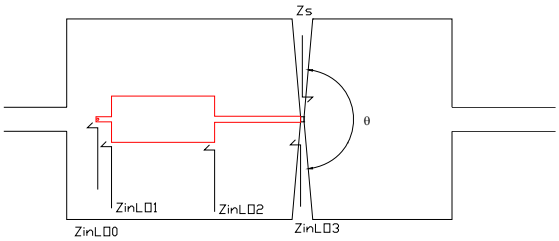

Fig. 5. The tuning circuit and impedance transformers for an end-loaded design, where $Z_{inLO\,i}$, i = 1, 2, and 3, is the input impedance of the junction after each section of transmission line at LO frequencies, and Z_s is the feed-point impedance.

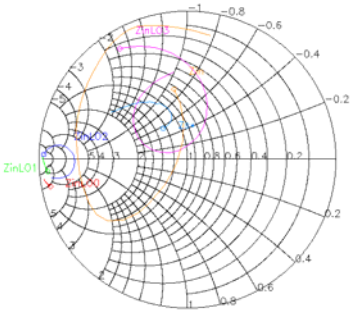

Fig. 6. Loci of the input impedance of the junction, Z_{inLO0} and those after each section of transmission line ($Z_{inLO\,i}$, i = 1, 2, and 3) of the end-loaded design at LO frequencies from 380 to 540 GHz. Z_{in} is the input impedance at signal frequencies. Z_s* is the complex conjugate of the feed point impedance. Circles indicate the start of impedance loci at 380 GHz. After the series inductor (or the end-loaded stub), the imaginary part of junction admittance is mostly cancelled, while the remaining resistance is on the order of 1 Ω. After 2 impedance transformers, the input impedance Z_{inLO3} is close to where Z_s* is on the Smith chart.

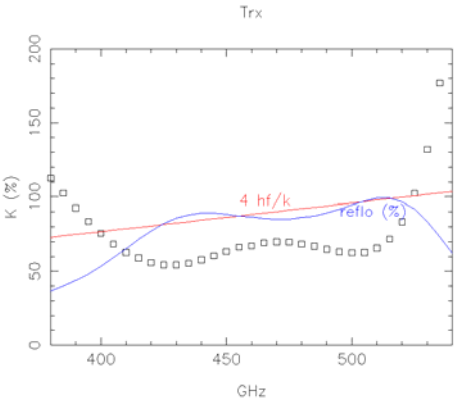

Fig. 7. The simulated SSB T_{RX} (square markers) of the series-inductor-tuned mixer design shown in Fig. 5. Four times quantum noise is plotted (red line) as a reference. The LO coupling (blue trace) is also shown. It is seen that good LO coupling corresponds to good T_{RX}, with a little displacement caused by the effects of G_m and T_{IF}.

In Fig. 8, for the design using a parallel inductor, a quarter-wavelength low-impedance open stub presents an RF short to a short, high-impedance stub as the inductor. The remaining resistance of the junction is about 18 Ω, close to the optimum resistance of 22 Ω derived from an empirical formula[7]

$$G_s = \frac{1}{2} + \frac{1}{4\omega}. \tag{1}$$

Since there is still some impedance difference, one transformer is placed between the junction and the feed-point. The impedance loci are shown in Fig. 9. The simulated T_{RX}, similar to that of the end-loaded design, is shown in Fig. 10.

IV. Optimum Embedding Impedance for Low Receiver Noise Temperature

To explore the optimum embedding impedance for lower receiver noise temperature, it is clear to look at the junction tuned with a parallel inductor so that the junction input impedance would not be transformed to a very small value after the inductor as in the end-loaded case. For the configuration in Fig. 7 without the transformer, Junction's capacitance is cancelled at LO of 485 GHz for our design. After calculations of the receiver noise temperature T_{RX}, the mixer noise temperature T_m, the mixer conversion gain G_m and the LO coupling over the Smith chart, as in Fig. 11, we can plot the contour enclosing the region where the T_{RX} is less than 70 K. Similarly, contours for T_m less than 40 K, G_m better than -2 dB, and LO coupling better than 95% can be drawn. Here

$$T_{RX} = T_m + \frac{T_{IF}}{G_m}. \tag{2}$$

All these values are for the single side band and the noise temperature of the IF chain T_{IF} is assumed to be 15 K. From Fig. 11, it can be seen that low T_{RX} can be achieved over a rather broad range on the Smith chart. The T_m contour does not coincide with the T_{RX} contour because the effects of T_{IF} and G_m.

On the other hand, the T_m contour is quite aligned with the LO coupling. Here the LO coupling is defined as the portion of available LO power delivered to the junction, namely

$$\frac{4\,\mathrm{Re}(Z_s)\,\mathrm{Re}(Z_{inLO})}{|Z_s + Z_{inLO}|^2}.$$

Since T_m is mainly due to correlation of the shot noise excited by the LO current[5], it is interesting to see that low T_m can be achieved when LO coupling is optimized.

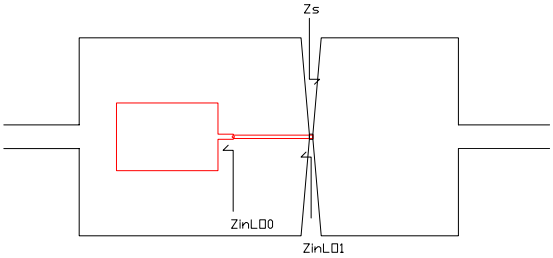

Fig. 8. Tuning circuit and impedance transformer for a SIS junction tuned with a parallel inductor.

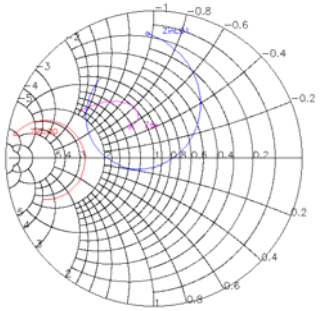

Fig. 9. Loci of the input impedance of the tuned junction Z_{inLO0} and that after the impedance transformer Z_{inLO1}, along with the complex conjugate of the feed point impedance Z_s* at LO frequencies from 380 to 540 GHz.

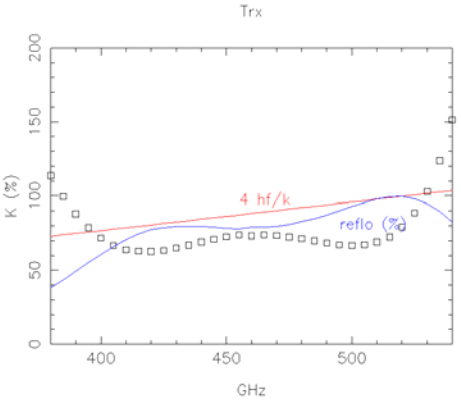

Fig. 10. The simulated SSB T_{RX} (squares), 4 times quantum noise limit (the red line), and the LO coupling (the blue trace) for the parallel-inductor-tuned mixer design shown in Fig. 8.

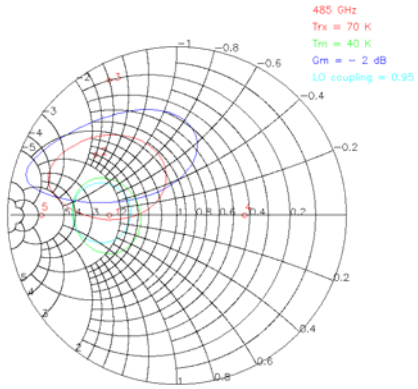

Fig. 11. Contours of T_{RX} (red), T_m (green), G_m (blue), and LO coupling (cyan) on the Smith chart for the design with a parallel inductor tuning circuit at 485 GHz, where junction's parasitic capacitance is cancelled. The optimum source conductance to give better T_m is around 2.5 (normalized to 1/50 Ω^{-1}), which corresponds to a source resistance of 20 Ω, consistent with the value given by (1).

V. Testing

A. Parallel-inductor- tuned

From receiver noise temperature measurements using the standard hot/cold load technique, some samples with a parallel inductor show a bandwidth not as wide as designed, as shown in Fig. 12. There are 2 factors that might cause this discrepancy. One possibility is the low R_n seen in these devices. Another factor might be the frequency response of the open stub used as a short to the parallel inductor. The bandwidth of a 1/4 wavelength open stub might be narrower, compared to a radial open stub. In addition, the discontinuity (the abrupt width change) between the open stub and the inductor is not modeled yet during simulation. There is an intention to have some designs using radial stubs for further verification.

We also did some analysis to break-down each contribution to the receiver noise temperature at several LO frequencies from the measurements of one device (460NTHU-1-1 IAA-C2-063) as shown in Table I.

TABLE I Receiver Noise Temperature Decomposition

LO Freq (GHz)	T_{RX} (K)	T_{RF} (K)	$T_{RF} + T_m/G_{RF}$ (K)	T_{IF} (K)	$G_{RF}\,G_m$ (dB)	T_{RX}' (K)
432	94.7	30.8	60.1	8.9	-3.9	82.2
452	126.7	35.3	90.9	8.9	-5.4	121.6
464	134.7	43.2	97.6	9.0	-5.4	128.7
488	126.7	49.9	94.9	9.2	-4.3	119.4

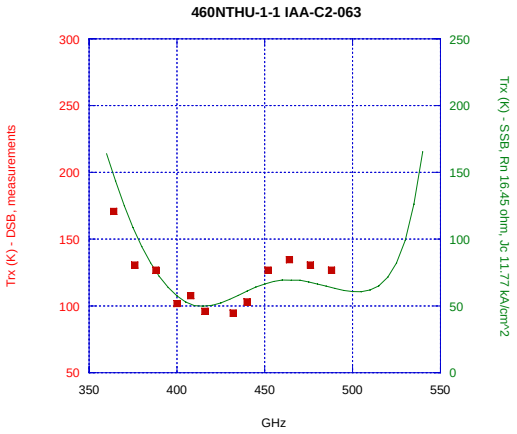

Fig. 12. Measured and simulated T_{RX} as a function of LO frequencies. The square is the double-side-band (DSB) T_{RX} measured from a sample (460NTHU-1-1 IAA-C2-063) with a parallel inductor, R_n = 16.5 Ω (lower than the design value of 19.5 Ω) and Jc = 11.8 kA/cm^2. The green trace is the simulated SSB T_{RX} from the design with the same junction parameters as the sample. Simulation results imply that besides the low R_n, there might be other factor responsible for the narrower bandwidth.

In Table I, at each LO frequency, T_{RX} is the measured DSB noise temperature. As shown in Fig. 13, T_{RX} can be decomposed into 3 terms, namely T_{RF} from the optical loss, T_m from the mixer itself, and T_{IF} from the IF amplifier, associated with the optical loss $1/G_{RF}$, and the mixer conversion gain G_m. The noise contribution from the optical loss T_{RF} is estimated using the intersecting-line method[8, 9]. T_{IF} is extrapolated along with the shot noise[10] of the junction above the gap voltage. Through this procedure, the correspondence between the noise temperature at mixer output and the measured IF power is established, from which we can figure out the overall conversion gain, i.e. $G_{RF}G_m$ of the system from the hot/cold load data. At last, $T_{RF} + T_m/G_{RF}$ can be estimated from the Y factor method with a modified Y factor as

$$Y' = \frac{P_{hot} - P_{gap}}{P_{cold} - P_{gap}} = \frac{T_{hot} + T_{RF} + T_m / G_{RF}}{T_{cold} + T_{RF} + T_m / G_{RF}}, \quad (1)$$

where P_{gap} is the IF power measured as the junction is biased at the gap voltage where the mixer conversion gain G_m can be considered as zero and the IF power output is due to T_{IF} alone[11]. The last column T_{RX}' is the sum of $T_{RF}+T_m/G_{RF}$ and $T_{IF}/(G_{RF}G_m)$. We can see that there are about 6 – 13 K discrepancy between the measured T_{RX} and the added-up one.

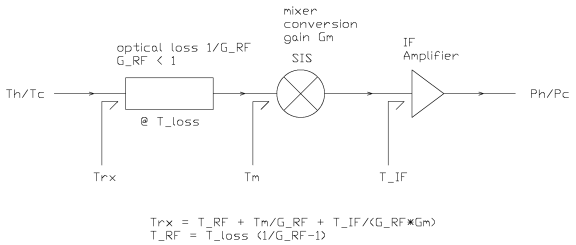

Fig. 13. Break-down of a receiver noise temperature (T_{RX}).

Using $T_{m,DSB}$ from simulations, we can further process the data to estimate G_{RF}, $G_{m,DSB}$, and T_{loss}, and compare with the $G_{m,SSB}$ from simulations for consistency check, as shown in Table II. At 432 and 488 GHz, $G_{m,DSB}$ agrees well with $G_{m,SSB}$ as $G_{m,DSB} = G_{m,SSB} + 3$ dB. The optical loss includes the loss (~ 0.07 dB) through the 5° LO coupling wire grid, the vacuum window, the IR blocking filter, the Teflon lens in front of the mixer block, and waveguide loss inside the mixer block. This might explain the low T_{loss} derived since the mixer block is anchored to 4 K.

TABLE II G_{RF}, $G_{m,DSB}$, AND T_{loss} DERIVED USING $T_{m,DSB}$ FROM SIMULATIONS

LO Freq (GHz)	$T_{m,DSB}$ (K)	T_m/G_{RF} (K)	G_{RF} (dB)	$G_{m,DSB}$ (dB)	$G_{m,SSB}$ (dB)	T_{loss} (K)
432	19.1	29.3	-1.9	-2.1	-4.8	57.2
452	21.0	54.7	-4.2	-1.2	-6.0	22.0
464	23.5	54.4	-3.7	-1.8	-5.9	32.9
488	26.3	45.0	-2.3	-1.9	-5.1	69.9

For direct detection, the sample was used as the detector in a Fourier transform Spectrometer (FTS). The results show that the device has reasonable response within the designed frequency range as shown in Fig. 14. One major factor that affects the FTS response is the product of the intrinsic current responsivity R_i of the junction to the radiation and the (LO) coupling, as plotted as the green trace in Fig. 15. As both T_{RX} and FTS response closely related to the (LO) coupling, proximity of low T_{RX} and the peak of the FTS response is observed.

For a sample with higher R_n (18.8 Ω, closer to the design value of 19.5 Ω), the frequency response has a wider bandwidth and agrees well with the simulation, except at higher frequencies near 500 GHz, as shown in Fig. 16. Limited by the LO available above 500 GHz at the moment, further tests above 500 GHz are required to verify the rising T_{RX} near 500 GHz.

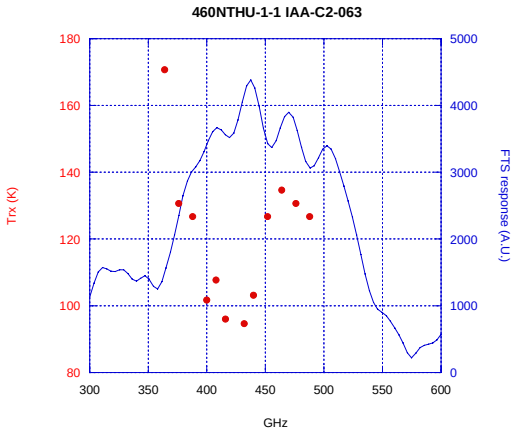

Fig. 14. T_{RX} as a function of LO frequencies and the measured FTS response. The lowest T_{RX} is close to where the peak FTS response is, with few GHz offset. Radiation intensity from the FTS is not yet calibrated.

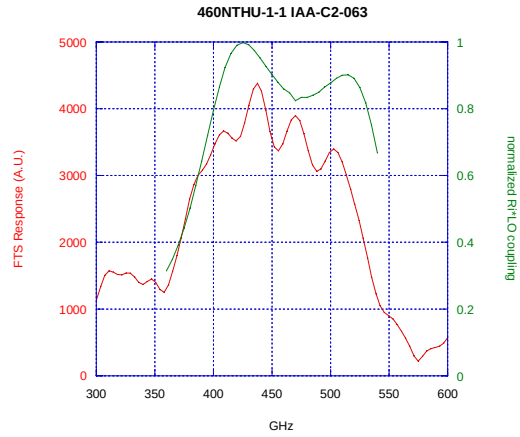

Fig. 15. The measured FTS response (red) and the simulation (the green trace as the product of the junction intrinsic current responsivity to LO - R_i and the LO coupling, normalized to its peak value). From simulation, R_i decreases monotonically to 65% from 360 GHz to 540 GHz while the LO coupling exhibits the 2-hump structure.

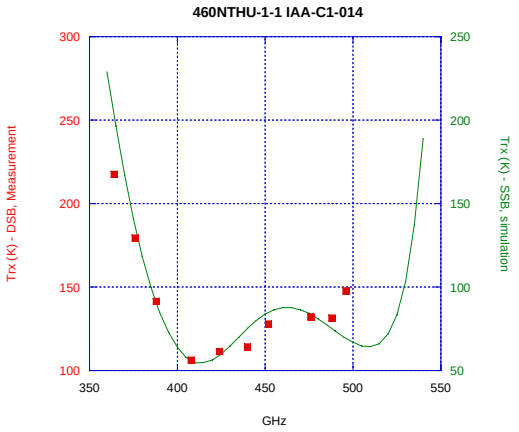

Fig. 16. Measured DSB T_{RX} of a device (460NTHU-1-1 IAA-C1-014) with a higher R_n (18.8 Ω, closer to the design value of 19.5 Ω) and simulations as a function of LO frequencies. The squares are the measured DSB T_{RX}. The green curve is the simulated SSB T_{RX} from the same design with R_n = 19.5 Ω, junction area of 1 μm^2 and junction capacitance of 90 fF. The measurements were done with 10° LO wire grid (94% transmission) and a un-blazed Teflon lens in front of the mixer block. As a result, the noise contribution from the optical loss (T_{RF}) is between 60 - 70K.

B. End-loaded scheme

For devices with an end-loaded inductive stub, despite the 2 quarter wavelength transformers used to transform the low impedance (< 1 Ω) of the tuned junction to the level of the embedding impedance, the test results show this kind of design exhibits a comparable bandwidth, as shown in Fig. 17 and 18. Similar noise analysis is done for one device (460NTHU-1-1 IAA-C5-047), listed in Table III. The difference between the measured T_{RX} and the added-up one is now less than 10 K.

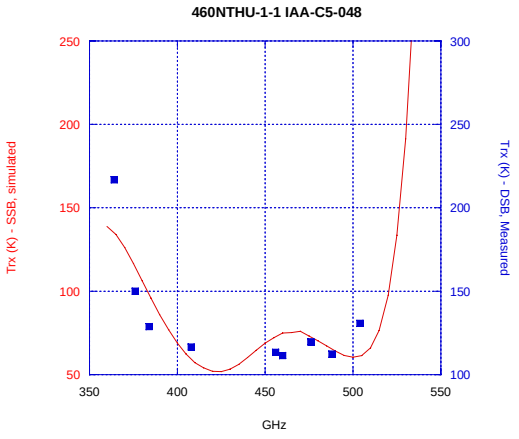

Fig. 17. T_{RX} of a device (460NTHU-1-1 IAA-C 5-048) with an end-loaded tuning stub as a function of LO frequency. The blue squares are measured DSB T_{RX}, while the red trace represents the simulated SSB T_{RX} with the same junction normal state resistance R_n, junction area, and the super current density J_c as the sample. The measurements follow the simulation quite well, except at 1 or 2 data points. During the testing, the noise contribution from the IF amplifier T_{IF} is estimated to be around 17K. The noise due to optical loss T_{RF} is estimated to be from 66 to 77K. T_{RF} is rather large because of the large degrees of LO coupling wire grid (10°, corresponding to 94% transmission) and a Teflon lens without anti-reflection blazing used in front of the mixer block.

VI. Conclusion

SIS junction mixers with 2 different tuning schemes were designed and tested for SMA 400-520 GHz band. The design with a parallel inductor has the advantage of higher input resistance. Thereby the matching between the junction and the probe can be and more compact and less complicated. However, from both simulations and measurements, two schemes have similar performances, with regard to receiver noise temperature or bandwidth. The optimum embedding impedance for low mixer noise temperature T_m is found to be where the LO coupling is efficient. Further testing is required to verify the mixer response above 500 GHz, as well as the effect of the open stub in the parallel-inductor-tuned design.

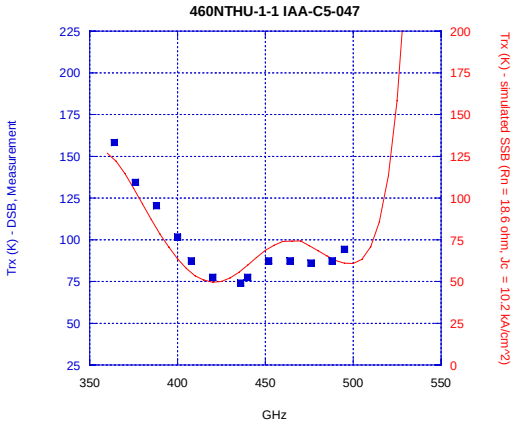

Fig. 18. Measured and simulated T_{RX} of another device (460NTHU-1-1 IAA-C5-047) also with an end-loaded tuning stub as a function of LO frequency. The blue squares are measured DSB T_{RX}, while the red trace represents the simulated SSB T_{RX} with the same junction normal state resistance R_n, junction area, and the super current density J_c as the sample. During the test, a smaller LO wire grid angle (5°, corresponding to 98.5% transmission, except at 495 GHz, where the wire grid is 10°) and a Teflon lens with anti-reflection blazing were used. Break-down of receiver noise contribution is listed in Table III.

TABLE III Receiver Noise Temperature Decomposition

LO Freq (GHz)	T_{RX} (K)	T_{RF} (K)	$T_{RF} + T_m/G_{RF}$ (K)	T_{IF} (K)	$G_{RF}\ G_m$ (dB)	T_{RX}' (K)
436	79.8	49.8	67.2	7.7	-2.5	80.9
452	93.3	52.7	70.0	7.6	-2.7	84.1
464	93.3	50.6	69.1	7.5	-3.1	84.4
488	93.3	57.6	75.6	7.9	-2.0	88.2

References

[1] R. Blundell, C. E. Tong, D. C. Papa, R. L. Leombruno, X. Zhang, S. Paine, J. A. Stern, H. G. LeDuc, and B. Bumble, "A wideband fixed-tuned SIS receiver for 200-GHz Operation," *IEEE Trans. Microwave Theory Tech.*, vol. 43, pp. 933-937, 1995.

[2] C. E. Tong, R. Blundell, S. Paine, D. C. Papa, J. Kawamura, X. Zhang, J. A. Stern, and H. G. LeDuc, "Design and characterization of a 250-350 GHz fixed-tuned superconductor-Insulator-superconductor receiver," *IEEE Trans. Microwave Theory Tech.*, vol. 44, pp. 1548-1556, 1996.

[3] A. V. Raisanen, W. R. McGrath, D. G. Crete, and P. L. Richards, "Scaled model measurements of embedding impedances for SIS waveguide mixers," *Int. J. IR and MM Waves*, vol. 6, pp. 1169-1189, 1985.

[4] A. R. Kerr, "Some fundamental and practical limits on broadband matching to capacitive devices, and the implications for SIS mixer design," *IEEE Trans. Microwave Theory Tech.*, vol. 43, pp.2-13, 1995.

[5] J. R. Tucker, "Quantum limited detection in tunnel junction mixers," *IEEE Journal of Quantum Electronics*, vol. QE-15, pp.1234-1258, 1979.

[6] W. H. Chang, "The inductance of a superconducting strip transmission line," *J. Appl. Phys.*, vol. 50, pp.8129-8134, 1979.

[7] Q. Ke, M. J. Feldman, "Optimum source conductance for high frequency superconducting quasiparticle receivers," *IEEE Trans. Microwave Theory Tech.*, vol. 41, pp.600-604, 1993.

[8] R. Blundell, R. E. Miller, and K. H. Gundlach, "Understanding Noise in SIS Receivers," *Int. J. IR and MM Waves*, Vol. 13, No. 1, pp. 3-26, 1992.

[9] Q. Ke and M. J. Feldman, "A technique for noise measurements of SIS receivers," *IEEE Trans. Microwave Theory Tech.*, 42, 752, 1994.

[10] D. P. Woody, R. E. Miller, and M. J. Wengler, "85-115 GHz receivers for radio astronomy," *IEEE Trans. Microwave Theory Tech.*, 33, 90, 1985.

[11] S. C. Shi, "Quantum-limited broadband mixers with superconducting tunnel junctions at millimeter and submillimeter wavelengths," Ph.D. Dissertation, 1996

An 800 GHz SIS Receiver for the RLT Incorporating a HIFI Band 3-type Mixer and SiGe LNA

A. Hedden, H. Li, E. Tong, S. Paine, R. Blundell, J. Kawamura, C. Groppi, C. Kulesa, C. Walker, G. de Lange, T. Klapwijk, T. Zijlstra, H. Mani, and S. Weinreb

***Abstract*—We have constructed an 810 GHz receiver system incorporating a superconductor-insulator-superconductor (SIS) mixer developed for Band-3 of the HIFI instrument for Herschel space observatory and a wide-band SiGe low noise amplifier (LNA) designed at Caltech. The instrument is currently installed at the RLT telescope (elevation 5500 m) in northern Chile. Hot/cold (280K/72K) load measurements performed at the telescope yield noise temperatures of 225 K (Y-factor = 1.7) including receiver optics. First-light observations indicate that the receiver is highly sensitive and functions stably. We present details of the receiver system, its performance at the telescope, and first-light observations with a Herschel mixer.**

***Index Terms*—radio astronomy, submillimeter wave receivers, submillimeter wave spectroscopy, superconductor insulator superconductor mixers**

I. INTRODUCTION

A key goal of upcoming space-based and airborne missions is improving our understanding of the structure of the Galactic interstellar medium (ISM) and the life cycle of interstellar clouds as a stepping stone to understanding the internal evolution of galaxies. Through the efforts of many researchers, the far-infrared (FIR) and terahertz (THz) atmospheric window, harboring important spectral line probes of molecular clouds and star formation, including high-J CO lines and N+ at around 1.3 and 1.5 THz, is becoming accessible with unprecedented sensitivity and resolution capabilities [1]-[4]. Complementary observations of key species in the 800 GHz atmospheric window are needed over large spatial scales (multiple square degrees) both for a more complete picture of the lifecycle of the ISM and for producing finder charts enabling the efficient use of new and upcoming THz observatories.

We have constructed and deployed (December 2008) a highly sensitive 810 GHz heterodyne receiver system to the RLT telescope in northern Chile [5] capable of making these much needed observations. At the heart of the receiver is an 800 GHz SIS mixer developed for Band-3 of the HIFI instrument [6, 7] to be launched in 2009. The mixer unit is connected to a wide-band SiGe LNA designed at Caltech [8]; the first of its kind to be used in a submillimeter (submm) receiver functioning at a telescope. The system operates with a 1-2 GHz IF capable of simultaneously observing important spectroscopic probes of star formation including neutral atomic carbon $^{12}C^0$ and $^{13}C^0$ J = 2-1 and carbon monoxide CO J = 7-6 lines near 809 GHz and 806 GHz, respectively.

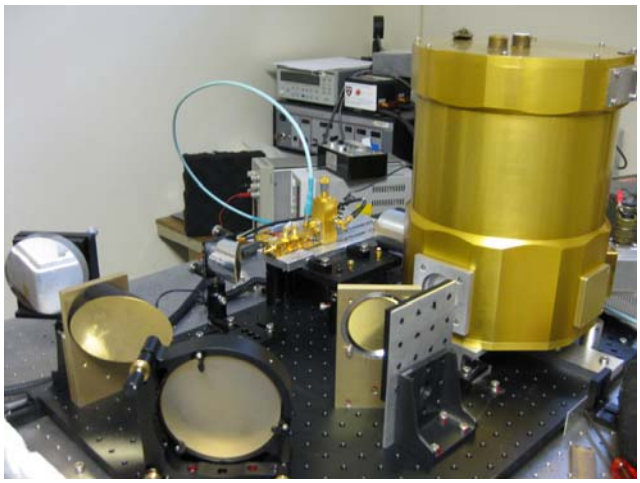

Fig. 1. Layout of the 810 GHz receiver system: view of receiver system operating in the laboratory complete with LO unit and all optics needed to couple the beam to the RLT.

Equipped with a spectrometer affording high spectral resolution (< 0.5 km/s) and coupled with a telescope beamsize of 1.9' at 810 GHz, this new RLT receiver system will provide important complementary observations to planned large-scale C+ and N+ surveys of the Galactic plane made by STO, an upcoming balloon-borne spectroscopic mission [9] in which

Manuscript received 20 April 2009.

A. Hedden*, H. Li, E. Tong, S. Paine, and R. Blundell are with the Harvard-Smithsonian Center for Astrophysics, Cambridge, MA 02138 USA (*corresponding author; phone: 617-495-7487; e-mail: ahedden@cfa.harvard.edu)

J. Kawamura is with the California Institute of Technology Jet Propulsion Laboratory, Pasadena, CA 91109 USA

C. Groppi, C. Kulesa, and C. Walker are with the University of Arizona Steward Observatory, Tucson, AZ 85721 USA

G. de Lange is with SRON, 9700 AV Groningen, the Netherlands

T. Klapwijk and T. Zijlstra are with the Kavli Institute of Nanoscience, Faculty of Applied Sciences, Delft University of Technology, Delft, the Netherlands

H. Mani and S. Weinreb are with the Dept. of Electrical Engineering, California Institute of Technology, Pasadena, CA 91125 USA

members of our team are involved. We present details of the receiver system, including results and performance at the RLT, and first-light observations obtained with a Herschel mixer.

II. Overview of the Receiver System

A. HIFI Band-3 Type Mixer Unit

The mixer assembly is a pre-flight spare for Band-3 of the HIFI instrument modified for use over a 1-2 GHz intermediate frequency (IF) range. The mixer is specified to operate between 800 and 960 GHz. It is projected to achieve a noise temperature of about 150 K at 800 GHz in the spacecraft under typical operating conditions. The details of the design and construction of the mixer are described in [10]. We have installed the mixer block in a liquid helium cooled cryostat equipped with an anti-reflection coated quartz vacuum window and infra-red blocking filters. Two off-axis parabolic mirrors, one placed inside the cryostat and a second one mounted outside the cryostat couple the beam emerging from the corrugated feed of the mixer block to the main telescope optics. The optical design was carried out with the use of the ZEMAX software package. The layout of our instrument is shown in Fig. 1.

B. SiGe Low Noise Amplifier

The mixer is connected to a SiGe IF amplifier [8] by a 10 cm long coaxial cable. This is the first use of a SiGe amplifier in a submm receiver system deployed on a telescope. Housed in a small package of about 3 cm x 2 cm x 1 cm, it has very low noise from 0.2 GHz to 4 GHz in addition to low power dissipation. Unlike most cryogenic HEMT amplifiers which require a servo loop to adjust the gate voltage so as to maintain a constant drain current and hence a stable gain, this SiGe amplifier can simply be operated with a fixed drain voltage. We have chosen a drain voltage of 1.4 V, which represents a compromise between several considerations (see Fig. 2). At lower bias voltage, the power dissipation is reduced and the gain flatness is improved. However, by increasing the bias voltage, higher gain and a lower noise temperature can be obtained. At our operating voltage, the power dissipation is only about 7 mW for a noise temperature of close to 4.5 K over the 1-2 GHz IF range. The gain of the amplifier is 38 dB at 1 GHz, decreasing to 36 dB at 2 GHz and to 33 dB at 4 GHz. The gain slope is further accentuated by the 1 meter long stainless steel coaxial cable connecting the amplifier to the output port of the cryostat. Gain equalization is achieved using the external IF processor resulting in a 2.5 dB variation in the power output spectrum.

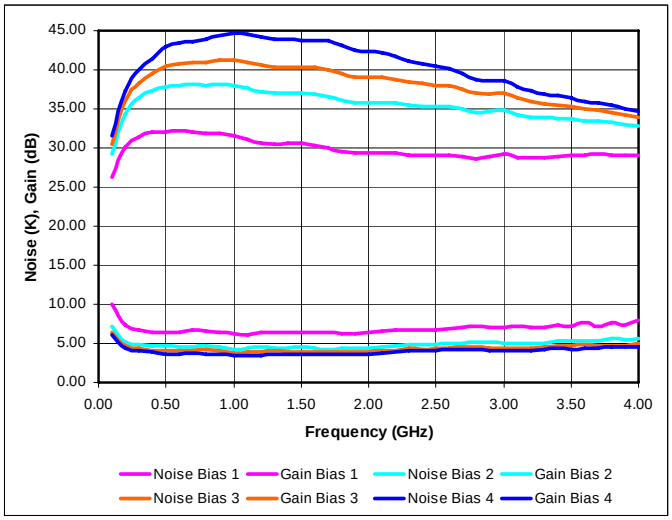

Fig. 2. Gain (top 4 curves) and noise (bottom 4 curves) characteristics of the SiGe LNA operated at 20 K with different drain voltages (cases 1-4 correspond to 1.1 V, 1.2 V, 1.3 V, and 1.6 V drain voltage). For operations with the 810 GHz receiver, a drain voltage = 1.4 V was used.

C. 810 GHz Local Oscillator Unit

The local oscillator (LO) unit used in this system incorporates a fixed-tuned planar diode doubler cascade developed by Jet Propulsion Laboratory for the Herschel space mission [11, 12]. The primary source is a Gunn oscillator operating at around 101 GHz. After passing through a compact coupler with an integrated harmonic mixer diode for phase-locking purposes, the output power of the Gunn oscillator is amplified by 2 stages of a W-band power amplifier to about 200 mW. This drives a cascade of 3 stages of frequency doublers to yield ~0.2 mW of radiated output power at 808 GHz. An off-axis mirror couples the LO power to the mixer through a wire grid polarizer oriented to reflect a small fraction of the LO output power which can be controlled by varying the drain bias voltage on the power amplifiers.

D. IF Setup and Backend Spectrometer

The purpose of the receiver is achieving simultaneous observations of three astronomically significant lines including neutral atomic carbon and carbon monoxide lines at around 809 GHz and 806 GHz, respectively. For this reason, the SIS mixer is operated in double-side-band mode at a fixed LO frequency of about 808 GHz. Using a 1-2 GHz IF, the carbon lines appear in the upper-side-band, and the CO line appears in the lower-side-band. A digital autocorrelator made by Spaceborne, Inc. with 1024 channels and a maximum bandwidth of 1 GHz was used as a backend spectrometer, resulting in a channel width of 1 MHz and a corresponding spectral resolution of 0.4 km/s at 810 GHz.

III. Results

A. Lab Measurements and Characterization

The SIS mixer operates best with a magnetic field that delivers 2 quanta of magnetic flux to the junction. This corresponds to a coil current of around 15 mA. At higher field strength, the quality of the SIS device is visibly degraded while at lower levels, receiver stability is poor. The optimal operating bias point of the mixer is found to be at 2.1 mV and 50 μA. To achieve this operating condition, we set the wire grid polarizer angle at about 5 degrees to the LO for signal coupling. This is equivalent to about 1.5% LO coupling and results in minimal loss to the signal beam. Even at this low coupling level, the LO unit does not need to be operated at full power. Standard hot/cold load sensitivity measurements were performed at the input pupil of the complete receiver system. A Y-factor of 1.7 was recorded, which translates into a receiver system noise temperature of 235 K (Rayleigh-Jeans temperature), averaged over the entire IF pass-band. This sensitivity compares favorably to lab measurements reported by the HIFI Band-3 development team [10] given that our bath temperature is at 4.2 K, the entire optics train is included in our measurement, and the mixer is being operated over an IF range different to the Band-3 design.

Before installation of the warm optical components, the beam emerging from the cryostat was mapped both in amplitude and phase by a near-field scanner with an open waveguide probe. Adjustments were made so that the axis of the measured beam coincided with the normal to the center of the cryostat window. Then the warm optical components were positioned after careful optical alignment. Finally, the receiver beam profile at the input pupil of the receiver system was measured for final adjustment and verification. This two-step radio/optical alignment procedure was introduced in the deployment of a 1.5 THz superconducting receiver [13] but this work confirms the utility of this method by the reproducibility and validity of the near-field measurements. In practice, this method has proven to be invaluable for producing good, repeatable alignment between the cryostat, SIS mixer, and the receiver / telescope optics, in addition to minimizing optical alignment efforts at high elevation.

B. Performance at the Telescope

The RLT telescope is located 40 km north of the ALMA site in northern Chile at an elevation of 5525 m, one of the best ground-based sites for terahertz astronomy with atmospheric transmission as high as 50% above 1 THz [5,14]. A Fourier Transform Spectrometer (FTS) is also located at the site and operates continuously, providing measurements of sky brightness to determine atmospheric opacity over the 350 GHz – 3 THz range [15] and calibration information for RLT spectroscopic observations. The telescope's primary mirror is 80 cm in diameter, resulting in a 1.9' beam at 800 GHz. The excellent observing conditions and modest beamsize (~5 pc at the Galactic center, capable of resolving star-forming clumps in nearby Giant Molecular clouds) make this telescope well suited to conducting large-scale surveys in the 800 GHz atmospheric window. To this end, the SIS receiver system described in this work was deployed to the RLT in early December 2008 and began its first observing campaign.

Fig. 3 shows receiver response measured at the RLT, including plots of mixer current vs. bias voltage with and without the local oscillator signal (pumped and unpumped IV curves) and receiver output power as a function of bias voltage for ambient temperature (280 K) and liquid nitrogen (72 K) blackbody loads (PV hot/cold curves) positioned at the input pupil of the receiver system. Optimal receiver response was achieved at a mixer bias of 2.3 mV and 55 μA, yielding a 225 K (Y = 1.7) receiver noise temperature at 808 GHz, an improvement of 10 K over lab performance and a factor of 5 better than noise levels achieved with the 800 GHz HEB receiver that this system replaced. This new receiver achieves a performance that is comparable to 800 GHz SIS receiver systems currently operating at similar sites, including CHAMP+ [16] on the APEX telescope (SSB noise

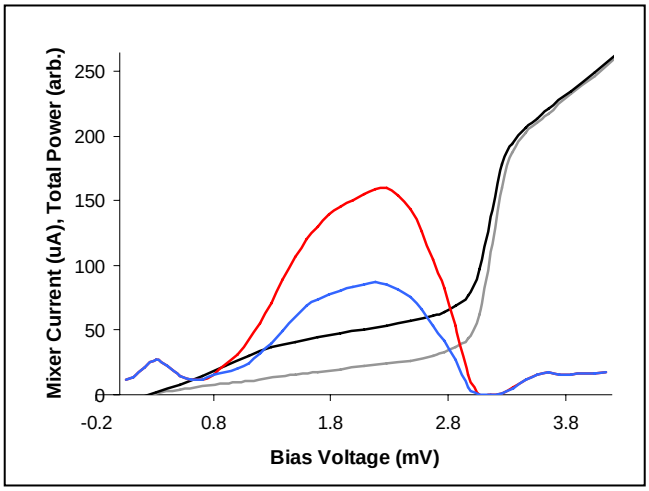

Fig.3. Performance at the RLT at 808 GHz, including pumped (black) and unpumped (gray) IV curves and hot (red) / cold (blue) total power measurements (PV curves; note that total power is in arbitrary units, arb.) Optimal performance (Y = 1.7) was achieved at a mixer bias of 2.3 mV and 55 μA, resulting in receiver noise temperature of 225 K.

temperatures of ~700 K at 810 GHz) and the SMART array [17] on NANTEN 2 (DSB noise temperatures of 200-400 K after recent upgrades).

The weather during the December 2008 observing campaign was good overall, with a zenith transmission equal to year-round median levels (40% at 810 GHz) throughout the run. This resulted in system noise temperatures of 1000-2100 K at the elevation of our sources (~60°) throughout the observing run. First light observations made with the new SIS receiver system toward the NGC 2024 star-forming region indicate that the receiver is sensitive and reveal its power as a large-scale mapping instrument (see Fig. 4). The spectrum shown represents a total on-source integration time of 0.6 minutes and clearly shows both CO J = 7-6 (left, LSB) and weaker neutral carbon line (right, USB) with a high signal-to-noise (S/N) ratio, > 15 at the $^{12}C^{0}$ line center and ~4-5 in the

CO line wings. The LO frequency was changed during observations to verify the identity of these lines. The resolution of this spectrum is 0.4 km/s, adequate for resolving features in complex line profiles, enabling multiple clouds along the line of sight to be distinguished, and disentangling signatures of bulk gas motions such as rotation and outflow. This spectrum is part of a larger 20'×20' map made toward NGC 2024 in ~8.5 hours of total observing time, including telescope overhead, with the new SIS receiver on the RLT.

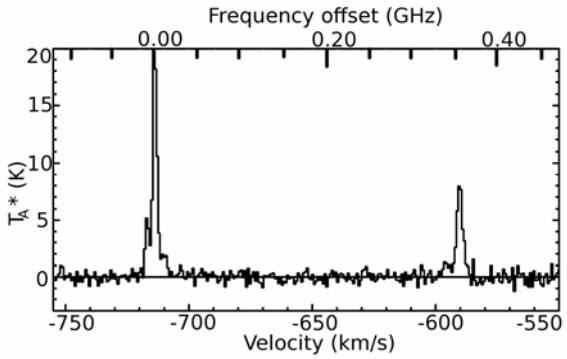

Fig. 4. Spectrum showing CO J = 7-6 (*left*, LSB) and $^{12}C^0$ J = 2-1 (*right*, USB) toward NGC 2024 made with the 810 GHz SIS receiver at the RLT. Axes show observed antenna temperature corrected for optical depth at source elevation and telescope scattering efficiencies (T_A^*) as a function of frequency offset from the CO line center (GHz), *top*, and velocity (km/s), *bottom*. These are first light observations for a Herschel Band-3 type mixer at a telescope.

IV. Conclusion

We have constructed and deployed an 810 GHz receiver system incorporating a HIFI Band-3 pre-flight spare SIS mixer developed for Herschel and a wide-band SiGe LNA to the RLT telescope (elevation 5500 m) in northern Chile. Receiver sensitivity achieved at the telescope is slightly improved over laboratory measurements, resulting in noise temperatures of 225 K (Y = 1.7) measured at the input pupil of the receiver system. This compares favorably to measurements reported by the HIFI Band-3 team, given differences in operating conditions, and to the performance of 800 GHz SIS instruments currently operating at similar sites. We present first-light observations with a Herschel Band-3 type mixer at a telescope and the results indicate that the 810 GHz SIS receiver system is sensitive, stable, and functions as a good large-scale mapping instrument. The location of the RLT and its primary beamsize at 800 GHz coupled with the sensitivity of this new receiver system and high spectral resolution capabilities add to its appeal as a survey instrument. Our team is embarking on a CO/C^0 selective survey of molecular clouds in the Galactic plane, providing an important complement to upcoming THz spectroscopic surveys with the STO balloon-borne mission.

References

[1] D. P. Marrone, J. Battat, F. B. Bensch, R. Blundell, M. Diaz, H. Gibson, T. Hunter, D. Meledin, S. Paine, D. C. Papa, S. Radford, M. Smith, and E. Tong, "A Map of OMC-1 in CO J = 9-8," *Astrophysical Journal.,* vol. 612, no. 2, pp. 940-945, September 2004.

[2] D. P. Marrone, R. Blundell, E. Tong, S. N. Paine, D. Loudkov, J. H. Kawamura, D. Luhr, and C. Barrientos, "Observations in the 1.3 and 1.5 THz Atmospheric Windows with the Receiver Lab Telescope," *Proc. 16th Int. Symp. Space THz Tech.*, S04-05, May 2005.

[3] M. C. Wiedner, G. Weiching, F. Bielau, K. Rettenbacher, N. H. Volgenau, M. Emprechtinger, U. U. Graf, C. E. Honingh, K. Jacobs, B. Vowinkel, K. M. Menten, L. A. Nyman, R. Güsten, S. Philipp, D. Rabanus, J. Stutzki, and F. Wyrowski, "First observations with CONDOR, a 1.5 THz heterodyne receiver," *Astronomy & Astrophysics.,* vol. 454, no. 2, pp. L33-L36, August 2006.

[4] C. E. Oberst, S. C. Parshley, G. J. Stacey, T. Nikola, A. Löhr, J. I. Harnett, N. F. H. Tothill, A. P. Lane, A. A. Stark, and C. E. Tucker, "Detection of the 205 μm [NII] line from the Carina nebula," *Astrophysical Journal.,* vol. 652, no. 2, pp. L125-L128, December 2006.

[5] D. P. Marrone, R. Blundell, H. Gibson, S. Paine, D. C. Papa, and C. E. Tong, "Characterization and status of a Terahertz telescope," *Proc. 15th Int. Symp. Space THz Tech.*, pp. 426-432, April 2004.

[6] M. Harwit, "The Herschel mission," *Advances in Space Research.,* vol. 34, no. 3, pp. 568-572, 2004.

[7] T. de Graauw, and F. P. Helmich, "Herschel-HIFI: The Heterodyne Instrument for the Far-Infrared", *The Promise of the Herschel Space Observatory*, ESA SP-460, pp. 45-51, 2001.

[8] S. Weinreb, J. C. Bardin, and H. Mani, "Design of cryogenic SiGe low-noise amplifiers," *IEEE Trans. Microwave Theroy Tech.,* vol. 55, pp. 2306-2312, November 2007.

[9] C. K. Walker, C. A. Kulesa, C. E. Groppi, E. Young, T. McMahon, P. Bernasconi, C. Lisse, D. Neufeld, D. Hollenbach, J. Kawamura, P. Goldsmith, W. Langer, H. Yorke, J. Sterne, A. Skalare, I. Mehdi, S. Weinreb, J. Kooi, J. Stutzki, U. Graf, C. Honingh, P. Puetz, C. Martin, and M. Wolfire, "The Stratospheric Terahertz Observatory (STO) an LDB experiment to investigate the life cycle of the interstellar medium," *Proc. 19th Int. Symp. Space THz Tech.*, pp. 28-32, April 2008.

[10] G. de Lange, B. D. Jackson, M. Jochemsen, W. M. Laauwen, L. de Jong, M. Kroug, T. Zijlstra, and T. M. Klapwijk, "Performance of the flight model HIFI band 3 and 4 mixer units," *Proc. SPIE* , vol. 6275, pp. 627517, July 2006.

[11] I. Mehdi, E. Schlecht, G. Chattopadhyay, and P.H. Siegel "THz local oscillator sources: performance and capabilities," *Proc. SPIE,* vol. 4855, pp. 435-446, 2003.

[12] I. Mehdi, G. Chattopadhyay, E. Schlecht, J. Ward, J. Gill, F. Maiwald, and A. Maestrini, "Terahertz multiplier circuits," *IEEE MTT-S Symposium Digest*, pp. 341-344, June 2006.

[13] C. E. Tong, D. N. Loudkov, S. N. Paine, D. P. Marrone, and R. Blundell, "Vector measurement of the beam pattern of a 1.5 THz superconducting HEB receiver," *Proc. 16th Int. Symp. Space THz Tech.,* pp. 453-456, May 2005.

[14] R. Blundell, J. W. Barrett, H. Gibson, C. Gottleib, T. R. Hunter, R. Kimberk, S. Leiker, D. Marrone, D. Meledin, S. Paine, D. C. Papa, R. J. Plante, P. Riddle, M. J. Smith, T. K. Sridharan, C. E. Tong, and R. W. Wilson, "Prospects for Terahertz radio astronomy from northern Chile," *Proc. 13th Int. Symp. Space THz Tech.*., pp. 159-166, March 2002.

[15] S. Paine, R. Blundell, D. C. Papa, J. W. Barrett, and S. J. E. Radford, "A Fourier Transform Spectrometer for measurement of atmospheric transmission at submillimeter wavelengths," *Publications Astron. Soc. Pacific,* vol. 112, pp. 108-118, January 2000.

[16] C. Kasemann, R. Güsten, S. Heyminck, B. Klein, T. Klein, S. D. Philipp, A. Korn, G. Schneider, A. Henseler, A. Baryshev, T. M. Klapwijk, "CHAMP+: a powerful array receiver for APEX," *Proc. SPIE*, vol. 6275, pp. 62750N, July 2006.

[17] U. U. Graf, S. Heyminck, E. A. Michael, S. Stanko, C. E. Honingh, K. Jacobs, R. T. Scheider, J. Stutzki, and B. Vowinkel, "SMART: the KOSMA Sub-Millimeter Array Receiver for Two frequencies," *Proc. SPIE*, vol. 4855, pp. 322-329, June 2003.

M2E

Broadband SIS mixer for 1 THz band

A. Karpov[1], D. Miller[1], J. A. Stern[2], B. Bumble[2], H. G. LeDuc[2], J. Zmuidzinas[1,2]
*1 California Institute of Technology, Pasadena, CA 91125, USA *,*
2 Jet Propulsion Laboratory, Pasadena, CA 91109, USA
* Contact: Karpov@submm.caltech.edu,
This work is supported by the USRA SOFIA instrument development program.

***Abstract*— We report the development of a low noise and broadband SIS mixer aimed for 1 THz channel of the Caltech Airborne Submillimeter Interstellar Medium Investigations Receiver (CASIMIR), designed for the Stratospheric Observatory for Far Infrared Astronomy, (SOFIA). The mixer uses an array of 0.24 μm2 Nb/Al-AlN/NbTiN SIS junctions with critical current density of 30-50 KA/cm2. The junctions are shaped in order to optimize the suppression of the Josephson DC currents. We are using a double slot planar antenna to couple the mixer chip with the telescope beam. The RF matching microcircuit is made using Nb and gold films. The mixer IF circuit is designed to cover 4 - 8 GHz band. A test receiver with the new mixer has a low noise operation in a 0.87 – 1.12 THz band. The minimum DSB receiver noise measured at 1 THz is 260 K (Y=1.64), apparently the lowest reported up to date. The receiver noise corrected for the loss in the LO injection beam splitter and in the cryostat window is 200 K. The combination of a broad operation band of about 250 GHz with a low receiver noise is making the new mixer a useful element for application at SOFIA. We will discuss the prospective of a further improvement of the sensitivity and extension of the upper frequency of operation of SIS mixer.**

Session M3

THz Sources

Chair: Imran Mehdi

Monday, April 20
2:20 – 3:20

M3A

Terahertz Local Oscillator Sources

T.W. Crowe*, J.L. Hesler, W.L. Bishop, G.S. Schoenthal, and K. Hui
Virginia Diodes, Inc., Charlottesville, VA 22902
* Contact: Crowe (a) VADiodes.com, phone (434)297-3257

***Abstract*—High quality local oscillator sources are required for astronomical receivers throughout the terahertz frequency range. This paper is focused on the development of sources for frequencies greater than 1 THz for use with Hot Electron Bolometric (HEB) mixers, specifically on the Stratospheric Observatory For Infrared Astronomy (SOFIA). One of the great advantages of HEB mixers is their very low LO power requirements, of order one microwatt per pixel (including coupling losses). However, the challenges of achieving even this power level at such high frequency remain significant, and the goals for significant tuning bands to enhance the measurement capability of the receiver are formidable. Also, there is great interest in developing array receivers, which will increase the required power level by a factor of ten.**

VDI's terahertz sources are based on high power amplifiers, typically near 40GHz, and a series of frequency multipliers that translate the power to higher frequency, albeit with very significant losses. For example, three years ago VDI (in collaboration with SRON) presented a 1.3THz source that generated of order 10uW and was electronically tunable over 100GHz of bandwidth. This source used an amp/x2x2x3x3 configuration, where the doublers were high power varactors and the triplers were broadband varistor multipliers. In fact, the triplers were shown to operate with similar performance across the entire waveguide band (1.1-1.7THz) without any tuning whatsoever. These same triplers have been used to generate greater than 30uW, when stronger driver components have been used.

More recently VDI has focused on the 1.9 and 2.7THz bands that are of interest for the German Receiver for Astronomy at Terahertz Frequencies, which is being developed by the Max-Planck-Institut für Radioastronomie (MPIfR) and the Universität zu Köln for use on the SOFIA aircraft. At 1.9 THz VDI has delivered an initial LO chain that generates a few microwatts of power, which is marginally sufficient to pump the receiver when the coupling losses into the dewar are included. In this paper VDI will describe this LO chain and the ongoing efforts to increase the output power by an order of magnitude for use on a future receiver array. The 2.7 THz frequency band is significantly more challenging, owing to the increased inefficiency of Schottky multipliers at the higher frequency. The goal is to generate enough power for a single pixel receiver with significant frequency tuning. To date VDI has demonstrated the required driver module at 300GHz and is presently working on an improved tripler to 900GHz. The final tripler to 2.7THz has been designed and is awaiting fabrication. First results for the new components are expected to be available in time for the conference presentation.

M3B

Tunable THz Source with Harmonic Multiplier Based on Superlattice Structures

V.L.Vaks[1*], A.N.Panin[1], S.I.Pripolzin[1], D.G.Paveliev[2], and U.I.Koshurinov[2]
1 Institute for Physics of Microstructures of Russian Academy of Science, Nizhny Novgorod, Russia
2 Nizhny Novgorod State University, Nizhny Novgorod, Russia
* Contact: Vax@ipm.sci-nnov.ru, phone +7-831-460-76-48

***Abstract*— The traditional approach to obtain high-stable generators has involved frequency multiplication of high-stable reference synthesizers. The Schottky diodes are widely employed for developing of multipliers, mixers and detectors of THz frequency range. However, for a successful operation in the THz region, it is necessary to increase cutoff frequency of Schottky diodes that has proven quite difficult due to fundamental restrictions (high inertness of electron pass through an active zone and parasitic capacitances). Use of superlattice structures are expected to be more effective for frequency transformation since the lower values of inertness and parasitic capacitances and presence of negative differential conductivity (up to 1 THz) on the volt-ampere characteristic. In the report we present high stable tunable radiation sources (frequency synthesizers and generator of harmonics), operating up to 6.3 THz. It is based on solid-state Gunn generator (97.5-117.5 GHz) and frequency multiplier on superlattice structures. Spectral parameters of generated harmonics are investigated. The elaborated source was used in THz spectrometer.**

Terahertz Sideband Generator Array on Extended Silicon Dielectric Lens

Haiyong Xu, *Member IEEE*, Sami H. Hawasli, *Member IEEE*, Lei Liu, Member IEEE, Jeffrey L. Hesler, *Member IEEE* and Robert M. Weikle, II, *Senior Member, IEEE*

***Abstract*— Terahertz Sideband generator (SBG) array on an extended Silicon (Si) hemisphere lens has been investigated in this paper. High power handling capacity is achieved compared with single varactor waveguide design. The SBG array is fabricated on a GaAs substrate. The unit cell dimension is determined to be 40 μm × 40 μm with considering of only single Transverse Electromagnetic (TEM) mode propagation. Schottky planar varactor diode parameters have been chosen to match the optimized embedding impedance. The simulated diode anode diameter is 1 μm, and the finger length is 14 μm.**

***Index Terms*— Schottky diode frequency converters, lens antennas, submillimeter wave devices, submillimeter wave generation.**

I. INTRODUCTION

SIDEBAND generators have been investigated for many years to produce tunable high frequency signals, that have wide applications in scale radar range systems and molecular spectroscopy [1]. State-of-the-art performance, more than 55 μW, has been achieved using single whisker-contact diode waveguide-based SBG's at 1.6 THz [2]. To improve the robustness and reliability, planar varactor circuit waveguide based SBG's are investigated with an output power of 40 μW [3]. Nowadays the Far-Infrared (FIR) laser can produce a fixed 184 μm spectrum line (1.63 THz) with more than 147 mW power and 118 μm line (2.52 THz) with 143 mW, such as Coherent SIFIR-50 system [4], which exceeded a single varactor SBG power handling capability (approximately 10 mW at 1.6 THz). However, it is difficult to explore multi-diode topologies using waveguide-based SBG's over 1 THz due to limited space and assembling challenges. To address these problems, an integrated planar array, which is easy to assemble and has high power handling capacity, is investigated in this paper. This array is placed on a high-resistivity Si substrate lens, leading to high gain patterns and high Gaussian coupling efficiency [5] [6]. The layout of the 1.6 THz SBG array assembled on an extended Si substrate lens is shown in Fig. 1. A movable mirror acts as a tunable backshort to optimize the embedding impedance. The SBG array is fed by a coplanar-waveguide (CPW) transmission-line (Tline) as shown in Fig. 2. This SBG array contains 16 planar Schottky diodes fabricated on a GaAs substrate. The IF microwave signal and DC bias are fed into the array through the CPW Tline.

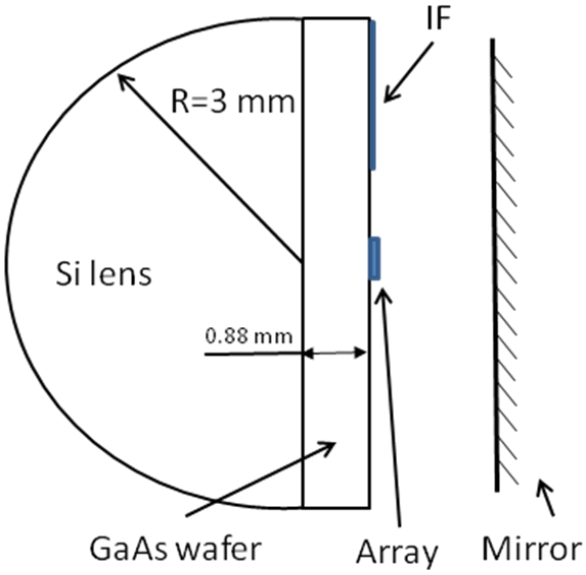

Fig. 1. SBG array assembled on an extended silicon substrate dielectric lens. Movable mirror acts as a backshort to tune the embedding impedance.

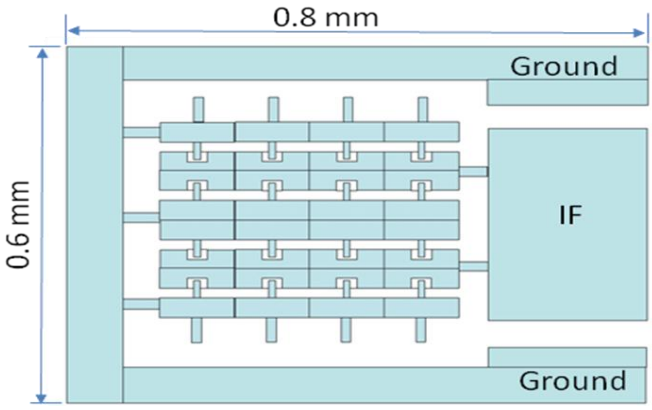

Fig. 2. The layout of SBG array consisting of 16 elements. CPW Tline is used to feed the array. The unit cell dimension is 40 μm × 40 μm.

Manuscript received 17 April 2009. This work was supported by the U.S. Army National Ground Intelligence Center (NGIC) under contract W911W5-06-R-0001.

Haiyong Xu, Sami H. Hasasli, Lei Liu and Robert M. Weikle, II are with the Charles L. Brown Department of Electrical and Computer Engineering, University of Virginia, Charlottesville, VA 22904, (phone: 434-924-6575, e-mail: hx4g@virginia.edu)

J. L. Hesler is with the Virginia Diodes, Inc., 979 2nd Street NE, Suite 309, Charlottesville, VA 22903, USA.

II. SBG DESIGN AND SIMULATION

SBG using a single varactor diode is first simulated in Agilent's Advanced Design System (ADS) software. An equivalent circuit model is shown in Fig. 3. The varactor junction is modeled by a junction capacitor C_j, a series resistor R_s, a finger inductor L_{fg}, a finger to pad capacitor C_{fp} and a pad to pad capacitor C_{pp}. The initial design goal is to determine the varactor parameters required to produce a low loss and 180^o phase shift, which means low SBG conversion loss [7]. To achieve the largest phase modulation, the junction capacitance is initially set to resonate with the finger inductance at the frequency of interest. This results in a short circuit and a reflection coefficient phase of 180 degrees. Off-resonance, the resonance circuit should present as large an impedance as possible to approximate an open circuit. Furthermore, the SBG embedding impedances from the diode junction are simulated for different anode sizes. For 1 μm diameter anode, the zero bias junction capacitance is estimated at 1.6 fF, while the series resistance is approximately 20 Ω. The optimized embedding impedance is found to be, Zem=46+j100 Ω at 1.6 THz, as shown in Fig. 4. The corresponding conversion loss is less than 9 dB. Based on the ADS simulated results, the circuit physical parameters are obtained and modeled in the Ansoft's High Frequency Structure Simulator (HFSS) software, which will accurately take all the parasitic parameters into account [3].

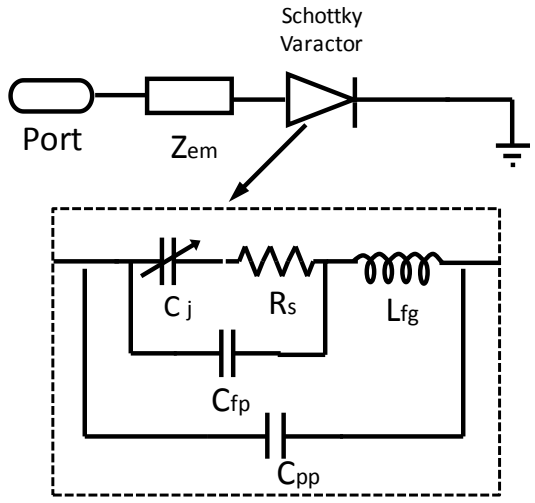

Fig. 3. Single planar Schottky varactor SBG equivalent circuit model. The varactor is modeled by finger inductance, junction capacitance, series resistance and parasitic capacitance

III. WAVEGUIDE SBG AT 1.6 THZ

Based on the simulation, a waveguide based SBG is designed, fabricated and measured. The integrated circuit includes a waveguide to microstrip transition, a planar varactor diode and a microstrip low pass filter, which is fabricated on a quartz substrate. A photograph of an integrated SBG circuit in a metal block is shown in Fig. 5. The integrated circuit width is 50 μm, and the thickness is 10 μm. The waveguide-to-microstrip transition is used to couple the LO power into the diode channel and sidebands (RF) back into the waveguide. The microwave IF signal is applied to pump the diode, while a low-pass microstrip filter integrated with the diode is used to resonate with the varactor and block the RF signal. After the assembling, the conversion loss measurement is conducted using one laser setup system. The output of laser beam is split into 2 parts. One part is used to pump the receiver mixer as a LO source. The other beam provides the RF carrier to the SBG. The output sidebands are reflected by a silicon etalon, which passes 99 % of the carrier laser power and reflects 80% of the sidebands. The sidebands are directed through a beam splitter by two mirrors to the mixer as the RF input signal. Finally, the mixer IF output is measured by a spectrum analyzer, which is the sideband power. After the path losses of the receiver system are calibrated, the SBG conversion loss is obtained and shown in Fig. 6.

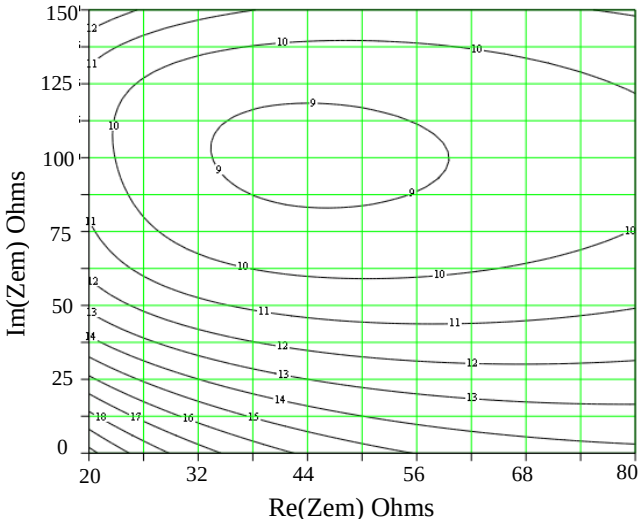

Fig. 4. ADS Simulated conversion loss corresponding to different embedding impedances for 1 μm diameter anode.

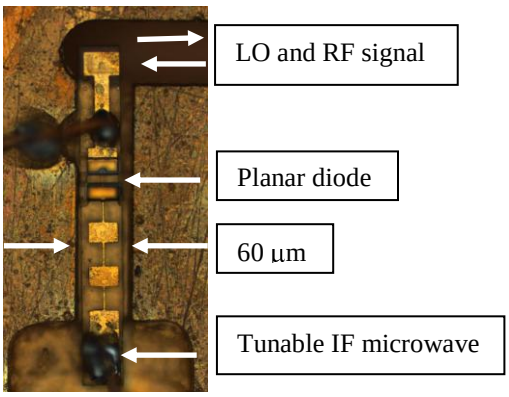

Fig. 5. Photograph of 1.6 THz integrated SBG circuit mounted in an open metal block. The circuit channel width is 60 μm. The varactor is pumped by a tunable IF microwave signal. The output RF signal will be LO +/- IF.

IV. ARRAY DESIGN

After the single varactor SBG measurement, the array is designed to achieve better power handling capacities. The Si lens diameter is first determined by balancing the Gaussicity

and directivity [5]. At 1.56 THz, the free space wavelength, λ_0, is approximate 0.19 mm. The hemispherical lens radius is chosen to be 3 mm, which will give the R/λ_0 ratio 15.8, where R is the radius of the lens. The extension of the hyperhemispherical lens is initially set to be R/n=0.88 mm, where n is the index of refraction of the lens, and the Si dielectric constant, ε_r, is 11.7.

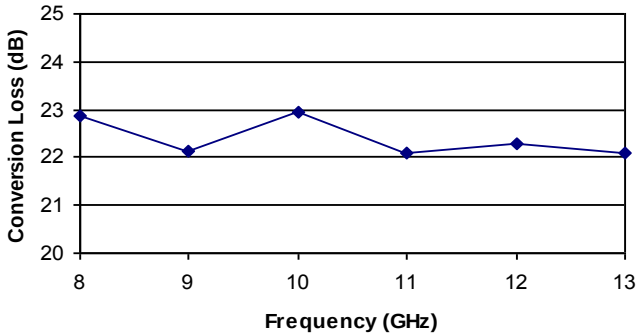

Fig. 6. Measured conversion loss of a signal varactor waveguide based SBG using a 1.6 THz FIR laser system.

An equivalent unit cell of the array is simulated with HFSS as shown in Fig. 7. Electric wall (E-wall) and magnetic wall (H-wall) planes are defined based on the array symmetry [8]. The two walls along the diode finger are H-walls, while the other two walls are E-walls. To avoid the higher order waveguide modes, the unit cell dimension must be less than a certain value. Based on the HFSS simulation, the unit cell dimensions are determined to be 70 μm × 70 μm for quartz substrate, while the unit cell dimensions for Si substrate will drop to approximately 40 μm × 40 μm. Ansoft's HFSS is used to optimized the diode parameters to match the best conversion loss as shown in Fig. 4. The varactor anode diameter is determined to be 1 μm, and the finger length is 14 μm, taking into account practical limitations on diode fabrication.

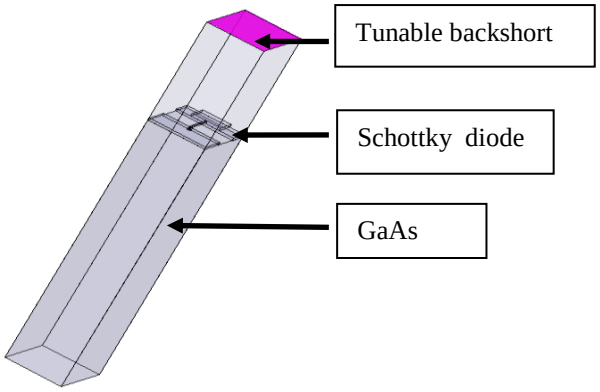

Fig. 7. An equivalent unit cell of SBG array using GaAs substrate. A mirror is used as a tunable backshort. E-walls are defined at two waveguide walls at the end of the diode, while H-walls are the two side waveguide walls parallel along diode finger. The array unit cell dimension is 40 μm × 40 μm.

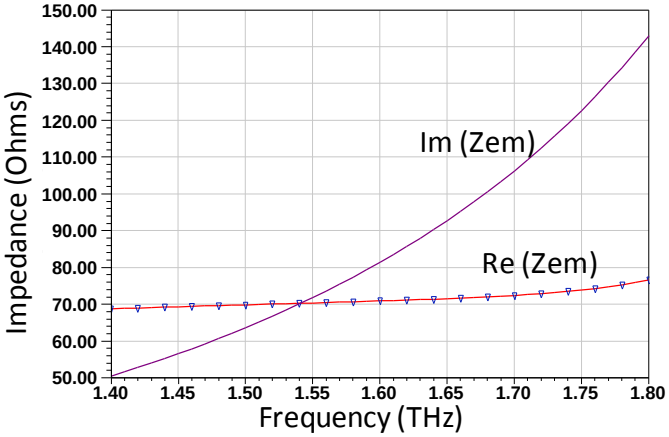

Fig. 8. Simulated embedding impedance of a unit cell. The diode anode size is 1 um, and the finger length is 14 μm.

The simulated embedding impedance versus frequency is shown in Fig. 8. The simulated embedding impedance is 70+j72 Ohms at 1.56 THz, which is expected to give a 10 dB conversion loss. This conversion loss doesn't account for circuit reflection and dielectric losses. Furthermore, the Gaussian beam coupling is calculated. The Gaussian laser beam is coupled into the array by an off-axis parabolic mirror with focus length 60 mm. To optimize coupling to the beam, the array is populated with 4 × 4 elements, and the array size will be 0.16 mm × 0.16 mm. The distance between the laser beam waist and the parabolic mirror is determined to 1.7 m, while the distance from the mirror to the Si lens is 61 mm.

V. Conclusion

A 1.6 THz SBG array with 16 elements on an extended silicon dielectric lens is investigated. Planar varactor diode parameters have been optimized to match the impedance, giving by a conversion loss contour map. The simulated SBG conversion loss is approximate 10 dB without considering of reflection and dielectric losses.

Acknowledgment

The authors would like to thank Dr. Zhiyang Liu from Tyco Electronics, Dr. Acar Isin and Dr. Bascom Deaver from Dept. of Physics, Univ. of Virginia, for their helpful discussion.

References

[1] P. H. Siegel, "THz technology," in *IEEE Trans. Microwave Theory and Techniques*, vol. 50, no. 3, pp. 910-928, March, 2002.

[2] D. S. Kurtz, J. L. Hesler, T. W. Crowe and R. M. Weikle, "Submillimeter-wave sideband generation using varactor Schottky diodes," in *IEEE Trans. Microwave Theory and Techniques*, vol. 50, no. 11, pp. 2610-2617, Nov, 2002.

[3] H. Xu, G. S. Schoenthal, J. L. Hesler, T. W. Crowe and R. M. Weikle, "Nonohmic contact planar varactor frequency upconverters for terahertz applications," in *IEEE Trans. Microwave Theory and Techniques*, vol. 55, no. 4, pp. 648-655, April, 2007.

[4] Coherent Inc. web site, http://www.coherent.com/Lasers/index.cfm?fuseaction=show.page&id=779&loc=834

[5] D. F. Filipovic, S. S. Gearhart, and G. M. Rebeiz, "Double-slot antennas on extended hemispherical and elliptical silicon dielectric lenses," in

IEEE Trans. Microwave Theory and Techniques, vol. 41, pp. 1738-1749, Oct., 1993.

[6] S. S. Gearhart and G. M. Rebeiz, "A monolithic 250 GHz Schottky-Diode Receiver," *IEEE Trans. Microwave Theory and Techniques,* vol. 42, no. 12, pp. 2504-2511, Dec., 1994.

[7] S. Kurtz, J. L. Hesler, T. W. Crowe and R. M. Weikle, "Submillimeter-wave sideband generation using varactor Schottky diodes", IEEE Trans. On Microwave Theory and Techniques, vol. 50, no. 11, pp. 2610-2617, Nov., 2002

[8] R. M. Weikle, "Quasi-Optical Planar Grids for Microwave and Millimeter-Wave Power," Dissertation California Institute of Technology, March, 1992.

Diamond Heat-Spreaders for Submillimeter-Wave GaAs Schottky Diode Frequency Multipliers

Choonsup Lee, John Ward, Robert Lin, Erich Schlecht, Goutam Chattopadhyay, John Gill, Bertrand Thomas, Alain Maestrini, Imran Mehdi, and Peter Siegel

***Abstract*—We have attached CVD diamond film as a heat-spreader to our existing 250 GHz GaAs Schottky diode frequency tripler chip in o rder to improve its power handling capability. Using this first generation device, we were able to produce 40 mW at 240 GHz from a single frequency tripler with 350 mW input power at room temperature. We have also run finite-element thermal simulations and seen that the 30 µm thick diamond film dropped the temperature of the anodes by about 200° C. This break-through in thermal management increases the output power of frequency multipliers by nearly 100%.**

***Index Terms*—Diamond, Frequency multipliers, Heat-Spreader, THz source.**

I. Introduction

THE planar GaAs Schottky diode frequency multiplier chain is a very good candidate for compact reliable tunable terahertz sources due to low mass, wide electronic tunability, narrow line-width, low noise, and room temperature operation [1]. However, the output power of frequency multiplier chains is relatively low compared to recent quantum cascade laser (QCL) results in the 2-3 THz band [2]. Frequency multipliers are cascaded in chains to create terahertz sources. Thus, in order to generate high power at the output in the 2-3 THz range, we need to have high driving power in the first stage of the chain, typically in the 200 to 400 GHz range. In order to increase the power handling capability and output power, the doping concentration of the Schottky contact can be adjusted to increase the breakdown voltage, or the number of anodes per multiplier chip can be increased [3]. However, due to thermal issues the most promising technique to increase output power has been to power-combine two or more parallel stages. For example, the power available at 300 GHz can be doubled by using a 300 GHz dual-chip power combiner [4].

Currently, up to 800 mW of continuous-wave (CW) tunable W-band power is available by four-way power combining MMIC amplifier chips at W-band [5]. However, current-generation submillimeter-wave frequency multipliers cannot handle the input power of 800 mW due to thermal management problems. Therefore, we propose to use a diamond film as a heat-spreader in order to remove the heat more efficiently, resulting in increased power handling and output power.

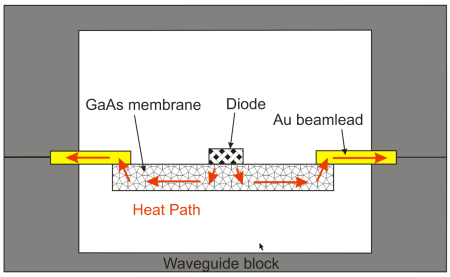

(a)

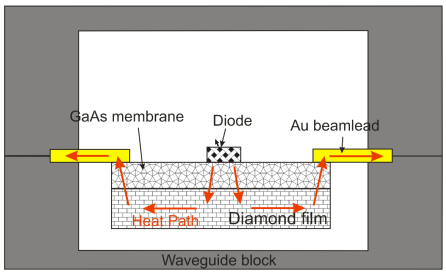

(b)

Figure 1. Simplified schematic view (not to scale). (a) Heat laterally transfers through GaAs membrane (thermal conductivity=46 W/m·K) to heat sink. (b) Heat laterally transfers through the CVD diamond film (thermal conductivity = 1000-1200 W/m·K) to heat sink.

II. Thermal Analysis

Figure 1 (a) shows the nominal schematic view of the 250 GHz tripler as placed in the split waveguide block. The heat generated at the anode transfers through a few-micrometer thick GaAs membrane and gold beamlead to the waveguide

Manuscript received 20 April 2009. The research described in this paper was carried out at the Jet Propulsion Laboratory, California Institute of Technology, under a contract with the National Aeronautics and Space Administration.

C. Lee, R. Lin, E. Schlecht, G. Chattopadhyay, J. Gill, B. Thomas, I. Mehdi, and P. Siegel are with the California Institue of Technology Jet Propulsion Laboratory, Pasadena, CA 91109 USA (Choonsup.Lee@jpl.nasa.gov) (Imran.Mehdi@jpl.nasa.gov)

A. Maestrini is with Université Pierre et Marie Curie Curie-Paris 6, LERMA, Paris, France (alain.maestrini@obspm.fr)

J. Ward is now with Raytheon Co., Fort Wayne, Indiana, USA. (John.S.Ward@raytheon.com)

block, which is a heat sink. The thermal conductivity of GaAs is approximately 46 W/m·K and this thermal conductivity value decreases as the temperature increases. Figure 1 (b) shows the proposed schematic view of the 250 GHz tripler with a diamond film bonded to the backside of the GaAs substrate to remove the heat more efficiently. The polycrystalline diamond film works as a heat spreader which removes the heat by thermal conduction to a heat sink. In this structure, the heat goes to the diamond film and then transfers through the diamond film laterally and goes back to the gold beamlead and waveguide block which is a heat sink. The thermal conductivity of CVD diamond is 1000-1200 W/m·K and is 20 times greater than GaAs (46 W/m·K) and three times higher than silver (430 W/m·K). Since the thermal resistance of the chip is about three times lower with diamond than without, it reduces the maximum temperature rise by a similar factor.

III. Microfabrication

A. Diamond Etching Process

Polycrystalline diamond deposited by hot-filament chemical vapor deposition (CVD) has been selected as the material for providing thermal management due to the high thermal conductivity (1000-1200 W/m·K). It is an electrical insulator (resistivity = 10^{15} Ω/cm) and has a moderate relative dielectric constant of 5.7. Because it is the hardest material known and it is chemically inert, it is extremely difficult to pattern the diamond, especially thick films. In order to etch the thick diamond film, the RF power, the gas flow, chamber pressure, and the bias voltage have been investigated in inductively coupled plasma (ICP) RIE. An etch rate of 550 nm/min has been used.

B. Microfabrication

JPL's Monolithic Membrane-Diode (MOMeD) process that results in extremely low parasitic Schottky diode chips has been discussed previously [6]. The frontside processing forms the Schottky diode, RF components and on-chip capacitors. The backside processing is used to remove the substrate and enable chips that are made on a very thin layer of GaAs to improve RF tuning. We have modified the backside processing sequence to allow us to mount a diamond film to the membrane. The diamond is patterned using an Inductively Coupled Plasma Reactive Ion Etching (ICP-RIE) system. The patterning of the diamond allows us to shape the diamond substrate, keeping the beamleads free for mounting and DC contacts. Figure 2 shows the front-side view of the 250 GHz tripler. The front-side view is the same as the tripler without the diamond. However, the back-side has the bonded diamond film for removing the heat efficiently.

IV. Measured Results

Figure 3 shows the measured 250 GHz tripler's output power and conversion efficiency as a function of the input power at 238.8 GHz. At 200 mW input power, the efficiency

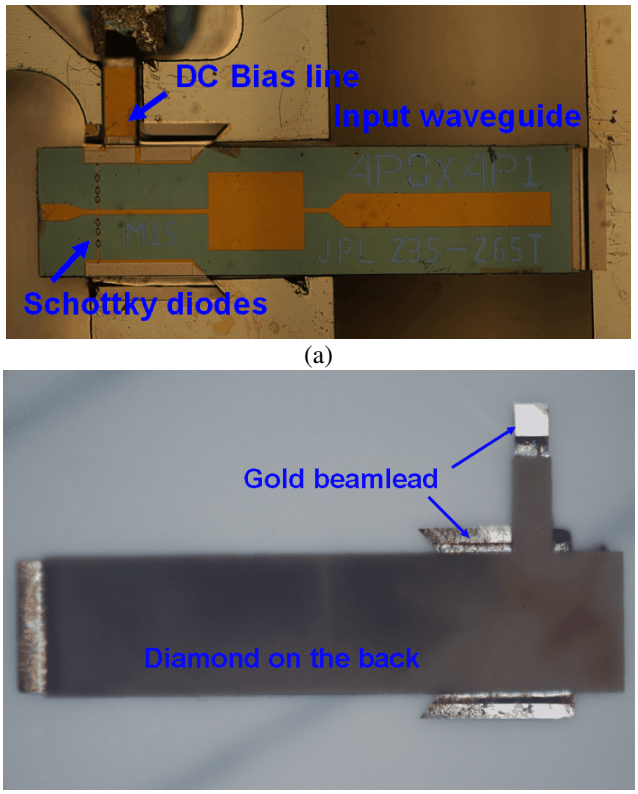

Figure 2. (a) Front view of the 250 GHz tripler when mounted in one half of the split waveguide block. (b) View of the 250 GHz tripler chip showing the diamond film.

was approximately 14 % for one with the diamond, and 11% for one without diamond. However, above 200 mW of the input power, the efficiency drops more slowly for the tripler with the diamond compared to the tripler without the diamond. The output power of the tripler without diamond peaks at 22 mW for the input power of 200 mW and thereafter starts to drop rapidly and fails at the input power of 240 mW. However, for the tripler with the diamond heat-spreader, the output power continues to climb as the input power increases. An output power of 40 mW at 350 mW input has been achieved from a single chip without any sign of degradation. In addition, reduction of operation temperature of Schottky diodes can increase the reliability.

Figure 4 shows the output power versus output frequency plot of the 250 GHz tripler for a chip with diamond and a chip without diamond. A frequency sweep was performed using flat input power levels at 100 mW, 200 mW, and 300 mW. The tripler without the diamond suffered a catastrophic failure at about 250 mW input power, and therefore no data was obtained for this chip at 300 mW. As the plot shows, adding the diamond layer improves the output power without degrading the bandwidth.

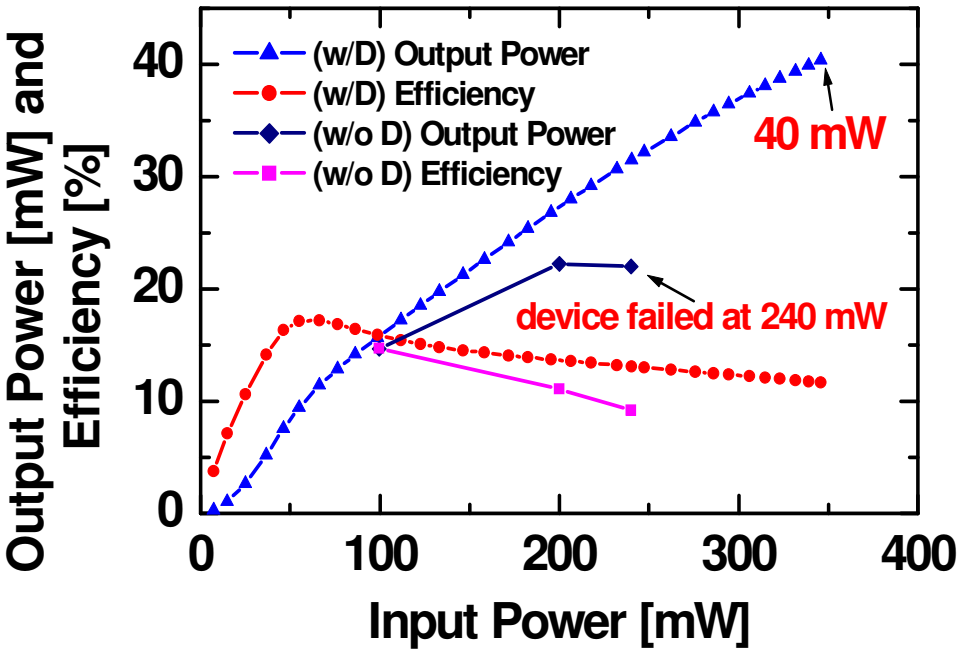

Figure 3. Output power and efficiency versus input power measured at 240 GHz for triplers operated at room temperature both with and without diamond heat-spreaders.

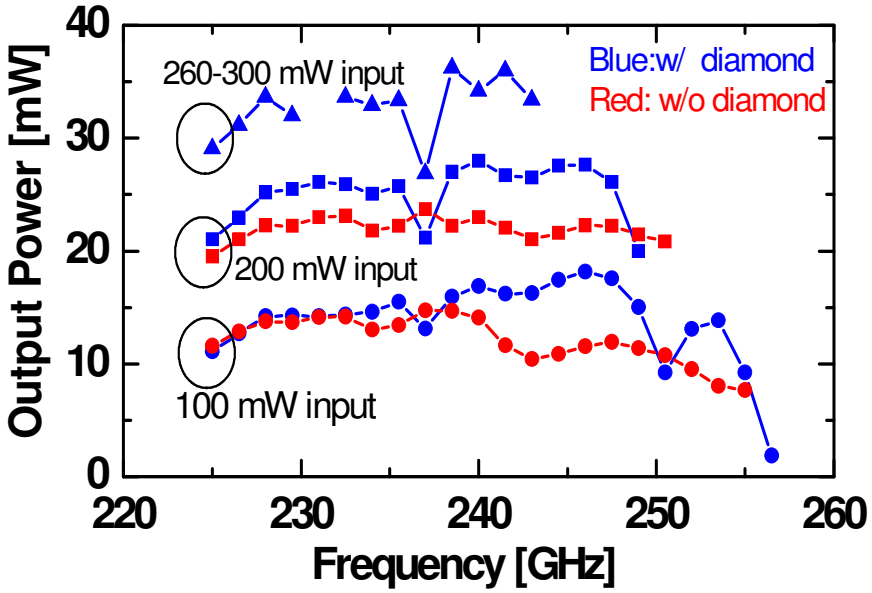

Figure 7. Output power versus output frequency for the 250 GHz tripler at room temperature. Chip without the diamond heat spreader suffered a catastrophic failure at 240 mW input.

V. Conclusion

This superior thermal management achieved with diamond provides a 100% increase in power handling capability. For example, we have achieved 40 mW output power at 240 GHz from a frequency tripler with 350 mW input power, while identical triplers without diamond suffered catastrophic failure at 250 mW input power. Optimizing the Schottky diode chips and waveguide circuits for the presence of the diamond substrate is expected to further increase the achievable output power. This increase in output power in the 250-350 GHz band is expected to increase the usable range of Schottky diode frequency multiplier chains to beyond 3 THz.

References

[1] P. Siegel, "THz technology," IEEE Transactions on Microwave Theory and Techniques, vol. 50, no. 3, March 2002.

[2] B. S. Williams, "Terahertz quantum-cascade lasers", Nature photonics, pp. 517-525, September 2007.

[3] A. Maestrini, J. Ward, G. Chattopadhyay, E. Schlecht, and I. Mehdi, "Terahertz Sources Based on Frequency Multiplication and Their Applications," J. of RF-Engineering and Telecommunication, Issue 5/6, vol. 62, pp.118-122, June 2008.

[4] A. Maestrini, J. Ward, C. T.-Canseliet, J. Gill, C. Lee, H. Javadi, G. Chattopadhyay, I. Mehdi, "In-Phase Power-Combined Frequency Triplers at 300 GHz," IEEE MWCL vol. 18, no.3, pp. 218-219, 2008.

[5] J. Ward, G. Chattopadhyay, J. Gill, H. Javadi, C. Lee, R. Lin, A. Maestrini, F. Maiwald, I. Mehdi, E. Schlecht, P. Siegel, "Tunable Broadband Frequency-Multiplied Terahertz Sources," Proceedings, 33rd International Conference on Infrared, Millimeter, and Terahertz Waves, Pasadena, California, September 2008.

[6] S. Martin, B. Nakamura, A. Fung, P. Smith, J. Bruston, A. Maestrini, F. Maiwald, P. Siegel, E. Schlecht, I. Mehdi, "Fabrication of 200 to 2700 GHz Multiplier Devices Using GaAs and Metal Membranes," IEEE MTT conference, pp. 1641-1645, 2001.

Session M4

QCLs

Chair: Brian Ellison

Monday, April 20
3:20 – 3:50

M4A

Integration of Lithographically Microfabricated Rectangular Waveguides and THz Quantum Cascade Lasers

M.C. Wanke[1*], C.D. Nordquist[1], M. Lee[1], C.L. Arrington[2], A.M. Rowen[1], M.J. Cich[1], A.D. Grine[2], C.T. Fuller[1], E.A. Shaner[1], E.W. Young[3], and J.L. Reno[1]

1 Sandia National Laboratories, Albuquerque, NM, 87185

2 LMATA Government Services, Albuquerque, NM, USA

3 Now at Lumileds, San Jose, CA, USA

* Contact: mcwanke@sandia.gov, phone +1-505-844-2532

This work was supported by the LDRD program office at Sandia National Labs. Sandia is a multiprogram laboratory operated by Sandia Corporation, a Lockheed Martin Company, for the United States Department of Energy's National Nuclear Security Administration under contract DE-AC04-94AL85000.

***Abstract*—THz quantum cascade lasers are promising solid-state sources for use as local-oscillators in THz heterodyne receiver systems. However, many challenges must still be addressed for QCLs to become practical THz sources. Among these challenges are to shape the highly divergent and non-Gaussian output beam patterns observed from QCLs into a more useful and predictable beam shape, and to integrate QCLs into the existing, broadly used THz technical infrastructure.**

To address both the beam pattern problem and integrability/manufacturability issues we have developed a lithographic method to microfabricate small, single mode rectangular waveguide structures on-a–chip. To explore the performance of the waveguides as well as the integration with active THz lasers, we have tested both stand-alone waveguides and waveguides integrated on-chip with THz quantum cascade lasers .

The 75 µm wide by 37 µm tall waveguide structures were designed to be single mode between 2 and 4 THz, and were fabricated using patterned electroplating of thick gold sidewalls around a photoresist form, followed by electroplating of a gold lid, and lastly removal of the polymer form by solvation. The waveguides were coupled to free space using 2-dimenstional H-plane horn flares.

Measurements on stand-alone waveguides with different lengths revealed a loss of 1.4 +/- 0.15 dB/mm corresponding to 0.14 db/λ. This is roughly a factor of two higher than HFSS models predict for perfect gold walls, but it still compares favorably to 0.2 db/λ at 100 GHz and 0.6 db/λ at 300 GHz for commercially available waveguides. Initial beam pattern measurements yielded qualitative data in agreement with predictions, but displayed strong high-spatial frequency amplitude oscillations. Recent measurements have identified the cause of this oscillation as being due to interference between alternate paths between the horn and detector resulting from reflections of intermediate optics. New beam pattern measurements eliminating the reflections will be presented.

We have also successfully fabricated the rectangular waveguides directly onto a chip containing multiple THz QCLs. Even though thermal stress issues caused by the need to cool the lasers resulted in a high failure rate in initial designs, we have observed QCL emission from the horns of single-spatial-mode integrated waveguides, some using only 0.2 W of input power at threshold.

Phase-locking of a 2.7-THz quantum cascade laser to a microwave reference

A.M. Baryshev, P. Khosropanah, W. Zhang, W. Jellema, J.N. Hovenier, J.R. Gao, T.M. Klapwijk, D.G. Paveliev, B.S. William, S. Kumar, Q. Hu, J.L. Reno, B. Klein, J.L. Hesler

***Abstract*—We demonstrate phase-locking of a 2.7-THz metal-metal waveguide quantum cascade laser (QCL) to an external microwave signal. The reference is the 15th harmonic, generated by a semiconductor superlattice nonlinear device, of a signal at 182 GHz, which itself is generated by a multiplier-chain (x2x3x2) from a microwave synthesizer at 15 GHz. Both laser and reference radiations are coupled into a hot electron bolometer mixer, resulting in a beat signal, which is fed into a phase-lock loop. Spectral analysis of the beat signal (see fig. 1) confirms that the QCL is phase locked. This result opens the possibility to extend heterodyne interferometers into the far-infrared range.**

***Index Terms*—Quantum Cascade Laser, Schottky Diode Multiplier, Superlattice Electronics Device, phase locking**

I. INTRODUCTION

TERAHERTZ quantum cascade lasers (QCLs) [1] are promising sources for various applications such as high-resolution heterodyne spectroscopy, sensing, and imaging. In particular, QCLs hold great promise for local-oscillator (LO) applications because of their demonstrated performances: a broad frequency coverage of 1.2 - 5 THz, high output power (1 mW), and compactness. Recently, their suitability as LOs has been demonstrated [2], [3] in hot electron bolometer (HEB) receivers with free-running QCLs, calibrated with a broadband blackbody radiation. To proceed with the applications of THz QCLs as LOs in a heterodyne spectrometer, stabilization of the frequency or phase is required to either eliminate the frequency jitter or to reduce the phase noise. For a heterodyne interferometer either on the Earth [4] or in space [5], phase locking of multiple LOs to a common reference at low frequency is essential.

Phase locking [6] a laser to a reference means to control the phase of the laser radiation field precisely. This serves not only to stabilize the frequency but also to transfer the line profile of the reference to the laser. In the case of frequency-locking, the laser's average frequency is fixed, but its linewidth remains equal to the laser's intrinsic linewidth. Until now, only two experiments [7], [8] to stabilize a THz QCL have been published. One is the frequency locking of a 3.1 THz QCL to a far-infrared (FIR) gas laser [7], the other is the phase-locking of the beat signal of a two lateral modes of a THz QCL to a microwave reference [8]. These experiments have suggested the feasibility of phase-locking, but have not led to a practical scheme for a LO. For a practical solution the phase needs to be locked to an external reference that can be generated conveniently and should preferably be far below the LO frequency. Therefore, an important challenge is the demonstration of phase-locking of a single-mode THz QCL to a microwave reference signal (MRS), which is the scheme commonly used in existing solid-state LOs. The MRS should be multiplied to a THz frequency in the vicinity of the laser frequency in order to obtain a beat note or an intermediate frequency (IF). As demonstrated in the measurements of FIR gas laser frequency, the harmonics of MRS at 3.8 THz [10] and at 4.3 THz [11] can be generated by Josephson junction harmonic mixers, resulting in a beat between the laser and the up-converted frequencies. Another commonly used harmonic generator is a Schottky diode [12]. Recently phase-locking has also been demonstrated in a THz photomixer source operated at 0.3 THz to an optical frequency comb of a femtosecond laser [13]. In contrast to THz QCLs, such a source has so far not demonstrated sufficient output power at frequencies above 1 THz.

In this contribution, we report the phase-locking of a 2.7 THz QCL to a harmonic generated from a MRS by a semiconductor superlattice (SL) nonlinear device in combination with a multiplier chain [9]. In addition to its immediate application in LOs, this work also demonstrates that the frequency of a QCL, as a photonic source, can be controlled precisely with an electronic source. This is a unique feature of THz QCLs which is not available to other lasers (gas lasers or solid-state lasers at higher frequencies).

Manuscript received 20 April 2009.

This effort is supported by the European Community Framework Programme 7, Advanced Radio Astronomy in Europe, grant agreement no.: 227290.

A.M. Baryshev is supported by a personal NWO/STW VENI grant "Advanced Heterodyne Mixers for THz Applications".

The work at MIT is supported by AFOSR, NASA and the NSF. Sandia is a multi-program laboratory operated by Sandia Corporation, a Lockheed Martin Company, for the US Dept. of Energy under Contract DE-AC04-94AL85000.

A.M. Baryshev, P. Khosropanah, W. Zhang, W. Jellema, J.R. Gao are with the SRON Netherlands Institute for Space Research, Postbus 800, 9700 AV Groningen, The Netherlands.

J.N. Hovenier and J.R, Gao and T,M, Klapwijk are with Kavli Institute of NanoScience, Faculty of Applied Sciences, Delft University of Technology, Lorentzweg 1, 2628 CJ, Delft, The Netherlands

D.G. Paveliev is with Laboratory of Semiconductor Devices, Radiophysics faculty. State University of Nizhny Novgorod, Russia

B.S. William, S. Kumar and Q. Hu are with Department of Electrical Engineering and Computer Science and Research Laboratory of Electronics, Massachusetts Institute of Technology, Cambridge MA 02139, U.S.A.

J.L. Reno is with Sandia National Laboratories, Albuquerque, NM 87185-0601, U.S.A.

B. Klein is with Max-Planck-Institut für Radioastronomie (MPIfR), Auf dem Hügel 69, 53121 Bonn, Germany

J.L. Hesler is with Virginia Diodes, Inc., Charlottesville, VA 22902, U.S.A.

Contact: a.m.hesper@sron.nl, phone +31-50-363 8287

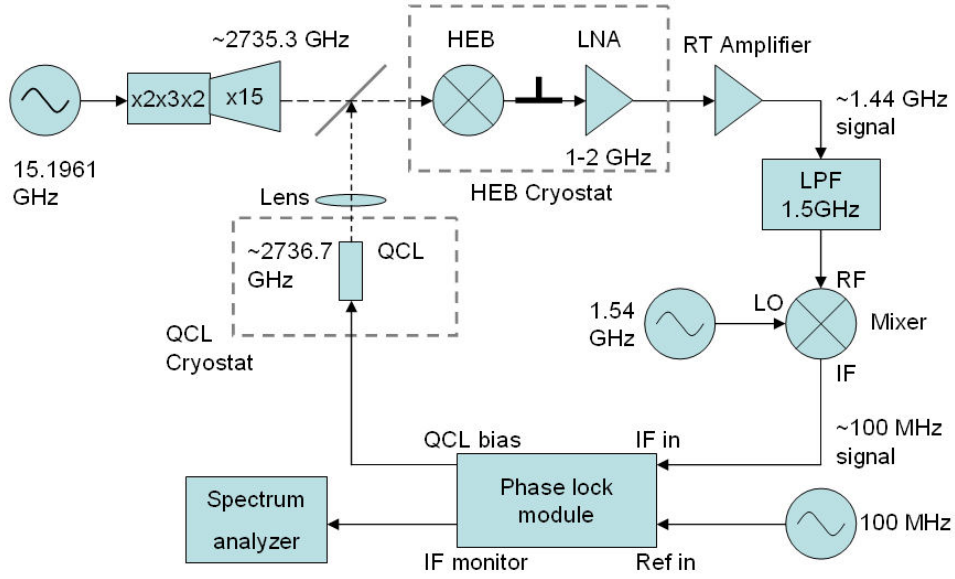

Fig. 1. Schematic diagram of the experimental setup to phase lock a THz QCL at 2.7 THz to a microwave reference. Not shown is that all the spectrum analyzer and signal generators are phase locked to a common 10 MHz reference.

II. Experimental setup

The QCL used is based on the double-resonant-phonon depopulation design with an active region containing 104 GaAs/$Al_{0.15}Ga_{0.85}As$ quantum-well modules (labeled FTP104, wafer EA1126) with a total thickness of 10 μm [14]. The Fabry-Pérot cavity of the QCL is a double-sided metal waveguide, which is 19 μm-wide and 800 μm-long. The QCL is operated with a current of 53 mA and a voltage of 12 V, and is cooled in a liquid-Helium cryostat. The maximum output power is 0.38 mW in CW mode. The emission spectrum measured by a Fourier-transform spectrometer shows a single-mode line at 2.735 THz. To realize a THz reference from a MRS we apply two stages of frequency multiplication; first with a multiplier chain consisting of a Schottky-doubler and -tripler ($\times 2 \times 3$), a power amplifier, and a varactor-doubler ($\times 2$), and then with a harmonic generator based on a superlattice (SL) nonlinear device [15], [16], operated at room temperature, whose higher order harmonics are at THz frequencies. The core of such a device is a MBE-grown superlattice structure with 18 periods. Each period consists of 18 monolayers of GaAs and 4 monolayers of AlAs. The superlattice is homogeneously doped with Si (2 1018 cm^{-3}). The area of the mesa device is 2-3 μm^2. The SL device is mounted on a block consisting of a diagonal horn to couple out the THz radiation and of a waveguide for pumping. As demonstrated [16], such a device can generate harmonics up to 3 THz. In comparison with a Schottky diode, it has a broader bandwidth because of a shorter response time and a smaller specific capacitance. Thus, it is more suitable for generating harmonics at higher frequencies.

To obtain the beat signal between the QCL and the THz reference, we use a lens-antenna coupled superconducting NbN HEB mixer [17]. It requires low LO power (< 300 nW). This turns out to be crucial for our phase-locking experiment because the QCL has a divergent far-field beam with strong interference patterns [18], resulting in a limited amount of usable power coupled into the mixer.

Fig. 1 shows a schematic diagram of the complete setup. The reference starts with a microwave synthesizer (Agilent 83640B) operated at 15.196 GHz followed by the multiplier chain that brings up the frequency to 182.352 GHz with a power level of 20-30 mW. The latter is used to pump the SL device to generate the 15th harmonic at 2.73528 THz, which is in the vicinity of the QCL's frequency, with a power level of 1-2 pW. The QCL is biased by a DC current, supplied by a phase-lock module (XL Microwave 800A-801, typically for

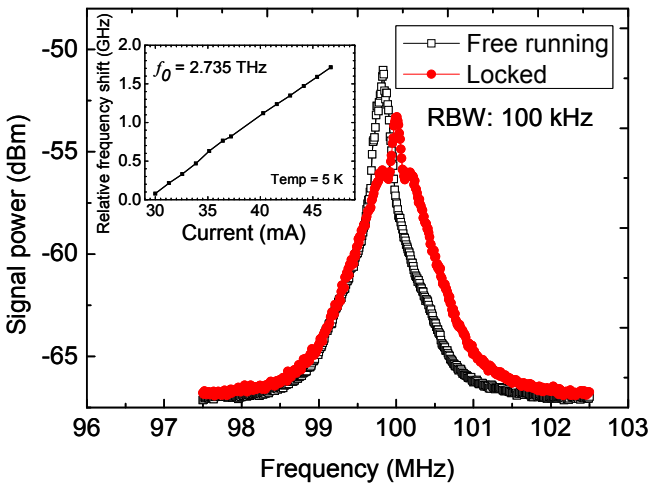

Fig. 2. A typical power spectrum of the beat signal of the THz QCL that is phase locked to a microwave reference recorded by the spectrum analyzer with a low resolution bandwidth (RBW) of 100 KHz. For comparison, a spectrum of the free-running QCL is also shown. The inset shows a relative frequency shift of the free-running QCL emission line versus the biasing current at 5 K. The starting frequency is 2.735 THz.

Gunn diode and YIG oscillators). The reference signal and output of the QCL are combined in the HEB mixer via a beam-splitter. The beat signal is amplified by an IF chain [17] consisting of an isolator, a cryogenic low noise amplifier, and room temperature amplifiers.

III. Measurement results and discussion

We first monitored the beat signal of the free-running QCL by a spectrum analyzer (alternatively by a fast Fourier transform spectrometer19), which is connected directly to the output of the IF chain. From the spectrum we obtain the frequency of the QCL to be 2.73673 THz. With this technique we can determine the frequency with a very high precision. By varying the current bias of the QCL, as shown in the inset of Fig. 2, the lasing frequency shifts monotonically and increases by 1.6 GHz from 30 to 46 mA (corresponding to 10.8 to 11.4 V), with the rate of 98 MHz/mA. This blue shift is most likely due to the frequency pulling of a Stark-shifted gain spectrum [20]. This observation indicates that the QCL behaves as a voltage controlled oscillator for the bias range of interest, which is required for phase-locking [7], [8]. To close the phase-lock loop (PLL), the beat signal, as shown in Fig. 1, is fed into a low-pass filter and then down-converted to about 100 MHz by a microwave mixer that has a microwave source at 1.54 GHz as LO. This is technically necessary since our phase-lock module is designed to lock an input signal close to a 100 MHz reference. The phase error signal is fed back into DC bias to the QCL. The PLL gain bandwidth is 1 MHz. All the instruments (the spectrum analyzer and signal generators) are phase locked to a common 10 MHz reference.

Fig. 2 shows a power spectrum of the beat under the phase-locking condition, recorded using a low resolution bandwidth (RBW) of 100 KHz. For comparison, a free-running spectrum is also plotted in the same figure. It is clear that using the PLL the beat signal is characterized by an additional, stable peak in the center.

To further demonstrate phase-locking, we monitor the power spectra of the beat by systematically reducing both RBWs and spans of the spectrum analyzer. Fig. 3 shows a selected set of power spectra of the beat for RBWs from 3 KHz down to 1 Hz. As indicated, the 3 dB-linewidth appears to decrease as the RBW is reduced. The linewidth of the beat can be as narrow as 1 Hz, limited by the minimum RBW of the instrument, while the S/N increases from 15 dB for a RBW of 3 kHz to 50 dB for 1 Hz. These spectra are reproducible and stable for an indefinitely long time. Since the spectra of the beat only reflect the relative phase noise spectral density between the laser and the reference, the extremely narrow linewidth of the beat implies that the line profile and stability of the reference are now transferred to the QCL [6], [21]. Thus, the THz QCL is phase locked. To quantify the phase-locking performance, we estimate how much power is in phase with the reference using the same method as in Ref [22]. Based on the peak power of -47 dBm within 1 MHz and -56 dBm within 1 Hz RBW we find about 13% of the QCL power to be concentrated in the narrow band of the reference. This low value can be explained by a narrow ($\ll$ 1 MHz) effective regulation bandwidth of

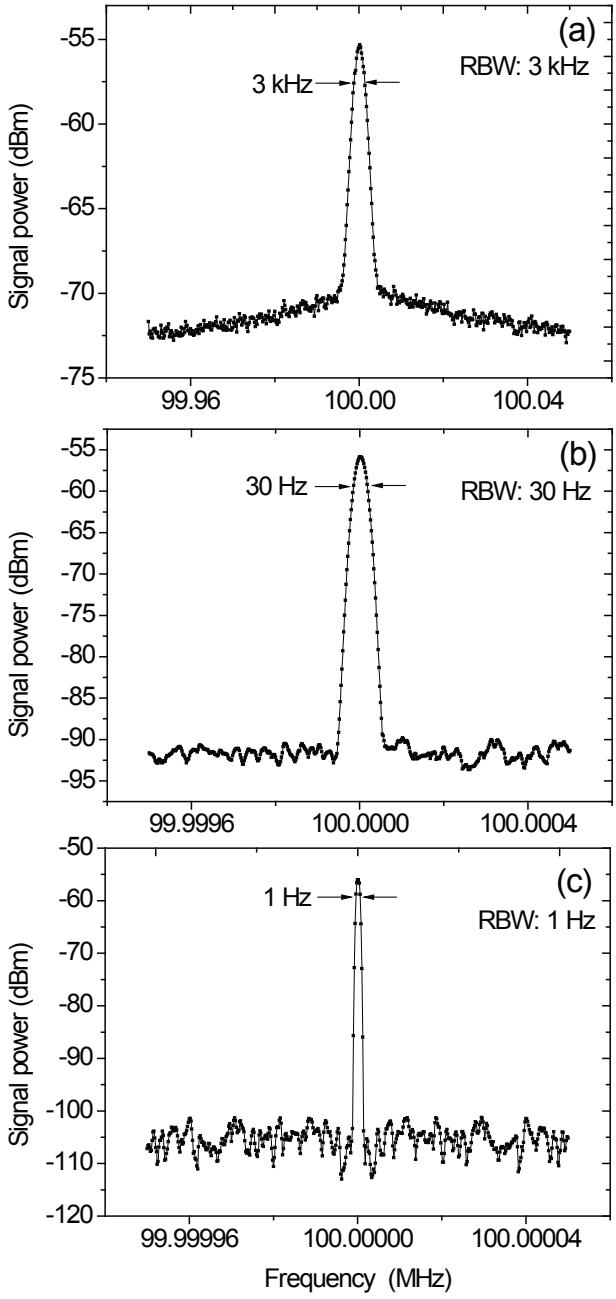

Fig. 3. Power spectra of the beat signal of the THz QCL that is phase locked to a microwave reference recorded by the spectrum analyser with different resolution bandwidths (RBW) and spans, but a fixed video bandwidth (VBW) of 300 Hz. A 3-dB linewidth of the beat signal is also indicated. To avoid confusion, we note that this linewidth is not the actual linewidth of the QCL (see text).

PLL system, due to total length of the cables included in the regulation loop, that caused additional delay. It is the complexity of the set-up for this demonstration phase locking experiment, which consists of two separate IR-labs cryostats, frequency down converter, optical coupling scheme and several synthesizers – all included in the feed back loop, that did not allow for shorter total delay. The measured line shape outside the regulation bandwidth of PLL is mainly determined by a phase noise of a reference synthesizer, emphasized by a a total

frequency multiplication of 180 times ($S/N \sim 180^{-2}$.

The total phase locked power can be improved significantly in the future by integrating harmonic generator and frequency down convertor in one cryostat or even integrating it with QCL itself as it was suggested in [**?**].

IV. Conclusion

In summary, we have demonstrated true phase-locking of a 2.7-THz QCL to a high-order harmonic from a microwave synthesizer generated by a superlattice harmonic generator. By extending harmonics of the superlattice device to the high end of THz range (3-6 THz), our phase-locking scheme can be potentially used in many applications of THz QCLs as local oscillators, in particular, for a space heterodyne interferometer5. Additionally, the phase-locked QCLs, with at least an accuracy of 1 part in 1012, determined by the microwave synthesizer, have potentials for other applications such as THz frequency standard and precision molecular spectroscopy.

Acknowledgement

The authors acknowledge NASA-JPL for the use of a W-band power amplifier chain used for spectral tests of Herschel-HIFI.

References

[1] B.S. Williams, Nature Photonics, **1**, 517 (2007). See references therein.
[2] J.R. Gao, J.N. Hovenier, Z.Q. Yang, J.J.A. Baselmans, A. Baryshev, M. Hajenius, T.M. Klapwijk, A.J.L Adam, T.O. Klaassen, B.S. Williams, S. Kumar, Q. Hu, and J.L Reno, Appl. Phys. Lett. **86**, 244104 (2005).
[3] H.-W. Hübers, S. G. Pavlov, A. D. Semenov, R. Köhler, L. Mahler, A. Tredicucci, H. E. Beere, D. A. Ritchie and E. H. Linfield, Optics Express, **13**, 5890 (2005).
[4] http://www.eso.org/public/astronomy/projects/alma.html
[5] F.P. Helmich and R.J. Ivison, Experimental Astronomy, **23**, 245 (2009)
[6] M. Zhu and J.L. Hall, J. Opt. Soc. Am. **B10**, 8029 (1993).
[7] A.L. Betz, R.T. Boreiko, B. S. Williams, S. Kumar, and Q. Hu, Opt. Lett. **30**, 1837 (2005).
[8] A. Baryshev, J.N. Hovenier, A.J.L. Adam, I. Kažalynas, J.R. Gao, T.O. Klaassen, B.S. Williams, S. Kumar, Q. Hu, and J. L. Reno, Appl. Phys. Lett. **89**, 031115 (2006).
[9] D. Rabanus, U.U. Graf, M. Philipp, O. Ricken, J. Stutzki, B. Vowinkel, M.C. Wiedner, C. Walther, M. Fischer and J. Faist, Opt. Express, **3**, 1159 (2009)
[10] D.G. McDonald, A.S. Risley, J.D. Cupp, K.M. Evenson, and J.R. Ashley, Appl. Phys. Lett. **20**, 296 (1972).
[11] T.G. Blaney, N.R. Cross, D.J.E. Knight, G.J. Edwards, and P.R. Pearce, J. Phys. D: Appl. Phys., **13**, 1365 (1980).
[12] F. Maiwald, F. Lewen, B. Vowinkel, W. Jabs, D.G. Paveljev, M. Winnewisser, and G. Winnewisser, IEEE Microwave and Guided Wave Lett., **9**, 198 (1999).
[13] Q. Quraishi, M. Griebel, T. Kleine-Ostmann, and R. Bratschitsch, Opt. Lett, **30**, 3231(2005).
[14] B.S. Williams, S. Kumar, Q. Qin, Q. Hu, and J. L. Reno, Appl. Phys. Lett. **88**, 261101 (2006).
[15] C. P. Endres, F. Lewen, T. F. Giesen, S. Schlemmer, D. G. Paveliev, Y. I. Koschurinov,V. M. Ustinov and A. E. Zhucov, Rev. Sci. Instrum. **78**, 043106 (2007);
[16] D.G. Paveliev, Yu.I. Koschurinov, V.M.Ustinov, A.E. Zhukov, F. Lewen, C. Endres, A.M. Baryshev,P. Khosropanah, W. Zhang, K. F. Renk, B. I. Stahl, A. Semenov and H.-W. Hübers, 19th International Symposium on Space Terahertz Technology, Groningen, The Netherlands, 28-30 April 2008 (unpublished)
[17] P. Khosropanah, J.R. Gao, W.M. Laauwen, M. Hajenius and T.M. Klapwijk, Appl. Phys. Lett., **91**, 221111 (2007).
[18] A. J.L. Adam, I. Kažalynas, J.N. Hovenier, T.O. Klaassen, J.R. Gao, E.E. Orlova, B.S. Williams, S. Kumar, Q. Hu, and J. L. Reno, Appl. Phys. Lett. **88**, 151105 (2006).
[19] B. Klein, S.D. Philipp, R. Güsten, I. Krämer, D. Samtleben, Proc. of the SPIE, Millimeter and Submillimeter Detectors and Instrumentation for Astronomy III. **6275**, 627511, (2006).
[20] L. A. Dunbar, R. Houdré, G. Scalari, L. Sirigu, M. Giovannini, and J. Faist, Appl. Phys. Lett. **90**, 141114 (2007).
[21] F. Bielsa, A. Douillet, T. Valenzuela, J-P. Karr, and L. Hilico, Opt Lett. **32**, 1641(2007)
[22] K. Döringshoff, I. Ernsting, R.-H. Rinkleff, S. Schiller, and A. Wicht, Opt. Lett, **32**, 2876(2005).
[23] M.C. Wanke, C.D. Nordquist, M. Lee, C.L. Arrington, A.M. Rowen, M.J. Cich, A.D. Grine, C.T. Fuller, E.A. Shaner, E.W. Young, and J.L. Reno, *Integration of Lithographically Microfabricated Rectangular Waveguides and THz Quantum Cascade Lasers*, this conference, to be published (2009)

Session T1

First Light THz Instruments

Chair: Anthony Kerr

Tuesday, April 21
9:20 – 10:20

First 1.3 THz Observations at the APEX Telescope

C. Risacher, D. Meledin, V. Belitsky, *Senior Member, IEEE* and P. Bergman

***Abstract*—The Atacama Pathfinder EXperiment (APEX) 12m telescope is operating on the Llano Chajnantor, Chile, since 2003 and a set of state of the art sub-millimeter receivers have been installed for frequencies spanning from 150 GHz to 1500 GHz. In 2008, a balanced 1.3 THz Hot Electron Bolometer (HEB) receiver was installed for the atmospheric window 1250-1380 GHz. This instrument is part of a 4-channel receiver cryostat with the other channels being 211-275 GHz, 275-370 GHz and 380-500 GHz Sideband Separating (SSB) SIS receivers. This paper presents the first observations obtained so far with the 1.3 THz band during its first months of operation. The sky measurements were taken during opportunistic commissioning and science verification phases, when the weather conditions were sufficiently good with a Precipitable Water Vapor (PWV) below 0.25 mm, which was the case only a few nights during these months. We present the first observations of the molecular transition CO J=(11-10) line on different sources such as Orion-FIR4, CW-Leo and SgrB2(M). We describe the many challenges and difficulties encountered for achieving successful THz observations from a large sub-millimeter ground-based telescope.**

***Index Terms*— Balanced receiver, HEB mixer, sub-millimeter waves, THz**

I. INTRODUCTION

THE 12 meter APEX telescope [1] is currently the largest sub-millimeter dish in operation in the southern Hemisphere. It is an early prototype of the Atacama Large Millimeter Array (ALMA) [2] Vertex antenna and its additional Nasmyth cabins (see Fig. 1) together with the Cassegrain cabin, allow the operations of a full suite of instruments. The different receivers installed, both heterodyne and continuum detectors, cover the frequency range from 150 GHz to 1500 GHz [3].

The chosen site at an altitude of 5100 m, is one of the best on Earth for its atmospheric conditions, which opens atmospheric windows up to ~1500 GHz [4]. This 1.3 THz receiver (known as apex-T2), was delivered by the Gard group in Chalmers University with the Onsala space observatory in Sweden, and it covers the atmospheric window from 1250 to 1380 GHz. Figure 2 shows the corresponding calculated atmospheric transmission for Precipitable Water Vapor (PWV) of 0.1, 0.2, and 0.3 mm. Terahertz observations are only worth performing for PWV below ~0.25 mm when the zenith atmospheric transmission gets above 20%. Such good atmospheric conditions are only achieved on average ~20 nights a year or ~5% of the year (statistics from 2003-2008).

Fig. 1. APEX 12 m antenna located on the Llano Chajnantor at 5100 m altitude in Northern Chile. On the picture, a crew of two people is adjusting the 5-screw panels to improve the surface accuracy. This is normally performed once a year after a holography session and is needed to allow efficient THz observations.

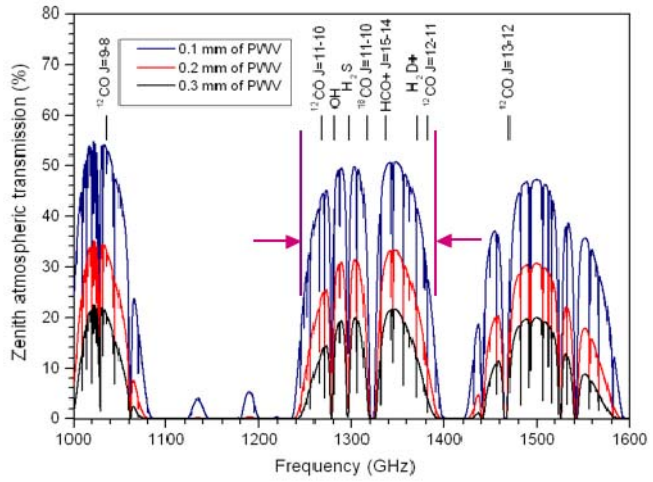

Fig. 2. Atmospheric transmission on the Llano Chajnantor for different weather conditions from 0.1 to 0.3 mm PWV. 0.3 mm is already considered excellent condition for observations until ~900 GHz, but is insufficient for the 1.3 THz window.

Manuscript received the 21st of April 2009.

C. Risacher was at the time of this work with the European Southern Observatory (ESO) in Chile. He is currently with the Netherlands Institute for Space Research (SRON), Postbus 800, 9700 AV Groningen, NL (phone: +31503634022; e-mail: crisache@sron.nl).

D. Meledin, and V. Belitsky are with the Chalmers University in Gothenburg, Sweden (e-mail: denis.meledin@chalmers.se and victor.belitsky@chalmers.se).

P. Bergman is with the Onsala Space Observatory, Sweden (e-mail: perbergman@chalmers.se).

Atmospheric conditions are only one of the many challenges for successful THz observations. At 1.3 THz, the telescope beam is about 4.5", which becomes comparable with the telescope absolute pointing accuracy (~2-3" rms). As there are basically no pointing sources at those frequencies, the pointing has to rely on relative measurement with the lower frequency bands.

Also, the antenna surface accuracy becomes increasingly critical at those wavelengths and requirements for THz observations are precisions below 18 μm rms.

II. Receiver Design

The apex-T2 receiver is a balanced HEB receiver operating from 1250 to 1380 GHz. A full description of the receiver is published in [5]. The balanced scheme is shown in Fig. 3. The RF and LO signals are combined through a 3 dB-90 ° waveguide hybrid built with a combination of photolithography of a thick photoresist and fine copper electroplating, which allow reaching unprecedented accuracy of far less than 2 μm and with better than 100 nm surface roughness for the waveguides [6]. The waveguide outputs are then connected to two block pieces incorporating the HEB mixer chips (Fig. 4). The chips are done in quartz substrate of 17 μm thickness.

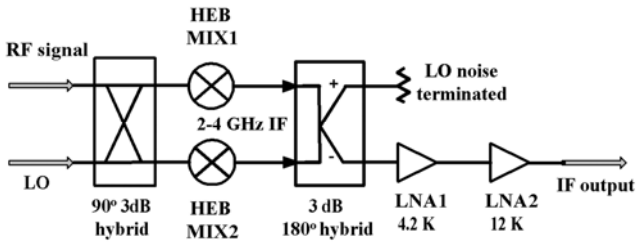

Fig. 3. Mixer layout. The balanced scheme is achieved by using 2 very similar mixers using as inputs the combination of the RF and LO signals through a 3 db-90 º hybrid.

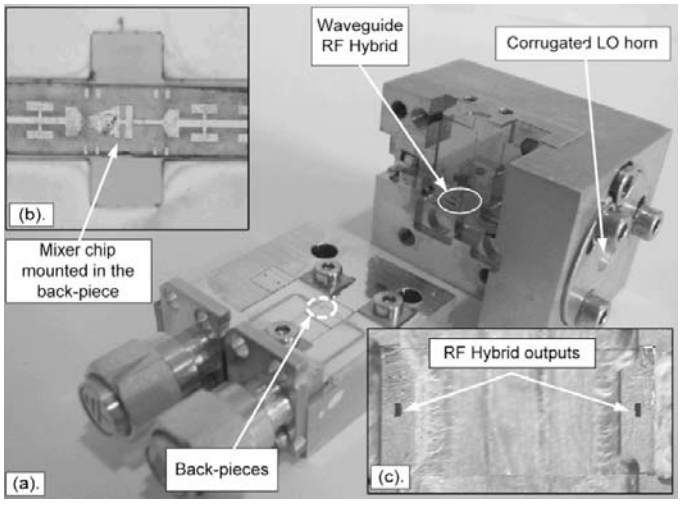

Fig. 4. Picture of the mixer block.

The IF signal outputs from the HEB mixers are then fed into a commercial 3 dB-180 ° hybrid from 2-4 GHz. One of its output is terminated with a 50 Ohm load, corresponding to the LO noise, and the other output is the signal of interest, and is amplified by state of the art cryogenic low noise amplifiers for 2-4 GHz [7].

This balanced scheme has many advantages. There is no need of a beamsplitter or diplexer to inject the LO, and all of the LO power is used advantageously. Furthermore, the LO amplitude modulated noise is terminated onto the load. Also, any unwanted spurious responses are well rejected. These help considerably for example for stability considerations.

The drawback is the need of using similar junctions, which proved to be very difficult for those components, frequency ranges and mounting considerations. Figure 5 shows the measured IV curves unpumped and pumped for the selected HEB mixers.

The receiver is mounted on the 4 K cold plate of a cryostat containing 3 other channels for frequencies 211-275 GHz, 275-380 GHz and 380-500 GHz. This receiver is the Swedish Facility (SHFI) described in [8]. The cooling machine is a closed cycle 3-stage cooler, providing a 4 K cold stage temperature. A temperature-stabilization is implemented in the coldest stage to stabilize the 4 K temperature of the different bands at levels ±2 mK. Having the ability to reach exactly the same physical temperatures allows efficiently using lookup tables.

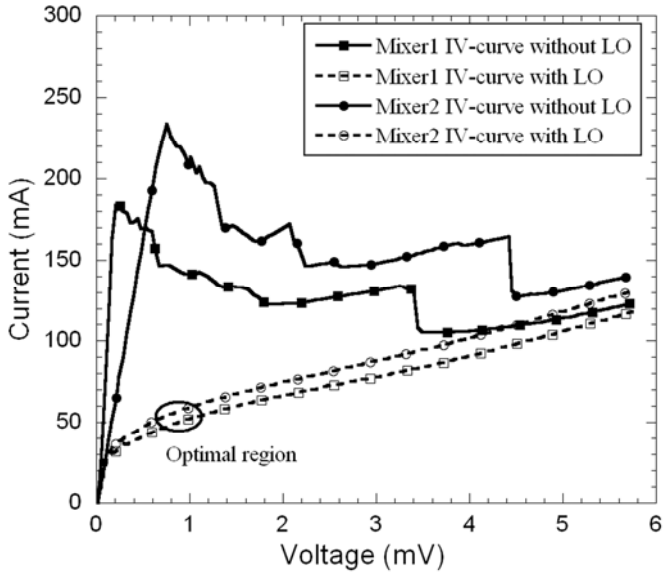

Fig. 5. IV curves for unpumped and optimally pumped conditions for the selected HEB junctions.

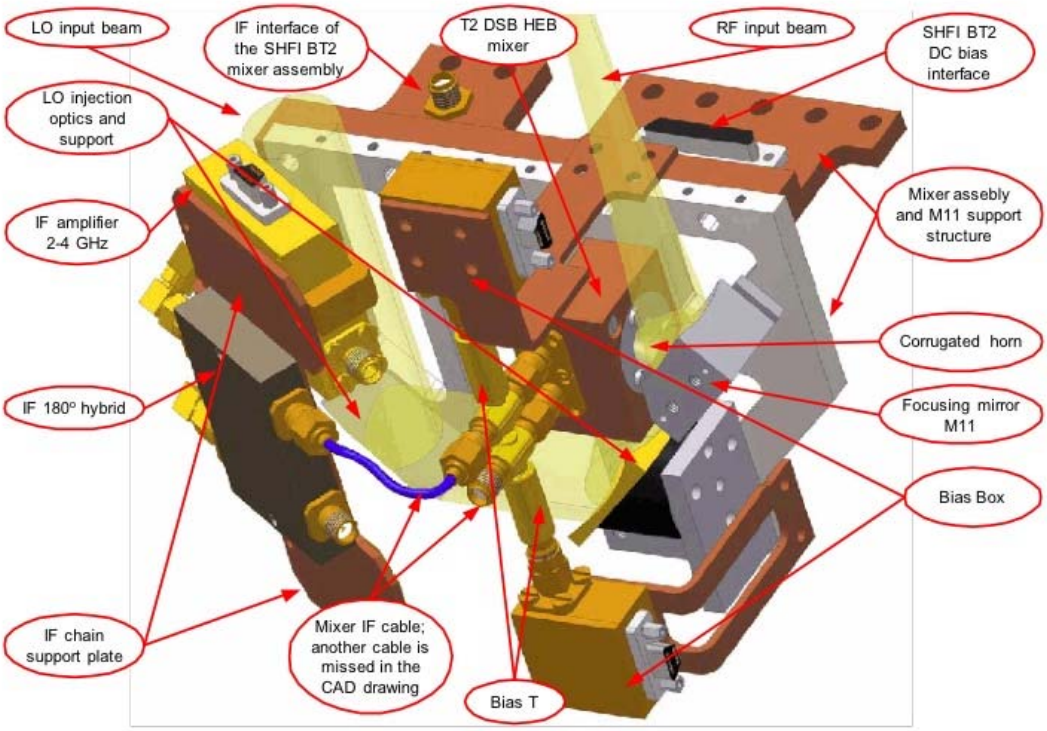

Fig. 6. The whole mixer assembly is mounted on a hexagonal plate which is thermally connected to the cryostat 4K cold stage through flexible copper wires.

III. Receiver Characterization

A. Receiver noise temperature

The receiver noise temperature were first measured on-site with external hot and cold blackbody loads of ~300 K and 77 K, put directly in front of the cryostat window. The Nasmyth A cabin incorporates a calibration unit module, providing hot and cold loads for the routine observations calibrations. At 1.3 THz, the loads coupling coefficients are far from unity, and they were adjusted to fit the external loads measurements.

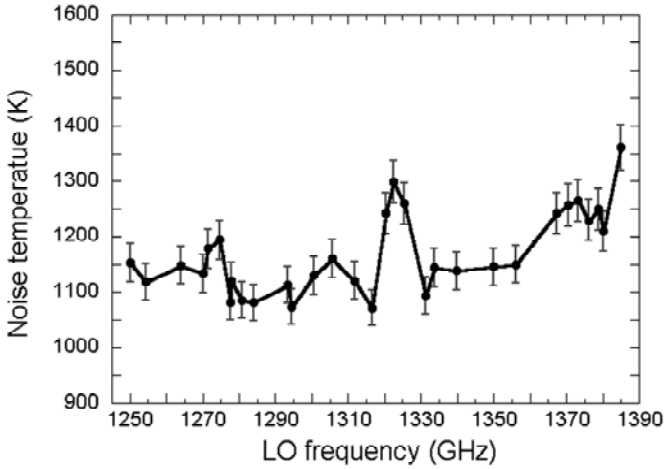

Fig. 7. Receiver noise temperatures as measured in the laboratories. On-site measurements are comparable.

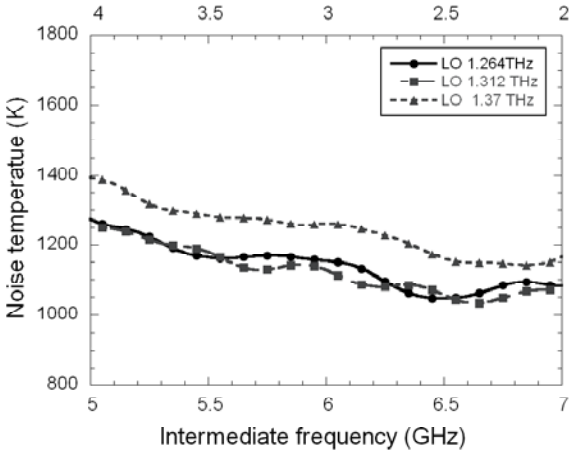

Fig. 8. Noise temperature across the IF band The 2-4 GHz IF output is unconverted to 7-5 GHz. Note that though there is no isolator between the HEB mixer and low noise amplifier, there are no IF standing waves.

Figure 7 shows the receiver noise temperature measured in the laboratory across its whole RF range. The noise temperature function of the IF frequency is shown in Fig. 8. Characteristics on site are very similar.

Although there are no isolators between the mixers IF outputs and the low noise amplifiers, the IF band-pass is very smooth and there are no visible IF ripples, quite strong for example in HIFI HEB bands [9, 18], where the HEB IF outputs are directly connected to the LNA inputs.

B. Receiver stability

The receiver stability was measured on site looking at a hot blackbody load of about 300 K. The backend is a Fast

Fourier Transform Spectrometer FFTS [10], which recorded during several hours the IF signals with a resolution bandwidth of 1 MHz. A standard way of characterizing the receiver stability is the Allan Variance [11-12].

Total power stabilities of ~50 seconds are achieved and spectroscopic stabilities are higher than 100 seconds. These numbers are comparable to SIS receivers and unusually good compared to other HEB receivers [13]. Results are even more impressive given that the HEB receiver is mounted on a closed-cycle cooling machine, which generates relatively strong 1 Hz vibrations.

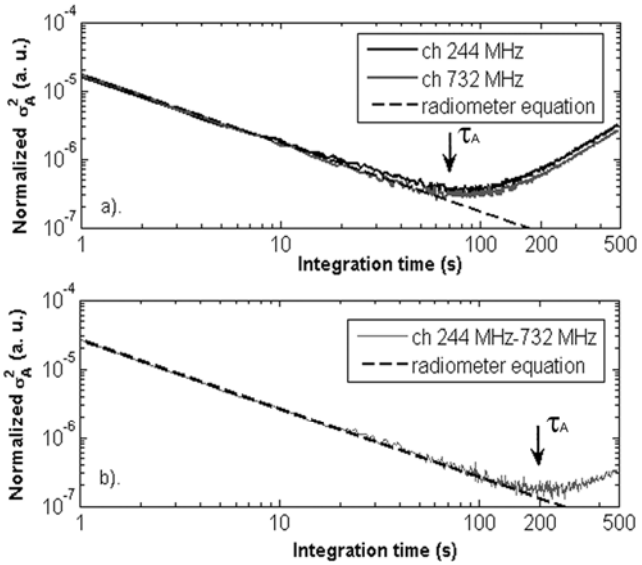

Fig. 9. Total power and spectroscopic Allan Variances measured at the 1316 GHz LO frequency. The backend bandwidth was of 1 GHz and channels corresponding to 244 and 732 MHz at IF were selected randomly to calculate the spectroscopic Allan Variance.

IV. Telescope

A. Pointing

During the first years of operations, it was noticed that the telescope tilt (defined as the telescope azimuth rotation axis) was drifting and could change in very short timescales. Figures 10 and 11 show the tilt direction and angle in a 1-year timescale. The reason for this is unknown, but causes significant problems at high frequencies, where the tilt changes can be comparable or larger than the beam sizes. The long-term variations are most likely due to seasonal and geographic variations (also seen with ALMA antennas) but the very rapid and short-term variations are not understood yet.

To minimize this effect, a standard calibration routine is performed daily at APEX, consisting in measuring the telescope tilt with a set of tiltmeters and correcting the pointing model for the change in tilt. With this correcting scheme, the absolute pointing accuracy can still be of about 2-3" rms as it can be seen with the low frequency receivers.

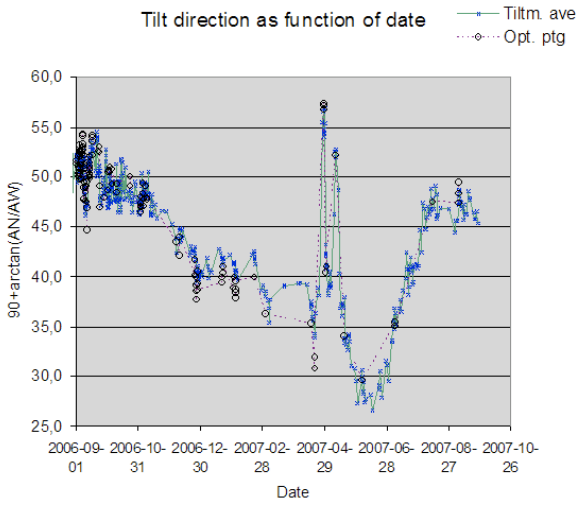

Fig.10. Tilt direction change during a 1 year period. Very sudden changes were seen on few occasions in April 2009.

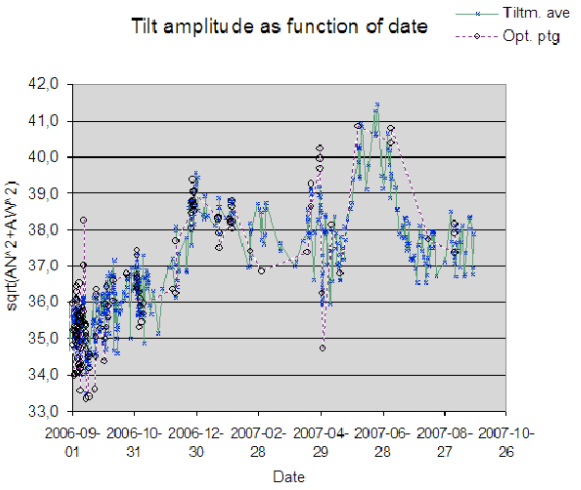

Fig. 11. Tilt amplitude change during a 1 year period.

When performing apex-T2 observations, as there are basically no pointing sources strong enough at those wavelengths, the idea is to use one of the low frequency bands within SHFI, either the 230 GHz or the 345 GHz and use them for pointing towards a source nearby the selected target. The relative pointing offsets and focus offsets are not expected to change and once derived, the switching between the different bands takes less than 5 minutes, all included. The difficulty lies in deriving the initial relative offsets between the bands, but once this is done, this would ensure efficient observing.

B. Telescope Surface accuracy

The ALMA 12 m antennas have a specification for their surface accuracy of 18 μm rms. This is sufficient for observations up to ~1 THz but for higher frequencies, requirements are greater. Holography sessions are typically ran once a year to check the surface accuracy and if needed adjust the panels to improve it. The 12 m telescope is made of 264 small aluminum panels in 8 rings on a Carbon Fiber

Reinforced Plastic (CFRP) backup structure, which ensures thermal stability.

Figure 12 shows the surface accuracy after the panels had been adjusted. This is about the best settings that can be achieved. However, this is measured at an elevation of ~13 degrees (the holography transmitter is located on a neighboring mountain), so a correction for the expected gravity deformation is done to optimize the surface for 50 degrees elevation.

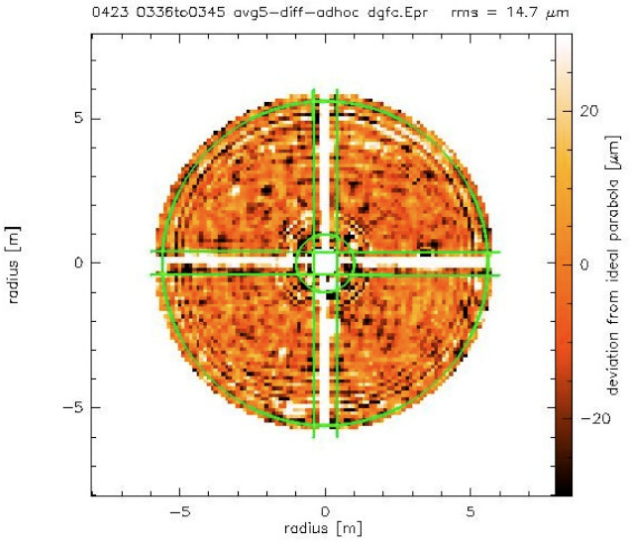

Fig. 12. Surface accuracy of the APEX dish after a successful holography run and subsequent panel adjustment in 2007. The achieved rms was of 14.7 μm.

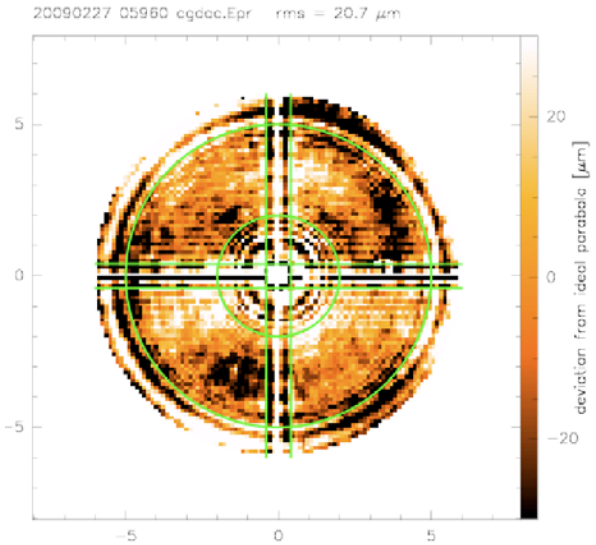

Fig. 13. Surface accuracy of the APEX dish after a holography run in 2008. The measured average rms is of 20.7 μm.

After several months, the surface might degrade and Fig. 13 shows the accuracy when measured in 2008. The antenna surface is very sensitive to temperature changes and the temperature control in the Cassegrain helps maintaining stable temperature. The latest measurements in 2008 show a worsening, and the surface accuracy during the THz observations presented in this paper were more likely to be between 20-25 μm, which is consistent with the derived beam efficiencies.

Figure 14 shows the aperture efficiency dependency on the surface accuracy of the antenna. It can be seen for example that from 15 to 20 μm surface accuracy rms, the aperture efficiency drops a factor of 2 at 1.3 THz.

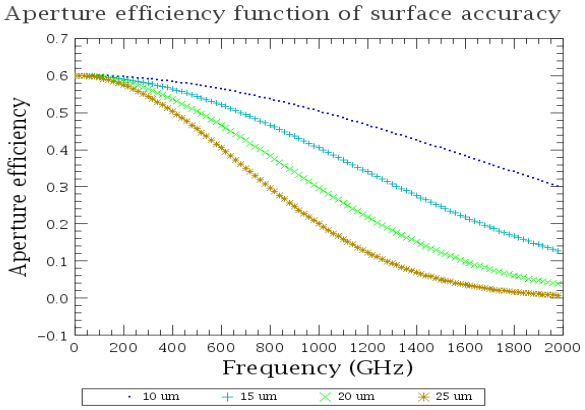

Fig. 14. Aperture efficiency dependency on surface accuracy. Best achievable results seem to be about 15 μm rms after a panel adjustment session but 20 μm rms is more likely to be the average value after few months.

V. First Observations

A. Astronomical lines of interests

The installation of this 1.3 THz receiver was motivated by the relative good atmospheric transmission achievable from this site. Also several important molecular transitions are observable within this window. Table 1 summarizes the most important lines.

TABLE 1 Molecular lines in the 1.3 THz window

Molecular transition	Frequency (GHz)
CO(11-10)	1267.014486 GHz LSB
HNC(14-13)	1268.200385 GHz LSB
CS(26-25)	1270.952878 GHz USB
H2CO(422-303)	1274.49247 GHz USB)
C18O(12-11)	1316.244114 GHz USB
HCN(15-14)	1328.302232 GHz LSB
LiH(3-2)	1329.41543 GHz LSB
HCO+(15-14)	1336.71492 GHz LSB
C17O(12-11)	1347.115 GHz LSB
HDO(303-202)	1353.77657 GHz USB
HNC(15-14)	1358.612610 GHz USB
CS(28-27)	1368.234047 GHz USB
H2D+(101-000)	1370.146 GHz USB
CO(12-11)	1381.995105 GHz USB

Among the most important lines in this band are the high-J transitions of CO, the J=11-10 and J=12-11. These lines can be emitted only from hot (T>100 K) and dense (n□$10^{5.5}$cm^{-3} or higher) molecular gas.

One of the most interesting lines in this frequency range is the ground-state para-H_2D^+ transition at 1370 GHz. This molecule is an appropriate tracer for the deeply embedded parts of dark cloud cores where other molecules freeze out onto the grains surface. The ground-state ortho-H_2D^+ transition at 372 GHz was already detected in several sources, however, the p-H_2D^+ has never been detected so far, and therefore its first detection is one of the receiver priorities.

It is worth noticing that the HIFI instrument does not cover this frequency range, and therefore both instruments could benefit from each other. The HIFI band 5 currently reaches 1271 GHz, therefore at least the CO(11-10) and CS(26-25) are observable with both receivers, which is very important for cross calibration purposes.

B. Initial pointing, focus on Jupiter

Only the Moon and the brightest planets, e.g. Jupiter are possibly detectable with total power continuum observations. Jupiter was only detected at high elevations and with PWV less than 0.25 mm, when the T_{SYS} is below 15000 K. To take advantage of the maximum atmospheric transparency, the receiver is tuned to 1353 GHz USB, where although the T_{REC} is slightly worse than at lower frequencies, the overall T_{SYS} is better. Unfortunately, only 1 GHz of the 2 GHz IF range is currently handled at APEX (backend limitations), so a factor of 1.4 in sensitivity is directly lost.

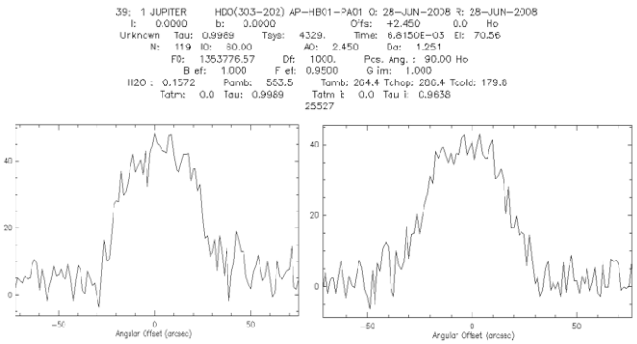

Fig. 15. Jupiter pointing in elevation (left) and azimuth (right).

Figure 15 show the pointing on Jupiter under very good weather conditions, and high source elevation. After the telescope pointing corrections were taken into account, the focus is normally found by moving the sub-reflector in every direction and finding the maximum of flux, which corresponds to a focused telescope. However for Jupiter, which is extended (~30") for the T2 beam, this procedure doesn't work well as a defocused beam still ends up on Jupiter.

A smaller sized planet such as Mars would work better, but it was not visible at the time and was also too weak for this purpose (too far from the Earth at the time).

Therefore, until now, few pointing measurements were performed and only initial relative offsets were found between the different bands within SHFI. More measurements are needed to fully cover this part and the focus relative positions should be performed whenever possible when Mars will be strong enough.

Calculations and models from [1], show that we expect a first error beam of ~80".

C. Observations of Orion-FIR4

The very first spectroscopic observations were done on the 14th of March 2008, looking at the very strong line of CO(11-10) in Orion-FIR4 [17]. The telescope was not pointed (nor focused) properly, explaining the narrower line width and lesser intensity than expected (Fig. 16). This region is very extended; therefore the line was easily detected.

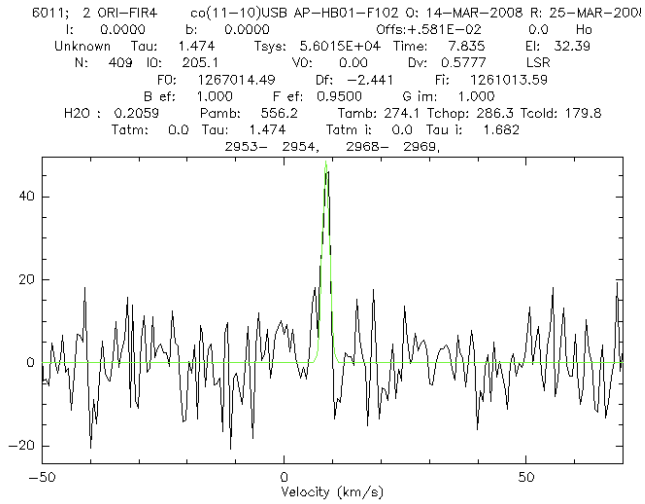

Fig. 16. First light on Ori-FIR4. Telescope was not pointed, nor focused, explaining the lower T_{MB} than expected (~ 200K).

D. Observations of CW-Leo (IRC-10216)

During the Science verification of the SHFI receiver, the evolved Carbon star CW-Leo (also know as IRC-10216) was observed at CO(11-10) (Fig. 17) and the line was clearly detected with a T_{mb} of ~ 41 K. This source is routinely used as pointing source for low frequency receivers and will be intensively observed by HIFI.

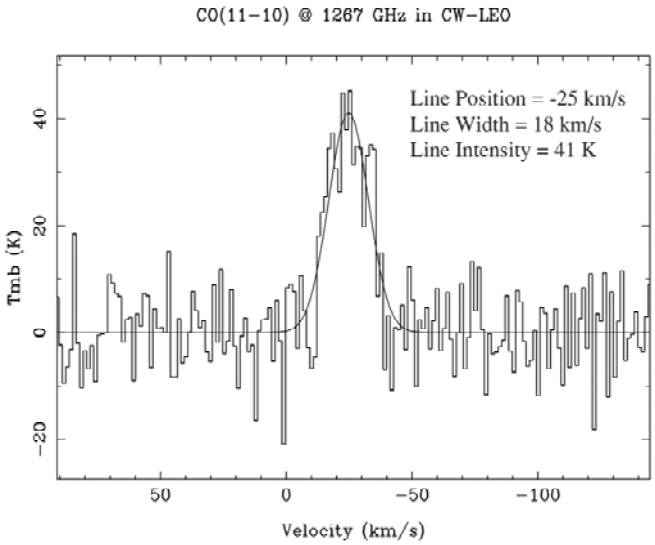

Fig. 17. CO(11-10) observations performed on April 2008.

E. Observations of Sagittarius B2 (SGR-B2(M))

The normal operation of the apex-T2 receiver is an opportunistic one. As the observations can only be done during few nights a year, whenever the conditions are good enough, the high frequency receivers have priority and take over the observations.

During one of those opportunities, commissioning observations were done on the Sagittarius B2 region. Several transitions were looked for, namely CO(11-10), CO(12-11), HCN(15-14) and SH. Only the first one was clearly detected and is shown in Fig. 19. The T_{MB} is of ~20K. The line shows a strong dip in the center, pointing to different causes. Either the line is excited enough and shows here self-absorption (which is seen at the lower J transitions) , either the reference OFF position during the observation had emission; therefore the ON-OFF will cause a similar line profile. More observations are needed to disentangle between both scenarios.

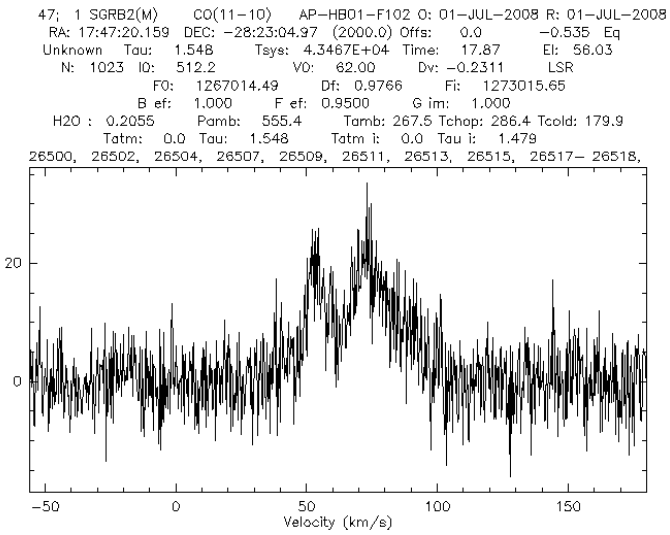

Fig. 18. CO(11-10) in SGR-B2(M) during T2 commissioning opportunistic observations.

VI. Conclusion

A state of the art balanced HEB receiver was installed at the APEX telescope in 2008, achieving excellent sensitivities and stability. Only a few nights of observations on sky were performed so far, but already several detections were readily performed.

The main challenges at those frequencies are:

- Weather conditions should be better than 0.25 mm PWV, which is the case only ~5% of the time.
- The antenna surface accuracy needs to be below 18 μm rms to achieve acceptable aperture efficiencies, however the antenna surface accuracy seems to be degrading with time and was probably above that threshold.
- Pointing is very difficult due to the absence of pointing sources, to variations in the telescope tilt causing change of several arcseconds, which is then comparable to the 1.3 THz beam of 4.5". Also, pointing to Jupiter can be very difficult due to the previous point, with a poor aperture efficiency.

Therefore, a prerequisite for efficient use of the 1.3 THz receiver is to have the best antenna surface possible, which would in turn allow an easier pointing and focus estimation using planets, and tie those to lower frequency bands. Also, an improvement would be to use the full IF bandwidth to improve the sensitivities.

This would allow very efficient use of the THz receiver as it can be readily used any time and take advantage of opportunistic weather conditions. This receiver covers a frequency band that won't be observed with the HIFI instrument of Herschel [18]. As such, the apex-T2 receiver, in combination with the 12 m APEX antenna at the Chajnantor site, offers excellent opportunities for THz astronomy, to complement and cross calibrate HIFI. Especially, APEX follow-up studies can be envisioned whenever higher spatial resolution is needed.

Acknowledgment

We would like to thank the APEX staff for their support during the receiver installation and observations.

References

[1] R. Guesten et al., "APEX, The Atacama Pathfinder EXperiment", in Proc. SPIE, 2006, 6267, 626714.

[2] Atacama Large Millimeter/submillimeter Array (ALMA) (http://www.alma.nrao.edu/

[3] APEX Instrumentation (http://www.apex-telescope.org/instruments)

[4] J.R. Pardo, J. Cernicharo, E. Serabyn, "Atmospheric Transmission at Microwaves (ATM): an improved Model for Millimeter - Submillimeter Applications", *IEEE Transactions on Antennas and Propagation*, Vol. 49, Issue 12, pp. 1683-1694, December 2001.

[5] D. Meledin et al.. "A 1.3 THz Balanced Waveguide HEB Mixer for the APEX Telescope", in *IEEE Trans. Microwave Theory and Techniques*, vol. 57, Issue 1, pp: 89-98, 2009.

[6] A. Pavolotsky, D. Meledin, C. Risacher, M. Pantaleev, V. Belitsky, "Micromachining approach in fabricating of THz waveguide components"*, Microelectronics J.,"* vol. 36, pp. 683-686, 2005

[7] C. Risacher, E. Sundin, V. Perez Robles, M. Pantaleev, and V. Belitsky," Low Noise and Low Power Consumption Cryogenic Amplifiers for Onsala and Apex Telescopes," in *Proc. 12th GAAS Symp.*, Amsterdam, 2004,pp. 375-378.

[8] Vassilev et al. "A Swedish heterodyne facility instrument for the APEX telescope", in Astronomy and Astrophysics, 490, 1157–1163 (2008).

[9] R. Higgins and J. Kooi, "Electrical standing waves in the HIFI HEB mixer amplifier chain ", in Proceedings of the SPIE, Volume 7215, pp. 72150L-72150L-10 (2009).

[10] B. Klein, S. D. Philipp, I. Krämer, C. Kasemann, R. Güsten and K. M. Menten, "The APEX digital Fast Fourier Transform Spectrometer," *Astron. & Astrophys.*, vol. 454, pp. L29-L32, 2006

[11] D W. Allan, "Statistics of Atomic Frequency Standards", *Proc. IEEE*, Vol. 54, No. 2, pp 221-230, 1969.

[12] R. Schieder, G. Rau, B. Vowinkel, "Characterization and Measurement of System Stability," in *Proc. SPIE*, vol. 598, 1985, pp. 189-192.

[13] J. Kooi and V. Ossenkopf, " HIFI Instrument Stability as measured during the Thermal Vacuum Tests of the Herschel Space Observatory", this issue.

[14] Cherednichenko, V. Drakinskiy, T. Berg., P. Khosropanah, and E. Kollberg, "Hot-electron bolometer terahertz mixers for Hershel Space Observatory," *Rev. Sci. Instrum.*, vol.79, 034501, 2008

[15] D. Marrone, R. Blundell, E. Tong, S. Paine, D. Loudkov, J. Kawamura, et al., "Observations in the 1.3 and 1.5 THz Atmospheric Windows with the Receiver Lab telescope," in *Proc. 15th Int. Symp. Space THz Technology*, Gothenburg, 2005, pp. 64-67

[16] D. Marrone, J. Battat, F. Bensh, R. Blundell, M. Dias, H. Gibson, et al., "A map of OMC-1 in CO J=9→8," *Astrophys. J.,* vol. 612, pp. 940-945, Sept. 2004

[17] M. Wiedner, G. Wiehning, F. Bielau, K. Rettenbacher, N. Volgenau, M. Emprechtinger, et al., "First observations with CONDOR, a 1.5 THz heterodyne receiver," *Astron. & Astrophys.*, vol. 454, pp. L33-L36, 2006

[18] P. Dieleman et al. "Performance of HIFI in flight conditions", this issue.

T1B

First Light of the TELIS instrument

Gert de Lange[1*], Pavel Yagoubov[2], Hans Golstein[1], Arno de Lange[1], Bart van Kuik[1], Joris van Rantwijk[1]
Ed de Vries[1], Johannes Dercksen, [1] Ruud Hoogeveen[1,] Valery Koshelets[3], Oleg Kiselev[3],
Andrey Ermakov[3]

1 SRON Netherlands Institute for Space Research, the Netherlands
2 ESO, Garching, Germany
3 Institute of Radio Engineering and Electronics (IREE), Moscow, Russia
* Contact: gert@sron.nl, phone +31-50-363 4074

***Abstract*— The TELIS (Terahertz and sub-millimeter limb sounder) instrument is a three-channel heterodyne receiver developed for observations of the stratosphere. TELIS is mounted together with the MIPAS-B2 instrument on a balloon platform of the Institute for Meteorology and Climate Research of the University of Karlsruhe (IMK, Germany). TELIS can observe both in the sub-millimeter range (480-650 GHz) and at 1.8 THz, while MIPAS-B2 observes trace-gases in the thermal infrared. Results will be used to refine and constrain numerical chemical transport models.**

The SRON contribution to TELIS is the 480-650 GHz Superconducting Integrated Receiver (SIR) channel. This is a unique superconducting on-chip heterodyne receiver, consisting of a double dipole antenna, a SIS mixer, a flux-flow Local Oscillator, and a superconducting harmonic mixer used for phase locking of the LO-signal. The bandwidth of the Digital Autocorrelator IF-backend of the SIR-receiver channel is 2 GHz, centered at 6 GHz. The lowest noise temperature of the receiver is 120 K DSB, measured over the full IF bandwidth. Although the concept of an integrated receiver has been explored for some years, the actual use of such a receiver for scientific observations so far has not been demonstrated.

The first flight campaign with TELIS/MIPAS was in June 2008 from Teresina (Brazil). The SIR channel was operating well during the 2 hour ascent, but a major problem with the TELIS cryostat occurred at flight altitude (40 km) and this prevented scientific data retrieval. A second flight of TELIS is scheduled early 2009 from Kiruna (Sweden). This flight will focus on the Arctic ozone chemistry. The actual flight date depends on the occurrence of favourable meterological conditions.

In the presentation we will discuss the operation of the SIR-channel in the laboratory and at the Teresina campaign and may include the results of the Kiruna flight.

Performance of HIFI in flight conditions

Pieter Dieleman, David Teyssier, Thomas Klein, John C. Pearson, Willem Jellema, Jacob W. Kooi, Jonathan Braine, Pat. W. Morris, Albrecht R.W. de Jonge, Rob de Haan, Wouter. M. Laauwen, Heino P. Smit, Nick D. Whyborn, Peter R. Roelfsema, Frank P. Helmich, and Thijs W.M de Graauw, on behalf of the HIFI team.

***Abstract*— HIFI, the Heterodyne Instrument for the Far-Infrared is one of three instruments on board the ESA Herschel mission, planned for launch in May 2009. The HIFI instrument was tested in representative flight conditions during the Thermal Balance / Thermal Vacuum (TBTV) test in ESA's Large Space Simulator (LSS) last December 2008. In particular HIFI's local oscillator could finally be tested over its full frequency range.**

The system noise temperature is similar to that found during instrument testing at the laboratory. Stability is measured to be slightly worse for the SIS bands and better than before for the HEB mixers, the latter most likely due to the absence of vibrations of mechanical cryocoolers. A new diplexer calibration approach was used, LO purity tests around 930 and 1900 GHz to remove spurious signals were successfully performed. Standing waves in both the signal-and LO optical paths were measured to provide input for spectrum baselines optimization schemes.

***Index Terms*—Submillimeter wave receivers, superconductor-insulator-superconductor devices, quasioptical mixers, Infrared spectroscopy.**

I. INTRODUCTION

THE Heterodyne Instrument for the Far-Infrared (HIFI) [1] is one of three instruments on board of the ESA Herschel satellite [2]. It spans a frequency from 480 – 1270 and 1430 to 1901 GHz, with a spectral resolution of up to 140 kHz. HIFI has 7 dual-polarisation mixer bands. Bands 1-5 consist of SIS mixers, bands 6 and 7 use HEB mixers [3]. The local oscillator (LO) frequency range is split into 14 frequency bands, each with its own LO chain. The LO is placed outside the cryostat to limit the heat load on the helium. A dedicated radiator will cool the LO to 125 K once in flight (see Fig. 1). The downconverted Intermediate Frequency (IF) signal is fed to two types of spectrum analyser: to an Acousto-Optic Spectrometer (WBS) with an IF band of 4-8 GHz and a resolution of 1.1MHz and to an auto-correlator (HRS) with an adjustable IF bandwidth up to 2 GHz and a resolution of up to 140 kHz.

HIFI was delivered to ESA for integration onto the Herschel satellite in June 2007. HIFI was fully integrated by April 2008. Most of the performance tests were executed in the summer of 2008. However n these tests the LO frequency coverage was limited, since the LO is mounted outside the cryostat and is hence at ambient temperature in normal clean room test environment. The available LO power at room temperature is insufficient for the band 6 and 7 HEB mixers. The Herschel Thermal Balance / Thermal Vacuum test was therefore the first opportunity to test the HIFI over its full frequency range. In this article the calibration scheme, some optimizations and the final performance as measured during the TBTV test are reported.

Manuscript received 20 April 2009.

P. Dieleman, W. Jellema, A.R.W. de Jonge, R. de Haan, W.M. Laauwen, H.P. Smit, P.R. Roelfsema and F.P. Helmich are with SRON, the Netherlands Institute of Space Research, Groningen, the Netherlands (+31-50-3638286, mail: P.Dieleman@sron.nl).

D. Teyssier is with the European Space Astronomy Centre, Madrid, Spain (e-mail: dteyssier@sciops.esa.int).

T. Klein is with the Max Planck Institute für Radio Astronomie, Bonn, Germany (e-mail: tklein@mpifr-bonn.mpg.de).

J.C. Pearson is with the Jet Propulsion Laboratories, Pasadena, California, USA (e-mail: john.c.pearson@jpl.nasa.gov).

J.W. Kooi is with the California Institute of Technology, Pasadena, California, USA (e-mail: kooi@phobos.caltech.edu.

J.Braine is with the Observatoire de Bordeaux, Bordeaux, France (e-mail: Jonathan.Braine@obs.u-bordeaux1.fr).

P.W. Morris is with IPAC, California Institute of Technolog, Pasadena, California, USA (e-mail: pmorris@ipac.caltech.edu).

N.D. Whyborn and M.W.M de Graauw are with the Atacama Large Millimeter/sub millimeter Array, Las Condes, Chile (e-mail: nwhyborn@alma.cl).

II. HERSCHEL THERMAL BALANCE TEST

November 2008 the Herschel satellite was lowered into the LSS, (Fig. 1) and the cool-down of the Large Space Simulator (LSS) [4] at the ESA test center ESTEC started.

The entire satellite was radiatively cooled in the LSS. Thermal equilibrium at 130 K was reached after 5 days for the LO. To save time a dissipative heater was used to avoid cooling the LO to its equilibrium temperature without dissipation. The heater power was set to the average LO dissipation in operation. Throughout the TBTV tests and in flight the dissipation of the LO was kept constant, either by operating the unit or by using this heater.

The warm units (spectrometers, electronic control and supply units) cooled to 5ºC in 24 hours, after which satellite heaters prevented further cooling. After HIFI switch-on, the temperature went up to 10 - 20ºC within 24 hours.

The thermal equilibrium temperature of the HRS appeared to be too low to maintain the clock speed of the HRS ASICs; satellite heaters were used to increase the temperature at the mounting interface to 25ºC. The thermal stability requirement of 0.3 mK/s of the WBS and HRS spectrometers units is guaranteed by a PID control.

Fig. 1. Herschel lifted to be placed into the LSS. The 3.5 meter telescope is covered by a protection cloth. The rear side of the solar panel is covered by multilayer thermal insulation (MLI) blankets. The black central cylinder contains the 2500 liters He and the focal plane units of the instruments. The lower section, covered with black MLI contains the warm electronics that will be kept at room temperature by their own dissipation . Clearly visible is the LO radiator close to the solar panel, this will allow the LO to cool to 125 K in flight.

III. HIFI TUNING

After thermal equilibrium was reached and a series of health checks was successful performed, the diplexers and LO settings could be tuned to provide optimum signal coupling and LO power to the mixers.

Diplexers in the Focal Plane Unit provide LO and signal coupling for 4 mixer bands. These diplexers are unbalanced and hence need re-adjustment once without gravity in flight.

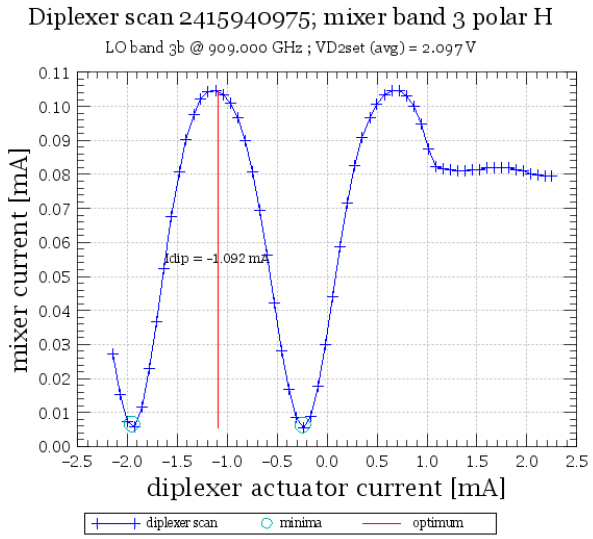

Fig. 2. A typical example of a diplexer scan. In this case the diplexer hits the end-stop beyond 1 mA, hence the flat region. The optimum is calculated as the average of the minima.

The diplexer calibration starts with a coarse tuning to optimize the LO – mixer coupling. Fig. 2 shows the result of a coarse diplexer scan.

Since neither the optimum LO power not the optimum diplexer setting is known a priory, the diplexer scan is executed for 7 LO power settings to hit at least one proper setting. The LO output power is controlled by the drain voltage setting of the 2nd power amplifier in the chain, before the multipliers. In Fig. 3 the mixer current as function of LO drain voltage (Vd2) is shown for mixer band 4 and LO subband 4a.

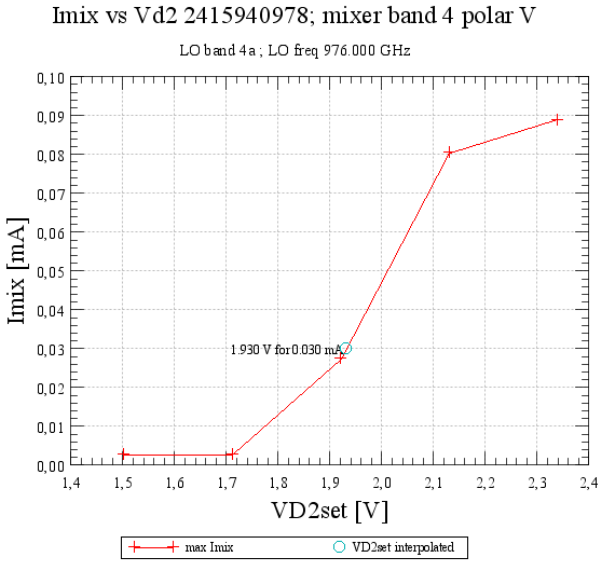

Fig. 3. The relation between 2nd power amplifier drain voltage and mixer current. The interpolated drain voltage setting is indicated as well.

This Vd2-mixer current relation is needed for the diplexer fine calibration, in which the diplexer setting for the signal path is optimized. The reason to include this test is that the LO alignment may differ from the signal path alignment. Since the diplexer function is based on path lengths variation, and the path length is dependent on the angle of the beam, any unequal alignment of the two beams would result in a different diplexer optimum setting. The signal path coupling optimization is performed by measuring the noise temperature using the internal hot-cold calibration loads for 20 diplexer settings around the expected optimum. A typical result of the diplexer fine calibration can be found in Fig. 4.

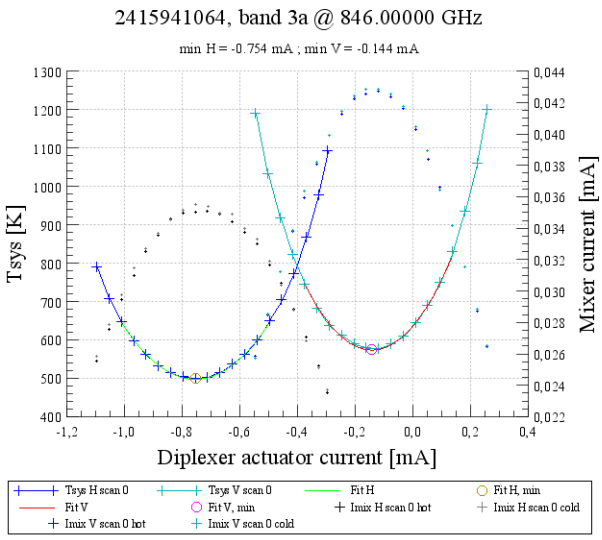

Fig. 4. Noise temperature versus diplexer setting for the H and V polarizations. The optima for the signal path are quite close to those found for the LO path.

The resulting diplexer calibration relation is shown in Fig. 5.

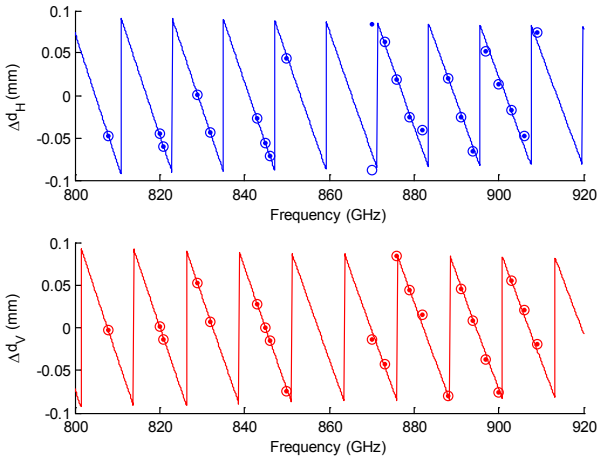

Fig. 5. Saw-tooth result for the diplexer setting as function of LO frequency. Clearly the model (line) fits the data (open circles) very well.

Generally the fine-tuning confirmed the course calibration results. Deviations were too small to be discerned mainly because of the limited accuracy of the noise temperature measurements due to standing waves and drift. The final accuracy is better than 2% of a wavelength, and hence the signal coupling losses are negligible.

The LO settings need adjustment with respect to the ILT found values since the LO attenuator values were different from those used in ILT, furthermore the output power is dependent on the LO temperature and the LO harness was now at 100 K rather than room temperature. The LO output power was calibrated by scanning the Vd2 and measuring the resulting mixer current for every 2 GHz over the full HIFI bandwidth. This procedure is performed with the diplexer already at the optimum LO coupling setting. The result is similar to that presented in Fig. 3, but with 10 points for optimum interpolation accuracy. An example of the HEB mixer current for the full LO power for LO subband 6b is shown in Fig. 6.

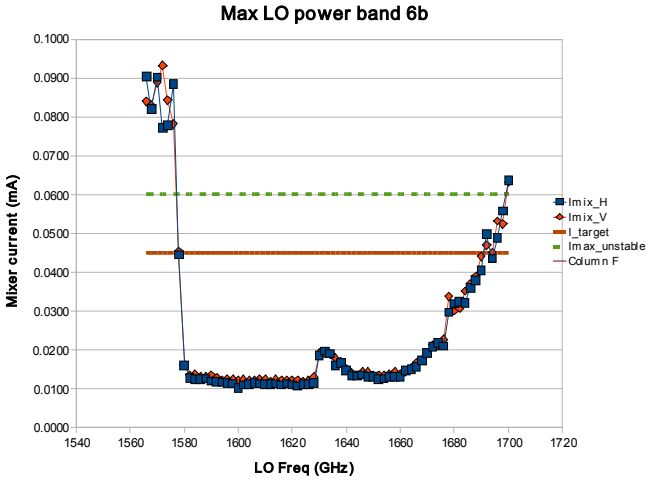

Fig. 6. Mixer current versus LO frequency for the maximum LO power. The brown line indicates the mixer current for best noise temperature. Clearly there is ample LO power over a 120 GHz range in this LO subband.

IV. HIFI Performance Test

With the diplexers and LO well tuned, the mixer magnet settings for maximum suppression of Josephson noise could be optimized. The method is described in [5]. The results are similar to those previously measured at ILT and during Herschel integration with the LO at room temperature.

The system sensitivity of HIFI was measured using the internal hot (100K and cold (10K) calibration loads for every 2 GHz. External loads or line signals could not be used since the Herschel cryocover was not opened during the TBTV test. The result is shown in Fig. 7. The noise temperature is similar to that measured in the Instrument Level Tests (ILT) just before delivery to ESA. At a number of frequencies the LO settings could be optimized to achieve an increased pump level at the mixer compared to ILT, so drop-outs at isolated frequencies could be removed. Since two mixers (horizontal and vertical polarization) function simultaneously, one could add the spectra and arrive at a combined system noise temperature that is square root 2 lower than the individual noise temperature, provided the noise temperatures and stabilities are similar.

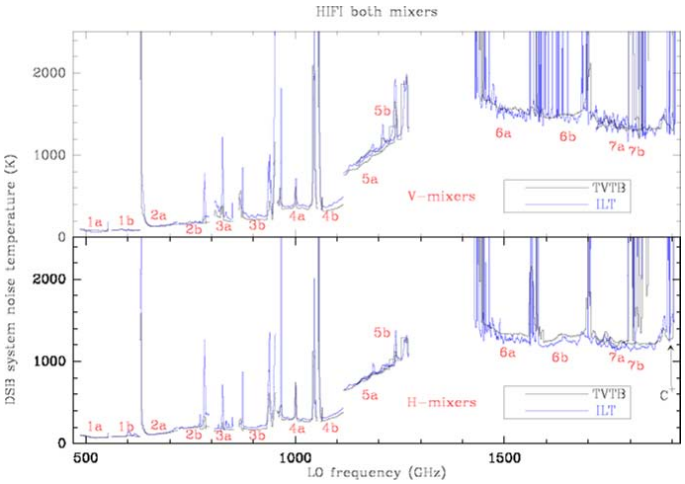

Fig. 7. System noise temperature as function of LO frequency. The plotted noise temperature values are the median values over the IF range.

V. LO PURITY

In the instrument level tests in the laboratory just before delivery it was found that LO subbands 3b and 7b had frequency regions where most of the LO power produced was not at the commanded frequencies. This behavior became apparent not only from dedicated spurious signals tests with external signal sources, but also by examining the diplexer scans in these frequency ranges. The diplexer can act as a Fourier transform spectrometer (FTS), albeit with a limited frequency resolution since the optical path length modulation is a mere 2 to 7 wavelengths. Since in the LSS an external signal source could not be used, the LO purity level could only be determined by diplexer scans. The diplexer model established as a result of the diplexer coarse test is then used to determine the mechanical path length and hence the LO frequency.

A typical example of the LO impurity is the spare band 3b output spectrum as shown in Fig. 8. The spare band 3b chain exhibited very similar behavior and hence the recipe to cure the problem could be determined and tested offline as a preparation for the TBTV test.

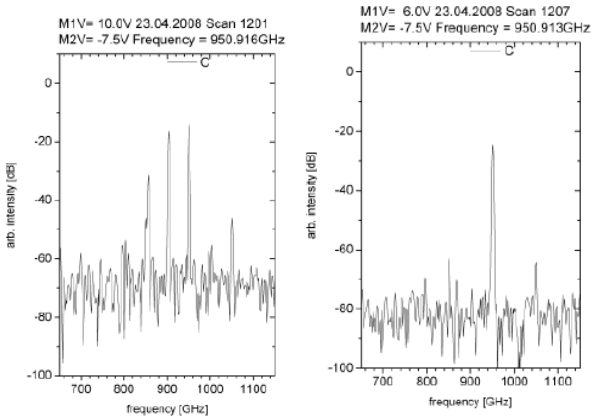

Fig. 8. LO output spectra measured with an FTS on the spare 3b LO chain. Commanded frequency is 950.916 GHz. The left plot shows the multi-tone with the default multiplier settings, the right plot shows the cleaned-up spectrum with settings optimized for single tone at the correct frequency.

It was found that the 1st (M1) and often also the 2nd multiplier (M2) stage bias voltages directly impact the purity of the LO signal.

The 3b TBTV purity test consisted of collecting the voltages and currents of the chain as well as taking diplexer scans for a 2-D grid of M1 and M2 voltage settings. A second parameter relating to the LO purity appeared to be the M2 current. For 3b the M1 needed to be biased more forward, M2 needed sometimes a more reverse bias voltage. To ensure these settings would not affect the lifetime of the multipliers, the 3b spare chain was lifetime tested at a worst case 8µA M2 reverse current for twice the expected flight operation time.
The test result is good: 9 out of 12 LO frequencies could be purified and the expectation is that the last 3 can be cured as well with extrapolated M2 voltages.

LO subband 7b was known to have purity problems above 1890 GHz. Unfortunately most of the observation proposals are centered around the CII line of 1901 GHz, that requires an LO frequency between 1897-1898 to measure the line in the upper side band. The purity effort in TBTV concentrated on this line. For band 7b it was found in ILT that the cure lies in operating the 1st multiplier at more negative voltage bias. However the LO band 7b was already used with M1 voltages close to half the reverse breakdown voltage, the general 'rule of thumb' safe limit to avoid damage to the diode. Hence the importance of lifetime tests was emphasized. A test was performed on a 200 GHz flight spare multiplier. In this test the device survived more than -9V of reverse bias with 100mW of RF. Although the I,V curve of the diode did change substantially, it stabilized and the output power hardly changed after 1000 hours of testing. The input power of the flight multiplier will be below 100mW, and the reverse bias will be -8.5 V or less. The 7b purity test was successful: the CII line is now clean.

For the diplexer bands 3,4,6 and 7 diplexer scans were taken for every 2 GHz with the aim to examine the LO purity. In this diplexer survey no new impure regions were found, except for bands 7a and 7b. Fig. 9 shows that regions a few GHz wide are present in these bands that show deviating LO frequencies. Curing these fell outside the scope of the TBTV test. With the knowledge obtained these can be addressed, although this will have to be in flight.

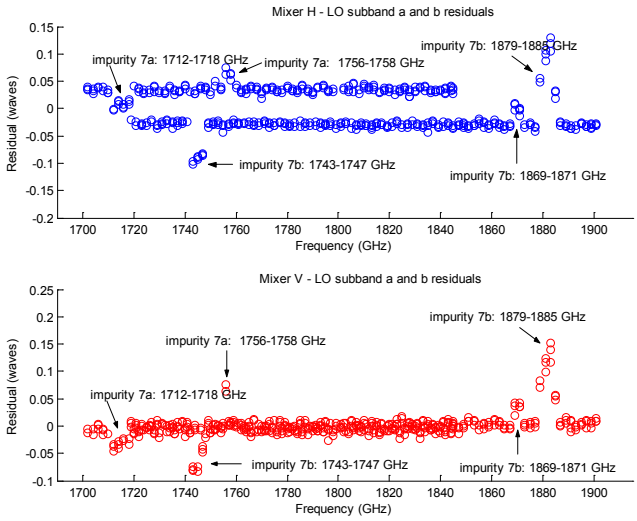

Fig. 9. Deviation of the measured versus commanded LO frequencies in terms of wavelength fractions. The CII (1900 GHz) region is clean.

VI. Standing Wave Tests

Dedicated tests were performed to find amplitude and periods of standing waves in both the LO and signal paths. The method chosen is to measure the mixer current and take I spectra during a retune the LO in steps of 14 MHz, with the mixer and diplexer tuned for the middle frequency of the range. For the signal path, the IF spectra were divided by the first spectrum and an FFT was calculated. The thus normalized IF spectrum is shown in Fig. 10.

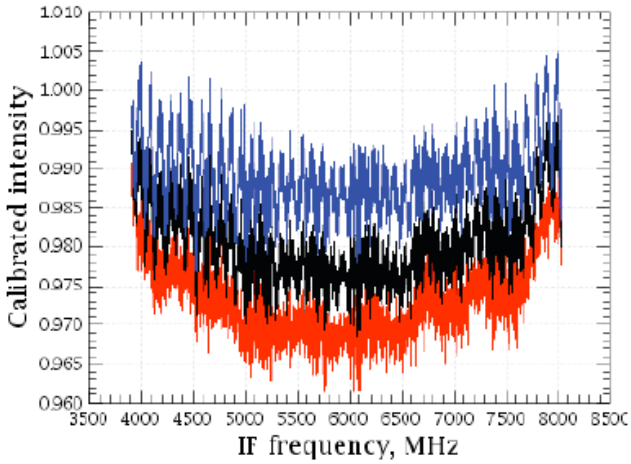

Fig. 10. Normalized spectra used in the signal standing wave calculation. The deviation from 1 is an indication of the mixer current and IF impedance match variation over the LO frequency range of 0.5 GHz.

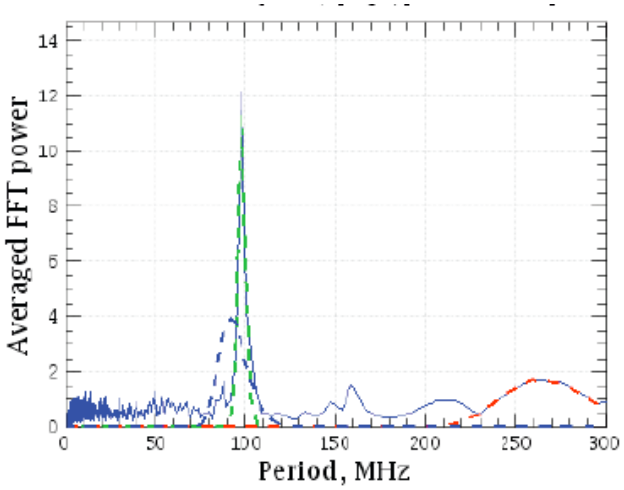

Fig. 11. FFT of the IF spectrum of Fig. 10. The peak at 92 MHz corresponds to the optical path length of 1.63 meters between the mixer and internal hot calibration source. The cold source – mixer distance is shorter (1.53 m), resulting in a frequency of 98 MHz.

The standing wave in the mixer – LO path was measured by monitoring the mixer current during the LO frequency retuning. The resulting curve shows a clear sinusoidal pattern, as can be seen in Fig. 12.

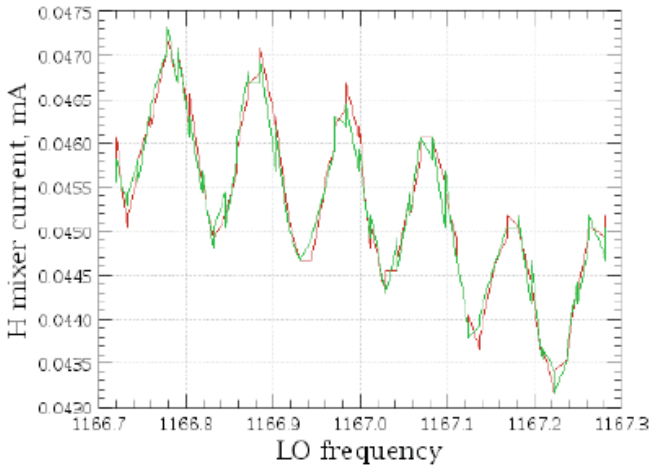

Fig. 12. Mixer current versus LO frequency. The frequency is typically 92 MHz, since the length of the mixer – LO path is (unintentionally) identical to the mixer – hot source.

Main standing waves found when looking at the Cold or Hot calibration loads are presented in Table 1.

TABLE I HIFI STANDING WAVE FREQUENCIES

Dominant Frequency	Path	Other frequencies
92 MHz	Mixer – Hot source	320, 650 MHz
98 MHZ	Mixer – Cold source	320, 650 MHz
92 MHz	Mixer – LO	320, 650 MHz

The higher frequencies are seen in the diplexer bands only, and the 650 GHz corresponds to 22 cm which is the distance between the diplexer rooftop and the mixer. The 320 MHz may be due to the combined rooftop reflection and the

interaction between the 2 mixer – LO paths, which causes an additional total coupling modulation.

The aim of the standing wave test is not only to measure the magnitude of the standing waves as such, but also to indicate the optimum frequency throw for frequency switched observations. Frequency switching is a popular observing mode for heterodyne systems since both in the "on" (At LO frequency f_1) as in the "off" (LO frequency $f_2=f_1+f_{throw}$) state the signal can be observed and dead time is minimized [7]. The frequency throw was chosen equal to the mixer – LO standing wave frequency of 92 MHz. This to ensure the mixer is pumped to the same mixer current level for f_1 and f_2 and that the difference in LO dissipation between f_1 and f_2 is minimal, providing a thermal drift as low as possible. Unfortunately most HIFI bands exhibit a slope on top of the sine, as seen in Fig. 12. For this reason retuning of the LO power is required when going from f_1 to f_2, and the resulting small difference in mixer currents and LO dissipations for the 2 frequencies does affect the baseline quality [6].

The HIFI stability was measured extensively, for various observing modes. The results are described in [6]. Generally the stability especially for the bands 6 and 7 is better than measured during the instrument level tests. The main reason may be the absence vibrations from mechanical cryo-coolers in the Large Space Simulator, which caused significant path length and hence LO power modulations in ILT where both the FPU and LO cryostats were cooled by separate mechanical coolers.

VII. HIFI STATUS AND OUTLOOK

The HIFI TBTV tests finished December 10th. After warm-up the satellite was moved to the Ariane Espace Launch site in Kourou, French Guyana. March 9th the last HIFI health check was performed, confirming that HIFI survived transport in good health and is ready for launch. The Herschel launch is expected to be in May 2009. One week after launch HIFI will be cooled down to its equilibrium temperature and can be switched on. The commissioning phase duration is 2 months, in which part of the TBTV tests are repeated to obtain the final flight performance of HIFI

ACKNOWLEDGMENT

P. Dieleman thanks the HIFI team for their thorough preparation, enthusiastic round-the-clock support during the TBTV test, and detailed analysis of all the data taken. ESA, TASF and ASED are thanked for their comradeship and cooperation throughout the entire Herschel integration and test phase.

REFERENCES

[1] T. de Graauw, "The Herschel Heterodyne Instrument for the Far-Infrared (HIFI)", Proc. SPIE 6265, 62651Z, 2006.

[2] G.T. Pilbratt, "Herschel space observatory mission overview", *IR Space Telescopes and Instruments*, J.C. Mather, Ed. SPIE 4850 (2003), pp. 586–597.

[3] G. de Lange, "Performance of the superconducting mixers for the HIFI Instrument", *Proceedings 19th International Symposium on Space Terahertz Technology*, pp 98-105.

[4] http://www.esa.int/esaTQM/1082551446328_facilitiesestec_0.html

[5] P. Dieleman *et al*, HIFI flight model testing at instrument and satellite level", *Proceedings 19th International Symposium on Space Terahertz Technology*, pp 106-110.

[6] J.W. Kooi *et al*, these proceedings

[7] A.P. Marston, "The Herschel-HIFI instrument observing modes and astronomical observation templates (AOTs)," in *Astronomy in the Submillimeter and Far Infrared Domains with the Herschel Space Observatory*, L. Pagani and M. Gerin, Ed. EAS Publications Series, 34 (2009) pp 21–32.

T1D

HIFI instrument stability as measured during the Thermal Vacuum tests of the Herschel space observatory

J. W. Kooi [1] and V. Ossenkopf [2, 3]
[1]*California Institute of Technology, Pasadena, CA 91125, USA*
[2]*KOSMA, I.Physikalisches Institut der Universitat zu Köln, Germany*
[3]*SRON Netherlands Institute for Space Research, Groningen, the Netherlands*
kooi@phobos.caltech.edu

***Abstract*—** HIFI, the high resolution far infrared heterodyne instrument for ESA's Herschel satellite consists of seven dual polarization sensitive mixer bands (SIS and HEB), and fourteen local oscillator channels. It is without a doubt the most complex and unique heterodyne instrument ever put together. To verify instrument performance and observation efficiency, we have investigated the HIFI instrument IF and System stability during thermal vacuum (TV) tests in the European Space Agency (ESA) Large Space Simulator (LSS) at ESTEC, Noorwijk, the Netherlands. During these tests the Local oscillator unit (LOU) was cooled to 110 K, mimicking flight operation.

As part of the Thermal Vacuum tests particular emphasis was given to:

- Verification and operational performance of frequency switch observations in all LO subbands. If successful this observation mode is particular useful in, for example, time efficient mapping of extended line sources.
- Verification of the instrument total power and spectroscopic stability. The results will be compared to that obtained during the instrument level test phase (2007).
- LO warm-up.
- In-band LO settling time.

Complicating the situation is that the local oscillator (LO) injection in HIFI is accomplished via quasi-optical beam-splitters (SIS mixer bands 1, 2, 5) and diplexers (SIS mixer bands 3, 4, and HEB mixer bands 6, 7). Especially in the diplexer bands we find evidence of significant baseline distortion during frequency switching, even when the frequency jump was between two peaks (or troughs) of the dominant optical standing wave between mixer and local oscillator.

In the talk we present an overview of the Allan Variance method, the measured SIS and HEB stability results, LO time constants, and how they impact baseline quality and observation efficiency.

Session T2

Direct Detectors

Chair: Brian Jackson

Tuesday, April 21
10:55 – 12:10

T2A

Development of low-noise multiband imaging arrays using microwave kinetic inductance detectors (MKID) for ground-based submillimeter astronomy

O. Noroozian[1*], N.G. Czakon[1], P.K. Day[2], J.-S. Gao[1], J. Glenn[3], S. Golwala[1], H. LeDuc[2], P.R. Maloney[3], B. Mazin[4], D. Moore[1], H. T. Nguyen[2], J. Sayers[1], J. Schlaerth[3], J. E. Vaillancourt[1], A. Vayonakis[1], and J. Zmuidzinas[1]

*1 California Institute of Technology *, Pasadena, CA 91125*
2 Jet Propulsion Laboratory, Pasadena, CA 91109
3 University of Colorado, Boulder, CO 80309
4 University of California, Santa Barbara, CA 93106
* Contact: omid@caltech.edu, phone +1(626)3952647

***Abstract*—The population of submillimeter-bright galaxies (SMGs) at high redshifts, first studied with the JCMT/SCUBA instrument in 1997, is potentially a very rich source of information for advancing our understanding of the formation and evolution of galaxies over cosmic history, and especially elucidating the role of galaxy merger events. While single-band imaging surveys have now revealed hundreds of SMGs, further progress will require multi-band information in order to measure spectral indices and luminosities and for selecting objects for targeted follow-up observations, e.g. with ALMA. The first steps in this direction are already being taken: the 10m South Pole Telescope is finding galaxies at 150 GHz and 220 GHz using TES bolometer array cameras, and the BLAST balloon instrument has made galaxy surveys at 250, 350, and 500 microns. Ultimately, surveys with bigger telescopes (such as the proposed 25m CCAT) equipped with large multiband imagers will be needed.**

As a step toward this ultimate goal, we are constructing MKIDCam, a 576 spatial pixel 4-band (750, 850, 1100, 1300 microns) camera to be deployed at the Caltech Submillimeter Observatory (CSO) in 2010. The focal plane arrays, optics, readout electronics, and cryogenics are currently under development. The focal plane will consist of 24 x 24 spatial pixels responding simultaneously to all four bands and assembled as a mosaic of 16 tiles. Each 6 x 6 pixel tile will have 144 frequency-multiplexed Microwave Kinetic Inductance Detectors (MKIDs). Individual pixels consist of a phased-array planar antenna, on-chip filters for band separation, and four MKIDs for simultaneous measurement of the four bands. The MKID readout will be performed using cryogenic HEMT amplifiers followed by room-temperature FPGA-based channelization electronics.

At present, tests on prototype 4x4 two-band arrays are being performed and critical properties such as responsivity, noise, quasiparticle lifetime, optical efficiency, optical bandpass response, and magnetic field sensitivity are being measured. The MKID resonators show excess frequency noise due to perturbations in the dielectric constant of a surface layer containing two-level system (TLS) fluctuators. Based on a semi-empirical TLS noise model, we have designed and fabricated new resonators using modified geometries such as interdigitated capacitors. Measurements of these devices have confirmed a reduction in frequency noise by roughly an order of magnitude compared to our previous conventional CPW resonators. These results suggest that the optically-loaded frequency-readout NEP for these devices could be appropriate for reaching the photon background limit at the CSO ($5 – 15 \times 10^{-17}$ W Hz$^{-1/2}$). A second engineering run with a 6x6 pixel 3-band array prototype camera incorporating the new lower noise resonator designs is planned at the CSO in 2009.

T2B

Noise Measurements in Ti Hot-Electron Nanobolometers

S.V. Pereverzev [1], D. Olaya [2], M.E. Gershenson [2], R. Cantor [3], and B.S. Karasik [1,*]
1 Jet Propulsion Laboratory, California Institute of Technology, Pasadena, CA 91109
2 Rutgers University, Piscataway, NJ 08854
3 Star Cryoelectronics Inc., Santa Fe, NM 87508
* Contact: boris.s.karasik@jpl.nasa.gov, phone +1-818-393-4438

***Abstract*—We present the current progress for the titanium (Ti) hot-electron nanobolometers operating at ~ 0.04-0.4 K. The ultimate goal of the work is to develop a submillimeter direct detector with the noise equivalent power NEP = 10^{-18}-10^{-20} W/Hz$^{1/2}$ for the moderate resolution spectroscopy and CMB studies on future space telescope (e.g., SAFIR, SPECS, SPICA, CMBPol) with cryogenically cooled (~ 4-5 K) mirrors.**

Recently [1], we have achieved the extremely low thermal conductance (~ 2 fW/K at 300 mK and ~ 0.1 fW/K at 40 mK) due to the electron-phonon decoupling in Ti nanodevices with Nb Andreev contacts fabricated on Si. This thermal conductance translates into the NEP ≈ 3×10^{-21} W/Hz$^{1/2}$ at 40 mK and NEP ≈ 10^{-18} W/Hz$^{1/2}$ at 300 mK. These record data indicate the great potential of the hot-electron nanobolometers for meeting many application needs. As the next step towards the practical demonstration of the HEDD, we fabricated and tested somewhat larger devices (~ 4 μm × 0.4 μm x 40 nm) whose critical temperature is well reproduced and is in the range 300-350 mK. The output electrical noise measured in these devices in the voltage-bias mode with a low-noise (~ 2 pA/Hz$^{1/2}$) dc SQUID amplifier was completely dominated by the thermal energy fluctuations (phonon noise). The corresponding electrical NEP was in the range (2-7)$\times10^{-18}$ W/Hz$^{1/2}$ depending on the detector device size. The time constant of these devices was too short to be measured directly with the available SQUID readout electronics and is estimated to be of the order of a μs or less.

Beside the record low NEP, the ultimately small nanobolometers have a very low electron heat capacitance that makes them promising for detecting single THz photons. The larger devices studied in this work were tested using NIR photons (wavelength 1550 nm). Depending on the average number of photons per pulse, a typical Poisson-like statistics of counts has been observed. The photon numbers greater than 2 were, however, difficult to observe since the detector output was almost saturated by just a single photon of this wavelength. The minimum detectable energy for these devices is estimated to be about h×5THz.

The on-going effort is aimed at fabrication of the antenna-coupled detector devices and direct optical measurements of the NEP at 650 GHz. A setup for single THz photon detection utilizing a pulsed quantum cascade laser is also being built. The progress in these areas will be reported during the meeting.

[1] J.Wei et al., *Nature Nanotechnology* 3, 496 (2008).

T2C

Low Thermal Conductance Transition Edge Sensor (TES) for SPICA

P. Khosropanah[1*], B. Dirks[1], J. van der Kuur[1], M. Ridder[1], M. Bruijn[1], M. Popescu[1], H. Hoevers[1], J.-R. Gao[1], D. Morozov[2], and P. Mauskopf[2]

1 SRON Netherlands Institute for Space Research, Utrecht/Groningen, The Netherlands
2 School of Physics and Astronomy , Cardiff University, UK

* Contact: P.Khosropanah@sron.nl, phone +31-50-363 3465

***Abstract*—** Transition edge sensor (TES) is one of four detector options for SAFARI FIR Imaging Spectrometer (focal plane arrays covering a wavelength range from 30 to 210 μm) in Japanese SPICA telescope. Since the telescope is cooled down to 4.5 K, the instrument sensitivity is limited by the detector noise. Therefore among all the requirements, a crucial one is the sensitivity, which should reach an NEP (Noise Equivalent Power) as low as 2×10^{-19} W/√Hz at an operating temperature of 50 mK. TES detectors are used or planned in many ground-based telescopes in addition to airborne, balloon-borne, and space-borne instruments. In those ground-based applications the sensitivity is nearly two orders of magnitude lower than what SAFARI demands. The challenge of TES for SAFARI is to develop detectors which have a much higher sensitivity than what currently employed in various instruments in combination with a time constant of about 10 ms.

In collaboration with European TES team, led by a group at University of Cardiff, UK, SRON is developing TiAu TES on Si_3N_4 membrane, where narrow Si_3N_4 membrane legs act as low thermal links between TES and the bath. We have succeeded in fabricating and testing such devices with a critical temperature of 80 mK and obtained a very low thermal conductance, from which we expect an NEP of 1.7×10^{-19} W/√Hz, taking only an ideal case of phonon noise into account.

Some of these detectors are integrated with Ta absorbers for optical sensitivity test. IR radiation is coupled to the absorber by a circular feed horn antenna in combination with a metal back short. All hardware is in place and in principle the samples are ready for seeing first light.

We will report our latest experiments on dark and optical tests.

Effect of Lifetime Broadening of Superconducting Energy Gap on Quasiparticle Tunneling Current

Takashi Noguchi, Toyoaki Suzuki, Akira Endo, Masato Naruse, Yasunori Hibi,

Hiroshi Matsuo and Yutaro Sekimoto

Abstract—We numerically study the quasiparticle tunneling current of SIS junctions by taking into account the lifetime broadening of energy gap. It is demonstrated that calculated dc I-V curves agree well with those of the SIS junctions measured at temperatures below 4.2 K. It is predicted that the subgap current is strongly dependent on bias voltage at low temperatures unlike the prediction of the BCS tunneling theory. It is also interesting to note that the decrease of a subgap current always saturates at a certain temperature when the temperature goes down. These predictions on the subgap current at low temperatures are consistent with the behavior of the subgap current of SIS junctions experimentally obtained. It is indicated that it is essential to suppress the lifetime broadening of energy gap as low as possible to invent SIS junctions with an extremely low subgap current at low temperatures.

***Index Terms*— Leakage currents, Submillimeter wave detectors, Superconductor-insulator-superconductor devices, Superconducting device noise, Tunneling**

I. INTRODUCTION

We have been developing Superconductor-Insulator Superconductor (SIS) junction detectors as single pixel elements for large direct detector arrays at submillimeter wavelengths [1]. Although up to date, SIS-junction detectors with $NEP \approx 10^{-19}$ $\mathrm{W}/\sqrt{\mathrm{Hz}}$ have been demonstrated [2, 3], such detectors must have background-limited sensitivity in future space observatories and further effort is needed to achieve SIS-junction detectors with background-limited sensitivity, $NEP \approx 10^{-19}$ $\mathrm{W}/\sqrt{\mathrm{Hz}}$. In order to achieve such high- sensitivity SIS detectors it is most essential to reduce electrical noise of SIS junctions.

The electrical noise of a SIS junction is proportional to square root of its subgap current I_{SG} as

$$NEP = \frac{h\nu}{\eta}\sqrt{\frac{I_{SG}}{e}} \quad \left(\frac{\mathrm{W}}{\sqrt{\mathrm{Hz}}}\right), \qquad (1)$$

where η is the quantum efficiency of the detector and I_{SG} is the quasiparticle current at an operating voltage V and is dependent on temperature as

$$I_{SG} \propto \exp\left(-\frac{\Delta}{k_B T}\right), \qquad (2)$$

where k_B and T are Boltzmann's constant and temperature, respectively. The large discrepancy between the sensitivity theoretically predicted and that experimentally obtained comes from the fact that the measured I_{SG} at low temperature is several orders in magnitude greater than that expected from (2). Such a discrepancy between measured and calculated I_{SG} at low temperatures has been generally reported in many papers on SIS junctions [2, 4, 5]. It has been widely recognized that extra current passing through defects or conductive paths in the tunneling barrier dominates over the intrinsic thermally-excited quasiparticle tunneling current at low temperatures. Thus a lot of efforts have been made to improve the quality of the tunneling barrier of SIS junctions to reduce the excess current. Nevertheless, such a SIS junction with a subgap current as low as that predicted by the BCS theory has never been invented. We have found evidences that the subgap leakage current at 4.2 K weakly depends on the quality of Nb films. To verify the hypothesis that the subgap leakage current is dependent on the quality of Nb films, we have been making theoretical calculations of the quasiparticle tunneling current in SIS junctions [6]. In this paper, we describe the procedure of the calculations of the quasiparticle tunneling current in a Nb/Al·AlO_x/Nb SIS junction with an ideal tunneling barrier, taking into account the imaginary part of the gap energy of Nb films as a parameter representing their quality. It will be shown that the calculated dc *I-V* characteristics for Nb/Al·AlO_x/Nb SIS junctions are consistent with those measured at 4.2 K. It will be also demonstrated that the calculated quasiparticle current at a subgap voltage in the SIS junction shows strong voltage dependence at low temperatures unlike the prediction of the BCS theory. Then we are investigating subgap tunneling current of Nb/Al·AlO_x/Nb SIS junctions experimentally and theoretically to find a way to lower it.

II. CALCULATION OF QUASIPARTICLE CURRENT

A. Quasiparticle states inside the gap

The quasiparticle tunneling current I_T through an ideal tunneling barrier in a SIS junction is generally given by

$$I_T = A\int_{-\infty}^{\infty} N_r(E-eV)N_l(E)\{f_r(E-eV) - f_l(E)\}dE\,, \quad (3)$$

where A is a constant and $N_{r,l}(E)$ and $f_{r,l}(E)$ are densities of states and Fermi distribution function at energy E, respectively, and defined as

$$N_{r,l}(E) = \Re\left[\frac{E}{\sqrt{E^2 - \Delta_{r,l}^2}}\right] \quad (4)$$

and

$$f_{r,l}(E) = \left\{\exp\left(\frac{E}{k_B T}\right) + 1\right\}^{-1}, \quad (5)$$

where the subscripts r and l represent right and left superconductors and $\Delta_{r,l}$ are the gap energies for the superconductors on both sides [7]. Since the gap energy $\Delta_{r,l}$ are assumed to be real in the conventional calculations of tunneling current I_T, there is no quasiparticle state inside the energy gap and quasiparticle densities of states show an infinitely steep peak at the gap energy. Thus a very sharp step-like rise of current is predicted at the gap voltage on the I-V characteristics of a SIS junction. However, the current rise at the gap voltage is rounded in the actual SIS junctions. To explain the rounded I-V characteristics near the gap voltage, a complex superconducting energy gap, expressed as $\Delta_{r,l} = \Delta_1 - i\Delta_2$, has been introduced [8, 9], where Δ_1 and Δ_2 are real numbers. Calculated densities of states using (4) for superconducting Nb with (dotted and solid lines) and without (thin line) the imaginary part of gap energy Δ_2 are shown in Fig.1. It is clearly shown that the infinitely steep peak at the gap energy is suppressed by the existence of imaginary part of the gap energy Δ_2. It is also interesting to note that a little but finite numbers of quasiparticle states are caused at energy deep inside the gap if the gap energy has an imaginary part.

In Fig.1 calculated dc I-V curves using (1) and (2) with complex gap energies are plotted. It should be noted here that a finite amplitude of tunneling current through the quasiparticle states inside the energy gap is predicted at the subgap voltages. The amplitude of the quasiparticle tunneling current at a subgap voltage increases as the magnitude of the imaginary part of gap energy Δ_2 increases.

To determine the magnitude of the imaginary part of the gap energy Δ_2 of Nb films in actual Nb/Al·AlO$_x$/Nb junctions, curve fitting between calculated and measured I-V characteristics at 4.2 K is made. A small knee structure just above the gap voltage and a reduction of gap voltage are usually observed on the dc I-V curves of Nb/Al·AlO$_x$/Nb SIS junctions, which come from the superconducting proximity effect at the Nb/Al interface of the bottom electrode. The proximitized gap energy in the Al layer is obtained by solving McMillan's recursive equations [10], taking a complex number of energy gap for Nb into account, and is used to calculate the tunneling current. The energy gap of the top electrode is assumed to be free from the proximity effect and identical to that of the Nb film in the bottom electrode. The imaginary part of energy gap Δ_2 is determined so as to give a best fit to the measured I-V curve at 4.2 K.

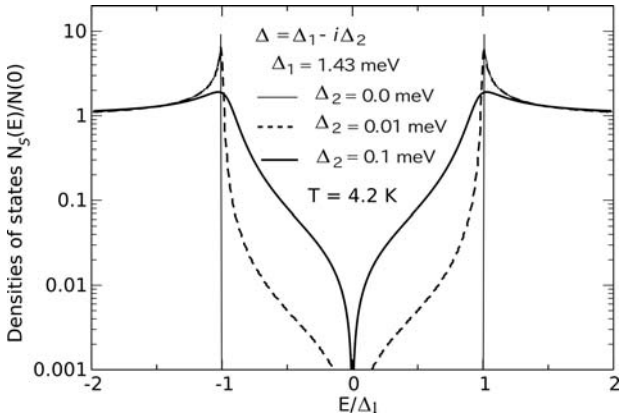

Fig. 1. Densities of states of Nb films having superconducting gap energy with (dotted and solid lines) and without (thin line) an imaginary part.

The measured dc I-V curve of a Nb/Al·AlO$_x$/Nb SIS junction at 4.2 K is plotted by open circles in linear (upper panel) and logarithmic (lower panel) scales in Fig.2. Solid lines in Fig.2 represent calculated quasiparticle tunneling current as a function of voltage. The measured dc *I-V* characteristics is quite consistent with calculated one by taking into account the imaginary part of gap energy Δ_2. It is also noted that amplitude of calculated quasiparticle tunneling current at a subgap voltage quantitatively agrees well with the measured one as shown in the lower panel of Fig. 2. This indicates that the measured subgap current is nearly identical to the theoretical lower limit of quasiparticle tunneling current in magnitude and indicates

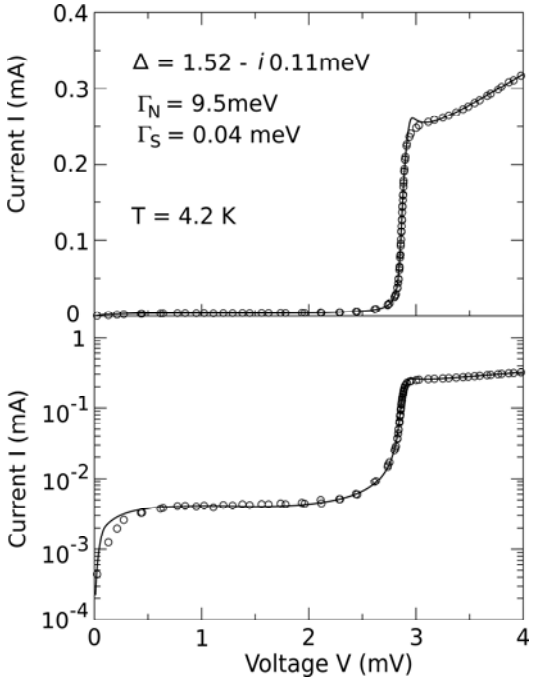

Fig. 2. Measured (open circles) and Calculated (solid lines) dc *I-V* curves of a Nb/Al·AlO$_x$/Nb SIS junction plotted in linear (upper panel) and logarithmic (lower panel) scale.

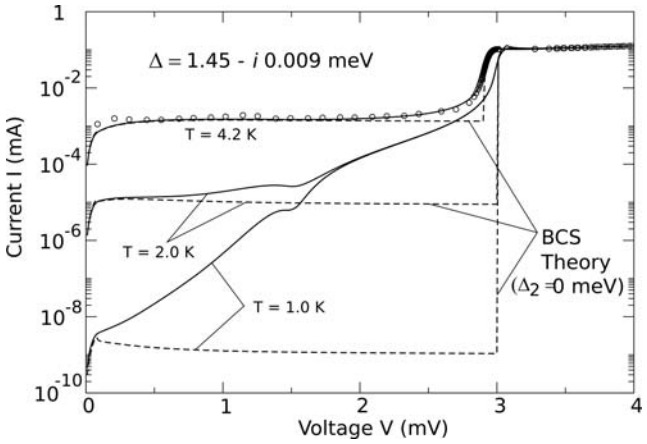

Fig. 3. Calculated dc I-V curves of a Nb/Al·AlO_x/Nb SIS junction at temperatures of 4.2, 2.0 and 1.0 K assuming that a Nb film has a complex superconducting gap energy. An imaginary part of the complex gap energy Δ_2 used in the calculation is determined from the fitting to the measured dc I-V curve at 4.2 K shown by open circles. dc I-V curves calculated by the conventional BCS theory at the respective temperatures are also shown by dotted lines.

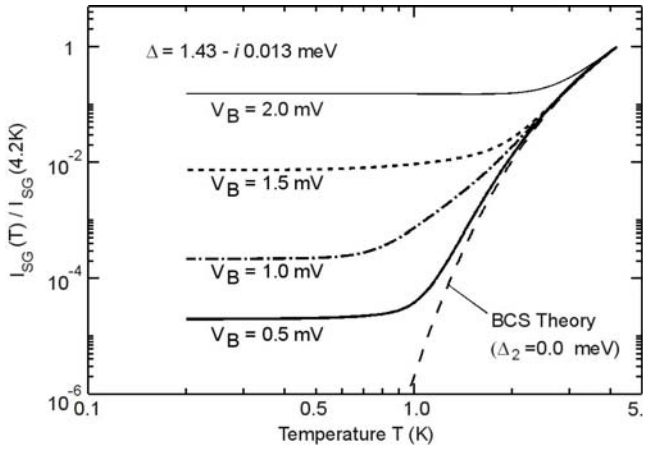

Fig. 4. Calculated subgap current of a Nb/Al·AlO_x/Nb SIS junction at bias voltages of 2.0, 1.5, 1.0 and 0.5 mV as function of temperature assuming that Nb film has complex superconducting gap energy. The dashed line represents a sugap current calculated by the conventional BCS theory as a function of temperature.

that an almost ideal tunneling barrier is achieved in the present SIS junction.

B. Quasiparticle current at low temperatures

It has been shown by Dynes et al. that the imaginary part of the gap energy Δ_2 in strong-coupling superconductors is independent on temperature below $T_C/2$, where T_C is a superconducting transition temperature [8]. According to their result, the imaginary part of the gap energy Δ_2 of Nb can be assumed to be constant below 4.2 K and it would be possible to predict the quasiparticle tunneling current of a Nb/Al·AlO$_x$/Nb SIS junction at low temperatures using eq. (1) with the imaginary part of gap energy Δ_2 of Nb obtained from the measured I-V curve at 4.2 K, while temperature dependence of the real part Δ_1 is assumed to be given by the BCS gap equation [7].

In Fig.3 calculated dc I-V curves at temperatures of 4.2, 2.0 and 1.0 K are shown together with those calculated by the BCS theory without any imaginary part of gap energy. It is clear that the subgap current at a temperature below 2.0 K is strongly dependent on voltage unlike those predicted by the BCS theory. This is because there is tunneling current flowing through quasiparticle states inside the energy gap in addition to the thermally-excited quasipaticle current. At high temperatures (> 2 K) the subgap current of the SIS junction is dominated by thermally-excited quasiparticle tunneling current, while it is dominated by the tunneling current through quasiparticle states inside the energy gap at low temperatures. Because the thermally-excited quasiparticle tunneling current reduces exponentially as temperature goes down, while the tunneling current through the number of quasiparticle states inside the energy gap is approximately independent on temperature. It is another remarkable feature that the subgap current at a voltage above $V = \Delta/e$ does not decrease as temperature goes down below ~2 K and seems to be saturated. Such a saturation of subgap current at low temperatures has been frequently found in SIS junctions [2, 4, 5]. In Fig.4 calculated subgap current at bias voltages of 0.5, 1.0, 1.5 and 2.0 mV are plotted as a function of temperature. It is clearly shown that any subgap current shows a saturation in magnitude at low temperatures, which is qualitatively consistent with the experimental results previously reported [2, 4]. It has been left unresolved why such a saturation of subgap current appears at low temperatures for a long time. Now it is clear that the saturation of subgap current occurs when the tunneling current through the quasiparticle states inside the energy gap dominates over the thermally-excited quasiparticle current at low temperatures.

The amplitude of the tunneling current through quasiparticle states inside the energy gap must be dependent on the magnitude of the imaginary part of the gap energy Δ_2, because

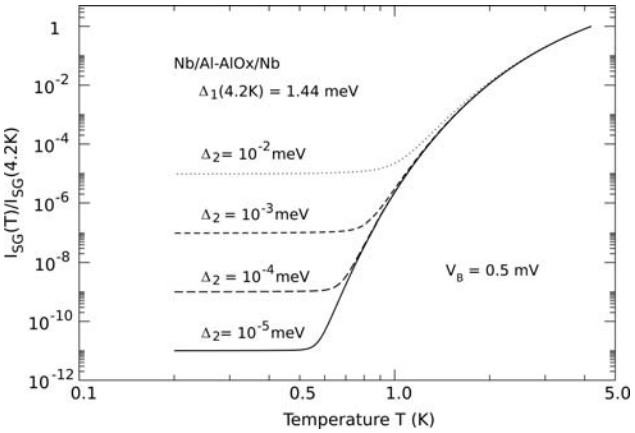

Fig. 5. Calculated subgap current of a Nb/Al·AlO_x/Nb SIS junction at a bias voltage of 0.5 mV as a function of temperature for different magnitudes of imaginary parts of gap energy Δ_2. Each subgap current is normalized to that at 4.2 K. The dashed line represents a sugap current normalized to that at 4.2 K predicted by the conventional BCS theory as a function of temperature.

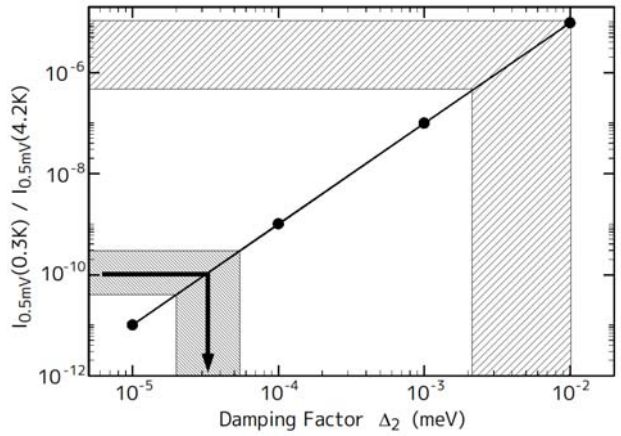

Fig. 6. Calculated subgap current of a Nb/Al·AlO_x/Nb SIS junction at T=0.3 K as a function of magnitudes of the imaginary part of gap energy Δ_2 at 4.2 K. Each subgap current is normalized to that at 4.2 K.

the number of quasiparticle states inside the energy gap strongly depends on the magnitude of Δ_2. In Fig.5 are plotted the calculated temperature dependence of the subgap current at a bias voltage V=0.5 mV for SIS junctions with different magnitudes of the imaginary part of the gap energy Δ_2 from 10^{-5} to 10^{-2} meV. Each subgap current is normalized to that at 4.2 K in order to clearly show the rate of change against the temperature. It is demonstrated that the saturation level of subgap current at 0.5 mV decreases as the magnitude of the imaginary part of the gap energy Δ_2 is reduced as expected.

Nb/Al·AlO_x/Nb .

In Fig. 6 calculated subgap current at 0.5 mV and 0.3 K is plotted as a function of the magnitude of Δ_2. The subgap current at 0.5 mV, which is sufficiently saturated, the upper right shaded region shows typical magnitude of Δ_2 of Nb-based SIS junctions reported up to date. The corresponding subgap current in this region is consistent with those ever achieved [2,5]. The lower left shaded region with thick arrow shows the our target value of the subgap current of SIS junctions for the background-limited sensitivity detectors. This indicates that is possible to reduce the saturated subgap current by 3 to 4 orders of magnitude, if the magnitude of Δ_2 can be achieved by approximately 2 orders of magnitude smaller than those of present Nb films.

III. COMPARISON TO EXPERIMENTAL DATA

We have made a high quality Nb/Al·AlN/Nb SIS junction with a quality factor at 4.2 K, where and are a subgap resistance at 2 mV and normal resistance of the SIS junction [11]. Measured dc I-V curves of the SIS junction at 4.2, 1.6 and 0.4 K are shown in Fig. 7 by open circles. Thin lines represent calculated ones using (3) by taking the imaginary part of the energy gap Δ_2 into account. The calculated dc I-V curve for 4.2 K shows a very good agreement with the measured one, whereas discrepancies between the calculated and measured ones at low temperatures are found.

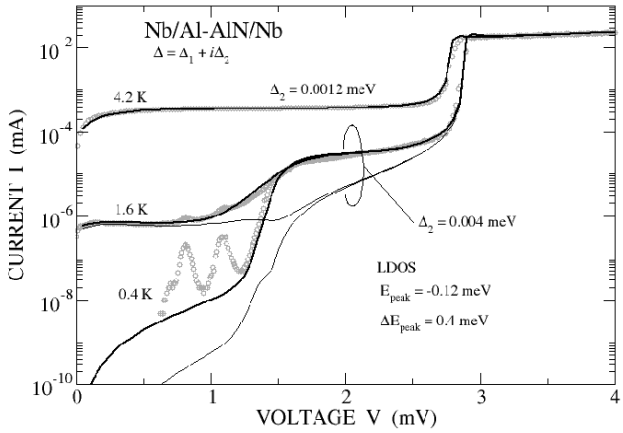

Fig. 7. Comparison between the calculated and measured I-V characteristics of a Nb/Al·AlN/Nb SIS junction at T=4.2, 1.6 and 0.4 K. Open circles represent measured data. Thin lines represent calculated ones using (3) by taking the imaginary part of the energy gap Δ_2. Thick solid lines represent calculated ones using (3) by taking the localized density of states (LDOS) in addition to the imaginary part of the energy gap Δ_2.

Especially, although there appears a remarkable structure just below 1.4 mV or a half gap voltage $V = \Delta_1 / e$ on the measured I-V curves at 1.6 and 0.4 K, no such a large structure is found on the calculated ones. It is also noted that the calculated subgap current below 1 mV at 0.4 K is an order of magnitude greater than measured one, whereas above 1.6 K the calculated subgap current below 1 mV is quite consistent with measured values. These discrepancies indicate that there are additional quasiparticle states inside the energy gap in addition to those induced by the imaginary part of the energy gap. In order to explain the measured dc I-V curves at low temperatures, we introduced a localized density of states (LDOS) inside the energy gap in addition to those induced by the imaginary part of the energy gap. The solid lines in Fig. 7 correspond to the calculated dc I-V curves including LDOS in addition to those induced by the imaginary part of the energy gap. The density of states used in the calculation is shown by the solid line in Fig. 8. The LDOS, shown by the broken line in Fig. 8, is assumed to have a Lorentzian-type energy dependence which is independent on temperature. It is found that calculated dc I-V curves agree well with measured ones.

Similar comparison between the calculated and measured dc I-V curves has been made for an Al/AlO_x/Al SIS junction reported by Teufel *et al* . [12]. In Fig. 9 calculated dc I-V curves with and without LDOS are shown by the solid and thin lines, respectively. The density of states used in the calculation is shown in Fig.10. It is noted here that there is a LDOS peak just below $E = 0$ or the Fermi level as in the case of Nb-based junction described above.

IV. DISCUSSION

We have shown that dc I-V characteristics of SIS junctions can be well described by the quasiparticle tunneling theory assuming that there are finite numbers of quasiparticle states inside the energy gap. We think that those quasiparticle states

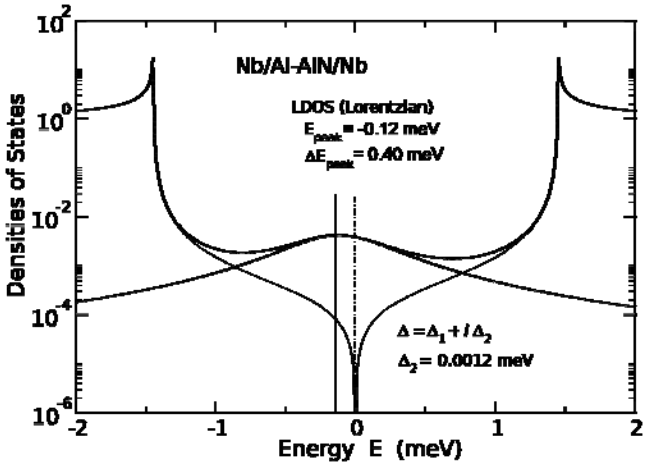

Fig. 8. Thick solid line represents the density of states which gives the best fit to the measured I-V curves of Nb/Al-AlN/Nb SIS junctions shown in Fig. 7. This density of states is decomposed into two parts; one is the quasiparticle density of states caused by the imaginary part of the energy gap (thin lines) and the other is a localized density of states (LDOS) inside the energy gap (broken line)..

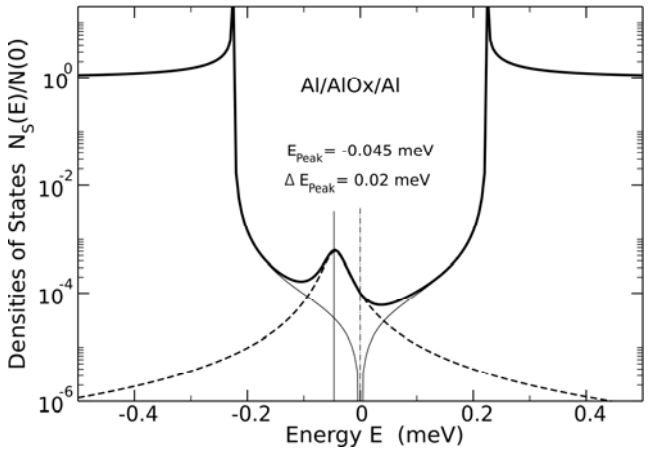

Fig. 10. Thick solid line represents the density of states which gives the best fit to the measured I-V curves of Al/AlOx/Al SIS junctions shown in Fig. 9. This density of states is decomposed into two parts; one is the quasiparticle density of states caused by the imaginary part of the energy gap (thin lines) and the other is a localized density of states (LDOS) inside the energy gap (broken line).

are decomposed into two major components; one is a localized quasiparticle states inside the energy gap and the other is attributed to the broadening of the density of states caused by the imaginary part of the energy gap. It is theoretically predicted that such a localized quasiparticle state or LDOS can be formed by the magnetic impurity scattering in a superconductor [13]. Although origin of the LDOS is not fully understood at present, it is thought to be quite important to reduce the numbers of the LDOS in order to achieve extremely small subgap current at low temperatures.

The imaginary part of the gap energy was theoretically taken into account to explain Q-values of superconducting cavities [14], damping of the Riedel singularity [15, 16] and broadening of a current step at gap voltage in I-V characteristics of SIS junction [8]. However, little attention has been paid to the fact that a small number of quasiparticle states are caused at energy deep inside the gap. Subgap current of SIS junctions at low temperatures are dominated by the tunneling current through those quasiparticle states, while a number of thermally-excited quasiparticles are extremely small at the temperature.

The imaginary part of the gap energy Δ_2 can be assumed to be inversely proportional to residual resistance ratio, $RRR=R(300K)/R(10K)$, which represents quality of a superconducting film, where R(300K) and R(10K) are resistance of the superconducting film at 300 K and 10 K, respectively. The *RRR* of our Nb films is 4–5, whereas *RRR*>200 has been obtained in crystalline Nb films [17]. Thus, in principle, it is possible to reduce the magnitude of the imaginary part of energy gap of a Nb film approximately 2 orders of magnitude smaller than that of present Nb films. If such a high-quality Nb film would be available, extremely low subgap current of a SIS junction can be obtained at low temperature.

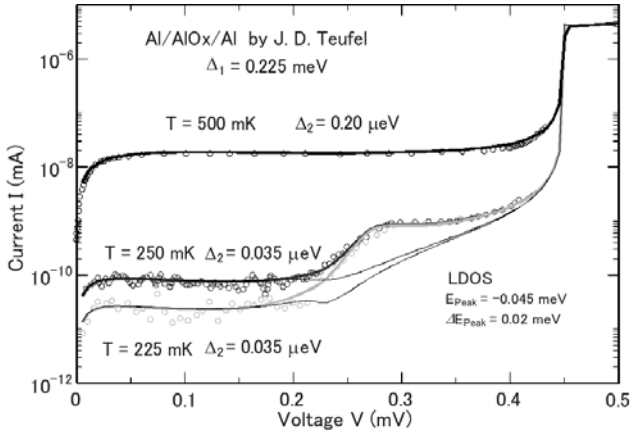

Fig. 9. Comparison between the calculated and measured I-V characteristics of a Al/AlOx/Al SIS junction at T=500, 250 and 225 mK. Open circles represent measured data. Broken lines represent calculated ones using (4) by taking the imaginary part of the energy gap Δ_2. Thick solid lines represent calculated ones using (4) by taking the localized density of states (LDOS) in addition to the imaginary part of the energy gap Δ_2.

V. SUMMARY

We have demonstrated that the quasiparticle states inside the energy gap plays an important role in the behavior of subgap current of a SIS junction at low temperatures. It has been shown that the imaginary part of superconducting gap energy causes small but finite numbers of quasiparticle states even at an energy deep inside the gap and that localized quasiparticle states are induced inside the energy gap. Quasiparticle tunneling through those quasiparticle states occurs at subgap voltages and dominates over the thermally-excited quasiparticle tunneling at low temperatures. These results indicate that much effort must be made to improve the quality of electrode films of SIS junctions in addition to make a very good tunneling barrier, in order to invent a high-sensitivity SIS photon detector with an extremely low subgap current at low

temperatures.

ACKNOWLEDGMENT

The authors thank Drs. Sergey Shitov and Matthias Kroug for useful discussions.

REFERENCES

[1] H. Matsuo, S. Ariyoshi, C. Otani, H. Ezawa, J. Kobayashi, Y. Mori, H. Nagata, H. M. Shimizu, M. Fujiwara, M. Akiba, and I. Hosako, Proc. SPIE 5498 (2004) 371.

[2] S. Ariyoshi, H. Matsuo, C. Otani, H. Sato, M. Shimizu, K. Kawase, T. Noguchi, IEEE Trans. Appl. Supercond. 15 (2005) 920.

[3] D. E. Prober, J. D. Teufel, C. M. Wilson, L. Frunzio, M. Shen, R. J. Schoelkopf, T. R. Stevenson and E. J. Wollac, IEEE Trans. Appl. Supercond. 17 (2007) 241.

[4] R. Monaco, R. Cristiano, L. Frunzio and C. Nappi, J. Appl. Phys. 71 (1992) 1888.

[5] H. Nakagawa, G. Pepe, H. Akoh, L. Frunzio, R. Cristiano, E. Esposito, S. Pagano, G. Peluso1, A. Barone and S. Takada, Jpn. J. Appl. Phys. 32 (1993) 4535.

[6] T. Noguchi, T. Suzuki, A. Endo and T. Tamura, Physica C, (2009) in press.

[7] M. Tinkham, Introduction to Superconductivity, McGraw Hill, New York, 1975, 48.

[8] R. C. Dynes, V. Narayanamurti and J. P. Garno, Phys. Rev. Lett. 41(1978) 1509.

[9] B. Mitrovic and L. A. Rozema, J. Phys., Condens. Matter 20 (2008) 015215.

[10] W. L. McMillan, Phys. Rev. 175 (1968) 537.

[11] A. Endo, Ph.D. thesis, Tokyo Univ., (2009).

[12] J. D. Teufel, Ph.D. thesis, Yale Univ., (2008).

[13] A. V. Balatsky, I. Vekhter and Jian-Xin Zhu, Rev. Mod. Phys.78, (2006) 373.

[14] A. Philipp and J. Halbritter, IEEE Trans. Magn. MAG-19 (1983) 999.

[15] C. A. Hamilton, Phys. Rev. B 5 (1972) 912.

[16] S. Morita, S. Imai, I. Fukushi, S. Takaki, Y. Takeuti and N. Mikoshiba, J. Phys. Soc. Jpn. 52 (1983) 617.

[17] G. Oya, M. Koishi and Y. Sawada, J. Appl. Phys. 60 (1986) 1440.

T2E

Kinetic Inductance Detectors with integrated antenna's for ground and space based sub-mm astronomy

A. Baryshev[1],J.J.A. Baselmans[2], S. Yates[2], A. Neto[3], D. Bekers[3], G. Gerini[3], Y.J.Y. Lankwarden[2], Bernd Klein[5], R. Barends[4], H. Hoevers[2], T.M. Klapwijk[4]

1 SRON Netherlands Institute for Space Research, Landleven 12, 9747 AD Groningen, The Netherlands
2 SRON Netherlands Institute for Space Research, Sorbonnelaan 2, 3584 CA Utrecht, The Netherlands
3 TNO - Defence, Security and Safety , Oude Waalsdorperweg 63, 2597 AK, The Hague, The Netherlands
4 Kavli Institute of Nanoscience, Delft University of Technology, Lorentzweg 1, 2628 CJ Delft, The Netherlands
5 Max-Planck-Institut für Radioastronomie, Auf dem Hügel 6953121 Bonn, Germany
Contact: A.M.Baryshev@sron.nl, phone +31-50-363 8287.

***Abstract*— Very large arrays of Microwave Kinetic Inductance Detectors (MKIDs) have the potential to revolutionize ground and space based astronomy. They can offer in excess of 10.000 pixels with large dynamic range and very high sensitivity in combination with very efficient frequency division multiplexing at GHz frequencies. In this paper we present the development of a 400 pixel MKID demonstration array, including optical coupling, sensitivity measurements, beam pattern measurements and readout. The design presented can be scaled to any frequency between 80 GHz and >5 THz because there is no need for superconducting structures that become lossy at frequencies above the gap frequency of the materials used. The latter would limit the frequency coverage to below 1 THz for relatively high gap materials such as NbTiN.**

An individual pixels of the array consist of a distributed Aluminium CPW MKID with an integrated twin slot antenna at its end. The antenna is placed in the in the second focus of an elliptical high purity Si lens. The lens-antenna coupling design allows room for the MKID resonator outside of the focal point of the lens. The best dark noise equivalent power of these devices is measured to be NEP = $7 \cdot 10^{-19}$ W/√Hz and the optical coupling efficiency is around 30%, in which no anti-reflection coating was used on the Si lens. For the readout we use a commercial arbitrary waveform generator and a 1.5 GHz FFTS. We show that using this concept it is possible to read out in excess of 400 pixels with 1 board and 1 pair of coaxial cables.

Session T3

THz Systems

Chair: Patrick Pütz

Tuesday, April 21
2:20 – 3:20

GUBBINS: A novel millimeter-wave heterodyne interferometer

P.K. Grimes, M.J.R. Brock, C.M. Holler, J. John, M.E. Jones, O.G. King, J. Leech, A.C. Taylor, G. Yassin, K. Jacobs and C. Groppi

***Abstract*—GUBBINS is a prototype heterodyne interferometer currently under construction at Oxford with the aim of demonstrating high surface brightness mm-wave interferometery at modest spatial and spectral resolutions [1]. Once built and tested, the instrument will be used to carry out demonstration observations of the Sunyeav-Zeldovich effect in bright galaxy clusters and measurements of atmospheric phase stability, as well as other tests of ground based interferometery. In this paper we give an update on the progress of the GUBBINS project, in particular, the development of the new technologies employed in this novel instrument.**

***Index Terms*—interferometery, heterodyne, SIS mixer, analogue correlator.**

I. Introduction

WE are currently designing and building a prototype single-baseline 220 GHz tracking heterodyne interferometer for high brightness sensitivity astronomical observations. This instrument, GUBBINS (220-GHz Ultra-BroadBand INterferometer for S-Z), will use two small antennas on a short baseline with ultra-wide IF bandwidth SIS mixers developed in collaboration with Cologne University and an ultra-wideband analogue correlator developed in collaboration with the University of Maryland. After extensive laboratory testing the instrument will be deployed for test astronomical observations at the Chajnantor Observatory, Chile, adjacent to ALMA. Although the instrument will make useful astronomical measurements, it will be used primarily for the development of new technologies for mm-wave interferometry.

The technology developed for this instrument will also have applications in other areas of astronomy, particularly in the design of very wide IF bandwidth SIS receiver arrays.

A. Use of interferometry in CMB observations

Cosmic microwave background astronomy requires extremely high brightness sensitivity and very good control of systematic and instrumental effects. The use of interferometric techniques allows total power fluctuations from the atmosphere to be subtracted. The use of heterodyne mixers allows each receiver to be phase switched independently by phase switching the local oscillator, so that the individually modulated redundant baselines can be used to eliminate other instrumental systematic effects. Achieving high brightness sensitivity in interferometry requires that the instantaneous bandwidth of each baseline be as wide as possible, and that the array be as filled as is practical within the limits of antenna shadowing.

Interferometry has been widely used in cosmology instruments at centimetre wavelengths, particularly for observations of the primary temperature anisotropy and E-mode polarisation of the cosmic microwave background e.g. CBI, DASI, VSA, and in observations of secondary anisotropies such as the Sunyaev-Zel'dovich effect, e.g. AMI, CBI-2, SZA.

Although measurements of the CMB and S-Z effect at millimetre wavelengths are regularly carried out, the limitations of the low instantaneous (IF) bandwidth of SIS mixers and backend systems, and the poor noise performance of other mm-wave coherent detectors, have resulted in an absence of successful CMB instruments using heterodyne interferometry in the millimetre-wave band. Recent advances in SIS mixer design and wideband correlator technology make it feasible to build a mm-wave heterodyne interferometer capable of carrying out novel CMB observations.

II. Galaxy cluster science with GUBBINS

The Sunyaev-Zel'dovich effect is the distortion of the spectrum of the CMB due to inverse-Compton scattering off the hot gas in clusters of galaxies [2]. This tends to boost the energy of the CMB photons, leading to a decrease in the CMB brightness below a frequency of about $220\,\mathrm{GHz}$, and an increase above this frequency. One of the key features of the S-Z effect is that its surface brightness is independent of the distance to the cluster, although the angular size on the sky does decrease with distance. This means that S-Z measurements can be used to study galaxy clusters over a very wide range of redshifts [3], [4].

The exact null frequency varies with the temperature of the cluster gas (thermal S-Z effect) and the peculiar velocity of the cluster (kinematic S-Z effect) (fig. 1). The shift in the null frequency due to the thermal S-Z effect is approximated by $217 + 0.45T\,\mathrm{GHz}$ where T is the cluster gas temperature in keV. A typical rich cluster has a gas temperature in the range $5 - 15\,\mathrm{keV}$, leading to shift in the null frequency of $2.5 - 7.5\,\mathrm{GHz}$. Hence by measuring the SZ spectrum and finding the null frequency we can measure the cluster temperature without the need for X-ray spectral measurements.

P.K. Grimes, C.M. Holler, M.E. Jones, O.G. King, J. Leech, A.C. Taylor and G. Yassin are with the Astrophysics group, Department of Physics, University of Oxford, UK.

M.J.R. Brock and J. John are with the Department of Physics, University of Oxford, UK.

K. Jacobs is with KOSMA, I. Physikalisches Institut, University of Cologne, Germany.

C. Groppi is with the Steward Observatory Radio Astronomy Laboratory, University of Arizona, AZ, USA

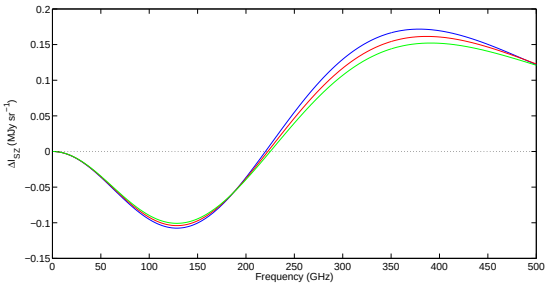

Figure 1. The change in CMB spectrum due to the thermal Sunyeav-Zeldovich effect in a galaxy cluster for three cluster gas temeperatures: $5\,\mathrm{keV}$ (blue), $10\,\mathrm{keV}$ (red) and $15\,\mathrm{keV}$ (green).

Table I
TARGET PERFORMANCE FOR GUBBINS PHASE I

Frequency	$185 - 275\,\mathrm{GHz}$
Antenna aperture	$0.4\,\mathrm{m}$
Baseline	$0.5 - 0.6\,\mathrm{m}$
Primary beam (220 GHz)	$11.4'$ FWHM
Spatial resolution (220 GHz)	$7.5' - 11.4'$
IF band	$3 - 13\,\mathrm{GHz}$
Instananeous bandwidth	$2 \times 10\,\mathrm{GHz}$
Correlator channels	16
Correlator bandwidth	$2 - 20\,\mathrm{GHz}$
Channel bandwidth	$1.125\,\mathrm{GHz}$
Target system temperature	$50\,\mathrm{K}$
Brightness sensitivity per channel	$1.5\,\mathrm{mK}/\sqrt{\mathrm{s}}$
Total brightness sensitivity	$350\,\mu\mathrm{K}/\sqrt{\mathrm{s}}$

GUBBINS will be able to detect a the brightest galaxy clusters in the sky in one night's observing per cluster, and will be able to constrain the null frequency of the S-Z effect to $\pm 1\,\mathrm{GHz}$ with several nights observing. In conjunction with low frequency S-Z data e.g. from CBI-2 ($26 - 36\,\mathrm{GHz}$), we should be able to measure the cluster gas temperature to within a few keV.

III. INSTRUMENT DESIGN

The design goals of this instrument are somewhat different to current mm-wave interferometers, in that we want to achieve maximum sensitivity to extended continuum sources, but with only moderate spatial and spectral resolution. The specifications of the GUBBINS instrument are given in Table I. These figures are for the initial GUBBINS design, but future developments are planned, particularly to increase the mixer IF bandwidth to the full $2 - 20\mathrm{GHz}$ band of the correlator and backend.

The prime design targets are for a single $0.5\,\mathrm{m}$ baseline (dictated by the angular size of the brightest S-Z clusters) with the maximum achievable filling factor; a target system temperature of $50\,\mathrm{K}$; a total instantaneous bandwidth of at least $10\,\mathrm{GHz}$ in each sideband divided into at least 8 spectral channels and an LO tuneable by at least $20\,\mathrm{GHz}$ either side of the nominal null in the S-Z effect at $217\,\mathrm{GHz}$.

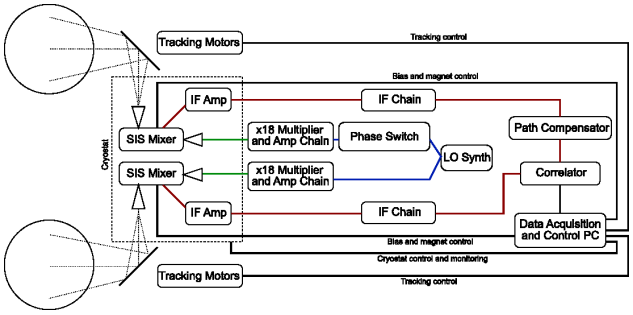

Figure 2. System diagram for the GUBBINS instrument. Data and DC signals are shown as black lines, LO signals as blue (low frequency, coaxial cables) and green (mm-wave, quasioptical) and IF signals as red. The optics are on the left of the diagram.

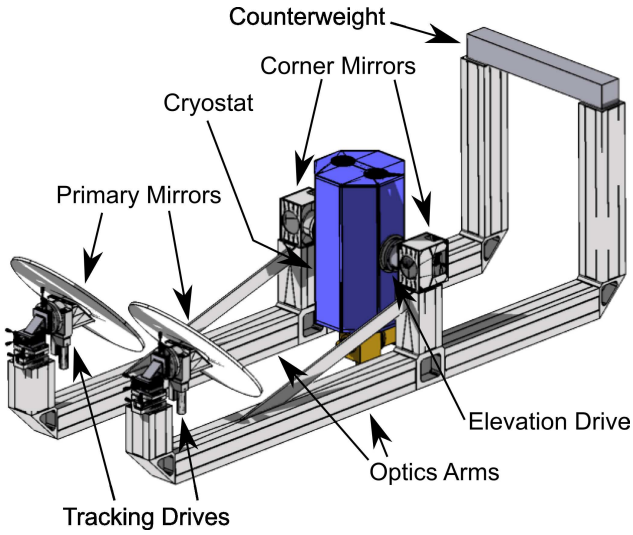

Figure 3. CAD model of the GUBBINS instrument. The telescope is supported on the base of the cryostat body, between the two optics arms.

A diagram of the GUBBINS system is given in Fig. 2 and a CAD model of the complete instrument in Fig. 3. To avoid the complexity and cost of using two cryostats and coolers, both SIS receivers are mounted in a single cryostat at the centre of the instrument, with the optics for each antenna mounted on either side. The SIS mixers mounted on either side of the coldhead, looking out of opposite sides of the cryostat, with LO signals being fed into cryostat through windows in the top of the cryostat, before being coupled to the mixers via smooth-walled horns and waveguide directional couplers.

A. Optics design

The optical design of each telescope employs the maximum primary mirror size that can be accommodated on a $0.5\,\mathrm{m}$ baseline without shadowing. If the antennas are to be scanned up to $45°$ from the zenith, the no shadowing condition gives a primary mirror projected aperture of $\sim 0.4\,\mathrm{m}$. The optical layout is shown in Fig. 5 and Fig. 4. Each telescope is fed by corrugated horn-reflector antenna with a $7°$ FWHM beam at $220\,\mathrm{GHz}$. The primary mirror is a $45°$ offset paraboloid with a focal length of $1020\,\mathrm{mm}$. GRASP simulations of the telescope beam are shown in Fig. 6.

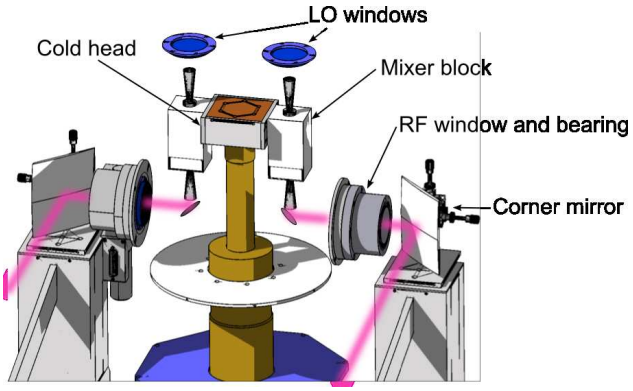

Figure 4. CAD model of the inside of the GUBBINS cryostat. The beams from the sky are shown in pink, and are reflected into the cryostat from the corner mirrors and through the elevation motor and bearings before passing through the cryostat windows and radiation shields to the horn-reflector antennas.

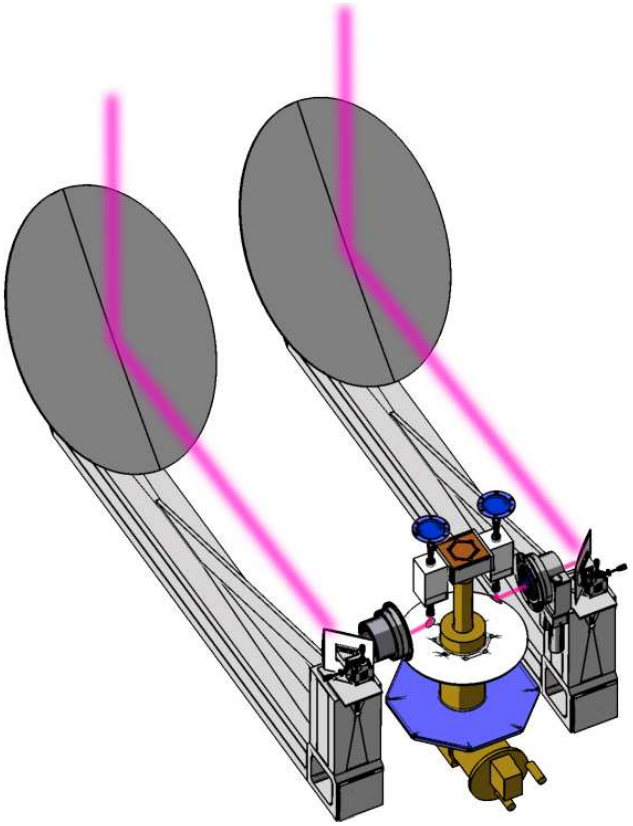

Figure 5. CAD model of the GUBBINS optics. The beams from the sky are shown in pink, and are reflected from the 45° offset primary mirrors to the 45° offset corner mirrors and into the cryostat. The telescope is pointed by rotating the primary mirrors about the axis between the primary mirrors and the corner mirrors, and by rotating the entire optics arm assemblies in elevation about the axis between the corner mirrors and horn-reflector antennas.

In order to allow the necessary degrees of freedom in the optics so that the telescopes can be pointed in elevation and azimuth, the telescopes are folded by a 45° offset corner mirror between the primary mirror and feed. The corner mirror is a convex paraboloid (focal length $-120\,\mathrm{mm}$) to reduce the length of the telescopes, at the expense of introducing slight aberrations when the telescopes are pointed far from the zenith.

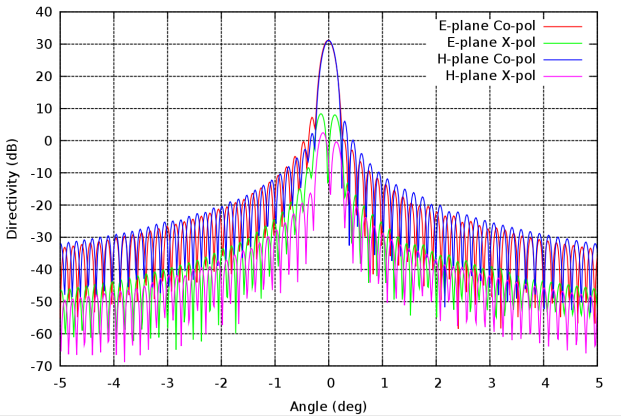

Figure 6. GRASP simulation of the primary beam of the GUBBINS optics.

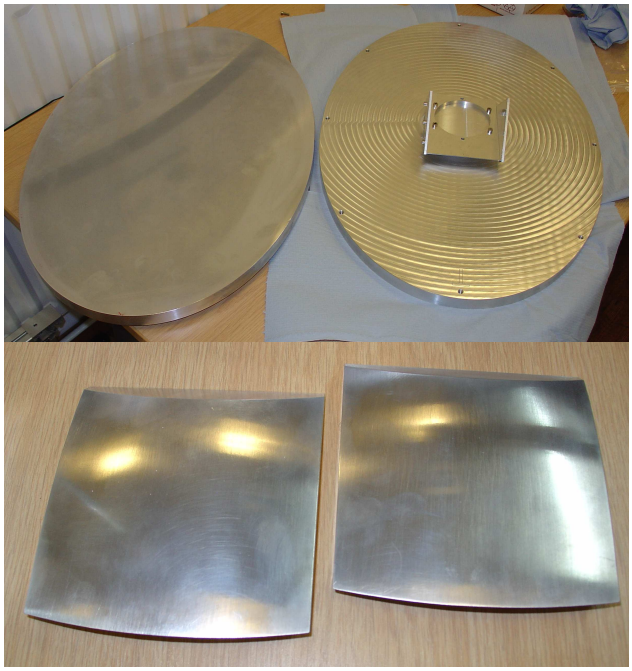

Figure 7. The GUBBINS primary (top) and corner mirrors (bottom) prior to assembly.

Both the primary and corner mirrors have been CNC machined from aluminium billets (fig 7). The surface figure has been measured on a CMM, giving a measured surface figure deviation of slightly less than $\pm 10\,\mu\mathrm{m}$. The corner mirrors are mounted on 2-axis goniometers, while the primary mirrors and drives are mounted on 2-axis tip/tilt stages and XYZ stages to allow the optics to be aligned.

B. Telescope mount and cryogenics

The two optics arms supporting the telescopes are mounted on a ring bearing and a servo motor fixed around the cryostat windows, and are connected by a counterweight at the rear end of the arms (see Fig. 3). The telescopes are tracked across the sky by rotating the primary mirrors on two servo motors about the optical axis between the primary and secondary mirrors. This allows both antennas to be pointed individually

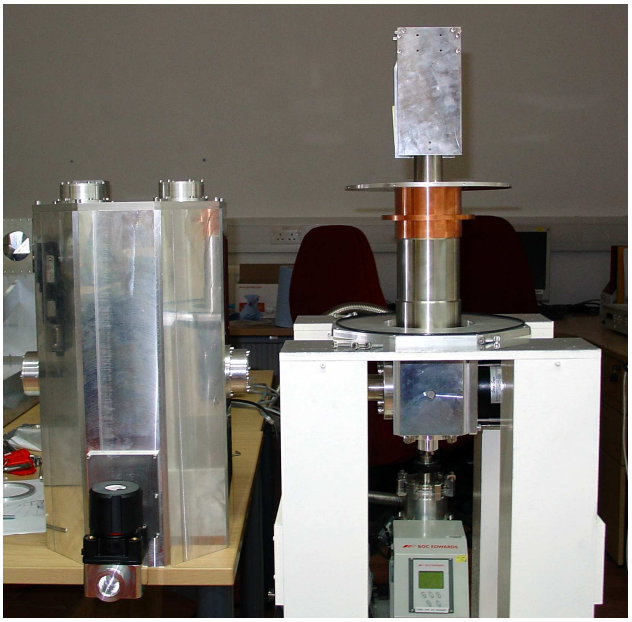

Figure 8. The GUBBINS cryostat, mounted on the telescope support pillar, and open to show the G-M cold-head, mixer mounting jig and radiation shield support.

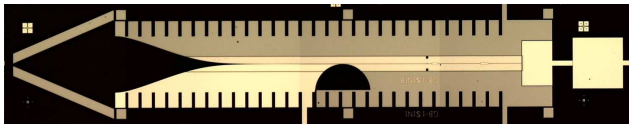

Figure 9. GUBBINS wide-IF band finline SIS mixer chip [5].

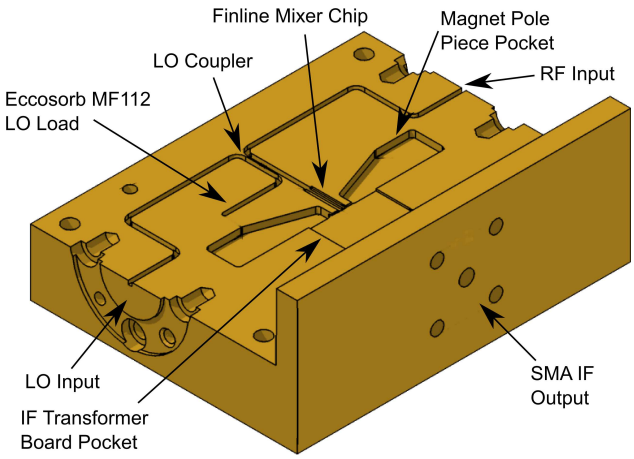

Figure 10. CAD model of the lower half of the GUBBINS mixer block.

in azimuth, while keeping the number of drive components to a minimum.

The whole instrument is supported on a pillar attached to the base of the cryostat and to a concrete plinth on the ground. The instrument is mounted on the plinth on a bearing, and can be secured in a number of orientations, allowing the projected baseline direction to be changed.

The cryostat is a structural element of the instrument mount, and is being custom designed and built by Oxford Physics (figs. 4 and 8). The cryostat is cooled by a two stage Gifford-McMahon cooler from Sumitomo Heavy Industries. It provides $1\,\mathrm{W}$ of cooling power to the $4\,\mathrm{K}$ stage, where the SIS mixers and first stage IF amplifiers are mounted, and $40\,\mathrm{W}$ to the $40\,\mathrm{K}$ stage where the electrical connections are heat sunk, and the second stage IF amplifiers are mounted.

C. SIS mixers and cryogenic IF amplifiers

GUBBINS will use the single-ended ultra-wide IF band finline mixers described in [5], with a waveguide directional coupler in a split mixer block for coupling LO to the mixer. These ultra-wide IF band mixers are based on an earlier $230\,\mathrm{GHz}$ finline mixer design [6], with a number of additions and improvements for ultra-wide IF band operation. An RF band-pass filter is used between the finline taper and the mixer tuning circuit to prevent the IF signal from leaking into the finline. The mixer tuning circuit and RF choke use relatively narrow microstrip lines to keep reactances in the IF band low, and a 5-stage microstrip transformer is used to match the $16.5\,\Omega$ SIS junction(s) to the $50\,\Omega$ input of the IF amplifiers over the $2-20\,\mathrm{GHz}$ IF band.

The first batch of SIS mixer chips (fig. 9), fabricated at KOSMA, are currently being tested in Oxford without the microstrip IF transformer and using a $4-6\,\mathrm{GHz}$ IF system with the GUBBINS $3-13\,\mathrm{GHz}$ cryogenic LNAs.

The split mixer block (Fig. 10) contains a $-16\,\mathrm{dB}$ directional coupler used to combine the LO signal with the astronomical signal, a termination load to dump the uncoupled LO power and the mounting position for the SIS mixer chip. The mixer block also holds the IF transformer board used to transform the $16.5\,\Omega$ output of the mixer to the $50\,\Omega$ input impedance of the IF amplifier and the SMA IF/DC bias connector. A superconducting electromagnet is mounted to the block to provide the magnetic field required to suppress Josephson tunnelling in the mixer, with magnet iron pole pieces used to concentrate the field at the mixer chip. The mixer block is currently being machined by Chris Groppi at the University of Arizona.

The $-16\,\mathrm{dB}$ directional coupler uses three $0.4\,\mu\mathrm{m}$ thick gold radial probes connected by suspended stripline and deposited on $65\,\mu\mathrm{m}$ thick quartz chips to couple power between the waveguides (fig. 11). The coupling of each chip is chosen according to the binomial distribution, with each chip and suspended stripline being one quarter wavelength long. The chips are glued into shallow slots between the waveguides, spaced at quarter wavelengths along the waveguides. The design parameters of the coupler are shown in table II, and the HFSS simulated performance in fig. 12. This design of coupler gives excellent return loss, directivity and insertion loss, while avoiding the difficulty of machining narrow and deep slots in the split mixer block.

The astronomical signals are coupled into the mixer block via corrugated horns mounted to waveguide flanges on the mixer block, while the LO signals are coupled via drilled, smooth-walled horns. The IF outputs from the mixer blocks are connected to commercial bias tees before being amplified by the first stage IF amplifiers. The cryogenic first stage IF amplifiers are $3-13\,\mathrm{GHz}$ InP LNAs supplied by Sander Weinreb at Caltech. They have excellent measured performance at $20\,\mathrm{K}$

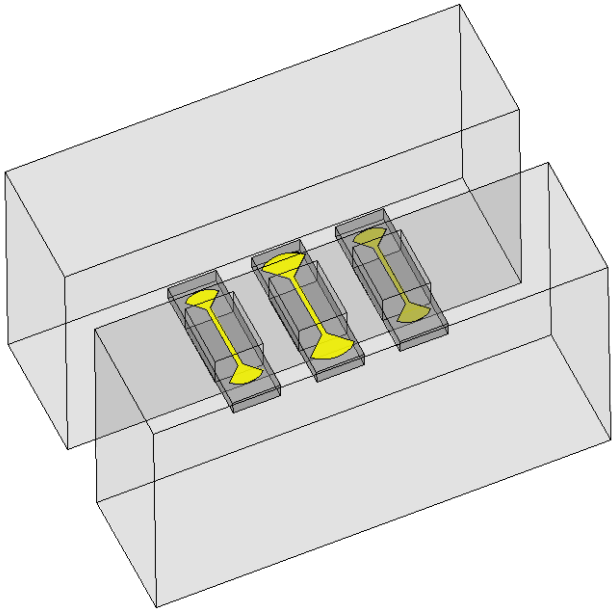

Figure 11. HFSS model of the waveguide directional coupler. The quartz chips (dark grey) are supported in shallow slots in the waveguide wall (light grey). 3 radial probes couple power between waveguides via suspended stripline.

Table II
DIMENSIONS OF THE WAVEGUIDE DIRECTIONAL COUPLER

Waveguide size	WR-4
Coupler spacing	350 μm
Waveguide slot width	200 μm
Waveguide slot height	130 μm
Coupler chip thickness	65 μm
Coupler chip width	190 μm
Coupler chip length	600 μm
Stripline width	20 μm
Stripline length	275 μm
Outer probe radius	100 μm
Inner probe radius	130 μm

over > 10 GHz bandwidth, which should be slightly improved on further cooling to 4 K.

D. LO system

Two 180° phase-switched LO signals are coupled into the two SIS mixers blocks via smooth wall horns on each of the mixer blocks and on the LO sources. The feed horns on the mixer blocks are coupled through two windows on the top of the cryostat via two Gaussian beam telescopes to the LO sources mounted on the side of the cryostat (fig. 13).

The LO signals are generated by two $195 - 260$ GHz multiplied LO sources from Radiometer Physics GmbH, with a multiplication factor of 18 and an output power level of 200 μW with ± 3 dB flatness across the LO band. Both LOs are driven by a single $10.8 - 14.5$ GHz synthesizer. To provide the required 180° phase shift between the two LO signals, the

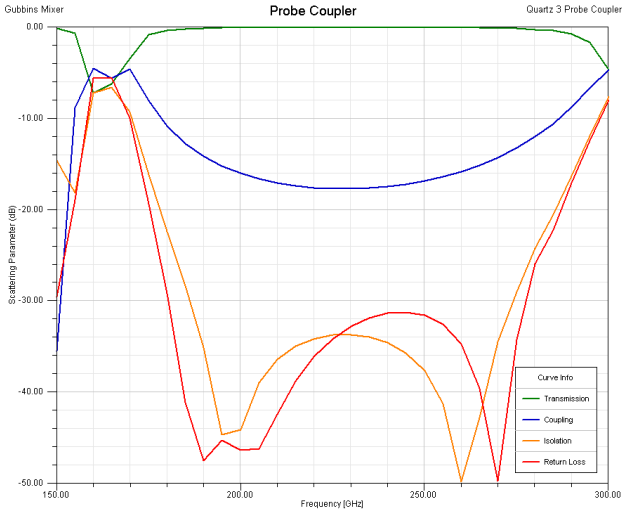

Figure 12. HFSS simulation of the LO directional coupler.

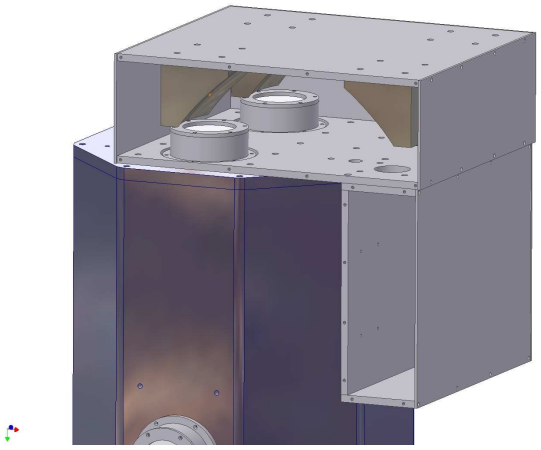

Figure 13. CAD model of the LO box and injection optics on top of the GUBBINS cryostat. The two RPG LO multipliers are housed in the box on the right, and coupled into the windows on top of the cryostat via two Gaussian beam telescopes.

input to one (or both) multiplier chains will be phase switched by a 10° Schiffman phase switch.

We also intend to investigate 180° phase switching the SIS receivers by switching the bias voltage of the SIS mixers from the positive to negative side of I-V curve. Since SIS mixers have antisymmetric I-V characteristics, switching the direction of the bias voltage changes the sign of the down-converted signal.

We are also working in collaboration with the Millimetre Technology Group at Rutherford Appleton Laboratories who are developing phase-locked photonic LO sources for use in SIS receivers [7]. These have the potential to greatly simplify the LO injection scheme of GUBBINS by providing individual phase switched LO sources for the SIS mixers, directly coupled to mixer blocks inside the cryostat.

E. IF chain

The IF signals from the cryogenic LNAs are then further amplified and individually processed before entering the

correlator. The latter stages of IF amplification are provided by a number of gain blocks, each of which uses two Hittite HMC462LP5 $2-20\mathrm{GHz}$, $13\,\mathrm{dB}$ cascadable amplifiers in surface mount packages. These gain blocks show excellent performance for a relatively low cost device, with a noise figure of $3.5\,\mathrm{dB}$ at room temperature. The noise of these amplifiers can be significantly improved by cooling, and we have successfully measured noise temperatures below $80\,\mathrm{K}$ for these amplifiers at $4\,\mathrm{K}$. Although we have plenty of gain available from the cryogenic LNAs, the first gain block will be mounted on the $40\,\mathrm{K}$ stage of the cryostat, to ensure that the noise figure of the first of these gain blocks has minimal effect on the overall system noise.

As well as being amplified, the IF signals are also band-pass filtered and have slope compensation applied across the IF band. The final step before correlation is to apply path compensation to the signal to remove the path delay introduced by scanning the two antennas of the telescope. The path compensator is made up of seven time delay switches, providing 2.5, 5, 10, 20, 40, 80 and $160\,\mathrm{mm}$ of path compensation, and made up of differential lengths of microstrip line switched by Hittite HMC547 $0-20\,\mathrm{GHz}$ FET surface mount packaged switches.

F. Correlator and data acquisition

The IF signals from the two antennas are combined in an analogue correlator, developed at Oxford in collaboration with Andrew Harris at University of Maryland. The correlator is a 16 lag complex Fourier transform correlator, with the full 2-20 GHz bandwidth being processed simultaneously. The architecture of a single-sideband version of the correlator is shown in Fig. 14.

The correlator cross-correlates the IF signals from the two antennas at discrete time delay steps, forming both real and imaginary parts of the cross-correlation. A sideband separating version of the correlator, capable of working with double-sideband receivers is made by duplicating the single-sideband version but applying the quadrature split to the IF signal from the other antenna, thus forming all linear combinations of IF signals. Applying a discrete Fourier transform to the set of lag data gives two independent complex power spectra for each of the receiver sidebands.

For each half of the double-sideband correlator, one half of IF signal from one antenna is split in a commercial quadrature hybrid, with other split in phase using a Wilkinson power divider, before being fed to two 16 lag correlator boards. The two signals on each board are then split sixteen ways using Wilkinson power divider trees before they are combined and detected by Gilbert Cell multiplier MMIC chips. The Wilkinson power dividers are a seven-stage design fabricated on alumina with a $50\,\Omega/\square$ resistive sheet used to define the resistive elements. These dividers show excellent performance from $1.5-23\,\mathrm{GHz}$.

Gilbert Cell multiplier MMICs are used to both combine the two IF signals and to detect the combined signal. These devices (Fig. 16) were developed by Andrew Harris at University of Maryland and Steve Maas at Nonlinear Technologies Inc. [8]. These devices provide both the sum and difference measurements of the combined signals, each replacing two power splitters, a 180° phase shift and two detector diodes in a conventional diode detector correlator [9].

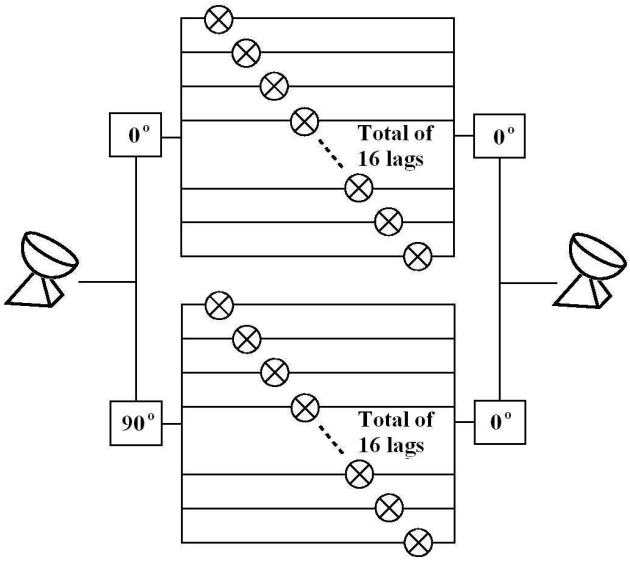

Figure 14. Architecture of one half of the GUBBINS $2-20\,\mathrm{GHz}$ analogue complex correlator. The other half is duplicated, but with the 90° phase shift applied to the signal from the other antenna, allowing the cross-correlations for both receiver sidebands to be obtained.

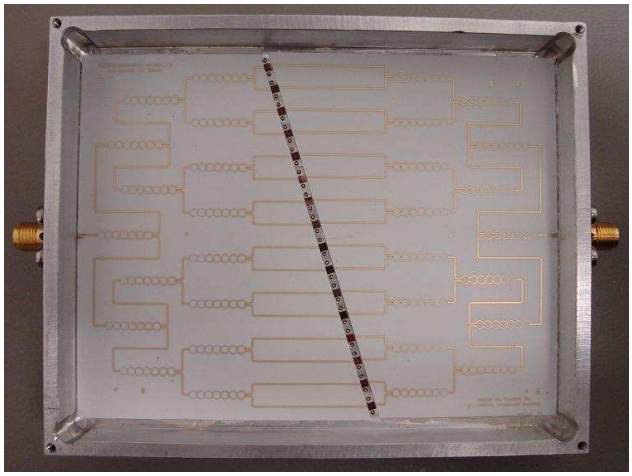

Figure 15. The prototype GUBBINS correlator board. Signals from each antenna are fed from the SMA connectors at each end of the board, and divided 16 ways in the Wilkinson power splitter trees, before being delayed in the lengths of microstrip and combined and detected in the multiplier chips along the centre of the board.

The full correlator board is fabricated on two wafers of alumina, with the multiplier chips being mounted between the two boards (figs. 15, 16). The aluminium box is used as the ground plane for both the microstrip boards and the multiplier chips. Each multiplier chip is biased and read by two pins inserted through the back of the correlator box and bonded to the multiplier chips.

The first prototype 16 lag correlator board has now been fabricated and tested [10]. The frequency response, lag spacing uniformity and required power input are shown in figs. 17, 18

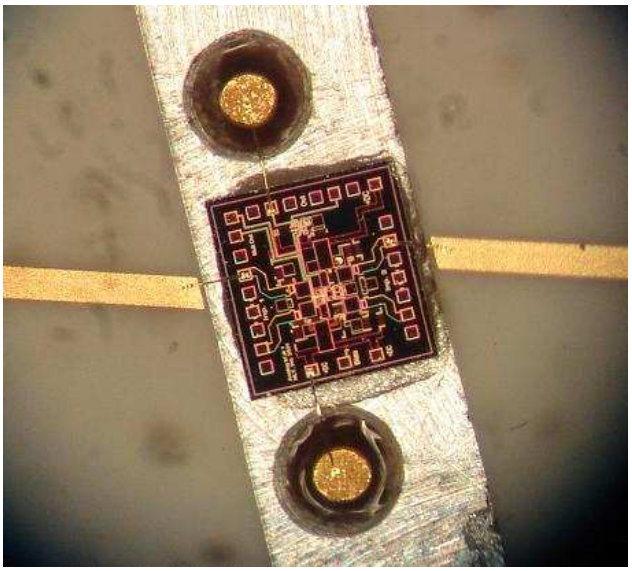

Figure 16. Close-up of a Gilbert Cell multiplier chip in the GUBBINS correlator.

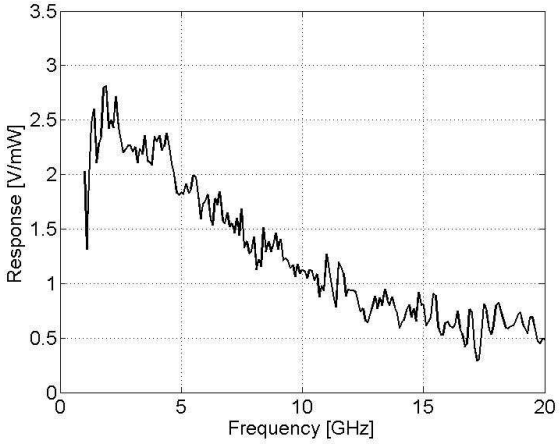

Figure 17. Frequency response of the prototype GUBBINS correlator board.

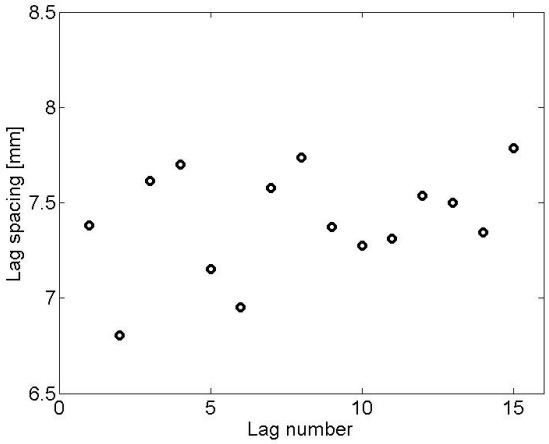

Figure 18. Lag spacings for the 16 lags on the prototype GUBBINS correlator board.

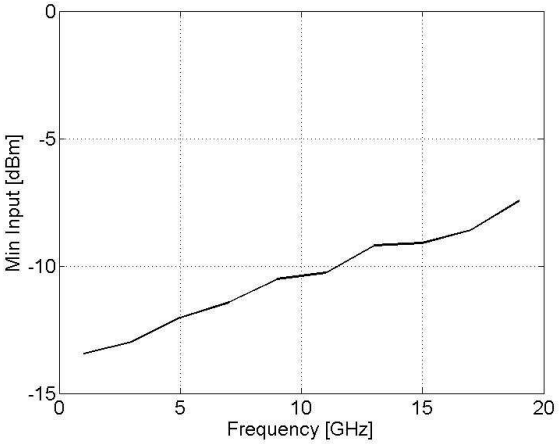

Figure 19. Required input power for the GUBBINS correlator.

and 19.

The multiplier chips are read by low noise amplifiers and an A-to-D conversion board developed by the Oxford Central Electronics Group. This board uses 2.8 MSps ADCs feeding an FPGA processor that demodulates the phase switching of the signals and provides a USB output to the data acquisition computer. The required readout boards are now in production at Oxford (fig. 20).

IV. Conclusions

We are building a prototype single-baseline mm-wave heterodyne interferometer to demonstrate high brightness sensitivity mm-wave interferometry. This instrument will accommodate many of the new technologies we are currently developing in Oxford, particularly ultra-wide IF band SIS mixers, ultra-wide band analogue correlators and phase switched photonic LO sources.

The instrument is in the middle of construction, with prototypes of the SIS mixers, IF system and correlator having been tested. The GUBBINS cryostat and optics are being assembled, and final versions of SIS mixers, LO system, correlator and read-out are currently being produced.

There is a niche for a future mm-wave interferometer with exceptional brightness sensitivity and wide field of view, complementary to ALMA and large mm-wave single dish telescopes, with key science goals of following up on the large numbers of S-Z clusters detected by current surveys, and for wide field imaging of faint extended continuum sources over wide frequency ranges. GUBBINS is intended to be an initial proving ground for the technology required for such an instrument.

Acknowledgements

The construction of GUBBINS is funded by the Royal Society under the Paul Instrument Fund scheme. We thank Andrew Harris and Steve Maas for use of the Gilbert Cell multiplier chips and their help with the development of the correlator.

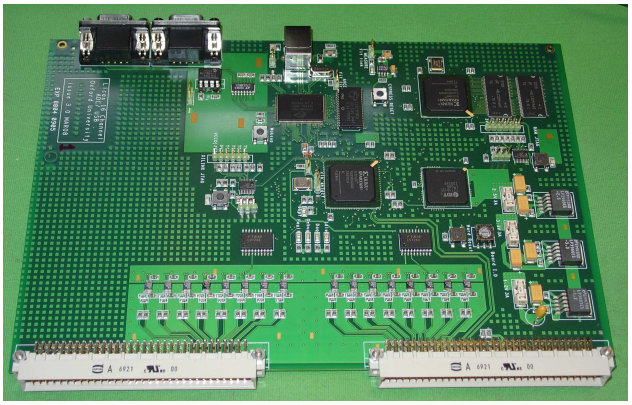

Figure 20. A GUBBINS correlator readout board. Signals from the correlator are read via the backplane connectors at the bottom, before being filtered and amplified in the lower section of the board. The signals are then digitised and processed by the FPGAs in the centre of the board, and then sent to the telescope control computer via the USB connection at the centre top of the board.

REFERENCES

[1] P. Grimes, M. Brock, C. Holler, K. Jacobs, M. Jones, O. King, J. Leech, A. Taylor, and G. Yassin, "A novel heterodyne interferometer for millimetre and submillimtre astronomy," in *Proc. 19th Int. Symp. Space THz Tech.*, 2008.

[2] R. A. Sunyaev and Y. B. Zeldovich, "Small-scale fluctuations of relic radiation," *Astrophysics and Space Science*, vol. 7, p. 3, 1970.

[3] M. Birkinshaw, "The Sunyaev-Zel'dovich effect," *PhysRep*, vol. 310, pp. 97–195, Mar. 1999.

[4] J. E. Carlstrom, G. P. Holder, and E. D. Reese, "Cosmology with the sunyaev-zel'dovich effect," 2002.

[5] P. Grimes, K. Jacobs, and G. Yassin, "Design of finline sis mixers with ultra-wide if bands," in *Proc. 19th Int. Symp. Space THz Tech.*, 2008.

[6] G. Yassin, R. Padman, S. Withington, K. Jacobs, and S. Wulff, "Broadband 230 GHz finline mixer for astronomical imaging arrays.," *Electronics Letters*, vol. 33, pp. 498–500, Mar. 1997.

[7] A. Fontana, Y. Bortolotti, B. Lazareff, A. Navarrini, P. Huggard, and B. Ellison, "Cryogenic photonic local oscillator for 2mm band sis heterodyne astronomical receiver array," *Electronics Letters*, vol. 43, pp. 1121–1123, 27 2007.

[8] A. Harris and S. Maas, "Gilbert cell multiplier measurements iii: Response from 2-30 GHz," *University of Maryland Technical Report*, 2002.

[9] C. M. Holler, T. Kaneko, M. E. Jones, K. Grainge, and P. Scott, "A 6-12 GHz analogue lag-correlator for radio interferometry," *A&A*, vol. 464, pp. 795–806, Mar. 2007.

[10] C. Holler, "2-20 GHz analogue lag-correlator for radio interferometry," *In prep.*, 2009.

SuperCam: A 64 pixel heterodyne array receiver for the 350 GHz Atmospheric Window

Christopher Groppi, Christopher Walker, Craig Kulesa, Dathon Golish, Jenna Kloosterman, Sander Weinreb, Glenn Jones, Joseph Barden, Hamdi Mani, Tom Kuiper, Jacob Kooi, Art Lichtenberger, Thomas Cecil, Gopal Narayanan, Patrick Pütz, Abby Hedden

Abstract— **We report on the development of SuperCam, a 64 pixel imaging spectrometer designed for operation in the astrophysically important 870 micron atmospheric window. SuperCam will be used to answer fundamental questions about the physics and chemistry of molecular clouds in the Galaxy and their direct relation to star and planet formation. The Supercam key project is a fully sampled Galactic plane survey covering over 500 square degrees of the Galaxy in ^{12}CO(3-2) and ^{13}CO(3-2) with 0.3 km/s velocity resolution**

SuperCam will have several times more pixels than any existing spectroscopic imaging array at submillimeter wavelengths. The exceptional mapping speed that will result, combined with the efficiency and angular resolution provided by the HHT will make SuperCam a powerful instrument for probing the history of star formation in our Galaxy and nearby galaxies. SuperCam will be used to answer fundamental questions about the physics and chemistry of molecular clouds in the Galaxy and their direct relation to star and planet formation. Through Galactic surveys, particularly in CO and its isotopomers, the impact of Galactic environment on these phenomena will be realized. These studies will serve as "finder charts" for future focused research (e.g. with ALMA) and markedly improve the interpretation, and enhance the value of numerous contemporary surveys.

In the past, all heterodyne focal plane arrays have been constructed using discrete mixers, arrayed in the focal plane. SuperCam reduces cryogenic and mechanical complexity by integrating multiple mixers and amplifiers into a single array module with a single set of DC and IF connectors. These modules are housed in a closed-cycle cryostat with a 1.5W capacity 4K cooler. IF signals are downconverted to baseband with a custom surface-mount board with 8 channels of IF processing. An Omnisys AB real time FFT spectrometer processes these IF signals to produce 64x250 MHz spectra with 0.25 km/s velocity resolution. The Supercam system is largely complete, and is now undergoing final fabrication and assembly, and should be deployed on the HHT this observing season.

***Index Terms*— Submillimeter wave spectroscopy, Submillimeter wave imagimg, Submillimeter wave mixers, Submillimeter wave receivers**

Manuscript received 20 April 2009.

C. Groppi (NSF Astronomy and Astrophysics Postdoctoral Fellow), C. Walker, C. Kulesa, D. Golish & J. Kloosterman, are with Steward Observatory, University of Arizona, Tucson, AZ 85721 USA (520-626-1627; fax: 520-621-1532; e-mail: cgroppi@as.arizona.edu).

S. Weinreb, G. Jones, J. Bardin & H. Mani are with the Department of Electrical Engineering, California Institute of Technology, Pasadena, CA, 91125 USA.

J. Kooi is with the Caltech Submillimeter Observatory, California Institute of Technology, Pasadena, CA 91125 USA.

T. Kuiper is with the NASA Jet Propulsion Laboratory, Pasadena, CA 90220, USA.

A. Licktenberger & T. Cecil are with the Department of Electrical and Computer Engineering , University of Virginia, Charlottesville, VA 22904 USA.

G. Narayanan is with the Department of Astronomy, University of Massachusetts, Amherst, MA 01003 USA.

P. Pütz is with the I. Physikalisches Institut, Universität zu Köln, Köln, Germany.

A. Hedden is with the Harvard Smithsonian Center for Astrophysics, Cambridge, MA 02138.

I. INTRODUCTION

SUPERCAM has been designed to operate in the astrophysically rich 870μm atmospheric window. The Heinrich Hertz Submillimeter Telescope has a 13μm RMS surface, making it one of the most accurate large submillimeter telescope currently in operation. In addition, the 10,500ft elevation site on Mt. Graham offers weather sufficient for observing in this window more than 50% of the observing season, 24 hours per day. The receiver is an 8x8 array constructed from integrated 1x8 mixer modules, with state of the art mixer, local oscillator, low noise amplifier, cryogenic and digital signal processing technologies.

SuperCam will have several times more pixels than any existing spectroscopic imaging array at submillimeter wavelengths. The resulting exceptional mapping speed, combined with the efficiency and angular resolution provided by the HHT will make SuperCam a powerful instrument for probing the history of star formation in our Galaxy and nearby galaxies. SuperCam will be used to answer fundamental questions about the physics and chemistry of molecular clouds in the Galaxy and their direct relation to star and planet formation. Through Galactic surveys, particularly in CO and its isotopomers, the impact of Galactic environment on these phenomena will be realized. These studies will serve as "finder charts" for future focused research (e.g. with ALMA) and markedly improve the interpretation, and enhance the value of numerous contemporary surveys.

II. SUPERCAM SCIENCE

From the Milky Way to the highest-redshift protogalaxies at the onset of galaxy formation, the internal evolution of galaxies is defined by three principal ingredients that closely

relate to their interstellar contents:

- The transformation of neutral, molecular gas clouds into stars and star clusters (star formation).
- The interaction of the interstellar medium (ISM) with the young stars that are born from it, a regulator of further star formation.
- The return of enriched stellar material to the ISM by stellar death, eventually to form future generations of stars.

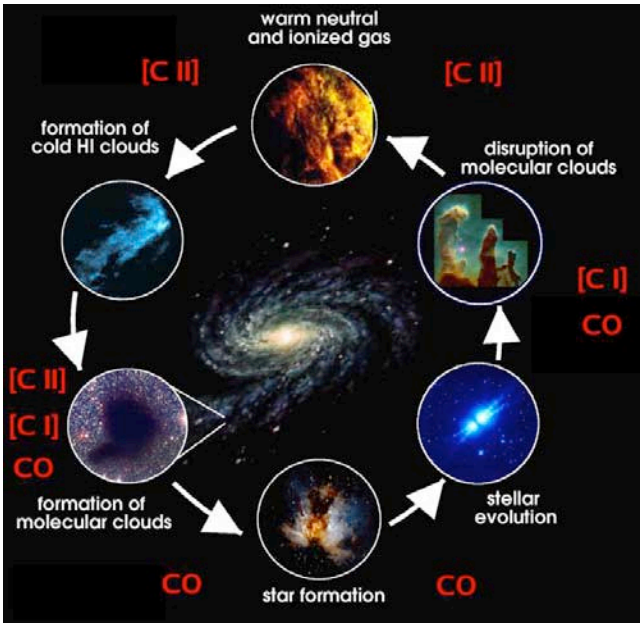

Figure 1: Life cycle of the ISM.

The evolution of the stellar population of galaxies is therefore determined to a large extent by the life cycles of interstellar clouds: their creation, starforming properties, and subsequent destruction by the nascent stars they spawn. The life cycle of interstellar clouds is summarized pictorially in Figure 1. Although these clouds are largely comprised of neutral hydrogen in both atomic and molecular form and atomic helium, these species are notoriously difficult to detect under typical interstellar conditions. Atomic hydrogen is detectable in cold clouds via the 21 cm spin-flip transition at 1420 MHz, but because the emission line is insensitive to gas density, cold (T~70K) atomic clouds are not distinguishable from the warm (T~8000K) neutral medium that pervades the Galaxy. Furthermore, neither atomic helium nor molecular hydrogen (H_2) have accessible emission line spectra in the prevailing physical conditions in cold interstellar clouds. Thus, it is generally necessary to probe the nature of the ISM via rarer trace elements. Carbon, for example, is found in ionized form (C^+) in neutral HI clouds, eventually becoming atomic (C), then molecular as carbon monoxide (CO) in dark molecular clouds. The dominant ionization state(s) of carbon accompany each stage of a cloud's life in Figure 1. In general, however, only global properties can be gleaned from the coarse spatial resolution offered by studies of external galaxies. Therefore detailed interstellar studies of the widely varying conditions in our own Milky Way Galaxy serve as a crucial diagnostic template or "Rosetta Stone" that can be used to translate the global properties of distant galaxies into reliable estimators of star formation rate and state of the ISM.

SuperCam has been designed to complete a key project Galactic plane survey in the ^{12}CO(3-2) and ^{13}CO(3-2) transitions of carbon monoxide. This survey, covering 500 square degrees of the Galaxy including a fully sampled survey from l=0º-90º and -1º<b<1º in addition to many molecular cloud complexes visible from the northern hemisphere, will improve the spatial resolution of existing surveys by more than a factor of 10. In addition, this will be the first submillimeter CO Galactic plane survey, providing a census of molecular gas actively participating in star formation. When combined with existing CO(1-0) surveys, a complete excitation temperature map of the survey region can be constructed. The depth of the survey is sufficient to detect CO to a level consistent with Av~1, detecting all CO that has formed in-situ.

III. SuperCam Instrument Description

A. Instrument Design

In the past, all heterodyne focal plane arrays have been constructed using discrete mixers, arrayed in the focal plane. SuperCam reduces cryogenic and mechanical complexity by integrating multiple mixers and amplifiers into a single array module with a single set of DC and IF connectors. Well conceived, efficient packaging is essential to the successful implementation of large format systems. The enormous complexity of even a small discrete system suggests a more integrated approach for larger systems [1,2]. At the heart of the array is an 8 pixel linear integrated array of low-noise mixers. The array mixer contains first stage, low-noise, MMIC IF amplifier modules with integrated bias tees. Eight of these modules are then stacked to produce the final 64 pixel array.

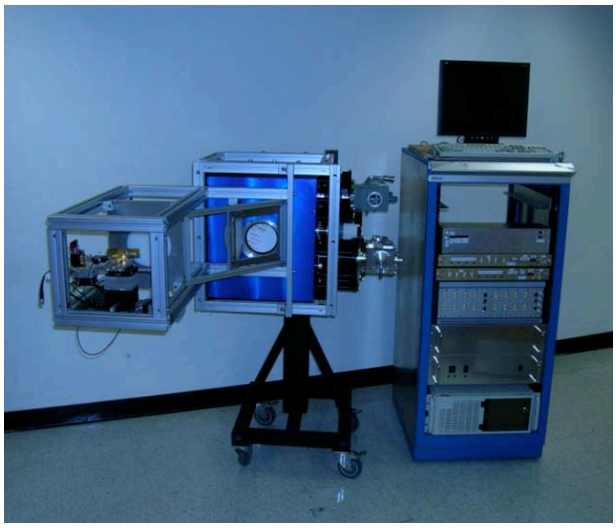

Figure 2: The SuperCam cryostat, LO optics and support electronics.

B. Cryogenics

The SuperCam systen with attached LO optics, frontend support electronics and backend electronics is shown in Figure 2. The cryostat was constructed by Universal Cryogenics in Tucson, Arizona, USA. Light from the telescope enters the cryostat through a 150 mm diameter AR coated, crystalline quartz vacuum window and passes through a Teflon coated crystalline quartz IR filter on the 40 K radiation shield before illuminating the 4 K mixer array. The Teflon layers on this filter serve as both the IR blocking filter and the antireflection coating. SuperCam uses a Sumitomo SRDK-415D cryocooler. The cooler has 1.5 W of thermal capacity at 4.2 K and 45W at 40K with orientation-independent operation. The operating temperature of the cryocooler is stabilized by the addition of a helium gas pot on the 2nd stage. A CTI cryogenics CTI-350 coldhead supplements the cooling of the 40K shield, and provides 12K heatsinking for the 64 stainless steel semi-rigid IF cables. The addition of this second coldhead permits the use of moderate lengths of standard coaxial cable while maintaining low heat load at 4K. Annealed and gold plated copper straps with a flex link connect the 4K cold tip to the cold plate, with less than a 0.2K temperature differential. Tests using heaters on the 4K cold plate, and system tests using prototype 1x8 mixer modules demonstrate adequate performance of the cryogenic system with the expected heat load from all 64 pixels.

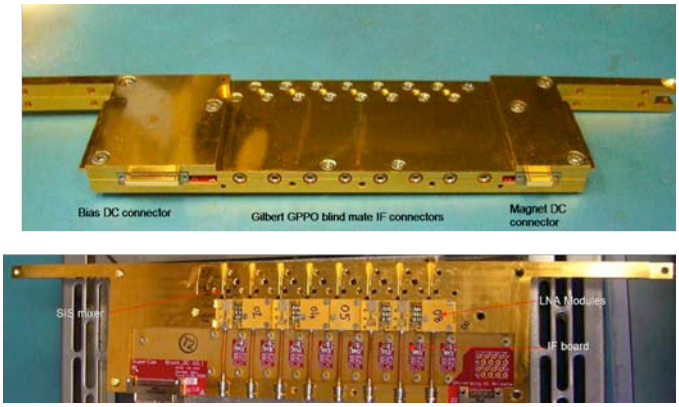

Figure 3: A completed Supercam 1x8 mixer module, fully assembled (top) and with the top cover removed (bottom).

C. Mixer Array

The SuperCam 64 beam focal plane is constructed from eight linear array modules with eight pixels each. Each pixel consists of a sensitive single ended SIS mixer optimized for operation from 320-380 GHz. The array mixers utilize SIS devices fabricated on Silicon-On-Insulator (SOI) substrates, with beam lead supports and electrical contacts [3]. The waveguide probe and SIS junction are based on an asymmetric probe design currently in use at the Caltech Submillimeter Observatory in their new facility 350 GHz receiver [4]. The 1x8 mixer subarrays are constructed from tellurium copper using the splitblock technique. Stainless steel guide pins and screws are used to ensure proper alignment and good contact between parts. Figure 3 shows a photograph of a production gold plated tellurium copper 1x8 mixer array fabricated at the University of Arizona using a Kern MMP micromilling machine. This block meets all design specifications, with 3 μm dimensional accuracy for all waveguide circuits. A diagonal feedhorn extension block is bolted to the front of the mixer array assembly, extending the diagonal horns to 11mm aperture size. This eliminates the need for dielectric lenses and their associated manufacturing and alignment difficulties. The energy in the horn passes through a 90° waveguide bend before reaching the device. The waveguide environment is designed around full height rectangular waveguide, with a fixed quarter wave backshort. The SIS device is suspended and self-aligned above the suspended stripline channel via eight small beamlead supports. The hot beamleads are tack-bonded with a wirebonder to the MMIC module input pads. Ground beamleads are glued to the mixer block using Epo-tek H20E conductive epoxy. The mounting method is designed such that the block can be opened repeatedly without disturbing the SIS devices. Single devices can be removed and replaced without disturbing neighboring devices. The mixer blocks are fabricated at the University of Arizona using a Kern MMP micromilling machine purchased for this project. This numerically controlled mill can fabricate structures to micron accuracy with a high level of automation. A SuperCam 1x8 module can be produced in ~8 hours of machine run time. The machine's 24 position tool changer allows a complete block to be fabricated with minimal user intervention during the machining process. Integrated workpiece and tool metrology systems, along with sophisticated computer aided manufacturing (CAM) software result in high part yield. Verification of fabricated parts though a high precision measurement microscope and 3D interferometric microscope insure dimensional accuracy and waveguide surface finish are within design tolerance. Testing, described in section IV, has been carried out using a single-pixel version of the SuperCam mixer design in a test cryostat, and with both prototype and production 8-pixel mixer modules. All mixer blocks are complete and are now undergoing gold plating and assembly.

D. Local Oscillator

With an array receiver, LO power must be efficiently distributed among pixels. Depending on the mechanical and optical constraints of the array, a balanced distribution can be achieved using quasioptical techniques or waveguide injection. With the quasioptical approach, dielectric beam splitters or holographic phase gratings are used to divide the LO energy between array pixels. We have chosen to use a hybrid waveguide/quasioptical LO power injection scheme. The LO power for the array will be provided by a single solid-state, synthesizer-driven source from Virginia Diode Inc. The active multiplier chain consists of a high power solid-state amplifier followed by a series of tunerless broadband multipliers. The output of the multiplier is coupled to an eight-way waveguide corporate power divider with splitblock machineable waveguide twists. Each of the eight outputs provides the drive power for a 1x8 subarray via an identical 8 way corporate divider with diagonal waveguide feedhorn outputs [5,6]. Figure 5 shows the complete 64-way power

divider constructed with the Kern micromilling machine at the University of Arizona. The power pattern of this divider and its injection optics is also shown in figure 5. Power division is equal to the ~10% level. In addition, we have constructed a 8 channel linear power divider for testing single mixer units with a lower power laboratory LO source. This power divider has been used in system tests with the prototype and production 1x8 mixer arrays, with excellent results. An extended diagonal horn array similar to the mixer horn extension blocks then matches the LO beams to the mixers through a Gaussian beam telescope comprised of two large dielectric lenses. A 1.0 mil Mylar beamsplitter is used to inject the LO power. Testing has shown that a 2mW LO source is sufficient to optimally pump a 1x8 mixer array with this scheme, running at only ~20% of the maximum power output. An already purchased 12 mW source from Virginia Diodes will be more than sufficient to pump the final 64 pixel array, also with a 1.0 mil Mylar diplexer. This scheme ensures uniform LO power in each beam since the waveguide path lengths are identical for each beam. In addition, the waveguide feedhorns provide well controlled and predictable LO power distribution and coupling to each mixer.

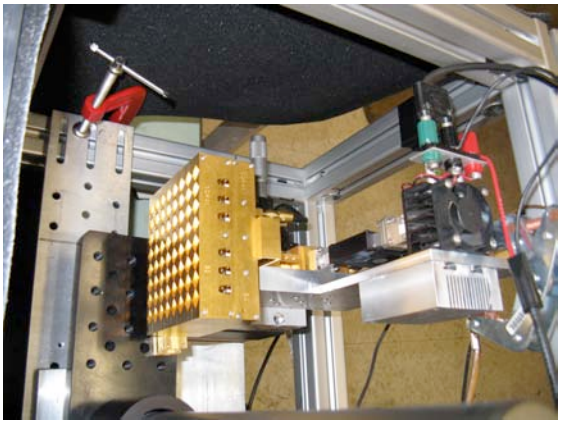

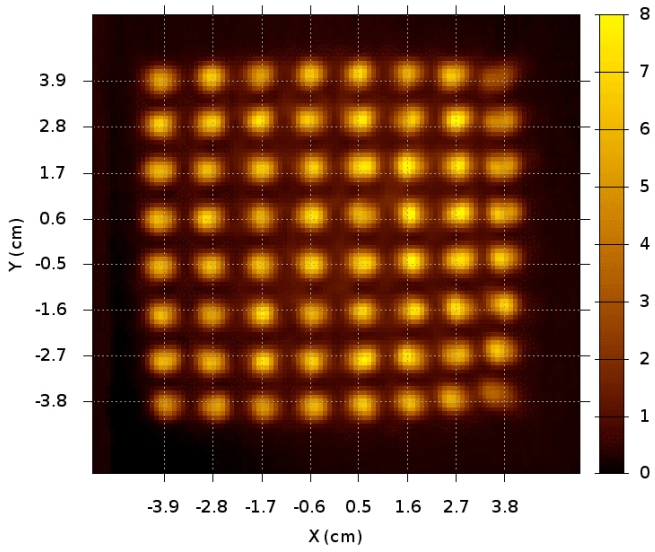

Figure 4: Supercam 64-way waveguide LO power divider (top) and measured power pattern from this divider (bottom). Amplitude scale is linear. Power is evenly divided to the +/- ~10% level. Some asymmetrical barrel distortion is evident, due to optical misalignment in the test setup.

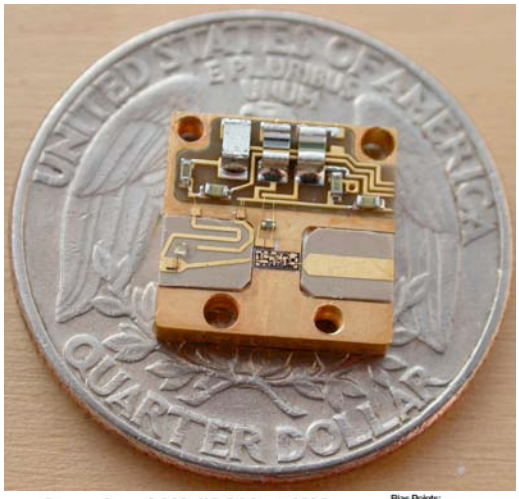

Figure 5: A SuperCam MMIC amplifier module (top), and typical measured results at 13K bath temperature (bottom) for several bias points. Amplifier noise remains low for bias powers as low as 6 mW. Gain remains above 30 dB.

E. IF/Bias Distribution System

The IF outputs from the SIS devices are bonded directly to the input matching networks of low-noise, InP MMIC amplifier modules located in the array mixers. These amplifier modules have been designed and fabricated by Sander Weinreb's group at Caltech. The IF center frequency of the array is 5 GHz. The MMIC chip is contained in an 11mm x 11mm amplifier module that contains integrated bias tees for the SIS device and the amplifier chip. The module achieves noise temperature of ~5 K and delivers 32 dB of gain while consuming 8 mW of power. An example is shown in figure 4, with measured gain and noise data at 4 mW through 20 mW power dissipation. Noise remains virtually unchanged down to 6 mW power dissipation, while gain is reduced modestly (Figure 5). Several tests have been performed with these modules to ensure oscillation free operation, low noise, high stability, and no heating effects on the SIS device. Modules have been integrated into both single pixel and 1x8 array mixers, and have shown performance as good or better than expected with connectorized amplifiers. No heating effects are visible, although care must be taken to avoid oscillation due to

feedback.

In addition to the LNA modules, the Caltech group has designed and constructed a warm IF system for SuperCam that will condition the IF signal for use with the SuperCam Array Spectrometer (figure 6). This IF system consists of a single large microwave printed circuit board with 8 channels of signal conditioning mounted in a modular chassis. The module contains a 5 GHz gain stage, switchable filters for both 250 MHz and 500 MHz bandwidth modes, baseband downconversion and baseband amplification.

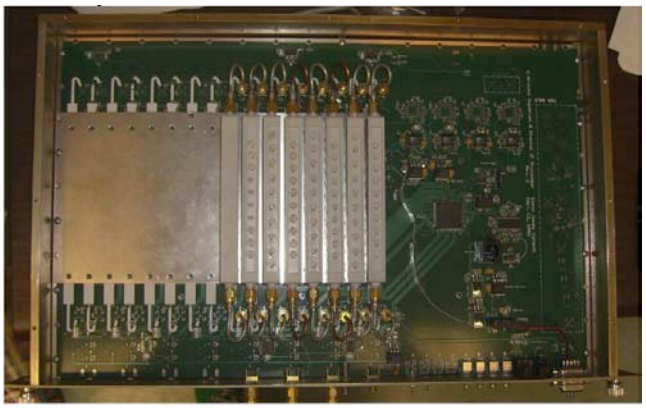

Figure 6: The inside of a SuperCam IF processor. This module provides amplification, programmable attenuation, passband filtering and total power detection for 8 channels.

F. Array Spectrometer

The SuperCam spectrometer delivers 64 channels at 250 MHz/channel with 250 kHz resolution, or 32 channels at 500 MHz with 250 kHz resolution. The system will be capable of resolving lines in all but the coldest clouds, while fully encompassing the Galactic rotation curve. The system is easily extendible to deliver 64 500 MHz bandwidth channels or 32 1 GHz bandwidth channels. This leap in spectrometer ability is driven by the rapid expansion in the capabilities of high speed Analog to Digital Converters (ADCs) and Field Programmable Gate Arrays (FPGAs). The SuperCam spectrometer, built by Omnisys AB of Sweden, is based on a polyphase filterbank architecture. High speed ADCs digitize the incoming RF signal at 8 bits resolution, preventing any significant data loss as with autocorrelation based schemes. A polyphase filterbank spectrometer is implemented on a FPGA. In our board architecture, 4 ADCs feed a single Xilinx Virtex 4 FPGA on each spectrometer board. Each board can process 4 500 MHz IF bandwidth signals or two 1 GHz IF bandwidth signals at 250 kHz resolution. These systems are fully reconfigurable by loading new firmware into the FPGAs. In addition, the spectrometer can be easily expanded to increase bandwidth. We have received an 8 board system capable of processing 64x250 MHz, 32x 500 MHz or 16x1GHz IF signals (figure 7). In the 64x250 MHz mode, we power combine two IF signals into one spectrometer input. Stability testing shows the spectrometer is capable of delivering a spectroscopic Allan time of ~650s, including the effects of the IF processor described in section III.E.

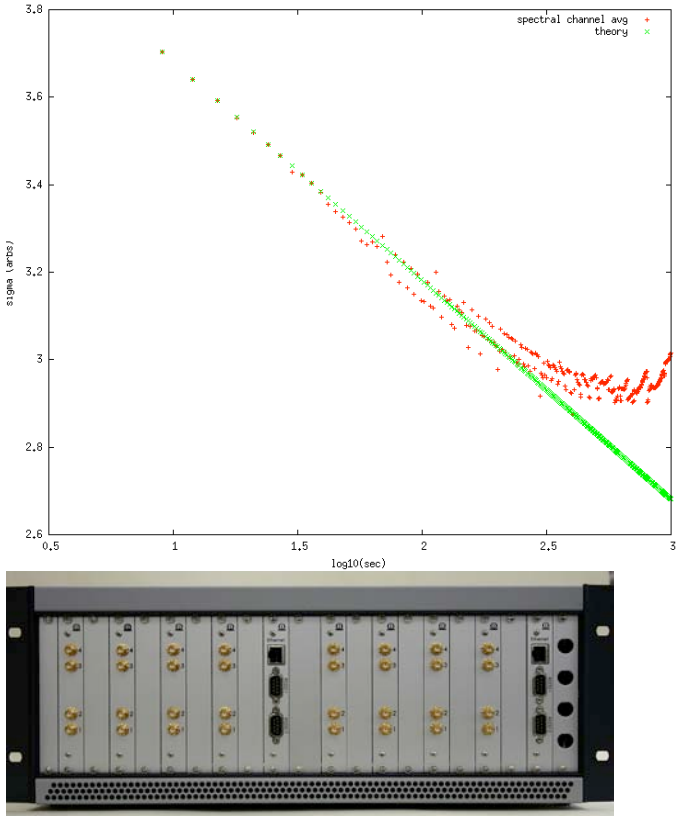

Figure 7: Measured Allan variance of the Supercam spectrometer system, including the Caltech IF processor. Allen time is 650s (top). The Supercam spectrometer system, built by Omnisys AB (bottom). This single 3U crate can process 16 GHz of IF bandwidth at 250 kHz spatial resolution. It consumes less than 200W of AC power.

G. Optics

The existing secondary mirror of the Heinrich Hertz Telescope provides a f/13.8 beam at the Nasmyth focus. The clear aperture available through the elevation bearing prevents the possibility of a large format array at this position. To efficiently illuminate a large format array like SuperCam, the telescope focus must fall within the apex room located just behind the primary. A system of re-imaging optics located in the apex room transforms the f number of the telescope to f/5 (figure 8). Since the physical separation between array elements in the instrument focal plane scales as $2f\lambda$, lower f/#'s serve to reduce the overall size of the instrument. The reimaging optics are composed of two offset parabolas and several flat mirrors. All the reimaging optics can be mounted on a single modular optical frame. This frame can be completely constructed, aligned and tested off the telescope, disassembled into modules and reassembled in the apex room. All electronics, including the backend, are located in the apex room. The cryostat and optics frame have been designed using finite element analysis to minimize gravitational deflection, and the calculated deflections have been fed into the tolerancing of the optical design. The optical system was initially designed and optimized with Zemax, and was then verified by BRO research using their ASAP physical optics package. The system's efficiency exceeds 80% for all pixels, and has been verified to be robust to alignment and fabrication tolerances.

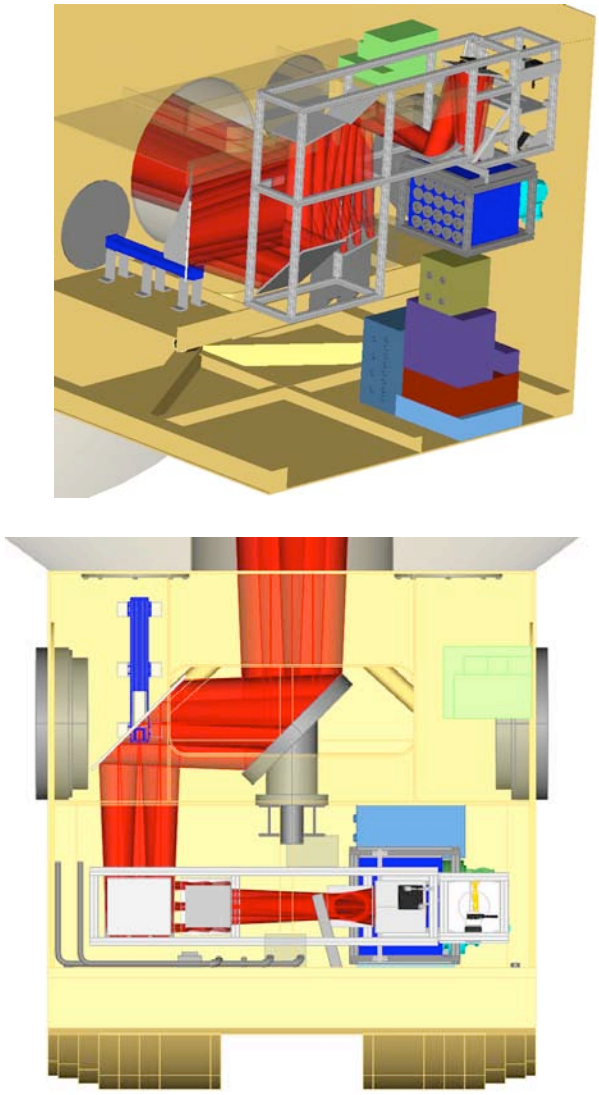

Figure 8: The Supercam optical design viewed from behind the primary reflector, (top), and viewed from the top (bottom). The apex room is transparent to visualize the design. The beam bundles are displayed in red.

IV. Laboratory Testing

For testing the SuperCam mixer design in the laboratory, we have designed two single pixel mixers. The first design uses an existing SIS junction design from the DesertStar 7-pixel array [2], but incorporates the Caltech designed MMIC module. This work has been reported in other papers [7]. We determined that the SIS receiver with integrated MMIC amplifier worked as well as a receiver with a separate connectorized amplifier and cryogenic amplifier, and resulted in no heating effects at the SIS device from the close proximity of the amplifier. We later designed a second single pixel amplifier that is an exact copy of a single pixel of the 1x8 mixer array design discussed in section III.B. This mixer was designed to test the self-aligning beam-lead-on-SOI SIS devices that will be used in the SuperCam array, as well as the compact, low power electromagnet, MMIC amplifier module and extended diagonal feedhorn.

This mixer has been extensively tested for noise performance across the band, frequency response using a Fourier Transform Spectrometer, and stability measurements using the complete backend system. Tests with the latest wafer of SIS on SOI devices from UVa show close to optimal tuning, and measured noise temperatures of ~65 K with less than 10K variation across the measured band (LO limited to 330 to 365 GHz). A plot of uncorrected receiver temperature versus LO frequency is shown in figure 9.

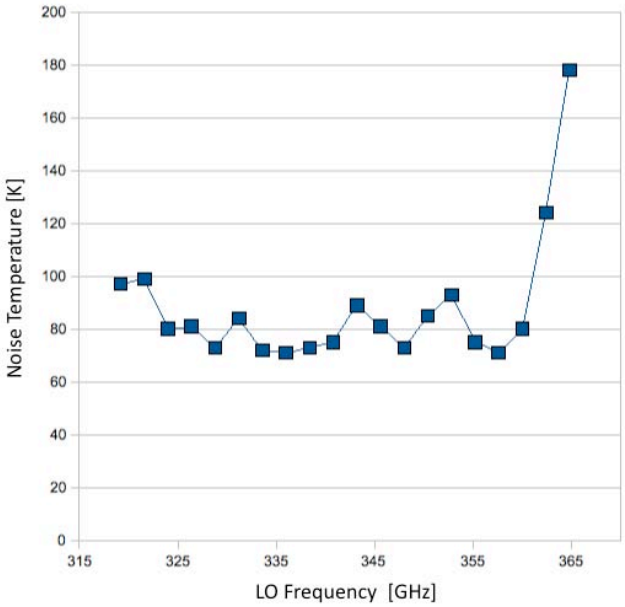

Figure 9: Supercam single pixel test mixer noise vs. LO frequency. Noise performance at the low and high ends of the band are influenced by lack of available LO power from our LO chain. The "bumps" in noise performance are due to residual sideband noise from the LO source, and are not present when measured with a Gunn diode driven LO.

In addition, measurements of both a prototype and production 1x8 mixer array have been completed using prototype or final electronics for the entire system. Performance testing of the first production mixer module is summarized in figure 10. The SIS devices for this test were selected randomly and screened only for their room temperature resistance. Device yield was 100% after this screening process. Noise temperatures have been corrected for the loss introduced by the currently uncoated quartz vacuum window. In addition, these measurements were made using a Goretex GR infrared filter rather than a Teflon coated quartz IR filter. The significantly increased IR load resulted in a higher than desired mixer temperature (~5K), also increasing noise somewhat. With an AR coated vacuum window and quartz IR filter, we expect to achieve the same noise performance as we have measured using the single pixel test mixer.

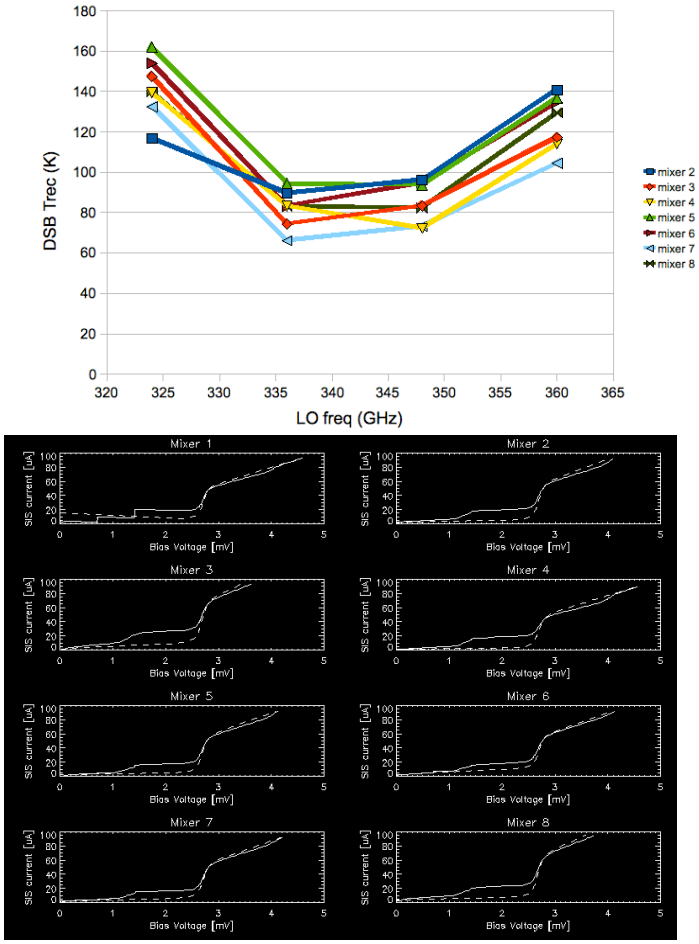

Figure 10: Noise vs. frequency measurements (top) and pumped and unpumped IV curves, of the eight pixels in the first Supercam production mixer (bottom). Mixer #1's magnet was not functioning during this test, and is not included in the noise measurements. LO sideband noise is contaminating the noise measurements at the low and high ends of the measured band.

V. Conclusion

We are constructing SuperCam, a 64-pixel heterodyne imaging spectrometer for the 870 µm atmospheric window. A key project for this instrument is a fully sampled Galactic plane survey covering over 500 square degrees of the Galactic plane and molecular cloud complexes. This ^{12}CO(3-2) and ^{13}CO(3-2) survey has the spatial (23") and spectral (0.25 km/s) resolution to disentangle the complex spatial and velocity structure of the Galaxy along each line of sight. SuperCam was designed to complete this survey in two observing seasons at the Heinrich Hertz Telescope, a project that would take a typical single pixel receiver system 6 years of continuous observing to complete. Prototypes of all major components have been completed and tested. Fabrication of the final waveguide components is now complete, and assembly is underway. One 1x8 mixer module is installed in the cryostat for testing at the University of Arizona, while the remaining modules are being assembled at Caltech. We expect to complete the instrument this summer, and deploy on the HHT during the fall observing season.

Acknowledgment

Supercam was supported by the NSF Major Research Instrumentation Program, Award AST- 0421499. CG is supported by an NSF Astronomy and Astrophysics Postdoctoral Fellowship under award AST-0602290.

References

[1] Walker, C. K., Groppi, C., d'Aubigny, C., Kulesa, C., Hungerford, A., Jacobs, K., Graf, U., Schieder, R., & Martin, C., 2001, PoleSTAR: A 4-Pixel 810 GHz Array Receiver for AST/RO, "Proceedings of the 12th International Symposium on Space Terahertz Technology", San Diego, CA, Eds. Mehdi & McGrath, JPL.

[2] Groppi, C.E., Walker, C.K., Kulesa, C., Puetz, P., Golish, D., Gensheimer, P., Hedden, A., Bussmann, S., Weinreb, S., Kuiper, T., Kooi, J., Jones, G., Bardin, J., Mani, H., Lichtenberger, A., Narayanan, G. SuperCam, a 64- Pixel Superheterodyne Camera, Proceedings of the 17th International Symposium on Space Terahertz Technology, 2006.

[3] R.B. Bass, J.C. Schultz, A.W. Lichtenberger (University of Virginia); C. Walker (University of Arizona); J. Kooi (CalTech), "Beam Lead Fabrication Using Vacuum Planarization", submitted to Proceedings of the Fourteenth International Symposium on Space THz Technology, May 2003.

[4] J.W. Kooi, C.K. Walker, and J. Hesler, "A Broad Bandwidth Suspended Membrane Waveguide to Thin Film Microstrip Transition", 9th Int. Conference on Teraherz Electronics, 15th - 16th October 2001.

[5] Ward, J.S. & Chattopadhyay, G., A 220-320 GHz 90° Polarization Twist for Integrated Waveguide Circuits, MWCL, submitted 2006.

[6] A. R. Kerr, "Elements for E-Plane Split-Block Waveguide Circuits," ALMA Memo 381, 1 July 2001.

[7] Puetz, P., Hedden, A., Gensheimer, P., Golish, D., Groppi, C., Kulesa, K., Narayanan, G., Lichtenberger, A., Kooi, J., Wadefalk, N., Weinreb, S., Walker, C., 345 GHz Prototype SIS Mixer with Integrated MMIC LNA, Int. J. Infrared Milli. Waves, 27, 1365, 2006.

Clover - Measuring the cosmic microwave background B-mode polarization

P. K. Grimes[4], P. A. R. Ade[1], M. D. Audley[2], C. Baines[3], R. A. Battye[3], M. L. Brown[2], P. Cabella[4], P. G. Calisse[1], A. D. Challinor[5,6] , P. J. Diamond[3], W. D. Duncan[7], P. Ferreira[4], W. K. Gear[1], D. Glowacka[2], D. J. Goldie[2], W. F. Grainger[1], M. Halpern[8], P. Hargrave[1], V. Haynes[3], G. C. Hilton[7], K. D. Irwin[7], B. R. Johnson[4], M. E. Jones[4], A. N. Lasenby[2], P. J. Leahy[3], J. Leech[4], S. Lewis[3], B. Maffei[3], L. Martinis[3], P. Mauskopf[1], S. J. Melhuish[3], C. E. North[1,4], D. O'Dea[2], S. M. Parsley[1], L. Piccirillo[3], G. Pisano[3], C. D. Reintsema[7], G. Savini[1], R. Sudiwala[1], D. Sutton[4], A. C. Taylor[4], G. Teleberg[1], D. Titterington[2], V. Tsaneva[2], C. Tucker[1], R. Watson[3], S. Withington[2], G. Yassin[4], J. Zhang[1] and J. Zuntz[4].

***Abstract*—Clover is a UK-led experiment to measure the B-mode polarization of the cosmic microwave background. The instruments are currently under construction and deployment to the Pampa La Bola site in the Atacama Desert is planned for 2010. It consists of two 2-m class telescopes feeding background limited imaging arrays of ~100 dual polarization pixels at each of 97, 150 and 225 GHz. The waveguide and antenna fed TES bolometers are limited by unavoidable photon noise from the atmosphere, and read-out using NIST's time domain multiplexing scheme. The entire instrument has been designed for exceptionally low systematic errors in polarization measurements, which has necessitated novel designs for the instrument optics, horn arrays, OMTs and detector feeds, as well as careful development of the scan strategy, field location and data analysis methods.**

The experiment aims to measure the polarization of the CMB with an angular resolution of $5.5' - 8'$ across $1000\,\mathrm{deg}^2$ of sky (angular multipole range $20 < l < 1000$) to a sensitivity of $8\,\mu$K-arcmin after foreground cleaning. If all systematics are adequately controlled this will allow the detection of the primordial B-mode CMB anisotropies down to tensor to scalar ratios of 0.03, as well as providing extremely accurate measurements of the CMB temperature, E-mode polarization, and B-mode lensing polarization. Detecting or constraining the level of the primordial B-mode signal will allow constraints to be placed on the energy scale of inflation, providing an unprecedented insight into the physics of the early Universe.

We describe the current status of the Clover project, including the current instrument design and construction status, and the development of the novel technology involved.

***Index Terms*—Cosmic Microwave Background, B-mode polarization, ground-based telescope, cosmology**

I. Introduction

PRECISE measurements of the polarization of the cosmic microwave background (CMB) can provide constraints on a number of cosmological parameters, possibly including the energy scale of inflation. A measurement of the energy scale of inflation would tell us about the physics of the Big Bang itself for the first time [1].

CMB polarization fluctuations are usually decomposed into two orthogonal modes; a "grad-like" E-mode with electric field-like parity, and a "curl-like" B-mode with magnetic field-like parity [2]. Primordial density perturbations in the early universe give rise to both the large scale distribution of matter in the universe and to the CMB intensity anisotropies. These density perturbations also generate the purely E-mode polarization fluctuations, or "E-modes" at about 10% of the intensity fluctuations (rms level $\sim 5\,\mu$K).

Magnetic field-like polarization fluctuations, or "B-modes" are not generated directly by primordial density perturbations. B-modes can be either generated by gravitational lensing of the primordial CMB intensity and E-mode polarization fluctuations by matter after decoupling of the CMB (the "B-mode lensing signal"), or by tensor fluctuations at the surface of last scattering, caused by primordial gravity waves. These primordial B-modes are a key diagnostic of inflationary cosmology theories, with the intensity of the gravity wave fluctuations giving a key insight to the energy scale and form of the inflationary field. As such, the CMB primordial B-mode signal provides a key insight into the physics of the very early universe, allowing us to probe physics at energy scales around $10^{16}\,\mathrm{GeV}$.

Based on the current $\Lambda\mathrm{CDM}$ concordance cosmology model, the primordial B-mode signal is expected to be at least 10-100 times weaker than the E-mode signal. Therefore its detection and characterization will require novel dedicated experiments with at least 1-2 orders of magnitude more sensitivity than current CMB polarization experiments.

A. The Clover project

Clover is a UK-led project that aims to measure the primordial B-mode CMB signal, or to constrain its level to a tensor-to-scalar fluctuation ratio $r < 0.026$ in an angular multipole range of $20 < l < 1000$ ($8'$ to $10°$). This is a factor of 10 lower than the current limits, and would confirm or rule out a number of theories of inflation.

[1]School of Physics and Astronomy, Cardiff University, UK.
[2]Cavendish Laboratory, University of Cambridge, UK.
[3]School of Physics and Astronomy, University of Manchester, UK.
[4]Astrophysics, Dept. of Physics, University of Oxford, UK.
[5]Institute of Astronomy, University of Cambridge, UK.
[6]DAMTP, University of Cambridge, UK.
[7]National Institute of Standards and Technology, USA.
[8]University of British Columbia, Canada.
P. Cabella is now with the University of Rome, Italy.
B.R. Johnson is now with the University of California, Berkeley, USA

Clover will spend two years making polarimetric observations of approximately 1000 square degrees of the sky from Pampa la Bola on the ALMA site in the Atacama Desert, Chile. Clover consists of two ~2 m Compact Range Antenna telescopes feeding imaging arrays of 96 dual polarized antenna-coupled Transition Edge Sensor (TES) bolometers at each of 97, 150 and 225 GHz. The Clover instruments use a number of techniques, including rapid constant elevation scanning, polarization modulation via half-wave plates, and absorbing ground shields to reduce systematic errors.

The two Clover telescopes are currently being assembled by the Astrophysics group at the University of Oxford, with the receivers undergoing cryogenic tests in the Astronomical Instrumentation Group at Cardiff University. The science grade detectors are currently being fabricated at the Detector Physics Group, Cavendish Laboratories, Cambridge and the 97 GHz array feed-horns and OMTs are being tested at University of Manchester. The two Clover instruments will then be integrated and tested at Oxford, before shipping to Chile for installation and commissioning.

B. Ancillary Science Goals

Clover will also make precise measurements of the CMB intensity and E-mode signals, and will measure the non-primordial B-mode lensing signal. These measurements will provide tighter constraints on cosmological parameters and will complement measurements made by Planck and other instruments. Clover will also be sensitive to a number of effects due to exotic physics in the early universe, particularly parity violation which results in correlations between the CMB intensity and E-mode signals and the B-mode signal, and B-mode signal from a background population of topological defects such as cosmic strings.

II. Instrument Description

A. Instrument requirements

The ambitious science goals of Clover mean that the requirements on both sensitivity and control of systematic errors are extremely stringent [3]. Some of the major requirements are listed in Table I.

Characterizing the B-mode fluctuation power spectrum for a tensor-to-scalar ratio of $r = 0.026$ requires mapping a sky area of $\sim 1000\,\mathrm{deg}^2$ to an rms noise of $1.4\,\mu$K per $5.5'$ pixel for the $150\,$GHz instrument. To reach the overall sensitivity across the survey areas in a reasonable integration time, the system noise must be comparable or lower than the unavoidable photon noise from the atmospheric and astronomical background. This results in stringent requirements on the detector noise, the instrument efficiency and on spillover from the optics.

Separating the CMB polarization signal from the strongest polarized astrophysical foreground signals (dust [4] and galactic synchrotron radiation [5]), requires that observations are made at three or more frequency bands across the expected foreground minimum at $\sim 100\,$GHz. The chosen Clover bandpasses and the expected atmospheric photon noise and transparency are shown in Table II.

Table I
Summary of requirements on the Clover instruments

Instrument Characteristic	Requirement
Stokes parameters measured	I, Q and U at each pixel
Multipole range	$20 < l < 1000$
Resolution	$8'$
Mapped area	$1000\,\mathrm{deg}^2$
RMS Noise per $5.5'$ map pixel (Q, U)	$1.4\,\mu$K
Instrument noise limit	Unavoidable photon noise
Detector NET (97, 150, 225 GHz)	$150,\ 225,\ 590\,\mu\mathrm{K}\sqrt{\mathrm{Hz}}$
Detector NEP (97, 150, 225 GHz)	$2,\ 4,\ 8\times 10^{-17}\,\mathrm{W}/\sqrt{\mathrm{Hz}}$
# FPA pixels (97, 150, 225 GHz)	$96, 96, 96$
Field of view (97, 150, 225 GHz)	$4.10^\circ,\ 3.42^\circ,\ 4.81^\circ$
Residual Q $\longleftrightarrow$ U rotation (Cross-pol)	0.24° ($< 1.4\%$)
Q, U loss (depolarization)	$< 10\%$
Residual T $\longleftrightarrow$ Q, U mixing	$< 0.015\%$
Polarization beam misalignment	$< 0.2\%$ FWHM
Beam ellipticity	< 0.85
Differential beam ellipticity	< 0.012
Polarization modulation efficiency	$> 90\%$
Absolute calibration	$< 5\%$

Table II
Clover observing bands. Mean τ and NEP_{sky} are calculated at the zenith for a 50% quartile atmosphere [6].

Band Pass	Mean τ	$NEP_{sky}\,(\times 10^{-17}\,\mathrm{W}/\sqrt{\mathrm{Hz}})$
$82 - 112\,$GHz	0.014	1.67
$125 - 175\,$GHz	0.023	3.08
$192 - 258\,$GHz	0.047	5.43

In order to prevent instrumental polarization of the CMB intensity fluctuations from swamping the B-mode polarization signal, the instrumental (de-)polarization (Stokes's I to Q, U mixing) and the beam's differential eccentricity must be well controlled. To prevent conversion of the E-mode signal into B-mode signals the residual instrumental cross-polarization (Stokes's Q to U rotation) after calibration must be below $-50\,$dB. In order to characterize and subtract these systematic effects, a number of modulation schemes are required.

B. Overall instrument design

The two Clover instruments are polarimetric imaging arrays on dedicated telescopes and mounts, with a 96 pixel focal plane array centered at 97 GHz on one telescope (the Low Frequency Instrument) and a mixed focal plane array of 96 pixels centered at each of 150 and 225 GHz on the second telescope (the High Frequency Instrument). The chosen frequency bands are given in Table II.

Each telescope is a $\sim 1.5 - 1.8\,$m compact range antenna (CRA) on an alt-az mount with an additional axis allowing rotation of the whole instrument about the pointing direction

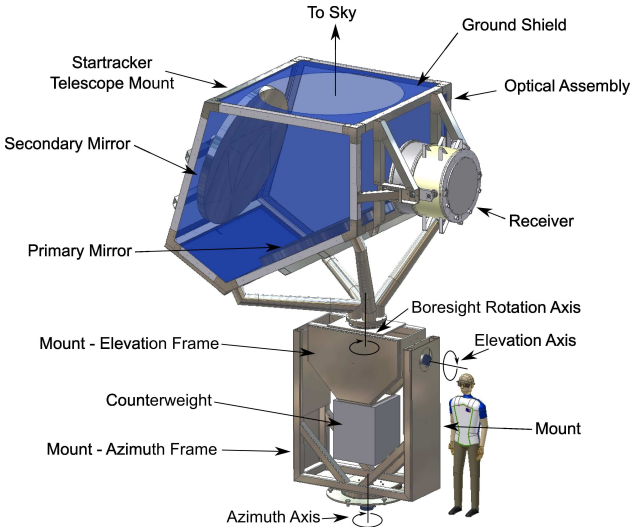

Figure 1. CAD drawing of one of the two Clover instruments. The receiver is on the left, with the absorbing ground screen surrounding the optics shown in blue.

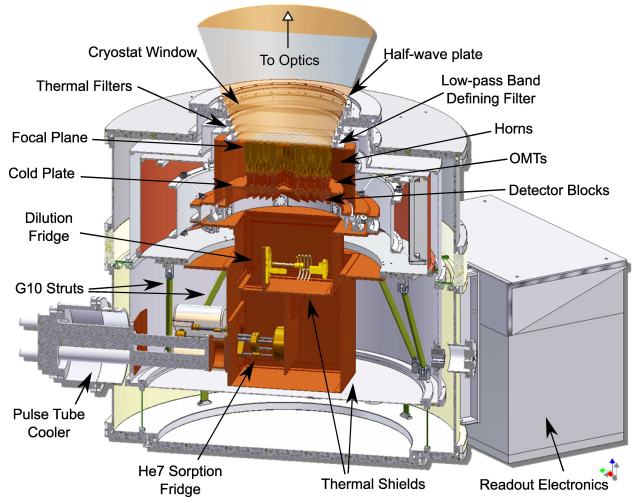

Figure 2. Cross-section through the LF instrument receiver. From the top, the signal from the telescope passes through the AHWP, cryostat window and filter stack. The focal plane array of horns and OMTs are positioned just behind the filter stack, with the blocks of 16 detectors mounted on the other side of the 100 mK cold plate. The detectors are readout by a TDM SQUID readout system mount on the 4 K stage, which is in turn read by the multi-channel electronics mounted on the right hand side. The cold plate is cooled by the miniature dilution fridge at the centre of the receiver, which is in turn cooled by the He7 sorption fridge and pulse tube cooler at the lower left.

of the telescope. The optics are designed to give extremely low sidelobes (below 1.6% spillover power) and very low cross-polarization across a large, flat focal plane[7]. In order to reduce the effect of polarized sidelobes from the instrument, the receiver and optics are surrounded by co-mounted absorbing ground screens that provide a constant background load for all sidelobes. An artist's impression of one of the two Clover instruments is shown in fig. 1.

All the pixels consist of profiled corrugated horns, feeding turnstile waveguide OMTs [8] in the low frequency instrument (LF), and circular waveguide probe OMTs [9] integrated into the detector chips in the 150 and 225 GHz pixels in the high frequency instrument (HF). The outputs of the OMTs are used to feed microstrip coupled molybdenum-copper transition edge sensor bolometers [10], via finline-to-microstrip transitions [11] in the low frequency instrument, and directly from the waveguide probes in the high frequency instrument. The bolometers are read using time division multiplexed (TDM) SQUID amplifiers developed by NIST and room temperature multi-channel electronic (MCE) systems developed by University of British Columbia [12], [13].

During CMB observations, the primary modulation of the sky signal is provided by rapidly scanning the instruments across the sky at a constant elevation, to provide a constant atmospheric power contribution, while the sky field drifts through the scanning elevation. The telescopes and mounts have been designed for scanning speeds up to $10^\circ/\mathrm{s}$ across a 20° diameter field, although slower scan speeds are likely to be preferred, to provide seperation between the pixel crossing rate and polarization modulation rate, and to reduce the observing time overheads associated with turning the telescopes around at the end of each scan [14].

Polarization modulation is provided by two methods; firstly a rotating metal mesh half-wave plate is used to provide rapid polarization modulation at the input to the focal plane arrays. This half-wave plate may be operated either in a continuously rotating mode, or with a stepped rotation between scans. Additionally, the entire instrument, including the optics, can be rotated about the pointing direction. This modulation is slow, and so is likely to be used between sets of several scans, or between observing sessions [15].

C. Optics

The Clover optics design is based on the compact range antenna design described in [7]. This design of antenna has been shown to give excellent cross-polarization performance across a large flat focal plane, allowing a large number of detectors to be fed directly without requiring additional focusing optics that may introduce chromatic aberrations or cross-polarization, or the complexity of a curved focal plane.

The key parameters of the design of the optics for the two instruments are given in table III. The performance of both optical systems has been extensively simulated using the GRASP physical optics package to minimize the cross-polarization and spillover performance while retaining the large focal plane areas. A summary of the optical performance results is given in table IV.

In order to prevent a 300 K background seen by spillover sidelobes from overloading the TES bolometers, the total power in the sidelobes has to be kept below 1.6%. The residual far out sidelobes are terminated on a co-mounted absorbing ground shield to provide a stable polarization signal background when the telescope is pointed in different directions. The calculated spillover pattern for a pixel at the edge of the focal plane on the LF instrument is shown in fig. 4.

Each of the Clover mirrors was CNC machined from a single piece of aluminum. The back of the mirror is light-weighted by machining away most of the backing material, leaving a number of ribs to provide structural strength and

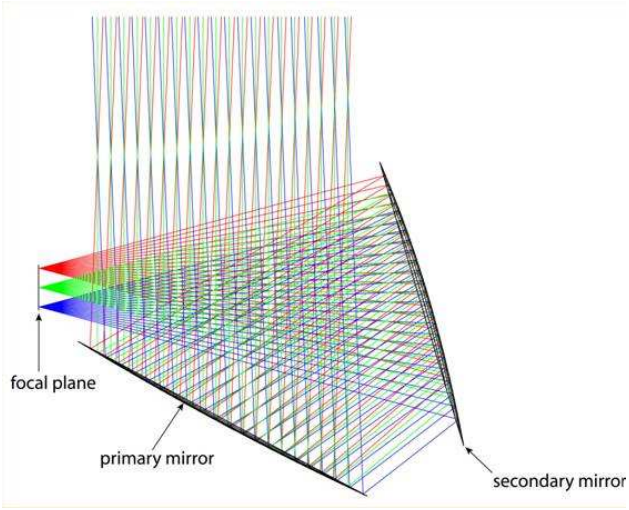

Figure 3. Schematic of the Clover CRA optics. Light from the sky is reflected from the parabolic primary mirror to the concave hyperboloidal secondary mirror before being focused on the focal plane, positioned perpendicular to the incoming wavefront from the sky.

Table III
PARAMETERS OF THE CLOVER OPTICS

Parameter	97 GHz	150, 225 GHz
Projected aperture	1.80 m	1.50 m
Effective focal length	2961 mm	2700 mm
F/#	1.64	1.80
Primary/secondary angle	65°	65°
Feed/secondary angle	25°	25°
Primary focal length	6350 mm	5790 mm
Primary offset	−6778 mm	−6180 mm
Secondary foci distance	8740 mm	7950 mm
Secondary vertex distance	−4227 mm	−3845 mm
Secondary eccentricity	−2.0674419	−2.0674419
Feed FWHM	14.5°	14.4°, 9.4°

Table IV
PERFORMANCE OF THE CLOVER OPTICS. IN EACH CASE, THE BEST AND WORST PERFORMING PIXEL IS SHOWN

Parameter	97 GHz	150 GHz	225 GHz
Beamwidth	7.5′, 7.7′	5.46′, 5.55′	5.28′, 5.34′
Beam eccentricity	0.11, 0.21	0.14, 0.27	0.11, 0.19
Cross-polarization	−39, −38 dB	−43, −41 dB	−45, −42 dB
First sidelobes	−35, −22 dB	−31, −19 dB	−44, −26 dB
Far-out sidelobes	< −70 dB	< −70 dB	-
Spillover	1.26, 1.62%	1.85, 2.60%	0.08%, 0.27%

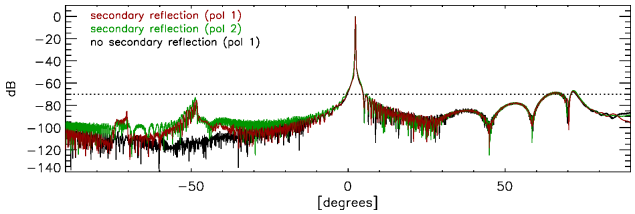

Figure 4. Far out sidelobe pattern calculated by GRASP for an edge pixel on the Clover LF instrument.

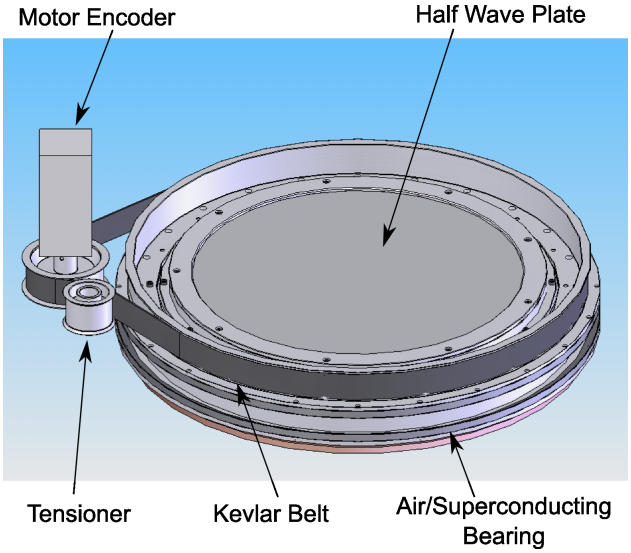

Figure 5. CAD model of the HF instrument achromatic half-wave plate on its superconducting magnetic levitation bearing and with the Kevlar belt and motor used to drive the AHWP.

location for three adjustable mounting points per mirror. The optical assembly skin is lined with Eccosorb HR-10 open cell foam absorber, with a closed cell polythene foam covering the Eccosorb HR-10 to provide weather protection for the absorber. The reflectivity of this absorber system has been measured as less than 3% at 150 GHz [16].

D. Half-wave plate, vacuum window and filter stack

Polarization modulation is applied to each array by an achromatic half-wave plate (AHWP) placed in front of each focal plane. Each AHWP is of hot-pressed metal mesh on plastic design of similar construction to the thermal and low-pass filters. By stacking alternate layers of capacitive and inductive grid patterns, phase differences of 180° can be achieved between orthogonal polarizations across large bandwidths.

The Clover LF AHWP operates over a 30% bandwidth centered at 97 GHz, and is mounted just in front of the cryostat window in a dry air flushed chamber. The AHWP runs on a large air bearing and is driven by a motor/encoder system via a Kevlar belt. This system provides accurate position control of the AHWP both in motion and when held in one place.

The HF AHWP has to cover two 30% wide bands, centered at 150 GHz and 225 GHz simultaneously. This means that considerably more layers are required to produce the AHWP, and so to reduce the absorption loss, the HF AHWP is placed

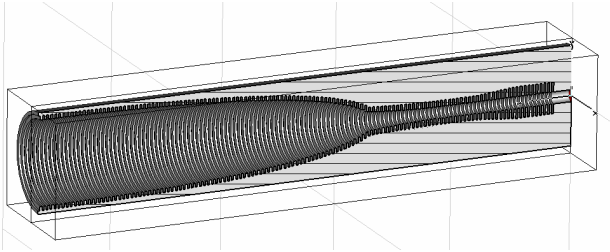

Figure 6. The profiled corrugated horn design for the Clover LF instrument.

just inside the cryostat window and thermally anchored to the 60 K radiation shield stage. The HF AHWP rotates on a superconducting magnetic levitation bearing, and is driven by a motor and Kevlar belt as on the LF instrument system (Fig. 5).

The window of each cryostat is made of ultra-high molecular weight polythene with a very low absorption coefficient. To withstand the 1 bar pressure difference over the 300 mm window diameter, the window needs to be 8 mm thick. Anti-reflection coatings of porous PTFE are used to reduce the Fabry-Perot fringing due to the thick dielectric.

The thermal load on the cold stage of the cryostat is reduced by using a number of reflective metal mesh low-pass filters with low emissivity near the observing bands. Since these dielectric material used to support the metal mesh becomes opaque in the mid-infrared, a number of low pass thermal filters are required, mounted on various thermal shields to gradually reduce the emission towards the cold-stage.

In the LF instrument, the upper edge of the observing band is defined by a multistage metal mesh filter placed across the whole focal plane. The low edge of the band is defined by a constriction in the throats of the horns. The mixed frequency nature of the HF focal plane means that individual low-pass filters are required on each horn to define the upper edge of the band individually for each pixel.

E. Feed horns and focal plane arrays

All the feed-horns are individually electroformed profiled corrugated horns with a high-pass corrugated waveguide filter at the throat to define the lower edge of the observation band (Fig. 6). The measured beam pattern for a 97 GHz horn is shown in fig. 7.

In the LF instrument, the detectors are gathered in linear blocks of 16, fed by eight horns and OMTs, and arranged as shown in fig. 8. Each detector block contains a single time-domain SQUID multiplexer chip that reads all 16 detectors.

In the HF instrument, the detectors and horns are gathered in 2×4 blocks, with one row of four offset from the other to allow for close hexagonal packing. The detector blocks are arranged as shown in fig. 8, with the 150 GHz detectors at the centre of the array, and the 225 GHz pixels at the edge of the array. Due to the strong under-illumination of the optics by the 225 GHz horns, placing the 225 GHz pixels at the edge of the focal plane does not significantly degrade the optical performance for these detectors.

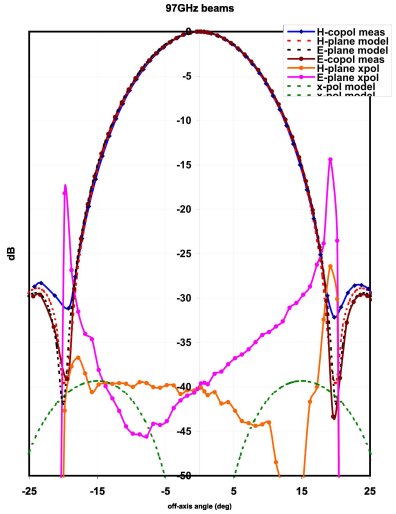

Figure 7. Measured beam pattern for a Clover LF horn. The cross-polarization measurement is limited by the accuracy of alignment between the transmitter and receiver horns.

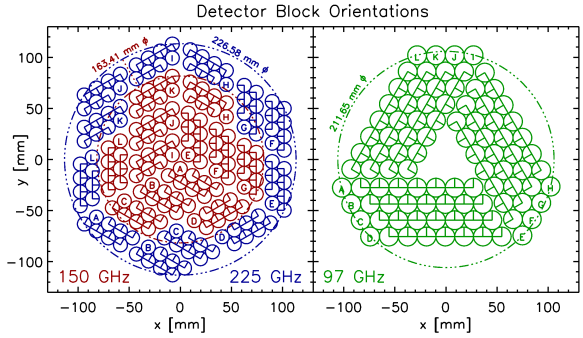

Figure 8. Layout of the two focal plane arrays. The H-plane polarization direction is shown by the short half-line on each circle. The dashed circles show the radius from the center of the array to the centre of the outermost pixel at each frequency.

F. OMTs

The low frequency instrument uses individual electroformed waveguide OMTs to separate the polarization components. The OMT is a turnstile design (fig. 9) fed by the circular waveguide from the feed-horn, and with tapered Y-junction waveguide power combiners that include a 90° twist in one arm to provide parallel waveguides at the outputs to the detector block [8]. Measured performance of the OMTs is shown in fig. 10.

The high frequency instrument uses four rectangular probes integrated onto the detector chip [9], [10] to both split the polarization components and to feed the TES detectors (figs. 11 and 12). The four rectangular probes are fabricated in niobium on a silicon nitride membrane that is mounted across the circular waveguide in front of a fixed back-short. The silicon nitride membrane is extended $\lambda/4$ into the waveguide walls in a narrow gap formed by extending the lower half of the circular waveguide walls into the well in the silicon detector chip that supports the membrane. The probes feed the microstrip inputs to the TES absorbers across a grounding ring that sits just above the end of the circular waveguide and capacitively couples to the edges of the gap in the waveguide. The signal

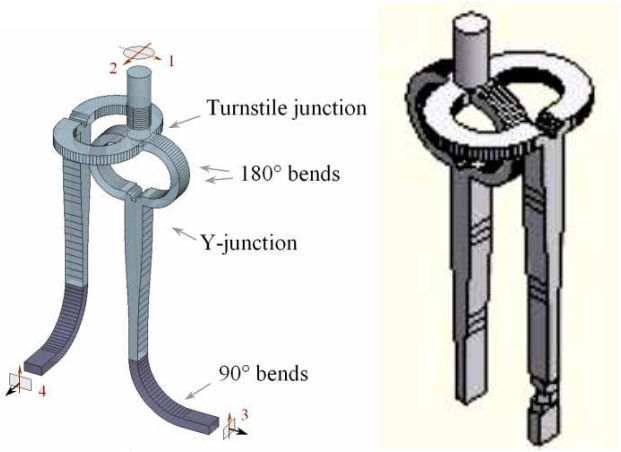

Figure 9. The prototype LF OMT (left) and the final design incorporating the waveguide twist required to bring both polarization components out in parallel waveguides.

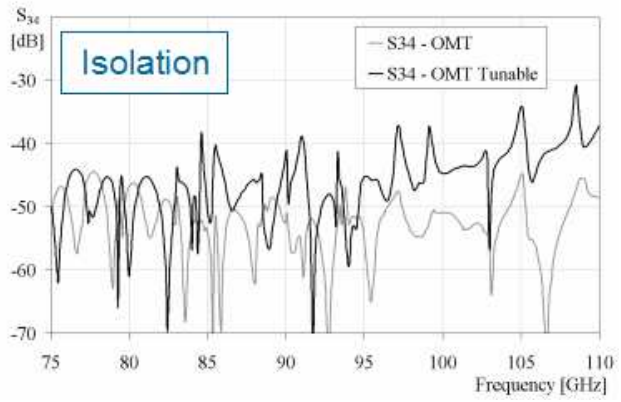

Figure 10. Measured polarization isolation (cross-polarization) for the LF prototype OMT and for an alternative prototype with a tunable turnstile stub.

from each polarization component is split 50:50 between the two probes on opposite sides of the OMT. These signals are recombined incoherently on the TES islands.

G. Detectors

In the low frequency instrument, the TES bolometers are fed from the waveguide OMTs via unilateral finline waveguide-to-microstrip transitions on the $225\,\mu\mathrm{m}$ thick silicon detector substrate [10], [17]. The design of the finline transition is described in [11]. To prevent the excitation of higher order modes in the finline, the WR-10 waveguide is reduced in height from $1.27\,\mathrm{mm}$ to $1.1\,\mathrm{mm}$, and the finline has serrations placed in the support slots at either side of the chip. The finline detectors are mounted in a copper E-plane split waveguide block that houses 16 detectors, as well as the TDM readout chips.

In the high frequency instrument, the output of the rectangular probes on silicon nitride membrane are coupled to three section quarter-wave transformers, implemented in microstrip, to match the $50\,\Omega$ probe output to the $23\,\Omega$ microstrip line that feed the TES bolometers [10]. The two probes that couple to each polarization component are connected to two

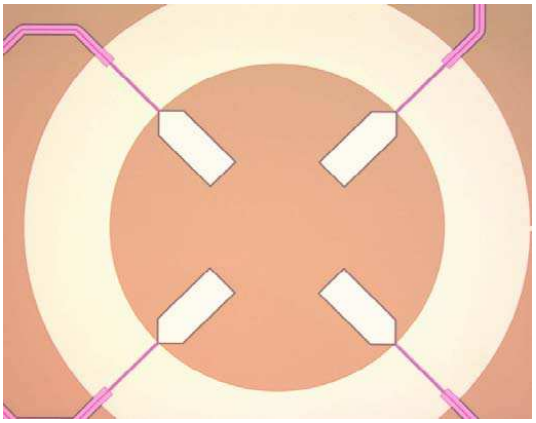

Figure 11. The HF microstrip coupled probe OMT, showing the probes, grounding ring, silicon nitride membrane and output microstrips. The circular waveguide output from the horn is aligned with the inner edge of the niobium grounding ring (yellow) and a quarter wave back-short waveguide is built into the detector block (see fig. 15).

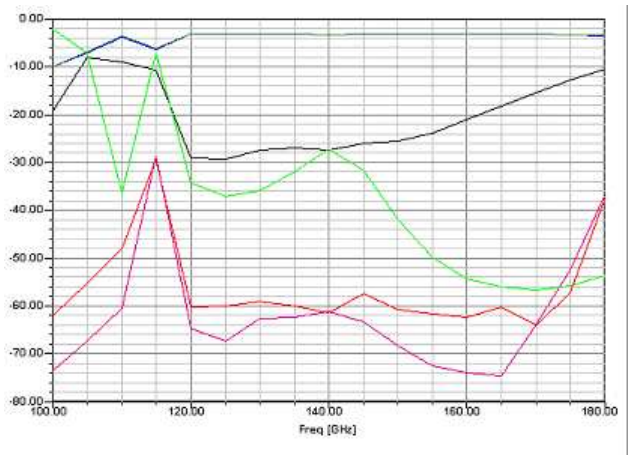

Figure 12. Results of HFSS simulations of the $150\,\mathrm{GHz}$ probe OMT, including the microstrip transformer.

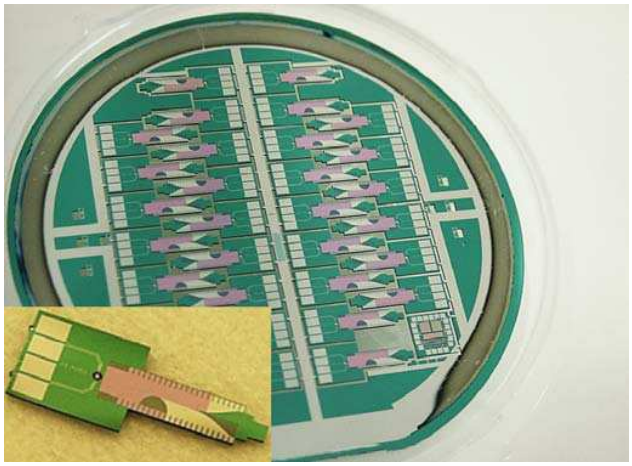

Figure 13. The 97 GHz second generation detectors.

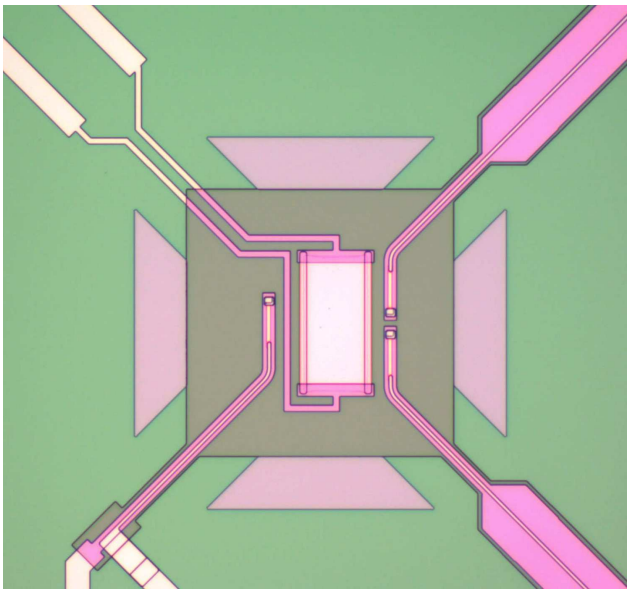

Figure 14. The HF detector's TES island, with two microstrip inputs from the two probes at the bottom, the TES bias wiring at the top left and the heater wiring at the top right.

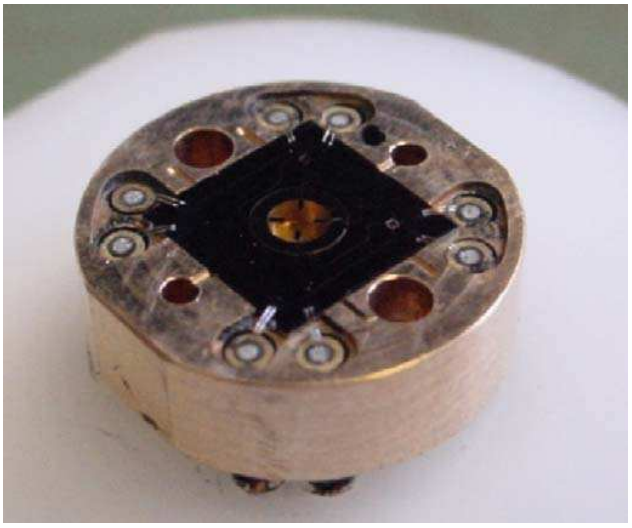

Figure 15. A prototype HF detector mounted in the detector module block. Bias signals and heater power are taken from the two TES detectors on superconducting pins through the block to the readout system on the back of the focal plane array. The circular waveguide back-short is visible through the centre of the detector chip.

resistors on a single TES island, so that the power is combined incoherently (fig. 14).

In both instruments, the niobium microstrip transmission lines carry the signal along one of the silicon nitride legs onto islands where the signal is converted to heat in a termination resistor made of gold/copper alloy. The termination resistor is matched to input microstrip line impedance, giving a return loss better than $-25\,\mathrm{dB}$.

The input signal is detected by molybdenum/copper proximity effect bi-layer transition edge sensors with a transition temperatures of $190\,\mathrm{mK}$ for the $97\,\mathrm{GHz}$ and $150\,\mathrm{GHz}$ detectors and $430\,\mathrm{mK}$ for the $225\,\mathrm{GHz}$ detectors. The TES are fabricated on islands suspended on four $0.5\,\mu\mathrm{m}$ thick silicon

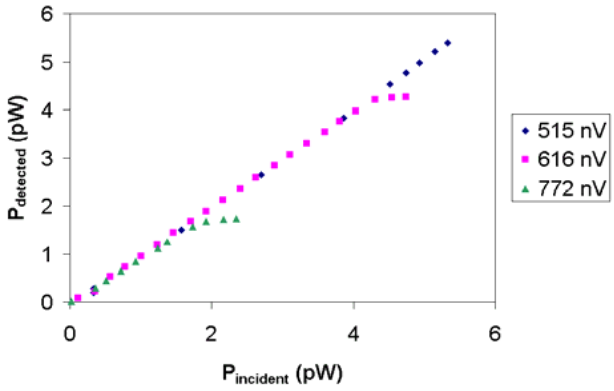

Figure 16. Detected power verses incident power at a variety of bias voltages for the prototype 97 GHz finline TES detectors [17].

nitride legs for thermal isolation. The input RF signal is carried on microstrip down one or two legs, while the TES readout leads run down one of the other legs. The fourth leg is used to carry DC power to a resistor, matched to the RF termination resistor for calibration purposes and to keep the received power on the TES constant in the presence of a changing power load from the sky. Interdigitated copper fingers are used to suppress excess noise in the TES due to internal thermal fluctuation noise by improving the thermalisation across the TES.

The detectors are fabricated on $225\,\mu\mathrm{m}$ silicon substrates with $0.5\,\mu\mathrm{m}$ low stress silicon nitride membrane. The Mo/Cu TES, copper fingers and banks are deposited first, followed by the niobium transmission line ground plane and TES contact leads, silicon dioxide insulation layer, Au/Cu resistors and niobium transmission line wiring layer. The detector chip is shaped by deep reactive ion etching (DRIE), which is also used to etch the well under the TES island. All detector fabrication processes apart from the DRIE are carried out by the Detector Physics Group at the Cavendish Laboratory [18].

Prototypes have been fabricated for both the low and high frequency detectors, and production of the science grade 97 GHz detectors is complete. Dark NEPs have been measured at $\sim 1.7 \times 10^{-17}\,\mathrm{W}/\sqrt{\mathrm{Hz}}$ with time constants $\tau \sim 10^{-4}\,\mathrm{s}$ for the 97 GHz detector design [17], comfortably within the performance requirements for Clover. Optical tests have been carried out at 97 GHz, using a temperature controlled blackbody load within the test cryostat. These indicate that the optical efficiencies of the science grade 97 GHz detectors are better than 70%.

H. Readout

In order to reduce the heat load on the cold stage of the cryostat, the TES detectors are read by a time division multiplexing system supplied by NIST [12]. This significantly reduces the number of wires required between the cold stage and room temperature. Each TES is operated in a flux locked loop to its own first stage SQUID. These SQUIDs are addressed in sequence to provide multiplexing and the current is amplified by an on-chip second-stage SQUID and then by a seperate SQUID series array. Each NIST SQUID multiplexing chip is capable of reading up to 32 TES, with one additional

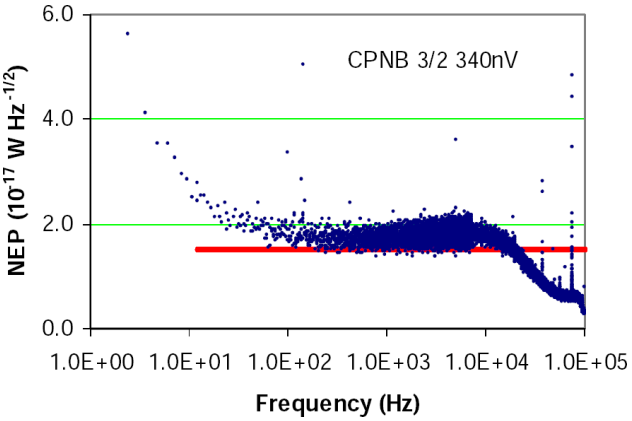

Figure 17. Measured noise spectrum for a prototype 97 GHz finline TES detector [17].

dark channel. In Clover, only 16 TES will be connected to each multiplexing chip due to packaging constraints. However, this scheme has the important advantages of reduced aliasing noise and allowing the selection of the most similar first stage SQUIDs on each chip and bypassing failed channels. The output of the SQUID TDM system is read by room temperature multichannel electronics supplied by University of British Columbia [13].

I. Cryogenics and magnetic shielding

Both Clover's focal plane arrays are cooled in closed-cycle three-stage cryostats. A CryoMech PT410 pulse tube cooler, modified for lower vibration operation, provides of $1\,\mathrm{W}$ of cooling power at $4\,\mathrm{K}$, as well as the $50\,\mathrm{K}$ stage used to cool the radiation shields (and AHWP in the HF instrument). A closed cycle "He-7" $^3\mathrm{He}/^4\mathrm{He}$ sorption fridge is mounted on the $4\,\mathrm{K}$ stage, providing $400\,\mu\mathrm{W}$ at $400\,\mathrm{mK}$. On the $400\,\mathrm{mK}$ stage a closed cycle miniature dilution refrigerator [19] is used to provide $3\,\mu\mathrm{W}$ of cooling power at $100\,\mathrm{mK}$ to the TES detectors. The temperature of the $100\,\mathrm{mK}$ stage is actively controlled to provide a temperature stability of $60\,\mathrm{nK}/\sqrt{\mathrm{Hz}}$ at $100\,\mathrm{mK}$, with a long-term variation of $< 3.5\,\mu\mathrm{K}$ over a 24 hour duty cycle. Additional temperature stages at $3\,\mathrm{K}$, $1.1\,\mathrm{K}$ and $700\,\mathrm{mK}$ are available for heatsinking various components of the sorption and dilution fridges, gas gap heat switches and cables.

A major difficulty with the cryogenics has been the requirement that the cryostat must be tipped as the telescopes point around the sky. By carefully choosing the mounting angles of the cryocoolers and limiting the range of allowed boresight and elevation angles, then the angle of the cryocoolers can be kept to within 45° from the vertical, while pointing the telescope up to 60° from the zenith with an adequate range of boresight angles to allow polarization systematics to be detected. This requirement has necessitated the development of novel designs of He-7 sorption coolers and miniature dilution refrigerators. At specific boresight angles, the telescopes can point to the horizon, allowing sky dips and other calibration observations to be made.

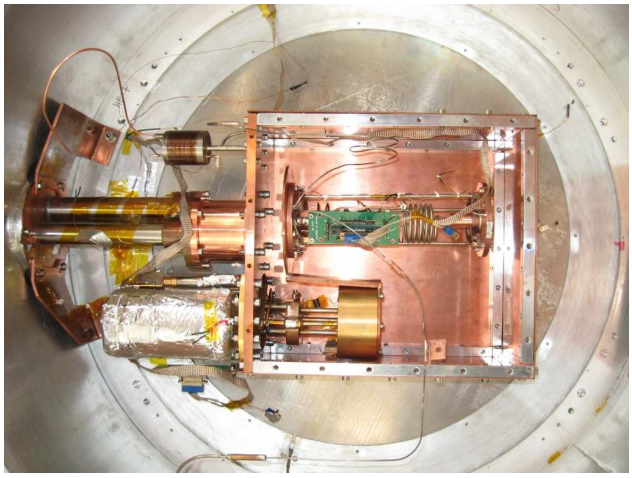

Figure 18. Pulse tube cooler head (left), $4\,\mathrm{K}$ box, He-7 sorption fridge (centre bottom) and prototype dilution fridge (centre) installed in the Clover LF cryostat.

J. Telescope mounts

Each of the two Clover instruments has its own three-axis mount. Both mounts are alt-az mounts with an additional boresight rotation axis used to rotate the whole telescope about its pointing direction to allow for the calibration of instrumental polarization. Each axis is driven by an extremely compact Harmonic Drive motor/encoder assembly. The mounts are able to maintain a pointing accuracy of 20", with a long-term tracking accuracy of 60", while being able to carry out constant elevation scans at speeds of up to $10\,\mathrm{deg/s}$ with turn-around accelerations up to $20\,\mathrm{deg/s^2}$.

Each mount has an optical pointing telescope mounted on the optical assembly behind the secondary mirror, for pointing calibration during commissioning and observations. These telescopes are based on the commercial photographic lens and CCD design used on the BLAST balloon-borne telescope [20], with a change of lens and CCD to accomodate Clover's resolution and field of view.

K. Site

Clover will be sited at Pampa la Bola, on the edge of the ALMA site in the Atacama desert near San Pedro de Atacama, Chile. This $4800\,\mathrm{m}$ altitude site provides excellent atmospheric transparency and stability at millimeter wavelengths, as well as the possibility of sharing some infrastructure with a number of other instruments and observatories on the site.

The latitude of the site (23° S) means that a good proportion of the sky is observable at relatively high elevations, and thus low air-mass. This allows observing fields to be selected that have very low levels of foreground contamination, and that overlap with surveys undertaken by other CMB instruments.

III. Observations and Data Analysis

A. Observing fields, modes and calibration

Contamination from Galactic foregrounds is a major issue for deep polarization observations of the CMB. In order to maximize the observing efficiency for Clover, the required

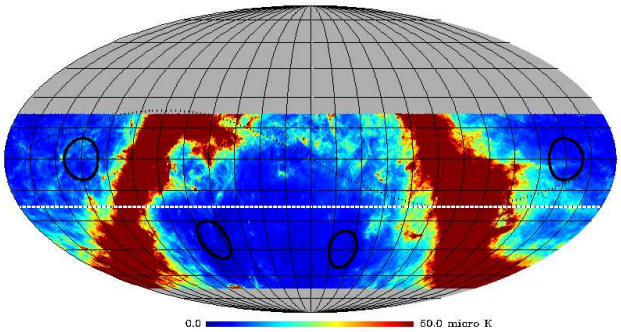

Figure 19. Clover observing fields, chosen to give year-round night time observing in regions of very low foreground contamination.

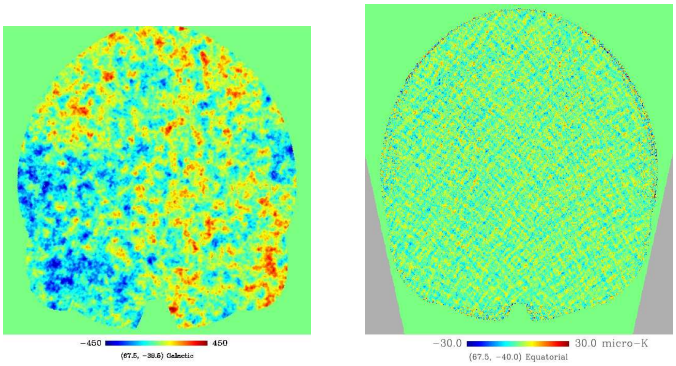

Figure 20. Sample Stokes' I (temperature) and U (polarization) maps recovered from simulated Clover observations by destriping.

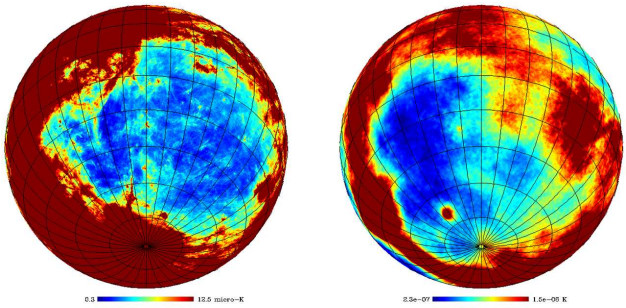

Figure 21. Template maps for foregrounds for synchrotron (left) and dust (right) contamination of the CMB sky.

$1000\,\mathrm{deg}^2$ survey area is split into four convex fields, spread roughly evenly in right ascension, with the declination and exact right ascensions chosen to place the fields in the area of minimum foreground contamination, estimated from all-sky CMB observations and Galactic polarization surveys. The optimized Clover survey fields are shown in fig. 19.

To reduce contamination from changing sky brightness and atmospheric fluctuations, Clover will perform fast, constant elevation scans over each field as it rises and falls each night. The observations will continue for two years, giving ~ 0.8 years integration time required to achieve the required map sensitivity.

The calibration of CMB polarization experiments is challenging, as there are few well-characterized stable polarized astronomical sources at mm wavelengths. Possible calibration sources are extra-galactic radio sources such as Tau A, or planets (although planets are not highly polarized). An absolute intensity calibration uncertainty of 5% should be possible from WMAP and Planck data. For polarization calibration it may be necessary to calibrate off unpolarized sources, using a weak wire grid polarizer across the cryostat aperture. It may also be possible to use artificial sources for characterizing subtle systematic effects, either in the laboratory or in the field.

B. Data analysis

The analysis of the Clover data will be difficult, mainly due to the large amounts of data expected (~ 100TB for a 2-year campaign). After some minimal processing of the raw time-ordered data, maps of the T, Q and U Stokes parameters (fig. 20) will be constructed using a combination of naive and near-optimal (but computationally efficient) destriping techniques [21].

In order to estimate the E- and B-mode power spectra from these maps, we will adopt a Monte-Carlo based "pseudo-C_l" approach, augmented by an optimal maximum-likelihood analysis for the largest angular scales. In general, such an approach requires detailed simulations of the experiment to quantify uncertainties, correct for noise and any filtering applied to the data, and to test for systematic contaminants. We have already used our initial simulation and analysis pipeline to investigate a number of possible instrumental systematic effects [15] and are currently using it to assess the performance of a number of alternate foreground removal techniques.

Detecting B-mode polarization will require the removal of foreground signals, particularly those from Galactic synchrotron and dust emission, as well as other, weaker foreground signals such as anomalous spinning dust. The spectral coverage of Clover means that some degree of component separation and removal will be possible, although removing more than two bright foreground components will require additional data or modeling of the foregrounds from other experiments.

IV. Performance predictions and timescale

A. Performance predictions

After 0.8 years of integration time, Clover will have mapped $\sim 1000\,\mathrm{deg}^2$ of the lowest foreground emission areas of the sky to a sensitivity of $1.7\,\mu$K per $8'$ pixel at 97, 150 and 225 GHz. It is expected that signals due to systematic effects will result in a bias in the measured tensor-to-scalar ratio of < 0.001. The expected angular power spectra and error bars for Clover are shown in fig. 22, for the current concordance ΛCDM cosmological model and tensor-to-scalar ratios $r = 0.1$ and $r = 0.026$, as well as the expected levels of foreground signals. The sensitivity and systematic effect estimates here are based on the current Clover performance requirements, given above. Detection of the primordial B-mode signal will determine the energy scale of inflation, while a non-detection of the B-mode signal at tensor-to-scalar ratio

$r > 0.026$ will provide an upper limit on the energy scale of less than $\sim 2 \times 10^{16}$ GeV.

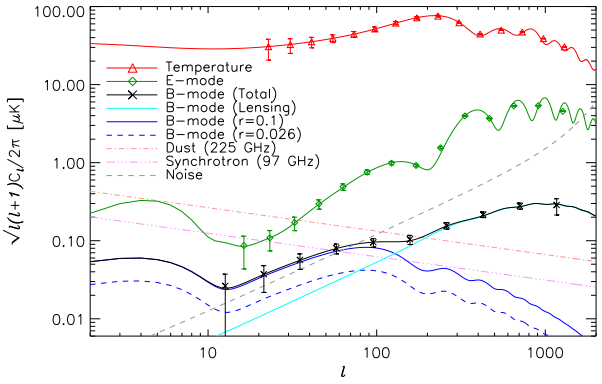

Figure 22. Predicted power spectra for Clover after 0.8 years integration time, as well as the expected instrumental noise and foreground levels before subtraction.

B. Progress and timescale

Both Clover instruments are currently in the component integration phase, with the telescopes and mounts being assembled and tested in Oxford, the cryostat, cryogenic systems and quasi-optical components (AHWPs, windows and filters) being assembled and tested in Cardiff and LF feed-horns and OMTs undergoing testing in Manchester. The production and testing of science grade LF finline detector modules and testing of the TDM readout is ongoing in Cambridge, in parallel with the final prototyping of the HF probe OMT detectors.

Assembly, integration and testing of the receivers and entire LF instrument is planned during mid to late 2009 in Cardiff and Oxford respectively, before shipping to the Clover site in Chile in early 2010 for commissioning. The HF instrument is due to follow a few months behind the LF instrument. Work on setting up the Clover site infrastructure in Chile is due to start in the next few months.

REFERENCES

[1] A. Challinor, "Constraining fundamental physics with the cosmic microwave background," *ArXiv e-print*, vol. astro-ph/0606548, 2006.

[2] W. Hu and M. White, "A CMB polarisation primer," *New Astronomy*, vol. 2, no. 323, 1997.

[3] D. O'Dea, A. Challinor, and B. R. Johnson, "Systematic errors in cosmic microwave background polarization measurements," *MNRAS*, vol. 376, no. 4, p. 1767, 2007.

[4] D. P. Finkbeiner, M. Davis, and D. J. Schlegel, "Extrapolation of Galactic Dust Emission at 100 microns to Cosmic Microwave Background Radiation Frequencies using FIRAS," *ApJ*, vol. 524, p. 867, 1999.

[5] G. Giardino, A. J. Banday, K. M. Górski, K. Bennett, J. L. Jonas, and J. Tauber, "Towards a Model of Full-sky Galactic Synchrotron Intensity and Linear Polarisation: A re-analysis if the Parkes data," *A&A*, vol. 387, p. 82, 2002.

[6] A. Otarola, M. Holdaway, L.-E. Nyman, S. Radford, and B. Butler, "Atmospheric transparency at Chajnantor: 1973-2003," *ALMA Memo Series*, vol. 512, 2005.

[7] G. Yassin, P. K. Grimes, and S. B. Sorenson, "Compact optical assemblies for large-format imaging arrays," in *Proceedings of the 16th Int. Symp. on Space THz Tech.*, (Gothenburg, Sweden), 2005.

[8] G. Pisano, L. Pietranera, K. Isaak, L. Piccirillo, B. Johnson, B. Maffei, and S. Melhuish, "A Broadband WR10 Turnstile Junction Orthomode Transducer," *IEEE Microwave Compon. Lett.*, vol. 17, no. 4, p. 286, 2007.

[9] P. K. Grimes, O. G. King, G. Yassin, and M. E. Jones, "Compact broadband planar orthomode transducer," *Electronic Letters*, vol. 43, no. 21, p. 1146, 2007.

[10] M. D. Audley, D. M. Glowacka, D. J. Goldie, V. N. Tsaneva, S. Withington, P. K. Grimes, C. E. North, G. Yassin, L. Piccirillo, G. Pisano, P. A. R. Ade, P. Mauskopf, R. V. Sudiwala, J. Zhang, K. D. Irwin, M. Halpern, and E. Battistelli, "Microstrip-coupled TES bolometers for CLOVER," in *Proceedings of the 19th Int. Symp. on Space THz Tech.*, (Groningen), Apr. 2008.

[11] G. Yassin, P. K. Grimes, O. G. King, and C. E. North, "Waveguide-to-planar circuit transition for millimetre-wave detectors," *Electronic Letters*, vol. 44, no. 14, 2008.

[12] C. D. Reintsema, J. Beyer, S. W. Nam, S. Deiker, G. C. Hilton, K. D. Irwin, J. Martinis, J. Ullom, and L. R. Vale, "Prototype system for superconducting quantum interference device multiplexing of large-format transition-edge sensor arrays," *Rev. Sci. Instrum.*, vol. 74, no. 10, p. 4500, 2003.

[13] E. S. Battistelli, M. Amiri, B. Burger, M. Halpern, S. Knotek, M. Ellis, X. Gao, D. Kelly, M. Macintosh, K. Irwin, and C. Reintsema, "Functional Description of Read-out Electronics for Time-Domain Multiplexed Bolometers for Millimeter and Sub-millimeter Astronomy," *J. Low Temp. Phys.*, vol. 151, p. 908, May 2008.

[14] C. E. North, B. R. Johnson, P. A. R. Ade, M. D. Audley, C. Baines, R. A. Battye, M. L. Brown, P. Cabella, P. G. Calisse, A. D. Challinor, W. D. Duncan, P. G. Ferreira, W. K. Gear, D. Glowacka, D. J. Goldie, P. K. Grimes, M. Halpern, V. Haynes, G. C. Hilton, K. D. Irwin, M. E. Jones, A. N. Lasenby, P. J. Leahy, J. Leech, B. Maffei, P. Mauskopf, S. J. Melhuish, D. O'Dea, S. M. Parsley, L. Piccirillo, G. Pisano, C. D. Reintsema, G. Savini, R. Sudiwala, D. Sutton, A. C. Taylor, G. Teleberg, D. Titterington, V. Tsaneva, C. Tucker, R. Watson, S. Withington, G. Yassin, and J. Zhang, "Detecting the B-mode Polarisation of the CMB with Clover," *ArXiv e-prints*, vol. astro-ph/0805.3690, May 2008.

[15] M. L. Brown, A. Challinor, C. E. North, B. R. Johnson, D. O'Dea, and D. Sutton, "Impact of modulation on CMB B-mode polarization experiments," *ArXiv e-print*, vol. astro-ph/0809.4032.

[16] K. W. Yoon, P. A. R. Ade, D. Barkats, J. O. Battle, E. M. Bierman, J. J. Bock, J. A. Brevik, H. C. Chiang, A. Crites, C. D. Dowell, L. Duband, G. S. Griffin, E. F. Hivon, W. L. Holzapfel, V. V. Hristov, B. G. Keating, J. M. Kovac, C. L. Kuo, A. E. Lange, E. M. Leitch, P. V. Mason, H. T. Nguyen, N. Ponthieu, Y. D. Takahashi, T. Renbarger, L. C. Weintraub, and D. Woolsey, "The Robinson Gravitational Wave Background Telescope (BICEP): a bolometric large angular scale CMB polarimeter," *Proceedings of the SPIE*, vol. 6275, July 2006.

[17] M. D. Audley, D. M. Glowacka, D. J. Goldie, V. N. Tsaneva, S. Withington, P. K. Grimes, C. E. North, G. Yassin, L. Piccirillo, P. A. R. Ade, and R. V. Sudiwala, "Performance of microstrip-coupled TES bolometers with finline transitions," *Proceedings of the SPIE*, vol. 7020, p. 70200G, 2008.

[18] D. Glowacka, D. Goldie, S. Withington, M. Crane, V. Tsaneva, M. Audley, and A. Bunting, "A fabrication process for microstrip-coupled superconducting transition edge sensors giving highly reproducible device characteristics," *J. Low Temp. Phys.*, vol. 151, p. 249.

[19] G. Teleberg, S. T. Chase, and L. Piccirillo, "A Cryogen-Free Miniature Dilution Refrigerator for Low-Temperature Detector Applications," *J. Low Temp. Phys.*, vol. 151, no. 3-4, p. 669, 2008.

[20] E. Pascale, P. A. R. Ade, J. J. Bock, E. L. Chapin, J. Chung, M. J. Devlin, S. Dicker, M. Griffin, J. O. Gundersen, M. Halpern, P. C. Hargrave, D. H. Hughes, J. Klein, C. J. MacTavish, G. Marsden, P. G. Martin, T. G. Martin, P. Mauskopf, C. B. Netterfield, L. Olmi, G. Patanchon, M. Rex, D. Scott, C. Semisch, N. Thomas, M. D. P. Truch, C. Tucker, G. S. Tucker, M. P. Viero, and D. V. Wiebe, "The Balloon-borne Large Aperture Submillimeter Telescope: BLAST," *ApJ*, vol. 681, pp. 400–414, July 2008.

[21] D. Sutton, B. R. Johnson, M. L. Brown, P. Cabella, P. G. Ferreira, and K. M. Smith, "Map making in small field modulated CMB polarization experiments: approximating the maximum likelihood method," *MNRAS*.

T3D

A Test Flight Instrument for the Stratospheric Terahertz Observatory (STO)

C. Walker[1*], C. Kulesa[1], C. Groppi[1], E. Young[1], P. Bernasconi[2], H. Eaton[2], N. Rolander[2], C. Lisse[2], D. Hollenbach[3], J. Kawamura[4], P. Goldsmith[4], W. Langer[4], H. Yorke[4], J. Sterne[4], A. Skalare[4], I. Mehdi[4], S. Weinreb[5], J. Kooi[5], J. Stutzki[6], U. Graf[6], C. Honingh[6], P. Puetz[6], C.L. Martin[7]

1 University of Arizona, Steward Observatory, Tucson, AZ 85721

2 Johns Hopkins University Applied Physics Laboratory, Laurel, MD, 20723

3 SETI Institute, Mountain View, CA 94043

4 NASA Jet Propulsion Laboratory, Pasadena, CA 91109

5 California Institute of Technology, Pasadena, CA 91125

6 University of Cologne, Cologne, Germany 50937

7 Oberlin College, Oberlin, OH 44074

* Contact: cwalker@as.arizona.edu, phone +1-520-621-8783

***Abstract*—The Stratospheric Terahertz Observatory (STO) is a NASA-funded long duration balloon (LDB) experiment designed to address a key problem in modern astrophysics: understanding the life cycle of star-forming molecular clouds in our Milky Way Galaxy. To accomplish this goal, STO will first survey a section of the Galactic Plane in the luminous interstellar cooling line [C II] at 158 microns (1.90 THz) and the important star-formation and ionized gas tracer [N II] at 205 microns (1.45 THz). With a telescope aperture of 80 centimeters illuminating two focal plane arrays of (heterodyne) HEB mixers at 1.4 and 1.9 THz, STO will have the arcminute angular resolution and sub-km/s spectral resolution to resolve and disentangle ionized, atomic, and molecular clouds throughout the Galactic Plane. By building a three-dimensional picture of the interstellar medium of the Galaxy, STO will be able to study the creation and disruption of star-forming clouds in the Galaxy, determine the parameters that govern the star formation rate, and provide a template for star formation and stellar/interstellar feedback in other galaxies.**

In rapid preparation for a September 2009 test flight from Fort Sumner, New Mexico, an international team is actively developing a prototype instrument payload. This test flight package consists of a liquid helium dewar supporting operation of an HEB mixer in each of the 1.4 and 1.9 THz bands, in addition to an ambient-temperature Schottky receiver operating at 330 GHz. Here, we will present the implementation of the test flight instrument architecture, including HEB mixers, IF processing, spectrometers, telescope optics and gondola subsystems. We will highlight the close relationship between this prototype instrument and the array receiver package for STO's long duration Antarctic flight in late 2010.

T3E

Main Parameters and Instrumentation of Millimetron Space Mission.

A.M. Baryshev[1*], W. Wild[1,5], S.F. Likhachev[2], V.F. Vdovin[2,3], G.N. Goltsman[2,4], and N.S. Kardashev[2]
1 SRON Netherlands Institute for Space Research, Landleven 12, 9747 AD Groningen, The Netherlands
2 Astro Space Center, Lebedev Physical Institute, 84/32 Profsoyuznaya st., Moscow, 117997, Russian Federation
3 Institute of Applied Physics of Russian Academy of Sciences, Nizhniy Novgorod, Russia (IAP RAS)
4 Physics Department, Moscow State Pedagogical University, Moscow 119435, Russia
5 European Southern Observatory, Karl-Schwarzschild-Strasse 2, D-85748 Garching bei München, Germany
* Contact: A.M.Baryshev@sron.nl, phone +31-50-363 8287

***Abstract*—Millimetron (official RosKosmos name "Spectrum-M") is a part of ambitious program called Spectrum intended to cover the whole electromagnetic spectrum with world class facilities. It is an approved mission included in Russian space program with the launch date in 2017..2019 time frame.**

The Millimetron satellite has a deployable 12 m diameter antenna with inner solid 4..6 m dish and a rim of petals. The mirror design is largely based on Radioastron mission concept that will be launched in 2009. If the antenna is passively cooled by radiation to open space, it would operate at approx. 50 K surface temperature, due to presence of a deployable three layer radiation screen. As a goal, there is a consideration of active cooling of antenna to 4 K, but this will depend on resources available to the project. Lagrangian libration point L2 considered for Millimetron orbit.

There are four groups of scientific instruments envisioned:

- **SVLBI instruments Space-Earth VLBI. It will allow to achieve unprecedented spatial resolution. Millimetron mission will attempt to achieve a mm/submm wave SVLBI. For that purpose, a SVLBI instrument covering selected ALMA bands and a standard VLBI band is envisioned, accompanied by a maser reference oscillator, a data digitizing and memory system, and a high speed data transmission link to ground. The ALMA bands can be extended to cover water lines if detector technology allows. Type of detector – heterodyne.**
- **Photometer/polarimeter. Recent progress in direct detector cameras with low spectral resolution, allows to propose a large format (5-10 kPixel) photometer camera on board of Millimetron mission. This camera can cover 0.1 - 2 THz region (with adequate amount of pixels per each subband).**
- **Wide band moderate resolution imaging spectrometer. Wide band moderate R = 1000 imaging spectrometer type instrument similar to SPICA SAFARI is planned, taking advantage of large cooled dish. It will cover the adequate spectral range allowable by antenna and will also work below 1 THz, as no ground instrument can have a cold main dish.**
- **High resolution spectrometer. For high resolution spectroscopy a heterodyne instrument is proposed, conceptually similar to HIFI on Herschel. This instrument will cover interesting frequency spots in 0.5..4 THz frequency range (using central part of antenna for higher frequency). It is sure that advances in LO and mixer technology will allow this frequency coverage.**

Session T4

Components & Novel Applications

Chair: Thomas Crowe

Tuesday, April 21
4:00 – 5:00

New Results on Terahertz Detection by Carbon Nanotubes

Enrique Carrion, Martin Muthee, Jason Donovan, Richard Zannoni, John Nicholson, Eric Polizzi and K. Sigfrid Yngvesson, *Life Fellow, IEEE*

Abstract—Since our first report on terahertz detection by bundles of single wall carbon nanotubes (SWCNTs) at the ISSTT2008, we have fabricated a large number of additional antenna-coupled SWCNT devices that all show terahertz detection. The maximum voltage responsivity (S_V) is about 25 V/W (intrinsic value 50 V/W) at 4.2 K, and S_V decreases slowly with temperature up to about 100 K. In this paper we further explore different fabrication procedures and the bolometric detection process. We also demonstrate diode type detection at terahertz frequencies in SWCNTs for the first time. We present results of circuit simulations and *ab initio* simulations of the electronic properties of SWCNTs.

***Index Terms*—Nanotechnology, carbon nanotubes, detectors, terahertz.**

I. INTRODUCTION

Our first paper at the **ISSTT** symposia on the topic of Terahertz detection in carbon nanotubes (CNTs) was presented at **ISSTT2005** [1]. We also discussed this topic in ref. [2]. At the **ISSTT2006** we presented results of microwave (MW) direct and heterodyne detection in *metallic* single wall carbon nanotubes (m-SWCNTs) [3],[4]. Very recently, the Yale group of D. Prober reported MW detection in m-SWCNTs [5], as well as a tentative terahertz detection [6]. Other groups have also demonstrated MW detection in SWNTs, primarily in *semiconducting* tubes (s-SWCNTs) [7]-[11]. McEuen et al. [12] used THz time-domain techniques for detection in a quasi-metallic (qm) SWCNT FET type device. The effective frequencies in that experiment were in the range of a few hundred GHz. Photoconductive detection in SWCNTs is very weak [13], but Itkis et al. [13] have developed a sensitive *bolometric* Near Infrared detector based on a Carbon Nanotube (CNT) film. Our group reported the first terahertz detection in bundles containing m-SWCNTs [14], up to 2.5 THz. The SWCNT bundles were coupled to log-periodic antennas in much the same manner as is used to couple NbN HEBs. At **ISSTT2008** we gave further results for this detector [15], as well as accurate characterization of the devices at microwave frequencies (up to 20 GHz). We also interpreted the experimental terahertz detection based on a general bolometric model. In the present paper, we further explore this bolometric model to interpret measured data for a large number of additional devices, which have been fabricated employing new methods. We also report a diode type of detection mode that was previously only seen at MW frequencies, but that we have now demonstrated in two devices up to frequencies as high as 1.6 THz.

CNTs are a promising medium for future terahertz detectors based on some general features based on their small diameters (1-2 nm) which lead to very low heat capacity and low capacitance. They can also have near ideal transport properties (ballistic transport) for both electrons and phonons. Detection in m-SWNTs can occur due to two basic mechanisms: (1) *a diode type* mechanism, as was proposed for terahertz in [7] and demonstrated at microwaves in [4]-[6]; (2) a *bolometer type* mode, similar to that in HEBs and other terahertz bolometers [5],[6],[14]-[16]. Both modes will be discussed below.

II. CHARACTERISTICS OF CARBON NANOTUBES

It is important to first review some general characteristics of CNTs. CNTs can be grown using several different methods, the main ones being laser ablation of carbon targets and chemical vapor deposition (CVD). Depending on the specific conditions during growth either multi-wall CNTs (MWCNTs) or SWCNTs may be formed. Although any type of CNT might be considered for terahertz detection we have concentrated on SWCNTs. SWCNTs can be conceptually viewed as a sheet of hexagonally arranged carbon atoms (called grapheme) that has been rolled up into a tube. This process can "work" for a large number of different wrapping angles, resulting in CNTs that differ in terms of their chirality. It was quickly realized that SWCNTs of different chirality can either be metallic (no bandgap at the Fermi level) or semiconducting (with bandgaps of from a few tenths of eV to about 1 eV, inversely proportional to the tube diameter). In a typical process about one third of the tubes are metallic, two thirds semiconducting. They can be distinguished experimentally since the resistance of the s-SWCNTs can be varied by application of a gate voltage to a back-contact substrate gate (or a top gate). The m-SWNTs then show constant resistance independent of the gate voltage. There are also cases in which tubes are nominally

Manuscript received 20 April 2009. This work was supported in part by the U.S. National Science Foundation under Grants ECS-0508436 and ECS-0725613.

All authors are with the Department of Electrical and Computer Engineering, University of Massachusetts/Amherst, Amherst, MA 01003, USA (corresponding author can be reached at phone: 413-545-0771; fax: 413-545-4611; yngvesson@ecs.umass.edu).

metallic, but in which perturbations create a small bandgap, typically 10 meV. Small bandgap tubes (also called quasi-metallic tubes, qm-SWNTs) and actual m-SWCNTs are often difficult to distinguish experimentally. In this paper we will characterize both as m-SWCNTs, unless otherwise noted.

As grown SWCNTs naturally form bundles of tubes due to the strong interaction between individual tubes. Many different surfactants have been used to separate the tubes. However, it has been found that the surfactants that remain on the tubes often cause the contacts to be unreliable and to have high resistance. In our work so far, we have usually employed bundles of tubes, although our initial MW detection [3],[4] was performed on single tubes. For both bundles and single tubes, special methods must be used to achieve low contact resistance. Tubes deposited on top of the contact metal usually result in contact resistances in the hundreds of kΩ for a single tube, even after a typical annealing procedure of two hours at 200°C-300°C. Lower contact resistance requires that the contact metal be deposited *on top of* the CNT, or surrounding it completely. The best known contact metal is palladium. In this case the total contact resistance can approach the quantum resistance of $h/4e^2$ = 6.45 kΩ. Although it may appear that SWCNTs with high contact resistance would not have good potential as terahertz detectors, we have discovered that this is not necessarily true, as we described at the last ISSTT [15]. Specifically, our MW probe measurements showed that the contacts include a large capacitance (1-20 fF) in parallel with the contact resistance that effectively shunts the contact resistance at terahertz frequencies. These measurements were performed on a different Coplanar Waveguide structure, not the same as the antennas we employed at THz. It is therefore likely that the range of contact capacitance for our THz devices is different, as will be discussed further below. All of the above types of tubes show nonlinear IV-characteristics that may potentially be considered for terahertz detection. We show typical examples below. The first example is a single m-SWNT with high contact resistance from our early work [3],[4].

This IV-curve has a nonlinearity at low bias voltage that is known as a "Zero-Bias Anomaly (ZBA)" [17]. The ZBA is interpreted as being due to tunneling through a barrier at the contacts. Higher bias voltage *increases* the tunneling current in this case. The resistance *increases* at lower temperatures as fewer electrons are able to tunnel. Bundles of tubes, as used in all of our more recent experiments show a very similar nonlinearity [15]. In this case we interpret the conductance of the bundle as being almost entirely due to the metallic tubes, since the s-SWCNTs are know to generally have much higher resistance.

An example of an IV-curve for a device with low contact resistance is given in Figure 2 below. This device was fabricated with Ti+Pd contacts below the CNTs, and Pd+Au above.

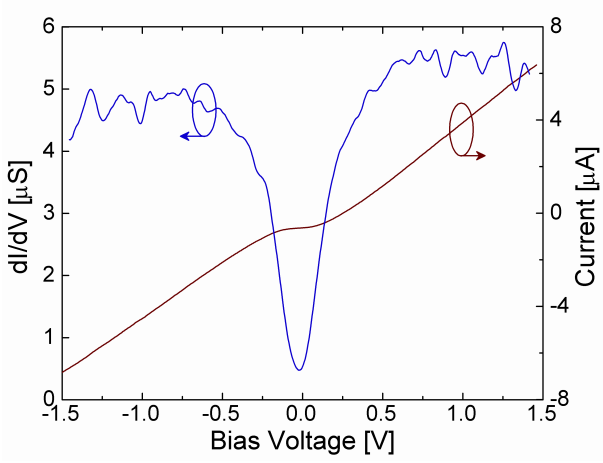

Figure 1. Typical IV-curve for a single m-SWCNT with high resistance contacts, from [4].

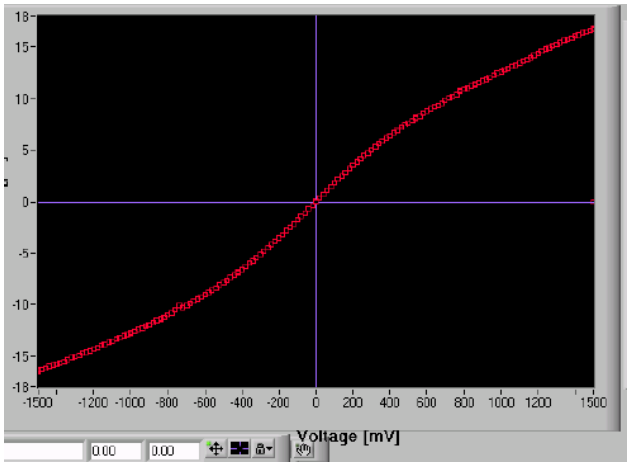

Figure 2. IV-curve for device with low contact resistance.

Clearly, the curvature in this case is in the opposite direction to that in Figure 1. The resistance is known to increase for bias voltages above 0.15 V due to optical phonon emission [17]. The resistance *decreases* at lower temperatures where fewer phonons exist that can scatter the electrons, as measured for example in [5]. The IV-curves shown in Figures 1 and 2 are for tubes supported by the silicon substrate. *Bundles of tubes* with low contact resistance have IV-curves with the same curvature [18].

Metallic SWCNTs can also be fabricated such that they are suspended across a trench that has been etched between the contacts. In this case the IV-curve at high voltages actually develops a negative slope (a negative differential resistance, NDR) due to very strong heating of the tubes [19].

In this work, we used nonconductive sapphire, silicon on sapphire (SOS) or high-resistivity silicon substrates. The choice of these substrates was crucial since for example highly doped silicon substrates show very strong absorption of THz. The sapphire, SOS and high resistivity silicon substrates have similar dielectric permittivity and are expected to all work well with the silicon lens quasi-optical coupling scheme we

employ (see Sec. IV.A). So far we have found no significant differences between these substrates.

We fabricated the CNT devices by the dielectrophoresis (DEP) method [20]. Typically, we apply a 5 - 50 MHz voltage of about 8V peak to Au contacts made by UV photolithography, such as those shown in Figure 3. We employed two types of log-periodic toothed antennas. LPA1 has about an 8 μm gap, as shown in Figure 3 (left). LPA 1 has an estimated upper frequency limit of 1.5 THz. We also fabricated LPAs with a smaller gap, about 1 μm (LPA2), as well as smaller teeth, see Figure 3 (right). LPA 2 has an estimated upper frequency limit of 3.5 THz. The LPA2 design is identical to one we used in our earlier NbN HEB work [21].

A drop of a suspension of CNTs in isopropyl alcohol [22] was applied to these structures. In the devices presented here we did not use surfactants, and consequently expect the tubes to be present in bundles. The CNTs will drift to the narrow gap in the contacts and attach to these, when the RF voltage is applied across the contacts. We monitor the DC resistance simultaneously through a bias tee. The DEP process is halted when the dc resistance is sufficiently low. All devices were annealed in air at 200 ^{o}C for two hours which decreased the contact resistance. The result is a small number of CNTs bundles contacted in parallel across the gap. The lower resistance of these devices, compared with the typical single SWCNTs, from 7 to 80 kΩ, facilitates matching of terahertz radiation to the CNTs. The IV-curves of all devices display the same "ZBA" that we had previously observed for the single m-SWNTs. The nonlinearity of the IV-curves is more pronounced the lower the temperature is, see Figure 4. We conclude that the IV-curves are due to a number of parallel metallic tubes in the bundles. Although DEP tends to primarily align m-SWCNTs, the bundles undoubtedly contain s-SWCNTs but these do not have any effect on the DC resistance.

In our initial device fabrication using antennas LPA1 and LPA2 we found by SEM and AFM imaging that the CNTs did not only attach to the smallest gap. Examples are shown in Figure 5. By using lower concentrated solutions and by centrifuging the solution to separate out impurities we obtained improved results.

We were also concerned about minimizing the thermal conductance, as discussed in Sec. IV.C. and therefore fabricated antennas that had an etched trench in the gap. These devices were fabricated on an oxidized high-resistivity silicon substrate with antennas of type LPA2 employed as etching mask for RIE. We term LPA2 antennas with a trench "LPA3".

Figure 3. Log-periodic antenna LPA1 (left) and LPA2 (right).

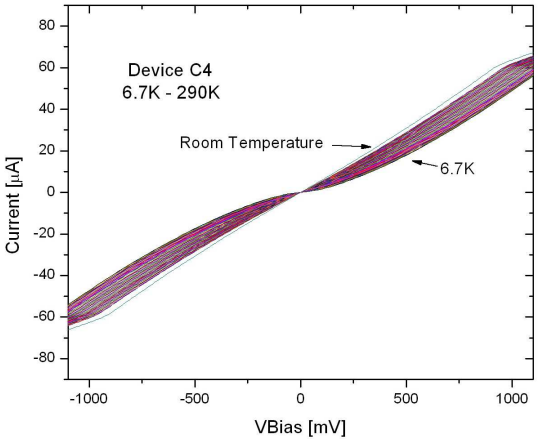

Figure 4. IV-curves as a function of temperature. Note that the non-linearity increases with decreasing temperature.

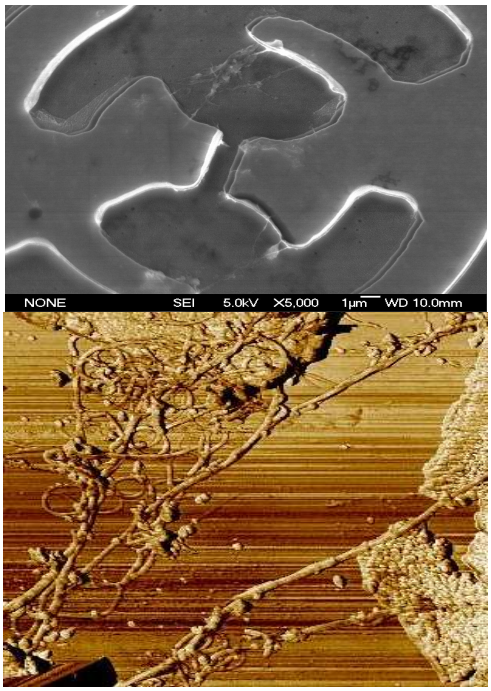

Figure 5. SEM and AFM pictures showing CNT bundles attached to some of the outer teeth of the antenna.

To further improve the probability of placing the tubes in the antenna gap we also applied photo resist and etched a small window that covered the antenna gap, see Figure 6. The DEP was then performed on the devices in this form. After the photoresist was dissolved, the CNTs remained in the gap (see Figure 7). It is not easy to ascertain from such pictures whether the tubes are actually suspended, and further SEM/AFM will be performed to answer this question.

III. DETECTION MODELS

Before presenting our experimental results we want to review the different models for the THz detection process in SWCNTs that we will consider.

A. The "diode" model

The voltage responsivity (S_V) and the current responsivity (S_I) are defined as

$$S_V = \Delta V/P_{THz} = S_I * R \qquad (1)$$

From standard microwave diode detector theory it is known [23] that

$$S_I = (1/4)*(d^2I/dV^2)*V^2_{THz}/P_{THz} \qquad (2)$$

Here, ΔV is the detected change in dc voltage, V_{THz} is the *peak* THz voltage and P_{THz} is the available THz power from the source.

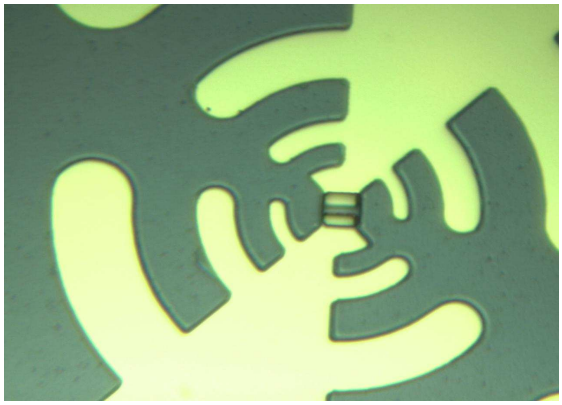

Figure 6. Optical photograph of an LPA3 antenna with an etched window for improved CNT placement in the antenna gap.

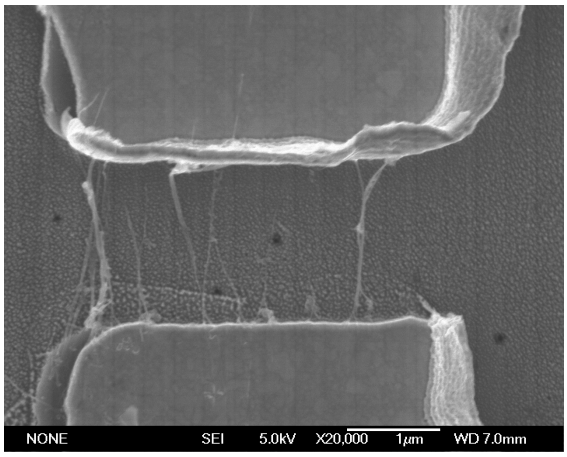

Figure 7. SEM picture of the gap region of an LPA3 antenna with several CNT bundles across the gap.

The only difference between the m-SWNT detector and MW diodes is that the m-SWNT IV-curve is symmetric. In [3],[4],[15] we showed that the MW voltage responsivity varies with bias voltage as $R*(d^2I/dV^2)$, which was obtained from the measured IV-curves. The agreement with Equations (1) and (2) was excellent. Note that for the devices in [3],[4],[15] the contact resistance was much larger than the actual CNT resistance, i.e. the nonlinearity of the IV curve could be ascribed to the contact resistance. Diode model fits could also be obtained for devices with low contact resistance, with IV-curves such as that in Figure 2, and by devices fabricated by the Yale group in [5,6]. In this case the nonlinearity is due to the CNT resistance, not the contact resistance. The Yale group reports a voltage responsivity of close to 400,000 V/W, measured at 77K and a frequency of 17 MHz [6]. **This makes it clear that the potential performance of SWCNTs as terahertz detectors is excellent.**

B. Bolometer Models

In bolometric detection the device changes its resistance in response to absorption of RF radiation. As the bolometer is heated by the terahertz power and biased by the dc current I_0, its temperature increases from T_0 to $T_0 + \Delta T$. If we define the factor $b = (1/R)*dR/dT$, then the voltage responsivity of the bolometer will be (neglecting electro-thermal feedback which is only important when the responsivity is very high) [24]:

$$S_V = \Delta V/P_{THz} = \frac{I_0 * R * b}{[G_{th} + i\omega C_h]}(V/W) \qquad (3)$$

A block-diagram of a bolometer is shown in Figure 8. The thermal time-constant of the bolometer is determined by $\tau_{th} = C_h/G_{th}$. In MW measurements on single qm-SWCNTs the Yale group showed that the response was typically consistent with a bolometer process due to heating of the SWCNTs [5],[6] (the contacts had very low resistance). This group measured dR/dT and showed that the change in resistance with temperature could be directly related to the DC heating as the bias voltage was increased. In this case DC heating and MW heating have equivalent effects on the resistance as in the "*standard model*" of HEBs [25]. RF absorption causes an *increased* resistance for the single tube case [5],[6].

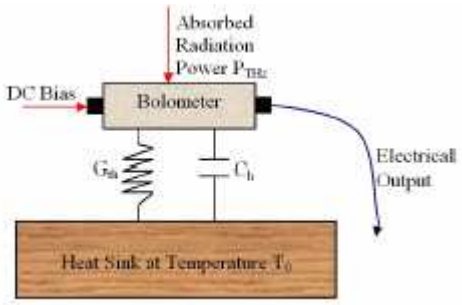

Figure 8. A bolometer model

We mention the above data in order to compare with our own THz detection results. A different type of bolometer model will be used below to interpret these: The *two-step bolometer model*. In this model, the THz radiation is absorbed in the m-SWCNTs which are therefore heated. The heated electrons in the CNTs then create an increased dc tunneling current through the contacts. The result of the THz absorption is thus a *decreased* resistance, equivalent to what happens when the entire device is heated. The net result is that equation (3) can still be used, by inserting measured values of dR/dT. One difference to the standard model case is that dR/dT depends on the bias voltage even under constant temperature conditions.

IV. TERAHERTZ MEASUREMENTS AND MODEL ANALYSIS

A. THz Measurement Setup

For the terahertz measurements, a device chip with dimensions 6x6 mm^2 was inserted in a fixture available from our earlier work with NbN HEB receivers [21]. The fixture allowed quasi-optical coupling to terahertz radiation, as well as bias input and detector output through a coaxial cable. Gold bond wires were used to connect to the contact pads of LPA1, while indium wires could be employed for LPA2, which has considerably larger contact pads. The fixture was then mounted in a liquid helium dewar. A 4 mm diameter ellipsoidal silicon lens was attached to the substrate for quasi-optical coupling to the antenna as shown in Fig. 9.

A 100 kΩ resistor is connected in series with the carbon nanotube, and the Keithley Source Meter is connected directly to the resistor (Figure 10). The dc voltage across the two terminals of the carbon nanotubes is sensed at the V_{sense} port. The Source Meter also measures the current through the carbon nanotubes. A change in the device current gives rise to a voltage drop across the 100 kΩ resistor that is measured with a lock-in amplifier (EG&G 7260), which has an input impedance of 1 MΩ, through two 200 kΩ resistors. A 1 kHz signal from a function generator was employed as reference for the lock-in amplifier.

Terahertz radiation was introduced through the dewar window and the silicon lens from a CO_2-laser (Coherent/DEOS GEM-50) pumped terahertz gas laser that had a typical output power of 2-5 mW (Figure 11). The power was measured with a Scientech (Astral AA30) power meter. The laser was modulated from the same 1 kHz function generator by inserting an acousto-optic modulator (IntraAction AGM-406B21) after the CO_2 pump laser, as indicated in Figure 10.

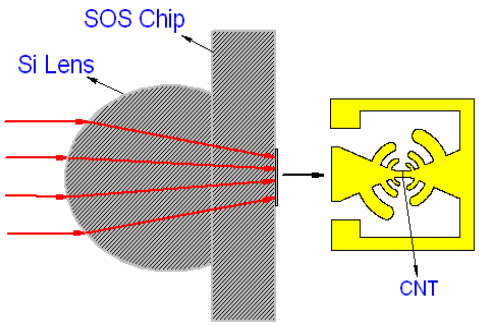

Figure 9. The quasi-optical coupling configuration.

B. Overview of Terahertz Measurement Results

Using the configuration described in section IV.A we have demonstrated THz detection in CNT bundles at several different frequencies (from 0.694 THz to 2.54 THz). We have measured the response for 18 devices of quite different resistances; see Table I for some examples. The resistance values given are for 300 K and low bias voltage.

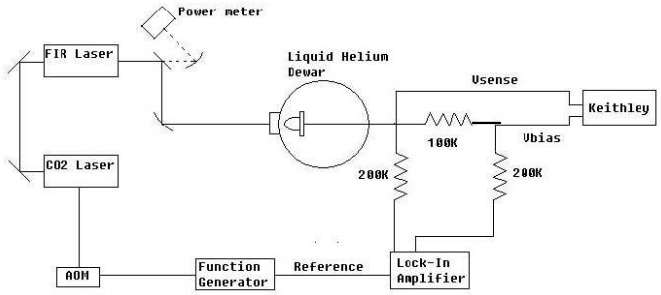

Figure 10. THz measurement setup.

Figure 11. Photograph of the terahertz gas laser source.

TABLE I.

Device	Resistance (kΩ)	Antenna	# Active m-SWNTs
B2	20	LPA1	50
C1	7	LPA2	30
C4	16	LPA2	15
1C4	80	LPA3	20
2D1	70	LPA3	20
3C3	50	LPA3	10*
4B2	40	LPA3	80*
4A2	22	LPA3	7*
4A3	48	LPA3	40*
2B1	16	LPA3	20*

*Estimates based on SEM imaging.

A summary of the voltage responsivity for selected terahertz detections is given in Figure 12. The terahertz power was measured outside the window of the dewar, and the response was linear in power. There is a roughly 3 to 4 dB optical loss between the dewar window and the antenna terminals, which was not corrected for. It is clear that there is a general type of detection process that works for a wide range of terahertz frequencies. There appears to be a pattern of decreasing responsivity from 0.694 THz to 1.63 THz, except for Device B2 that increased its responsivity at 2.54 THz.

Some devices show no or only very weak detection at 300 K, but Device 1μmB2 is an exception to this rule (not shown in Figure 13 or Table I). Up to about 100 K, the responsivity depends only weakly on temperature, typically decreasing only a factor of two or less from 4.2 K to about 25 K. The largest responsivity measured is about 25 V/W, which would

correspond to an intrinsic responsivity (correcting for optical losses) of over 50 V/W. We first discuss the results which can be interpreted using the bolometric model.

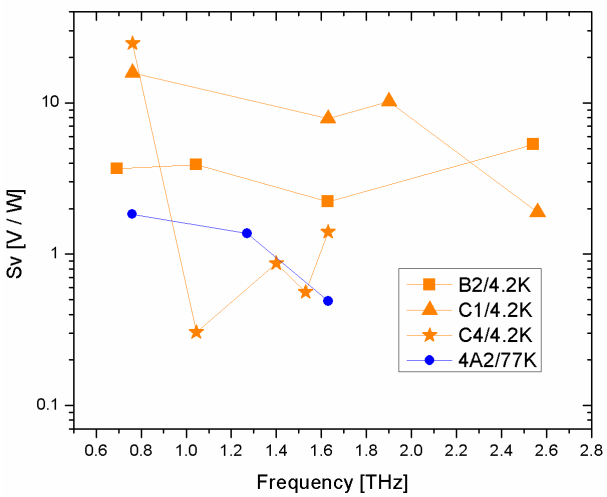

Figure 12. Summary of measured THz responsivity versus frequency.

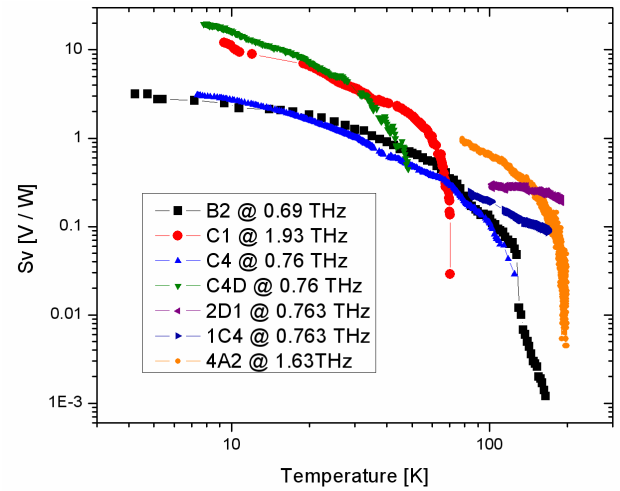

Figure 13. Summary of measured THz responsivity versus temperature.

C. Devices That Conform to The Bolometric Model

The criterion for whether a device conformed to the bolometer model was whether the responsivity followed Eq. (3) as the voltage bias was varied. We first measured R(T) versus voltage at several different temperatures, see Figure 14, and then calculated the factor b = 1/R*(dR/dT), Figure 15. Using this data we then varied the unknown factor G_{th} to obtain a best fit to Eq. (3), see Figures 16 and 17. Good fits were obtained for all devices (excepting two devices discussed in the next section), and at all frequencies at which they were measured. On the other hand, it was not possible to obtain a fit to Equations (1) and (2) for the diode mode. The voltage for which S_V peaks is about 60 mV at 5 K and 700 mV at 77 K. Note that the device temperature is not expected to change as the bias voltage is changed, since there is negligible DC heating of the CNTs. We thus expect that a single value of G_{th} should be valid for the entire curve. We have plotted G_{th} as a function of temperature in Figure 18, and compared with G_{th} for a single tube, as measured in [5,6]. The temperature dependence for single tubes and bundles appears to be quite similar at the lowest temperatures, but somewhat faster for the bundles above 60 K.

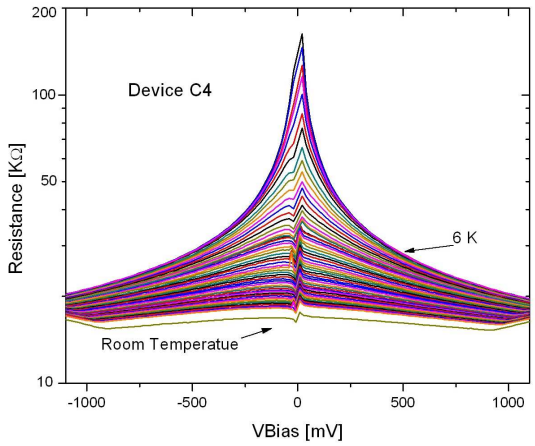

Figure 14. Measured resistance of device C4 for several different temperatures from 300 K to 5 K, versus bias voltage.

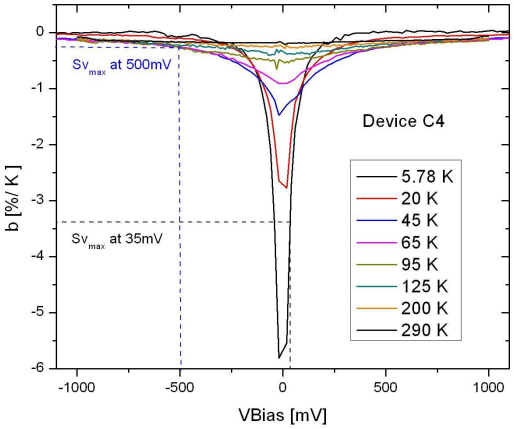

Figure 15. Plots of the factor 'b' in Eq. (3) for device C4 versus bias voltage for several different temperatures.

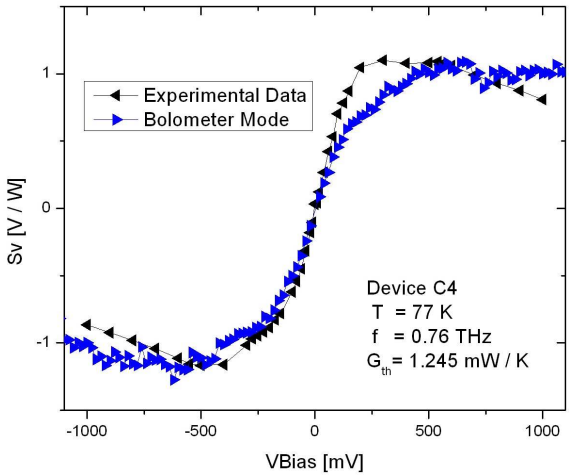

Figure 16. Plot of the measured responsivity of device C4 versus bias voltage (black points) compared with the prediction from the bolometer model (blue points). Detection was measured at 77 K at 0.76 THz.

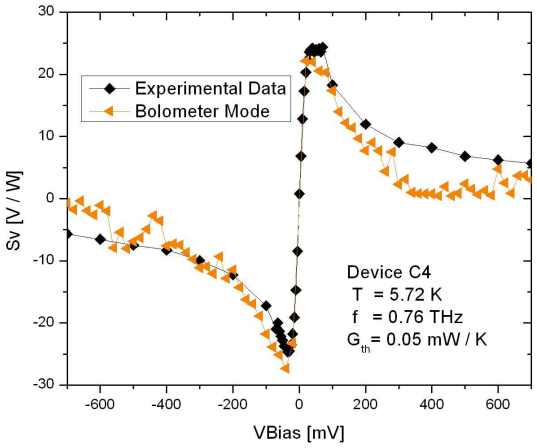

Figure 17. Plot of the measured responsivity of device C4 versus bias voltage (black points) compared with the prediction from the bolometer model (orange points). Detection was measured at 5.7 K at 0.76 THz

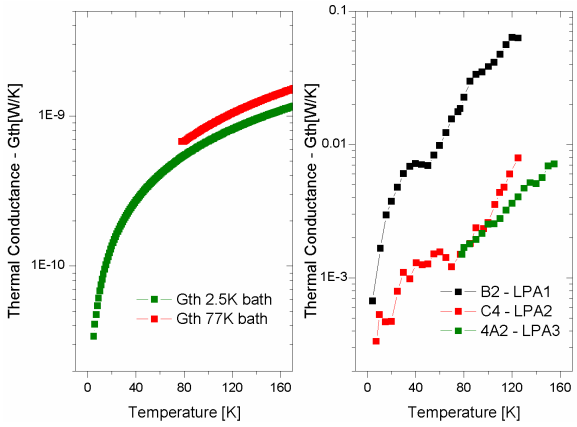

Figure 18. Plots of G_{th} measured for single SWCNTs in [5,6] (left). Plots of G_{th} versus temperature as derived from fits to Eq. (3) for three of our devices.

However, the values we obtain for G_{th} are about five to six orders-of-magnitude larger than for a single tube. To understand this we need to modify Eq. (3) to take into account additional effects that may occur.

$$S_V^{(1)} = \Delta V / P_{THz,abs} = \frac{V_0 * b}{[G_{th} + i\omega C]} \left[\frac{\eta}{L_{opt} L_{mism}} \right] (V/W) \quad (4)$$

First, the devices we measured consisted of a number of tubes which will increase the total thermal conductance. We do not presently have an accurate estimate for the effective number of tubes, but it is likely to be in the range 10-100 (see Table I). The thermal conductance of bundles of tubes, as versus single tubes, is not well known. Any optical (L_{opt}) or mismatch (L_{mism}) losses to the THz radiation would also be interpreted as an increased G_{th}, as indicated in Eq. (4). In [15] we estimated such losses to be about 16 dB. A more accurate estimate would require having better models for terahertz propagation on CNTs in bundles than we presently have. Finally, the factor η is introduced to take into account the efficiency with which electrons that are heated in the CNTs are able to diffuse out and tunnel through the contacts, a factor that is very difficult to estimate. To fully account for our data, η may have to be assumed to be quite small. One factor that may also influence the coupling loss (L_{mism}) is if terahertz energy is lost from the active metallic tubes to other inactive tubes in the bundles.

D.Devices That Conform to The Diode Model

We found two devices for which the diode models produced good fits to the measured $S_V(V_{bias})$. An example is shown in Figure 19 below (device 4A2). The fit is good except for some deviation at the highest voltages that may be due to an additional bolometric effect. However, it is clear that the bolometer model does not fit the data over-all. Similar fits were obtained for this device at 0.76 THz, 1.27 THz and 1.63 THz. Interestingly, when the same device was measured at 5.7 K, we found that both models could be used to fit the data.

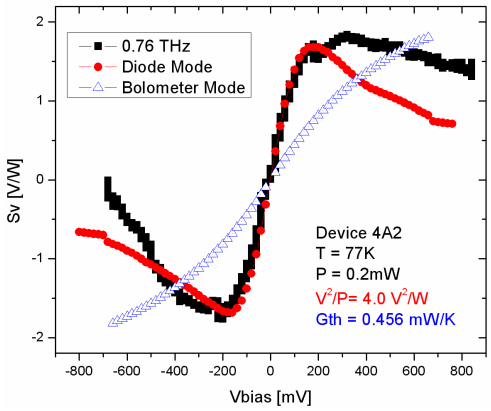

Figure 19. Measured responsivity of device 4A2 versus bias voltage (black) compared with predictions from diode model (red) and bolometer model (blue points). Detection measured at 77K and 0.76THz.

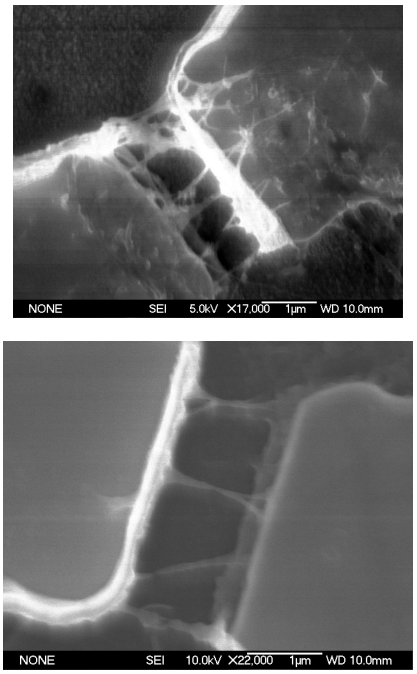

Figure 20. SEM pictures of devices that showed bolometric detection (top) and diode mode detection (bottom). Scale bar: 1µm.

This is the first time, as far as we know, that diode mode detection in CNTs has been demonstrated at such high frequencies. We ascribe this detection to the contact nonlinearities, as outlined in Sec. III.A. Figure 20 shows two

devices of which the one at the top showed bolometer mode detection, while the one at the bottom showed diode mode detection. Both devices that showed diode mode detection have tubes that appear to terminate on the edges of the antenna as the one shown in Figure 20. However, some devices that appear similar to the diode mode devices in SEM pictures also conform to the bolometer mode, so this question requires further study.

The diode model fits and the measured IV-curves enable us to obtain estimated values of the factor V^2_{THz}/P_{THz} in Eq. (2). With a given antenna impedance of 100 Ω, this factor should ideally be 200 Ω, if the entire terahertz voltage were coupled to the contacts (note that V_{THz} in Eq. (2) is the peak value). From the fits to the experimental data we instead find V^2_{THz}/P_{THz} = 8.0, 5, and 1.7 Ω at 0.76 THz, 1.27 THz, and 1.63 THz, respectively. We have corrected these values for an estimated 3 dB of optical loss in order to find the intrinsic values, at the antenna terminals. The best result (at 0.76 THz) corresponds to a 14 dB coupling loss for the THz power, significantly better than the total efficiency for the bolometer devices. To analyze the coupling loss of our diode mode devices we use a circuit model shown in Figure 21, based on the transmission line (TL) model for the high-frequency properties of SWCNTs from P. Burke [26]. The model has been modified by assuming nonlinear contact resistances, R1 and R2, with parallel contact capacitances, C1, and C2. Between the contacts we insert the Burke TL model for the m-SWCNT. This model assumes that the electron coupling effects in the m-SWCNT produce a Tomonaga-Lüttinger plasmon propagation mode for the electrons with a propagation velocity of about $2.4*10^6$ m/s. Plasmon resonances are predicted whenever the CNT length is a multiple of half the plasmon wavelength [26]. We have simulated this model using the ADS package [27]. We used contact resistances that match the measured DC resistance, R_{CNT} = 2 kΩ in agreement with [28], tube length of 1.3 µm, a plasmon velocity of $2.4*10^6$ m/s [26], and a characteristic impedance of the TL of 9.7 kΩ. We also assumed ten SWCNTs thus modelled, connected in parallel (Figure 21 for simplicity shows only one of these).

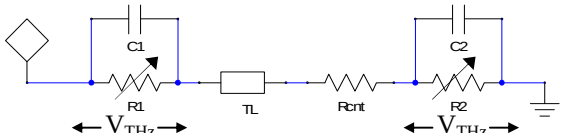

Figure 21. Circuit model for the m-SWCNT operating in the diode mode.

The main characteristic of the measured data is that the responsivity decreases as the frequency increases. If we initially neglect the effect of the plasmon transmission line, but not the m-SWCNT resistance, R_{CNT}, then this decrease could be caused by shunting of the contact resistance due to the contact capacitance. This case is illustrated in Figure 22.

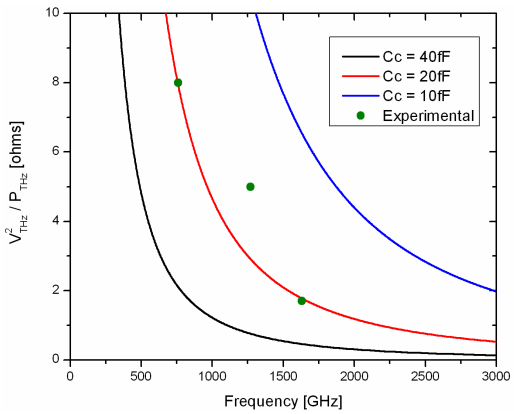

Figure 22. Simulation of the circuit in Figure 21 for the case that the plasmon TL is neglected. The green points are experimentally measured, and corrected for optical loss.

The measured data could thus be explained if the contact resistance was about 20 fF, a somewhat high value, but within the range of values we have measured at microwave frequencies [15]. Of, course, there may also be other unknown frequency-independent loss mechanisms such as particles from the original CNT solution, etc. If there were such losses, the capacitance value required would be smaller. The validity of the plasmon model has not been completely demonstrated yet, which is why we might neglect the TL. For example, McEuen et al. [12] detected resonances on a SWCNT using time-domain terahertz spectroscopy, but obtained a propagation velocity equal to the Fermi velocity, more than three times faster than the predicted plasmon velocity. This would shift the resonances to higher frequencies by that factor.

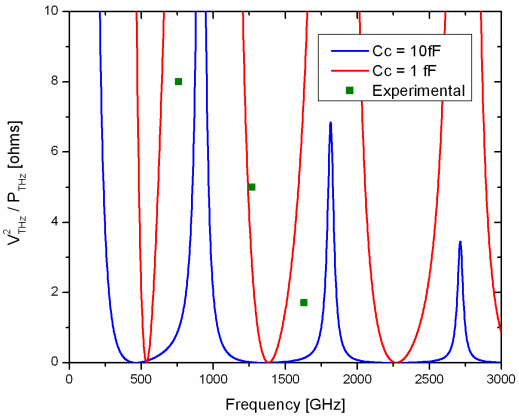

Figure 23. Simulation of the circuit in Figure 21 for the case when the plasmon TL is included. The green points are again experimentally measured.

We next compare a simulation with the plasmon TL model included, see Figure 23. In this case, the plasmon resonances clearly have a major effect on the voltage across the contacts. The experimental data are fairly close to the red curve for C_c (= C1+C2) = 1 fF. Measurements at a few more frequencies would quickly establish which of these general pictures (Figure 22 or Figure 23) is more correct. The main point here is that for devices that detect in the diode mode it should be feasible to check this type of circuit models, and answer questions such as what the propagation velocity is, does the TL model apply to bundles of tubes, etc.. We note that [29] and [30] predict yet again different values for the TL propagation velocity. In any case, it appears much more

straightforward to do this type of model fitting for the diode mode than for the bolometer mode. The circuit model fitting to terahertz data could also be combined with further microwave measurements, as we did in [15].

V. PROGRESS IN LARGE-SCALE ATOMISTIC SIMULATION

In order to obtain the different component characteristics presented in the equivalent circuit model in Fig.21, we aim to go beyond the current state-of-art capabilities for simulating CNTs by developing large-scale *ab-initio* atomistic approaches. Our proposed atomistic Density Functional Theory (DFT) and Kohn-Sham equation approach has the potential to clear up our understanding of many experimental issues, and to offer the high degree of reliability and accuracy needed to characterize the following macroscopic quantities: kinetic inductance, contact resistance and contact capacitance, quantum capacitance and CNT resistance.

An atomistic description of a long CNT up to 100nm (~ 10,000 atoms), which has been so far considered as a formidable task, could however provide important insights into the electronic properties of the device. In order to achieve this goal efficiently, we have been developing innovative numerical modeling strategies using a real-space mesh technique framework and a combination of mathematical methodologies and high-performance parallel algorithms such as the CMB strategy [31,32] (CMB stands for mode approach/contour integration/banded solver). Using our CMB strategy, the typical electron density of 20nm long CNT composed by ~2500 atoms can be computed in only`90 seconds using only one core of current workstation which is orders of magnitude faster than any other existing *ab-initio* techniques. In addition the CMB strategy is fundamentally designed for making a competitive parallel implementation possible at different levels of the modeling process.

Recently, a highly efficient and innovative numerical algorithm for solving the symmetric eigenvalue problem, FEAST, has been proposed and described in detail in [33]. This general algorithm is fundamentally different from the traditional Krylov subspace iteration based techniques and takes its inspiration from the density matrix representation and the contour integration techniques in quantum mechanics. In contrast to the CMB strategy, FEAST can calculate all the eigenpairs (eigenvalues and eigenvectors) and its main computational tasks consist of solving few (standard) independent linear systems with multiple right-hand sides along the complex contour. Using the mode approach, the obtained banded linear systems can be solved using highly efficient SPIKE-based algorithm [34]. .TABLE II summarizes the timings obtained for computing the electron density of a (5,5) CNT using both the CMB strategy and the FEAST algorithm. Both algorithms exhibit linear scaling performances when the size of the system increases and can then be potentially used to simulate very long CNTs. CMB is faster than FEAST but this latter is more accurate since it provides as well all the exact eigenpairs (i.e. the integration along the complex contour benefits from an iterative refinement technique which minimizes the numerical quadrature error).

#unit cells	1	3	6	24	48
N	199,874	331,298	528,434	1,711,250	3,288,338
$N_1 * M$	6278	9438	14861	48125	92477
$L(nm)$	0.73	1.23	1.98	6.51	12.55
$\#atoms$	20	60	120	480	960
T_{CMB} (s)	2.24	3.26	4.87	16.5	30.1
T_{FEAST} (s)	10.2	15.0	24.6	221	491

TABLE II. Comparisons of the simulation times for computing the electron density of a metallic (5,5) CNT using the CMB strategy and the FEAST algorithm which computes all the eigenpairs. The calculations are performed using only one core of an Intel-Clovertown system (2.66GHz, 16Gb).

In order to illustrate the efficiency of our modeling technique for handling both finite and periodic systems, we have compared in Figure 24 the density of states (DOS) of the (5,5) CNT calculated using (i) the bandstructure diagram of periodic (infinite) system, (ii) the histogram of all the eigenvalues obtained considering different lengths for the tube as reported in TABLE II. . As expected, the numerical results between the periodic and finite systems become closer as the length of the CNT increases. The boundary effects at the edge of the finite tube are noticeable for short-lengths where they let appear some states in the region around the Fermi-level which is in principle flat (constant) for the periodic system. These effects/states almost completely disappear for the 48-unit cell CNT.

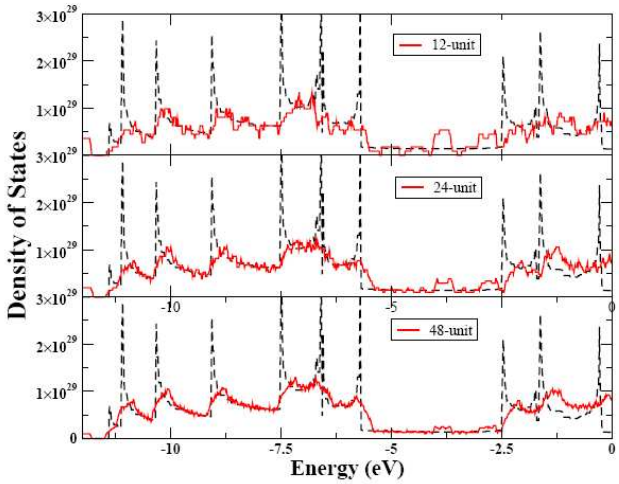

Figure 24. Comparisons of the density of states obtained for the periodic (5,5) CNT and the finite (5,5) CNT (isolated system) using three different length 12-unit, 24-unit and 48-unit cells

In order to perform the time-dependent simulations using TDDFT calculations (Time dependent DFT), we have recently investigated two different numerical strategies: (i) a scheme based on the Crank Nicolson procedure that will allow us to adapt the transient simulation approach proposed in [35], and (ii) a scheme based on spectral decomposition (solving the integral equation). This latter associated with innovative numerical quadrature techniques for decomposing the time evolution operator, shows promises for simulating long time-scale and then capturing the essential physics of the terahertz experimental data [36].

VI. Conclusion

We have demonstrated detection of terahertz radiation in a number of devices that couple integrated antennas to CNTs. The DEP fabrication is very convenient and reliable. While the voltage responsivity, which is interpreted as due to a bolometer effect, is much lower than for similar microwave devices [3],[4], the present configuration enables a variety of studies of CNTs at THz frequencies. The new demonstration of diode mode detection up to 1.6 THz shows stronger coupling of the terahertz radiation to the CNTs and should be useful for exploring the high-frequency models of m-SWCNTs, such as the properties of the Tomonaga-Lüttinger liquid plasmons, in future work. We are presently working on fabrication methods that should result in low-resistance contacts to both bundles and single tubes, and much higher responsivities are expected, as discussed in Sections II and III. These experimental studies will be interpreted with the help of the *ab initio* simulations. A final step is the expansion to heterodyne detectors and the first determination of the thermal time-constant of m-SWCNT detectors (in the frequency domain). The time-constants are expected to be very short [1,2].

References

[1] K.S. Yngvesson, "A New Hot Electron Bolometer Heterodyne Detector Based on Single-Walled Carbon Nanotubes," *16th Intern. Symp. Space Terahertz Technol.*, Göteborg, Sweden, May 2005, p. 531.

[2] K.S. Yngvesson, "Very wide bandwidth hot electron bolometer heterodyne detectors based on single-walled carbon nanotubes," *Applied Phys. Lett*, vol. **87**, p. 043503 (2005).

[3] K.S. Yngvesson, F. Rodriguez-Morales, R. Zannoni, J. Nicholson, M. Fishetti, and J. Appenzeller, "Microwave Detection and Mixing in Metallic Single Wall Carbon Nanotubes and Potential for a New Terahertz Detector," *17th Intern. Symp. Space Terahertz Technol.*, Paris, France, May 2006, p. 135.

[4] F. Rodriguez-Morales, R. Zannoni, J. Nicholson, M. Fischetti, K. S. Yngvesson, and J. Appenzeller, *Appl. Phys. Lett*. **89**, 083502 _2006_.

[5] D.F. Santavicca and D. Prober, "Terahertz Resonances and Bolometric Response of a Single Walled Carbon Nanotube", paper 1646, 33rd Intern. Conf. Infrared, Millimeter and Terahertz Waves, Sept. 2008, CalTech, Pasadena, CA.

[6] D.F. Santavicca, J. Chudow, A. Annunciata, L. Frunzio, D. Prober, M. Purewal and P. Kim, "Terahertz resonances on a single-walled carbon nanotube," Intern. Workshop on Optical Terahertz Science and Technol., Santa Barbara, CA, March 7-11, 2009.

[7] H.M. Manohara, E.W. Wong, E. Schlecht, B.D. Hunt, and P.H. Siegel, *Nano Lett.* **5**, 1469 (2005).

[8] S. Rosenblatt, H. Lin, V. Sazonova, S. Tiwari, and P.L. McEuen, *Appl. Phys. Lett*. **87**, 153111 (2005).

[9] A. A. Pesetski, J.E. Baumgardner, E. Folk, J. Przybysz, J. D. Adam, and H. Zhang, *Appl. Phys. Lett.*, **88**, 113103 (2006).

[10] M. Tarasov, J. Svensson, L. Kuzmin, and E. E. B. Campbell, *Appl.Phys.Lett.*, **90**, 163503 (2007).

[11] C. Rutherglen and P. Burke, "Carbon Nanotube Radio," *Nano Letters*, **7**, p. 3296 (2007).

[12] Z. Zhong, N.M. Gabor, J.E. Sharping, A.L. Gaeta, and P.L. McEuen, "Terahertz time-domain measurement of ballistic electron resonance in a single-walled carbon nanotube," *Nature Nanotechnol.* **3**, 201 (2008).

[13] M.E. Itkis, F. Borondics, A. Yu and R.C. Haddon, *Science*, **312**, 413 (2006).

[14] K. Fu, R. Zannoni, C. Chan, S.H.Adams, J. Nicholson, E. Polizzi and K.S. Yngvesson, "Terahertz detection in single wall carbon nanotubes," *Appl. Phys. Lett.*, **92**, 033105 (2008).

[15] K.S. Yngvesson, K. Fu, B. Fu, R. Zannoni, J. Nicholson, S.H. Adams, A. Ouarraoui, J. Donovan and E. Polizzi, "Experimental detection of terahertz radiation in bundles of single walled carbon nanotubes," Proc. 19th Intern. Symp. Space Terahertz Technol., Groningen, The Netherlands, April 28-30, 2008, p. 304.

[16] K. Fu, "Metallic Carbon Nanotubes, Microwave Characterization and Development of a Terahertz Detector," *M.Sc. thesis, University of Massachusetts, Amherst, MA* (2008).

[17] Z. Yao, C.L. Kane, and C. Dekker, *Phys. Rev. Lett.* **84**, 2941 (2000).

[18] Th. Hunger, B. Lengeler, and J. Appenzeller, Phys. Rev. B, **69**, 195406 (2004).

[19] E. Pop, D.A. Mann, K. Goodson, and H. Dai, J. Appl. Phys., **101**, 093710 (2007).

[20] R. Krupke and F. Hennrich, *Adv. Eng. Mater*. **7**, 111 _2005.

[21] E. Gerecht, C. Musante, Y. Zhuang, K. Yngvesson, T. Goyette, J. Dickinson, J. Waldman, P. Yagoubov, G. Gol'tsman, B. Voronov, and E. Gershenzon, *IEEE Trans. Microwave Theory Techn.*, vol. **47**, pp. 2519–2527, (1999).

[22] Cheap Tubes, Brattleboro, Vt.. Purified 90% SWCNTs, grown by CVD, nominal diameter from 1 to 2 nm., average length of 50 μm before ultrasonication.

[23] K.S. Yngvesson, "*Microwave Semiconductor Devices*", Kluwer Academic, Norwell, MA (1991).

[24] P.L. Richards, *J. Appl. Phys*., **76**, 1 (1994).

[25] S. Yngvesson and E. Kollberg, "Optimum Receiver Noise Temperature for NbN HEB Mixers According to the Standard Model," *10th International Symposium on Space THz Technology*, Charlottesville, VA, March 1999, pp. 566-582.

[26] P. J. Burke, "Lüttinger liquid theory as a model of the gigahertz electrical properties of carbon nanotubes," *IEEE Trans. Nanotech*. **1**, 129 (2002).

[27] Agilent, Inc., Santa Clara, CA.

[28] M. S. Purewal, B. H. Hong, A. Ravi, B. Chandra, J. Hone, and P. Kim, "Scaling of Resistance and Electron Mean Free Path of Single-Walled Carbon Nanotubes", *Phys.Rev.Lett*. **98**, 186808 (2007).

[29] G.W. Hanson, "Fundamental Transmitting Properties of Carbon Nanotube Antennas", *IEEE Trans. Antennas Propagat.*, **53,** 2426 (2005).

[30] M. V. Shuba, S. A. Maksimenko and A. Lakhtakia "Electromagnetic wave propagation in an almost circular bundle of closely packed metallic carbon nanotubes" *Phys. Rev. B*., **76,** 155407 (2007).

[31] D. Zhang and E. Polizzi, "Efficient Modeling Techniques for Atomistic-Based Electronic Density Calculations", J. Comp. Elec., Vol. 7, N. 3, pp 427-431 (2008).

[32] D. Zhang and E. Polizzi, "Linear scaling techniques for first-principle calculations of large nanowire devices", 2008 NSTI Nanotechnology Conference and Trade Show. Technical Proceedings, Vol. 1 pp12-15 (2008).

[33] E. Polizzi, "Density-Matrix-Based Algorithms for Solving Eingenvalue Problems" Phys. Rev. B. Vol. 79, 11512 (2009).

[34] E. Polizzi, A. Sameh. "A Parallel Hybrid Banded System Solver: The SPIKE Algorithm", *Parallel Computing*, **32**, 2, pp. 177-194 (2006).

[35] O. Pinaud, "Transcient simulations of resonant tunneling diode", *J. Appl. Phys.* **92**,1 p1987 (2002).

[36] Z. Chen, E. Polizzi, (unpublished,).

In situ Quantitative THz Gas Analysis

John C. Pearson, Brian J. Drouin, Ken B. Cooper, and Robert A. Stachnik

Abstract— **The rotational spectrum of gas phase molecules offers the potential to be an extremely powerful tool for analytical chemistry. Every polar molecule features a unique rotational spectrum with a band origin at DC. The resolution of phase locked microwave techniques can easily be 1 part in 10^{10} while the Doppler limited line widths are one part in 10^6. In the absence of significant optical depth the intensities of Doppler limited lines are linearly proportional to the total column. For *in situ* applications a microwave source illuminates the gas and power is measured as a function of frequency allowing the comparatively narrow lines to be detected even when there is significant gain or power structure. The illuminating source can easily have a brightness temperature greater than 10^{14}K so that extremely weak features can be detected. The result is that rotational techniques facilitate extremely sensitive chemical identification and have the potential for very accurate total abundance determination. The development and calibration of ambient temperature *in situ* rotational spectroscopic systems operating between 0.1 and 0.6 THz for planetary science is presented. Optimization of this type of system requires some rather different considerations than are typical for space based remote sensing instruments. The system considerations, the calibration and potential applications of *in situ* spectroscopy are discussed.**

***Index Terms*—Gas detectors, Spectroscopy, Signal Detection, Heterodyning**

I. INTRODUCTION

THE idea of employing microwave spectroscopy as an analytical chemistry tool was first extensively discussed in 1948 by Gordy [1]. An entire chapter of the classic 1955 text Microwave Spectroscopy by Townes and Schawlow [2] was devoted to the subject. With the exception of a massive, late 1960's, commercial, system produced by Hewlett Packard, microwave spectroscopy has yet to be commercially exploited or used in any real sense for *in situ* analytical chemistry. However, microwave spectroscopy has proven to be a valuable remote chemical analysis tool in Limb Sounding and Radio Astronomy applications. The reasons for the microwave spectroscopic technique not achieving its *in situ* chemical analysis potential are primarily due to some rather significant technological challenges in generating and detecting submillimeter radiation that had to be overcome. The rapid improvements in digital electronics and wide bandwidth submillimeter sources have now eliminated the last of these original technical obstacles and building small powerful gas analysis systems are now feasible.

Manuscript received 16 April 2009. This work was performed by the Jet Propulsion Laboratory, California Institute of Technology under contract with the National Aeronautics and Space Administration.

J.C. Pearson, B.J. Drouin, K.B. Cooper and R. Stachnik are with the Jet Propulsion Laboratory, California Institute of Technology, 4800 Oak Grove Dr., Pasadena, CA 91109. Phone: 818-354-6822; fax 818-393-2430; e-mail: John.C.Pearson@jpl.nasa.gov

Design and optimization of an *in situ* gas detector requires a different approach than passive remote sensing where the sensitivity and performance is driven by minimizing the effective T_{sys}. First, the *in situ* implementation requires detection of a small change in power on a high power carrier signal caused by a molecular absorption in the sample gas. The relevant figure of merit is then the smallest change in power, rather than the smallest power that can be detected. Second, an *in situ* design must be able to do quantitative analysis in an absolute sense, extracting the total column of absorbing gas and determine with the help of a pressure and temperature measurement the fractional abundance of the observed molecule. In the planetary science application a key aspect is determination of the isotopic ratios of simple molecules for derivation of information about the evolution of the body in question relative to the initial solar nebula. From a spectroscopic point of view the isotopes are distinct molecules the so quantitative analysis of both determines the isotope ratio.

In this paper we discuss the three aspects of in situ rotational gas spectroscopy that are most critical to a system design: an understanding of the "target" signatures as a function of conditions, the fundamental limits of system performance as well as what is required to detect and quantify, and the practical system considerations that can prevent an instrument from reaching theoretical limits.

II. MOLECULAR ABSORPTION

All molecules with different atoms have polar bonds. As long as there is not accidentally high symmetry such as in CO_2 (OCO) or benzene (C_6H_6 in a ring), all molecules with dissimilar atoms have a permanent dipole moment and exhibit a rotational spectrum. Unlike infrared and electronic bands, the rotational band of all molecules features an origin at zero in frequency. Therefore, every polar molecule features transitions which can be accessed with millimeter and submillimeter techniques. The great promise of microwave spectroscopy is that a single detection system can in theory detect and quantify any molecule that is polar in sufficient abundance to be detectable.

The critical element of spectroscopic detection is the line strength with emission and absorption being completely correlated through the Einstein A and B coefficients [3]. The integrated absorption intensity of any molecular gas transition at any wavelength is calculated from the following equation [4]:

$$I(T) = \int_0^\infty \alpha_\nu d\nu = \left(\frac{8\pi^3}{3hc}\right) \nu S \mu^2 \left[e^{-E''/kT} - e^{-E'/kT}\right] / Q \,. \quad (1)$$

Here α_ν is the frequency dependent absorption coefficient, *h* is Planck's constant, *c* is the speed of light, ν is the frequency, *E"* and *E'* are the upper and lower state energies, respectively, *k* is Boltzmann's constant, *T* is the temperature, *S* is the geometrical projection of the transition moment, μ is the transition dipole moment and *Q* is the partition function. In rotational spectroscopy the transition dipole is the permanent electric dipole moment and the energy exponent is a few percent unless the temperature is very low. The transition line width of the absorption is determined by summing in frequency space the spontaneous emission line width (inverse of Einstein A coefficient), the Doppler line width and the collisional line width. Spontaneous emission line widths are proportional to the transition frequency cubed and are only a few kHz for the strongest submillimeter transitions [4]. The Doppler width is given by Equation (2), below, and is typically less than 1 MHz for frequencies less than 700 GHz. The pressure broadening width (typically 5-15 MHz/Torr) is linear in pressure, independent of wavelength, and is a function of quantum state and broadening gas. Pressure broadening can be ignored by operating only in the Doppler limit i.e. at very low pressure (<10 mTorr) gas. The Doppler half width at half maximum in MHz is [4]:

$$\Delta\nu_d = 1.17221\times10^{-6}\times\nu_{ab}\sqrt{\left(\frac{T}{300K}\right)\left(\frac{28}{m}\right)}\ , \qquad (2)$$

where ν_{ab} is transition frequency in MHz, T is the gas temperature and m is the mass in atomic units. Doppler limited transitions in the submillimeter are only a few 100 kHz wide, but increase linearly with frequency. In the Doppler limit, the line width is on the order of one part in 10^6 of the frequency. This is effectively a very high Q which makes it comparatively easy to avoid interference on the same scale from either electronic or optical effects. The other implication of the narrow line width is that Doppler limited spectroscopy in the millimeter and submillimeter with a modest fractional bandwidth will cover about a million line widths. Since pressure broadening in an unknown gas mixer is an intractable problem [2] staying in the Doppler limit is an obvious operational requirement for a practical system. The peak absorption [4] is given by:

$$\alpha = I(T)\, f \,/\, \Delta\nu_d \times 1.51149 cm^{-1}\ . \qquad (3)$$

Here Δν is the Doppler half width at half maximum of a Doppler limited 10 mTorr pressure and *f* is the fraction of molecules of a given species. In the Doppler limit the peak line strength is linear with column density. Fractional concentration can be directly converted to a column using the ideal gas law where there are $3.9\text{x}10^{14}$ molecules/cm^2 in a 1 cm long column at a pressure of 10 mTorr at 300 K. There are several public rotational line catalogs http://spec.jpl.nasa.gov and http://www.astro.uni-koeln.de/site/vorhersagen/, which tabulate line strengths, *I(T)*, and provide some instruction and software (JPL) to do so for other molecules.

The power absorbed per unit length *l* of gas is given by:

$$P_x = P_0 e^{-\alpha d}\ . \qquad (4)$$

Where P_0 is the power applied to the absorbing gas and *l* is the path length of propagation in the medium. For the line to be detectable P_x must be larger than the receiver ΔP_{min} in the measurement period.

Molecules feature a number of transitions depending on their structure. In just about all cases there is a line every 2B or B+C where these are the inverse moments of inertia along the axes of rotation. In symmetric top and asymmetric top molecules there will be additional series due to projection (K quantum number) on the molecular axis. As a result, a system with a modest fractional bandwidth can detect at least several lines of all but the lightest molecules. In heavy molecules thousands of lines will likely be present in a wideband spectrum. The relative intensity and the line width are determined by Equations (1) and (2) adding to the confidence in any detection.

The last molecular consideration is picking a frequency band which is ultimately a compromise between light and heavy target molecules with light molecules like water being much stronger at high frequency while heavy molecules are better suited for lower frequencies. A very good compromise at room temperature is the 300 GHz range where the heavy molecules will be near the Boltzmann peak and the light ones, which are generally easier to detect, are usually still present. For planetary applications lower temperature suggest lower frequency, however the light molecules like HCl and ammonia are often the primary science targets and these require submillimeter detection.

III. Spectroscopic Detection

The ultimate figure of merit for an absorption spectrometer is the smallest change of power that can be detected. In general it is easy to detect power and compare the power level to the noise floor of the detector to determine a carrier-to-noise floor ratio (CNR). For small signals the detector noise dominates, but in the large signal limit, noise related to the source always plays a significant role. A previous paper discusses the fundamental detection limits and compares in situ to active remote (standoff) detection [5].

The subject of sensitivity limitations for absorption spectrometers where large signals are involved was first discussed by Townes and Geschwind [6] who pointed out on the basis of amplitude modulation that the theoretical minimum detectable change in power of a large signal is proportional to the geometric mean of the noise and the signal powers:

$$\Delta P_{\min} \propto \sqrt{kT\,\Delta\nu P_{rx}}\ , \qquad (5)$$

where *k* is Boltzmann's constant, *T* is the receiver's physical noise temperature in the absence of signal power, $\Delta\nu$ is the detection bandwidth and P_{rx} is the received signal power. Historically, spectroscopic systems have been operated in the small signal power regime, so that the minimum detectable absorbed power is determined by non-source noise terms not

related to the source, such as the NEP of the detector. However, the improvements in sources at THz frequencies have resulted in the source noise being an essential consideration.

Practical detection systems require choices be made in the sort of detector employed. Historically the emphasis has been on achieving thermal background limited detection, however, this is not necessarily the best optimization for a large signal detection system.

Equation (5) states that the smallest detectable signal is at best proportional to the square root of the received power. The sensitivity limit can be rigorously derived from the Rician probability distribution of signal detection as has been done for radar detection by Levanon [7]. The result also agrees with radar cross section measurement theory discussed by Dybdal [8] and proportionality factor is of order unity:

$$\Delta P_{\min} = \sqrt{2kT\Delta\nu P_{rx}} \quad . \tag{6}$$

An intuitive justification is that any power detector squares the sum of a signal and a noise voltage, $P=(Vs+Vn)^2$, so that for large signals, the cross-term $2Vs\cdot Vn \propto \sqrt{Ps\cdot Pn}$ dominates the fluctuations of the measured power. In heterodyne detection, the system temperature, $T_{sys,}$ includes quantum noise, intrinsic mixer noise (conversion loss), as well as the thermal background noise. As a result, T_{sys} is the relevant quantity in Equations (5-6) for all heterodyne detection of changes in transmitted power.

The minimum detectable power absorption of Equation (6) must also apply to the signals received by a direct detector. However, analysis of direct detectors is complicated by the fact that a direct detector's NEP almost always quantifies the dominant noise that is additive after the square law action, rather than multiplicative prior to squaring as in Equation (6). In the large signal limit, the internal NEP must eventually become irrelevant in the absence of saturation. Direct detectors also have quantum efficiency, γ, that is less than unity. The performance of direct detector systems have been discussed at length by many authors, however we will adopt the formalism derived by Brown [9]. The SNR at the detector output includes the background modulation term, the background seen by the detector, the shot noise, and the intrinsic NEP.

$$SNR^2 = \frac{P_{rx}^2}{\Delta P_{\min}^2} = \frac{P_{rx}^2}{2P_{rx}kT\Delta\nu + 2(kT)^2\Delta\nu\Delta f + 2P_{rx}h\nu_c\Delta\nu + NEP^2\Delta\nu} \tag{7}$$

Here Δf is the input bandwidth and $\Delta\nu$ is the output bandwidth. In the limit $h\nu<<kT$, the cross-term noise will always dominate the shot noise. The SNR with respect to the detector input can be derived by multiplying Equation 7 by the quantum efficiency.

It is instructive to compare direct detectors using Equation 7 with heterodyne detectors in an ideal case where $T_{sys}\sim T$ (no mixer conversion loss or shot noise) and unity quantum efficiency. Regardless of input bandwidth and NEP both detection schemes ultimately converge to the same value: $SNR=(CNR/2)^{1/2}$, where *CNR* is the carrier to thermal noise at the detector input.

The figure of merit for a heterodyne detector is the transmit temperature at which the IF starts to compress relative to T_{sys}. In a direct detector it is generally better to be able to accept higher input power levels as long as Equation (6) is not dominated by the NEP term, then a better detector is advantageous. Detector selection ultimately requires an understanding of the available source power and actual detector properties such as saturation, NEP, and load curves.

An interesting consequence of the sensitivity being proportional to the square root of input power and detection (output) bandwidth is that the absolute absorption can be almost trivially determined. The real CNR is proportional to the number of counts between the unilluminated detector and the illuminated detector in the absence of gas and the SNR can be obtained by taking the appropriate square root. The square root of the number of counts of the absorption line counts relative to the CNR is the absolute fractional absorption of the line which can be used in equation 3 to derive the fractional abundance of the gas. A challenge is to assure that the detector is very close to linear and not dominated by some intrinsic noise (NEP). The signal-to-noise of a heterodyne detection system used to measure a change in power on a carrier is always proportional to the square root of input power as long as the IF is not compressed. Direct detectors have a signal to noise proportional to the square root of the change in counts, but the zero (noise floor) or a strong absorption will always sample the NEP limited regime making the calibration significantly more difficult.

It is useful to consider the sensitivity of a system in a 1 Hz bandwidth with a mixer that has a 10 dB conversion loss (T_{sys}=3000 K) and starts to compress with a signal level of 100 μW of RF (10 μW at the IF). In this case $\Delta P_{min}=2.88\text{x}10^{-12}$ Watts and the signal-to-noise is $3.5\text{x}10^7$. After taking into account the square root of the input power level, it is hard to conceive of a system with a signal-to-noise better than $1\text{x}10^8$ or, equivalently, a minimum detectable absorption of 1 part in 100 million. So for existing technology this can be considered an upper limit on the possible performance of the microwave portion of the system.

IV. Detection Requirements

A. Calibration of Absorption

An analytical chemistry system must be able to determine the absolute abundance. The test requirements associated with determining the absolute absorption in a direct detector make it highly advantageous for *in situ* applications to choose heterodyne detection as does the general requirement for ambient temperature detection in planetary applications. In principle most of the issues subsequently discussed apply to both kinds of detection, however for simplicity heterodyne detection will be considered hereafter. In the heterodyne system measurement of an absolute concentration corresponds to a calibration test where the IF compression is carefully measured as a function of RF frequency at the IF frequency. Calibration requires a "dark" or "cold" input level for the

mixer which is just the pumped mixer looking at the ambient environment. This can be accomplished by simply turning off the transmitted signal, but it must be done periodically in frequency since T_{sys} will be a function of frequency. The "hot" level is the illuminated mixer with no gas in the cell. It should be noted that this can usually be well determined even with gas in the cell because the spectrum is rarely completely line confused.

The difference between the hot and cold is required for calibration but only a relative scale in arbitrary count units is needed. This is due to the fact that measurement of the absorption is effectively a % absorbed result and is normalized to such in the data reduction. The % absorbed is an absolute number that can be traced directly to the fractional abundance of the molecule in question. The accuracy of the abundance measurement can be determined by the noise (square root of hot counts) relative to the depth of the line plus the uncertainty in the depth measurement. In this case of a line absorbing 10% of the power would be dominated by the accuracy in determining the line depth while a signal-to-noise of 5 line would be dominated by the noise.

The other calibration considerations are that the path length of the absorbing column is known and that the temperature and pressure can be measured. Errors in these quantities correspond directly to errors in the determined abundance as can be seen from Equations (1-3).

B. Dynamic Range of Electronics

A general requirement for a heterodyne spectrometer is that its dynamic range be limited by the first mixer. The corollary to this requirement is the noise be preserved after the mixer IF amplifier combination and that no subsequent component significantly adds to the noise. Both are standard for heterodyne systems but the need to preserve a maximum dynamic range of 160 dB corresponding to the CNR must be considered carefully and is far from trivial.

Equation (6) states that the signal-to-noise is proportional to the square root of the input power. In the limit of a "dark" calibration pulse, or an optically thick absorption, the power at the detector is just its noise. Since counting from this "zero" is necessary for calibration the detection scheme must have enough dynamic range to count zero and full power on the same scale. In our limiting case of a signal-to-noise of $1x10^8$ this corresponds to 160 dB, which is a significant problem for the ultimate detector in the system. Unfortunately, only HEMT amplifiers generally have this sort of dynamic range, while diodes, digitizers, and other sorts of analog detectors do not achieve the required performance. However, lock-in amplification theory provides the basis of a solution. The 160 dB corresponds to the final filtered 1 Hz bandwidth. The electric field sampled in a much larger bandwidth will have a correspondingly lower signal-to-noise. The noise will increase 10 dB with every decade of bandwidth digitized so a digitizer with an 80 dB spur free dynamic range would have to digitize a 100 MHz bandwidth to have the digitizer noise not be the limiting factor. Sampling faster does not help since the digitizer noise also increases with the reduced time. The currently available state-of-the art 16 and 24 bit digitizers are close to this level of performance and improvements are constantly being made so that they will not likely be a future limitation. The signal can then be extracted from the noise with digital lock-in amplification techniques that narrow the bandwidth to the desired level by having the integration time define the detection bandwidth. Once sufficient bandwidth to have the signal-to-noise of the digitizer not be the limiting factor is digitized, then digital lock-in techniques can provide the bandwidth limitation and accumulate the necessary bits for the required accuracy. 160 dB corresponds to 54 bits so the digital lock-in should be a 64 bit implementation. Digitization and lock-in processing must be done with both the in phase and quadrature components due to the unknown and changing phase. The digitizer linearity is a calibration error and any fluctuations will appear as a system gain change. Any digitizer instability will be noise.

C. Lock-in Detection Approach

Microwave spectroscopy has traditionally utilized a modulation scheme to minimize the impact of 1/f noise in the detector and to minimize the impact of standing waves. Modulation is always less than unit efficiency so there is a sensitivity penalty when using it. As long as the mixer is not operated in a homodyne mode, 1/f will not be a problem in the conversion. The overall receiver system gain is subject to 1/f noise that will manifest itself as structure on the power spectrum (noise) and a calibration error (shift of zero). Phase or frequency modulation allows the phase to be detected, which is independent of the receiver gain. While this is advantageous, the phase in a heterodyne system is proportional to the path difference between the LO and signal path, and will in general depend on frequency as well as (to a lesser extent) the absorbing gas pressure. As a result, traditional lock-in amplifier type detection with a fixed phase shift will only work over a limited range of conditions and frequencies. The only solution is to capture a complete description of the electric field at the detector by detecting both in phase, I, and quadrature, Q. Early attempts at build heterodyne absorption spectrometers without IQ detection had major problems with phases and could only be used in narrow frequency bands. So detecting in phase and quadrature must be considered a detection requirement.

Modulation represents a trade-off between standing waves and system stability with the ultimate detection limit and calibration accuracy. Modulation may be advantageous in the final implementation, however the final minimum detectable concentration will be larger and there will be a calibration penalty due to the line width changing the modulation efficiency that will be particularly severe when lines are blended. In an ideal system modulation would not be necessary, however achieving this requires a number of aspects of the system to be carefully designed and tuned up. These are discussed in Section VI.

D. Other Considerations

The effective filtering in the detection scheme makes this

system sensitive to phase noise. All power that falls out of the detection band due to phase noise is effectively lost. For a high quality local oscillator and transmit signal, spectral purity only becomes a consideration at longer integration times where the bandwidth is effectively extremely narrow. In this case a phase reference (difference between LO and transmit) can be multiplied by the same factor and then be used in a second down conversion to cancel all phase noise within a bandwidth defined by path difference in two signal paths.

A variety of other standard microwave techniques such as the use of a correlation receiver can be used to suppress various sources of noise from other aspects of the system such as the local oscillator if necessary. However for planetary applications simplicity is preferred since mass, power and volume are extremely expensive.

V. General Requirements

A. Source and Reference

A general requirement is that the frequency is sampled on a fine enough grid so that each absorption feature is covered by at least 10 points with 20 or more being better whenever it is desirable to determine the absorption line width. This corresponds to a step size of 10 to 50 kHz at the transmit frequency. Since the signal-to-noise is proportional to the square root of integration time per point, there is a direct trade-off between speed and sensitivity and ultimately accuracy. A "discovery mode" would sample more coarsely in frequency with shorter integration times while careful measurement of isotope ratios will need to be done with a finer frequency step. The strict square root in the integration time means that there is no advantage to stepping slowly relative to averaging more samples as long as the system overhead is negligible. Unfortunately synthesizers suitable for significant fractional bandwidths with the ~1kHz step size required often take a few 10's of milliseconds to switch frequencies. Much faster synthesizers can be constructed at the cost of additional power. Ultimately, digital electronics will enable direct synthesis of any arbitrary waveform with good phase noise and low power. Currently this approach requires more DC power than a slow synthesizer however it should eventually become an extremely attractive option.

The fundamental synthesizer must cover the same fractional bandwidth as the resultant system and have a step size small enough to cover a molecular line with at least 20 points. Software control can degrade the resolution as desired. Faster switching is always desirable since this affords flexibility in the data collection, however this can be traded with system stability. A very stable system will follow the square root of integration time independent of the data collecting strategy, whereas in an unstable system averaging many fast frequency scans is significantly better.

Molecular line frequencies are constants of nature and cannot change. As a result, they define a frequency to the accuracy of their measurement. A trivial peak picking algorithm will determine line center to better than 10% of the line width. A more sophisticated algorithm, such as fitting the base line structure and line to a dispersion and a Gaussian line shape, will return the center frequency to better than 1% of the line width. Historically, microwave spectroscopy has utilized a highly accurate reference frequency to derive the absolute frequency of the signal absorbed by the molecules. However, the reference frequency can be calibrated to extremely high precision by making measurements of lines as long as it is stable in time. It is possible to implement a spectrometer without a locked reference or even without an electronic reference and still achieve frequency accuracy of better than 1 part in 10^7 [10]. However when unlocked, calibration becomes significantly more numerically intensive and signal averaging cannot be done without first calibrating and then re-gridding prior to averaging. For planetary application a frequency accuracy of about 1 part in 10^7 is sufficient and well in range of capability of temperature controlled crystal oscillators. Higher accuracy is better but only if the reference quality is free in terms of other system constraints.

The other major constraint on the synthesizer driving both the LO and the transmitter is that it does not blind the receiver with noise at the IF frequency. Generally this is not a problem as long as signal levels are maintained with significant margin above the noise. The dynamic range of a 10 dBm signal relative to thermal noise is 184 dBc/Hz. A 10 dB noise figure at the first step of amplification would reduce this to 174 dBc/Hz, which can in principle be preserved until the multiplication where the signal-to-noise degrades at least as fast as the conversion loss and in the case of other signals as 20 log(N) where N is the harmonic number. For the mixer to limit the system dynamic range, the carrier-to-noise ratio in the local oscillator and transmit signals must be better than in the mixer.

Several practical approaches can be applied. First is to saturate all amplifiers to effectively compress the amplifier noise. Second is to maintain large signal levels, never getting below a few dBm. Practically this means making sure the noise figure of the entire amplification chain is determined by the first amplifier.

B. Gas Handling

Gas handling is by definition separate from the problem of detection aside from the requirement that the sample must have at least the minimum absorption to be detected. The strength of the absorption is linearly proportional to the path length in the absorption cell. As a result longer sample cells allow for detection of lower concentrations. Unfortunately there is always a standing wave between the transmitter and the receiver doing the down conversion. This standing wave causes several significant problems. Most importantly it causes some fraction of the signal power to see a longer path length resulting in a direct error in the amplitude. Second it has a frequency dependent phase which results in an apparent distortion in power (a reason to modulate). If the path length is such that a standing wave period becomes close to the line width the system sensitivity is enormously degraded and no easy signal processing can retrieve the lost information. This results in a rule of thumb that the path length should at the

longest result in a standing wave period 10% of the line width. The worst case is at high frequency for a light molecule in a hot system. For example, NH_3 has a mass of 17 and a transition frequency of 572 GHz at 370 K, and it would have a full width at half maximum of 2 MHz. Applying the factor of 10 the system could tolerate a standing wave period of 20 MHz corresponding to a maximum tolerable path length of 15 meters. Longer is possible at lower frequencies and temperatures where the line widths are narrower.

Several gas collection strategies exist. The simplest is just to leak in the required amount of gas and then pump it out once the spectrum has been collected. If sensitivity is a problem a sorbate can be used to collect specific classes of molecules and the target molecules desorbed during filling. This makes it more challenging to determine absolute concentrations but it identifies the trace constituents. There are several considerations for the gas handling. Pumping is expensive in terms of power, and the smallest low power pumps have a finite lifetime. Thus, pumping should only be done when needed, requiring the absorption cell to be very vacuum tight. Another consideration is a strategy to keep previous fills of the cell from contaminating the current fill. Bake out heaters are effective in decontamination as is pure purge gas and pumping time.

C. Resources

The planetary application requires low power and very compact and light weight electronics as well as small volumes. These constraints are lifted in many other analytical chemistry applications. Limited data rates suggest that the ability to signal average and transmit only the resulting data is desirable. The other constraints push the design to use a phase locked oscillator and to focus on obtaining sufficient gain stability to not require rapid frequency switching.

Another obvious power saving consideration is to turn off the RF and detection electronics while gas handling operations are taking place. This will have the effect of averaging the power over the operation and will limit the maximum power. Realistically a complete *in situ* system could be implemented in less than 10 kg and would require less than 20 Watts. The details of the accommodation and other mission driven constraints could potentially have major implications to these values making the overall system architecture the single most important feature in saving mass and power.

D. Mixer and IF Amplifier

The best mixer is the one with the largest range between T system and T saturation, generally leading to a higher LO power implementation in a balanced configuration. Here the LO power requirement is increased but so is the compression point of the IF, while the noise temperature will be largely unaffected. Fundamental mixers generally have higher power levels at the right frequency so the IF compression sets in later as well as featuring slightly better noise temperatures.

The IF amplifier needs to comply with the usual receiver requirement of not dominating the system noise, but in this case the IF amplifier must also not compress on a macroscopic signal that can approach -15 dBm. As a result, linearity rather than ultimate noise figure is the more important selection consideration.

VI. Practical Considerations

A. Stability

Several important practical considerations must be made in optimizing the overall system. These include the choice of modulation, the averaging strategy and minimization of standing waves. The optimal choices depend on the RF system gain stability and the stability of the optical alignment. Dealing with the RF system gain stability is more challenging because gain changes can originate in local oscillator power level fluctuations, the mixer conversion efficiency, the transmitted power, the IF amplification gain or drifts in the digitizer. Like other radiometers temperature fluctuations are the major contributor to gain instability. If the temperature cannot be regulated or is expected to be highly variable, faster frequency sweeping and more regular transmit off pulses will be required for calibration. Sweeping the frequency fast enough will always make the impact of drifts on the scale of a line negligible even for highly unstable operational conditions. As a result, a very high quality system can be built even for conditions unsuitable for a radiometer, but this places a significant demand on the synthesizer performance. Any sweep rate that covers a line width at a frequency beyond the 1/f knee of the gain stability will achieve the desired end. Covering a line width at a frequency within the 1/f knee will degrade the performance. Allen times at representative operating conditions can be used to determine the 1/f knee.

B. LO and Transmit Hardware

A practical consideration is to utilize identical local oscillator and transmit hardware. This has a distinct cost and development complexity advantage, but it requires something close to -20 dB of the transmit signal not make it to the mixer to avoid saturation. The need for the loss significantly relaxes a number of optical throughput requirements and probably necessitates including additional optical loss in the system. The simplest implementation, unthinkable in other types of receivers, is to put an attenuator in front of the mixer signal port. The ideal implementation is to distribute the loss to minimize the standing waves in the system.

The challenge for the LO and transmit hardware is to have a relatively constant power over frequency. This will minimize the need to actively control bias parameters during measurements and will greatly simplify the control software. An obvious compromise can be made in accepting some LO power starvation at the mixer, since the system performance is only a weak function of T_{sys} as long as the IF compression is not dramatically reduced.

C. Optical Alignment

A second consideration is to assure that temperature does not change the alignment significantly and that the standing waves are at a small level. Several elements are highly desirable, first is to have separate RF and LO ports on the

mixer so that the LO can be injected through a waveguide eliminating LO alignment as a potential problem. The second consideration is to fabricate the entire optical system out of the same material, including the feed horns, sample cell and mirrors. If these are all hard mounted to a mechanical structure of the same material then alignment will be well preserved over temperature and there will be no dramatic changes in standing waves over temperature.

D. Optics

The excess transmit power affords many luxuries in the optical design. As such the critical aspect of the design must be a focused on minimization of standing waves over the entire frequency rather than optical throughput. Optical throughput should be traded for minimal standing waves in all cases. This means liberal use of aperture stops, not using all the mirror surfaces and introducing loss where advantageous. Unlike receiver signal paths which must use reflective optics, lenses in transmission may be used with no penalty as long as the surfaces do not cause standing waves. Since the RF system covers a significant fractional bandwidth it is highly desirable to design the optical system to be frequency independent. This requires designing the optics to take into account the constant radius of phase curvature in the feed horns rather than the usual beam properties which are frequency dependent. The bandwidth makes it difficult to use quarter wave plates, but the polarized nature of the source and detector make it possible to use the polarization as a means of standing wave control. The mechanical design should allow for optimization of standing waves before it is locked in place.

VII. Planetary System

The general design philosophy is to do as much of the signal processing as possible at frequencies below 20 GHz where high quality commercial components are available. The feasibility of this approach has been demonstrated in THz astronomy by the Heterodyne Instrument for Far Infrared (HIFI) [11] and in THz laboratory spectroscopy [12].

The basic building block for a planetary system would be to have two frequency channels implemented in a cross polarized configuration and launched into a common cell with a polarizing grid. The detection end would be accomplished in an identical way. The high frequency channel would cover the 530-630 GHz range while the low frequency channel would cover 225-330 GHz. The high frequency channel would be turned off when the common source is out of its frequency range. Software control would allow one or both channels to be operated simultaneously. A reference channel comprising the difference frequency multiplied by the correct harmonic number would be generated in common with the high frequency channel simply being the low frequency channel multiplied by two.

A synthesizer in the 12.5 to 18.4 GHz range with a 1 kHz step and a <1 ms switching time would drive the LO. The transmit signal would be derived by mixing the LO signal with a fixed oscillator used for the down conversion as well. It may prove advantageous to use the digital clock frequency for this purpose. The fundamental mixer would down convert to a MHz base band at approximately ¼ of the digitizer frequency, i.e. 32 MHz for a 16 bit 130 M sample per second digitizer collecting both the real and imaginary part over its Nyquist limited bandwidth.

From this point the signal would be digitally lock-in amplified increasing the number of significant bits to the desired level. One result for each sample point would be stored at the output. The scan strategy would be to integrate for 10 ms per point and signal average to the desired level. The gas cell could be a 5 meter long folded path avoiding beam overlap in a welded aluminum box with one wedged window for the beam entrance and exit. The total volume of the cell would be about 2 liters. Pumping would be accomplished with redundant micro turbo pumps similar to those designed for the Sample Analysis at Mars instrument suite on the Mars Science Lander. A molecular drag pump could serve as the backing pump.

One electronics board would provide the conditioned power, a second board would control all the bias lines, valves and pumps while the third would analyze the data and log the results as well as communicate with the rest of the instrument system.

An expected sensitivity calculation can be done assuming a mixer IF compression level of 5 μW at 300 GHz and 2 μW at 600 GHz and a conversion loss of 10 dB at 300 GHz and 13 dB at 600 GHz. Assuming a factor of two loss for standing wave, and instability and a 90% integration efficiency the signal-to-noise ratio at 300 GHz would be 1.1×10^6 in the 10 ms integration and 7×10^5 at 600 GHz. Assuming a 1 kHz step at the synthesizer, the step size at 300 GHz would be 18 kHz and 36 kHz at 600 GHz. The 300 GHz channel would cover 5.9 GHz per hour while the 600 GHz system would double this. In 10 ms at 300 K, HCN at 265.8 GHz could be detected at 4.5 parts per billion of the 10 mTorr sample. NH_3 at 572 GHz could be detected under the same conditions at 51 parts per billion. The detection sensitivity will improve at the square root of integration time. All of this is prior to any attempt to concentrate gas constituents or signal average.

VIII. Conclusions

Sophisticated and extremely sensitive gas analysis systems can now be constructed and calibrated thanks to a number of THz developments originally for heterodyne local oscillator development. Application of submillimeter technology promises to make a new generation of analytical chemistry instruments possible for planetary exploration as well as for applications in terrestrial chemical detection and identification. The chemical specificity is unparalleled due to the resolution of the rotational spectroscopic technique. Additionally, many more orders of magnitude in sensitivity can be obtained by using concentration techniques, potentially making this a valuable tool in civil defense and environmental regulation enforcement.

REFERENCES

[1] W. Gordy, "Microwave Spectroscopy," Reviews of Modern Physics 20, 1948, pp. 668-717.

[2] C.H Townes and A.L. Schawlow, *Microwave Spectroscopy*, New York, McGraw-Hill, 1955.

[3] L.I. Schiff, *Quantum Mechanics3rd Ed.*, New York, McGraw-Hill, 1949.

[4] W. Gordy and R.L. Cook, *Microwave Molecular Spectroscopy*, New York, John Wiley and Sons, 1984.

[5] J.C. Pearson, K. Cooper, and B.J. Drouin, "Spectroscopic Detection, Fundamental Limits and System Considerations," IEEE MTTs Proceedings of IRMMW-THz 2008, 2008, paper M3B2.

[6] C.H. Townes and S. Geschwind "Limiting Sensitivity of a Microwave Spectrometer" J. Appl. Phys. 19, 1948, pp. 795-796

[7] A. Levanon, *Radar Principles*. Toronto: Wiley-Interscience, 1988.

[8] R.B. Dybdal, "Radar cross section measurements," Proc. IEEE 75 (4), 1987, pp. 498-516.

[9] E.R. Brown, "Fundamentals of Terrestrial Millimeter-Wave and THz Remote Sensing," in Terahertz Sensing Technology Volume II: Emerging Scientific Applications and Novel Device Concepts, D. L. Woolard, W.R. Loerop, and M. S. Shur, Eds, Singapore: World Sci., 2003.

[10] D.T. Petkie, T.M. Goyette, R.P.A. Bettens, S.P. Belov, S. Albert, P. Helminger and F.C. De Lucia, "A Fast Scan Submillimeter Technique," Rev. Sci. Instrument. 68, 1997, pp1675-1683.

[11] J. Pearson, R. Guesten, T. Klein, and N. D. Whyborn, "Local Oscillator System for the Heterodyne Instrument for FIRST (HIFI)," *Proceedings of SPIE* **4013**, 2000, pp. 264-274.

[12] B.J. Drouin, F.W. Maiwald, and J.C. Pearson, "Application of Cascaded Frequency Multiplication to Microwave Spectroscopy," Rev. Sci. Instrum. 76, 2005, 093113.

Ultra-Gaussian Horns for ClOVER – a B-Mode CMB Experiment

P.A. Ade[1], R.J.Wylde,[2,3*] and J.Zhang[1]
1 School of Physics and Astronomy, Cardiff University, The Parade, Cardiff, CF24 3AA, U.K.
2 School of Physics and Astronomy North Haugh, St Andrews, Fife KY16 9SS, UK and
3 Thomas Keating Ltd, Station Mills, Billingshurst, West Sussex, RH14 9SH, UK

* Contact: r.wylde@terahertz.co.uk, phone ++44-1403782045

Abstract — **ClOVER is a UK funded experiment to be based in the Atacama Desert to measure the B-mode polarization of the Cosmic Microwave background between multipoles of 20 and 1000 down to foreground limited sensitivities. One of two telescopes will operate large focal plate arrays at 150 and 225 GHz, using TES bolometers.**

The feeds to these bolometers utilise corrugated horns with novel features which meet with two important performance requirements: very low sidelobes, to avoid uncontrolled signal contamination and high pass filtering to control the fields presented to the Radial Probe detectors.

The former is provide by a design, developed by Graham Smith in St.Andrews, to deliberately excite HE12 higher order modes in a sine-square profile section of the horn, followed by an extended parallel section designed to bring the HE12 mode into phase with the dominate HE11 mode. Surprisingly wide bandwidths – at the 30% level - with sidelobes well below minus 35dB are achieved. Analysis shows that close to 99.88% of the transmitted power (in a time reversed view) is in the fundamental Gaussian free space mode – hence the term, Ultra-Gaussian horn.

The later is provide by a filter section close to the transition into the detector module. The suppression of leaks well below the nominal HE11 cut-off provided an interesting computational and experimental challenge, requiring significant modelling effort in both HFSS and more traditional Mode Matching programs.

Special attention has been applied to the production engineering of these horns – given budgetary constraints and the large number required (100 in each band)

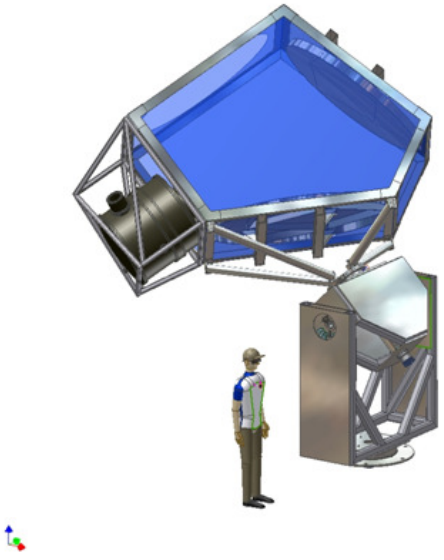

An image of the telescope with the horns places inside the black cryostat (Middle left of picture)

Introduction

ClOVER [1] is a UK funded experiment to be based in the Atacama Desert to measure the B-mode polarization of the Cosmic Microwave background between multipoles of 20 and 1000 down to foreground limited sensitivities. One of two telescopes will operate large focal plane arrays at 150 and 225 GHz, using a 4-probe Ortho-Mode Transducer (OMT) in circular waveguide with outboard TES bolometers to simultaneously detect the orthogonal polarizations.

Clover Horns

The form of a 150 GHz ClOVER focal plane module is shown in the two images below, indicating how a set of 8 closely packed horns are assembled to feed the 4-probe device which is supported on a silicon nitride membrane across the circular guide. A backshort behind the membrane enhances the probe absorption efficiency. Detail of the backshort design is presented in [2].

The horns mandrels are made on a modified Harding SuperPrecision lathe, and electroformed using a space-qualified process. To control costs, the outside form of the horn has been kept as simple as possible, allowing alignment to be provided by the assembly.

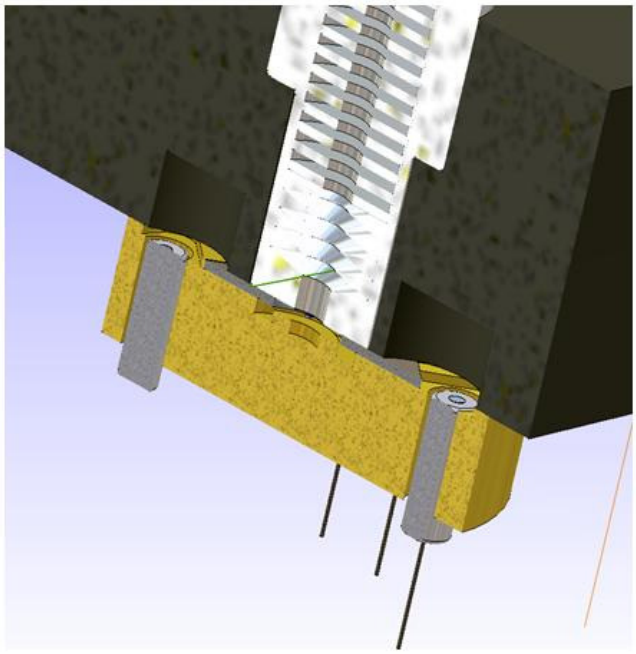

Sidelobes

A B-mode experiment requires critical control of the beam on the sky as any power contribution from strong polarized sources in the sidelobes will contamination the primeval signal. The cleanliness of the feed system is thus a crucial part of the design.

Traditionally, corrugated horns have be used for this task as they provide axially symmetric patterns over the wide spectral bandwidth needed for detection of the weak B-mode signature - but their sidelobes are typically at the –25 dB level.

Recently however, Graham Smith of St. Andrews University, devised a way of deliberately adding a HE12 component to the standard HE11 mode formed at the throat of a corrugated horn and then - with a phasing section - allowing the two modes to come into phase [3]. In principle it is possible to move from having 98% of the power in the fundamental mode in a standard corrugated horn to something like 99.88%.

This is the approach that we have taken for the ClOVER horns. The form of the horn is shown below, with a cosine squared profile to generate the appropriate amount of HE12 mode and then a phasing section to bring this mode into phase with the HE11 fundamental mode.

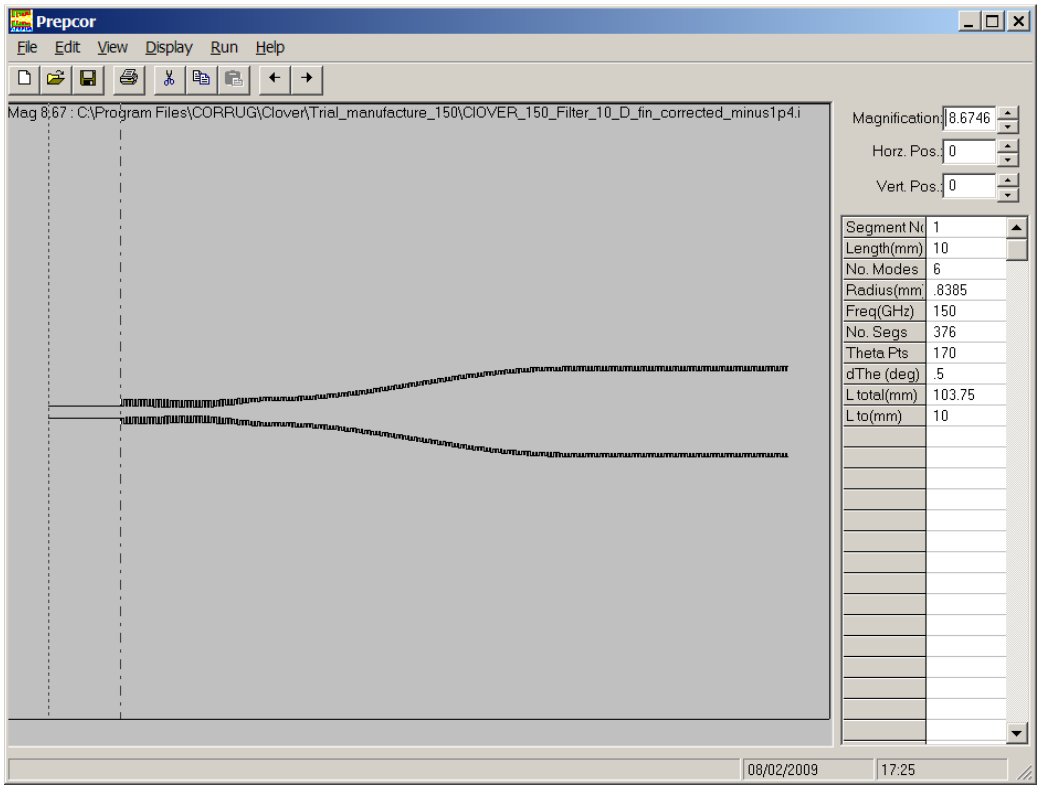

In this cross section, the profile section generated the HE12 mode, and the parallel section brings it into phase with the HE11 mode

Soe Min Tun of SMT Ltd has devised an addition to his CORRUG mode matching program to help us design such "Ultra-Gaussian" horns by providing amplitude and phase of the HE1n and EH1m mode sets, to allow computational adjustments to be made.

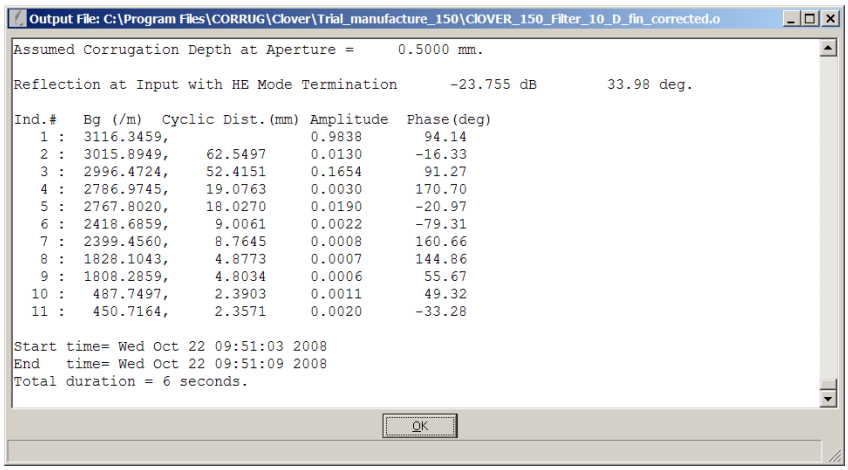

At the practical level one simply modifies the length of the cosine-square form to give the amplitude of HE12 mode desired and then adjusts the length of the parallel section to bring the modes into phase.

Performing this analysis over the wide band of frequencies detected, has shown that this technique is much more insensitive to changes in frequency than, for instance, Potter or Picket horns – which also rely upon the generation of higher order smooth wall modes to improve the antenna pattern.

The outcome of this analysis can be seen in the following plots of E& H pattern measurements made on a set of ClOVER horns at the middle and band edge frequencies. The black dots are the CORRUG mode matching predictions, and provide ample proof that both the analysis and construction of the horn are working well.

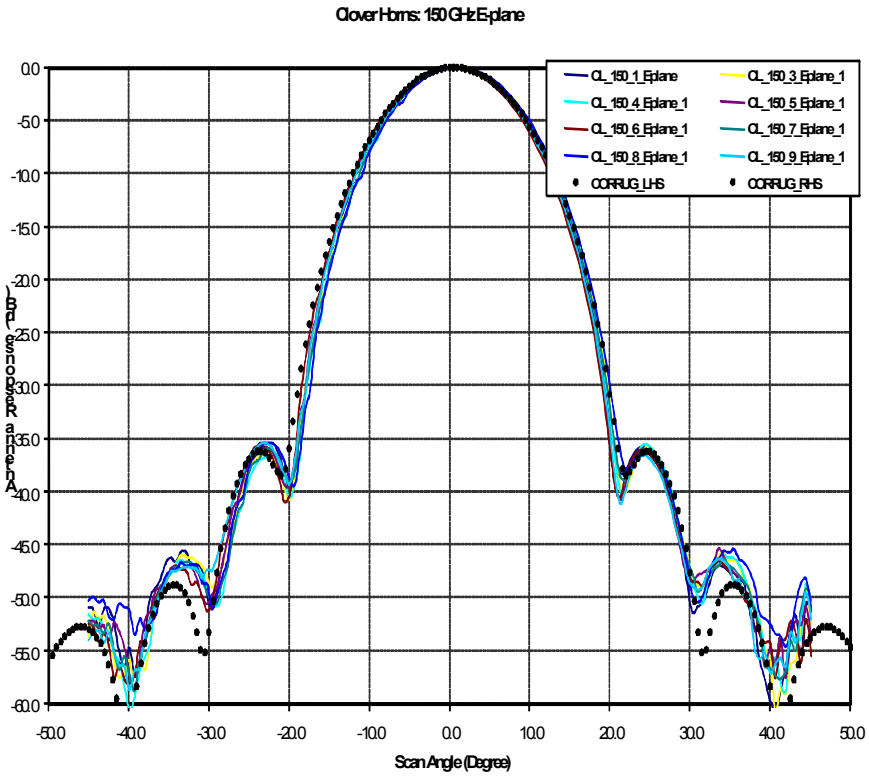
Clover Horns: 150 GHz E-plane
CL_150_1_Eplane
CL_150_3_Eplane_1
CL_150_4_Eplane_1
CL_150_5_Eplane_1
CL_150_6_Eplane_1
CL_150_7_Eplane_1
CL_150_8_Eplane_1
CL_150_9_Eplane_1
CORRUG_LHS
CORRUG_RHS
Response (dB)
Scan Angle (Degree)

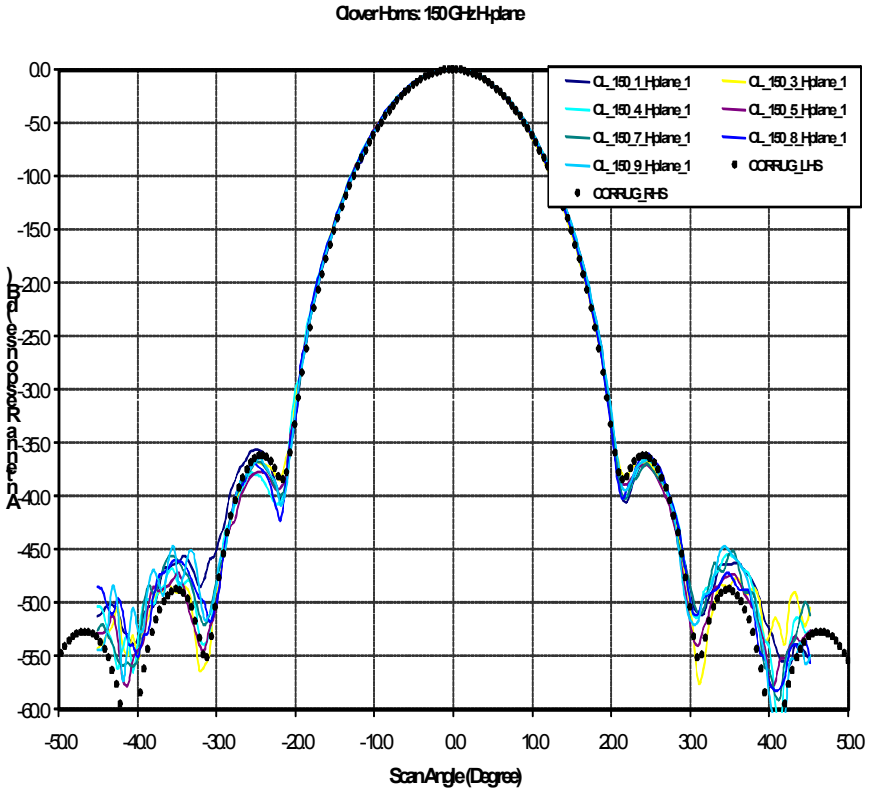
Clover Horns: 150 GHz H-plane
CL_150_1_Hplane_1
CL_150_3_Hplane_1
CL_150_4_Hplane_1
CL_150_5_Hplane_1
CL_150_7_Hplane_1
CL_150_8_Hplane_1
CL_150_9_Hplane_1
CORRUG_LHS
CORRUG_RHS
Response (dB)
Scan Angle (Degree)

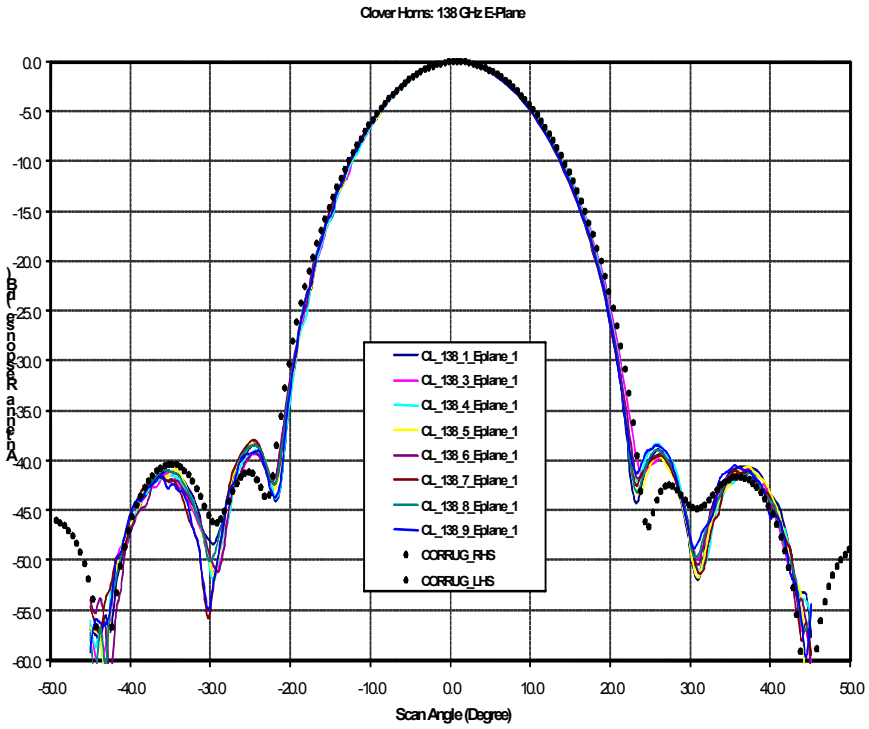
Clover Horns: 138 GHz E-Plane
Normalized Response (dB)
Scan Angle (Degree)
CL_138_1_Eplane_1
CL_138_3_Eplane_1
CL_138_4_Eplane_1
CL_138_5_Eplane_1
CL_138_6_Eplane_1
CL_138_7_Eplane_1
CL_138_8_Eplane_1
CL_138_9_Eplane_1
CORRUG_RHS
CORRUG_LHS

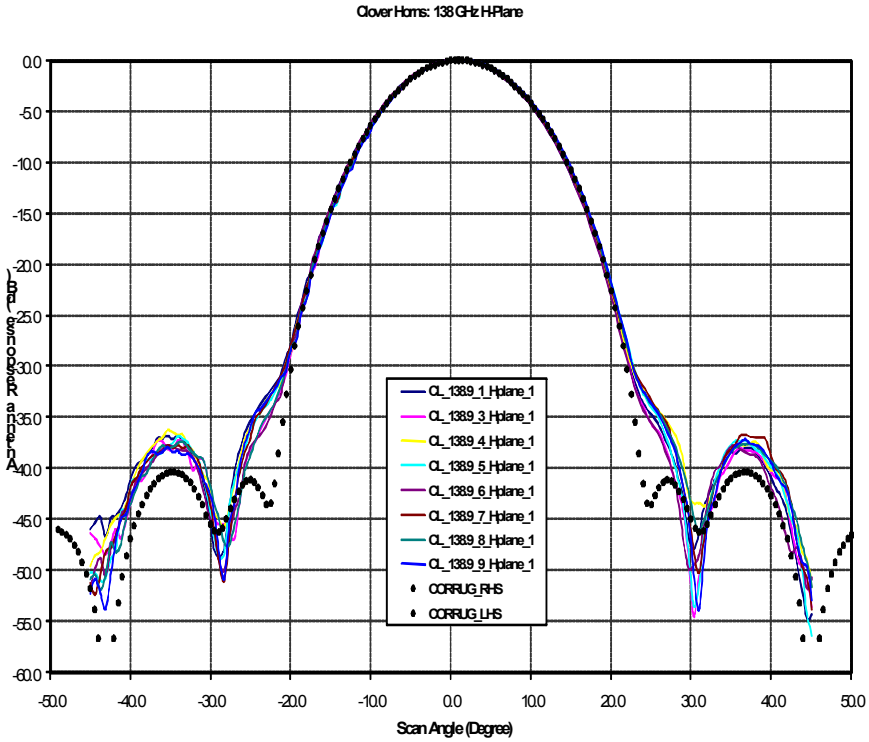
Clover Horns: 138 GHz H-Plane
Normalized Response (dB)
Scan Angle (Degree)
CL_1389_1_Hplane_1
CL_1389_3_Hplane_1
CL_1389_4_Hplane_1
CL_1389_5_Hplane_1
CL_1389_6_Hplane_1
CL_1389_7_Hplane_1
CL_1389_8_Hplane_1
CL_1389_9_Hplane_1
CORRUG_RHS
CORRUG_LHS

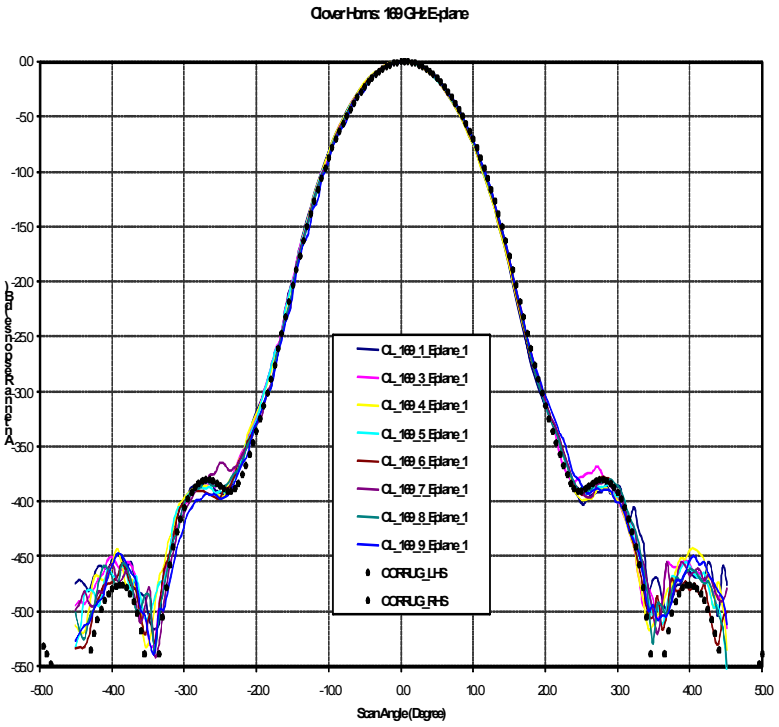
Clover Horns: 169 GHz E-plane
Response (dB)
Scan Angle (Degree)
CL_169_1_Eplane_1
CL_169_3_Eplane_1
CL_169_4_Eplane_1
CL_169_5_Eplane_1
CL_169_6_Eplane_1
CL_169_7_Eplane_1
CL_169_8_Eplane_1
CL_169_9_Eplane_1
CORRUG_LHS
CORRUG_RHS

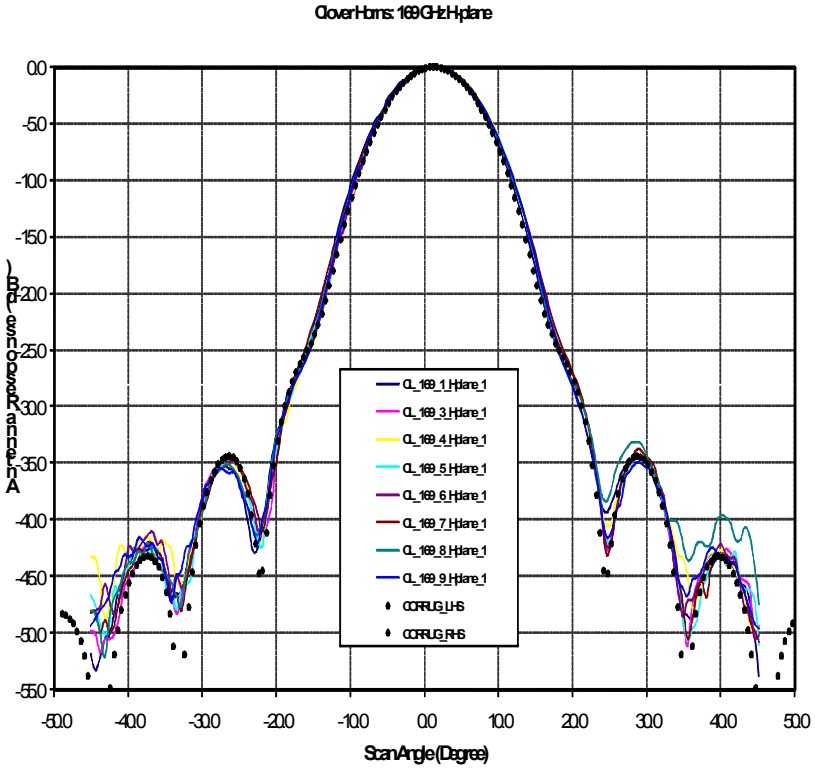
Clover Horns: 169 GHz H-plane
Response (dB)
Scan Angle (Degree)
CL_169_1_Hplane_1
CL_169_3_Hplane_1
CL_169_4_Hplane_1
CL_169_5_Hplane_1
CL_169_6_Hplane_1
CL_169_7_Hplane_1
CL_169_8_Hplane_1
CL_169_9_Hplane_1
CORRUG_LHS
CORRUG_RHS

Filtering

In addition to the low-sidelobe patterns, the horns also need to provide a high pass cut on to the detectors. The presence of a section of parallel guide - see in this expanded section of the horn - provide the cutoff.

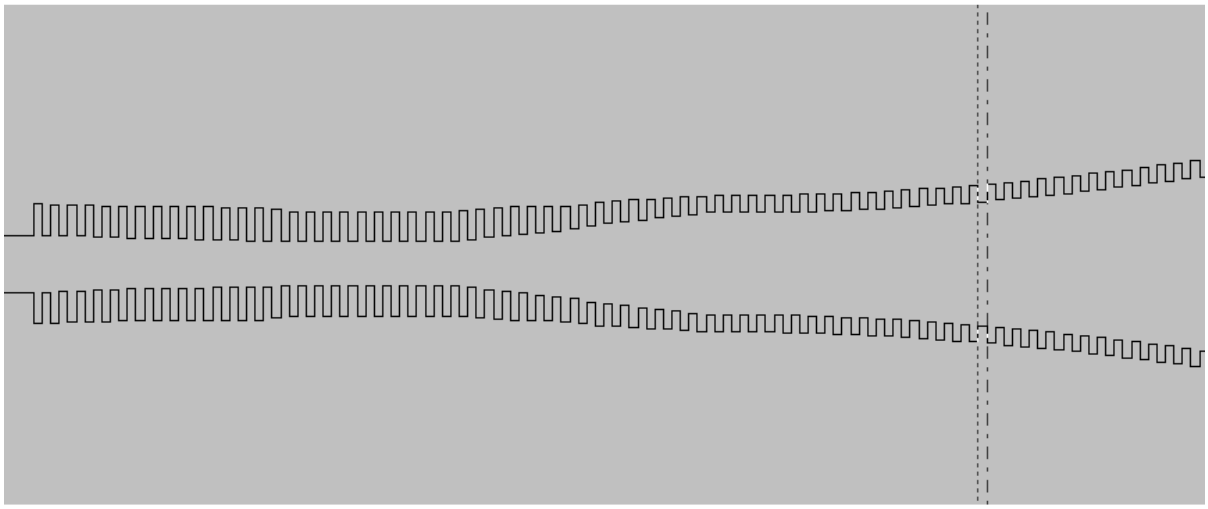

It turns out that the filtering action of HE11 guides is not a simple as one might expect. The dispersion curves for the structure are complex, and not at all intuitive. As other have found out [4], one can suffer leaks, often associated with slow wave propagation, at frequencies well below the nominal cut on.

We have used both HFSS and CORRUG to model the leakage below the cutoff band. The plot below gives details of the modeling results, showing the unwanted leakage around 110 GHz.

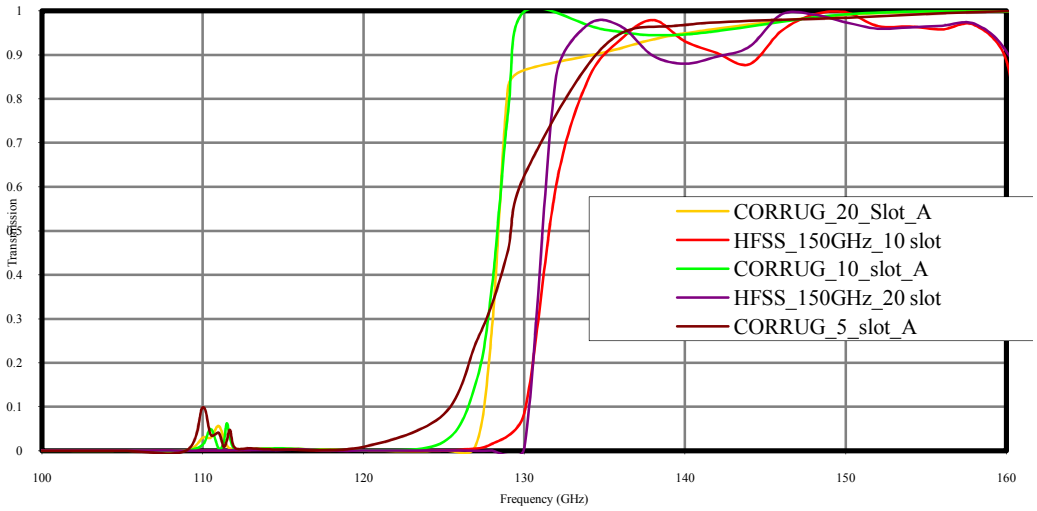

CORRUG and HFSS modeled Transmission from 100 to 160 GHz (3.33 to 5.33 wave numbers)

Filter sections of 5,10 and 20 slot were examined following a very careful heuristic design of the transition in and out of the filter section, with 10 slots proving to be sufficient. A set of trial horns was placed in the optical path of a long wavelength spectrometer to determine the spectral nature of the high frequency cut-on. As the presence of the horns modifies the optical matching to the spectrometer, the precise level of transmission is not important. These data show that the cut-on is occurring at the desired frequency and that low frequency leaks are absent.

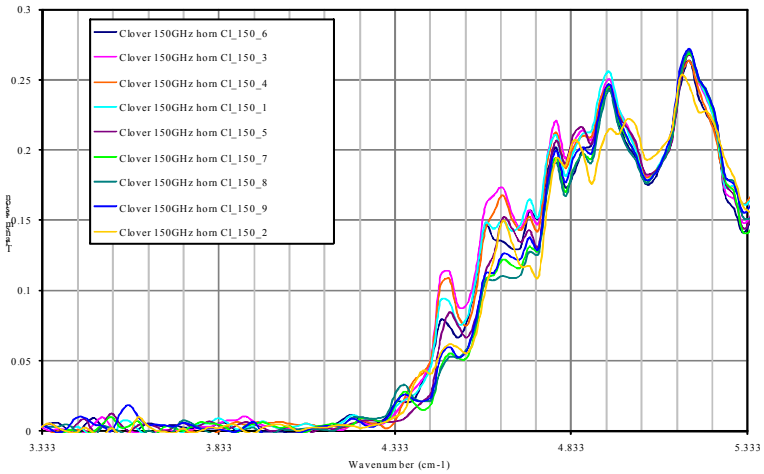

Measured Transmission from 3.33 to 5.33 wave numbers (100 to 160 GHz)

Conclusions

The design of corrugated horns had been though of as a mature technology, but these ClOVER horns employ some unexpected new developments[1] to give the required sidelobes for CMB measurements. Though careful modeling, problems associated with sub-band leakage though the filtering section have been overcome.

References

[1] Clover – Measuring the CMB B-mode polarization. C.E.North et al. 18th Int. Symp on Space Terahertz Technology, Pasadena, California, USA
[2] "Clover Polarimetric Detector - A Novel Design of an Ortho-Mode Transducer at 150 and 225 GHz". Mauskopf P., Zhang J., Ade P.A.R., Withington S., Grime P., Progress In Electromagnetics Research Symposium, 24th-28th March 2008, Hangzhou, China.
[3] "Reducing Standing waves in Quasi-optical Systems by Optimal Feedhorn Design". Paul A.S. Cruickshank, David R. Bolton, Duncan A. Robertson, Richard J. Wylde and Graham M. Smith, in Digest of IRMMW-THz2007 conference, Cardiff 2007, Volume 2 pp941-942
[4] "Corrugated waveguide band edge filters for CMB experiments in the far infrared" E.Gleeson, J.A.Murphy, D.Maffei, W.Lanigan, J.Brossard, G.Cahill, E.Cartwright, S.E.Church, J.Hinderks, E.Kirby, C.O 'Sullivan in Infrared Physics and Technology 46 (2005) 493-505

[1] It turn out that similar mode sets – with high levels of HE12 modes - were used in the Planck HFI horns, but without a proper understanding of the process which gave rise to the good sidelobes performance

Session W1

Schottky Mixers & Detectors

Chair: Heinz-Wilhelm Hübers

Wednesday, April 22
9:20 – 10:20

W1A

Broadband Schottky Receivers for Atmospheric Studies

K. Hui, J.L. Hesler, and T.W. Crowe*
Virginia Diodes, Inc., Charlottesville, VA 22902
* Contact: Crowe (a) VADiodes.com, phone (434)297-3257

***Abstract*—Microwave limb sounding of the Earth's atmosphere is well developed as a means to gain greater understanding of atmospheric chemistry; particularly with regard to ozone depletion and greenhouse warming. More recently scientists have considered long-duration missions to study the atmospheres of other planets, particularly Venus and Mars, as well as the atmospheres of the major moons of the gas giant planets. Of particular interest is the proposed Vesper mission to Venus which would use heterodyne receivers in the frequency band from about 440-590GHz. Schottky receivers are ideal for such a mission because they achieve the required sensitivity without any need for cooling and can be easily tuned across very significant frequency bands. Through a NASA SBIR project (Contract NNX09CA57C), VDI is developing an improved mixer technology that would be optimal for Vesper and other similar missions. Specifically, VDI is striving to simplify the Vesper receiver through the development Schottky receivers that can be tuned across the entire waveguide band without any mechanical or bias adjustments. For Vesper VDI proposes the use of a subharmonically pumped mixer that operates in the WR-1.9 waveguide band (400-600GHz). This mixer requires no bias and the Phase 1 study has shown that excellent sensitivity (Tmix ~ 1,000-2,000K, DSB) can be achieved across a very broad frequency band with only 1-2mW of LO power. In Phase 2 VDI will co-design the mixer and LO multipliers to achieve a receiver system that allows tuning of the LO frequency across the required Vesper band with no adjustments other than the frequency of the input oscillator, while maintaining the sensitivity noted above and potentially reducing the required LO power level. The presentation will review that performance of this mixer design, with emphasis on the work being done to achieve full waveguide band performance and discussion of the development of the LO oscillator chain.**

Sub-millimeter wave MMIC Schottky sub-harmonic mixer testing at passive cooling temperatures

B. Thomas, E. Schlecht, A. Maestrini, J. Ward, G. Chattopadhyay, R. Lin, J. Gill, C. Lee, and I. Mehdi

Abstract— **We report on the development of a cryogenic test bench for millimetre, sub-millimeter and terahertz MMIC Schottky mixers. The test set-up is used to measure an 874 GHz MMIC membrane sub-harmonic mixers at 300 and 120 K of ambient temperature, in vacuum environment. When cooled to temperatures compatible with passive cooling in space (120 K range), a DSB receiver noise temperature of approx. 3500 K with best value at 3000 K is obtained in the frequency range 850-910 GHz. Based on the latter topology, sub-harmonic mixer design has been extended up to 2 THz. It uses a novel custom Schottky electrical Schottky model compatible with ADS software suite to take into account effects related to the plasma resonance in doped GaAs at terahertz frequencies. Predicted performance is presented for room temperature operation.**

***Index Terms*— cryogenic test setup, terahertz frequencies, MMIC membrane Schottky sub-harmonic mixer, modeling.**

I. INTRODUCTION

The sub-millimeter wave and terahertz frequency range is rich in emission and absorption lines of various molecular species whose detection and mapping are important to understand the atmospheric circulation of planets. For instance, methane (CH4), carbon monoxide (CO), HCN and CS have strong spectral signatures lying in the range between 1 and 2.2 THz [1]. Schottky diode based heterodyne instruments have demonstrated high sensitivity and high spectral resolution up to 2.5 THz while operating at room temperature. Sub-millimeter wave heterodyne instruments that use such devices are envisaged for future atmospheric remote sensing instruments onboard several proposed missions such as LAPLACE, TANDEM (ESA/NASA candidate missions to outer planets) for Jupiter and Saturn [2], as well as future Mars/Venus missions. Moreover, future Earth observation missions dedicated to the monitoring of ice clouds in the troposphere/stratosphere could use frequency channels operating as high as 874 GHz, giving valuable information on the ice cloud particles size and their spatial distribution [3].

In that context, we report on the current status of development of MMIC Schottky diode sub-harmonic mixers from 0.5 THz up to 2 THz. First, a sub-millimeter wave sub-harmonic mixers centered at 874 GHz has been tested at room (295 K) and cryogenic (120 K) temperatures. For this purpose, a robust cryogenic test set-up for Schottky mixers has been developed and is presented hereafter. The amount of improvement that can be obtained by cooling it to temperatures compatible with passive cooling in space (approx. 120 K) has been quantified and is also presented.

Following the development of this prototype, the design of MMIC Schottky sub-harmonic mixers has been extended to cover various bands within the 1-2 THz range. In order to take into account some electrical effects which might be of importance at THz frequencies such as the displacement capacitance and carrier inertia, a custom electrical model of the Schottky Barrier has been developed and incorporated into the ADS software by the mean of a Symbolically Defined Device (SDD). Predicted performances give best DSB mixer conversion losses between 10 and 15 dB and DSB noise temperature between 2500 K and 5000 K at room temperature from 1 to 2 THz. When operated in the 120 K temperature range, the receiver noise temperature is expected to drop by a factor of 2.

II. CRYOGENIC TEST SETUP FOR SCHOTTKY MIXER TESTING

In order to perform measurements on sub-millimeter wave sub-harmonic mixers at room and cryogenic temperatures, a cryogenic test bench has been developed and is presented here. The test bench includes a vacuum cryogenic chamber connected to a vacuum pump and a cryo-cooler head, liquid nitrogen external Dewar, various DC/IF and RF vacuum feedthrough connectors, couple of vacuum windows, and internal hot/cold loads and chopper blade. An external and internal view of the cryogenic test set-up is presented in Fig.1 and Fig. 2 respectively.

To generate the LO signal, a commercial synthesizer followed by an active sextupler and a series of power-combined W-band amplifier chain is used to produce more than 150 mW in W-band. This powerful signal is then fed into the cryogenic

Manuscript received 20 April 2009. This work was supported by the Jet Propulsion Laboratory, California Institute of Technology under contract from the National Aeronautics and Space Administration.

B. Thomas, E. Schlecht, J. Ward,G. Chattopadhyay, R. Lin, J. Gill, C. Lee and I. Mehdi are with the Jet Propulsion Laboratory, California Institute of Technology, under contract from the National Aeronautics and Space Administration, Pasadena, CA 91109 USA (phone: 818-393-5902; fax: 818-393-4683; e-mail: Bertrand.C.Thomas@jpl.nasa.gov). J. Ward is now with Raytheon Inc. Fort Wayne, Indiana, USA.

A. Maestrini is with the Observatoire de Paris, LERMA, Paris, 75014 France, (e-mail: a.maestrini@obspm.fr).

test chamber via a W-band flange vacuum feed-through to the following multipliers. The receiver front-end, composed of the multipliers and sub-harmonic mixer, is thermally connected to the cold 100 K stage of the test chamber and temperature controlled by a couple of 25 W heaters mounted on the bottom of the bracket. Above the front-end chain, a vacuum stepper motor and gold plated 2-blades chopper is suspended from the lid of the vacuum chamber to present alternatively a hot and cold load to the mixers' feed-horn antenna. The hot load sitting on the bottom of the test chamber is isolated thermally from the cold stage. The cold load inside the test chamber is connected thermally to a liquid nitrogen Dewar positioned outside the test chamber. This Dewar has a thermal vacuum feed-through specially designed to avoid breaking the vacuum inside the chamber while cooling the cold load. DC and IF signal are connected to bias boxes and an IF pre-amplifier outside the test chamber via DC/IF vacuum feedthroughs. Finally, a fully automated IF processor, including filters, power detectors, and a computer that records the signal levels and drive the stepper motor is used to measure the Y-factor of the receiver chain.

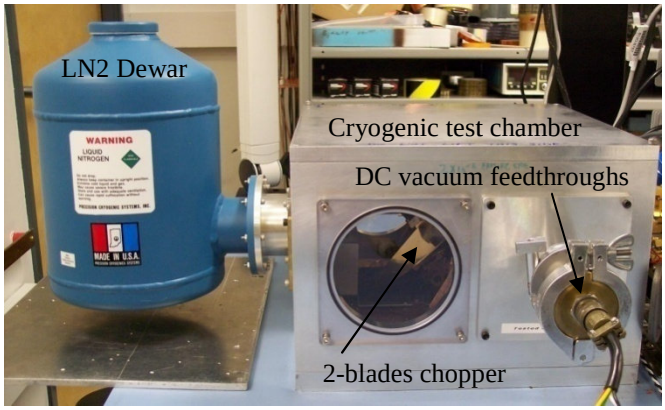

Fig.1. General view of the cryogenic test set-up used to characterize mixers at cryogenic temperatures (compatible with passive cooling in space).

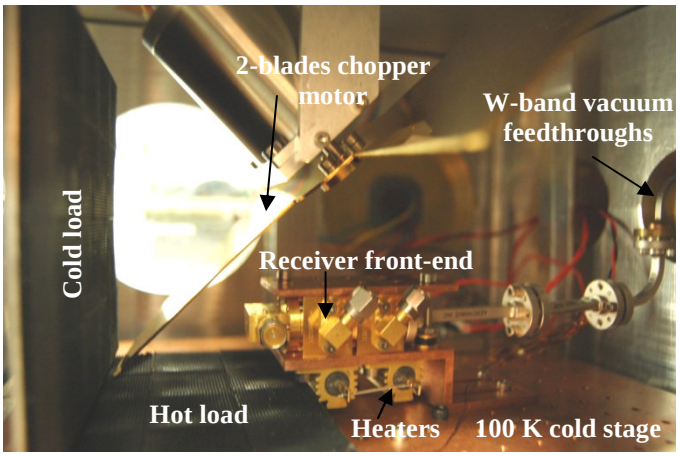

Fig. 2. Internal view of the cryogenic vacuum mixer test bench. The hot and cold calibration targets are inside the vacuum test chamber. The chopper blade is suspended from the 295 K lid inside the vacuum chamber. The cold target is thermally connected to an external liquid nitrogen Dewar shown in Fig. 1. The receiver front-end (multipliers and mixer) are attached to a copper bracket thermally connected to the 100 K stage of the chamber.

III. Cryogenic Testing of Sub-Millimeter MMIC Membrane Sub-Harmonic Mixer

An 874 GHz front-end chain has been tested. The Local Oscillator for the 874 GHz mixer is provided by either a 200 GHz doubler + 400 GHz doubler, or a 220 GHz tripler + 440 GHz doubler. A view of the 874 GHz front-end chain that includes both doublers and sub-harmonic mixer is shown in Fig. 3. Further details about the doublers design and performances can be found in [4], and for the sub-harmonic mixer in [5].

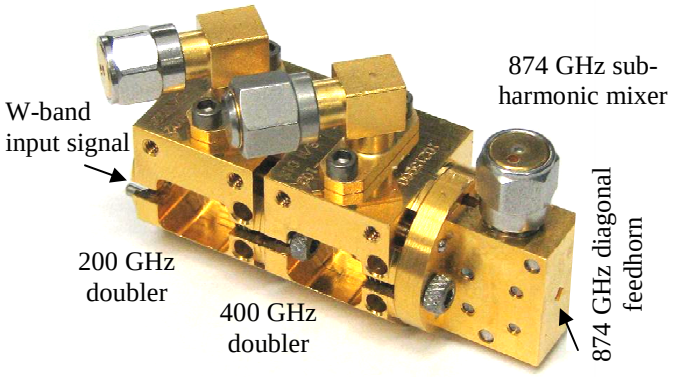

Fig.3. View of the 874 GHz receiver front-end, including a 200 GHz and 400 GHz doubler, and 820-910 GHz sub-harmonic mixer (on the right).

As indicated, several LO chains are required to cover the bandwidth of the 820-910 GHz sub-harmonic mixer, as the latter is unbiased and needs between 3 and 5 mW of input power in the 440 GHz range. As shown in Fig. 4, two chains are used to cover the 405-442 GHz frequency range when operating at room temperature. The output power was recorded with an Erickson calorimeter PM3 [6]. When cooled to 120 K, the tripler + doubler chain can output enough power to pump the mixer up to 450 GHz as shown in the next section.

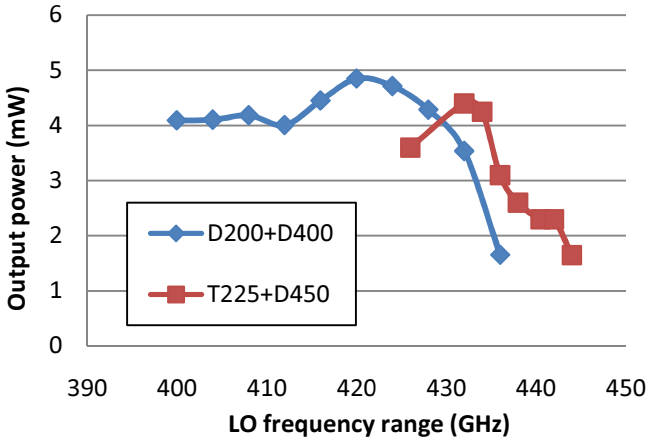

Fig.4. Output power of both LO chains used to drive the 874 GHz sub-harmonic mixer VS output frequency at room temperature. The 1st chain includes 200 GHz and 400 GHz doublers (blue diamonds), the 2nd 220 GHz tripler and 440 GHz doubler (red square).

A. Test results at 874 GHz

The DSB receiver noise temperature of the 874 GHz MMIC membrane sub-harmonic mixer for 295 K and 120 K of ambient temperatures is presented in Fig.5. As previously mentioned, it includes the contribution from the mixer, 1st LNA and IF processor chain. As shown in Fig. 5, at room temperature, the receiver noise temperature ranges from 4680 K to 6280 K from 840 GHz up to 885 GHz at room temperature (295 K). These values are consistent with independent measurements of the DSB mixer noise temperature ranging from 3000 K to 4000 K, with approx. 11.5 to 13 dB of estimated DSB conversion losses [5]. Above 885 GHz, the tripler + doubler LO chain does not give enough power at room temperature to reach optimal performance of the mixer, and receiver noise temperature degrades.

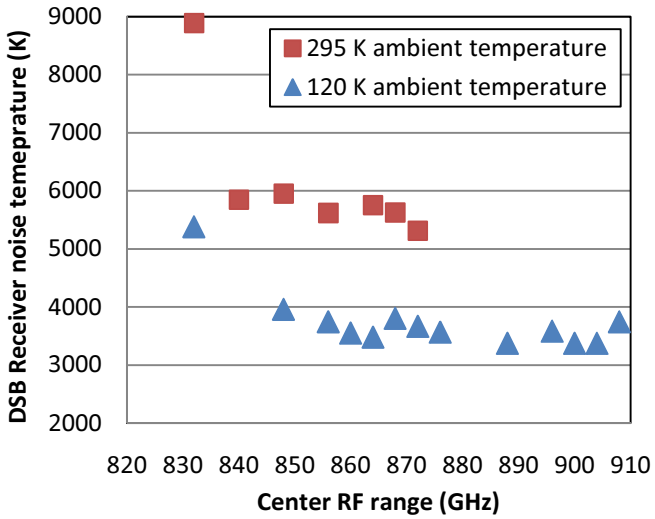

Fig.5. 295 K (red squares) and 120 K (blue triangles) ambient temperature performance of the 874 GHz receiver chain. The sub-harmonic mixer is located inside the cryogenic test chamber, whereas the 1st LNA is located outside and therefore always at room temperature.

When the mixer is physically cooled to 120 K, the DSB receiver noise temperature drops down in the 3000 K to 4000 K range. If the conversion losses are assumed to remain similar at about 11.5-13 dB while cooling, the resulting DSB mixer noise temperature drops from 4000 K to about 2500 K, giving an improvement in the DSB mixer noise temperature close to 2 dB as previously reported [7]. At 80 K of physical temperature, the best DSB receiver noise temperature measured was 3000 K at 888 GHz central RF range.

Further measurements are on-going to characterize accurately the DSB mixer noise temperature and DSB conversion losses in this frequency range *VS* operating temperature.

IV. Custom Schottky Diode Model for Terahertz Frequencies using Symbolically Defined Devices

At terahertz frequencies, several studies have shown that high frequency effects associated with plasma resonance in the doped GaAs epi-layer material can influence the performance of the mixer and therefore has to be included in the electrical model of the Schottky diode [8][9]. The standard ADS software suite (from Agilent [10]) model of the Schottky barrier does not include effects such as displacement capacitance, carrier inertia, and capacitance-voltage behavior above flat-band. Furthermore, the standard ADS Schottky noise model does not consider the heating of the electrons when passing through the Schottky barrier. We present here two complementary electrical models of the Schottky diode, one used to compute the conversion losses at terahertz frequencies, the other used to predict more accurately noise performances at room temperature. A schematic view of the custom SDD Schottky model and standard ADS Schottky model with improved noise model are shown in Fig. 6a&b.

First, a custom ADS electrical model of the Schottky barrier that uses the Symbolically Defined Devices (SDD) toolbox has been developed specifically for the prediction of conversion losses and optimal embedding impedances necessary to accurately design MMIC Schottky mixers at terahertz frequencies. This custom SDD electrical model is presented in Fig. 6a. It also includes modified C/V equations above flat-band [11]. This part of the SDD model has been validated on a broadband 170-205 GHz MMIC frequency doubler [12]. The SDD model also includes a non-linear capacitance from the contribution of the displacement capacitance and a non-linear inductance from the contribution of the carrier inertia [8]. It is believed that these effects play an increasing important role when the frequency of operation of Schottky devices is getting closer to the plasma resonance of doped GaAs. Simulation results on terahertz sub-harmonic mixers presented in the next section seem to confirm this assumption. Finally, the I/V equation defined in the SDD is similar to the one used in the standard ADS Schottky model.

Second, a custom noise model of the Schottky barrier that approximates the effect of hot electron noise in addition to the standard shot and thermal noise embedded in the ADS Schottky diode model has already been reported [13] and is used here. A schematic drawing of this Schottky noise model is presented in Fig. 6b. In order to compute the total mixer noise temperature using ADS, a first simulation of the mixer circuit including the standard ADS Schottky model is performed to determine the harmonic LO currents passing through the diode. In a second step, an external noise source proportional to the sum of the square of the harmonic LO currents is added in series to the Schottky diode model, and the mixer noise temperature is computed. This model has been validated on a 330 GHz sub-harmonic mixer using an anti-parallel pair of planar Schottky diode [14]. This model is used to predict mixer noise performances at terahertz frequencies, as shown in the next paragraph.

Unfortunately, until now, it is not possible to use an SDD to predict noise performance with ADS, and therefore have one single custom Schottky model for conversion losses and noise temperature at the same time. Therefore, two separate models are still needed so far. Moreover, only room temperature noise predictions are believed to be relevant as harmonic currents change at cryogenic temperature and therefore affect the shot and hot electron noise generation. Further development of the model will therefore include a temperature dependent I/V curve for cryogenic operation.

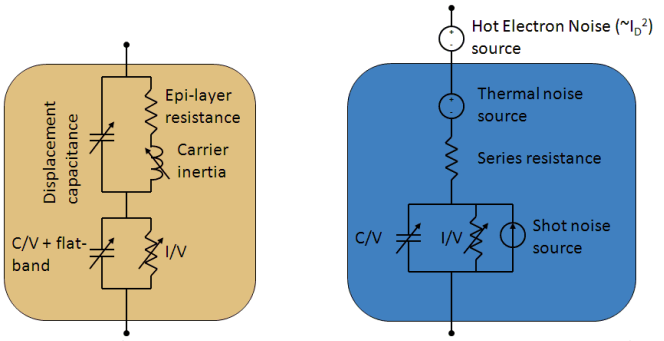

Fig. 6a&b. Left: custom ADS Schottky model that uses Symbolically Defined Device (SDD) for operation above 1 THz. Right: standard ADS Schottky electrical and noise model with enhanced Hot Electron Noise model (top).

V. Design of Terahertz MMIC Biasable Sub-Harmonic Mixers in the 1-2 THz Range

The design of 1-2 THz MMIC sub-harmonic biasable mixers based on the successful 874 GHz mixer topology [5] is presented here. Four different devices have been designed to cover respectively the following bands: 0.93-1.1 THz, 1.1-1.3 THz, 1.35-1.5 THz and 1.75-2 THz. A generic version of the mixers' architecture is shown in Fig. 7. As previously, both Schottky diodes on the circuit are in a balanced configuration. A MIM chip capacitor integrated to the circuit allows to forward bias the diodes and therefore reduce the amount of LO power required which is desirable especially at the high end of the LO frequency range (1 THz). The devices that use a thin GaAs membrane (typ. few microns thick) are suspended inside the cross-channel between the LO and RF waveguides using four grounded beamleads, and connected to an IF output circuit using a fifth beamlead.

The predicted performances for ambient temperature operation are shown in Fig. 8&9. In addition to the four circuits mentioned above, the predicted performance of the 810-910 GHz sub-harmonic mixer tested previously is also given for comparison. The conversion losses are calculated using the Harmonic Balance code of ADS.

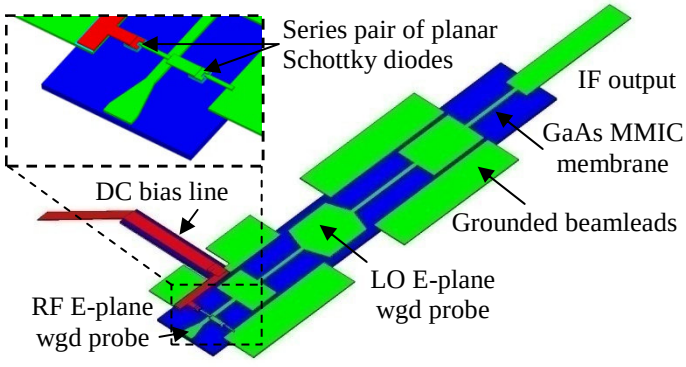

Fig.7. Isometric view of a generic MMIC membrane biasable sub-harmonic mixer chip. The chip is further "scaled" for various frequency ranges: 0.9-1.1 THz, 1.1-1.3 THz, 1.35-1.5 THz and 1.75-2 THz.

A series resistance in the range 20 to 25 Ω depending on the circuit is assumed, with an ideality factor of 1.3, and built-in potential of 0.8 V. The IF frequency and impedance are set to 5 GHz and 100 Ω respectively.

For the DSB conversion losses, Fig. 8a&b shows the simulation results for the custom SDD Schottky models (as presented in Fig. 6a), for both unbiased (see Fig. 8a) and biased (see Fig. 8b) configurations. For the un-biased configuration, an LO input power of 4 mW is assumed for the circuits up to 1.5 THz, and 6 mW is assumed for the 1.75-2 THz one. For the biased configuration, an LO power of 1.5 mW at half the RF frequency, and a bias voltage of 1V for both diodes in series is assumed. To predict the DSB mixer noise temperature at room temperature, only the standard ADS Schottky diode noise model enhanced with Hot Electron Noise source is used (see Fig. 6b). Fig. 9a shows the DSB mixer noise temperature for un-biased configuration, and Fig. 9b for the biased configuration, with similar LO power and DC bias values as before.

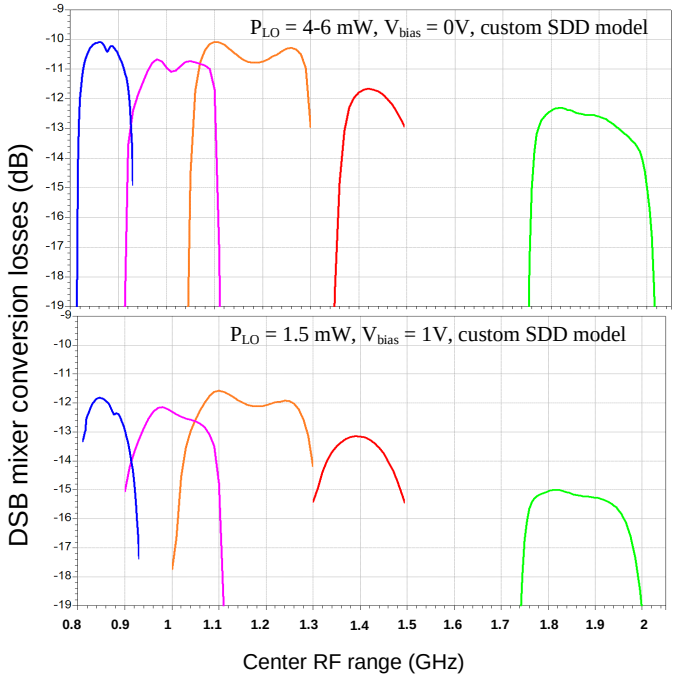

Fig. 8a&b. Predicted DSB mixer conversion losses for room temperature operation in the range 0.8-2 THz, using the custom SDD model. Fig. 8a are for unbiased devices and 4-6 mW of LO power, Fig. 8b are for biased devices at 1V for both diodes and 1.5 mW of LO power.

As shown in Fig. 8a&b, the predicted DSB mixer conversion losses extend from 10 to 13 dB using the custom SDD model when the mixer is pumped with enough LO power and without bias. When pumped with only 1.5 mW and biased, the DSB mixer conversion losses degrade by up to 2 dB. From the simulation results obtained in Fig. 9a&b, it can be seen that the predicted DSB mixer noise temperature ranges from 2000 to 4000 K when the device is pumped with sufficient LO power and without biasing, and from 3000 to 5000 K when pumped with 1.5 mW of LO power and biased at 1V. These values are for room temperature operation.

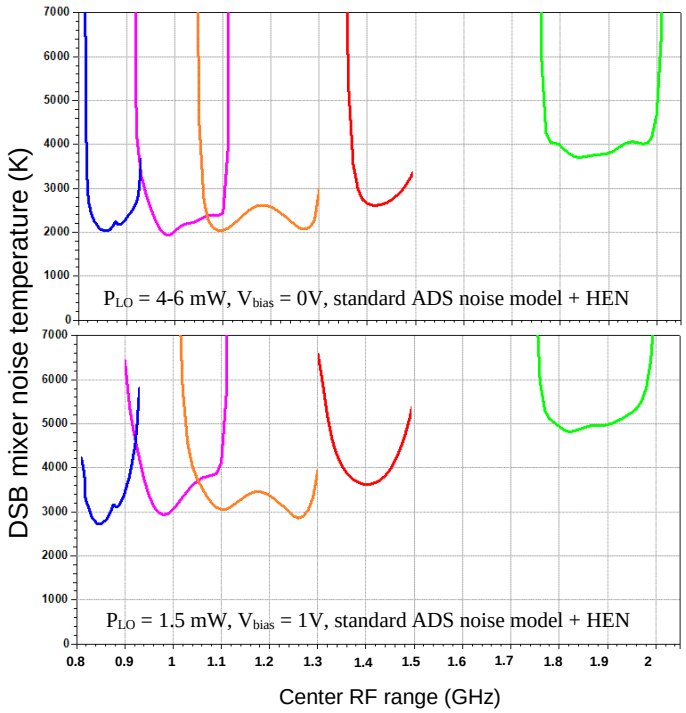

Fig. 9a&b. Predicted DSB mixer noise temperature for room temperature operation in the 0.8-2 THz range. It uses the standard ADS Schottky noise model enhanced with Hot Electron Noise source. In the unbiased case (Fig. 7b), LO power is 4-6 mW. In the biased case (Fig. 7b), LO power is 1.5 mW and applied voltage is 1V for both devices.

Finally, an example of the proposed architecture for an all-solid-state room temperature or passively cooled terahertz heterodyne receiver front-end is shown in Fig. 10. The LO chain relies on power-combined W-band power amplifiers, sub-millimeter MMIC Schottky Varactor multipliers [15], and uses the MMIC GaAs membrane sub-harmonic mixer described to reach frequencies up to 1.8 THz.

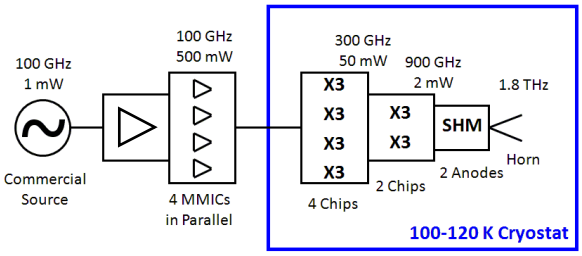

Fig.10. Proposed architecture for a 1.8 THz all-solid-state receiver chain. The LO chain is based on MMIC power-combined Schottky Varactor multipliers and power amplifiers, and uses the MMIC membrane sub-harmonic mixer described above.

ACKNOWLEDGMENT

The authors wish to acknowledge Dr. Anders Skalare and Dr. Robert Dengler at JPL for their advices and support in mounting the cryogenic test bench.

REFERENCES

[1] E. Lellouch et al., "A submillimeter sounder for the Titan Saturn System Mission (TSSM)", *European Planetary Science Congress*, EPSC Abstracts, Vol. 3, EPSC2008-A-00193, 2008.

[2] ESA Cosmic Vision 2015-2025 website: http://sci.esa.int/science-e/www/area/index.cfm?fareaid=100

[3] S.A. Buehler, "CIWSIR: A Proposed ESA Mission to Measure Cloud Ice Water Path,", proceedings of the Int. TOVS Study Conf., ITSC-XV Program, Maratea, Italy , 4-10 October 2006.

[4] E. Schlecht et al, "200, 400 and 800 GHz Schottky Diode "Substrateless" multipliers: Design and results", IEEE MTT-S, International Microwave Symposium, Vol. 3, May 2001.

[5] B. Thomas, A. Maestrini, D. Matheson, I. Mehdi and P. de Maagt, "Design of an 874 GHz Biasable Sub-Harmonic Mixer Based on MMIC Membrane Planar Schottky Diodes", *proceedings of the 33rd IRMMW-THz 2008 conference*, California Institute of Technology, Pasadena, CA, September 15-19, 2008.

[6] N. Erickson, "A fast and sensitive submillimetre waveguide power meter", *10th Int. Symp. on Space THz Technology*, Charlottesville, pp.501-507, 1999.

[7] J. Hesler, et al., "Fixed-tnued submillimeter wavelength waveguide mixers using planar Schottky-barrier diodes", IEEE Trans. on Microwave Theory and Techniques, Vol. 45, No. 5, pp. 653-658, May 1997.

[8] T. Crowe, "GaAs Schottky barrier mixer diodes for the frequency range 1–10 THz" *International Journal of Infrared and Millimetre Waves*, vol. 10, No. 7, pp. 765-777, July 1989.

[9] E. Schlecht. F. Maiwald, G. Chattopadhyay, S. Martin and I. Mehdi, "Design considerations for heavily-doped cryogenic Schottky diode Varactor multipliers", proceedings of the 12th International Symposium on Space Terahertz Technology, San Diego, California, February 15, 2001.

[10] Advanced Design System 2008, Agilent Technologies, 395 Page Mill Road, Palo Alto, CA 94304, USA.

[11] D. Porterfield, "Millimeter-wave Planar Varactor Frequency Doublers", PhD thesis, University of Virginia, August 1998.

[12] B. Thomas, J. Treuttel, B. Alderman, D. Matheson and T. Narhi "Application of transferred substrate to a 190 GHz doubler and 380 GHz mixer using MMIC foundry Schottky diodes", proceedings of the SPIE conf. on Astronomical Instrumentation, Marseille, France, June 2008.

[13] B. Thomas, A. Maestrini, JC. Orlhac, JM. Goutoule and G. Beaudin, "Numerical analysis of a 330 GHz sub-harmonic mixer with planar Schottky diodes", proceedings of the 3rd ESA workshop on millimetre-wave technology and techniques, Espoo, Finland, May 21-23, 2003.

[14] B.Thomas, A. Maestrini and G. Beaudin, "A Low-Noise Fixed-Tuned 300-360 GHz Sub-Harmonic Mixer Using Planar Schottky Diodes", IEEE MWCL, pp.865-867, vol.15, no.12, December 2005.

[15] A. Maestrini et al., "In-Phase Power Combining of Submillimeter-Wave Multipliers", *proceedings of the 33rd IRMMW-THz 2008 conference*, California Institute of Technology, Pasadena, CA, September 15-19, 2008.

A 200 GHz Schottky Diode Quasi-Optical Detector Based on Folded Dipole Antenna

L. Liu, *Member IEEE*, H. Xu, *Member IEEE,* Y. Duan, A. W. Lichtenberger, J. L. Hesler, *Member IEEE*, and R. M. Weikle, II, *Senior Member, IEEE*

***Abstract*—We report the development of quasi-optical Schottky diode detectors based on folded dipole antennas (FDAs) having high driving point impedances. For a prototype demonstration, we have designed a 200 GHz FDA on a silicon substrate with three turns and nearly 1100 Ω input impedance. For DC signal output, we designed a coplanar strip (CPS) low-pass filter which effectively suppresses the RF (200 GHz) current on the DC lines. The detector circuits are diced into octagons for alignment with the high resistivity silicon lens. Initial responsivity and antenna pattern measurements have been performed, and the results are presented. More research will be done to further optimize the detector design and performance.**

***Index Terms*—Terahertz, quasi-optical, detector, Schottky diode, folded-dipole antenna.**

I. INTRODUCTION

TERAHERTZ detectors have a wide range of applications in spectroscopy, imaging, astronomy and bio-sensing [1-3]. Compared to other detectors such as Golay cells [4, 5] or hot-electron bolometers (HEBs) [6, 7], Schottky diode based detectors [8] have the merits of both fast response and high responsivity. In addition, they can be operated at either room or cryogenic temperature. THz waveguide or quasi-optical detectors employing zero bias Schottky diodes (ZBDs) have been developed and promising results have been reported [8, 9]. However, due to the substantial impedance mismatch between ZBDs (~1000-3000 Ω) and waveguide or antenna structures (e.g. log-periodic or sinuous antennas), the power coupling efficiency is limited, resulting in relatively low detector responsivity.

In this paper, we introduce quasi-optical Schottky diode detectors based on folded dipole antennas (FDA) having high driving point impedances. For a prototype demonstration, we have designed a 200 GHz FDA on a silicon substrate with three turns (N=3) and nearly 1200 Ω input impedance. For DC signal output, we have designed a coplanar strip (CPS) low-pass filter which effectively suppresses the RF (200 GHz) current on the DC lines. The detector circuits are diced into octagons for alignment with the high resistivity silicon lens. Initial responsivity and antenna pattern measurements have been performed, and the results are presented. On the basis of the initial testing, an anti-reflection coating will be applied to the silicon lens to reduce the coupling loss. Further research will be done to optimize the detector design and performance.

Manuscript received 20 April 2009. This work was supported in part by the U.S. Army National Ground Intelligence Center under Grant W911W5-06-R-0001.

L. Liu. H. Xu, A. W. Lichtenberger, and R. M. Weikle, II are with the School of Engineering and Applied Science, University of Virginia, 351 McCormick Road, Charlottesville, VA 22904-4743, USA (email: ll8j@virginia.edu).

Y. Duan and J. L. Hesler are with the Virginia Diodes, Inc., 979 2nd Street NE, Suite 309, Charlottesville, VA 22903, USA.

II. DETECTOR DESIGN

A. Folded Dipole Antenna

In a typical quasi-optical THz detector design, antenna structures are employed for power coupling. The input impedances of those antennas, such as annular-slot antennas and broadband self-complementary antennas on a silicon substrate, are generally less than 100 Ω. The junction resistance for a zero-bias Schottky diode, however, is in the range of 1000 to 3000 Ω. The substantial impedance mismatch between the ZBDs and antennas limits the power coupling efficiency, resulting in relatively low detector responsivity.

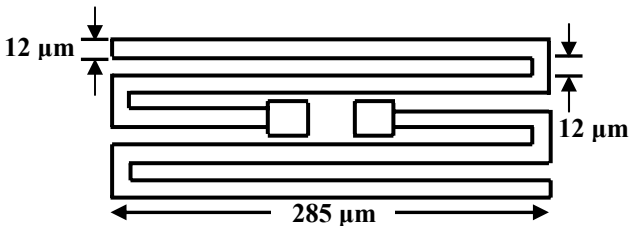

(a)

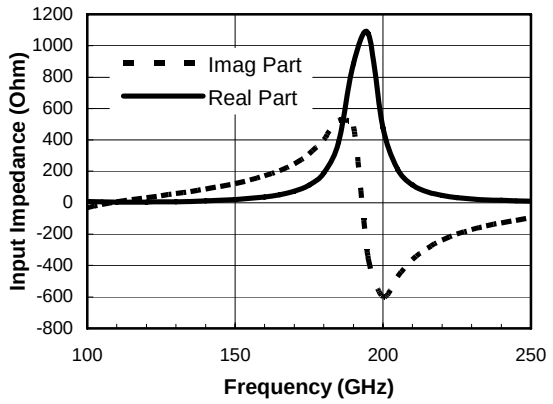

(b)

Fig. 1. Folded dipole antenna design and simulation, (a) schematic of the antenna structure for operation at 200 GHz., and (b) HFSS simulation results of the antenna input impedance.

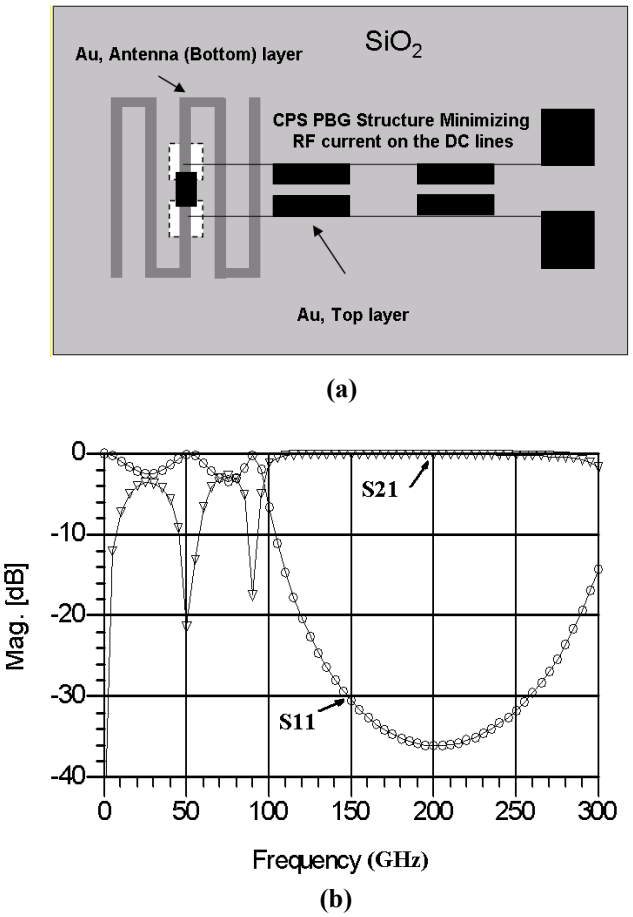

Fig. 2. (a) The overall design of the 200 GHz Schottky diode quasi-optical detector based on folded dipole antenna. The CPS PBG structure for DC signal output minimizes the RF current on the DC lines. (b) ADS Momentum simulated S parameters for the CPS low-pass filter.

A folded dipole antenna (N turns) may provide good matching characteristics for embedding ZBDs since its input impedance is determined by

$$Z_{in} = N^2 Z_0 , \quad (1)$$

where Z_0 is the impedance of the ordinary single dipole [10, 11]. For a prototype demonstration, we have designed an FDA on a silicon carrier with 3 turns that operates at nearly 200 GHz. As shown in Fig. 1 (a), the length of the antenna is 285 μm. Both the antenna arm width and arm gap are 12 μm. For flip-chip mounting of the zero bias Schottky diodes, the feed point gap is 30 μm, and the contact pads dimensions are 25 μm by 25 μm. The antenna input impedance is simulated using HFSS and shown in Fig. 1 (b). The resonant frequency is 195 GHz and the real part of the impedance is nearly 1100 Ω, while the imaginary part is zero. The simulated antenna radiation patterns (both E- and H-Planes) have 3-dB beam width of around 75°.

Folded dipole antennas with N = 2, 3, and 4, were also simulated using HFSS, and the resonant frequency impedance increases with increasing of N, as expected. The antenna arm width and arm gap also affect the antenna impedance as seen from the full-wave simulation. This provides an opportunity to fine tune the antenna impedance to match that of a given ZBD junction resistance. The resulting detector will have a narrow bandwidth of nearly 20 GHz.

B. Zero Bias Schottky Diode

The zero bias Schottky diodes used in this research were fabricated at Virginia Diodes, Inc. (VDI), in a flip-chip configuration using the process described in [12]. Typical chip dimensions are 180×80×40 μm (length×width×thickness), with device parameters of I_{sat} = 11 μA, R_s = 19 Ω, ideality factor, η = 1.13, and zero bias junction resistance, dV/dI = 1-3 k Ω [8].

C. DC Output Circuit

For DC signal output, we plan to sputter 4000 Å of SiO_2 over the antenna layer for insulation, and fabricate a coplanar strip (CPS) low-pass filter (or PBG structure) which effectively suppresses the RF (200 GHz) current on the DC lines. As shown in Fig. 2 (a), the CPS LPF consists of five sections with section length of 135 μm. For the high-impedance section, the line width is 2 μm, and the gap between two lines is 80 μm, while for the low-impedance section, the line width is 43 μm, and the gap is 2 μm. The s-parameters of the CPS LPF are shown in Fig. 2 (b), and the RF suppression at around 200 GHz is as high as 36 dB. Although not designed to work as a typical LPF (large ripples in the pass band), the CPS PBG structure provides good transmission for DC and very low frequency signals.

III. Detector Fabrication and Assembly

The detector circuits were fabricated in the Microfabrication Laboratory at the University of Virginia (UVML). For a prototype demonstration, folded dipole antennas with three turns that operate at nearly 200 GHz were fabricated on 0.5mm-thick high-resistivity (≥ 20000 Ω·cm) silicon wafer (ε_r = 11.8), using a traditional Au plating process. The antennas are connected to DC output pads using two meander lines (2 μm width) at both ends (see Fig. 3 (b)). In principle, the radiation due to RF currents on each of the meander lines cancel each other in the far field, thus reducing their influence on the folded dipole antennas.

The antenna will be mounted on an extended hemispherical high-resistivity (≥1000 Ω·cm) silicon lens (ε_r = 11.8) with radius R, of 5 mm. The total extension length (L) is chosen to be 1 mm (L/R ~ 0.2) for high Gaussian coupling efficiency. According to [13], most of the power is radiated into the dielectric side, and the use of a silicon substrate with high dielectric constant further enhances the power coupling efficiency for a receiving antenna. In addition, using the same material for both the substrate and lens eliminates the power loss to substrate modes [14].

As shown in Fig. 3, a quasi-optical detector mount has been employed for coupling the input power to the folded dipole antenna. The detector chips have been diced into octagons for alignment with the high-resistivity silicon lens. The zero bias Schottky diode is mounted at the center of the antenna using flip-chip mounting technique (see inset of Fig. 3 (b)). The

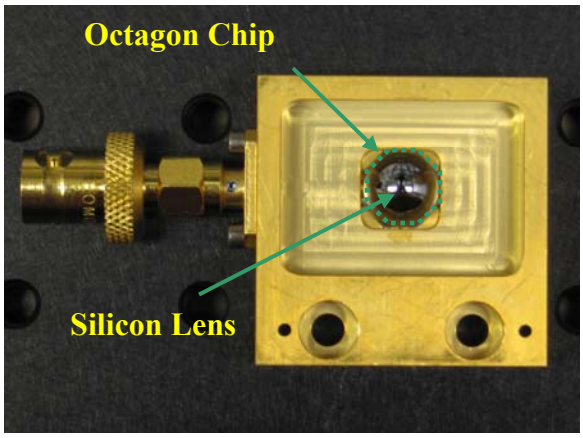

(a)

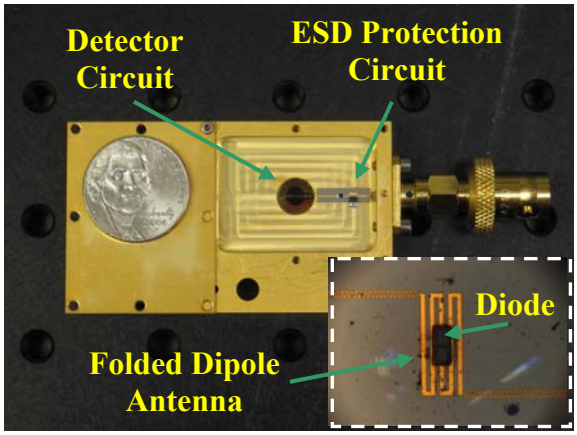

(b)

Fig. 3. The circuits and quasi-optical block of the 200 GHz folded dipole antenna detector. (a) The front-side view of the quasi-optical detector block with extended hemispherical silicon lens. (b) The back-side view of the detector with ESD protection circuit. The inset shows the folded dipole antenna with a flip-chip mounted ZBD and meander lines.

detector circuit is mounted on the back side of the block, and a high-resistivity silicon lens (R = 5 mm) is attached against the detector chip from the front side. An ESD protection circuit is also mounted and all connections are accomplished using wire-bonding techniques.

IV. Measurements

A. Detector Responsivity Measurement

The detector responsivity measurement setup is shown in Fig. 4. An Agilent microwave source together with a VDI 140-240 GHz FEM are employed to provide the THz radiation through a diagonal horn antenna. In between the VDI FEM and the horn antenna, a waveguide directional coupler is inserted to monitor the output power with an Ericson power meter. Two off-axis parabolic mirrors (f = 76.4 mm) are utilized to couple the THz radiation onto the ZBD folded dipole detector. The THz radiation is modulated with a chopper at 100 Hz, and the DC output signal from the detector is measured using a lock-in amplifier.

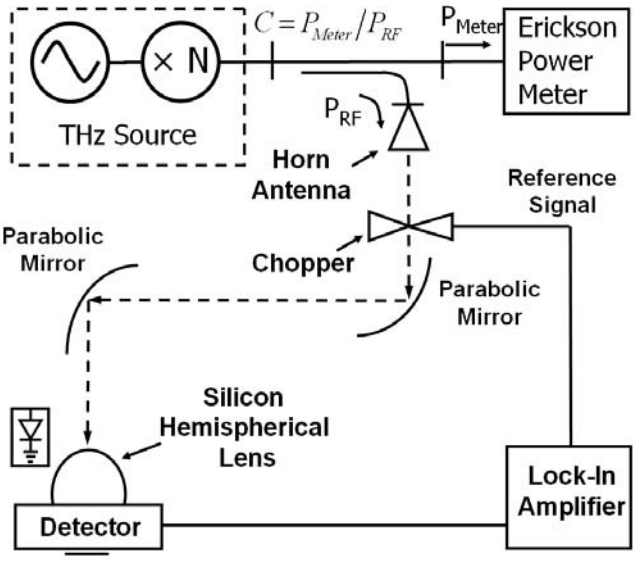

Fig. 4. The detector responsivity measurement setup for the frequency range of 140 GHz to 240 GHz. Two parabolic mirrors are utilized for coupling the RF power onto the detector. The DC output signal is modulated at 100 Hz and measured with a lock-in amplifier.

Fig. 5(a) shows the results for detector responsivity measurement at 140 to 240 GHz. A peak responsivity of around 280 V/W (without any corrections) is observed at 186 GHz. Compared to the designed working frequency of 195 GHz, the measured resonant frequency is shifted to a lower frequency. This might be a result of loading due to the meander lines at both of the antenna arm ends, which effectively increases the antenna electrical length. The detector responsivity decreases rapidly from the center frequency (186 GHz), and drops to below 100 V/W at 140 GHz, and is lower than 15 V/W at 240 GHz, showing the anticipated narrow bandwidth of this detector. The estimated bandwidth is approximately 20 GHz, which is close to the simulation results. The corresponding NEP is ~20 pW/√Hz at the resonant frequency, according to [8]. However, the peak responsivity of 280 V/W is much lower than what we expected, and analysis and discussion of this will be presented in section V.

B. Antenna Characterization

To ensure that the designed folded dipole antenna is working properly, the far-field radiation patterns of the antenna on an extended hemispherical silicon lens have been measured at ~190 GHz. In this measurement, VDI frequency extension modules (FEMs) cover the frequency range of 190 GHz to 210 GHz, were utilized for providing the THz radiation. The detector was mounted on a computer-controlled rotation stage and the output DC signal was modulated and detected by a lock-in amplifier. As shown in Fig. 5 (b), the measured radiation patterns show reasonable Gaussian-shape main beams with side-lobe level less than -14 dB. The 3-dB beam width of the folded dipole antenna is 10° at 190 GHz. The measured H-plane radiation pattern is slightly broader than the pattern in the E-plane, as expected, according to [13].

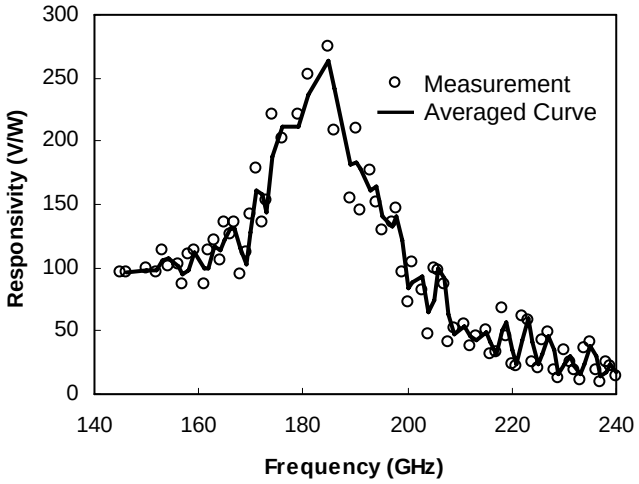

(a)

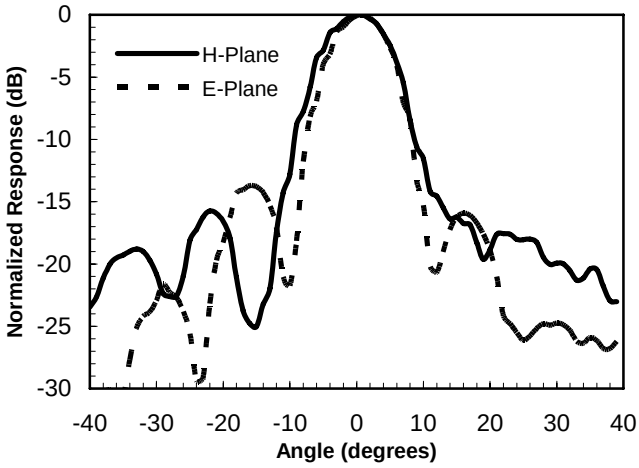

(b)

Fig. 5. Detector initial measurement results: (a) responsivity measurement in the frequency range of 140-240 GHz. A peak responsivity of ~280 V/W is observed at 186 GHz, (b) antenna radiation patterns measured at 190 GHz show good Gaussian-shape main beams.

V. Discussion and Comparison

To evaluate the performance of this quasi-optical Schottky diode detector based on the folded dipole antenna, we compare its responsivity to two different detectors. Using the same experimental setup as shown in Fig. 4, we measured the responsivity of a WR-5 waveguide detector with horn antenna, and a broadband quasi-optical detector (planar sinuous antenna) developed by our group in [9], in the frequency range of 140-240 GHz. The results are summarized in Fig. 6. The waveguide detector has a typical responsivity of 600-1200 V/W over the entire WR-5 frequency band, with good performance (~200 V/W) up to 230 GHz. The broadband quasi-optical detector exhibited a responsivity of 200-800 V/W over the entire frequency range. Its performance is slightly better than the waveguide version at frequencies higher than 210 GHz, demonstrating its broadband property. The folded dipole Schottky diode detector, however, shows a relatively low peak responsivity at 186 GHz.

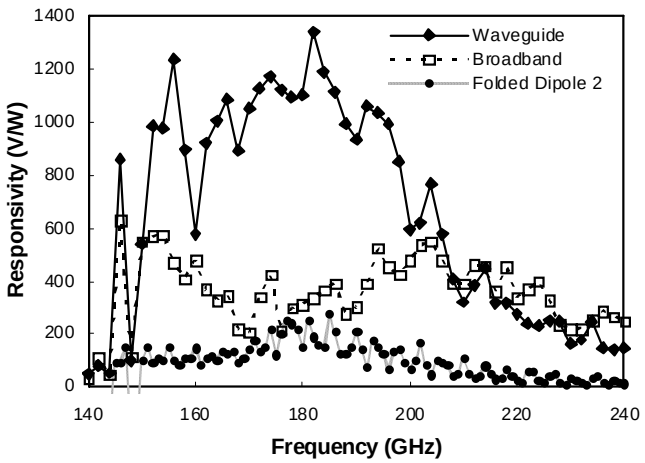

Fig. 6. Responsivity measurement of three different zero bias Schottky diode detectors comparing their performance in the frequency range of 140-240 GHz.

Although the antenna is working more-or-less as designed (as seen in Fig. 5), the center frequency responsivity is much lower than expected. With impedance matching between the antenna and ZBD, RF power reflection of up to nearly 80% are avoided, and a responsivity of 600-1500 V/W (3-5 times better than the broadband version), at resonant frequency, is expected. Since this detector is designed for narrow band applications, the goal responsivity of 1000-2500 V/W (quasi-optically) can be achieved, in principle, by applying anti-reflection coating to the silicon lens. We attribute the measured low responsivity to the following several factors: 1. the fabricated circuit is a simplified version (with meander lines for DC output) for quick diagnostics; 2. the Schottky diode chip is much larger than the designed contact pads for flip-chip mounting (see Fig. 3(b)), which effectively loads a metal layer (Au) and a dielectric (GaAs, $\varepsilon_r = 10.9$) layer at the antenna feed point, resulting in a different drive point impedance and resonant frequency; 3. the responsivity measurement system is not optimized.

On the basis of the above discussion, we plan to further simulate the fabricated detector structure with the loading of the metal and dielectric layers at the antenna feed point to understand its effect to the detector performance. Meanwhile, we will continue to fabricate the detector circuit described in Fig. 2, and measure the performance with an optimized experimental setup.

Acknowledgment

The authors would like to thank all the colleagues from the UVML, the Microwave Laboratory, and the FIR-THz Laboratory at the University of Virginia. The authors are also grateful for the assistance and advice of Professors Acar Isın and Bascom S. Deaver, Jr., both with the Department of Physics at the University of Virginia, Charlottesville, VA.

REFERENCES

[1] P. H. Seigel, "Terahertz technology," *IEEE Trans. Microwave Theory and Tech*., vol. 50, no. 3, pp. 910–928, March 2002.

[2] B. H. Deng, C. W. Domier, and N. C. Luhmann, Jr. *et al*., "ECE imaging of electron temperature and electron fluctuations," *Rev. Sci. Instrum.*, vol. 72, no. 1, pp. 301–306, Jan. 2001.

[3] D. Woolard *et al*., "The potential use of submillimeter-wave spectroscopy as a technique for biological warfare agent detection," *22nd Army Sci. Conf.*, Baltimore, MD, Dec. 12–13, 2000.

[4] P. R. Griffiths and J. A. de Haseth, "Fourier transform infrared spectrometry," *Wiley Interscience*, New York, pp. 209–212, 1986.

[5] P. R. Griffiths and C. C. Homes, "Instrumentation for far-infrared spectroscopy," *Handbook of Vibrational Spectroscopy*, vol 1–Theory and Instrumentation, Wiley, New York, 2001.

[6] J. Wei, D. Olaya, B. S. Karasik, S. V. Pereverzev, A. V. Sergeev, and M. E. Gershenson, "Ultrasensitive hot-electron nanobolometers for terahertz astrophysics," *Nature Nanotech.*, no. 3, pp. 496-500, July 2008.

[7] L. Liu, H. Xu, R. R. Percy, D. L. Herald, A. W. Lichtenberger, J. L. Hesler, and R. M. Weikle, "Development of integrated terahertz broadband detectors utilizing superconducting hot-electron bolometers," *IEEE Trans. Appl. Supercon.*, to be published, Jun. 2009.

[8] J. L. Hesler, and T. W. Crowe, "Responsivity and noise measurements of zero-bias Schottky diode detectors," *18th Intl. Symp. Space Terahertz Techn.*, Pasadena, March 2007.

[9] J. L. Hesler, L. Liu, H. Xu, and R. M. Weikle, II, "The development of quasi-optical THz detectors," *33rd International Conference on Infrared, Millimeter, and Terahertz Waves (IRMMW)*, Pasadena, California, USA, Sep. 2008.

[10] C. A. Balanis, "Antenna theory: analysis and design," 2nd Edition, *John Wiley & Sons, Inc.*, 1997.

[11] H. C. Ryu, S. I. Kim, M. H. Kwak, K. Y. Kang, and S. O. Park, "A folded dipole antenna having extremely high input impedance for continuous-wave terahertz power enhancement," *33rd International Conference on Infrared, Millimeter, and Terahertz Waves (IRMMW)*, Pasadena, California, USA, Sep. 2008.

[12] W. L. Bishop, E. Meiburg, R. J. Mattauch, T. W. Crowe and L. Poli, "A micron-thickness, planar Schottky diode chip for terahertz applications with theoretical minimum parasitic capacitance," *IEEE MTT-S Int. Micwave Symp. Digest*, pp. 1305–1308, May 1990. *r Quantities*, ANSI Standard Y10.5-1968.

[13] D. F. Filipovic, S. S. Gearhart, and G. M. Rebeiz, "Double slot antennas on extended hemispherical and elliptical silicon dielectric lenses," *IEEE Trans. Microwave Theory & Tech.*, vol. 41, pp. 1738-1749, Oct. 1991.

[14] D. B. Rutledge, and M. S. Muha, "Imaging antenna arrays," *IEEE Trans. Antennas Propagat.*, vol. AP-30, no. 4, pp. 535-540, July 1982.

Session W2

HEB Mixers & Receivers

Chair: Boris Karasik

Wednesday, April 22
10:55 – 12:10

NbN phonon-cooled hot-electron bolometer mixer with additional diffusion cooling

S. A. Ryabchun, I. V. Tretyakov, M. I. Finkel, S. N. Maslennikov, N. S. Kaurova, V. A. Seleznev, B. M. Voronov, and G. N. Gol'tsman

***Abstract*— We present low-noise and wide-bandwidth HEB mixers made from NbN-Au two-layer films *in situ* deposited on Si substrates. At 2.5 THz, the lowest double-side band receiver noise temperature was 750 K. The gain bandwidth measurements at T_c yielded a gain bandwidth of 6.5 GHz, exceeding by almost a factor of two the typical value of 3.5 GHz for phonon-cooled HEB mixers on Si substrates with no additional buffer layer. The record characteristics are attributed to the improved interface between the superconducting film and the gold contact pads.**

***Index Terms*—HEB mixer, phonon cooling, diffusion cooling, gain bandwidth, noise temperature**

I. INTRODUCTION

In the terahertz range, most informative for the radio astronomy of the early universe, hot-electron bolometer (HEB) mixers have long ago established themselves as the best detectors because they offer the lowest noise temperature and a reasonably wide gain bandwidth [1-5]. Such instruments as HIFI, CASIMIR, and GREAT will be using HEB receivers to cover certain frequency bands above 1 THz [6, 7]. It should be noted, however, that all the HEB mixers that will be employed in the above instruments are phonon-cooled [8] and their IF bandwidth does not exceed 4 GHz. At the same time, the increase of the gain bandwidth and the reduction of the noise temperature are important both for continuum and spectroscopic observations. The traditional approach to increase the gain bandwidth has been to improve the acoustic transparency of the interface between the film and the substrate, and to decrease the film thickness. Using an appropriate substrate material or buffer layer allows increasing the gain bandwidth up to 3.2 GHz for waveguide HEBs [3] and 4.8 GHz for quasioptical HEBs [9]. Decreasing the film thickness yields further increase of the gain bandwidth up to 5.2 GHz [2] but for thicknesses less than 2.5 nm NbN loses its superconducting properties. It has been reported that the noise temperature and gain bandwidth of phonon-cooled HEB mixers can be improved by cleaning the interface between the superconducting film and the contact pads [4, 5].

Manuscript received 17 April 2009. This work was supported in part by Grant No. 07-02-13626-O from the Russian Foundation for Basic Research. Funding for M. F. was provided by Grant No. MK-3098.2008.2 from the President of the Russian Federation Foundation for Young Russian Scientists.

All the authors are with the Department of Physics and Information Technology, Moscow State Pedagogical University, *29 Malaya Pirogovskaya St., Moscow, Russia 119992* (Sergey Ryabchun, phone: +7(499)246-6321; fax: +7(499)246-6321; e-mail: sryabchun@rplab.ru).

With respect to the cooling mechanism, HEB mixers fall into two classes: phonon-cooled HEBs (PHEBs) [8] and diffusion-cooled HEBs (DHEBs) [10]. Which cooling mechanism dominates depends on the mixer length. If $L << L_{th} = (D\tau_{th})^{1/2}$ (L being the mixer length, D the diffusion coefficient, and τ_{th} the electron temperature relaxation time) the hot electrons will leave the mixer before being scattered by phonons. Diffusion cooling is effective, however, only if there is no additional energy barrier at the interface between the film and the contact pads. In the opposite case ($L >> L_{th}$) the hot electrons will more likely give their excess energy to the lattice before leaving the film. Although Nb diffusion-cooled HEB mixers can offer a gain bandwidth as wide as 9 GHz [11] the decrease in the number of papers dedicated to this type of HEB mixer, together with the fact that mostly NbN phonon-cooled devices are installed in practical systems, suggests that there are serious problems in realizing low noise temperature and a wide gain bandwidth in the same device.

In this paper we propose a phonon-cooled NbN HEB mixer with additional cooling via diffusion of hot electrons into the normal contact pads. Being primarily of the phonon-cooled type, such a mixer offers simultaneously a record low noise temperature and a wide gain bandwidth. This is the first time a NbN HEB mixer with additional diffusion cooling has been proposed, and, as discussed in greater detail below, such a mixer has certain advantages compared to NbN PHEB and Nb DHEB counterparts.

II. DEVICE FABRICATION AND DC TESTING

The HEB mixers proposed in this paper were fabricated from NbN-Au two-layer films *in situ* deposited on high-resistivity polished Si substrates by DC magnetron sputtering. The films were patterned using e-beam lithography to obtain mixing elements with lengths 0.1 - 0.4 μm. Given an NbN film sheet resistance of about 500 Ω we chose a mixer length-to-width ratio of 0.1 to ensure better IF and RF match with the IF chain and the log-spiral antenna, respectively. Fig. 1 shows a SEM photograph of a part of an HEB device including the mixing element, the contact pads and a part of the spiral antenna. Also shown is a close-up of the inner part of the device including the mixing element and partly the contact pads. Referring to Fig. 2, our devices had two superconducting transitions: one at about 9 K of the mixer itself and the other around 7 K of the part of NbN film under the contacts due to the proximity effect. The critical current densities were about 4.5×10^6 A cm^{-2}, and the normal state resistances were 70-

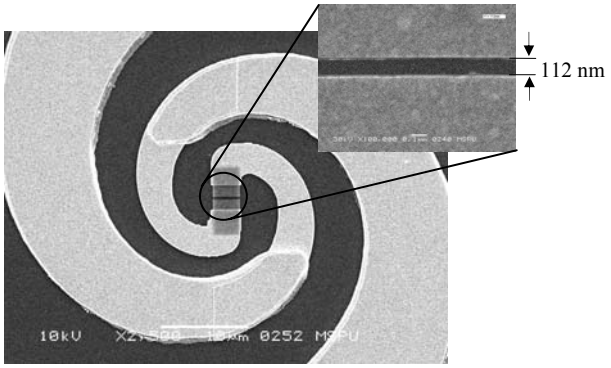

Fig. 1. A SEM photograph of an HEB device including the mixing element, the contact pads and a part of the spiral antenna. Also shown is a close-up of the inner part of the device including the mixing element and partly the contact pads; the length of the mixer is 112 nm.

80 Ω.

III. Experimental setups

A. Gain bandwidth measurements

HEB mixers are described most simply by the uniform-heating model, which applies best when the device is operated at the superconducting transition temperature T_c. In this case the heat balance equations governing the dynamics of the superconducting film become linear and allow for an analytical solution which can be interpreted unambiguously [12]. That is why we chose to perform gain bandwidth measurements at T_c, where the superconducting energy gap is almost completely suppressed, and so the local oscillator frequency is not an issue.

For the gain bandwidth measurements we employed the standard technique with two monochromatic sources (in our case two backward-wave oscillators operating at about 300 GHz). An HEB mixer chip containing a log-spiral antenna with a mixing element at its apex was glued to an extended hemispherical Si lens and installed into a mixer block which was mounted onto the cold plate of a liquid helium cryostat. The HEB mixer was IF-coupled to a 3 cm long coplanar waveguide with a subsequent transition to a coaxial cable which delivered the IF signal out of the cryostat to a room-temperature broadband bias-tee followed by an amplifier with a pass-band of 0.1-12 GHz and a gain of about 36 dB. The amplifier output was fed to a spectrum analyzer. The IF chain was calibrated using a network analyzer.

B. Noise temperature measurements

The receiver noise temperature was measured at a local oscillator frequency of 2.5 THz and an ambient temperature of 4.2 K. A mixer block containing devices with dimensions 0.1-0.3 μm × 1-3 was mounted into a cryostat with a 0.5 mm thick high density polyethylene window and a Zitex-104 cold infrared filter. In order to reduce the direct detection effect [13] we mounted a 2-3 THz bandpass mesh filter on the cold plate. A gas discharge H_2O laser provided local oscillator drive at 2.5 THz, which was combined with radiation from a blackbody with the use of a 6 μm thick Mylar beam-splitter. The receiver back end comprised a wideband bias-tee followed by a cryogenic amplifier with a built-in isolator, together forming a unit with a gain of 30 dB over a bandwidth of 1-2 GHz. The room temperature part of the IF chain included two amplifiers, each with a gain of 30 dB and a bandwidth of 0.01-2 GHz, separated by a tunable 50-MHz bandpass filter. The output of the second room-temperature amplifier was fed to a square-law power detector followed by a high precision voltmeter.

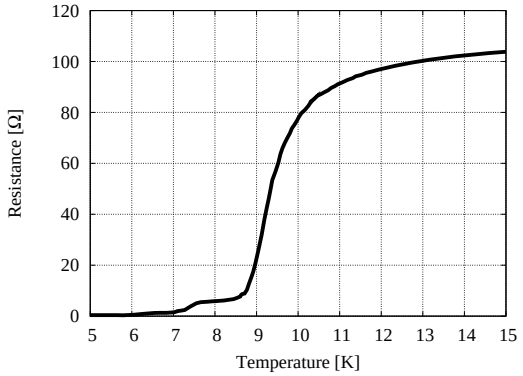

Fig. 2. Typical resistance-temperature curve for HEB mixers studied in this paper. As can be seen, besides the primary superconducting transition, there is also another one at lower temperature due to the proximity effect between the superconducting film and the normal contact pads.

IV. Experimental results and discussion

A. Gain bandwidth measurements

Our measurements showed that within an experimental error the noise temperature is independent of device dimentions so there is nothing special about the length 0.25 μm chosen for noise temperature measurements. However, to get a clear picture of the contribution of the diffusion channel, for the gain bandwidth measurements we chose devices with lengths from 0.12 μm to 0.35 μm. Fig. 3 shows the results of the gain bandwidth measurements for devices with the extreme lengths. Fitting the experimental data with

$$P(f_{IF}) = P_0/[1 + (f/f_{3dB})^2] \quad (1)$$

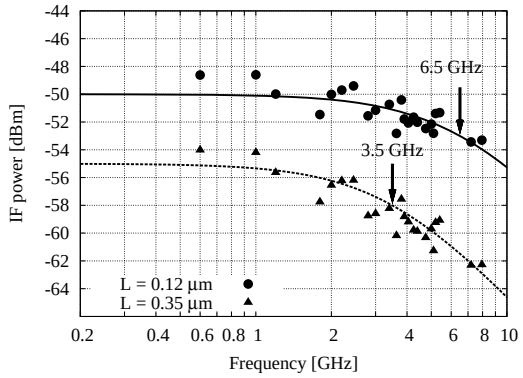

Fig. 3. The gain bandwidth measurement data for two HEB mixers with different lengths of the mixing element: 0.12 μm (circles) and 0.35 μm (triangles).

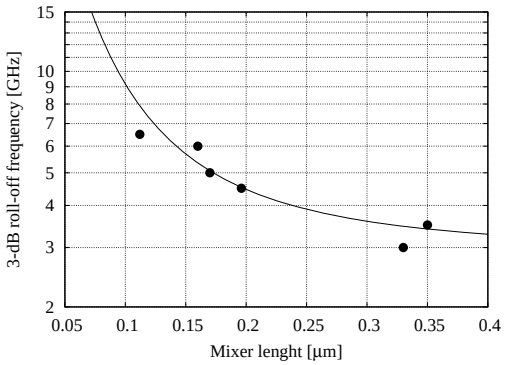

Fig. 4. The gain bandwidth as a function of the length of the mixing element. Solid curve is the theoretical dependence.

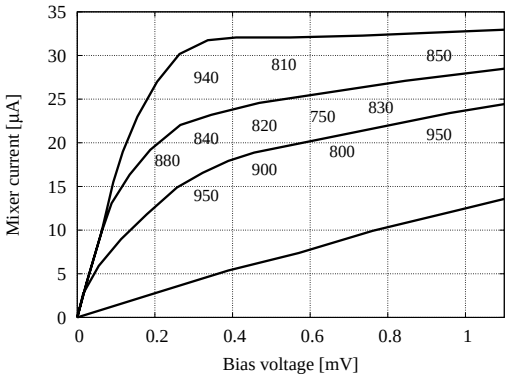

Fig. 5. A family of the current-voltage characteristics of an HEB mixer taken at different levels of the LO drive. The top curve is the least pumped one. Also shown is the receiver noise temperature at different operating points.

yields 3-dB rolloff frequencies of 6.5 GHz and 3.5 GHz for the lengths 0.12 μm and 0.35 μm respectively. The value 3.5 GHz is typical of PHEB mixers on Si substrates with no additional buffer layer.

For NbN HEB mixers studied in this paper, phonon cooling alone would result in a 3-dB rolloff of only about 3 GHz. That, combined with the experimental data, points to additional diffusion cooling, which is supported by theoretical estimations given below. As was shown in [14], the time constant of the DHEB equals

$$\tau_{\text{diff}} = L^2/\pi^2 D, \qquad (2)$$

where D is the diffusion coefficient of the material. In the case of a PHEB with additional diffusion cooling the total thermal conductance is $G_{\text{tot}} = G_{\text{ph}} + G_{\text{diff}}$, whence the mixer time constant is found to be

$$\tau_{\text{m}} = C_{\text{e}}/G_{\text{tot}} = (1/\tau_{\text{ph}} + 1/\tau_{\text{diff}})^{-1}, \qquad (3)$$

where C_{e} is the electronic heat capacity. Substitution of the relevant material parameters into Eqs. (2) and (3) yields 3-dB rolloff frequencies of 7.2 GHz and 3.5 GHz for mixer lengths of 0.12 μm and 0.35 μm respectively. Referring to Fig. 4, the gain bandwidth of several HEB mixers is shown as a function of the length of the mixing element; also shown is the dependence obtained with the use of Eq. (3). This result is of great fundamental and practical importance, since it provides a way to increase the gain bandwidth of NbN HEB mixers, which is limited by the electron-phonon interaction time and the escape time of nonequilibrium phonons into the substrate. The fact that at 4.2 K the film under the contact pads turns superconducting is not an issue at least for diffusion cooling, and measurements both at microwave [14] and terahertz [11] frequencies showed that the gain bandwidth results are in perfect agreement with equation (2). So, there is no doubt that further experiments at the low-noise operating point at terahertz frequencies and 4.2 K will show the contribution of the diffusion channel.

B. Noise temperature measurements

The noise temperature measurements were performed with the use of the standard Y-factor procedure. Although HEB mixers are known to suffer from the direct detection effect [4, 15], in our case this effect was found to contribute less than 5% to the receiver noise temperature in the IV plane due to the use of the mesh filter. Fig. 5 shows a family of the current-voltage characteristics of an HEB mixer with dimensions 0.25 μm × 2.5 μm taken at different levels of the local oscillator drive. The top curve is the least pumped one. Also shown is the receiver noise temperature at different operating points. The lowest value of the receiver noise temperature is 750 K, which is about 6 times $h\nu/k_{\text{B}}$ (k_{B} being Boltzmann's constant) at this frequency. As was shown by several authors [4, 5], the noise temperature can be lowered by decreasing RF loss in contacts. In situ gold contacts offer a simple and yet an essentially new solution to the problem of high contact resistance and RF loss.

For HEB mixers shorter than 0.2 μm the absorbed LO power estimated with the use of the isothermal technique was found to be 160 nW/μm^2 (the film thickness is 3.5 nm) and to within an experimental error independent of the mixer length. This can be understood by noting that, for PHEB mixers, as the mixer dimensions are scaled down, say by a factor of k, such as to keep the length-to-width ratio constant, the absorbed LO power decreases by k^2. This continues until the mixer length becomes comparable to L_{th}. At that point diffusion cooling becomes effective, and since the diffusion time is proportional to the length squared, the rate of energy outflow is scaled by $1/k^2$. So in our case in the first approximation the amount of absorbed LO power should not depend on the mixer dimensions.

The absence of kinks on the IV curves and the fact that the receiver noise temperature does not change drastically with the change of the operating point demonstrates that the device is quite stable. That can be qualitatively understood by noting that if the mixer length were much shorter than the thermal healing length L_{th} the normal domain would collapse almost immediately after the formation, which would show itself as kinks on the IV curve. At the superconducting transition temperature, for the NbN mixers studied in this paper $L_{\text{th}} \approx 0.1$ μm, whereas for a Nb mixer the thermal healing length would be $L_{\text{th}} \approx 0.4$ μm. This means that although it is much easier to ensure the condition $L < L_{\text{th}}$ in a Nb mixer, the increase of the gain bandwidth will be achieved at the expense

of the device stable performance.

We believe that allowing for atmospheric absorption and using an antireflection coating might bring the noise temperature down to about 550 K at 2.5 THz at the low-noise operating point.

V. Conclusion

We have demonstrated that the use of *in situ* gold yields an appreciable improvement of HEB mixer performance. A gain bandwidth as wide as 6.5 GHz was measured near the superconducting transition. This is almost twice as large as the usual value obtained for HEB mixers on Si substrates with *ex situ* gold contacts. The dependence of the gain bandwidth on the length of the mixing element further supports the conclusion that we have a PHEB mixer with additional diffusion cooling. At 2.5 THz the receiver offered a noise temperature of 750 K, which is 6 times $h\nu/k_B$. Eliminating contributions due to reflection off the Si lens and atmospheric loss should lower the receiver noise temperature by about 30%.

References

[1] Jonathan Kawamura, C.-Y. Edward Tong, Raymond Blundell, D. Cosmo Papa, Todd. R. Hunter, Ferdinand Patt, Gregory Gol'tsman, and Eugene Gershenzon, IEEE Trans. on Appl. Supercond., **11**, 952-954, (2001).

[2] Yury B. Vachtomin, Matvey I. Finkel, Sergey V. Antipov, Boris M. Voronov, Konstantin V. Smirnov, Natalia S. Kaurova, Vladimir N. Drakinski and Gregory N. Goltsman, in *Proc. of the 13th Int. Symp. on Space Terahertz Technology* (Harvard University, Cambridge, MA, 2002), pp. 259-270.

[3] Denis Meledin C.-Y. Edward Tong, Raymond Blundell, in Proc. of the 13th *Int. Symp. on Space Terahertz Technology* (Harvard University, Cambridge, MA, 2002), pp. 65-72.

[4] J. J. A. Baselmans, M. Hajenius, J. R. Gao, T. M. Klapwijk, P. A. J. de Korte, B. Voronov, G. Gol'tsman, Appl. Phys. Lett., **84**, 1958 (2004).

[5] P. Khosropanah, J. R. Gao, W. M. Laauwen, M. Hajenius, and T. M. Klapwijk, Appl. Phys. Lett. **91**, 221111 (2007).

[6] Sergey Cherednichenko, Vladimir Drakinskiy, Therese Berg,Pourya Khosropanah, and Erik Kollberg, Rev. Sci. Instrum., 79, 034501 (2008).

[7] Available: http://www.sofia.usra.edu/.

[8] E. Gershenzon, G. Gol'tsman, I. Gogidze, Y. Gusev, A. Elantiev, B. Karasik, A. Semenov, Sov. Superconductivity, **3** (10), 2143 (1990).

[9] S. Cherednichenko, M. Kroug, P. Yagoubov, H. Merkel, E. Kollberg, K. S. Yngvesson, B. Voronov, and G. Gol'tsman, in *Proc. 11th Int. Symp. on Space Terahertz Technology* (Ann Arbor, Michigan, University of Michigan, USA, 2000), p 219.

[10] D. E. Prober, Appl. Phys. Lett. **62**, 2119 (1993).

[11] R. A. Wyss, B. S. Karasik, W. R. McGrath, B. Bumble, and H. LeDuc, in *Proc. 10th Int. Symp. on Space Terahertz Technology* (Charlottesville, Virginia, University of Virginia, USA, 1999) pp. 215-228.

[12] N. Perrin, C. Vanneste, Phys. Rev. B, **28**, 5150 (1983).

[13] J. J. A. Baselmans, A. Baryshev, S. F. Reker, M. Hajenius, J. R. Gao, T. M. Klapwijk, Yu. Vachtomin, S. Maslennikov, S. Antipov, B. Voronov, and G. Gol'tsman, Appl. Phys. Lett., **86**, 163503 (2005).

[14] P. J. Burke, R. J. Schoelkopf, D. E. Prober, A. Skalare, B. S. Karasik, M. C. Gaidis, W. R. McGrath, B. Bumble, and H. G. LeDuc, J. Appl. Phys. **85**, 1644, (1999).

W2B

Quantum noise contribution to NbN hot electron bolometer receiver

W. Zhang[1,2*], P. Khosropanah[1], J.R. Gao[1,3], E.L. Kollberg[4], K.S. Yngvesson[5], T. Bansal[1,3], J.N. Hovenier[3], T.M. Klapwijk[3]

[1]*SRON Netherlands Institute for Space Research, Utrecht/Groningen, The Netherlands*

[2]*Purple Mountain Observatory, National Astronomical Observatories of China, Chinese Academy of Sciences, China*

[3]*Kavli Institute of Nanoscience, Delft University of Technology, Delft, The Netherlands*

[4]*Department of Microelectronics and Nanoscience, Chalmers University of Technology, Gothenburg, Sweden*

[5]*Department of Electrical and Computer Engineering, University of Massachusetts, Amherst, USA*

*Contact: W.Zhang@sron.nl, Phone: +31-50-363 2935

***Abstract*— Superconducting NbN hot electron bolometer (HEB) mixers are so far the most sensitive detectors for heterodyne spectroscopy in the frequency range between 1.5 THz and 5 THz. To reach the ultimate receiver noise temperatures in the high end of the THz range (3-6 THz), it is crucial to understand their fundamental noise contribution from different origins. With increasing frequency, the classical output noise contribution should remain unchanged, but the quantum noise contribution is expected to play an increasing role [1].**

This paper reports the first dedicated experiment using a single NbN HEB mixer at a number of local oscillator frequencies between 1.6 to 4.3 THz to address and quantify the contribution of the quantum noise to the receiver noise temperature.

We used a spiral antenna coupled NbN HEB mixer with a bolometer size of 2 μm×0.2 μm. In order to minimize uncertainties in the corrections of the optical losses, we use a vacuum hot/cold load setup [2] to eliminate the air loss, and an uncoated elliptical Si lens. Although other components, a 3 μm Mylar beam splitter and a QMC heat filter, also introduce frequency dependent optical losses, they can be accurately calibrated. Furthermore, to reduce uncertainties in the data, we measure Y-factors responding to the hot/cold load by fixing the voltage, but varying the LO power [2]. As LO, we use a FIR gas laser.

We measure the Y-factor at the optimal point at different frequencies by only varying LO frequencies, but keeping the rest exactly the same. We obtain DSB receiver noise temperatures, which are 842 K (at 1.6 THz), 845 K (1.9 THz), 974 K (2.5 THz) and 1372 K (4.3 THz). After the correction for the losses of the QMC filter and the beam splitter, the noise data show a linear increase with increasing frequency.

Using a quantum noise model [1] for HEB mixers and using a criterion for which the classical output noise must be constant at different frequencies, we analyze the results and find the excess quantum noise factor β to be around 2 and that 24 % of the total receiver noise temperature at 4.3 THz (at the input of the entire receiver) can be ascribed to quantum noise. Clearly the quantum noise has a small but measurable effect on the receiver noise temperature at this frequency.

We are still analyzing different alternatives of interpretation for the mismatch loss between the bolometer and the spiral antenna.

[1] E. L. Kollberg and K. S. Yngvesson, "Quantum-noise theory for terahertz hot electron bolometer mixers," IEEE Trans. Microwave Theory and Techniques, 54, 2077, 2006.

[2] P. Khosropanah, J.R. Gao, W.M. Laauwen, M. Hajenius and T.M. Klapwijk, "Low noise NbN hot-electron bolometer mixer at 4.3 THz," *Appl. Phys. Lett.*, 91, 221111, 2007.

Development of 1.5 THz Waveguide NbTiN HEB Mixers

L. Jiang, T. Yamakura, Y. Irimajiri, K. Shimbo, S. Shiba, T. Shiino, N. Sakai, P. G. Ananthasubramanian, H. Maezawa, S. Yamamoto

***Abstract*— We present results on the design, fabrication, and measurement of 1.5 THz waveguide niobium titanium nitride (NbTiN) superconducting hot electron bolometer (HEB) mixers. The NbTiN HEB mixer element is made from a 12 nm thick NbTiN thin film deposited on a crystalline quartz substrate at room temperature. The Fourier transform spectrometer (FTS) measurement shows that the response of the HEB mixer is centered near 1.3 THz with a bandwidth of about 400 GHz. The uncorrected DSB receiver noise temperature is measured to be 1700 K at 1.5 THz, whereas the mixer noise temperature is 1000 K after correction of quasi-optical and IF chain losses. The required LO power absorbed in the HEB mixer is evaluated to be 340 nW by using an isothermal technique. The IF gain bandwidth is supposed to be about 1.3 GHz or higher. The present results show that good performance can be obtained for the NbTiN HEB mixer even with a relatively thick film (12 nm) fabricated at the room temperature.**

***Index Terms*—Terahertz, Hot electron bolometer mixer, NbTiN film, Receiver noise temperature.**

I. INTRODUCTION

Superconducting mixers play a key role in astrophysics and atmospheric science in the terahertz region, which contains unique spectral lines of ions, atoms, and molecules that profoundly depict fundamental astrophysical and atmospheric processes. In particular, low noise superconductor-insulator-superconductor (SIS) mixers have realized high sensitive astronomical observations on ground-based, airborne, and space-based telescopes [1-2]. However, its sensitivity degrades drastically owing to the abrupt increase of the loss of superconducting film above the energy gap frequency (~700 GHz for niobium, for instance). Superconducting hot electron bolometer (HEB) mixers have matured as the most sensitive heterodyne detectors at frequencies between 1.2 to 6 THz [3-8]. In principle, the RF bandwidth of HEB mixers is not limited by the superconducting energy gap. The superconducting HEB mixers can be operated from millimeter wave up to far infrared without degradation in performance, and show good performance of double-sideband (DSB) receiver noise temperature approaching six times the quantum limit ($6h\nu/k$) with the required local oscillator (LO) power of only a few tens of nanowatt (nW). Therefore, they are being employed for astronomy and atmospheric applications as sensitive detectors to observe faint signals in the THz region [9-11].

Currently the state-of-the-art phonon-cooled HEB mixers are fabricated from a thin niobium nitride (NbN) film. However, the niobium titanium nitride (NbTiN) HEB mixer is an alternative option as well for the HEB mixers [12-13], since its physical and chemical properties are quite similar to those of NbN. In contrast to the NbN film, the NbTiN film can readily be fabricated on quartz substrate, and hence, it can readily be used for a waveguide mixer, which gives a well-defined beam pattern. In spite of this merit, studies on the NbTiN HEB mixers have so far been limited in comparison with the NbN mixers. In this paper, we present our continuous efforts to realize a 1.5 THz waveguide NbTiN HEB receiver for ground-based astronomical observations [14-15].

II. WAVEGUIDE COUPLED NBTIN HEB MIXER

A. Fabrication

Our HEB device is based on an NbTiN superconducting thin film that is deposited on a Z-cut crystalline quartz substrate by the reactive sputtering of an NbTi (weight ratio of Nb:Ti = 4:1) alloy target in a mixture of Ar and N_2 gas at room temperature. By employing an RF plasma assisted sputtering system, the NbTiN film is deposited in a low pressure condition (0.4 Pa) to ensure high film quality.

Fig. 1 shows a sketch of the HEB structure. In the HEB device fabrication, the deposition of the microbridge consisting of a 12 nm NbTiN film and the contact pads (2 nm Ti and 40 nm Au bilayer) on the crystalline quartz substrate is carried out without breaking vacuum. This sputtering process is so-called *in situ* technique, which avoids the unfavorable

Manuscript received 20 April 2009. L. J. thanks Japan Society for the Promotion of Science, for financial support. This work is supported by Grand-in-Aid from the Ministry of Education, Culture, Sports, Science, and Technologies (14204013 and 15071201) of Japan.

L. Jiang, K. Shimbo, S. Shiba, T. Shiino, N. Sakai, and S. Yamamoto are with the Department of Physics, The University of Tokyo, Hongo 7-3-1, Bunkyo-ku, Tokyo 113-0033, Japan. (phone: +81-3-5841-4217; fax: +81-3-5841-4178; e-mail: ljiang@taurus.phys.s.u-tokyo.ac.jp).

T. Yamakura is with the Department of Physics, Graduate School of Pure and Applied Sciences, University of Tsukuba, Japan (e-mail: s0730335@ipe.tsukuba.ac.jp).

Y. Irimajiri is with the National Institute of Information and Communications Technology, Japan. (e-mail: irimaji@nict.go.jp)

P. G. Ananthasubramanian is with the Raman Research Institute, Bangalore, India. (e-mail: pgananth@gmail.com).

H. Maezawa is with the Solar-Terrestrial Environment Laboratory, Nagoya University, Japan. (e-mail: hiro@stelab.nagoya-u.ac.jp).

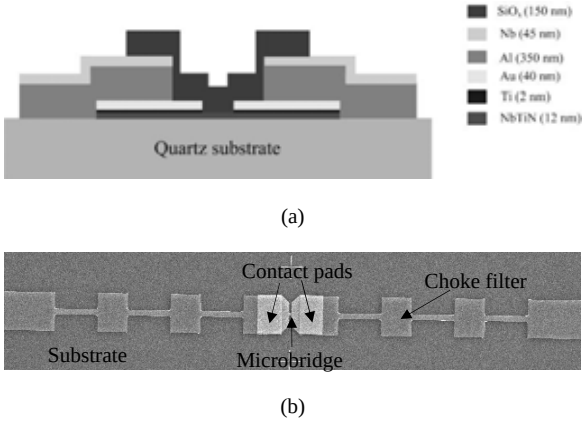

Fig. 1. (a) Cross section view of the microbridge, contact pads, choke filter, and passivation layer. (b) Scanning electron microscope (SEM) micrograph of the fabricated HEB element.

formation of an oxide layer on the NbTiN film surface. The choke filter structure is formed by a lift off process using a positive photo resist mask and *in situ* deposition of 350 nm Al and 45 nm Nb. The microbridge length is defined by a positive electron-beam resist mask and subsequent inductively coupled plasma (ICP) etching. As the last step, the microbridge area is covered by an SiO_x ($1< x <2$) passivation layer for protection. Since it is very difficult to measure the NbTiN film thickness with high accuracy, the film thickness is estimated as a product of the sputtering time and the deposition rate. The NbTiN film thickness is confirmed to be proportional to the sputtering time for films with thickness of a few tens nm. The dimensions of the NbTiN microbridge investigated in this paper are 0.3 μm in length and 1.5 μm in width. The cross section view of the HEB structure is shown in Fig. 1 (a), and a scanning electron microscope (SEM) micrograph of the HEB device in a front view is shown in Fig. 1 (b).

B. DC characterization and analysis

Here we discuss DC properties that indicate the quality of the devices. Fig. 2 shows the measured normal state resistance at 15 K ($R_{15\,K}$) as a function of the ratio of microbridge length to width (L/W) for different-sized devices, where L is the microbridge length and W the microbridge width. The $R_{15\,K}$ values clearly show a linear dependence on L/W, demonstrating good uniformity of the deposited ultra-thin NbTiN film. The linear relation can be represented as $R_{15\,K} = R_{C+A+L} + R_{\square,15\,K} \times (L/W)$, where $R_{\square,15\,K}$ is the square resistance at 15 K, and R_{C+A+L} is the resistance of the contact pads and the antenna structure of the mixer element including contact resistance among them as well as contribution from leads. From Fig. 2, the $R_{\square,15\,K}$ is evaluated to be about 170 Ω. In order to match waveguide coupled RF circuit, we select a device with proper $R_{15\,K}$ close to the waveguide embedding impedance. The device resistance versus temperature (R-T) curve is shown in Fig. 3. The R-T curve shows three superconducting transitions. $T_{c,contact}$ is due to the proximitized NbTiN film under the contact pads as a result of the superconducting proximity effect between the NbTiN film and the normal contact pads of the Au/Ti bilayer. $T_{c,bridge}$ is caused by the NbTiN microbridge itself, which is defined as the temperature at which the resistance becomes a half of the R_{15K}. $T_{c,antenna}$ is supposed to originate from the antenna structure composed of Al/Nb bilayer on top of the NbTiN. The measured $T_{c,bridge}$ is 9.7 K with a transition width ΔT_C of 2.9 K.

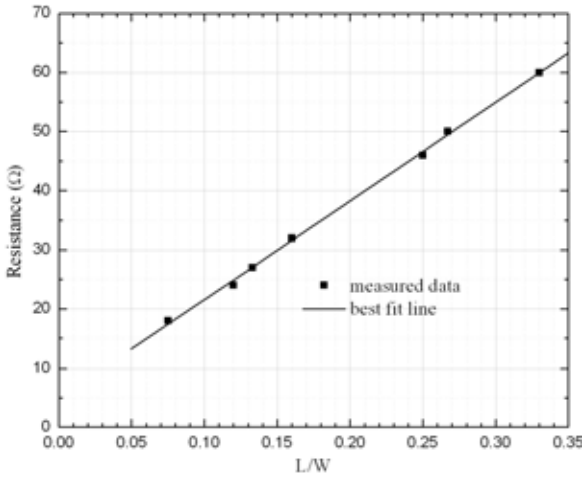

Fig. 2. Measured normal state resistance at 15 K ($R_{15\,K}$) as a function of the ratio of the microbridge length to the width (L/W). The square resistance ($R_{\square,\,15\,K}$) at 15 K is evaluated to be about 170 Ω from the slope of the best fit line.

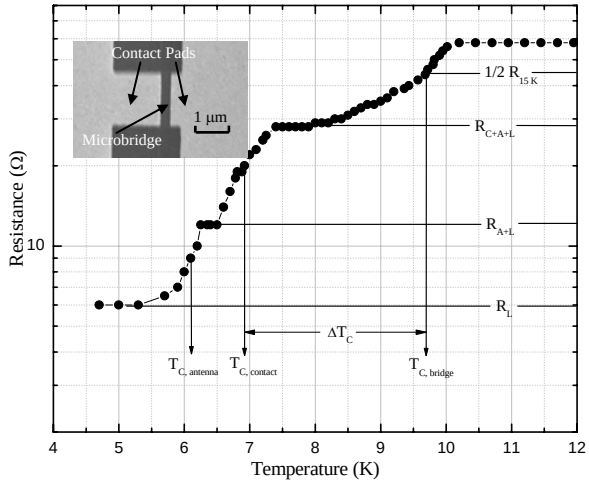

Fig. 3. Resistance versus temperature curve of the measured HEB device, R_{C+A+L} is the resistance above $T_{c,\,contact}$ with $T_{c,contact}$ the critical temperature of the stack layer containing the contact pads and antenna structure on top of the NbTiN film, R_{A+L} the resistance of the antenna and leads, $T_{c,bridge}$ the critical temperature of the NbTiN microbridge, R_L the leads resistance, and ΔT_C the transition width. Inset: zoomed SEM micrograph of the NbTiN microbridge between the contact pads.

C. Design of waveguide coupled RF circuit and characterization

The configuration of the 1.5 THz NbTiN HEB element is designed with the aid of high frequency structure simulator (HFSS) software. The waveguide has a 180 μm width and a 70 μm height. The mixer's RF choke filter is designed on the basis of a 42-μm-wide and 23-μm-thick quartz substrate (ε_r = 4.65), which is accommodated in a 64-μm square slot. A detail of the HFSS calculation is described elsewhere [15].

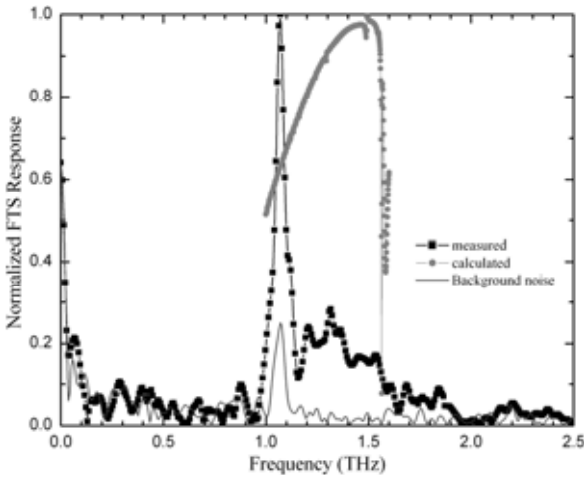

Fig. 4. Normalized direct detection response of the waveguide coupled HEB mixer measured after correction of optical components with a Fourier transform spectrometer. The simulated normalized response is also included for comparison. Note that the peak frequency appearing 1.07 THz is caused by the background noise in FTS measurement room.

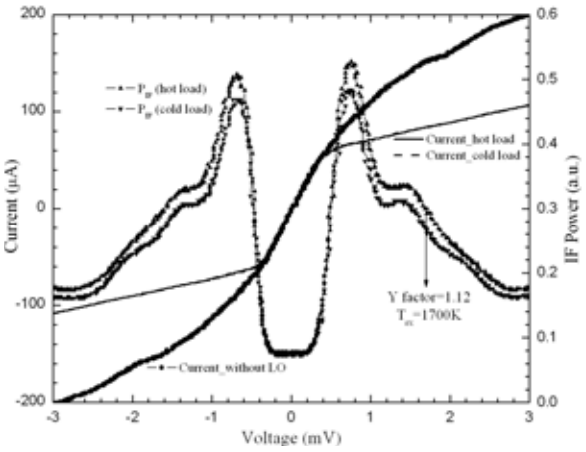

Fig. 5. Current-voltage curves of HEB mixer with and without LO at 1.5 THz, and receiver IF output powers P_{IF} (hot) and P_{IF} (cold) corresponding to the hot (295 K) and cold (77 K) loads respectively as a function of the bias voltage at the optimum LO pumping level. The maximum Y-factor (P_{IF} (hot) / P_{IF} (cold)) is 1.12, which corresponds to the receiver noise temperature of 1700 K.

The experimental characterization of the waveguide coupled mixer response is performed by an evacuated Fourier transform spectrometer (FTS) system with the HEB chip accommodated in the waveguide block. The signal beam of the FTS is collimated to the mixer horn by an elliptical mirror. Fig. 4 shows the measured FTS response of the HEB after correction for the frequency dependent transmission of the optical components of the FTS, including the beam splitter in the FTS and the vacuum window of the 4 K cryostat. The simulated response of the waveguide embedding circuit is shown in the same figure as well. The measured peak frequency appearing at 1.07 THz is due to the background noise of measurement environments. Regardless of the interference noise, the maximum FTS response is found to locate at 1.3 THz, which has a small deviation from the design frequency of 1.5 THz. The 0.2-THz frequency shift is probably caused by imperfect waveguide machining.

III. Measurement Setup

The characterization of the HEB mixer receiver is performed by a quasi-optical setup, which is similar to that reported in the previous paper [15]. The HEB mixer chip is housed in the waveguide mixer block, which is mounted on the cold plate of a GM two-stage 4 K close-cycled refrigerator. The LO source is a 1.4-1.5 THz multiplier chain [16], which provides a peak output power of 20 μW while operated at 1.47 THz. The output horn of the LO source is a diagonal feed horn designed for 1.5 THz. The LO beam is collimated with a parabolic mirror, and is combined with the RF signal of the blackbody radiation from a slab of Eccosorb at 295 K (hot load) and 77 K (cold load) through a 6 μm thick Mylar beam splitter.

The HEB mixer's IF output is connected via a bias-tee to a cooled isolator and a 0.9-1.3 GHz low noise amplifier, which is followed by a room temperature amplifier chain. The latter consists of two amplifiers, a directional coupler with through output followed by a spectrum analyzer, and coupling output filtered by a band pass filter, detected by a square law direct detector, and recorded by computer. The band pass filter has a bandwidth of 200 MHz at the center frequency of 1.1 GHz. The IF amplifier chain connected to the spectrum analyzer provides a gain of 80 dB with a noise temperature of 12 K.

IV. Measurement Results

A. Receiver noise temperature

We have employed the conventional Y-factor method to measure noise temperature of the waveguide NbTiN superconducting HEB mixer. Fig. 5 shows the measured IF output power and the bias current corresponding to the hot and cold loads as a function of the bias voltage at the optimum LO pumping level. The maximum Y factor of 1.12 is achieved at 1.5 THz, when the HEB is operated at the bias voltage of 1.7 mV and the current of 83 μA. We obtain the lowest receiver noise temperature of 1700 K based on the measured Y factor using a Callen and Welton temperature definition [17]. The measurement is performed at the IF frequency (1.1 GHz) at which the mixer gives the best sensitivity. This receiver noise temperature is comparable to those of the waveguide NbTiN HEB mixer receivers so far reported by other groups; 1900 K @ 1.3 THz [12] and 1600 K @ 1.5 THz [18]. We evaluate the required LO power P_{LO} by using an isothermal technique [19]. The LO power requirement at the optimum bias point is evaluated to be 340 nW for the HEB mixer with a 12 nm thick NbTiN film. We can reduce the required LO power by reducing the mixer size. The direct detection effect is not obvious, because the bandwidth of the waveguide HEB mixer is quite narrow according to the FTS measurement results.

We have also confirmed the heterodyne mixing by introducing a small output power of another 1.5 THz frequency source as the RF input. The heterodyne beat signal

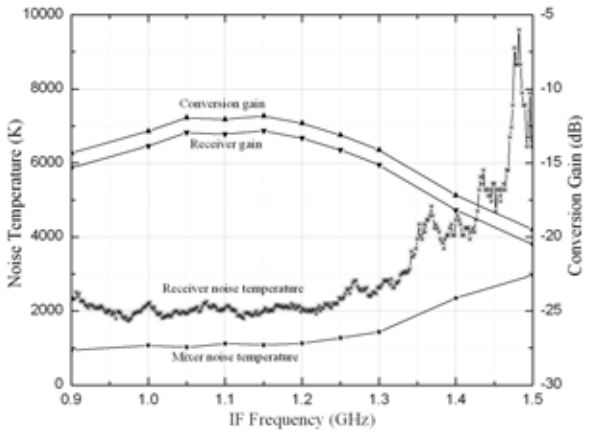

Fig. 6. Measured receiver noise temperature and conversion gain. The mixer noise temperature and conversion gain are obtained after correcting losses of the quasi-optical path and the IF amplifier chain.

is recognized easily in the IF output by a spectrum analyzer.

B. Intermediate frequency gain bandwidth

We have measured the DSB receiver conversion gain of the waveguide NbTiN superconducting HEB mixer with a U-factor technique [20] by measuring the hot and cold load output powers as a function of frequency. Fig. 6 shows the measured receiver and mixer noise temperatures and conversion gains at the optimum operating point. The HEB mixer noise temperature and conversion gain are obtained after correcting the losses in the quasi-optical path and the IF amplifier chain. Since the bandwidth of the IF amplifier chain is 0.9-1.3 GHz, the accurate receiver and mixer gains cannot be obtained below 0.9 GHz and above 1.3 GHz. Nevertheless, we can say that the IF gain bandwidth of the HEB mixer is about 1.3 GHz or higher, even though for a 12 nm thick NbTiN film.

C. Stability

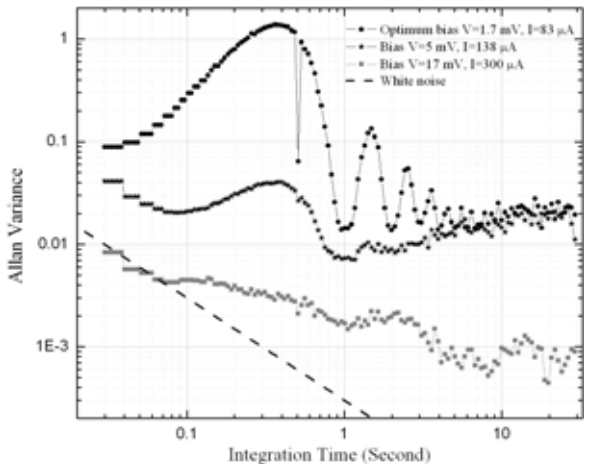

Fig. 7. Allan variance of the NbTiN HEB receiver operated at 1.5 THz obtained in a 200 MHz bandwidth at the optimum bias voltage and higher DC biases. The theoretical white behaviour and stability behaviour of the HEB mixer driven into normal state by high DC bias are included for comparison.

To evaluate the receiver system stability, we have measured, at the optimal operating conditions, the Allan variance [21] of the receiver system. We have performed the Allan variance measurement of the receiver system by monitoring the IF output power as a function of time. The bandpass filter is centered at 1.1 GHz with a 200 MHz bandwidth. In Fig. 7, the Allan variance is measured at the optimum bias point and higher DC biases. It is very clear that the 1 sec period temperature fluctuation and mechanical vibration caused by 4 K close-cycled refrigerator has distinct effect on the Allan variance. Its influence gradually decreases with DC bias voltage, but still exists at high DC bias (17 mV). The Allan time is estimated to be around 1 sec, even if the 1 sec period fluctuation is excluded with a mathematical analysis. This may reflect some instabilities in the IF amplifier chain.

V. CONCLUSION

In summary, we have successfully realized a terahertz heterodyne receiver system based on a superconducting NbTiN HEB mixer. The superconducting NbTiN ultra-thin film deposited on a crystalline quartz substrate at room temperature is used for the HEB mixer. We employ *in situ* fabrication of the NbTiN layer and the Au/Ti contact pads. The waveguide RF embedding circuit is designed by an HFSS software, and is characterized with an evacuated FTS in combination with the NbTiN HEB mixer. We have measured an uncorrected DSB receiver noise temperature to be 1700 K at 1.5 THz. The mixer noise temperature of 1000 K is obtained after the correction of losses of quasi-optical path and IF amplifier chain. The IF gain bandwidth is measured to be about 1.3 GHz or higher at the optimum operating point. The LO power requirement of the HEB mixer is evaluated to be 340 nW for a 1.5×0.3 μm^2 microbridge area. The Allan time is observed to increase with DC bias, and estimated to be about 1 sec while excluding the effect of intrinsic 1 sec period fluctuation by mathematical analysis.

It should be noted that the above performance is obtained based on a 12 nm NbTiN film which is thicker than that used by other groups (a few nm) for the phonon-cooled mixers, where the phonon-cooling is less effective for a thicker film. In contrast to conventional fabrication processes of phonon-cooled HEBs, we have employed an *in situ* process in the HEB fabrication, which ensures good transparency of hot electrons between the NbTiN film and Ti/Au contact layer. It would make the diffusion-cooling process work to some extent in addition to the phonon-cooling process [22]. Although this was pointed out for our 0.8 THz HEB mixers [15], the same effect has also been confirmed in the present 1.5 THz mixer. The attractive advantage of the diffusion-cooled HEBs is that wideband IF gain bandwidth can be achieved with a reasonable noise performance [23]. Therefore, in our HEBs, the existence of both of phonon- and diffusion-cooling mechanisms due to *in situ* process, makes the HEB receiver noise temperature be as low as 1700 K and a 1.3 GHz or higher IF gain bandwidth even with a 12 nm thick NbTiN

film.

ACKNOWLEDGMENT

We are grateful to Dr. Hiroshi Matsuo of NAOJ for allowing us to use his Fourier transform spectrometer.

REFERENCES

[1] B. D. Jackson, T. M. Klapwijk, "The current status of low-noise THz mixers based on SIS junctions," *Physica C 327-276*, pp. 368, 2002.

[2] Brian D. Jackson, Gert de Lange, Tony Zijlstra, Matthias Kroug, Jacob W. Kooi, Jeffrey A. Stern, and Teun M. Klapwijk, "Low-noise 0.8-0.96- and 0.96-1.12-THz superconductor-insulator-superconductor mixers for the Herschel space observatory," *IEEE Trans. Microwave Theory Tech.*, vol. 54, no. 2, 2006.

[3] E. M. Gershenzon, G. N. Golt'sman, I. G. Gogidze, A. I. Eliantev, B. S. Karasik, and A. D. Semenov, "Millimeter and submillimeter range mixer based on electron heating of superconducting films in the resistive state," *Sov. Phys. Supercond.*, vol. 3, pp. 1582, 1990.

[4] A. D. Semenov, H. –W. Hübers, J. Schubert, G. N. Golt'sman, A. I. Elantiev, B. M. Voronov, and E. M. Gershenzon, "Design and performance of the lattice-cooled hot-electron terahertz mixer," *J. Appl. Phys.*, vol. 88, no. 11, pp. 6758-6767, 2000.

[5] S. Cherednichenko, P. Khosropanah, E. Kollberg, M. Kroug, and H. Merkel, "Terahertz superconducting hot-electron bolometer mixers," *Physica C*, vol. 372-376, pp. 407-415, 2002.

[6] J. J. A. Baselmans, M. Hajenius, J. R. Gao, T. M. Klapwijk, P. A. J. de Korte, B. Voronov, and G. Gol'tsman, "Doubling of sensitivity and bandwidth in phonon cooled hot electron bolometer mixers," *Appl. Phys. Lett.*, vol. 84, no. 11, pp. 1958-1960, 2004.

[7] W. Zhang, P. Khosropanah, J. N. Hovenier, J. R. Gao, T. Bansal, M. Hajenius, T. M. Klapwijk, M. I. Amanti, G. Scalari, and J. Faist, "Demonstration of a heterodyne receiver for detection of OH line at 3.5 THz based on a superconducting HEB mixer and a distributed feedback quantum cascade laser," *Proc. of 19th Int. Symposium on Space Terahertz Tech.*, pp. 53-58, 2008.

[8] P. Khosropanah, J. R. Gao, W. M. Laauwen, M. Hajenius, and T. M. Klapwijk, "Low noise NbN hot electron bolometer mixer at 4.3 THz," *Appl. Phys. Lett.*, vol. 91, 221111, 2007.

[9] Göran L. Pilbratt, "Herschel mission overview and key programmes," *Proc. of 19th Int. Symposium on Space Terahertz Tech.*, pp. 97, 2008.

[10] Eric Becklin, "Stratospheric observatory for infrared astronomy," *Proc. of 19th Int. Symposium on Space Terahertz Tech.*, pp. 27, 2008.

[11] D. Meledin, V. Desmaris, S. –E. Ferm, M. Fredrixon, D. Henke, I. Lapkin, O. Nyström, A. Pavolotsky, M. Strandberg, R. Sundin, and V. Belitsky, "APEX band T2 1.25-1.39 THz waveguide balanced HEB receiver," *Proc. of 19th Int. Symposium on Space Terahertz Tech.*, pp. 181-185, 2008.

[12] D. Loudkov, C. –Y. E. Tong, R. Blundell, K. G. Megerian, and J. A. Stern, "Performance of the NbTiN hot electron bolometer mixer with AlN buffer layer at terahertz frequency range," *IEEE Trans. Appl. Supercond.*, vol. 15, no. 2, 476-479, 2005.

[13] Pedro Pablo Muñoz, Sven Bedorf, Michael Brandt, Thomas Tils, Netty Honingh, and Karl. Jacobs, "THz waveguide mixers with NbTiN HEBs on silicon Nitride membranes," *IEEE Microwave and Wireless Components Lett.*, vol. 16, no. 11, 2006.

[14] L. Jiang, S. Shiba, K. Shimbo, M. Sugimura, P. G. Ananthasubramanian, H. Maezawa, Y. Irimajiri, S. C. Shi, and S. Yamamoto, "Development of 0.8 THz and 1.5 THz Waveguide NbTiN HEB Mixers," *Proc. of 19th Int. Symposium on Space Terahertz Tech.*, pp. 409-412, 2008.

[15] L. Jiang, S. Shiba, K. Shimbo, N. Sakai, T. Yamakura, M. Sugimura, P. G. Ananthasubramanian, H. Maezawa, Y. Irimajiri, and S. Yamamoto, "Development of THz Waveguide NbTiN HEB Mixers," *IEEE Trans. Appl. Supercond.*, accepted.

[16] VDI user guide, 1.46 THz FEM, *Virginia Diodes Inc.*, 2005.

[17] Anthony R. Kerr, "Suggestions for revised definitions of noise quantities, including quantum effects," *IEEE Trans. Microwave Theory Tech.*, vol. 47, no. 3, pp. 325-329, 1999.

[18] M. C. Wiedner, G. Wieching, F. Bielau, K. Rettenbacher, N. H. Volgenau, M. Emprechtinger, U. U. Graf, C. E. Honingh, K. Jacobs, B. Vowinkel, K. M. Menten, L. –A. Nyman, R. Gusten, S. Philipp, D. Rabanus, J. Stutzki, and F. Wyrowski, "First observations with CONDOR, a 1.5 THz heterodyne receiver," *Astronomy & Astrophysics* 454, L33-L36, 2006.

[19] G. N. Gol'tsman, B. S. Karasik, O. V. Okunev, A. L. Dzardanov, and E. M. Gershenzon, "NbN hot electron superconducting mixers for 100 GHz operation," *IEEE Trans. Appl. Supercond.*, vol. 5, no. 2, pp. 3065-3068, 1995.

[20] Ling Jiang, Wei Miao, Wen Zhang, Ning Li, Zhen Hui Lin, Qi Jun Yao, Sheng-Cai Shi, Sergey I. Svechnikov, Yury B. Vakhtomin, Sergey V. Antipov, Boris M. Voronov, Natalia S. Kaurova, and Gregory N. Gol'tsman, "Characterization of a quasi-optical NbN superconducting HEB mixer," *IEEE Trans. Microwave Theory Tech.*, vol. 54, no. 7, 2006.

[21] D. W. Allan, "Statistics of Atomic Frequency Standards", *Proc. of the IEEE*, vol. 54, no. 2, pp. 221-230, 1966.

[22] S. A. Ryabchun, I. V. Tretyakov, M. I. Finkel, S. N. Maslennikov, N. S. Kaurova, V. A. Seleznev, B. M. Voronov, and G. N. Goltsman, "Fabrication and characterization of NbN HEB mixers with in situ gold contacts," *Proc. of 19th Int. Symposium on Space Terahertz Tech.*, pp. 62-67, 2008.

[23] I. Siddiqi, A. Verevkin, D. E. Prober, A. Skalare, W. R. McGrath, P. M. Echternach, and H. G. LeDuc, "Heterodyne mixing in diffusion-cooled superconducting aluminum hot-electron bolometers," *J. Appl. Phys.*, vol. 91, no. 7, pp. 4646-4654, 2002.

W2D

System Performance of NbTiN THz SHEB Waveguide Mixers and Cryogenic SiGe LNA

P. Pütz[1*], M. Schultz[1], C.E. Honingh[1], M. Justen[1], K. Jacobs[1], J. Bardin[2], G. Jones[2], H. Mani[2], and S. Weinreb[2]

1 KOSMA, 1. Physikalisches Institut der Universität zu Köln, 50937 Köln, Germany*

2 Department of Electrical Engineering, California Institute of Technology, Pasadena CA 91125

* Contact: puetz@ph1.uni-koeln.de, phone +49-221-470-3769

***Abstract*—Due to the intrinsic IF 3-dB roll-off frequency of a superconducting hot electron bolometer (SHEB) mixing device of only a few GHz, a large relative IF processing bandwidth with a lower band edge ≤ 1 GHz is important to exploit the full potential of a SHEB receiver. In particular this is mandatory for astronomical measurements in the THz frequency range.**

We present test receiver measurements of several NbTiN THz SHEB waveguide mixers in combination with a newly available 0.3–4 GHz cryogenic low noise amplifier (LNA) based on discrete SiGe heterojunction bipolar transistors. This SiGe LNA is especially suitable for SHEB mixer IF amplification because of its multi-octave bandwidth at low frequencies and low input reflection coefficient. As a result – contrary to current approach for stable SHEB receiver operation – neither an isolator nor a balanced LNA configuration for suppression of the reflected IF power at the amplifier input is required. An isolator severely limits the relative IF bandwidth to less than one octave and balanced amplifiers are too bulky for future array applications, even if one could accommodate the additional dissipation. We investigate the IF frequency response of the test receiver with regard to output power stability (i.e. Allan times), ripple and receiver noise and demonstrate that this receiver configuration is suitable for astronomical operation. With these LNAs the 1.4 THz and 1.9 THz SHEB receiver channels of the German Receiver for Astronomy at Terahertz Frequencies (GREAT) for the Stratospheric Observatory for Infrared Astronomy (SOFIA) and the balloon-borne Stratospheric Terahertz Observatory (STO) will get a substantial enlargement of available IF bandwidth.

Integration of a Mobile Terahertz Spectroscopic System based on HEB Heterodyne Detection

Jack T. Surek, Thomas J. Hofer, and Eyal Gerecht, *Member, IEEE*

***Abstract*—We are developing a mobile heterodyne terahertz system based on hot electron bolometer (HEB) mixer receivers to both image and obtain spectra from biological samples. An HEB mixer provides unprecedented sensitivity and spectral resolution at terahertz frequencies. We have recently demonstrated a low-noise heterodyne passive imager operating at 0.85 THz [1]. A heterodyned HEB detector integrated with a low noise amplifier and quasi-optical beam handling based on polymer lenses are central to this radiometric system. The current design is optimized for the atmospheric windows centered at 650 GHz and 850 GHz, but can be extended to any terahertz frequency. A state-of-the-art mechanical cooler with a very small footprint, high temperature stability, and low mechanical vibrations is also under development for our HEB receiver technology. Here we report the integration of these different elements into one platform that will result in a flexible, mobile, and versatile diagnostic instrument capable of long-term, low-maintenance operation in biomedical applications. We intend to perform real-time tissue diagnosis using broadband terahertz spectroscopy that is guided by terahertz imaging with a spot size of 500 micrometers or less with this mobile platform.**

***Index Terms*—Heterodyne detection, hot electron bolometer (HEB) detectors, quasi-optical coupling, radiometry, terahertz imaging, terahertz spectroscopy.**

I. Introduction

Terahertz spectroscopy and imaging have great potential for healthcare and a wide range of remote sensing applications. Terahertz frequencies correspond to unique vibrational and rotational energy level transitions in molecules. Terahertz radiation also has a shorter wavelength than that of the microwave to millimeter wave range, easily providing sub-millimeter spatial resolution.

Terahertz radiation can identify complex gas molecules in plasma by their resonant rotational energy absorption from the field. These have a wide range of remote sensing applications from astronomy, to monitoring semiconductor fabrication, to homeland security. If the molecules reside in a partially ionized plasma then terahertz spectroscopy is better than its optical and microwave competitors in detection sensitivity.

We are also developing terahertz systems for non-destructive evaluation (NDE) of materials and chemical sensing in terms of scattering parameters and noise. Similar measurements can be made on solutions of thin cross-section. So terahertz sensing will be a natural complement to microfluidic and similar lab-on-chip systems.

By using hot electron bolometer (HEB) heterodyne detectors in terahertz spectrometers, we can come close to quantum-noise-limited sensitivity with spectral resolution that approaches a few kilohertz. This potential for high resolution spectra is particularly important in measuring minute changes in terahertz absorption that occur with conformational changes such as protein folding, or complex formation between biomolecules. Here we detail the integration of an HEB receiver with a quasi-optical system to handle local oscillator and radiometric signals along with a state-of-the-art mechanical cryogenic cooler in a mobile platform for terahertz imaging and spectroscopy.

II. HEB Heterodyne Detection

HEBs are surface superconducting devices with extremely small parasitic reactances, even at the highest terahertz frequencies. HEB devices are able to absorb radiation up to the visible range due to their very short momentum scattering times. The detection signal comes from a change in device resistance as the quasi-particles warm. HEB devices are fabricated from 3.5 to 4 nm thick NbN films that are sputtered onto silicon. Typical device size can range from 2 micrometers wide by 0.5 micrometers long down to sub-micrometer dimensions. We direct beams carrying the local oscillator (LO) signal and the radiometric signal from a sample to this HEB detector using quasi-optics. A twin slot antenna couples the radiation to the HEB device, and this mixer/antenna combination is centered at the second focus of a 4 mm diameter silicon ellipsoidal lens to maximize optical coupling. The twin-slot antenna surrounding the HEB has a highly symmetrical and linearly polarized radiation pattern providing nearly perfect power coupling to the incident Gaussian beam. This gold monolithic terahertz antenna is patterned on a silicon substrate by use of an electron-beam metallization step followed by a lift-off step. The impedance of the HEB is matched to this antenna by adjusting its aspect ratio. In this configuration, radiation from the antenna becomes a plane wave in the aperture plane outside the lens. The combination of the silicon lens and the twin-slot antenna results in a far-field beam with a full width at half power (FWHP) of about 3 degrees.

HEBs made of NbN films have a thermal time constant that is determined by both the rate at which phonons are emitted by

Manuscript received 20 April 2009.

J. T. Surek and E. Gerecht are with the National Institute of Standards and Technology, Boulder, CO 80305 USA (phone: 303-497-4244; fax: 303-497-3970; e-mail: jsurek@boulder.nist.gov).

T. J. Hofer is with Bethel University, St. Paul, MN 55112 USA.

the electrons and the escape rate of the phonons from the NbN film to the substrate. NbN HEBs are, therefore, known as phonon-cooled HEBs and can exhibit conversion gain bandwidths of about 4 GHz, while the receiver noise temperature bandwidth can be up to twice the gain bandwidth. An operating temperature range for the HEB devices of 4 K to about 6 K is an advantage over most other far-infrared (FIR) devices, which require cooling to sub-Kelvin temperatures.

In a typical receiver system, the front-end mixer is integrated with a low-noise amplifier (LNA). We have demonstrated a design for integrating the HEB device and a monolithic microwave integrated circuit (MMIC) LNA in the same block [1]. A multi-section microstrip matching network is employed to achieve broadband coupling between the HEB and the MMIC LNA. The HEB device is located in close proximity to the MMIC chip, which is mounted in a narrow rectangular cavity for the purpose of eliminating possible amplifier oscillations. This particular MMIC LNA has been characterized against standards developed at the National Institute of Standards and Technology (NIST) and, by use of a recently developed measurement technique [2], exhibits noise performance of below 5.5 K from 1 GHz to 11 GHz. To power the device and extract the intermediate frequency (IF) signal from it, we use a bias "tee" circuit that is built into the mixer block.

We have also demonstrated an integrated design for a small focal plane array (FPA) with two pixels that allows for dual-frequency and dual-polarization operation [3]. Fig. 1 shows a photograph of the two-pixel HEB/MMIC-LNA integrated mixer block. The pixels operate independently of each other. SMA coaxial lines and connectors allow us to extract the two IF outputs from the sides of the block and two connectors provide all DC bias lines for the HEB devices and the MMIC LNAs. The optical configuration of the pixels in the array is of the "fly's eye" type, which allows ample space for other components in the focal plane. The performance of this FPA demonstrates the suitability of HEBs as mixer elements in much larger FPAs in the future. FPAs with two or more pixels will increase image scan rate and simultaneous operation of neighboring pixels at different frequencies or polarizations. They can also operate in correlation receivers. In summary, this general architecture is well suited for construction of FPAs with a large number of pixels to produce terahertz imagers and spectrometers with superior sensitivities and speeds.

III. Quasi-Optical System Design

Our previous terahertz imaging system relied on off-axis paraboloid (OAP) mirrors for beam handing [1]. While this approach minimizes optical power loss, aberrations from these mirrors limit the minimum spot size and shape that can be achieved. A better approach, which retains the high efficiency of free space propagation, uses a quasi-optical imaging system [4] based on lenses. Our approach uses three dielectric lenses that are machined from high density polyethylene (HDPE) to create convex surfaces at a design wavelength of 635 gigahertz. This provides diffraction-limited spatial resolution as measured by the beam width on the sample.

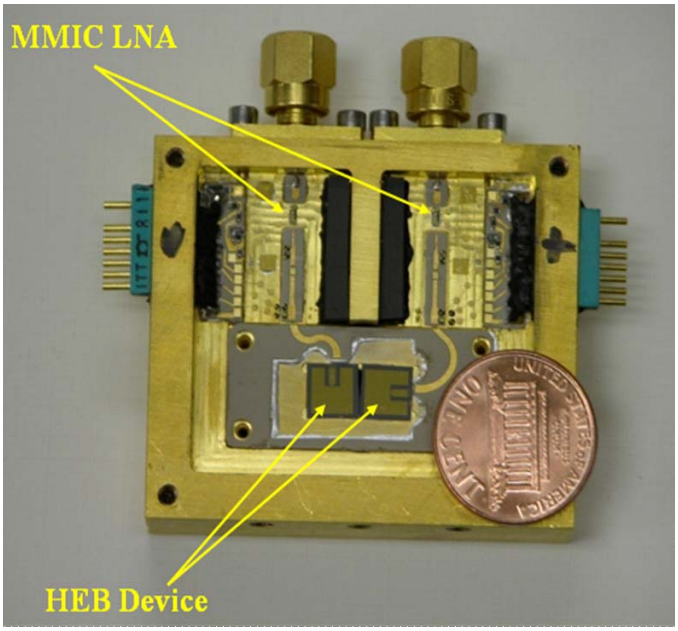

Fig. 1. Two-pixel integrated mixer block housing two HEB devices and two MMIC LNAs. This configuration maximizes SNR [3].

To relay the signal beam a distance of approximately 800 mm between sample surface and HEB receiver, lens structures were designed from the object (sample) plane, as follows: (1) an objective lens with its first surface focusing to a waist of ~1 wavelength at 25 mm and a second surface at infinite radius to generate a collimated beam, (2) a lens to collect this collimated beam that has both surfaces designed to focus at 100 mm, and (3) a much larger focusing lens with both surfaces machined to focus at 100 mm, designed to couple the beam into the 4 mm elliptical silicon lens, to which the HEB/antenna element is affixed. The radiometric signal beam is drawn over a photograph of our optical layout in Fig. 2. The collimated region allows compliance in beam path length for integration.

Lens positions were initially simulated using a custom graphical layout program that we developed and then tested by direct calorimetric measurements. To achieve this, the 635 and 850 gigahertz sources were placed at the HEB mixer position, reversing the light path to map the beam and measure beam waists at critical points. This was done by cutting the Gaussian beam with a razor blade assembly mounted to an XY stage driven by micro-stepping linear motors. Calorimetric measurements made as this beam was cut then resulted in data that approximated an error function curve.

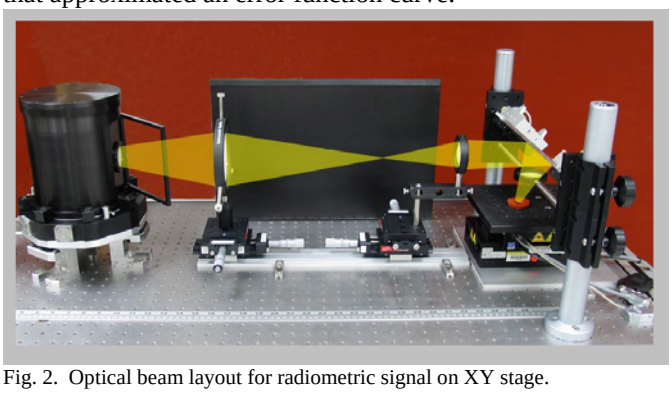

Fig. 2. Optical beam layout for radiometric signal on XY stage.

We differentiated and fit this curve to a Gaussian profile to determine beam width. Data from one of these fits is shown in Fig. 3. The minimum measured beam widths at the object plane for 635 GHz and 850 GHz were 600 micrometers and 500 micrometers, respectively. We also confirmed that using the 850 GHz source with the hyperbolic profile lenses, we designed for 635 GHz, increased focal distances by 3%.

IV. System Integration

A photograph of the mobile cart platform that we are assembling our new terahertz system on is shown in Fig. 4. With it we are engineering a robust platform for a terahertz system that ultimately will provide fixed-frequency imaging and chirped spectroscopy. It combines the HEB receiver, a custom mechanical cryocooler, a local oscillator source, quasi-optics for beam handling and a motion control/data acquisition system. The custom cooler is a 4K Stirling-type pulse tube design, developed through an ongoing collaboration with our colleagues in the NIST Chemical Sciences and Technology Laboratory [5]. Its operation at 30 Hz minimizes temperature fluctuations and mechanical vibrations at the HEB mixer block, thus reducing noise and gain fluctuations. Moreover, configuring the cryogenic system in this way allows for many months of operation without supervision or maintenance. An automated motion controller drives XY sample translators and acquires data in real-time.

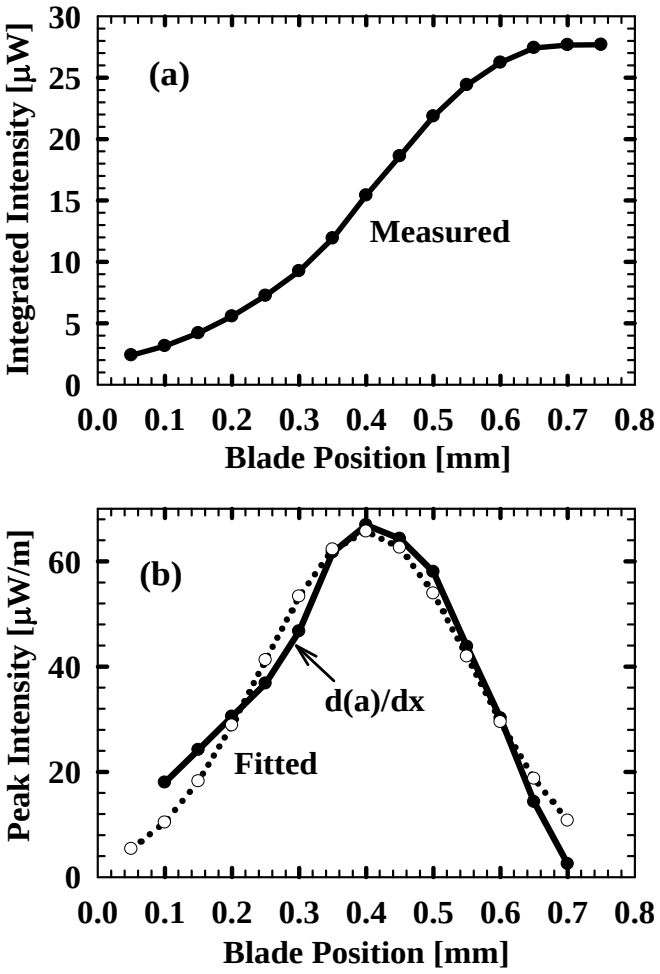

Fig. 3 An example of experimental beamwidth fitting. In (a), intensity is measured with a calorimeter as the beam is progressively opened past a razor edge that cuts/occludes it orthogonally. Note that while intensities are given units here, the absolute value depends on calorimeter placement and any collection optics used downstream of the cut. In (b) the first derivative of the data (averaging two points) is calculated from the data and a Gaussian peak is least squares fit to the result. Here the full width to e^{-2} of peak is 580 micrometers.

Fig. 4. Photograph of our terahertz imaging and spectroscopy system assembled on a mobile cart platform.

The practical choices of LO sources at terahertz frequencies include FIR lasers operating on a number of discrete spectral lines throughout the terahertz spectrum, and harmonic multiplier sources in the lower terahertz spectrum. We have chosen the harmonic multiplier architecture for our LO sources because of their compact size, ease of use, and availability for frequencies in the lower terahertz spectrum. We have deployed a number of commercially available harmonic multiplier sources [6] as the LO signal. Our 850 GHz source consists of a phase-locked dielectric resonance oscillator with an output signal at 11.8 GHz and a 72x multiplication chain. This source produces about 300 microwatts, which is sufficient for a small array of HEB mixers. A tunable range of about 10% was achieved with this multiplier source by replacing the low frequency signal that drives the multiplication chain with a microwave synthesizer having sub-hertz spectral resolution. Tunability is important because the next step will be to chirp this source for rapid spectral acquisition.

In order to combine the LO and radiometric signal along the final beam path into the mixer, we employ Mylar beam splitters, ranging in thickness from 6 to 25 micrometers, reflecting 28% to 1% of the incoming LO radiation, respectively. In future designs the material under measurement will be actively polarized with a source that also relies on harmonic multiplication.

V. Biomedical Applications

We are integrating hardware and sample handling methods in a mobile cart platform to perform terahertz imaging and spectroscopy aimed at sensing the large and increasing

number of diseases that are being identified as problems caused by protein excesses in the cell [7]-[9]. For cancer, protein production goes on unchecked, but in many more cases there are problems with the way a protein self-folds or with the cell machinery that helps it fold. Protein conformational problems lead to aggregated complexes, as in the case of amyloidosis or proteins that can't be recognized by the normal proteolysis machinery of the cell that takes out the garbage. Many important diseases result from protein conformational problems, e.g. Alzheimer's, Huntington's, the prion diseases, cystic fibrosis, type 2 diabetes and Parkinson's disease.

Terahertz spectroscopy on biological substances is still novel, but results so far suggest that it is sensitive to protein folding [10]-[11] and protein surface hydration [11]-[13] in isolated biochemical samples. While some authors have been investigating the degree to which terahertz spectroscopy can report structure down to the level of singular bonds, the conditions that allow such specificity are too restrictive and require extensive modeling [14]. Also, frequency-domain spectra of random biopolymers dried into 100 micrometer thick test films are too averaged to show spectral shapes characteristic of the small biomolecule constituent [15].

Terahertz spectra of good resolution can be achieved only through techniques which control the signal attenuation due to water absorption and spectral broadening caused by the thermal averaging. Both of these aspects demand techniques that limit the thickness of samples to tens of micrometers. To perform terahertz imaging and spectroscopy that are selective for the tissue surface, we plan to combine optical focusing with active polarization of the sample surface for real-time diagnostics during surgery. By imaging with a spot of 500 micrometers or less at the tissue surface it should be possible to identify the extent of diseased tissue during surgical removal. For clinical diagnostics outside of the operating theater, tissue and cell biopsies may additionally be flash-frozen to distinguish such protein imbalances with much greater sensitivity. We are integrating the above capabilities that will allow the efficacy of a drug treatment to be monitored over time, for example. Therefore we envision a vital role for frequency-chirped terahertz spectroscopy in clinical diagnostics and real-time surgical monitoring of protein conformational diseases.

VI. Summary

Terahertz imaging and spectroscopy can play an important role in bioscience and materials sensing applications. Like any other spectroscopic method, it has challenges and limitations to overcome to advance beyond a curiosity. Some of these are technical, such as incorporation of the HEB mixer for detection; but development of appropriate sample handling and stimulus methods are just as important to an optimized platform. Our efforts have therefore shifted toward a more balanced approach that leverages the best available technology to serve the needs of biological applications. While there are many challenges ahead, we see the integration of a highly frequency selective and sensitive HEB receiver-based system combined with quasi-optical methods of beam handling on a mobile cart platform as a critical step toward making terahertz spectroscopy and imaging a relevant tool for real-time diagnostics in life sciences. We anticipate that the same consideration will lead to very similar platforms for materials NDE as well.

References

[1] E. Gerecht, D. Gu, L. You and K. S. Yngvesson, "A passive heterodyne hot electron bolometer imager operating at 850 gigahertz," *IEEE Trans. Micr. Theory Tech.*, vol. MTT56, pp. 1083-1091, May 2008.

[2] J. Randa, E. Gerecht, D. Gu, and R. Billinger, "Precision Measurement Method for Cryogenic Amplifier Noise Temperatures Below 5 K," *IEEE Trans. Microw. Theory Tech.*, vol. 54, no. 3, pp. 1180–1189, Mar. 2006.

[3] D. Gu, E. Gerecht, F. Rodriguez-Morales, and S. Yngvesson, "Two-Dimensional Terahertz Imaging System Using Hot Electron Bolometer Technology", *17th Intern. Symp. Space THz Technol.*, Paris, France, April 10-12, 2006.

[4] P. F. Goldsmith, *Quasioptical Systems*, Piscataway, NJ: IEEE Press 1998.

[5] P. E. Bradley, E. Gerecht, R. Radebaugh, and I. Garaway, "Development of a 4 K Stirling-Type Pulse Tube Cryocooler for a Mobile Terahertz Detection System", *to be presented at the Cryogenic Engineering Conference and International Cryogenic Materials Conference 2009.*

[6] Virginia Diodes, Inc., Charlottesville, VA, 2006 [Online]. Available: http://www.virginiadiodes.com/multipliers.htm.

[7] L. M. Luheshi, D. C. Crowther, and C. M. Dobson, "Protein misfolding and disease: from the test tube to the organism," *Curr. Opin. Chem. Biol.*, vol.12, iss.1, pp. 25-31, February 2008.

[8] C. Reiss, T. Lesnik, H. Parvez, S. Parvez, and R. Ehrlich, "Conformational toxicity and sporadic conformational diseases," *Toxicology*, vol. 153, no.1-3, pp. 115-121, November 16, 2000.

[9] R. W. Carrell, "Cell toxicity and conformational disease," *Trends Cell Biol.*, vol. 15, no. 11, pp. 574-80, Epub October 3, 2005.

[10] Y. Qu, H. Chen, X. Qin, L. Li, L. Wang and T. Kuang, "Thermal denaturation of CP43 studied by Fourier transform infrared spectroscopy and terahertz time domain spectroscopy," *Biochimica et Biophysica Acta – Proteins & Proteomics*, vol. 1774, iss. 12, pp. 1614-1618, December 2007.

[11] S. J. Kim, B. Born, M. Havenith, and M. Gruebele, "Real-time detection of protein-water dynamics upon protein folding by terahertz absorption spectroscopy," *Angew. Chem. Int. Ed.*, vol. 47, pp. 6486-6489, 2008.

[12] S. Ebbinghaus, S. J. Kim, M. Heyden, X. Yu, M. Gruebele, D. M. Leitner and M. Havenith, "Protein sequence- and pH-dependent hydration probed by terahertz spectroscopy," *J. Amer. Chem. Soc.*, vol. 130, pp. 2374-2375, 2008.

[13] S. Ebbinhaus, S. J. Kim, M. Heyden, X. Yu, U. Heugen, M. Gruebele, D. M. Leitner and M. Havenith, "An extended dynamical hydration shell around proteins," *Proc. Natl. Acad. Sciences*, vol. 104, no. 52, pp. 20749-20752, December 26, 2007.

[14] D. F. Plusquellic, Siegrist, K., E. J. Heilweil and O. Esenturk, "Applications of terahertz spectroscopy in biosystems," *ChemPhysChem*, vol. 8, pp. 2412-2431, 2007.

[15] B. M. Fischer, M. Hoffman, H. Helm, R. Wilk, F. Rutz, T. Kleine-Ostmann, M. Koch. and P. U. Jepsen, "Terahertz time-domain spectroscopy and imaging of artificial RNA," *Optics Express*, vol. 13, no. 14, pp. 5205-5215, 11 July 2005.

Session W3

Receivers & Backends

Chair: Victor Belitsky

Wednesday, April 22
2:20 – 3:20

ATOMMS: the Active Temperature, Ozone and Moisture Microwave Spectrometer

Christopher Groppi, E. Robert Kursinski, Dale Ward, Angel Otarola, Kate Sammler, Michael Schein, Sarmad Al Banna, Brian Wheelwright, Steve Bell, Willy Bertiger, Mark Miller, Herb Pickett

Abstract— ATOMMS represents a new class of active, airborne, limb-viewing spectrometer that is a cross between Global Positioning System (GPS) occultations (e.g [1]) and NASA's Microwave Limb Sounder. ATOMMS will characterize atmospheric constituents by actively probing their cm and mm wavelength absorption lines. Two instrument packages are being constructed for NASA's WB-57F high altitude research aircraft, now equipped with precise WAVES gimbaled pointing systems. One aircraft will generate multiple tones near the 22 GHz water line and 183 GHz to 204 GHz absorption lines and transmit them across the Earth's limb through the atmosphere to receivers on a second aircraft. Flight paths of the two aircraft begin over the horizon, with the two aircraft flying at 65 kft altitude. This creates a rising occultation geometry as the aircraft fly towards each other. ATOMMS provides the sensitivity, resolution and accuracy needed to satisfy key monitoring needs for temperature, pressure, moisture and ozone. The 100 to 200 m ATOMMS vertical resolution will far surpass the 1 to 4 km vertical resolution of present state-of-the-art satellite radiometers opening a window into atmospheric scales previously inaccessible from space. Predicted precisions of individual ATOMMS temperature, pressure and moisture profiles are unprecedented at ~0.4 K, 0.1% and 1-3% respectively, extending from near the surface to the flight altitude of ~20 km. ATOMMS ozone profiles precise to 1-3% will extend from the upper troposphere well into the mesosphere. Other trace constituents such as water isotopes can be measured with performance similar to that of ozone. The ATOMMS experiment is a pathfinder experiment for eventual implementation on a constellation of satellites. Space observations from multiple satellites in precessing orbits will allow for global spatial coverage and increased altitude coverage. Our long term goal is a constellation of approximately a dozen small spacecraft making ATOMMS measurements that will provide dense, global coverage and complete cloud-penetration and diurnal sampling every orbit. The ATOMMS instrument packages are now being tested and assembled, with expected flight series in spring and early summer, 2009.

***Index Terms*—Remote Sensing, Terrestrial atmosphere, Microwave receivers, Microwave transmitters**

Manuscript received 20 April 2009.

C. Groppi (NSF Astronomy and Astrophysics Postdoctoral Fellow), M. Schein, S. Al Banna, B. Wheelwright and S. Bell are with Steward Observatory, University of Arizona, Tucson, AZ 85721 USA (520-626-1627; fax: 520-621-1532; e-mail: cgroppi@as.arizona.edu).

E.R. Kursinski, D. Ward, A. Otarola and K. Sammler are with the Department of Atmospheric Sciences, University of Arizona, Tucson, AZ 85721.

W. Bertiger, M. Miller and H. Picket are with the NASA Jet Propulsion Laboratory, Pasadena, CA 90220 USA.

I. INTRODUCTION

ATOMMS is a new remote sensing system that combines features of GPS RO with the Microwave Limb Sounder (MLS). It is an active limb viewing occultation system that promises performance that will make it a key observing system in the Global Climate Observing System (GCOS). We are building a prototype of the instrument for an aircraft to aircraft occultation demonstration of its performance. A high-level ATOMMS instrumental configuration is depicted in Figure 1.

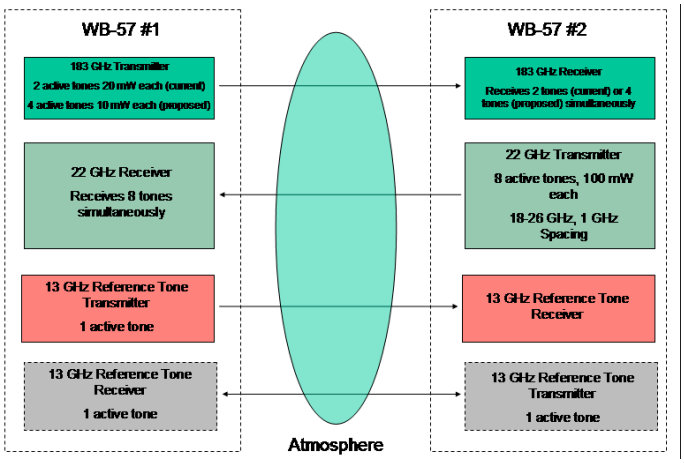

Figure 1: ATOMMS experiment configuration. The two payloads are referred to as ATOMMS-A and ATOMMS-B.

Figure 2 shows the key elements of the ATOMMS instrumentation demonstration on one of the two aircraft: (1) ATOMMS microwave instrument 13 GHz, 22 GHz and 183 GHz transmitters and receivers, (2) ATOMMS precise positioning system hardware consisting of a GPS receiver a 3 axis precision accelerometer system on each aircraft, (3) the WB57F aircraft and (4) the WAVE gimbal built by SRI for NASA that points the ATOMMS microwave instrument. Not shown are the ATOMMS retrieval system and the precise positioning system software.

During an occultation, each ATOMMS microwave transmitter radiates several monochromatic signal tones that pass through the atmosphere to the receiver on the opposite side of the atmosphere (as shown in Figure 1) which digitizes and records the signals. We have designed the ATOMMS transmitters and receivers to simultaneously sample water vapor at both the 22 and 183 GHz lines to create the dynamic range needed to profile water vapor from the surface into the

mesosphere as well as measure ozone at 195 GHz in the upper troposphere and middle atmosphere. The ATOMMS retrieval system later derives the phase and amplitude of the signals and combines them with the precise knowledge of the transmitter and receiver positions (estimated by the ATOMMS precise positioning subsystem) to derive profiles of atmospheric moisture, ozone, temperature and pressure.

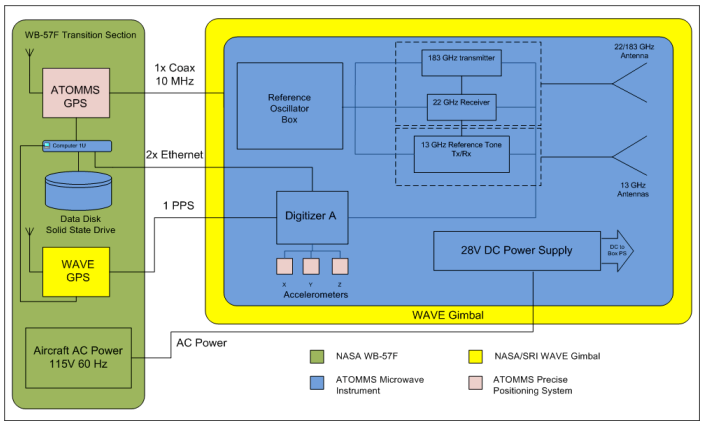

Figure 2: Block diagram of the ATOMMS A aircraft. With the exception of the science tone complement, ATOMMS B is identical.

The ATOMMS system has a unique set of strengths for monitoring climate and climate change as well as strongly constraining physical processes in the atmosphere, which are unmatched by any current or planned satellite-borne water vapor sensors. Some of the research benefits afforded by ATOMMS observations are briefly summarized in this section. A more complete description of the potential research benefits of ATOMMS can be found in [2].

II. Scientific Motivation

A. Accuracy and Vertical Resolution of Temperature and Water Vapor Profiles

Considering that average scale height for tropospheric water vapor is about 1.5 km, it is imperative that its vertical structure be resolved by measurements to a vertical resolution of 500 m or less. The recent GPS occultation experiments (GPS/MET [10], CHAMP[11], SAC-C[12], and COSMIC [13]) have demonstrated the ability of radio occultations to probe the atmosphere with a vertical resolution of ~200 m. ATOMMS retains this characteristic; a level of vertical resolution is simply not possible using a passive, nadir-viewing system (e.g., AIRS, IASI, AMSU). The highest vertical resolution claimed for these systems is on the order of 2 km. MLS also has 2-3 km vertical resolution. Thus, ubiquitous layering of water vapor in the troposphere with typical vertical scales of a few hundred meters [3] will remain invisible to passive sensors.

Only radio occultation can globally determine temperature and lapse rates at the sharp vertical scales at which they vary in both clear and cloudy conditions. However, accurate GPS RO temperatures are limited to the upper troposphere (limited by moisture) through the mid-stratosphere (limited by the ionosphere). In contrast, ATOMMS temperature and stability will extend throughout the free troposphere through the mesosphere under any conditions. Another key point is GPSRO measures temperature OR water vapor, not both. GPSRO has shown some of the potential for RO observations in the warmer regions of the lower and middle troposphere with accuracies of 0.2 – 0.5 g/kg [4]. ATOMMS will extend the dynamic range by orders of magnitude to precisely profile water from the 1-4% levels in the lower troposphere to the ppm levels in the mesosphere with 1-10% individual profiles and absolute accuracies with averaging perhaps an order of magnitude better (depending on spectroscopy), while simultaneously profiling temperature to sub Kelvin accuracy over the same range.

B. Upper Troposphere / Lower Stratosphere Retrievals

ATOMMS offers a remarkable improvement in our ability to measure temperature, water vapor and ozone behavior in the climatically critical upper troposphere and lower stratosphere (UTLS). Despite the critical roles this region plays in determining how our climate will change in the future, its behavior has been and continues to be very poorly observed. To place ATOMMS in context, a basic conundrum for understanding and predicting climate change has been that our ability to measure water vapor and temperature in the upper troposphere under all sky conditions has been close to nil. The existing observational techniques all have very different types of uncertainties, errors and resolutions. When comparisons have been made, the comparisons have not agreed very well. For instance, the observations assimilated (radiosondes and radiances from several remote sensing sensors) in the ECMWF 40-year reanalysis (ERA-40) database [15] shows ERA-40 water mixing ratios are considerably larger in the tropical upper troposphere than measurements from the MOZAIC (Measurements of Ozone and Water Vapor by Airbus In-Service Aircraft) program, while in the upper stratosphere ERA-40 has about 5% to 10% more ozone and 15% to 20% less water vapor than inferred from the Halogen Occultation Experiment and the Microwave Limb Sounder onboard the Upper Research Satellite [16].

This region is critical for climate because temperature changes in this region will produce very large changes in the outgoing long wave radiation that cools the Earth. Temperature changes in this region are also indicative of how realistic models are in transporting added heat from additional greenhouse gases from the surface up to the upper troposphere. There has been an issue for quite some time as to whether model simulations at the surface visa vis the free troposphere are realistic. One component is that a primary feedback is water vapor above 500 mb. It appears climate models have a tendency to produce more water vapor in the upper troposphere in response to increased greenhouse gas concentrations and warming at the surface than may be occurring in the real world. Unfortunately we don't really know whether or not this is true because the water vapor and temperature observations in the upper troposphere are simply not good enough.

C. Retrievals can be made in the presence of most clouds

Earth is at least two-thirds cloud covered [5] creating a

fundamental sampling problem for remote sensing systems that are unable to penetrate clouds, which includes all IR probing systems (e.g., AIRS, IASI) and limits MLS. Long-term data sets derived from these systems will be incomplete and dry-biased, which limits the ability to measure and understand processes that control climate and aid in weather prediction as well as making detection of climate change difficult. Again GPS occultation experiments have demonstrated the ability of radio occultations to make observations and retrievals in both clear and cloudy conditions. Coincident cloud observations and ATOMMS relative humidity in and around clouds will establish the relation between cloud properties and relative humidity at scales typically resolved by models including the frequency and amount of supersaturation, supercooled mixed phase clouds, all important but poorly observed and understood phenomena sorely waiting for new critical observational constraints. One can see from these discussions that with its global coverage once deployed in orbit, ATOMMS will provide something approaching a global field campaign for studying convection at the scales of GCMs.

III. ATOMMS Development Status

A. ATOMMS Microwave Instrument

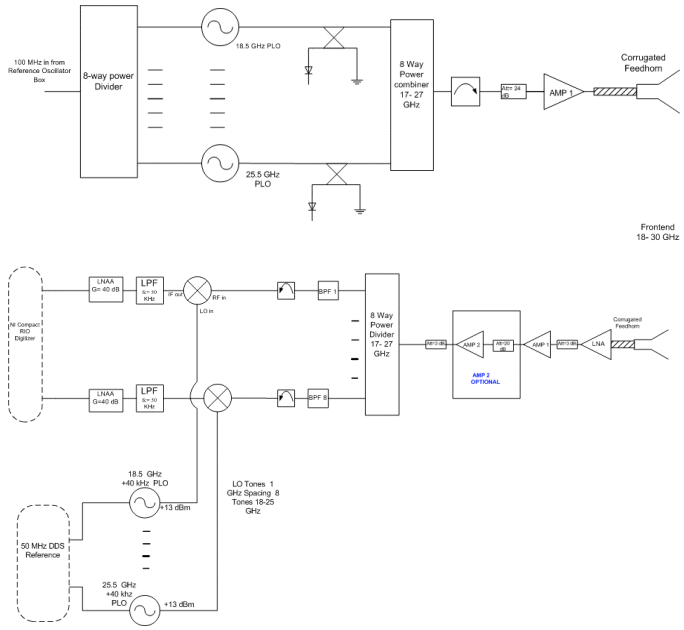

Figure 3: The ATOMMS 22 GHz transmitter (top) and receiver (bottom) subsystems. Two of the eight channels are shown in each block diagram for clarity.

The ATOMMS microwave instrument has been designed to take advantage of off-the-shelf telecommunications technology whenever possible, particularly for the 22 GHz channel. The basic instrument design uses very similar circuits for all channels. Figure 3 shows the block diagram of the 22 GHz transmitter and receiver. The transmitter uses eight separate phase locked YIG oscillators to generate the tones. These tones are individually power-monitored before they are power combined. A single amplifier then amplifies these eight tones to a level of ~100 mW per tone. Since ATOMMS measurements are effected by differential amplitude noise, a common power amplifier is used for all tones to attenuate differential amplitude fluctuations. The receiver amplifies all eight received tones simultaneously for the same reason. The amplified signal is then power divided into eight channels. Bandpass filters in each channel isolate a single received tone. These tones are then mixed with LO signals generated by YIG phase locked oscillators fed with a reference from a DDS synthesizer. This synthesizer is used to offset the frequency of the LO, generating a ~ 40 kHz IF frequency. The low frequency IF is then low pass filtered and amplified with a low noise audio frequency amplifier. The IF is then fed into a National Instruments Compact RIO real-time data acquisition system, where the time domain waveform is digitized and recorded. This data acquisition system has been shown to operate at ambient pressure in the WB-57F in previous experiments. The 13 GHz reference tone transmitter and receiver are identical to the 22 GHz system, but with a single transmitted and received tone rather than eight.

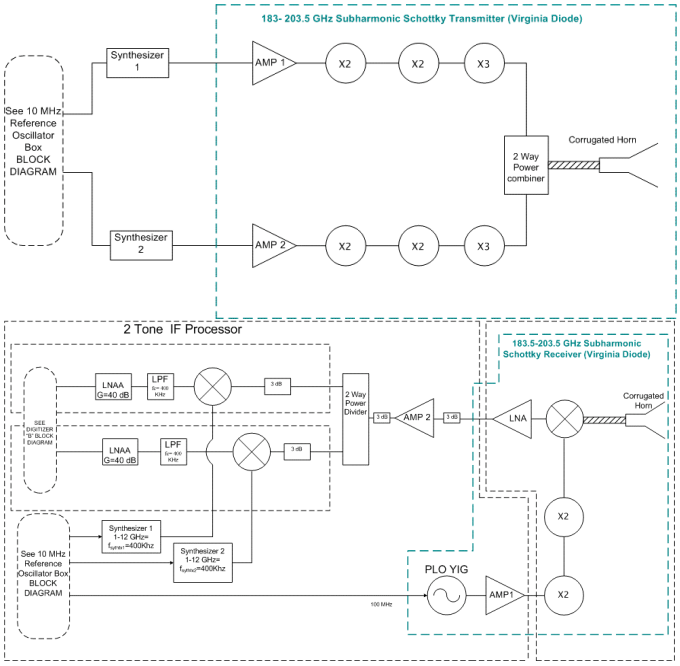

Figure 4: The ATOMMS 183 GHz transmitter (top) and receiver (bottom) system block diagrams.

The 183 GHz subsystem is based on a two tone transmitter and subharmonically pumped Schottky mixer receiver front end from Virginia Diodes. The transmitters each provide 40 mW of power from 180-203.5 GHz, and are power combined using a waveguide magic tee. Power monitoring diodes before the magic tee record the transmitted power level of each channel, for later removal of differential amplitude effects. After power combining, the transmitted power is ~20 mW per tone. The subharmonically pumped Schottky receiver has a measured noise temperature of ~1100K, and is flat across the band. A low noise amplifier with a 1-12 GHz bandwidth relays the IF signal to a downconverter module. The receiver IF downconverter is identical in architecture to the 22 GHz receiver system with the exception that tunable synthesizers

are used to generate the LO signals rather than fixed tuned oscillators. Block diagrams of the 183 GHz subsystem are shown in figure 4. Figure 5 shows the 183 GHz transmitter system mounted to the ATOMMS-A rear plate.

The ATOMMS antenna system uses a pair of coaxially mounted feedhorns to illuminate a single 30 cm diameter high density polyethylene lens, anti-reflection grooved for operation at 183 GHz. The design and fabrication of this optical system is covered in another paper in these proceedings [6].

A detailed link budget simulated the performance of the instrument using realistic antenna parameters and estimated losses. This link budget was used to specify all the components of the ATOMMS transmitter and receiver systems. The final configuration of both aircraft is shown in Figure 1 and 2. Transmitter and receiver pairs are mounted in opposite aircraft, with each aircraft containing a transmitter for one band and the receiver for the other band. This balances both the data acquisition and power needs for each instrument.

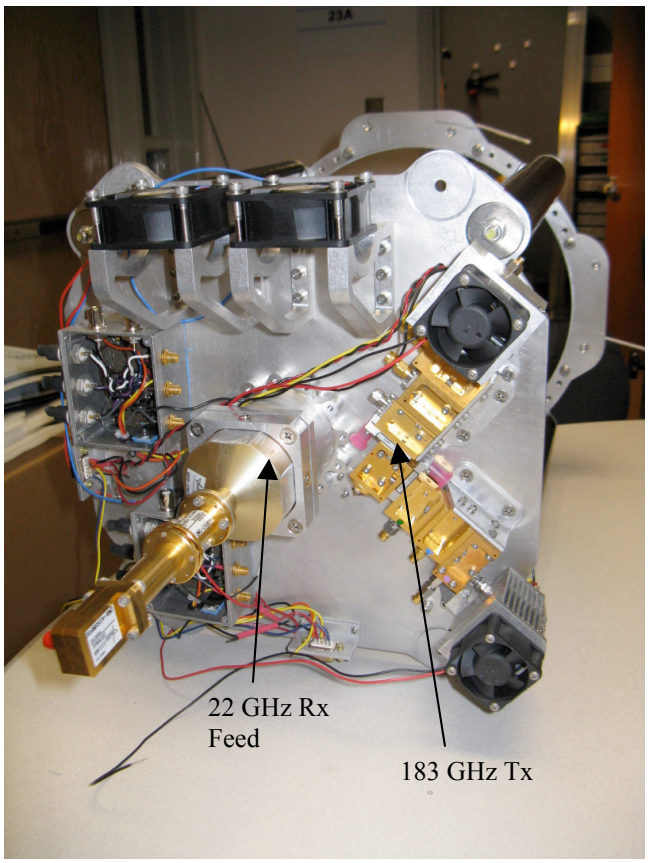

Figure 5: The ATOMMS 183 GHz transmitter system and 22 GHz receiver feed.

The ATOMMS instrument package mechanical aspects are as highly engineered as the electronics. Past experience in flying complex research instruments in the WB-57F aircraft have shown that a fairly sophisticated minimum level of integration of structure, power, thermal, vibration, low pressure and various other design factors are required to build a successful instrument. The ATOMMS instrument design, shown in figure 6, was engineered down to the level of fasteners, connectors and wiring using 3D Computer Aided Drafting (CAD) software before any manufacturing. Figure 7 shows the ATOMMS-A instrument, completely assembled and awaiting system testing.

With fully assembled electronics modules, we have completed testing of the electronics systems at the box level, and we are now verifying that instrument performance meets the specifications necessary to accomplish the scientific mission.

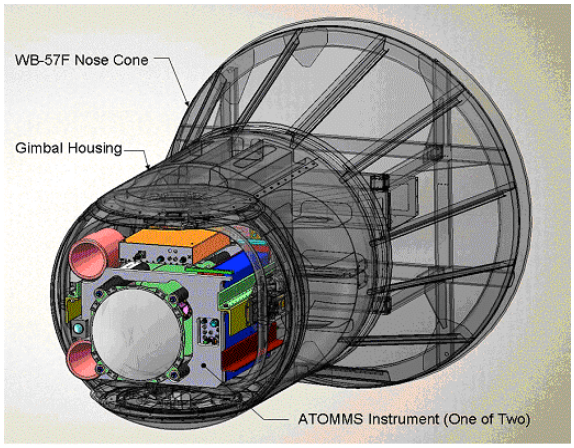

Figure 6: A 3D CAD model of one of the ATOMMS instruments in the SRI WAVE gimbal. The ATOMMS instrument was completely built in CAD before any fabrication took place.

Data acquisition duties are handled by National Instruments Compact RIO systems. These small chassis can be loaded with up to eight multifunction interface modules to handle science signal and housekeeping digitization, digital I/O and accelerometers readout. Each Compact RIO system communicates with a PC over two dedicated Ethernet cables. These PCs are mounted in a partially pressurized part of each aircraft, just behind the moving portion of the gimbal. Each PC is equipped with large capacity solid state hard drives, and runs Labview Realtime OS. These computers receive the data collected by the Compact RIO system mounted directly on the ATOMMS instruments and record the data to disk. They also are responsible for collecting the GPS observables from the JPL provided GPS receiver used as part of the Precise Positioning System.

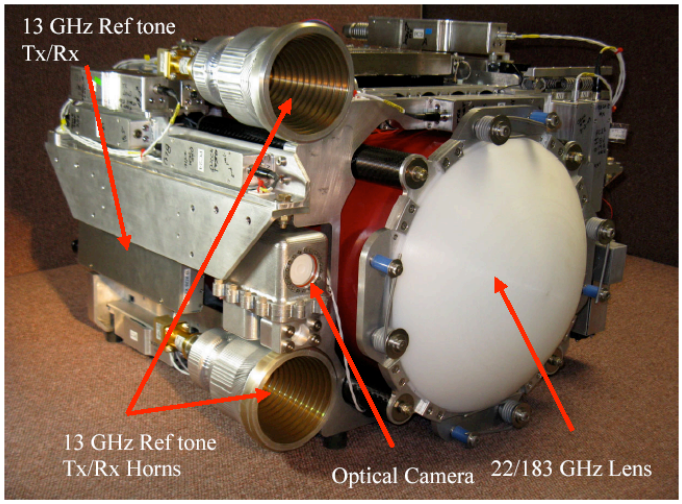

Figure 7: The fully assembled ATOMMS A instrument. Visible components are labeled. The 183 GHz Tx and 22 GHz Rx modules are not visible.

B. Precise Positioning System

The ATOMMS system will profile atmospheric temperature and pressure. This is derived from a profile of refractivity that is derived from a profile of bending angle derived in turn from a profile of Doppler shift versus time. In the aircraft to aircraft occultations, the atmospheric Doppler shift is much smaller than for the spacecraft occultation case because the aircraft move much slower (~200 m/sec) than the spacecraft (several km per second). At the uppermost altitudes, just below the altitude of the aircraft, the atmospheric bending angle is quite small. Therefore the atmospheric Doppler shift is quite small. In order to precisely determine atmospheric temperature and pressure, the ATOMMS system must measure very small bending angles at high altitudes. The system goal is to estimate the motion of the aircraft to an accuracy of 0.1 mm/sec.

Over the course of the experiment design, we refined our understanding of the necessity of this goal and how to achieve this small error. The ATOMMS Precise Positioning System consists of accelerometers and GPS receiver on each aircraft. Positions can be estimated very accurately from the GPS receiver data about every 100 seconds. In profiling the atmosphere via the ATOMMS occultations, we determined that we will use integration times of ~10 seconds or less. To achieve the high vertical resolution and performance over these short intervals, we determined that very accurate accelerometers must be used. Essentially the precise reconstruction of the time-varying aircraft positions and velocities will integrate the acceleration measured by the accelerometers to obtain the velocities of the two ends of the ATOMMS instrument. The GPS receiver data will essentially be used to estimate the bias and scale factor of the accelerometers. Extremely low-noise accelerometers (Endevco Model 86), developed for seismic research, were selected for the ATOMMS experiment after extensive analysis by the ATOMMS team at the University of Arizona and JPL.

High performance GPS receivers have been selected that could satisfy the ATOMMS requirements that were also familiar to JPL. The receivers already in the WB-57F aircraft were deemed insufficient to deliver the quality of phase data needed. JPL suggested a high performance Ashtech receiver that they use for other applications.

C. WB-57F Aircraft

NASA is providing the WB-57F aircraft time for the ATOMMS experiment. ATOMMS presently holds two flight slots in the WB-57F schedule, and a third is planned to be added. Currently, the first flight slot is a combination engineering test flight, followed immediately by an air to ground RF testing flight series. The second is a full up air to air, two aircraft flight test series. A minimum of 3 flights are anticipated for each flight series. As a risk reduction measure, we plan to separate the engineering test flights and air-to-ground single aircraft test flights, allowing more time to address any issues identified in the engineering test flights.

Figure 8: The WAVE system mounted on the nose of a WB-57F. ATOMMS will replace the optical telescope in this system. A microwave transparent radome will replace the front skin and optical window.

In support of these flight tests, Southern Research Institute and the University of Arizona have been defining the desired flight plans for each flight series, along with the task load for the WB-57 flight backseat operator (FBO).

D. NASA/Southern Research Institute (SRI) WAVE Gimbal Pointing System

The ATOMMS experiment takes advantage of NASA's WB-57F Ascent Video Experiment (WAVE) system, designed to optically image the space shuttle during launch. This system is a complete replacement nose for the WB-57F, containing a 2-axis gimbaled pointing system capable of 0.25 degree pointing accuracy (see figure 8). The system also contains an optical telescope with a high definition video camera and recorder. The ATOMMS microwave sensors replace this optical imaging package, but still use the replacement nose and gimbal.

ATOMMS does present several challenges for pointing and integration with the WAVE system. The ATOMMS instrument must be adequately balanced, and within weight limits for the gimbal. More importantly, ATOMMS is not an imaging detector, so pointing cannot be done with image recognition. In addition, the atmospheric attenuation effects we wish to measure will not allow pointing based on feedback from the microwave signal strength. Any atmospheric fluctuations would be interpreted as a pointing error, and would cause the pointing loop to become unstable. We have therefore developed, jointly with Southern Research Institute (SRI) a pointing system based on GPS coordinates. As a development effort with NASA, SRI has already proven the capability to point and track a known GPS coordinate to far better than 0.25 degree accuracy in level flight. This accuracy has been demonstrated by SRI on several WB-57 test flights with the WAVE optical sensor. Using an optical camera co-mounted with the ATOMMS instrument, we can calibrate this GPS pointing system using SRI's existing algorithm to allow ATOMMS to also point to within 0.25 degrees of a known GPS coordinate. The ATOMMS microwave beam will be measured in the lab relative to the center of this optical camera to compensate for any fixed pointing offset.

The next challenge was to predict the GPS coordinate for each aircraft, and provide that information to the other aircraft to allow them to point at each other. This will be done with a combination of a pre-computed flight plan based on GPS waypoints and times, and pseudo-real time updates of position provided by an Iridium phone data link between aircraft. Because of the slow speed and unreliability of the Iridium link, the primary location information will be the flight plan, which the pilots will attempt to fly as accurately as possible. Meeting the waypoint locations accurately is not a large challenge for the pilots, but timing arrival at those waypoints is a significant challenge. Therefore, the Iridium link will be used to provide time shifts along the flight path rather than for full position and time information. The code for this implementation has been written by SRI and is now undergoing testing.

Another requirement was the need for RF transparent nose skins in the SRI gimbal system. The windows and skin material in the existing gimbal nose skins is effectively opaque at microwave and millimeter wavelengths. They are presently in fabrication at Cobham Defense / Nurad Division in subcontract to SRI, and are scheduled for delivery in the early February 2009 time frame.

E. ATOMMS Retrieval System

1) Retrieval Software

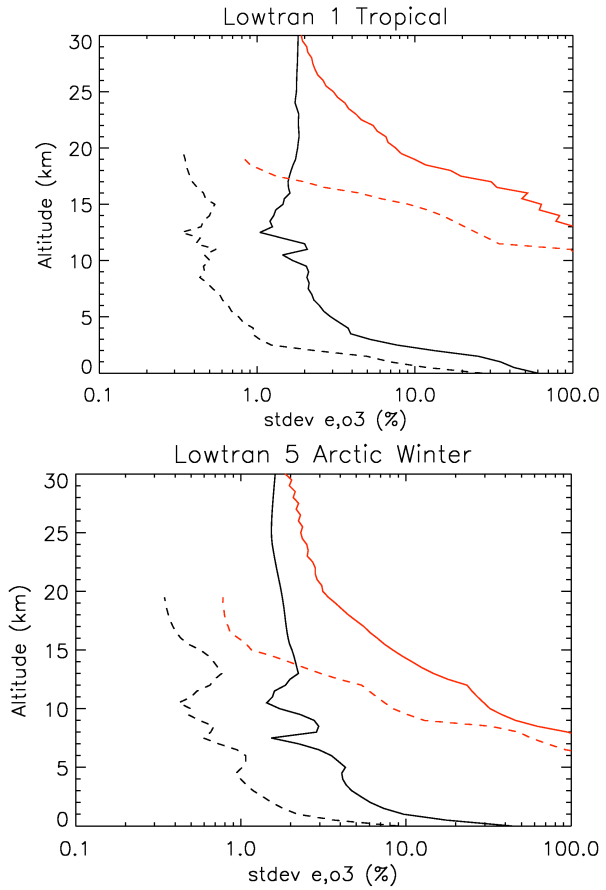

Figure 9. Standard deviation of simulated errors of H2O vapor (black) and O3 (red) from satellite (solid) and aircraft occultations (dashed). top: arctic winter conditions. bottom: tropical conditions. From [9].

Prior to this project, we developed simulations to investigate the accuracy of retrievals for an ATOMMS-type instrument in a satellite-to-satellite geometry. We have been adapting this code to perform retrievals in the MRI aircraft to aircraft geometry. We have used this code to understand how instrumental parameters, such as SNR and antenna gain pattern, will affect retrieval accuracy. We have also developed an improved method to deal with liquid water clouds distributed inhomogeneously along the occultation signal path. We developed a two relaxation dielectric model of liquid water for simulating ATOMMS retrievals when liquid clouds are present [14].

ATOMMS will retrieve the atmospheric profile of index of refraction using the method proven to work for GPS occultations, modified for the aircraft geometry. JPL has agreed to provide the JPL GPS occultation processing software to the UA that we will modify for the ATOMMS processing. Simulated errors based on this retrieval technique for water and ozone are shown in figure 9.

2) Atmospheric Turbulence

Amplitude scintillations ("twinkling of a star") are an unwanted source of amplitude variation that reduces the accuracy of how well we can isolate the absorption on the ATOMMS signals. To better understand this error, Angel Otarola's recently defended dissertation research [7] focused on atmospheric turbulence and its impact on the ATOMMS observations. We have coupled this effort to the retrieval system development to understand the impact these variations will have on the accuracy of the ATOMMS retrievals.

We have developed a relation between the scintillations due to the real part of the wet refractivity variations that allows us to estimate the magnitude of the scintillations due to water vapor knowing the average water vapor concentration. A paper is in preparation. Using high resolution radiosonde data, we have developed an understanding of the spectrum of turbulent variations in the vertical coordinate in particular the spectral transition from homogeneous turbulence at smaller scales to a different spectral dependence of turbulence at larger scales.

Prior to this work, the impact of turbulent variations in the imaginary component of refractivity has thus far been ignored by the radio occultation community. We are working towards generalizing the equations that describe the impact of turbulence variations in the real part of the index of refraction to include the contributions of the imaginary variations. This work is important because we now realize that the simple two tone amplitude ratioing method described by [8] will not work as well for the imaginary contributions. The two tone method cancels the real contributions well because of their weak frequency dependence, but does not perfectly cancel the contributions due to the imaginary component. Based on this new understanding, we feel that it is essential that we simultaneously measure more than two tones at our high band frequencies (180 – 203 GHz) to diagnose and minimize the effects of turbulence on our retrievals.

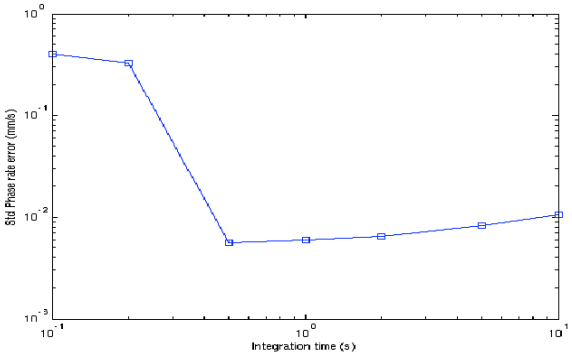

Figure 10: Standard deviation of the phase rate error for a 13 GHz signal generated and transmitted from one ATOMMS device, then received and digitized by the second ATOMMS device before processing

3) System Testing Support

We have been developing codes and testing strategies to support preliminary instrument tests: laboratory tests, ground based tests, and air to ground tests. Since each test has its own unique implementation and interpretative challenges, we have been developing separate software for each. With the hardware partially completed, we have begun to process and analyze signals recorded by the ATOMMS instrument in the lab. As an example, the ATOMMS MRI will utilize the 13 GHz channels to determine the atmospheric Doppler shift from which we will retrieve the atmospheric refractivity. To meet our accuracy goals, the 13 GHz signals need to be extremely phase stable. We expect the limiting error in determination of the atmospheric Doppler shift to be due to uncertainty in the estimation of the line of sight velocities of the aircraft, which is specified to be 0.1 mm/s or less. Digitized laboratory measurements from one of the 13 GHz transmit-receive chains has been analyzed for phase stability as a function of the signal integration time as shown in figure 10. The phase error has been translated into units of mm/s. The figure shows that for integration times greater than 0.5 s, the instrument performance is an order of magnitude better than the expected error in the line of sight velocity determination. As we plan to use integration times of 1-10s for signal extraction, the phase error of the 13 GHz signals is well within specification.

IV. CONCLUSION

ATOMMS offers a unique and unprecedented capability for measuring key atmospheric variables fundamental to climate independently from models and other climatological assumptions. The planned aircraft to aircraft occultations offer the only way to demonstrate and assess the ATOMMS concept and its performance without the very costly step of placing at least one if not both of the instruments in orbit. Assuming the aircraft demonstrations prove successful, they will pave the way for support from the larger science community for the ATOMMS concept and a NSF/NASA/NOAA spacecraft mission and a major new global research instrument for atmospheric science.

ACKNOWLEDGEMENTS

ATOMMS is supported by the NSF Major Research Instrumentation Program under award ATM-0723239. CG is supported by an NSF Astronomy and Astrophysics Postdoctoral Fellowship under award AST-0602290.

REFERENCES

[1] Kursinski, E.R., G.A. Hajj, J.T. Schofield, R.P. Linfield, and K.R. Hardy, Observing Earth's Atmosphere with Radio Occultation Measurements using the Global Positioning System, J. Geophys. Res., 102, 23429-23465, 1997.

[2] Kursinski, E. R. and D. Rind, The hemispherical asymmetry of the Tropical Water Vapor Distribution and Implications for the Water Vapor Feedback, submitted to GRL, 2007.

[3] Newell, R.E., V. Thouret, J.Y.N. Cho, P. Stoller, A. Marenco, and H.G. Smit, Ubiquity of quasi-horizontal layers in the troposphere, Nature, 398, 316-319, 1999.

[4] Kursinski, E.R. and G.A. Hajj, A Comparison of water vapor derived from GPS occultations and global weather analysis, Geophys. Res. Lett., 22, 2365-2368, 2001.

[5] Rossow, W.B. and R.A. Schiffer, Advances in understanding clouds from ISCCP, Bull. Amer. Meteor. Soc., 80, 2261-2288, 1999.

[6] AlBanna, S. et al., A single 30 cm Aperture Antenna Design for The Operation of 2 Widely Separated Frequency Bands for the Active Temperature, Ozone and Moisture Microwave Spectrometer, Proceedings of the International Symposium on Space Terahertz Technology, in press, 2009.

[7] Otarola, A.C., The effects of turbulence in an absorbing atmosphere on the propagation of microwave signals used in an active sounding system. Ph.D. dissertation, The University of Arizona, United States -- Arizona. ProQuest Digital Dissertations @ University of Arizona database. (Publication No. AAT 3336701) 2008.

[8] Kursinski, E.R., S. Syndergaard, D. Flittner, D. Feng, G. Hajj, B. Herman, D. Ward, T. Yunck, A Microwave occultation observing system optimized to characterize atmospheric water, temperature, and geopotential via absorption, J. Atmos. Oceanic Tech., 19, 1897-1914, 2002.

[9] Kursinski, E. R., et al., The Active temperature, ozone and moisture microwave spectrometer (ATOMMS), in ECMWF/EUMETSAT GRAS SAF Workshop Proceedings, The Applications of GPS Radio Occultation Measurements. S. Healy Ed. 2008.

[10] Ware, R., and Coauthors, 1996: GPS sounding of the atmosphere from low Earth orbit: Preliminary results. Bull. Amer. Meteor. Soc, 77, 19-40.

[11] Wickert, J. et al. (2001), Atmosphere sounding by GPS radio occultation: First results from CHAMP, *Geophysical Research Letters*, 28(17), 3263-3266.

[12] Hajj, and Coauthors, 2004: CHAMP and SAC-C atmospheric occultation results and intercomparisuns. J. Geophys. Res., 109, D06109, doi:10.1029/2003JD003909.

[13] Anthes, R. A., et al. (2008), The COSMIC/FORMOSAT-3 mission: Early results, *Bulleting of the American Meteorological Society*, 89(3), 313-333.

[14] Otarola A. (2006) The Complex Permittivity of Pure Liquid Water from Microwaves up to 1.5 THz.

[15] Uppala, S. (2001), ECMWF Reanalysis 1957-2001, Paper presented at Workshop on Reanalysis, Eur. Cent. For Medium-Range Weather Forecasts, Reading, UK, 5-9 Nov.

[16] Oikonomou, E. K., and a. O'Neill (2006), Evaluation of ozone and water vapor fields from the ECMWF reanalysis ERA-40 during 1991-1999 in comparison with UARS satellite and MOZAIC aircraft observations, J. Geophys. Res., 111, D14109.

[17] Soden, B.J., Jackson, D.L. Ramaswamy, V., Schwarzkopf, M.D., and Huang, X. (2005), The radiative signature of upper troposheric moistening, Science, 310 (4), 841-844.

[18] Dessler, A. E., Zhang, Z., and Yang, P. (2008), Water-vapor climate feedback from climate fluctuations 2003-2008, Geophysical Research Letters, 35, L20704.

Water Vapor Radiometer for ALMA

Dr. A. Emrich, S. Andersson, M. Wannerbratt, P. Sobis, Serguei Cherednichenko, D. Runesson, T. Ekebrand, M. Krus, C. Tegnader, U. Krus.

Omnisys Instruments AB
Gruvgatan 8 SE-42136 V.Frolunda
Sweden
Email: ae@omnisys.se

***Abstract*—Omnisys Instrument AB has developed a Water Vapor Radiometer for the ALMA project from scratch in 18 months and will deliver 50 units within the next 18 months. The radiometer includes an Optical Relay, Mounting Frame as well as the Radiometer core module. The radiometer core include optics and calibration system as well as a schottky mixer based front-end and a filterbank back-end. These subsystems are supported by a thermal management subsystem, control and communication subsystem as well as a power subsystem. The system and subsystems will be described in the paper.**

***Index Terms*—Radiometer**

I. INTRODUCTION

Omnisys Instrument AB has developed a Water Vapor Radiometer for the ALMA project from scratch in 18 months and will deliver 50 units within the next 18 months. The radiometer includes an Optical Relay, Mounting Frame as well as the Radiometer core module.

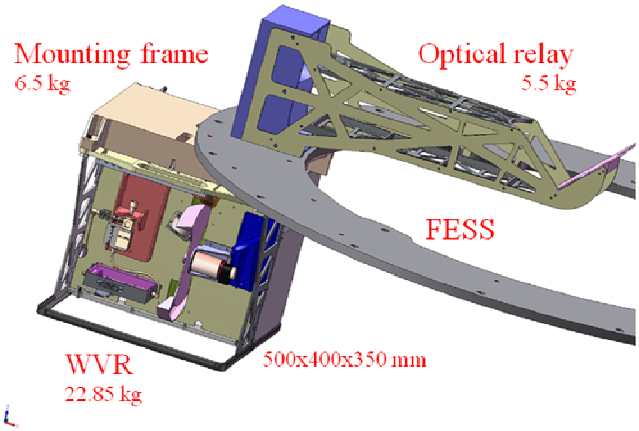

Fig 1. The Water Vapor Radiometer including Mounting Frame and Optical Relay, mounted on the FESS on an ALMA antenna.

The size and mass of the system is about a factor three lower than allocated and facilitates manual handing by one man.

The radiometer core include optics and calibration system as well as a schottky mixer based front-end and a filterbank back-end. These subsystems are supported by a thermal management subsystem, control and communication subsystem as well as a power subsystem.

II. RADIOMETER CORE

The optics in the radiometer core is shown below. The beam enters through a window (implemented in a tilted PPA30 sheet) and is reflected at two active mirrors (M2&M3) before the receiver horn and mixer. In between a chopper wheel is operated deflecting the beam on either the cold load or the hot load with the cycle: SKY-COLD LOAD-SKY-HOT LOAD.

Fig 2. Optics in the radiometer core.

In the RF chain, the signal is received by a corrugated horn, followed by a subharmonic schottky mixer and an LNA. The mixer is provided by Radiometer Physics Gmhb and the LNA

is provided by Miteq (custom implementation).

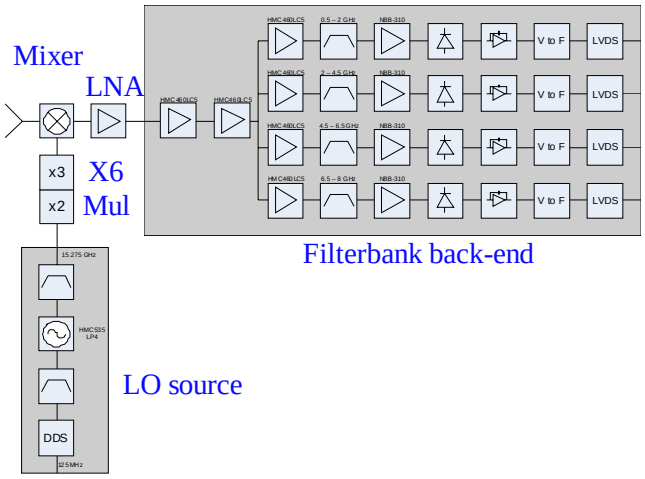

Fig 3. RF chain block diagram.

The LNA is followed by a filterbank. The local oscillator (LO) for the mixer is created by a 15.275 GHz synthesizer followed by an active x6 multiplier, both designed and produced by Omnisys. The active multiplier includes a high precision power output control function, enabling accurate LO power setting for each individual schottky mixer. The optimum power level varies with about a 2-3 dB.

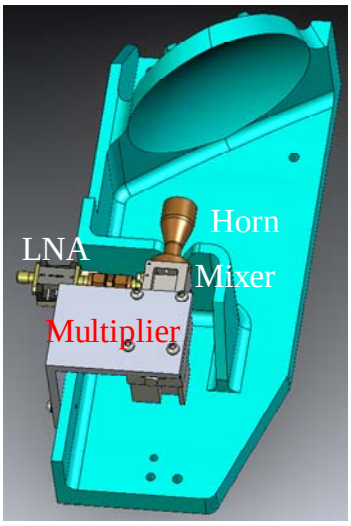

Fig 4. The M3 mirror with the front-end electronics.

III. Calibration Loads

The Cold Load use a Peltier cooler and the Hot load use resistive heaters for accurate temperature control. The nominal operating temperatures are 283 and 353 K respectively and the dew point at the ALMA site is avoided.

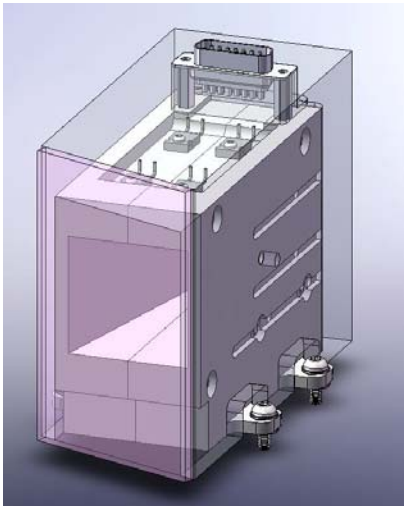

Fig 5. The Hot Load with isolation.

The Cold Load is 3 reflection design, while the Hot Load is a 7 reflection design, both implemented in aluminium coated with 1.2 mm CR-110 Eccosorb. The SWR and back scatter has been measured both on lab bench and in the system.

Both loads has been simulated in 3D in Solidworks simulation module CosmosWorks, as shown below. The internal thermal differences are within 50 mK.

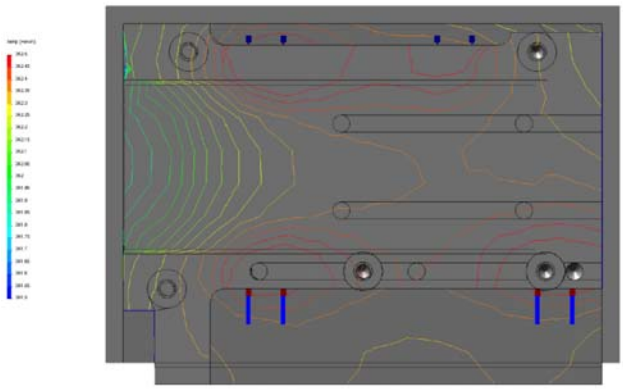

Fig 6. The Hot Load thermal simulation in CosmosWorks.

Several temperature sensors were used in the evaluation of the loads and two are used in each in the production model, to allow for a independent safety temperature monitoring function. A typical temperature variation is shown below and the variation is well below 10 mK.

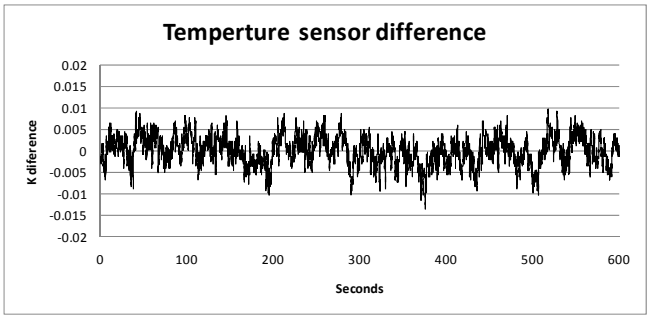

Fig 6. Thermal stability of the Hot Load.

IV. Filterbank

The back-end consist of a four channel filterbank covering 0.5-8 GHz. It is implemented in one box but in two compartments. One is used for bias electronics and thermal regulation and one, as shown below, for the microwave electronics.

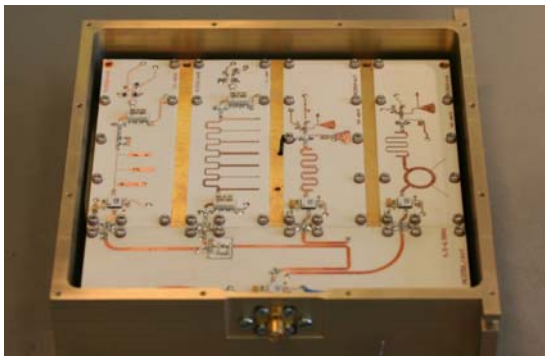

Fig 7. Microwave compartement of the Filterbank back-end.

Several types of microstrip, lumped and commercial filters are used in different configurations in the four channels to allow for sharp response as well as out of band rejection. Differential schottky diode detectors are use with voltage to frequency converters for the final detection. A typical frequency response is shown below for both sidebands.

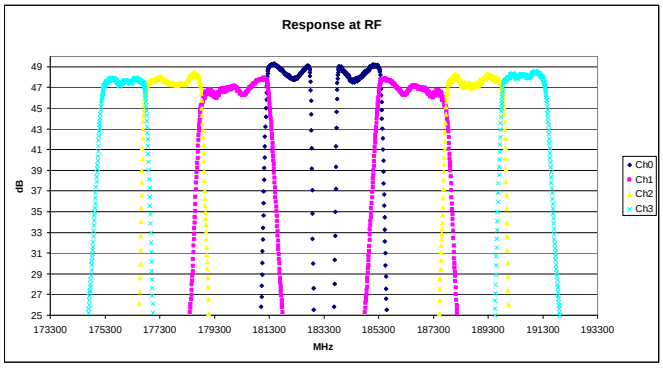

Fig 8. Frequency response of complete WVR.

V. Thermal Regulation

There has been extensive work in the design, test and optimization of the thermal control and regulation system. The Central Base plate in the radiometer core is regulated by the fan speed control in the cooling channel, while the calibration loads and the back-end have separate thermal regulation systems.

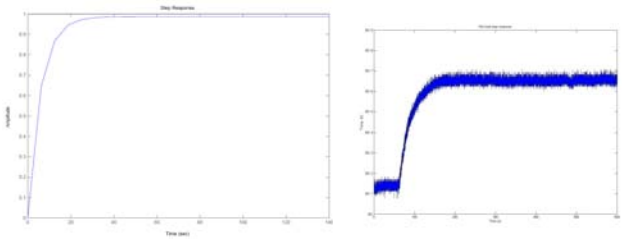

Fig 9. Simulated and tested step response of a thermal regulation function.

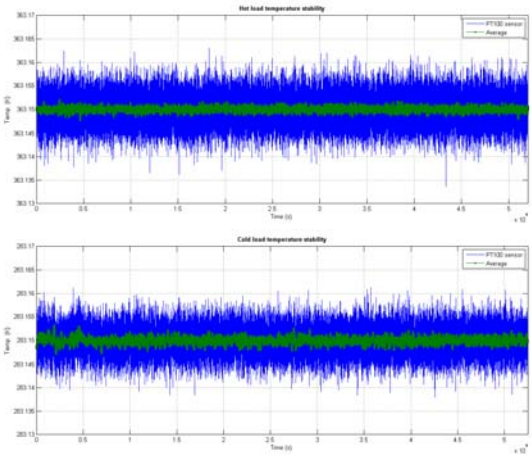

Fig 10. Long term (14 h) thermal stability of the Hot and Cold load.

Typical regulation accuracies are well below 10 mK and the system is compliant to operating between 16-21 C ambient temperature at 5000 m elevation. Start up from cold is also within specification.

Fig 11. The radiometer installed on an ALMA antenna.

VI. System tests

The first WVR has been tested at the site at 3000 m elevation and test data is shown below. Typical mounting and dismounting of the WVR at the antenna is below 30 minutes, due to a clever arrangement of mechanical/optical interface.

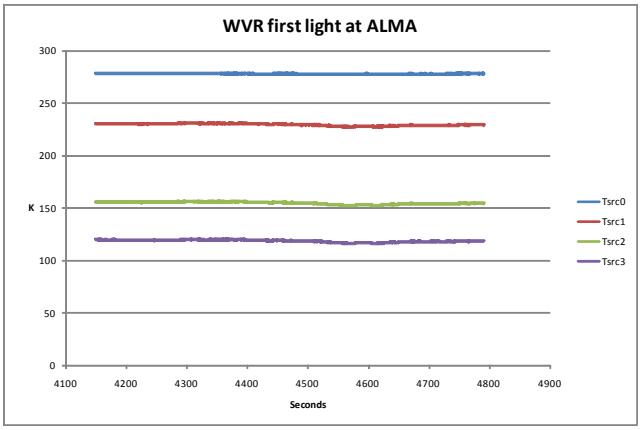

Fig 11. First light data from WVR #102 at the ALMA site.

VII. Conclusion

A new Water Vapor Radiometer has been developed by Omnisys Instruments for the ALMA project in 18 months. It is compliant to all requirements and adapted for long lifetime operations, limited and simple maintance and reasonable per unit cost. More than 50 units will be produced over the next 18 months.

Advanced mHEMT technologies for space applications

Axel Hülsmann, Arnulf Leuther, Ingmar Kallfass, Rainer Weber, Axel Tessmann,
Michael Schlechtweg, Oliver Ambacher

***Abstract*—Heterodyne receivers operating at THz frequencies can detect rotation spectra of several spurious gases. These receivers typically use sub harmonic Schottky diode mixers, which need a low phase noise local oscillator (LO) input generated by frequency multiplication and amplification. THz radiometry requires broadband receivers with low noise temperatures which are necessary for high temperature resolutions. All these systems benefit from low-noise transistors working at millimeter-wave (MMW) frequencies.**

***Index Terms*—mHEMT, MMIC, sub-millimeter-wave, frequency multiplier, low-noise amplifier (LNA), mixer, voltage controlled oscillator (VCO)**

I. Introduction

The frequency range above 300 GHz is of growing interest for space applications. Many spectroscopic signatures of tri atomic molecules and other substances are present at sub-millimeter-waves (SMW). This offers the possibility to remotely analyze the atmosphere and surface composition of planets or their moons. Up to now, this frequency regime can be handled only by sub harmonic Schottky diode based mixers, but as demonstrated in this paper, metamorphic high electron mobility transistor (mHEMT) technology is becoming available. However, heterodyne systems at least need an LO signal with sufficient power, as there is a high conversion loss of passive frequency multiplication by hetero barrier varactors (HBVs) or Schottky-diodes. For high spectroscopic resolution a low phase noise sub harmonic LO-signal has to be generated, multiplied and amplified. These components operate at the millimeter wave range, and can be cost efficiently fabricated by mHEMT technology on GaAs wafers. Some MMIC components that have been already realized are presented at this paper.

II. Metamorphic HEMT Technology

The use of In-rich InGaAs channels in HEMTs has resulted in SMW amplifiers at 300 GHz and above [1], [2] which had been the domain of Schottky diodes just some years ago. Also HBTs have been used to cover this frequency range [3]. HEMTs can be grown pseudomorphically on InP or metamorphically on GaAs with comparable results. Metamorphic means, that the lattice constant of the GaAs substrate is changed by a quaternary buffer to a value needed by the active device on top. The generated dislocations do not degrade the electron transport mechanism in the field effect transistors. InP substrates have a better thermal conductivity but GaAs is more robust, cheaper and thus MMICs can be fabricated on larger wafers. At IAF, we have developed a mHEMT technology suitable for monolithic SMW integrated circuits (S-MMICs). As shown in Fig. 1, the e-beam defined T-shaped gate, which is defined by a four layer PMMA resist, has a length down to 35 nm.

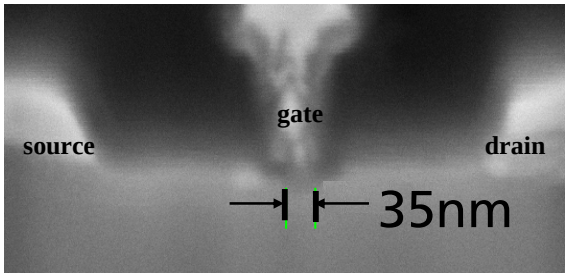

Fig. 1. Scanning electron microscopy of a 35 nm mHEMT cross-section.

The metamorphic HEMTs structure is grown by MBE on 4-inch GaAs wafers and has an $In_{0.80}Ga_{0.20}As$ channel with $In_{0.52}Al_{0.48}As$ barriers.

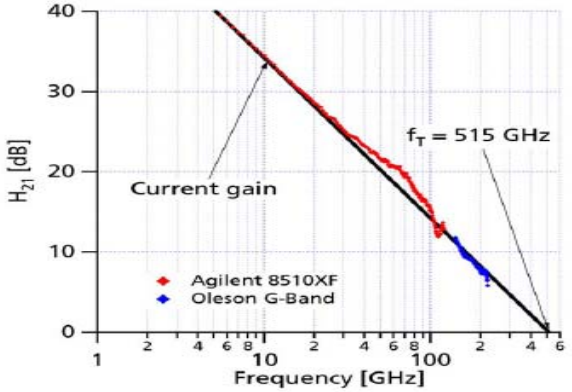

Fig. 2. Measured current gain of the 35nm mHEMT and extrapolated transit frequency.

The gate recess is carried out by selective wet chemical etching, and the device isolation by mesa etching. Source and drain contact resistances are as low as 0.03 Ω·mm. The gate to drain and drain to source breakdown voltages are 2.0 V and 1.5 V, respectively. The peek transconductance at a gate

Manuscript received 07 April 2009. This work was supported in part by the German federal ministry of defense (BMVg), the ministry of education and research (BMBF), and the Fraunhofer Society.

A. Hülsmann, A. Leuther, A. Tessmann, I. Kallfass, R. Weber, M. Schlechtweg, and O. Ambacher are with Fraunhofer Institute of Solid State Physics (Institut Angewandte Festkörperphysik, IAF), Tullastr. 72, D79108 Freiburg, Germany.

Corresponding author phone: +49 761 5159 325; fax: +49 761 5159 71 325; e-mail: axel.huelsmann@iaf.fraunhofer.de).

voltage of +0.2 V was measured to be 2500 mS/mm, and the maximum drain current is 1600 mA/mm. As shown in Fig. 2, the current gain cutoff frequency f_T is extrapolated above 500 GHz. Details of the 35 nm mHEMTs have already been published by Leuther et al. [4]. A comparison of mHEMT devices with different gate length is shown in Tab. I.

TABLE I Electrical DC- and RF-Parameters of the IAF Metamorphic HEMT Technologies

	l_g = 100 nm	l_g = 50 nm	l_g = 35 nm
R_c	0.07 Ω·mm	0.05 Ω·mm	0.03 Ω·mm
R_s	0.23 Ω·mm	0.15 Ω·mm	0.1 Ω·mm
$I_{D,\,max}$	900 mA/mm	1200 mA/mm	1600 mA/mm
V_{th}	-0.3 V	-0.25 V	-0.3 V
$BV_{off\text{-}state}$	4.0 V	2.2 V	2.0 V
$BV_{on\text{-}state}$	3.0 V	1.6 V	1.5 V
$g_{m,\,max}$	1300 mS/mm	1800 mS/mm	2500 mS/mm
f_T	220 GHz	380 GHz	515 GHz
f_{max}	300 GHz	500 GHz	> 700 GHz
MTTF	3×10^7 h	2.7×10^6 h	n.a.

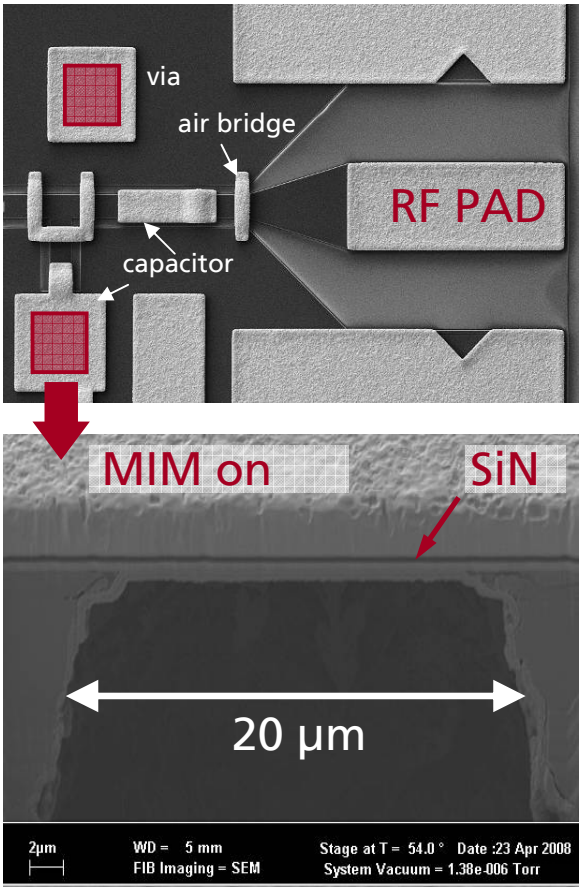

Fig. 3. Photo of a mHEMT MMIC. The top photo shows an output port with 14 µm ground to ground coplanar waveguides. The bottom photo shows a cross-section of an MIM capacitor on a 20 µm via hole.

We use grounded coplanar waveguides (GCPW) with different impedances from 30 to 70 Ohm on backside metalized 50 µm thinned wafers. A design library of passive and active devices has been implemented in Agilents ADS consisting of waveguides, MIM-capacitors, resistors, inductors, Schottky diodes and mHEMT devices. Details of an MMIC are shown in Fig. 3.

III. Integrated Circuits

Several MMICs have been realized using the above mentioned mHEMT technology. Depending on the MMIC frequency range, mHEMTs with 100 nm, 50 nm, or 35 nm gate length and grounded coplanar waveguides with ground to ground spacings of 14 µm or 50 µm have been used. All passive and active devices have been characterized up to H-band and a library of components like grounded coplanar waveguides, capacitors, T- and X-junctions, via holes, and RF pads were implemented in Agilents ADS, to build up IAFs circuit design library. Special care was carried out for the active devices models as published by Seelmann-Eggebert et al. [5].

Using 35 nm mHEMT devices, an H-band two-stage amplifier S-MMIC was designed to achieve broadband gain characteristic in combination with low noise figure. Fig. 4. shows the schematic cascode configuration of one utilized stage and Fig. 5 shows the chip photo of the realized circuit. Transistors with 2 x 10 µm gate width have been used for the compact coplanar layout. The on-wafer measured S-parameters of the amplifier are shown in Fig. 6, and a summary of the device performance is given in Tab. II. Further details of the circuit are published by Tessmann et al. [6].

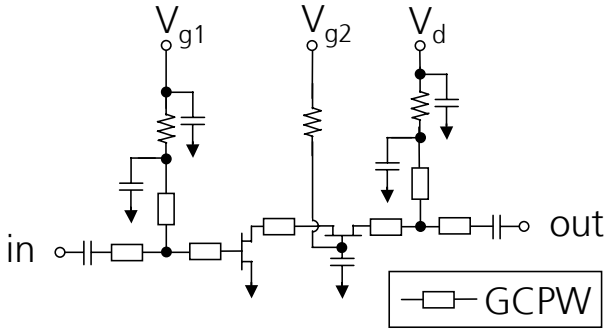

Fig. 4. Schematic circuit of one stage of the cascode amplifier.

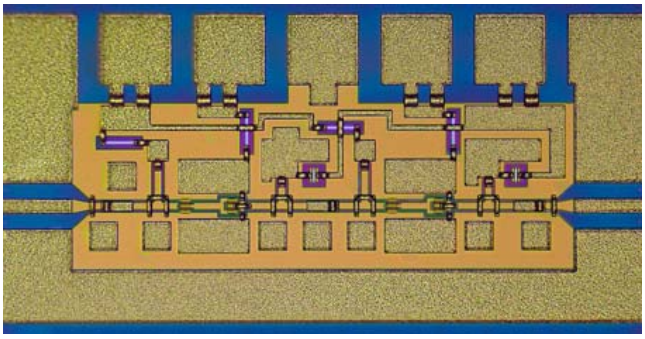

Fig. 5. Chip photo of the two-stage H-band cascode amplifier in 35 nm mHEMT technology.

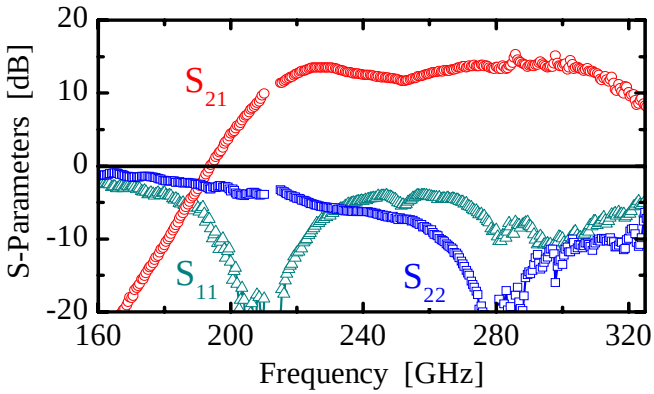

Fig. 6. On-wafer measured S-parameters of the two-stage H-band cascode amplifier S-MMIC from 160 to 325 GHz.

TABLE II AMPLIFIER PERFORMANCE

Bandwidth	220 … 320 GHz
Gain	13 dB
Input return loss @ 300 GHz	< -10 dB
Output return loss @ 300 GHz	< - 10 dB
Chip size	0.43 × 0.82 mm²

Furthermore an G-band four-stage low-noise amplifier MMIC was designed in 50 nm mHEMT technology with high gain at 210 GHz. A chip photograph of the realized four-stage low-noise amplifier MMIC is shown in Fig. 7. To achieve reasonable gain up to 220 GHz, the gate width of the common-source devices was chosen to be 2 × 10 µm.

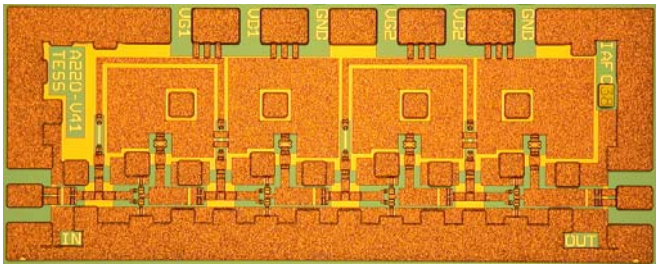

Fig. 7. Chip photograph of the four-stage 210 GHz low-noise amplifier MMIC fabricated in 50 nm mHEMT technology. The chip size is 0.65 × 1.5 mm².

The on-wafer measured small-signal gain of the MMIC is shown in Fig. 8. The LNA circuit achieved a linear gain of more than 16 dB. Furthermore, noise figure measurements were performed at room temperature (T = 293 K) from 180 to 206 GHz. The measured average noise figure of the low-noise amplifier was only 4.8 dB over the characterized frequency range. Details of the circuit are published by Tessmann et al. in [7].

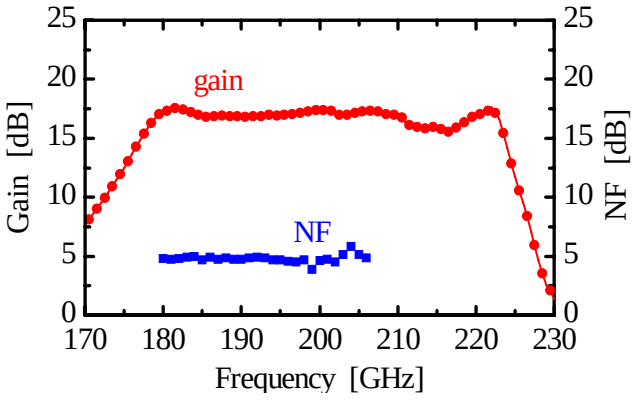

Fig. 8. On-wafer measured gain and noise figure (NF) of the four-stage 210 GHz low-noise amplifier MMIC.

Schottky diode detectors have been integrated for the mHEMT process using broadband impedance matching [8]. The diodes use the Schottky contact and epi-layers of the mHEMT which is not ideal for detectors, but enables easy integration. Different diode layouts have been analysed. Fig. 9 shows the voltage response at 135 GHz for a detector with shorted source and drain of a 100 nm mHEMT with 12.5 µm gate width as well as a design with 1.25 µm² square shaped diodes. The lower response of the mHEMT diode is due to higher ratio of edge length to contact area which degrades the n-factor. These detectors can be integrated with LNAs enabling single chip direct detection radiometer MMICs and are working at zero bias.

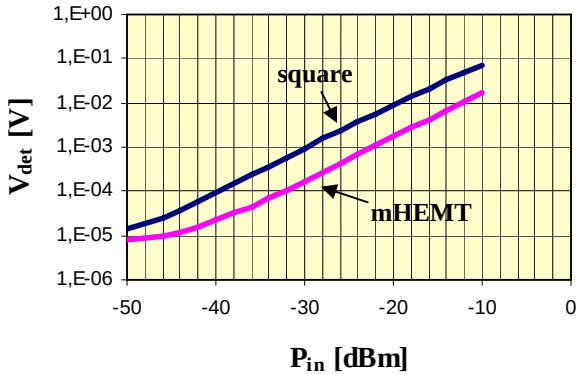

Fig. 9. Detector voltage response versus input power at 135 GHz for a 100 nm mHEMT with shorted source and drain and 12.5 µm gate width, in comparison to a design with 1.25 µm² square shape at zero bias.

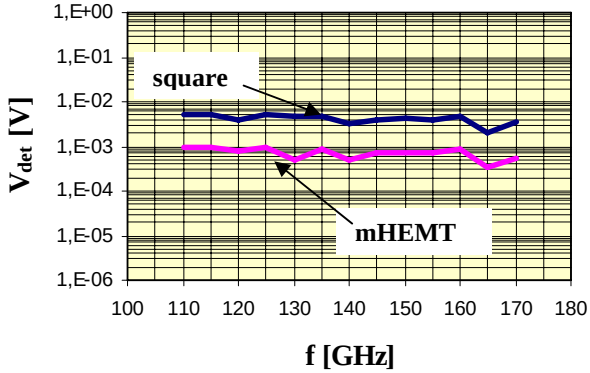

Fig. 10. Detector voltage response at an input power of -23 dBm versus frequency for a 100 nm mHEMT with shorted source and drain with 12.5 µm gate width, and a design with 1.25 µm² square shape diodes at zero bias.

Fig. 10 shows the broadband response of the detector circuit covering the complete D-band from 110 to 170 GHz. Again mHEMT and square layout of the Schottky diodes are compared, demonstrating the advantage of the square layout with a sensitivity of 1000 V/W at zero bias.

Using 100 nm mHEMT technology we demonstrate an active, sub harmonic down-conversion mixer operating beyond 200 GHz. Besides a lower conversion loss, the advantages of active FET mixers over conventional diode mixers include a potentially lower noise figure, lower local oscillator (LO) power requirements, and most important, the on-chip integration with other circuit components like LNAs to form multi-functional single-chip receivers. Fig. 11 shows the chip photograph of the realized G-band dual-gate FET mixer MMIC. Its total chip size is 1 × 1.5 mm². Details of the mixer are published by Kallfass et al. [9]. The mixer's conversion gain characteristic was evaluated on-wafer.

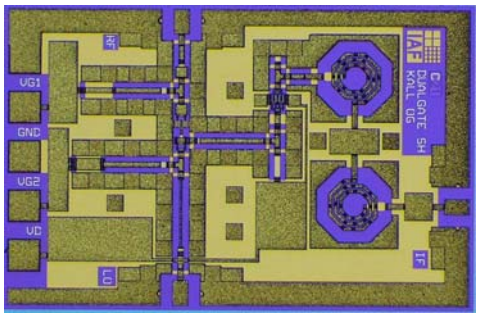

Fig. 11. Chip photograph of the sub harmonic dual-gate FET mixer. The chip size is 1.0 × 1.5 mm².

Fig. 12 shows the measured and simulated conversion gain performance of the subharmonic dual-gate mixer MMIC. The mixer was driven with 10 dBm LO power and the IF was measured at 400 MHz. The mixer MMIC achieved a maximum conversion gain of -4.7 dB at 214 GHz. Over the full measured bandwidth of 165 to 220 GHz, the conversion gain stayed above –10 dB. In-house nonlinear FET models were employed to predict the frequency translating effect.

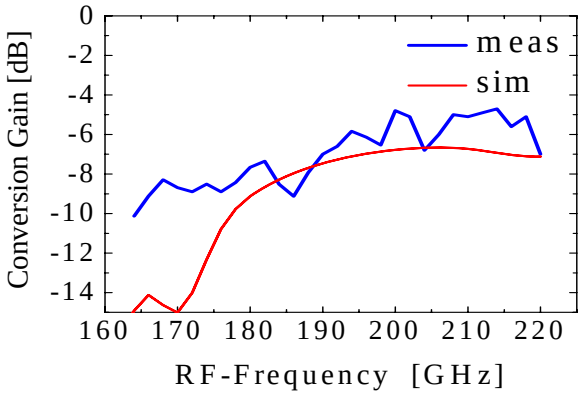

Fig. 12. Measured and simulated conversion gain versus RF frequency of the subharmonic dual-gate FET mixer MMIC at 10 dBm LO-power.

Fig. 13 shows the chip photograph of a sixtupler MMIC in 100 nm mHEMT technology. An active single-ended-to-differential-converter stage is followed by a balanced tripler and a doubler stage. With the balanced multiplier concept, broadband six-fold frequency multiplication from Ku-band into W-band could be demonstrated, overcoming the bandwidth limitations of conventional single-ended multiplier chains. The circuit employs an innovative cascode topology in its doubler stage. The realized sixtupler MMIC shows more than 7 dBm output power and over 6 dB conversion gain within a bandwidth of 78 to 104 GHz. This design enables broadband system designs and provides monolithic integration for broadband power measurement setups at W-band. Fig. 14 shows the output power versus frequency of the sixtupler. Details of the sixtupler are published by Kallfass et al. [10].

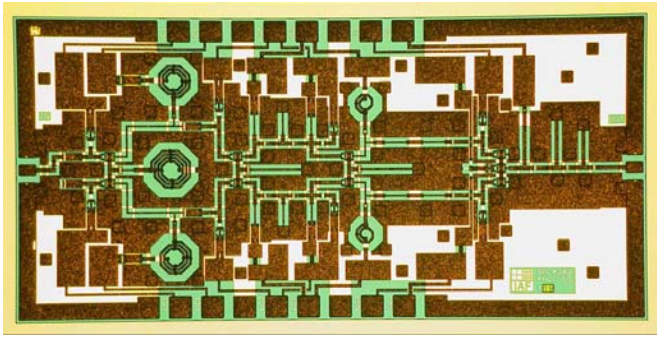

Fig. 13. Chip photograph of the sixtupler MMIC realized in metamorphic HEMT technology with a chip size of 3 x 1.5 mm².

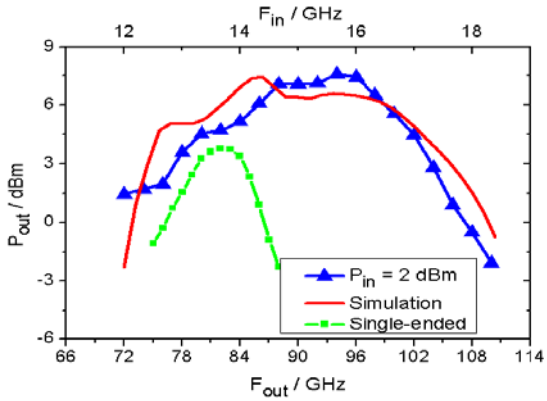

Fig. 14. Output power versus frequency of the sixtupler MMIC.

Using 100 nm mHEMT technology, a PLL-based stabilization technique for monolithic integrated W-band voltage controlled oscillators (VCOs) was demonstrated. A 92 GHz push-push oscillator in coplanar waveguide technology and a frequency divider-by-eight were developed and integrated on a single MMIC. Fig. 15 shows the chip photograph of the push-push VCO with divider.

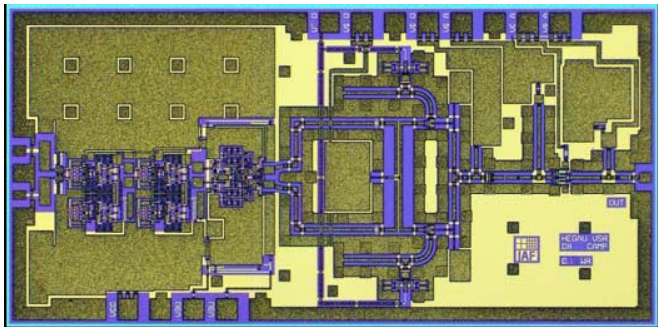

Fig. 15. Chip photograph of the VCO MMIC (chip size: 3.0 x 1.5 mm²).

The oscillator achieves a tuning range of 3.4 GHz around the center frequency of 92 GHz and an output power of more than 5.5 dBm. By applying this concept, the VCO was synchronized to a low frequency reference signal at 180 MHz using a commercially available PLL circuit. Compared to the free running oscillator, the phase-noise was improved by 24 dB to -77 dBc/Hz at 100 kHz offset from the carrier. Fig. 16 shows the measurement results. Details of the oscillator are published by Weber et al. [11].

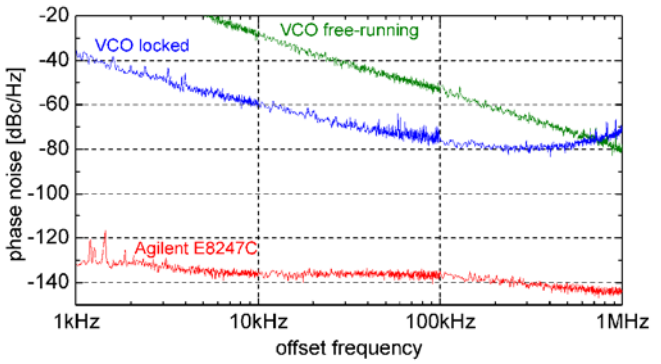

Fig. 16. Measured phase noise of the free-running and locked VCO at 92.16 GHz and the reference signal at 180 MHz.

IV. Conclusion

Metamorphic HEMT technology has been demonstrated to be highly suitable for the development of advanced millimeter-wave and sub-millimeter wave circuits for space applications. Sub-millimeter and millimeter wave amplifier circuits have been demonstrated with mHEMT devices of 35 nm and 50 nm gate length. Devices with 100 nm gate length were used for a mixer, a sixtupler and a PLL based VCO design operating at W-, D-, and G-band. The possible monolithic integration of special Schottky diode detectors with this technology was also presented.

Acknowledgment

The authors would like to thank their colleagues from the IAF technology department for MMIC processing. Additionally we like to thank Rainer Lösch for his excellent epitaxial layers, Michael Kuri and Herrmann Massler for their experienced RF measurements and Matthias Seelmann-Eggebert for his outstanding device modeling. This work was funded by the German Federal Office of Defense Technology and Procurement (BWB) in the framework of the TeraIC program.

References

[1] W. Deal, X. Mei, V. Radisic, P. Liu, J. Uyeda, M. Barsky, T. Gaier, A. Fung, R. Lai, "Demonstration of a S-MMIC LNA with 16-dB Gain at 340 GHz", 2007 IEEE Compound Semiconductor Integrated Circuits Symposium, pp. 1-4, Oct. 2007.

[2] D. Pukala, L. Samoska, T. Gaier, A. Fung, X. B. Mei, W. Yoshida, J. Lee, J. Uyeda, P. H. Liu, W. R. Deal, V. Radisic, R. Lai, "Submillimeter-Wave InP MMIC Amplifiers From 300–345 GHz", IEEE Microwave and Wireless Components Letters, vol. 18, no. 1, pp. 61-63, Jan. 2008.

[3] V. Radisic, D. Sawdai, D. Scott, W. R. Deal, L. Dang, D. Li, A. Cavus, A. Fung, L. Samoska, R. To, T. Gaier, R. Lai, "Demonstration of 184 and 255-GHz Amplifiers Using InP HBT Technology", IEEE Microwave and Wireless Components Letters, vol. 18, no. 4, pp. 281-283, April 2008.

[4] A. Leuther, A. Tessmann, H. Massler, R. Lösch, M. Schlechtweg, M. Mikulla, O. Ambacher, "35 nm Metamorphic HEMT MMIC Technology," 20th International Conference on Indium Phosphide and Related Materials, MoA3.3, May 2008.

[5] M. Seelmann-Eggebert, T. Merkle, F. van Raay, R. Quay, M. Schlechtweg,, "A Systematic State-Space Approach to Large-Signal Transistor Modeling", IEEE Trans. on Microwave Theory and Techn., vol. 55, pp. 195–206, February 2007.

[6] A. Tessmann, A. Leuther, H. Massler, M. Kuri, R. Loesch, "A metamorphic 220-320 GHz HEMT amplifier MMIC", IEEE Compound Semiconductor Integrated Circuit Symposium, CSICS 2008: 12-15 Oct. 2008, Monterey/Calif.. Piscataway, NJ: IEEE, 2008, pp. 31-34.

[7] A. Tessmann, I. Kallfass, A. Leuther, H. Massler, M. Schlechtweg, O. Ambacher, "Metamorphic MMICs for Operation Beyond 200 GHz," Gallium Arsenide Application Symposium Association -GAAS-: 3rd European Microwave Integrated Circuits Conference 2008. Proceedings: Held in Amsterdam, from 27 to 31 October 2008 as part of European Microwave Week 2008, EuMW. Amsterdam, 2008, pp. 210-213.

[8] A. Hülsmann, "Breitbandiger Mikro-, Millimeter- und Sub-Millimeter Detektor," patent pending, Deutsches Patent und Markenamt, 2008.

[9] I. Kallfass, H. Massler, A. Leuther, "A 210 GHz, Subharmonically-Pumped Active FET Mixer MMIC for Radar Imaging Applications," 2007 IEEE CSIC Symposium Digest, pp. 71-74, Oct. 2007.

[10] I. Kallfass, H. Massler, A. Tessmann, A. Leuther, M. Schlechtweg, G. Weimann, "A broadband frequency sixtupler MIMIC for the W-band with >7 dBm output power and >6 dB conversion gain," IEEE MTT-S, International Microwave Symposium Digest 2007. CD-ROM: 3-8 June 2007, Honululu/Hawai. Piscataway, NJ: IEEE, 2007, pp. 2169-2172.

[11] R. Weber, M. Kuri, M. Lang, A. Tessmann, M. Seelmann-Eggebert, and A. Leuther, "A PLL-stabilized W-band MHEMT push-push VCO with integrated frequency divider circuit," IEEE MTT-S, International Microwave Symposium Digest 2007. CD-ROM: 3-8 June 2007, Honululu/Hawai. Piscataway, NJ: IEEE, 2007, pp. 653-656.

Compact 340 GHz Receiver Front-Ends

Peter Sobis, Tomas Bryllert, Arne Ø. Olsen, Josip Vukusic, Vladimir Drakinskiy, Sergey Cherednichenko, Anders Emrich and Jan Stake

Abstract— **A compact 340 GHz room temperature receiver front-end has been developed consisting of a subharmonic Schottky diode mixer module with an integrated LNA. A novel sideband separation topology has been evaluated by using a pair of the developed mixers interconnected by external waveguide branch guide coupler hybrids for the LO and RF feedings and coaxial IF hybrids, measuring sideband suppression levels of 5 dB to 15 dB over the 315-365 GHz band.**

For efficient LO pumping of the sideband separating mixer, a novel high power LO chain based on a 5 x 34 GHz HBV quintupler (170 GHz LO source) has been developed with an ultra compact mechanical block housing, not much larger then a waveguide flange. We have also looked into a broadband medium LO power source consisting of a W-band active multiplier module, based on commercial MMIC chips from Hittite, followed by a medium power Schottky doubler from VDI.

The demonstrated compact receiver front end has a considerably reduced size and weight owing to the high multiplication factor of the compact LO chain and mixer with integrated LNA. The novel sideband separating topology that uses 90 degree hybrids for both LO and RF resolves the standing wave issue of a previously proposed topology, in which a matched Y-junction was used as an RF hybrid and a branch guide coupler with a 45 degree differential line phase shifter at the output, was used for the LO feeding. The proposed topology improves both the sideband suppression and reduces the standing waves at the LO and RF ports.

***Index Terms*—Submillimeter wave circuits, Submillimeter wave mixers, Submillimeter wave receivers, Submillimeter wave waveguides**

I. Introduction

There is a need for compact heterodyne receivers operating in the sub-millimeter wave band (above 300 GHz) for earth observation instruments and space science missions. The sub-millimeter wave or terahertz domain allows studying several meteorological phenomena such as water vapour, cloud ice water content, ice particle sizes and distribution, which are important parameters for the hydrological cycle of the climate system and the energy budget of the atmosphere.

In this paper an ultra-compact 340 GHz receiver front-end module is presented suitable for earth missions as well as future planetary missions. The receiver has specifically been designed to meet the specification of the STEAMR instrument, promoted by the Swedish Space Corporation (www.ssc.se), which constitutes the millimeter wave limb sounder in PREMIER [1], one of three ESA Earth Explorer Core missions that now have entered a feasibility study phase.

The STEAMR submm-wave front-end consists of 14 RT SSB or DSB receivers divided equally over two polarizations in a focal plane array configuration operating in the 310-360 GHz band. The broadening of spectral lines in the earth lower sphere layers motivates the use of SSB receivers while in the upper layers the narrow lines can be resolved using DSB configurations. In this work we propose a novel subharmonic sideband separating mixer topology that better can withstand LO port mismatches and variations in between the mixer pair.

The subharmonic sideband separation mixer topology that was suggested in [2] was employing a matched Y-junction to split the RF signal and a 45/135 degree phase shifter hybrid for the LO feeding. This topology is sensitive to standing waves at the mixer RF inputs, due to the poor isolation in between the mixers, leading to considerable ripple in the image rejection response. The proposed novel image rejection mixer topology circumvents this problem by using 90 degree hybrids for both the RF and LO, moreover it improves the LO and RF SWR as the reflected power is terminated. The quadrature feeding of the LO and RF port is possible, as the effective "fundamental" LO phase shift is translated to 180 degrees by the subharmonic x2 mixers.

II. Front-end Receiver Module

The STEAMR submm-wave front end consists of a total of 14 receiver modules divided into sub-arrays of 3-4 DSB or SSB mixers. In such a configuration there is room for optimization and partial integration of the front-end receiver modules and LO system. The system LO signal will be fixed to about 170 GHz with an IF band of 6-18 GHz SSB covering an RF band of 320-360 GHz instantaneously, where the goal is to reach a DSB noise temperature better than 2000 K for each individual receiver. In this context, a compact front-end receiver module architecture consisting of a subharmonic Schottky mixer and LNA integrated into one block has been developed, see figure 1.

Manuscript received 20 April 2009. This work was supported in part by the Swedish National Space Board and by the Swedish Research Council (VR).

J. Stake, V. Drakinskiy, S. Cherednichenko and J. Vukusic are with the Physical Electonics Laboratory, Department of Microtechnology and Nanoscience, Chalmers University of Technology.

P. Sobis and A. Emrich are with Omnisys Instruments AB, Gruvgatan 8, SE-421 30 (phone: +46-31-7343400; fax: +46-31-7343429; e-mail: ps@omnisys.se).

A. Olsen and T. Bryllert are with Wasa Millimeter Wave AB. (e-mail: info@wmmw.se).

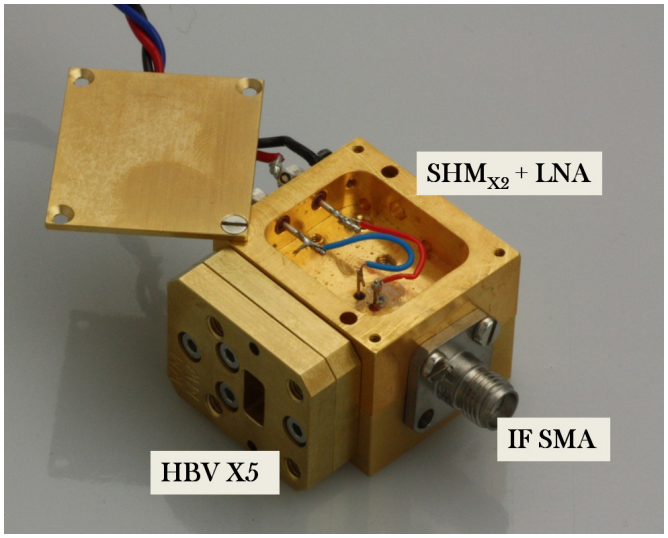

Figure 1. Photo of the novel compact 340 GHz front end receiver consisting of a mixer module with an integrated LNA and an ultra compact HBV x5 multiplier.

Furthermore, two LO source alternatives capable of pumping two or more mixers have been evaluated. The first LO chain is based on a high power x5 multiplier using HBV-technology [3] driven by a 0.5 W amplifier at 35 GHz while the other LO chain is using a medium power Schottky based x2 multiplier driven by an active W-band x6 module. See figure 2, for a schematic overview of the receiver front-end system showing the two LO chain alternatives.

III. SUBHARMONIC MIXER

The receiver mixer module design, presented in [4], is based on a subharmonic inverted suspended mixer circuit topology [6], and uses a 75 um thick fuzed quartz substrate and a commercial SC1T2-D20 antiparallel Schottky diode chip from Virginia Diodes Inc., that is soldered to the thin film circuit in a flip chip fashion. The mixer has been design for a LO bandwidth of about 5% and a RF bandwidth of more then 20%. The relatively long distance (5mm) in between the IF port and mixer diodes, limits the bandwidth of the IF response

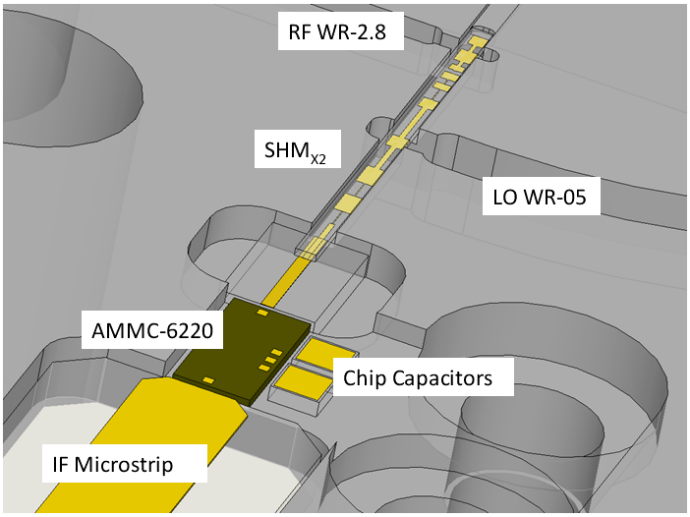

Figure 3. 3D-model of the developed 340 GHz mixer module with an integrated LNA (AMMC-6220).

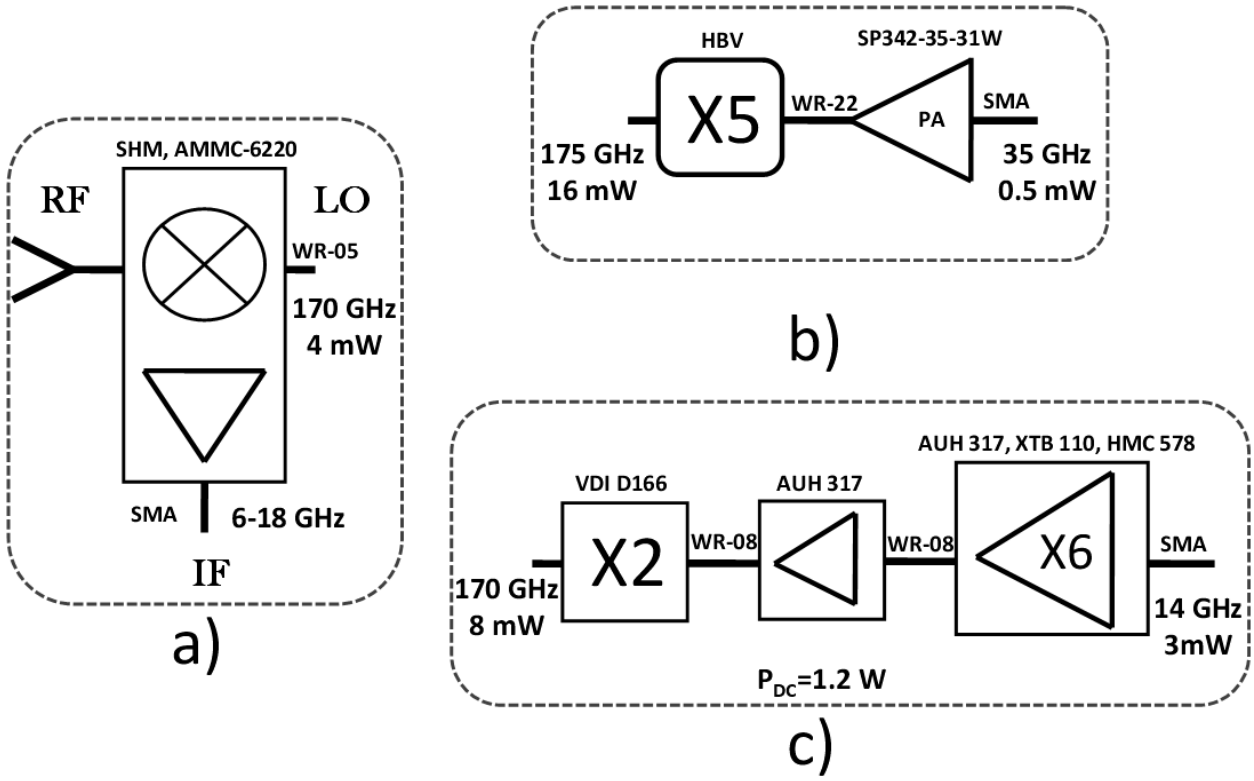

Figure 2. Schematic of the front-end receiver module a) the HBV quintupler LO chain b) and the Schottky doubler based LO chain c).

to about 30 GHz. The AMMC-6220 MMIC LNA with a typical noise temperature of 165 K has been integrated to the E-plane mixer splitblock using vertical DC feedthrus, see figure 3. A lid covers the outer side of the splitblock half which houses a small mounting cavity in which a simple DC bias circuit could be placed.

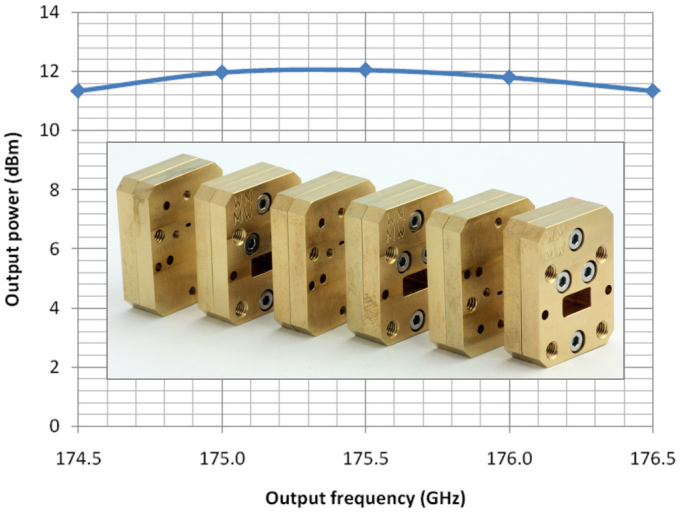

Figure 3. Measured output power for the HBV quintupler LO module.

A. HBV Quintupler

The quintupler source module features an ultra-compact block design, and a microstrip matching circuit on high-thermal-conductivity AlN to improve the power handling capability [3]. The HBV diode is flip-chip soldered onto a microstrip circuit that contains the impedance matching elements and waveguide probes [5]. The AlN circuit is then mounted in a waveguide block with waveguide input/output interfaces (WR-22 / WR-5). One of the ambitions of the work was to make a design that was reliable and reproducible – therefore care was taken to minimize the number of manual steps in the fabrication and mounting. No DC electrical connection between the microstrip circuit and the waveguide block was therefore used. The epimaterial is a generic HBV design with three barriers. High power HBV diodes are fabricated using standard III-V processing techniques and utilizes four-mesas in series (4 x 3 = 12 barriers) in order to increase the power handling capability.

The output power from multiplier module was evaluated using an Erickson power meter PM2 and a frequency synthesizer followed by a Spacek power amplifier providing the input signal. A waveguide isolator was also used between the power amplifier and the HBV multiplier. In figure 3 the output power is plotted as a function of frequency for a constant pump power.

B. The Schottky Doubler based x12 Module

A W-band active x6 multiplier module developed for the LO chain of the ALMA water vapour radiometer (www.almaobservatory.org), was used together with an additional packaged W-band amplifier chip AUH-317, to pump a low power Schottky x2 multiplier (D166) from Virginia Diodes Inc.. This configuration was able to produce sufficient output power to pump two mixers and had a relative broadband response, see figure 4. The output power was measured using an Erickson power meter (PM2).

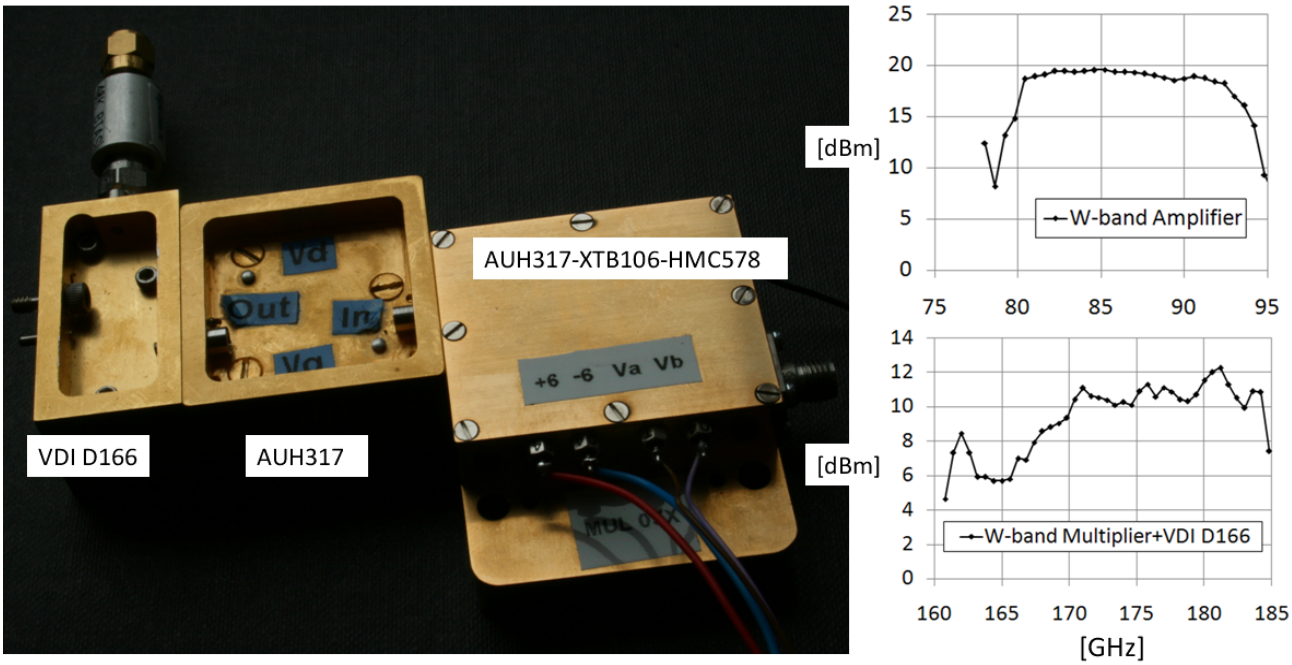

Figure 4. Photo of the medium power Schottky doubler based LO chain (left), and measured output powers from the W-band multiplier with an extra amplifier stage (top right) and from the Schottky doubler (bottom right).

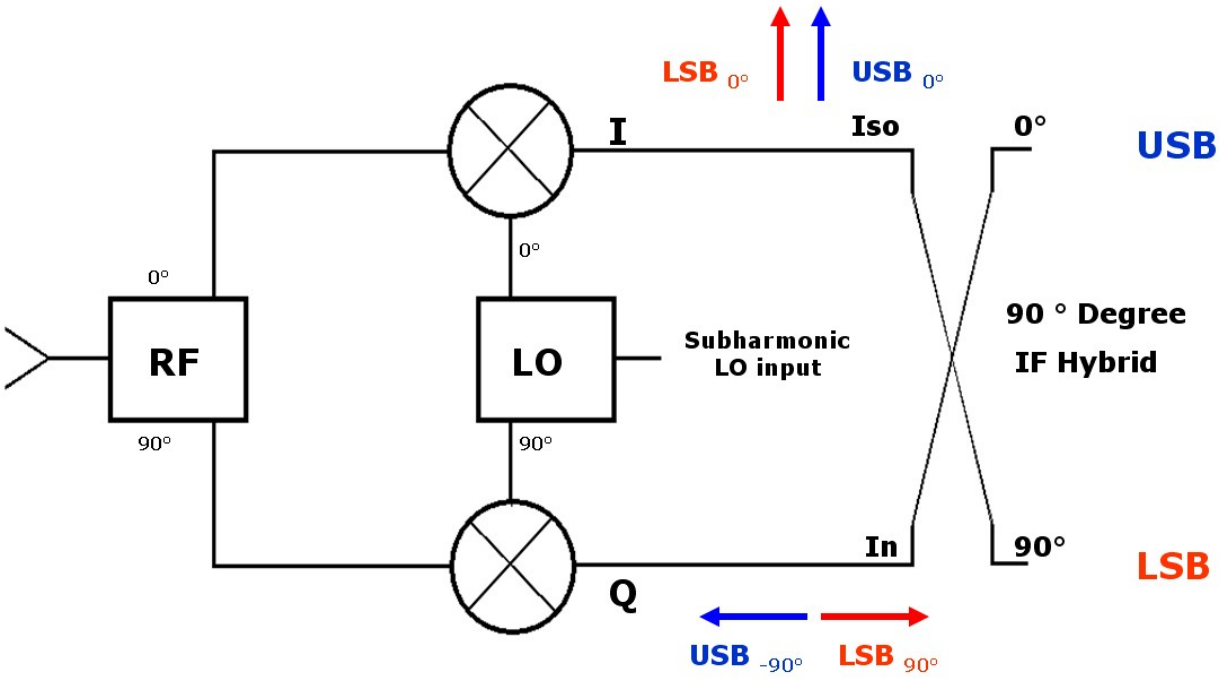

$$I = \sin\left(\omega_{RF,USB} - 2\omega_{LO}\right) + \sin\left(2\times\omega_{LO} - \omega_{RF,LSB}\right)$$

$$Q = \sin\left(\omega_{RF,USB} + 90° - 2\times\omega_{LO} - 2\times 90°\right) + \sin\left(2\times\omega_{LO} + 2\times 90° - \omega_{RF,LSB} - 90°\right)$$

Figure 5. Schematic of the proposed image rejection topology that uses 90 degree RF and LO hybrids.

IV. Novel Subharmonic Sideband Separating Topology

A novel sideband separation scheme has been developed for subharmonic mixers, see figure 5. The image rejection mixer topology uses 90 degree hybrids for both the RF and LO and is therefore more resilient to poor matching of the RF and LO ports which often is the case for submm-wave mixers. More important, standing waves can be a major source to ripple in the image rejection response, but also complicates the interconnection to adjacent LO and RF subsystems and could in worst case lead to system instabilities and system failure.

The RF and LO hybrids can easily be realised in waveguide technology with relative small losses, we have chosen to use oversized branch guide coupler hybrids that have been designed using the FEM based 3D-EM simulation CAD tool HFSS and machined in a EVO NCR system from Kern with a final block precision of 5 um or better.

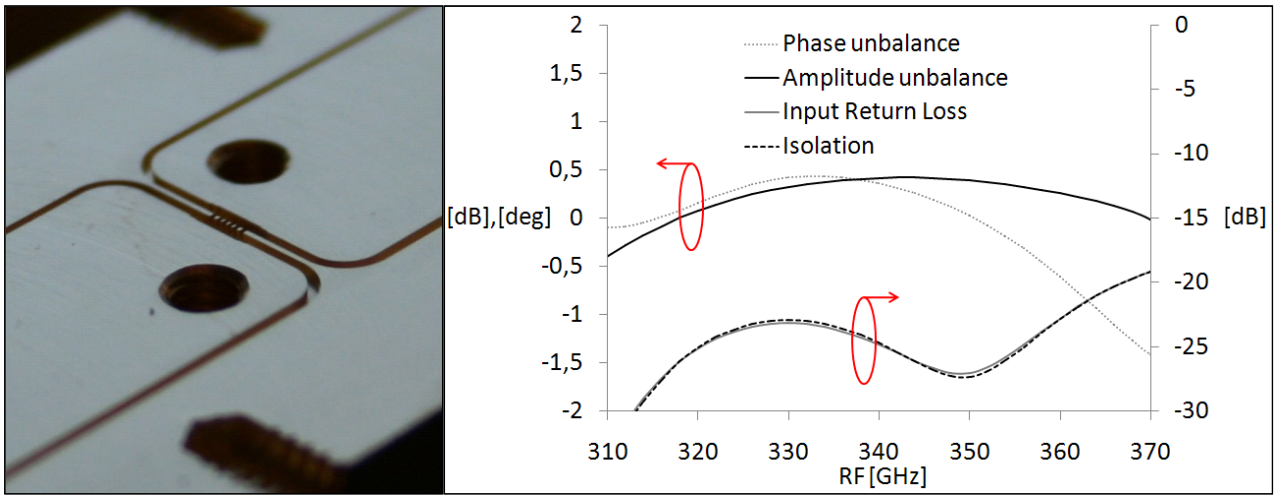

Figure 6. Photo of the WR-2.8 E-plane splitblock branch guide coupler hybrid (left) that was machined in brass using a 160 um diameter tool, the xyz-dimensions were measured in a digital microscope and are within 5 um. 3D-EM simulated performance using H-plane symmetry (right).

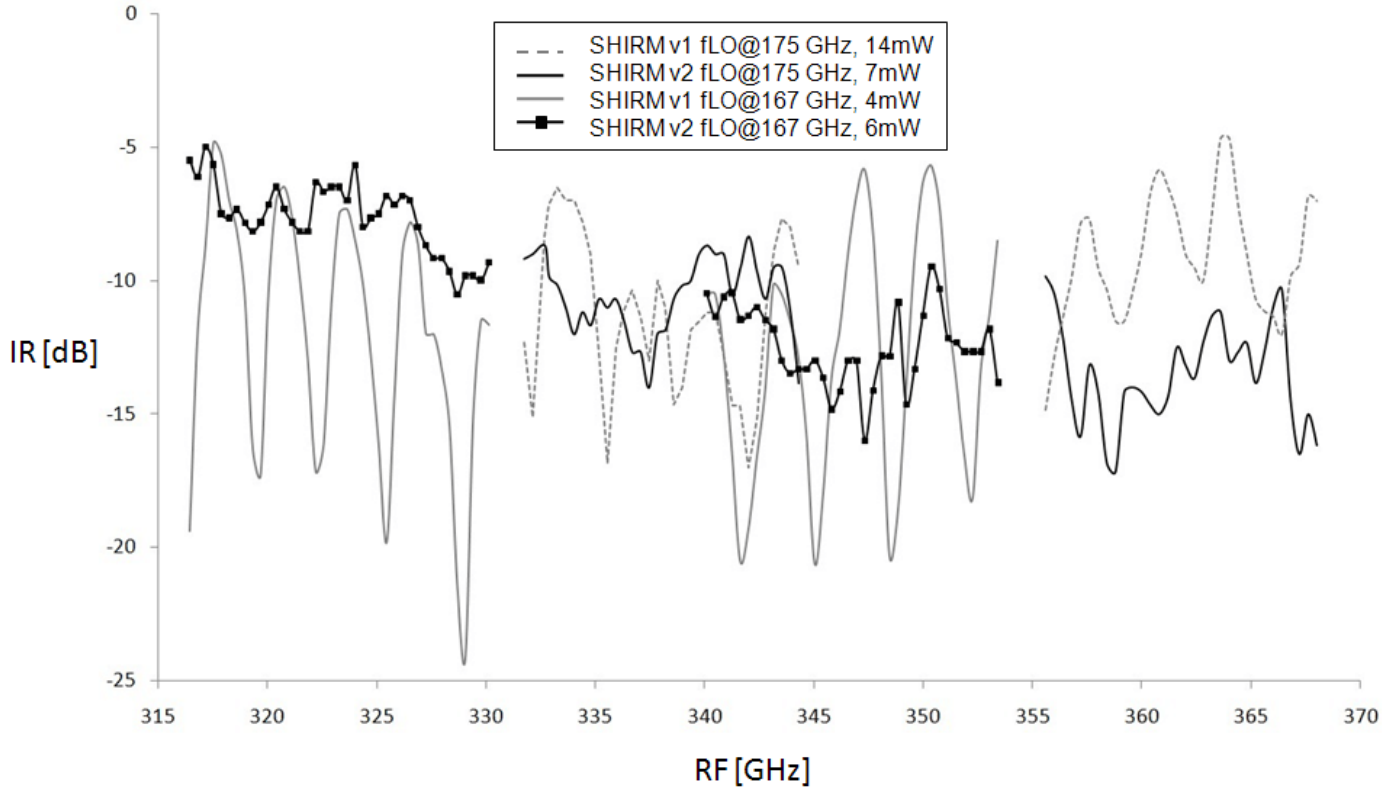

Figure 8. Measured sideband suppression vs. RF frequency of the novel (SHIRM v2, black) and previously proposed (SHIRM v1, grey) image rejection topologies at 167 GHz and 175 GHz LO frequency.

In order to evaluate both image rejection topologies a RF matched Y-junction was also designed and one of the LO hybrid sides comprised a 45 degree 3-stub loaded differential line phase shifter. In this way it could either be used as a 45/135 degree hybrid in one direction or as a 90 degree hybrid in the other direction. Both the RF Y-junction and the LO hybrid have measured a loss extending 1 dB due to the long waveguides used to separate the flange interconnects, the insertion loss of the developed RF 90 degree hybrid, see figure 6, is expected to be slightly higher as the input waveguide is longer.

V. RESULTS

Two mixers were assembled showing a divergence in receiver DSB noise temperature starting at 12 GHz IF, see figure 7. The commercial LNA's performance clearly affects the total receiver noise temperature comparing to the result obtained when using the same mixer design together with a custom 1-12 GHz MMIC LNA, with a typical noise temperature of about 75 K, developed at Chalmers University of Technology. The mixer conversion loss including waveguide, horn antenna and substrate losses has been estimated to around 9 dB broadband using a 3dB attenuator in between the mixer and LNA in a hot(RT)/cold(LN) load measurement setup.

The pair of assembled mixer modules was used to evaluate the two different SHIRM topologies at a LO frequency of 167.5 GHz (Schottky x2 based LO chain) and 175 GHz (HBV x5 LO chain) with an LO power of about 7 mW and 14 mW respectively, covering a RF bandwidth of 315 GHz to 365 GHz. Three IF hybrids from Anaren Inc were used to cover the 6-18 GHz band together with phase matched semi-rigid SMA cables and two broadband SMA packaged MITEQ amplifiers. A WR.2.8 comb generator from Virginia Diodes Inc was used to generate the RF signals.

The two sideband separation mixer prototypes are showing

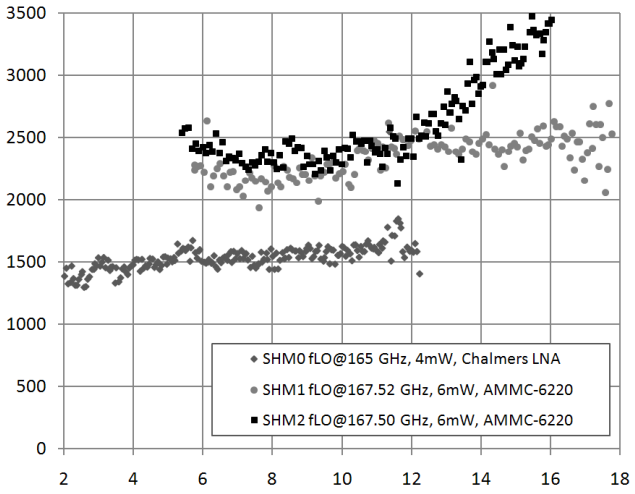

Figure 7. Receiver DSB noise temperature for three different mixer modules using Y-factor measurements.

sideband suppression levels of -5 to -15 dB over the RF band, see figure 8, where a satisfactory level can be considered to be -15dB or better. The ripple of the previously proposed topology coincides well with the half wavelength distance in between the mixers. A quick check to confirm that this ripple was in fact coming from a standing wave in between the two mixer RF ports, two WR-03 1" long waveguide pieces were inserted in between the mixers and the RF hybrid, leading to an equally relative increase of the ripple in the image rejection

response. Furthermore the novel topology had an improved image response in terms of ripple over the entire band and suppression level was improved over the upper half of the band. A test of the mixer IQ amplitude unbalance was showing no more than a 1.5 dB difference with typical values of around 0.5 dB suggesting the presence of a phase unbalance of about 40 degrees.

VI. CONCLUSIONS

The current Schottky doubler based LO chain is capable of pumping two mixers at optimum conditions, a high power Schottky doubler would however encompass variations in between the individual receiver chains and would therefore give better safety margins.

The developed HBV based LO chain, optimized for high power, makes an attractive alternative for pumping mixer arrays and image rejection mixers. The novel compact topology could also be optimized for medium to low power outputs to better match the requirements of a single receiver unit.

The receiver noise temperature could be improved further by cooling (about -60C degrees) but it is not yet clear whether a noise temperature of 2000 K DSB can be reached. By using a custom LNA design with similar performance as with the Chalmers 1-12 GHz MMIC LNA, we estimate that a DSB receiver noise temperature of less than 1700 K over the whole band can be reached.

The novel image rejection topology is showing a potentially improved performance compared to the other topology, however it needs to be evaluated further and acceptable sideband suppression levels must be reached. By better understanding the source of unbalance, further steps towards an improved performance can be taken. The RF hybrid design will be verified and more mixer modules must be assembled in order to assure a good balanced mixer pair. Integration of the hybrids with the mixers should of course remove any uncertainties coming from flange interconnects and long waveguides in the current setup. This would also reduce LO and RF losses significantly leading to a lower noise.

VII. ACKNOWLEDGMENTS

We wish to thank Carl-Magnus Kihlman for the excellent work of manufacturing the high precision prototype blocks. and Niklas Wadefalk for providing the state of the art LNA and for helpful discussions, both are with the Department of Microtechnology and Nanoscience at Chalmers University of Technology. The mixer and HBV quintupler development has been done under separate contracts with the Swedish National Space Board. This work was in part conducted under an industrial Ph.D project grant from the Swedish Research Council (VR).

VIII. REFERENCES

[1] ESA SP-1313/5 Candidate Earth Explorer Core Missions – Reports for Assessment: PREMIER – Process Exploration through Measurements of Infrared and millimetre-wave Emitted Radiation, 2008, ISBN 978-92-9221-406-7, ISSN 0379-6566

[2] P. Sobis, J. Stake and A. Emrich, "A 170 GHz 45 degree Hybrid for Submillimeter Wave Sideband Separating Subharmonic Mixers" *Microwave and Wireless Components Letters*, IEEE, vol. 18, NO. 10, pp. 680-682, Oct. 2008.

[3] J. Stake, T. Bryllert, A. O. Olsen and J. Vukusic, , "Heterostructure Barrier Varactor Quintuplers for Terahertz Applications" *Proc. of the 3rd European Microwave Integrated Circuits Conf.*, 2008.

[4] P. Sobis, J. Stake and A. Emrich, "Optimization and Design of a Suspended Subharmonic 340 Ghz Schottky Diode Mixer" *International Conference on Infrared and Millimeter Waves and 14th International Conference on Terahertz Electronics*, Shanghai, China, ISBN/ISSN: 1-4244-0400-2, pp. 193, 2006.

[5] T. Bryllert, A. O. Olsen, J. Vukusic, T. A. Emadi, M. Ingvarson, J. Stake and D. Lippens, "11% efficiency 100 GHz InP-based heterostructure barrier varactor quintupler" *Electronics Letters*, vol. 41, No. 3, February 2005.

[6] B. Thomas, A. Maestrini and G. Beudin, "A low-noise fixed-tuned 300-360-GHz sub-harmonic mixer using planar Schottky diodes" *Microwave and Wireless Components Letters*, IEEE, vol. 15, No. 12, pp. 865-867, Dec. 2005.

Session W4

Testing & Measurements

Chair: Bertrand Thomas

Wednesday, April 22
3:45 – 5:00

W4A

Modular VNA Extenders for Terahertz Frequencies

Y. Duan and J.L. Hesler*
Virginia Diodes, Inc., Charlottesville, VA 22902
* Contact: Hesler (a) VADiodes.com, phone (434)297-3257

***Abstract*—One of the major challenges of creating terahertz systems for radio astronomy and other applications is the lack of suitable test and measurement equipment. Over the past several decades researchers have developed and demonstrated broadband mixers and multipliers based on Schottky diodes that have been used primarily for scientific applications throughout this frequency band. As the performance of these basic components has improved and particularly as their tuning bandwidth has increased, it becomes possible to develop effective frequency extenders for standard test equipment, such as Vector Network Analyzers (VNAs) and Spectrum Analyzers (SAs). VDI's first effort in this area was in collaboration with ESA for the development of a VNA extender for their antenna test range in Noordwijk (see paper presented at the AMTA conference in St. Louis, Nov. 2007). For that effort VDI developed transmitter and receiver extenders to the WR6.5 and WR4.3 waveguide bands for a Rohde & Schwarz ZVA 40. These systems achieved transmit powers of ~0-5dBm and dynamic range in the range of 80-100dB across the waveguide bands.**

VDI is now developing a modular VNA extender system that will allow measurements across the frequency range from about 140 GHz through 1 THz, and eventually higher. The modular nature of the system allows the same lower frequency components, such as the LO and transmitter W-Band drivers, to be reused as additional frequency multipliers are added to move to higher frequency bands. Through the gradual improvement of the individual components, as well as the system design, VDI has recently demonstrated excellent performance (DR ~80dB) in the WR1.5 waveguide band. This talk will review the development of the modular VNA frequency extender system and present recent results for frequencies in the range from 500GHz through 1.5 THz.

A Simple Orthomode Transducer for Centimeter to Submillimeter Wavelengths

A. Dunning, S. Srikanth, and A. R. Kerr

***Abstract* –We describe a simple orthomode transducer suitable for operation from centimeter to submillimeter wavelengths with appropriate scaling. It is fabricated as a split-block assembly with all waveguides in the same plane, and requires no septum or polarizing wires. The OMT operates over a 1.3:1 frequency band, narrower than a full waveguide band (typically 1.5:1). For a WR-10 version of the OMT, covering 78-102 GHz, the polarization isolation is > 37 dB and the return loss at the rectangular waveguide ports > 24 dB. The practical upper frequency for this design is probably limited by the precision of alignment that can be achieved between the block halves, which affects the polarization isolation.**

***Index Terms* — Orthomode transducers, waveguide junctions, multimode waveguides, millimeter wave circuits.**

I. Introduction

In designing broadband orthomode transducers (OMTs) it is desirable to maintain symmetry about both input polarizations to prevent generation of higher-order modes. However, most schemes which have been devised to accommodate these symmetry conditions [1][2][3][4][5][6] result in considerable complexity compared with designs which are symmetrical about only one plane. At submillimeter wavelengths this extra complexity presents an additional obstacle to fabrication. We describe an OMT symmetrical about only one plane which can be fabricated as a simple split block assembly and which requires no polarizing wires or septum.

For an OMT with a square input waveguide and symmetrical about only one plane, strong coupling into the TE_{11} and TM_{11} modes is almost unavoidable at frequencies close to their common cutoff frequency. As a result, the TE_{11} and TM_{11} cutoff frequency may be taken as the upper frequency limit of such a design. Because coupling to the higher modes falls off very quickly below the cutoff frequency, the OMT can operate quite close to this limit with little degradation in performance. The lower frequency limit is given by the cutoff frequency of the TE_{01} mode. This would give a maximum bandwidth of 1.41:1. However, it is difficult to achieve an acceptable return loss close to the TE_{01} cutoff due to the rapid variation in guide wavelength. A bandwidth of ~1.3:1 is therefore a practical limit for such a design.

Manuscript received 19 April 2009.

A. Dunning is with the CSIRO Australia Telescope National Facility, Epping NSW Australia 1710.

S. Srikanth and A. R. Kerr are with the National Radio Astronomy Observatory, Charlottesville, VA 22903. Corresponding author: akerr@nrao.edu.

The National Radio Astronomy Observatory is a facility of the National Science Foundation operated under cooperative agreement by Associated Universities, Inc.

II. A Split-Block OMT

The OMT described here consists of an input section, a polarization separating junction, and an output section for each polarization. The structure of the waveguide is shown in Fig. 1. The input section is composed of a square input which is reduced to a smaller square waveguide, followed by a transition to a waveguide with a T-shaped cross section. The polarization separating junction removes one polarization via a mitered bend and allows the other to pass through. Finally each output section consists of a stepped transition to a larger rectangular waveguide. The OMT was designed in three stages beginning with the junction of the dual-mode waveguide with two rectangular waveguides. Then the transition between the T-waveguide and the square waveguide was designed, and finally the input and output transitions were added.

The internal geometry of the polarization separating junction is shown in Fig. 2. Using a T-shaped waveguide makes it possible to maintain only two propagating modes within the 1.3:1 frequency band and simultaneously achieve a waveguide

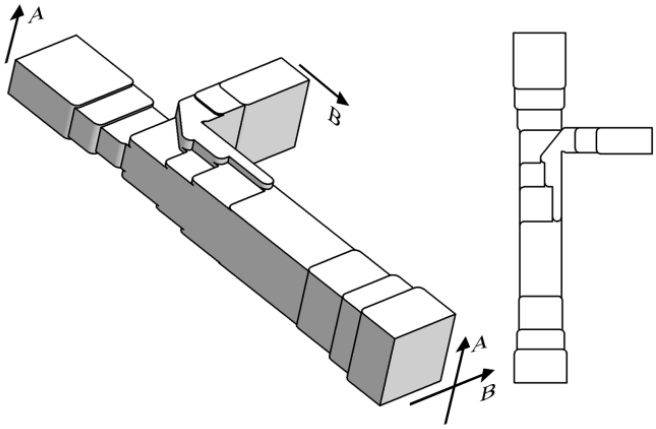

Fig. 1. Geometry of the OMT

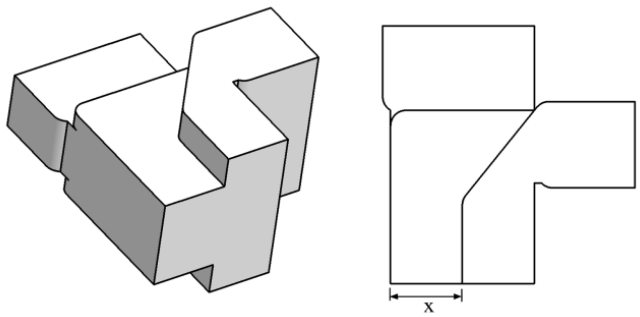

Fig. 2. Internal geometry of the polarization separating junction with the T-waveguide input.

impedance closely matched to that of the junction's rectangular waveguide outputs. The ratio of the cutoff frequency of the desired modes in the T-waveguide to the cutoff frequency of the next higher order mode is 1.73:1, which makes it possible for this junction to operate over a bandwidth of approximately 1.6:1. It is only the transition from square to T-waveguide that reduces this bandwidth to 1.3:1. The dominant modes in T-waveguide and their corresponding polarizations are shown in Fig. 3. The **A** polarization encounters a transition to rectangular waveguide via a linear increase in the narrow section of the T-waveguide (dimension *x* in Fig. 2.) until only a rectangular section remains. This transition presents a section of reduced impendence waveguide almost a quarter wavelength long that is compensated by reducing the impedance of the output waveguide. The **B** polarization is removed via a mitered bend through a rectangular waveguide at right angles to the T-waveguide. A small capacitive transverse ridge at the junction of the rectangular waveguide with the T-waveguide was found to improve the return loss of this polarization. Using a finite element electromagnetic simulator [7] all internal dimensions of the junction and the rectangular waveguide outputs were optimized for minimum reflection of the input signals.

The transition between the T-shaped waveguide and square waveguide consists of a two stage stepped transition. This transition was initially optimized alone and then in combination with the junction for optimal return loss in each polarization.

As a final step, quarter-wave transformers were added to the input and each output waveguide to transform to the required external waveguide sizes. The external square waveguide propagates four modes within the frequency band and therefore the smaller square waveguide section must be maintained for a significant distance from the junction to prevent generation of higher-order modes. Finally, the whole structure was optimized for maximum return loss in both polarizations simultaneously.

The original design was for ALMA Band 6 (211-275 GHz) but for ease of measurement we constructed and measured a scaled version for 78-102 GHz in WR-10 waveguide as shown in Figs. 4 and 5.

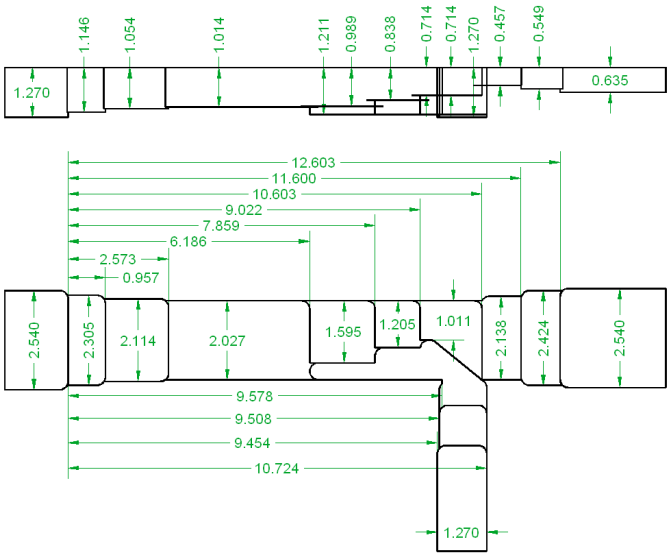

Fig. 4. Dimensions of the WR-10 OMT in mm. All corner radii are 0.216 mm.

Fig. 5. Photograph of the WR-10 OMT.

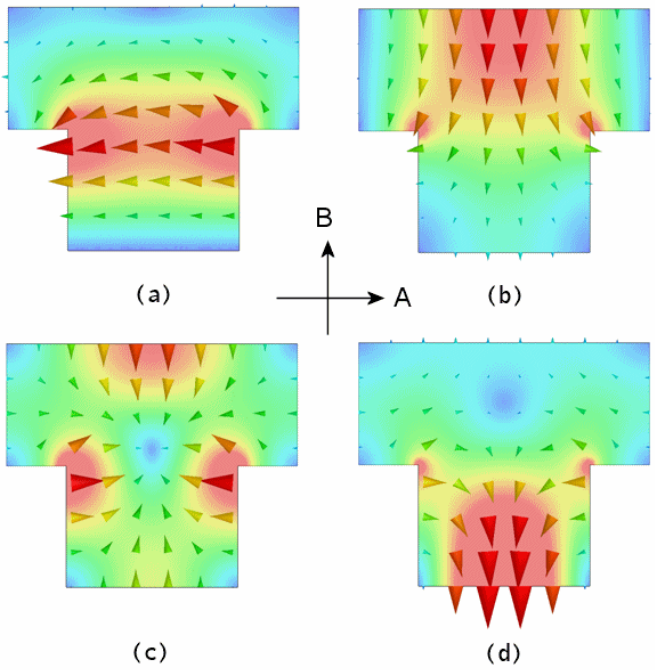

Fig. 3. Electric field of the first four modes of the T-waveguide. a) The mode corresponding to the TE_{01} mode in the square waveguide and the *A* polarization. b) The mode corresponding to the TE_{10} mode in the square waveguide and the *B* polarization. c) and d) show the next higher TM and TE modes, respectively.

III. Simulation and Measurements

The OMT was analyzed using the FDTD electromagnetic simulator QuickWave [8]. Fig. 6(a) shows the simulated transmission and reflection of the through and side paths (in Fig. 1, paths *A* and *B*, respectively).

Measurements were made using an HP8510C two port vector network analyzer with a square-to-rectangular waveguide transition on the square port of the OMT and a matched load on the rectangular port not connected to the VNA. Fig. 6(b) shows the measured transmission and reflection. The measured transmission shown in Fig. 6(b) has been corrected for the small loss of the square-to-rectangular transition.

Fig. 7 shows the polarization isolation measured with the VNA connected to the square port of the OMT and the isolated waveguide port.

The first OMT we made had poor polarization isolation as a result of misalignment between the block halves. To explore this, FDTD simulations were run with deliberately misaligned parts. Fig. 8 shows the effect of misalignments of 7, 14, and 28 μm on the polarization isolation.

IV. Discussion

The surprising sensitivity of the isolation of the OMT to small misalignments between block halves warrants further explanation. If the misalignment were simply equivalent to a twist in the square waveguide, the cross polarization would be much less than observed (and simulated). A 28 μm misalignment of a 2.54 mm square waveguide would cause a rotation of ~0.3°, corresponding to a -45 dB cross-polarized component independent of frequency. The actual cause of the frequency dependent cross-polarization can be explained with the aid of Fig. 9 which shows the misaligned square waveguide. Vector **A** represents the electric field of one incident linear polarization, and can be broken down into two components $\mathbf{A_1}$ and $\mathbf{A_2}$. Because of the misalignment of the two halves of the block, the two components see waveguides of slightly different effective width and thus have different phase velocities. This results in the generation of circular polarization. At lower frequencies, close to the cutoff frequencies of the $\mathbf{A_1}$ and $\mathbf{A_2}$ modes, the difference in phase velocity is more pronounced, leading to the frequency dependence of the isolation shown in Fig. 8.

In principle the OMT can be scaled to operate at any frequency. In practice, scaling to higher frequencies will be limited by the precision of alignment between the block halves and by the ability to machine the small channels of the T-waveguide section. The smallest commercially available end-mills have a diameter of ~25 μm [9][10], which would allow an OMT to be machined for operation at 1300-1700 GHz. However, the best machining techniques would only permit alignment of the upper and lower parts within perhaps 2 μm. This would give ~15 dB isolation at the low end of the band in an OMT scaled for operation at 540–700 GHz.

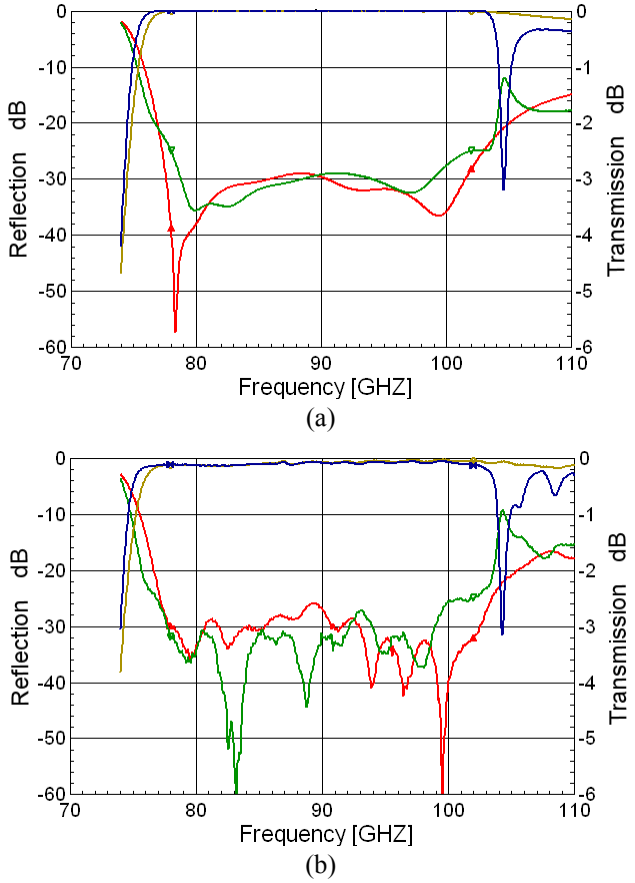

Fig. 6. S-parameters of the OMT: Transmission (side path blue, through path brown), and reflection coefficient (side arm green, through arm red) at the rectangular waveguide ports. (a) Simulated using QuickWave. (b) Measured. Markers at 78 and 102 GHz.

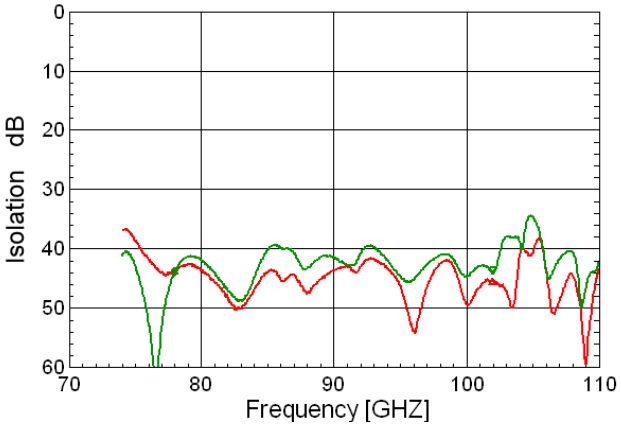

Fig. 7. Measured isolation of the OMT. Side-port isolation (red); through-port isolation (green). Markers at 78 and 102 GHz.

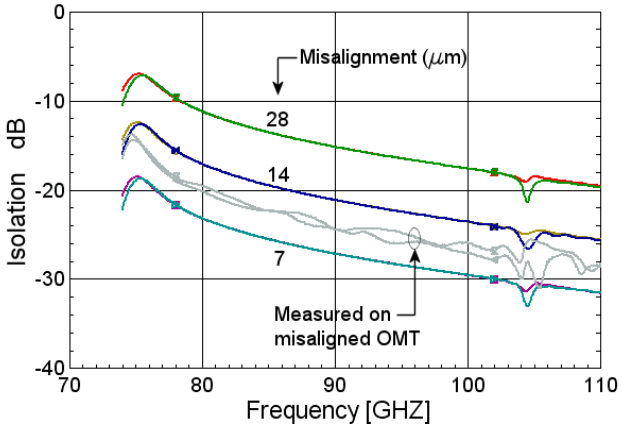

Fig. 8. Simulated polarization isolation as a function of misalignment between the block halves, for the side-port and through-port. Shown in gray are measurements on a misaligned OMT. Markers are at 78 and 102 GHz.

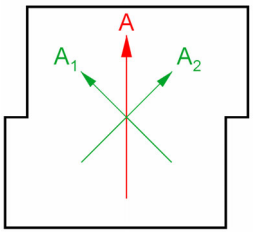

Fig. 9. Cross-section of the misaligned square waveguide. Components $\mathbf{A_1}$ and $\mathbf{A_2}$ of linearly polarized wave **A** have different phase velocities which results in generation of a cross polarized component..

It is interesting to speculate that in future receivers, in which the signal is digitized at the front end, it may be possible to correct the imperfect polarization isolation of an OMT digitally in the back end.

REFERENCES

[1] A. M. Bøifot, E. Lier, and T. Schaug-Pettersen, "Simple and broadband orthomode transducer," Proc. Inst. Elect. Eng., vol. 137, no. 6, pt. H, pp. 396–400, Dec. 1990.

[2] E. Wollack, "A Full Waveguide Band Orthomode Junction," Electronics Division Internal Report 303, National Radio Astronomy Observatory, May 1996. http://www.gb.nrao.edu/electronics/edir/edir303.pdf

[3] E. J. Wollack and W. Grammer, "Symmetric waveguide orthomode junctions," Proc. ISSTT, pp. 169, 2003, and ALMA Memo 425, 2002. http://www.alma.nrao.edu/memos/html-memos/alma425/memo425.pdf

[4] G. Narayanan and N. Erickson, "Full-Waveguide Band Orthomode Transducer for the 3 mm and 1 mm Bands," Proc. ISSTT, pp. 505-514, Mar 2002.

[5] G. Moorey, R. Bolton, A. Dunning, R. Gough, H. Kanoniuk and L. Reilly, "A 77-117 GHz cryogenically cooled receiver for radioastronomy," Proc. Workshop on the Applications of Radio Science (WARS2006), Leura, NSW, Australia, 15-17 Feb. 2006.

[6] A. Navarrini and R. Nesti, "Symmetric Reverse-Coupling Waveguide Orthomode Transducer for the 3-mm Band," IEEE Trans. Microwave Theory Tech. vol. 57, no. 1, pp. 80-88, Jan. 2009.

[7] HFSS, Ansoft LLC, Pittsburgh PA. http://www.ansoft.com/products/hf/hfss/

[8] QuickWave-3D, QWED Sp. z o.o., 02-010 Warsaw, Poland. http://www.qwed.com.pl/qw_3d.html

[9] Performance Micro Tool, Inc., Janesville, WI 53547. http://www.pmtnow.com/end_mills/tools/TR-2.asp

[10] Harvey Tool Co., LLC., Rowley, MA 01969. http://www.harveytool.com/products/

Six-Port Reflectometers for Waveguide Bands WR-15 and WR-2.8

Guoguang Wu, *Student Member, IEEE*, Zhiyang Liu, *Member, IEEE,* Lei Liu, *Member, IEEE,* Jeffrey L. Hesler, *Member, IEEE*, Arthur W. Lichtenberger, and Robert M. Weikle, II, *Senior Member, IEEE*

***Abstract*—Millimeter-wave six-port reflectometers for scattering parameter measurements in the WR-15 and WR-2.8 frequency bands have been designed and implemented. These reflectometers represent an effort to (1) develop a cost-effective measurement infrastructure that is scalable to terahertz frequencies and (2) to realize *in-situ* measurement instruments for monitoring the performance of millimeter-wave components. Performance of the six-ports has been assessed by applying them to measure the return loss for various components, including calibration standards and other common waveguide components. Measurement results have been found to be in close agreement with those obtained with a commercial HP8510C vector network analyzer. In addition, a WR-15 six-port reflectometer has been demonstrated as an *in-situ* sensor to monitor the mismatch between adjacent stages of a frequency multiplier chain.**

***Index Terms*—Six-port reflectometer, scattering parameters waveguide, return loss, frequency multiplier**

I. INTRODUCTION

SINCE it was demonstrated in 1977 by Engen [1]-[4], the six-port technique has been recognized as an attractive alternative to conventional four-port network analyzers due to its simple structure and requirement for fewer components. Because it is based only on power measurements, no phase-locked sources or wave splitters are necessary. Moreover, the size of the six-port can be compact compared to commercial network analyzers. For this reason, the six-port technique is promising as a technique for embedded sensing to measure mismatch between components internal to an instrument or system.

In this paper, we describe two six-port reflectometer architectures that (1) can be implemented to measure waveguide components at millimeter-wave frequencies and (2) can be applied as an embedded sensor for monitoring of the performance and operation of adjacent stages in a millimeter-wave circuit, such as a frequency multiplier chain.. By directly monitoring the impedance mismatch between adjacent stages using a six-port reflectometer, circuit designers are provided with a diagnostic tool that can be used for studying the behavior of multipliers as well as a guide for adjusting external operating parameters (such as bias conditions and drive power levels) that impact performance of the entire chain. To accomplish this a six-port reflectometer module designed to be inserted directly between adjacent multiplier stages, thus allowing continuous monitoring of the multiplier chain's operation by measurement of the input impedance presented to a source multiplier stage, is described. In the sections below, the design of the six-port modules are detailed as well as measurements used to characterize their performance.

Manuscript received 19 April 2009. This work was supported in part by the U.S. Army National Ground Intelligence Center (NGIC) under Grant 126900-GG10879-31875.

G. Wu is with the Department of Physics, University of Virginia, Charlottesville, VA 22904 USA (corresponding author to provide phone: 434-924-6575; fax: 434-924-4576; e-mail: gw9d@virginia.edu).

Z. Liu was with the University of Virginia, Charlottesville, VA22904 USA. He is now with Autoliv Electronics, 1011B Pawtucket Blvd, PO Box 1858, Lowell, MA 01853 USA.

L. Liu, A.W. Lichtenberger, and R.M. Weikle II are with the Department of Electrical and Computer Engineering, University of Virginia, Charlottesville, VA 22904 USA.

J.L. Hesler is with Virginia Diodes, Inc., 979 Second Street, S.E. Suite 309, Charlottesville, VA 22902 USA

II. REFLECTOMETER DESIGN

A. WR-15 Reflectometer Design

As a proof-of-concept demonstration, a prototype six-port reflectometer was designed for V-band (50–75 GHz) operation. The six-port module, shown in Fig. 1, consists of a section of WR-15 waveguide and three probe channels that accommodate microstrip waveguide probes with integrated zero-bias Schottky diode detectors. Note that because only three detectors are utilized, the reflectometer is actually a five-port (which can be considered a simplified version of the six-port). Provided the device to be measured is known apriori to be passive, only three detectors are required to uniquely determine its reflection coefficient [5]. The fourth detector may be used to enhance measurement accuracy, but strictly is not required. Bias protection circuits are included in the detector outputs to reduce the likelihood of damage to the zero-bias Schottky diodes through electrostatic discharge. Because the output power for the first multiplier stage (and drive power for the second multiplier stage) is typically large (on the order of several hundred milliwatts), coupling from the waveguide channel to the probes is designed to be small, less than −30 dB. In addition, two additional ports are included in the design to permit the reflectometer to be calibrated through null double injection technique [6]. Coupling between the two calibration injection ports and the waveguide channel is also designed to be small (less than −20 dB). As a consequence, the probe and calibration injection channels have a small loading effect on the reflectometer waveguide, a desirable feature that

reduces loading of these channels on the reflectometer as well the performance of the frequency multipliers connected to its input and output ports.

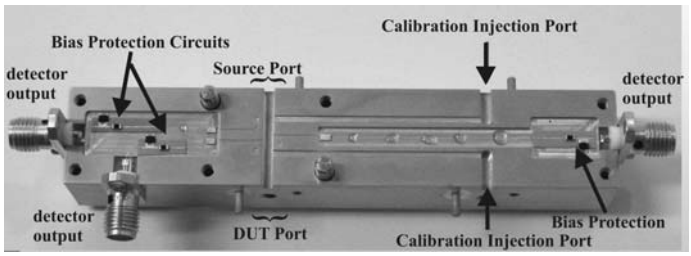

Fig.1. Photograph of the WR-15 six-port module.

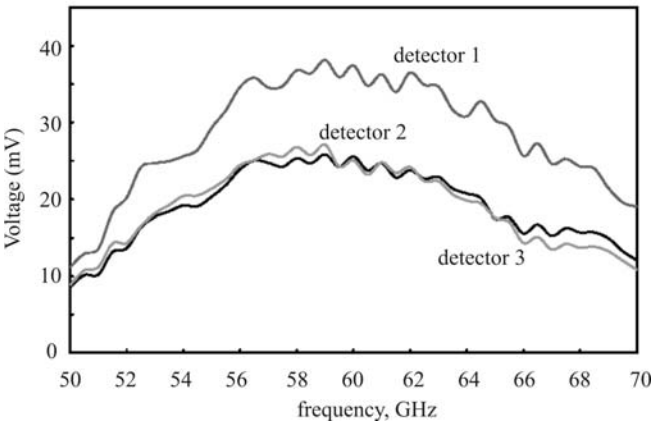

Fig.2. Detected voltages from the reflectometer. The input power is 7 dBm.

Fig. 2 shows the measured voltage response of the various detector diodes in the reflectometer. For this measurement, a source (7 dBm available power) is placed at one waveguide port and a HP W8486A power meter at the other. Detector voltages are monitored with a Keithley digital multimeter controlled by LabView. Initially, a resonance in the response of all the detectors was observed at 56 GHz. This resonance, which was associated with mismatch between the detector and the microstrip probe circuit, was eliminated by integrating a shunt titanium resistor (nominally 130 Ω) in parallel with the detector. This reduces the overall responsivity of the detectors, but also eliminates large variations in detected voltages as well as non-square-law operation of the diodes over the measurement bandwidth. From the measured detector voltages, available power to the waveguide, and waveguide-to-microstrip coupling values (modeled), the responsivity of the detectors is estimated to be 3000 V/W.

Fig. 3 shows the measured detector voltages (at 60 GHz) in response to a waveguide sliding short placed at the DUT measurement port of the reflectometer. Varying the short position allows the standing waves in the waveguide channel to be observed and allows proper operation of the reflectometer to be verified.

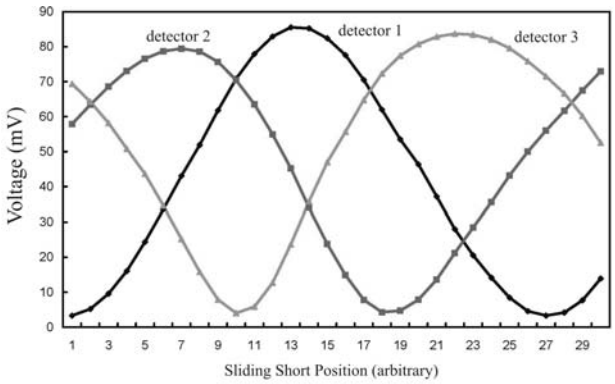

Fig.3. Voltage response of the diode detectors at 60 GHz in response to a waveguide sliding short.

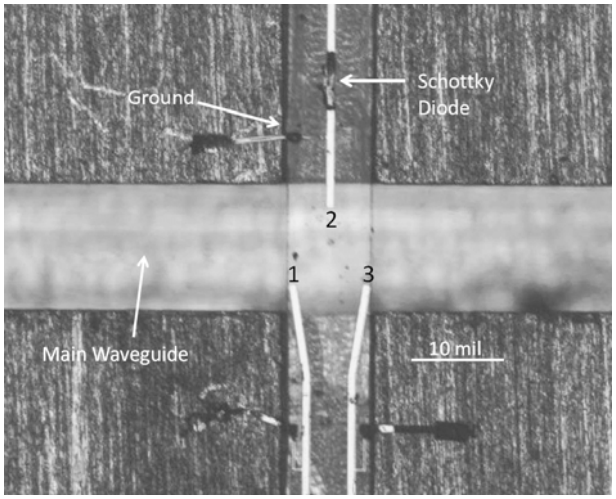

Fig.4. Microscope photo of WR2.8 six-port reflectometer probe structure.

B. WR2.8 Reflectometer Design

The basic design of WR-2.8 (270 GHz – 390 GHz) six-port is similar that of the WR-15 version, except that three probes were fabricated on a single substrate and placed into one common channel that crosses the primary waveguide. The rationale for using a single chip instead of three separate chips was ease of fabrication, simpler alignment and greater control over the passive circuitry performance. A photograph of the WR-2.8 reflectometer block and probe circuit is shown in Fig. 4. The primary waveguide channel is 28 mils × 14 mils and the widths of the probe circuit channel, quartz substrate, and microstrip lines are 10 mils, 9 mils, and 0.8 mils respectively. The quartz substrate is 1.5 mils thick and the distance between adjacent probes is 4.5 mils, or ~35° at the center frequency of 330 GHz.

The available power for measurements at WR-2.8 is slightly higher than 0.5 mW over the 275~335 GHz range, a frequency band that overlaps with the V03VNA-T/R Oleson Extension Module. This makes it possible to compare results obtained from the reflectometer with those of the commercial network analyzer.

III. Calibration Procedure

Fig. 5 illustrates the general architecture of the six-port reflectometer, where port 1 is the excitation port, the device under test (DUT) is placed at port 2, and ports 3—6 represent the power detection ports. To obtain the reflection coefficient for various DUT's from the power detection readings, calibration is necessary. A common and straightforward calibration method is Engen's sliding termination method [4]. With this method, the calibration consists of two steps. The first step effectively converts the six-port reflectometer to an equivalent four-port reflectometer and is used to determine the complex ratio b_3/b_4 from the set of power measurements. Once this is accomplished, the reflectometer is effectively a four-port that can be calibrated with one of several standard and familiar techniques.

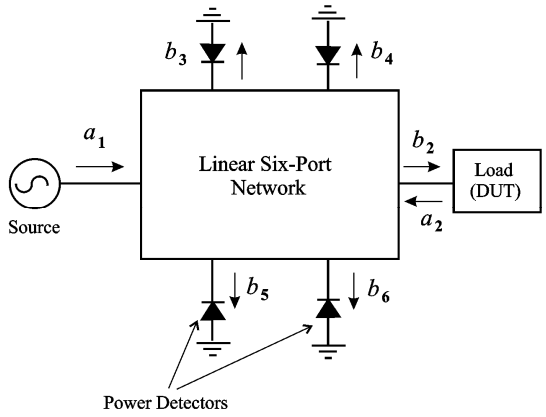

Fig.5. Diagram of a general six-port reflectometer.

For the first calibration step, a sliding termination is utilized so that the reflection magnitude remains unchanged as the position of the load is varied. The complex ratio, b_3/b_4, is obtained from a least-square fitting of data, which ideally forms an ellipse when the power ratios are plotted against one-another.

For the WR-15 six-port reflectometer, a sliding short is used for the first step of calibration. An example of data obtained from this measurement (at 61 GHz) is shown on the P_5/P_4 versus P_3/P_4 plot of Fig. 6. Data from twenty different positions with roughly equal intervals of 220 μm were chosen for this measurement.

For the WR2.8 six-port reflectometer, a different calibration termination is chosen because commercial sliding shorts are not readily available in this frequency band. Instead, seven fixed offset shorts with different delays were used for the first-step calibration. These seven offset shorts were designed to provide delays up to one wavelength over the entire waveguide band. The performance of the offset shorts has the same effect as a sliding short, except that only seven data points are available for fitting the ellipse. Fig. 7 shows the calibration ellipse plot for the WR-2.8 six-port reflectometer

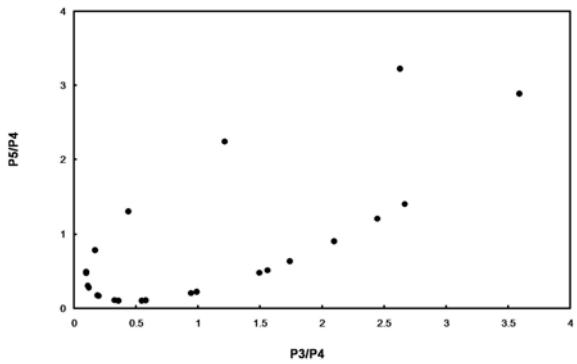

Fig.6. Ellipse curve from the first step calibration for WR15 six-port reflectometer at 61 GHz as an example.

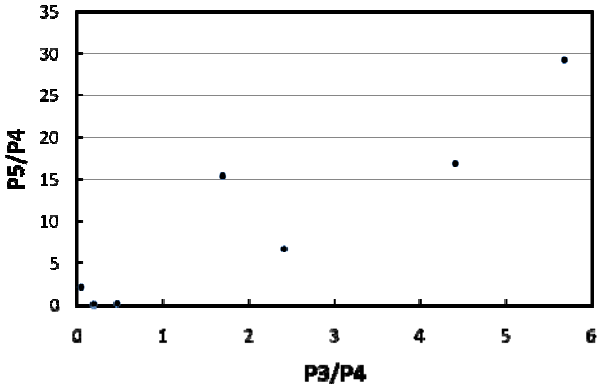

Fig.7. Ellipse curve from the first step calibration for WR2.8 six-port reflectometer at 290 GHz as an example.

from the seven offset shorts.

For the second-step of the calibration, the WR-15 and the WR-2.8 six-port reflectometers also employ different calibration standards. For the WR-15 reflectometer, a flush short, two sliding short positions (treated as delay shorts), and a matched load are used. For the WR-2.8 reflectometer, a flush short, two fixed offset shorts, and an open-ended waveguide are used. The open-ended waveguide was chosen for WR-2.8 six-port because its return loss is relatively well-understood and this standard is not subject to misalignment of the waveguide flange connection [7], which is a significant issue at frequencies higher than 100 GHz.

IV. Measurements

To assess the six-port reflectometer performance, the WR-15 reflectometer was used to measure a variety of WR-15 waveguide components and its performance was compared to scattering parameters obtained from the same components using an HP8510C vector network analyzer. Fig. 8 shows the results of these measurements which are in good agreement. Fig. 8(a) shows the return loss data for a waveguide directional coupler, Fig. 8(b) shows the return loss of a waveguide iris, and Fig. 8(c) the return loss of a horn antenna.

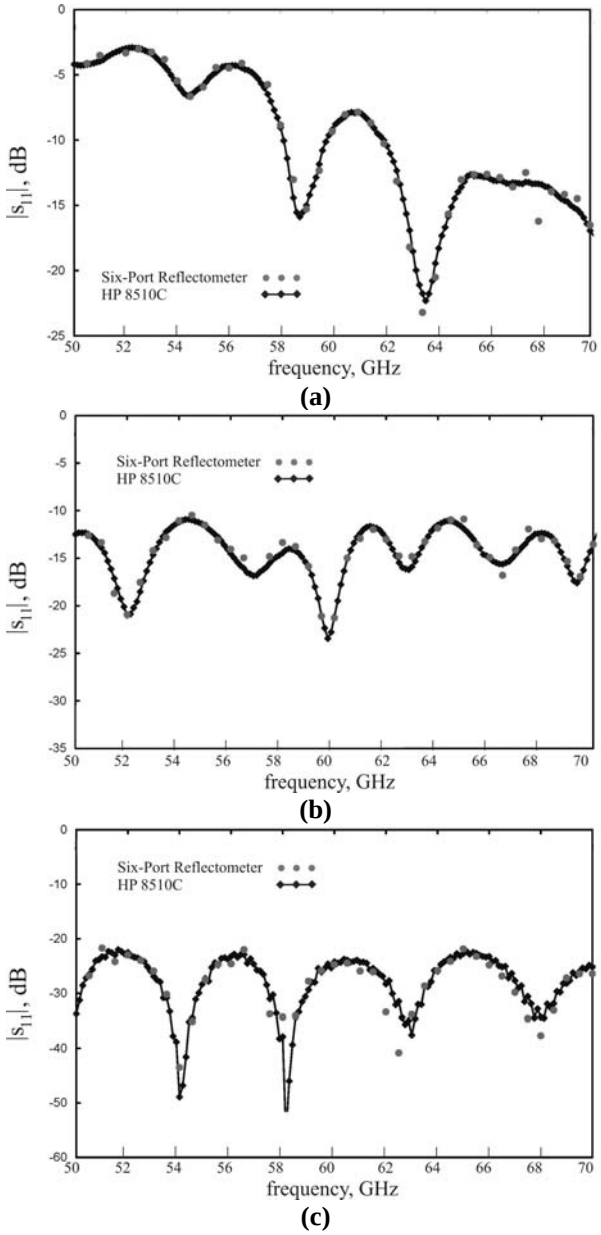

Fig.8. Measurement of return loss performed with the six-port reflectometer compared to data obtained with a HP8510C network analyzer. The devices measured are (a) a WR-15 waveguide coupler, (b) a waveguide iris, and (c) a horn antenna.

The WR15 six-port reflectometer was also implemented as an embedded sensor to monitor the mismatch between two adjacent stages in a frequency multiplier chain. The basic test setup is simple and consists of placing the six-port reflectometer between two adjacent doublers, both of which require a bias voltage. Prior to measuring the multiplier mismatch, a test was done was to examine changes in the multiplier chain performance resulting from introduction of the six-port. Fig. 9 shows the output power of the multiplier chain as a function of frequency for two different bias conditions. This measurement was repeated with WR-15 six-port reflectometer present. As seen from the data, the output power changes slightly, but the reflectometer does not have a drastic effect on the operation of the doubler chain.

Application of a WR-2.8 six-port reflectometer for mismatch measurement of two adjacent stages in corresponding frequency multiplier chains is a subject of ongoing work.

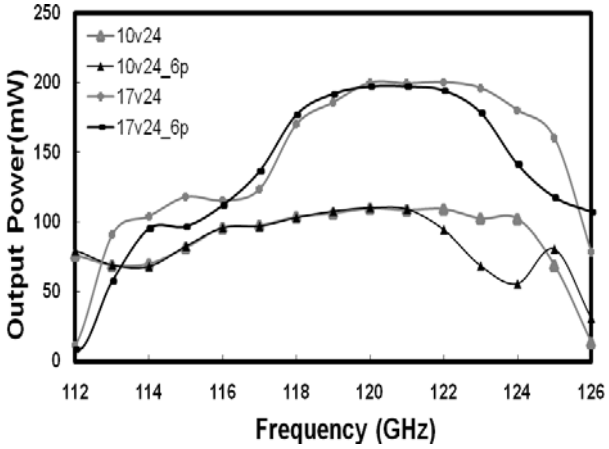

Fig.9. Output frequency dependence of output power at two different voltage bias conditions with and without six-port reflector. The input bias voltage for both bias conditions is 24 Volts, while there are two values for the output bias voltage, 10 Volts and 17 Volts.

V. SUMMARY

Six-port reflectometers at WR-15 and WR-2.8 have been designed and fabricated with initial tests completed. Results show a good agreement between measurements done with the WR-15 six-port and a commercial HP8510C vector network analyzer. As an initial test, the WR-15 six-port reflectometer has been also implemented as an embedded sensor placed between two adjacent stages in a frequency multiplier chain and it was found that the output power did not change dramatically by introduction of the six-port reflectometer. The next stages of this work will include full implementation of WR-2.8 six-port reflectometers studying the mismatch between frequency multipliers as well as full characterization of the performance of these prototype instruments (including dynamic range and measurement uncertainty).

REFERENCES

[1] G.F. Engen, and R.W. Beatty, "Microwave reflectometer techniques," in *IRE Trans. Microwave Theory Tech.*, pp. 351-355, July 1959.

[2] G.F. Engen, "The six-port reflectomter: an alternative network analyzer," *IEEE Trans. Microwave Theory Tech.*, vol. 25, no. 12, pp. 1075-1080, Dec. 1977.

[3] G.F. Engen and C.A. Hoer, "Application of an arbitrary 6-port junction to power measurement problems," *IEEE Trans. Instrum. And Meas.*, vol. 21, no. 6, pp. 470-474, Nov. 1972.

[4] G.F. Engen, "Calibrating the six-port reflectometer by means of sliding terminations," *IEEE Trans. Microwave Theory Tech.*, vol. 26, no. 12, pp. 951-957, Dec. 1978.

[5] C.A. Hoer, "Using six-port and eight-port junctions to measure active and passive circuit parameters," *National Bureau Stand. Tech.*, note 673, Sep. 1975.

[6] D. Hui and R.M. Weikle, II, "Calibration of six-port reflectometers using null double injection," in *67th ARFTG Microwave Measurement Conference Digest*, San Francisco, CA, pp. 164-179, June 2006.

[7] Z. Liu and R.M. Weikle, II, "A reflectometer calibration method resistant to waveguide flange misalignment," *IEEE Trans. Microwave Theory Tech.*, vol. 54, no. 6, June 2006.

Fast Fourier Transform Spectrometer

B. Klein, I. Krämer, S. Hochgürtel, R. Güsten, A. Bell, K. Meyer, and V. Chetik

***Abstract*—We review the development of our digital broad-band Fast Fourier Transform Spectrometers (FFTS). In just a few years, FFTS back-ends - optimized for a wide range of radio astronomical applications - have become a new standard for heterodyne receivers, particularly in the mm and sub-mm wavelength range. They offer high instantaneous bandwidths with many thousands spectral channels on a small electronic board (100 x 160 mm). Our FFT spectrometer make use of the latest versions of GHz analog-to-digital converters (ADC) and the most complex field programmable gate array (FPGA) chips commercially available today. These state-of-the-art chips have made possible to build digital spectrometers with instantaneous bandwidths up to 1.8 GHz and 8192 spectral channels.**

Our latest development step is a prototype compact FFTS board with a new 5 GHz 8/10-bit ADC and an outstanding instantaneous bandwidth of 2.5 GHz. An early version of the board has been successfully field-tested at the APEX telescope and we present a first spectrum observed in November 2008.

***Index Terms*—Fast Fourier Transform Spectrometer, FFTS, instrumentation, spectrographs**

I. INTRODUCTION

At the Max-Planck-Institute für Radioastronomie (MPIfR) we develop digital Fast Fourier Transform Spectrometer since ~6 years: Beginning with a bandwidth of just 2 × 50 MHz and 1024 (1k) channels in 2003 [1], 1.5 GHz with 8k channels in 2007 [2], [3], we are currently developing a wideband FFTS with an instantaneous bandwidth of 2.5 GHz and likely 32k spectral channels. This corresponds to an improvement in bandwidth by a factor of 50 over 6 years or ~400 MHz per year. Today, FFT spectrometers cover all the requirements of line observations in radio astronomy. They provide wide bandwidths for mm and submm-observations and very high spectral resolution (kHz range) for radio sky frequencies of a few GHz. The high dynamic range of today's ADCs (8/10-bit) allows using FFTS for planet observations with high background and strong maser lines. FFTS are very stable as measured by long Allan variance times; they are calibration- and aging free and can be easy manufactured. Our FFT signal processing is based on a generic approach, which makes it possible to generate FPGA cores with different bandwidths and spectral resolution on a short time scale. Unlike the usual window-FFT processing, we use a more efficient 4-tap polyphase filter-bank algorithm, with significant less frequency scallop loss, less noise bandwidth expansion, and faster sidelobe fall-off.

Manuscript received 20 April 2009.

B. Klein, I. Krämer, S. Hochgürtel, R. Güsten, A. Bell, K. Meyer and V. Chetik are with the Max-Planck-Institut für Radioastronomie (MPIfR), Bonn, Germany.

Send correspondence to Bernd Klein, e-mail: bklein@mpifr-bonn.mpg.de

II. AFFTS: THE 32 × 1.5 GHZ BANDWIDTH ARRAY-FFTS

To serve the requirements of today's and future receiver arrays (e.g., CHAMP$^+$, LAsMA [4]), we have developed a compact (100 × 160 mm) FFTS-board [5] with an on-board standard 100 MBits/s Ethernet interface, which simplifies the combination of many boards into an Array-FFTS, just by integrating of a common Ethernet switch. For use at the APEX telescope [6], we have combined 32 FFTS-boards in four 19 inch crates (Fig. 1). The APEX AFFTS has been successfully commissioned one year ago. In the current configuration, it provides a total bandwidth of 32 × 1.5 GHz = 48 GHz and 256k (32 × 8k) spectral channels. If requested the AFFTS bandwidth can be extended to 58 GHz (32 × 1.8 GHz) by uploading a new FPGA processing core and new ADC synthesizer parameters.

III. XFFTS: THE NEW 2.5 GHZ BANDWIDTH FFTS

With the availability of first samples of E2V's 5 GS/s 8-bit ADC in mid 2008, we have started the development of a new eXtended bandwidth FFTS (XFFTS) board [5]. The goal of this project has been to realize a digitizer board, which is able to analyze 2.5 GHz of instantaneous bandwidth. Already in Nov. 2008 we performed observations with this new XFFTS at the APEX telescope: the first light spectrum towards the extragalactic nucleus NGC253 is displayed in Fig. 2.

Still during this development a 10-bit 5 GS/s ADC became available by E2V with an even wider analogue input bandwidth: This new device allows capturing frequencies up to 3.85 GHz. To allow higher spectral resolution (the first test board was limited to just 256 spectral channels due to FPGA resources) we designed a new XFFTS board around E2V's novel 5 GS/s 10-bit ADC and replaced the Virtex-4 FPGA by a Xilinx Virtex-5 SX240T – one of the highest performance FPGA devices available today. In Fig. 3 we show a photo of our new XFFTS board that is currently undergoing first lab tests. It very likely, that FPGA resources will allow to implement a full polyphase filter-bank FFT signal processing pipeline with 32768 spectral channels for the 2.5 GHz wide band mode. By using our optimized filter coefficients, this FFTS will have a spectral resolution (equivalent noise bandwidth) of 88.5 kHz. This wideband high-resolution FFT spectrometer development aims at operational readiness for SOFIA's early science flights with GREAT in 2010 [7].

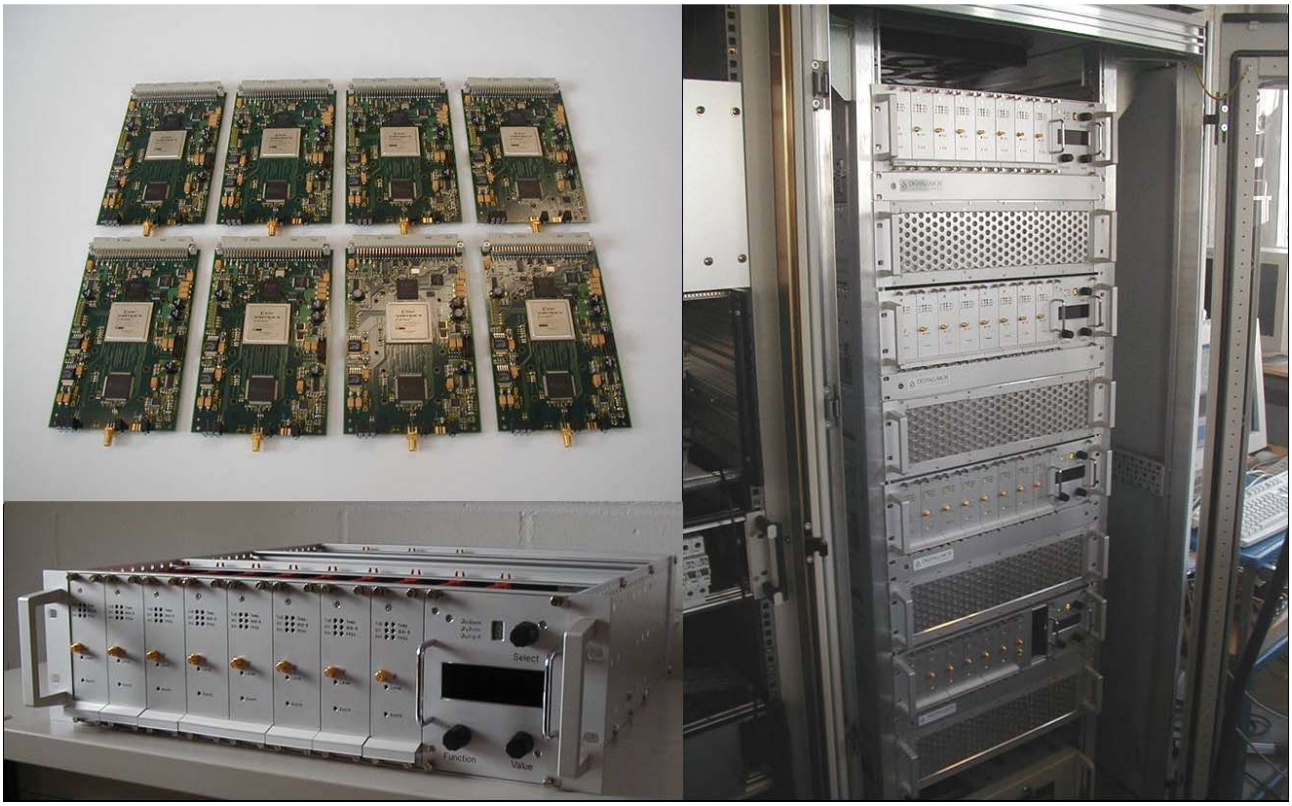

Fig. 1. The APEX wideband AFFTS consists of four FFTS-crates, each equipped with 8 FFTS boards and one FFTS-controller with LCD unit. The frequency resolution (equivalent noise bandwidth) for the standard board configuration with 1.5 GHz bandwidth and 8192 spectral channels per board is 212 kHz.

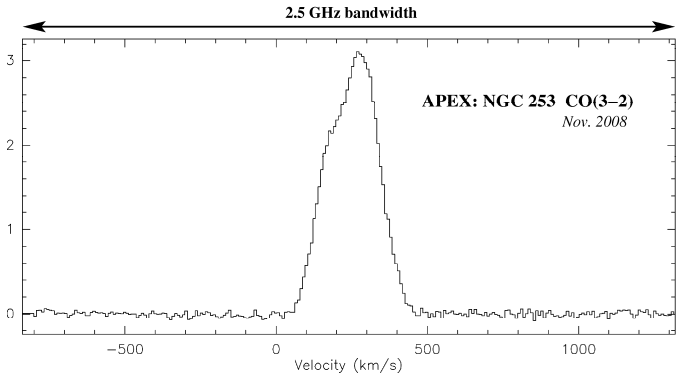

Fig. 2. First light spectrum of the new MPIfR 2.5 GHz XFFTS board towards NGC 253. The CO(3-2) transition at 345 GHz was observed with the APEX-2 facility receiver in November 2008.

Fig. 3. Currently in lab tests: The new 2.5 GHz bandwidth XFFTS, making use of a first sample of E2V's 5 GS/s 10-bit ADC and the high performance Xilinx Virtex-5 SX240T FPGA.

IV. Summary & Outlook

The potential advantages of our digital broadband Fast Fourier Transform Spectrometer are summarized:

- They offer high instantaneous bandwidth up to 2.5 GHz with many thousands frequency channels, thus offering wide-band observations with high spectral resolution. This simplifies the IF processing enormously, in terms of stability, aging, power dissipation, size and costs.
- FFTS provide very high stability by exclusive digital signal processing. Spectroscopic Allan variance times of several thousands seconds have been demonstrated routinely.
- Our optimized polyphase FFT signal processing pipeline provides a nearly loss-free time to frequency transformation with significantly reduced frequency scallop, less noise bandwidth expansion, and faster side lobe fall-off.
- Low space and power requirements allow to operate FFTS at high altitude (e.g., APEX at 5100-m) as well as on airborne observatories (SOFIA) and future satellites.
- FFTS production costs are low compared to traditional spectrometers through the use of exclusively commercial components and industrial manufacturing.
- The superior performance, high sensitivity and reliability of our FFTS have been demonstrated at many observatories world-wide, e.g., APEX (Chile), CSO (Hawaii), the IRAM 30-m (Spain) and the MPIfR 100-m Effelsberg telescopes. In addition, FFTS are used in atmospheric research and in radiometer laboratories.

Based on our reconfigurable FFTS technology, we have recently developed a read-out system, operating in frequency domain, for arrays of Microwave Kinetic Inductance Detectors (MKIDs). First measurements show no deterioration of the noise performance compared to low noise analog mixing. Thus, this technique allows capturing several hundreds of detector signals with just one pair of coaxial cables [8].

The announcements of new ADCs with even higher sample rates ($f_s \geq 10$ GS/s) and wider analogue input bandwidth, together with the still increasing processing power of future FPGA chips (e.g., XILINX Virtex-6 family), make it very likely that FFTS can be further pushed to broader bandwidth in the next years.

REFERENCES

[1] S. Stanko, B. Klein, J. Kerp, "A Field Programmable Gate Array Spectrometer for Radio Astronomy", A&A, Vol. 436, pp.391-395, 2005.

[2] B. Klein, S.D. Philipp, I. Krämer, C. Kasemann, R. Güsten, K.M. Menten, "The APEX Digital Fast Fourier Transform Spectrometer", A&A, Vol. 454, pp. L29-L32, 2006.

[3] B. Klein, S.D. Philipp, R. Güsten, I. Krämer, D. Samtleben, "A new generation of spectrometer for radio astronomy: Fast Fourier Transform Spectrometer", Proc. of the SPIE, Vol. 6275, pp. 627511, 2006.

[4] R. Güsten, et al., "Submillimeter Heterodyne Arrays for APEX", Proc. of the SPIE, Vol. 7020, pp. 702010-702010-12, 2008.

[5] B. Klein, I. Krämer, S. Hochgürtel, R. Güsten, A. Bell, K. Meyer, V. Chetik, "The Next Generation of Fast Fourier Transform Spectrometer", Proc. of the 19. ISSTT, 2008.

[6] R. Güsten, et al., "APEX: the Atacama Pathfinder Experiment", Proc. of the SPIE, Vol. 6267, pp. 626714

[7] S. Heyminck, R. Güsten, P. Hartogh, H.-W. Hübers, J. Stutzki, U.U. Graf, „GREAT: a first light instrument for SOFIA", Proc. of the SPIE, Vol. 7014, pp. 701410-701410-7, 2008

[8] S.J.C. Yates, A.M. Baryshev, J.J.A. Baselmans, B. Klein, R. Güsten, "Fast Fourier Transform Spectrometer readout for large arrays of Microwave Kinetic Inductance Detectors"

W4E

High Resolution Digital Spectrometer with Correlation and Image Rejection Capabilities

A. Murk[1*], C. Straub[2], D. Zardet[2] and B. Stuber[3]
1 University of Bern, 3012 Bern, Switzerland
2 University of Applied Sciences Northwestern Switzerland, 5210 Windisch, Switzerland
* Contact: axel.murk@iap.unibe.ch, phone +31-50-363 4074

We present a new digital back-end for Correlation and Spectrum Analysis (COSPAN), which will be used for remote sensing of the atmosphere and radio astronomy. Its hardware is based on a commercially available signal analyzer Acqiris AC240 from Agilent, which provides two input channels with 1GS/s sampling rate and an on-board FPGA signal processor. The original FFT firmware of this instrument allows to accumulate a total power spectrum with 1GHz bandwidth and 16384 channels (61kHz resolution) in real-time for a single input channel. Our new COSPAN firmware processes the data from both input channels in two separate FFT pipelines, which results in two 500MHz wide complex spectra with 30.5kHz resolution. These spectra can be then combined or analyzed by different user modes. The most straight forward one is the total power mode where the real and imaginary part is squared and added for each spectrum separately. This mode could be used, for example, to process two pixels of an array receiver. In the correlation mode the real and imaginary part of the product of the two spectra is accumulated, which corresponds to the complex cross-correlation spectrum of the two inputs. This mode has been implemented for our new 22GHz correlation receiver MIAWARA-C, in which the atmospheric signal and a reference signal from an active cold load are combined with an 3dB hybrid coupler and processed in two identical receiver chains. With the correlation mode the two input signals are continuously compared with each other, whereas the uncorrelated noise of the two receivers does not contribute to the accumulated spectra. As a result gain fluctuations are less critical and the stability of the instrument is highly improved. Another application area for the correlation mode are polarimetric observations. The third image rejection mode calculates the total powers of the sum and the difference of the two complex FFT spectra after applying an appropriate phase shift. When the two input channels are fed by an IQ Mixer the two resulting spectra represent the lower and the upper sideband. This mode is the equivalent to a conventional sideband separating mixer in which which the two IFs are combined by an analog hybrid coupler, but it provides a higher image rejection because the digital 90 degree phase shift is more accurate. To further improve the image rejection COSPAN allows to determine and correct the amplitude unbalance of the IQ mixer.

Poster Session

P1 Sources
P2 Waveguides, Antennas & Quasi-Optics
P3 Novel Devices & Measurements
P4 Schottky Diodes
P5 SIS Mixers
P6 Physics & Measurements of SIS Devices
P7 HEBs & Direct Detectors
P8 Receivers and Backends

Chairs: Eric Bryerton, Arthur Lichtenberger & Robert Weikle

Monday, April 20
7:00 – 9:00

P1A

Design study for the local oscillator injection scheme for the ALMA band 10 receiver

M. Candotti[1*], Y. Uzawa[1], Y. Fujii[1], T. Kojima[1]
*1 National Astronomical Observatory of Japan *, Osawa, Mitaka, Tokyo, 2-21-1, Japan*
* Contact: m.candotti@nao.ac.jp, phone +81-422-34-3909

***Abstract*— The ALMA band 10 receiver will cover the highest frequency range observable with ALMA covering the spectrum from 787 GHz to 950 GHz. The ALMA band 10 receiver front-end is currently under development. In this paper we introduce a novel concept of Local Oscillator (LO) injection scheme. Three solutions were studied for the band 10 receiver LO injection system. The first solution being investigated was a full waveguide scheme which main characteristic was to have the LO source (pair of triplers devices) connected to each other by an oversized waveguide. The first multiplier was located in the 110K thermal stage and the second tripler into the 4K thermal stage. The mixer then received the LO power from a waveguide 10 dB coupler connected to the 792-955GHz signal output. This scheme was tested and demonstrated to suffer of large standing waves, which eventually made the mixing process impossible due to lack of LO pumping power at some frequencies of band 10. The use of a double mirror coupling system together with a beam splitter for quasi-optical LO power injection was also investigated. However mechanical constrains made this design not practicable.**

The current design implies the use of a double mirror coupling system which purpose is to couple two identical horns in a so called horn-to-horn scheme. The 10 dB power coupler is then used for power injection to the mixer chip. The design and software analysis of the total power coupling between the two horns will be presented in this paper. Some initial measurements of beam pattern and total power being transmitted from horn to horn will be shown aiming at the concept validation for the nominal design room temperature.

A Novel Dual-Chip Single-Waveguide Power Combining Scheme for Millimeter-Wave Frequency Multipliers

José V. Siles, *Member IEEE*, Alain Maestrini, *Member IEEE*, Byron Alderman, Steven Davies, and Hui Wang

***Abstract*—In this work, we propose a novel dual-chip power combining scheme where two symmetrical MMIC chips are mounted on a single transmission waveguide. This configuration adds an extra degree of freedom in power combining as it allows to double the number of diodes in split-block waveguide multipliers, and thereby, to increase the power handling capabilities of frequency multipliers by an additional factor of 2. The two chips are symmetrically placed along the E-plane within the transmission waveguide. This adds an additional symmetry plane that simplifies the computational cost of the circuit simulations since just half of the structure can be simulated by defining a perfect H-plane boundary condition at the symmetry plane. The proposed topology is demonstrated throughout the design of a dual-chip biasless 190 GHz broadband Schottky doubler based on United Monolithic Semiconductor's (UMS) technology.**

***Index Terms*—Circuit simulation, Millimeter-wave circuits, Power combiners, Schottky diodes, Schottky diodes frequency converters.**

I. INTRODUCTION

BIG efforts have been made in the recent years to develop solid-state sources providing high local oscillator (LO) power levels at millimeter-wave bands. State-of-the-art sources have already demonstrated LO power levels up to 800 mW at 90-100 GHz, and up to several watts are expected at 100 GHz with MMIC amplifiers based on GaN transistors [1]. This represents a good opportunity to continue improving the LO power generation at THz frequencies by means of Schottky multiplier chains.

Manuscript received 20 April 2009. This work was supported by the European Space Agency ESA/ESTEC under contract ITT AO/1-5084/06/NL/GL and by the CNES of France.

J. V. Siles, was with LERMA, Observatory of Paris, 75014 Paris, France. He is now with the Department of Signals, Systems and Radio-communications, Technical University of Madrid, 28040 Madrid, Spain (phone: +34 657231217, fax: +34 913367362; e-mail: jovi@gmr.ssr.upm.es).

A. Maestrini is with LERMA, Observatory of Paris, 75014 Paris, France (e-mail: alain.maestrini@obspm.fr).

B. Alderman is with the Rutherford Appleton Laboratory, Chilton, Oxfordshire, OX11 0QX, UK (e-mail:B.Alderman@rl.ac.uk).

S. Davies is with the Department of Physics, University of Bath, Bath BA2 7AY, UK (e-mail:s.r.davies@bath.ac.uk).

H. Wang was with LERMA, Observatory of Paris, 75014 Paris, France. She is now with the Rutherford Appleton Laboratory, Chilton, Oxfordshire, OX11 0QX, UK (e-mail:hui.wang@stfc.ac.uk).

However, traditional multiplier chains based on GaAs Schottky diodes cannot handle such amount of LO power since chips featuring either a large number of diodes or excessively large anode areas would be required. In split-waveguide designs, the size of the chip is limited by the dimensions of the transmission waveguide and other constraints [2].

Several alternatives may be considered to deal with this problem. On the one hand, Schottky diodes based on semiconductor composites with larger bandgap than GaAs might be employed for the first multiplication stages of THz LO chains. In this context, GaN Schottky multipliers featuring 2 or 4 diodes could easily handle a 1 W input power at 100 GHz although conversion efficiencies would be around a 25 % lower than those achieved with GaAs Schottky diodes due to the lower electron mobility of GaN [3]. Novel materials like carbon nano-tubes and graphene, featuring both large bandgap and high electron mobilities, could be also employed in the near future for Schottky multipliers [4, 5].

On the other hand, power-combining schemes also offer a very good alternative to increase the power handling-capabilities of GaAs Schottky multipliers [1]. One possible power-combining scheme has been recently demonstrated with excellent results for a 300 GHz tripler. It consists of two mirror-image tripler circuits that are power-combined in-phase in a single waveguide block using compact Y-junctions at the input and output waveguides [2].

This work proposes a novel dual-chip single-waveguide power combining-scheme that adds an additional symmetry to the multiplier circuit, increasing by an additional factor of two its power handling capabilities. This topology is demonstrated through the design of a 190 GHz doubler with UMS technology. The most important design and technical difficulties connected to this topology are also outlined herein. The design of the doubler has been carried out at LERMA, Observatory of Paris, and the post-processing at the University of Bath. Block fabrication and assembly will be performed at Rutherford Appleton Laboratory, Oxford (UK). Results from the 1st foundry run were not satisfactory mainly due to wafer imperfections and difficulties in the block assembly as a consequence of the complex topology, For the 2nd run, a ~10 % efficiency over a ~15 % 3-dB bandwidth is expected.

II. Dual-Chip Single-Waveguide Power Combining Scheme for Multipliers

The dual-chip single-waveguide power combining scheme proposed in this work consists of two chips symmetrically placed along the E-plane of the transmission wave-guide, as it is shown in Fig. 1. With this topology, the power handling capability of a frequency multiplier is increased by a factor of two since it features double number of anodes than a single-chip design. In order to maximize the input power coupled to the diodes, the distance between the chips must be as lowest as possible so they are located near the center of the waveguide where the maximum of the exciting TE_{10} mode is.

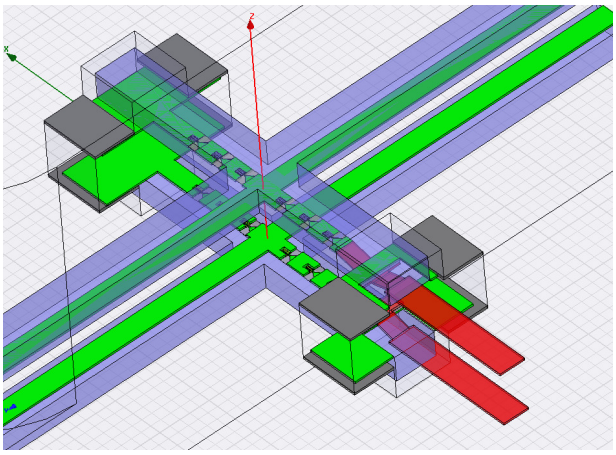

Fig. 1. Dual-chip single wave-guide scheme for frequency multipliers.

The two suspended microstrip lines can theoretically propagate two quasi-TEM modes (see Fig. 2). However, only one quasi-TEM mode (Fig. 2a) will be excited since the electric field lines of the second quasi-TEM mode (Fig. 3b) will be orthogonal to the input TE_{10} mode according to the geometry of the circuit. Note that the electric field corresponding to the 1st quasi-TEM mode (Fig. 2a) is tangential to the symmetry plane. Hence, if a perfectly symmetric circuit is assumed, only half the structure (with only one chip) can be simulated in HFSS by defining a perfect H-plane boundary condition at the symmetry plane. This reduces the computational cost of the design process.

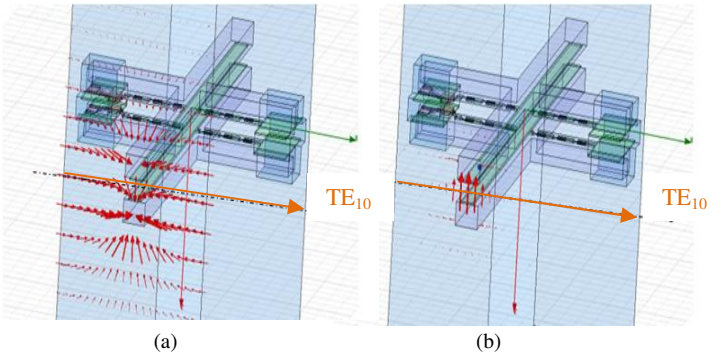

(a) (b)

Fig. 2. Theoretical quasi-TEM modes propagated by the two suspended striplines of the proposed dual-chip power combining scheme.

Contrarily to the in-phase power combining scheme shown in [2] (see Fig. 3), the topology proposed here does not use duplicated circuits combined by means of Y-junctions at the input and at the output because the two chips are embedded in a single waveguide. Hence, the complexity of the block is reduced. However, the assembly procedure in the dual-chip single-waveguide structure becomes much more complex because a very precise control in the positioning of the two chips is crucial in order to guarantee the symmetry of the circuit. This and other difficulties concerning the proposed scheme will be discussed in the following section.

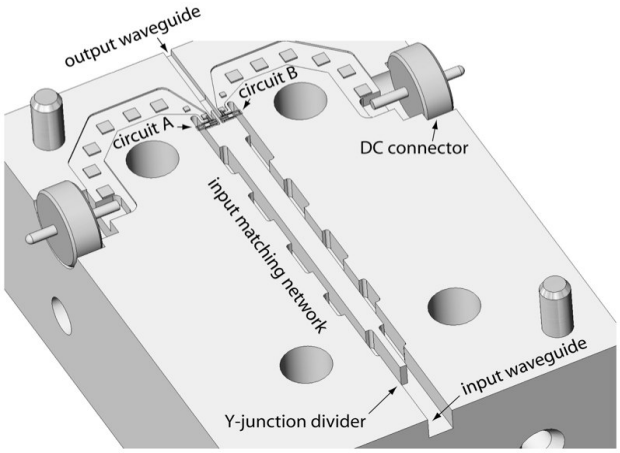

Fig. 3. In-phase power-combined dual-chip tripler at 300 GHz (proposed by A. Maestrini [2]). Each chip is assembled onto a different waveguide. Y-junctions are employed for power-combining.

It is important to remark that a combination of these two schemes might be employed in order to achieve a X4 increase in the power-handling capability of a traditional multiplier.

III. Fabrication Difficulties

The main difficulties concerning this novel dual-chip power-combining scheme are presented through the measurement results corresponding to the 1st foundry run of the design of a dual-chip 190 GHz Schottky doubler based on UMS technology (featuring 6 anodes per chip). This doubler was initially designed for a 100 mW input power and a -12 V reverse bias voltage per chip (-2 V per anode) since the nominal breakdown voltage provided by UMS was -6 V per anode. The expected efficiency was 25 % over a 6 % 3-dB bandwidth. However, the actual breakdown voltage of the chips was found to be -2 V per anode due to deficiencies in the wafer during the fabrication process, and thereby, a -12 V reverse bias voltage per chip could not be applied. Moreover, the actual GaAs-substrate thickness of the chips ranged between 32 µm and 36 µm, instead of the nominal value of 50 µm. The distance between the chips after the assembly was also measured and a non-uniform separation varying between 32 and 44 µm along the channel was found (nominal design distance between chips was 40 µm).

Under these circumstances, the measured performance of the doubler was extremely poor as it can be seen in Figs. 4 and 5. The bias voltage of each chip was optimized for each analyzed frequency in the tests in order to maximize the provided output power. The input power was fixed to 50 mW in order not to overpump the diodes. RF measurements showed an important asymmetry in the effective power coupled to each chip whereas the measured I-V curves at DC corresponding to each chip were found to be exactly

symmetrical. The measured maximum output power was 0.450 mW. It can be seen in Fig. 4 that only in the vicinity of the peak of efficiency both chips demand the same bias voltage for optimum performance of the doubler. Out of this zone, important discrepancies can be observed in the optimum bias voltage that was found for each chip. It was also noticed during the test that the doubler efficiency experiences a certain variation (from 0.7 % to 0.85 % in Fig. 4) when acting on the screws of the block. This could be due to the fact that this mechanical operation changes the distance between the chips compensating somewhat the asymmetries in this distance. The problem with the lack of symmetry becomes even more evident when measuring the DC current across each chip. Big discrepancies can be observed in Fig. 5 between the two chips even in the case when similar bias voltages are selected for each chip.

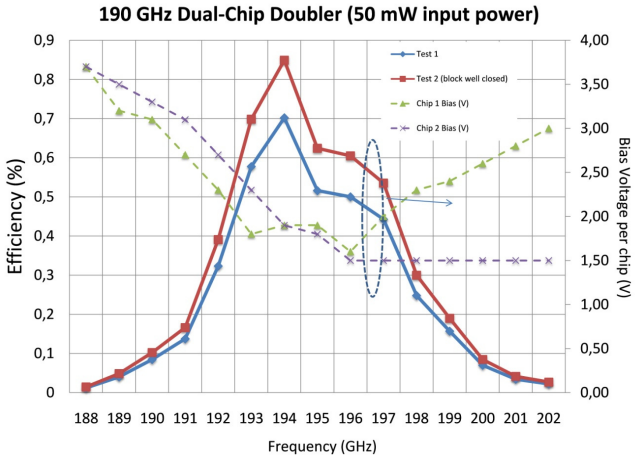

Fig. 4. Measured efficiency of the 190 GHz doubler (1st foundry run). Dashed lines indicate the optimum bias voltage for each chip to maximize measured efficiency.

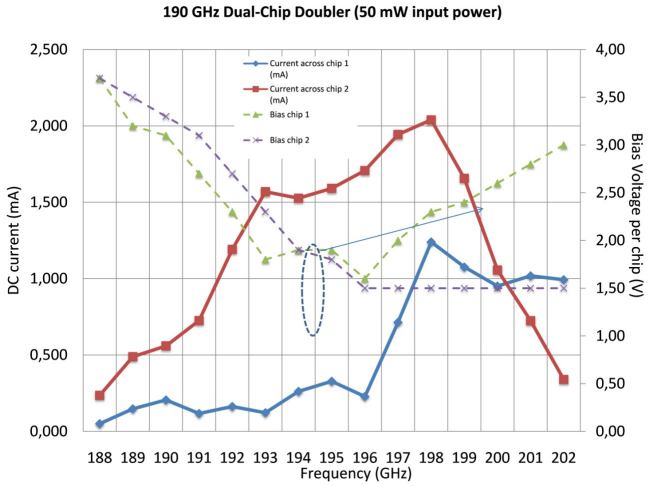

Fig. 5. Measured DC current across each chip of the 190 GHz doubler (1st foundry run). Dashed lines indicate the optimum bias voltage for each chip to maximize measured efficiency.

To summarize, it is evident that the sensitivity of the doubler to the distance between the chips is high so a larger separation between them is necessary due to the difficulty in precisely controlling this distance during the assembly if it is excessively small. Furthermore, a high accuracy is also necessary during the fabrication and post-processing of the chips in order to reduce as much as possible the asymmetries in the circuit.

IV. Design of a Dual-Chip Single-Waveguide 190 GHz Doubler (2nd Foundry Run)

The doubler is a split-block waveguide design that features twelve UMS Schottky planar diodes on two chips monolithically fabricated on a 50-µm GaAs-based substrate. Diodes on each chip are connected in series at DC and both chips are inserted within the output waveguide. Each of the two E-plane probes located in the input waveguide couple the signal at the fundamental frequency to each chip. The waveguide channel between the input and output waveguides prevents the second harmonic from leaking into the input waveguide. The distance between chips is 100 µm to favor the assembly and reduce the impact of misalignments. The general scheme of the 190 GHz doubler can be seen in Figs. 6 and 7.

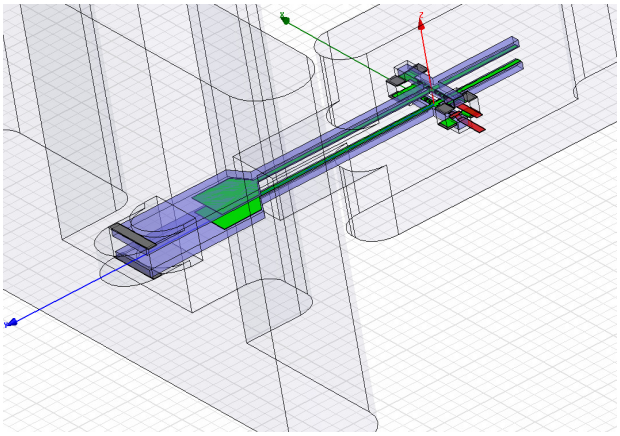

Fig. 6. General scheme of the dual-chip single-waveguide 190 GHz doubler.

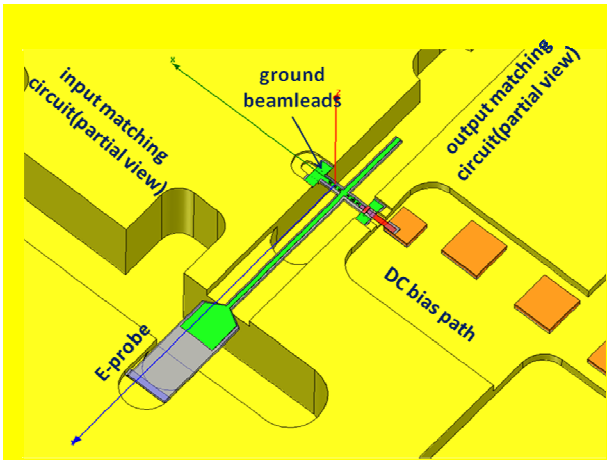

Fig. 7. 3D view of the bottom part of the waveguide block with the 190 GHz doubler bottom chip installed. It features 6 Schottky diodes in a balanced configuration. The upper part of the block contains the second chip, which is symmetrical to the bottom chip.

The circuit features additional matching elements in the input and output waveguides, made with a succession of waveguide sections of different heights and lengths (see Fig. 8).

The Schottky diodes provided by UMS for this work are adequate for mixers but not for multipliers. Both the epilayer

thickness and doping are not optimum for a state-of-the-art doubler design in terms of efficiency: diode epilayer is already fully depleted at ~ 0.1 V and the expected DC breakdown voltage for this wafer is ~ -5 V. Under these circumstances, the optimum bias voltage per anode should be around -3 V in order to maximize the power handling capabilities of each anode. However, a biasless design was finally considered in order to enlarge the frequency bandwidth and guarantee safe operation regime for the diodes. The use of a dual-chip topology for this design is necessary to increase the number of diodes, and thereby, the supported input power. Note that individual DC bias lines for each chip have been included in order to add a tuning parameter to deal with possible asymmetries between the two chips.

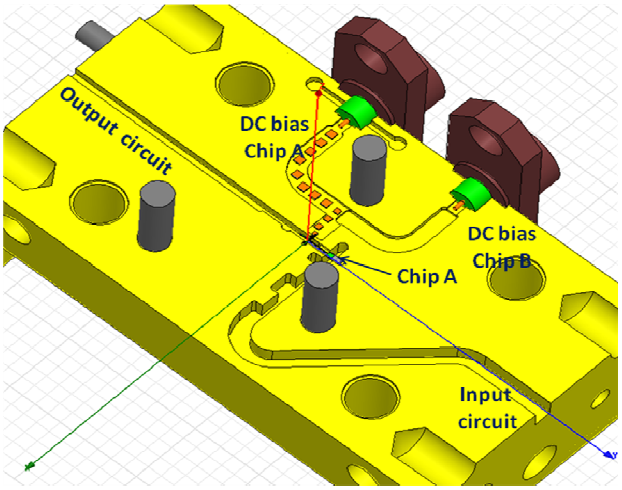

Fig 7: 3D view of the bottom part of the waveguide block, showing the two DC bias paths (one per chip).

The design methodology combines Agilent's ADS linear/nonlinear harmonic balance circuit simulation to optimize and compute the performance of the circuit, with Ansoft's HFSS 3D electromagnetic simulation to model accurately the diodes geometry and waveguide structures. Due to the special characteristics of the provided UMS diodes, simple analytical nonlinear Schottky diode models, like the standard Schottky diode model included in ADS, are not valid. The Schottky model employed for this design in ADS simulations has been specifically adjusted by means of empirical results and physics-based simulations.

A room-temperature conversion efficiency of a ~10% over a 15% 3dB-bandwidth is expected for the 2nd foundry run of the dual-chip single-waveguide 190 GHz doubler, as can be seen in Figs. 8 to 11. An available input power of 80 mW has been considered and the DC characteristics of the employed diodes are the following: a 18 fF zero junction capacitance (C_{j0}), a 4.4 Ω series resistance (R_s) and a ~$4 \cdot 10^{-14}$ A saturation current (I_s). The fabrication and post-processing have been improved with regards to the 1st foundry run in order to avoid some of the technical difficulties discussed in the previous section. Furthermore, the larger separation between the two chips makes it easier the assembly of the chips guarantying a more accurate control of the distance during the assembly.

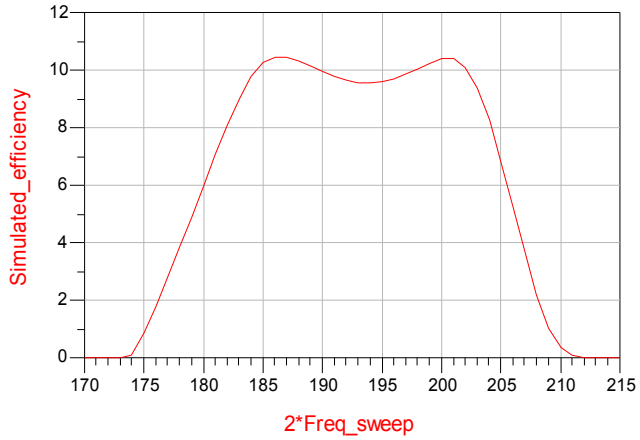

Fig 8: Predicted efficiency (%) of the 12-anode dual-chip 190 GHz balanced doubler at room temperature with 80 mW input power.

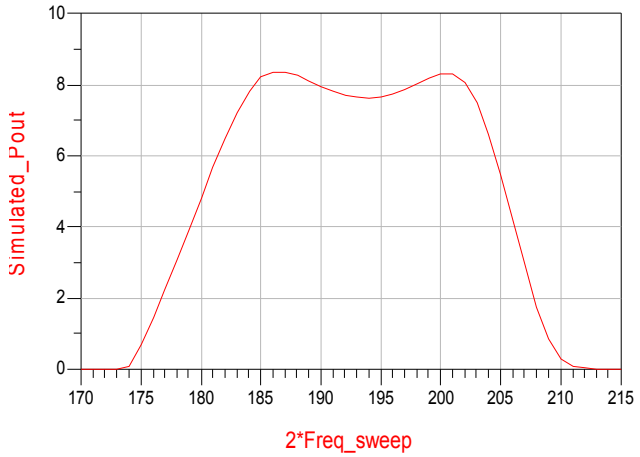

Fig 9: Predicted output power (mW) of the 12-anode dual-chip 190 GHz balanced doubler at room temperature with 80 mW input power.

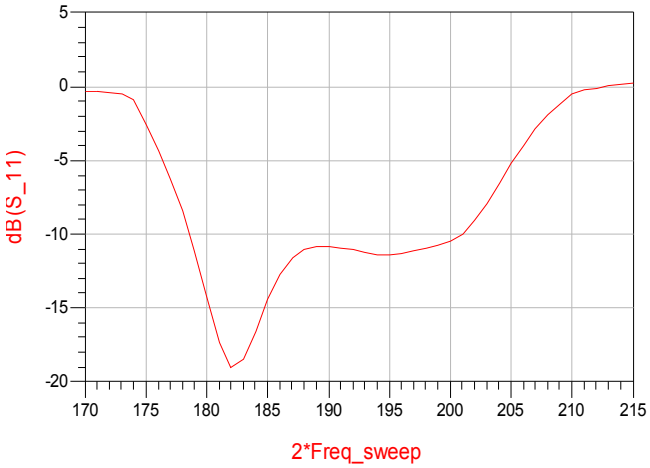

Fig 10: Predicted input matching of the 12-anode dual-chip 190 GHz balanced doubler at room temperature with 80 mW input power.

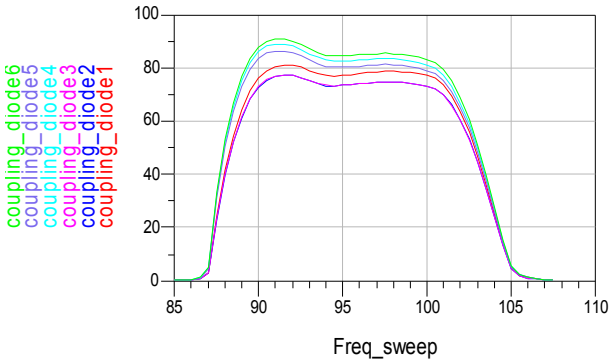

Fig 11: Predicted input coupling to each diode corresponding to the dual-chip 190 GHz balanced doubler at room temperature with 80 mW input power.

V. Conclusion

A novel dual-chip single-waveguide power combining scheme for frequency multipliers has been proposed and demonstrated through the design of a 190 GHz doubler. It allows to double the number of diodes in the design in order to increase the power handling capabilities of the multiplier. State-of-the-art efficiencies cannot be achieved with this specific design due to the limitations of the Schottky diodes provided by UMS to operate as multipliers. However, with an accurate control of the fabrication and assembly processes to guarantee the symmetry between the two chips and well optimized diodes (to be used as multipliers), state-of-the-art performances would be obtained without sacrificing efficiency or bandwidth compared with a single chip implementation. This work represents a further step to increase the LO power provided by multiplier-based solid-state sources beyond 1 THz.

Acknowledgment

The authors would like to thank UMS for providing the wafers for this work.

References

[1] J. S. Ward, G. Chattopadhyay, J. Gill, H. Javadi, C. Lee, R. Lin, A. Maestrini, F. Maiwald, I. Mehdi, E. Schlecht, and P. Siegel, "Tunable Broadband Frequency-Multiplied Terahertz Sources," *33rd International Conference on Infrared, Millimeter and Terahertz Waves*, September 2008.

[2] A. Maestrini, J.S. Ward,C.Tripon-Canseliet, J.J. Gill, C. Lee, H. Javadi, G. Chattopadhyay, and I. Mehdi, "In-phase power combined frequency triplers at 300 GHz," *IEEE Microwave and Wireless Components Letters*, vol. 18, no. 3, pp. 218-200, March 2008.

[3] J.V. Siles and J. Grajal, "Capabilities of GaN Schottky multipliers for LO power generation at millimeter-wave bands," *19th International Symposium on Space Terahertz Technology*, April 2008.

[4] H.M. Manohara, E.W. Wong, E. Schlecht, R.D. Hunt, and P.H. Siegel, "Carbon nanotube Schottky diodes for high frequency applications," *Joint 30th International Conference on Infrared and Millimeter-Waves and 13th International Conference on Terahertz Electronics,* vol.1, pp-285-286, September 2005.

[5] M.S.Fuhrer, "Carbon Nanotubes and Graphene for High-Frequency Electronics," *Physical Review Letters 101, 146805 (2008).*

Numerical Physical Model for Heterostructure Barrier Varactors

Jesús Grajal, Virginia Bernardo

***Abstract*— A physics-based CAD tool for the design of heterostructure barrier varactors (HBV) is presented. We analyse the impact of the material system and device structure on the limiting transport mechanisms in HBVs and on HBV-based frequency tripler performance.**

Index Terms—**CAD, heterostructure barrier varacto, harmonic balance, submillimeter-wave technology, frequency multiplier.**

I. Introduction

Varactor frequency multipliers play a key role in developing solid-state power sources at terahertz frequencies. Heterostructure barrier varactors represent a very interesting technological alternative to traditional Schottky diodes providing an alternative for the fabrication of frequency multipliers at millimetre-wave and submillimeter-wave bands [1], [2].

An HBV is a symmetric device composed of a high bandgap undoped or sligthly doped semiconductor (*barrier*), placed between two low band-gap highly doped modulation layers. When an external bias is applied across the device, electrons are accumulated on one side of the barrier and depleted on the opposite side providing a voltage-dependent depletion region in one of the modulation layers. When the structure presents symmetry, an even C-V characteristic is obtained.

HBV diodes show several advantages for the implementation of frequency multipliers:

- An easier power handling due to the possibility of stacking several barriers in a single device.
- The achievement of odd multiplication factors with no need of filtering the even harmonics of the RF signal.
- No bias is required for HBV multipliers with odd multiplication factors, contrarily to Schottky ones.

The electrical performance characteristics of HBV diodes have been studied with a one-dimensional physics-based HBV numerical model. It combines conventional drift-diffusion formulation with thermionic and thermionic-field emission currents imposed at the interface between layers. Tunnelling transport through the barriers is significant especially for HBV diodes with high doping in the modulation layer. The time-independent Schrödinger's equation is solved using the transfer matrix approach in order to calculate the transmission coefficient through the different barriers in the device.

This simulation tool incorporates different materials systems (*AlGaAs/GaAs* or *AlAs/AlGaAs/GaAs* on *GaAs* substrate, *InAlAs/InGaAs* or *AlAs/InAlAs/InGaAs* on *InP* substrate), non-constant doping and composition profiles for each layer, as well as variable number of barriers. This tool offers the possibility to understand some limiting mechanisms in HBVs, such as tunnelling transport through the barriers, avalanche breakdown due to impact ionization, or self-heating effects, and to mitigate them through a proper design.

This physics-based simulator has been integrated into an in-house circuit simulator based on the harmonic balance method. The integration of numerical simulators for active devices into circuit simulators avoids the need of equivalent-circuit model extraction, and provides another degree of freedom to improve the performance of circuits because they can be designed from both a device and a circuit point-of-view.

The physics-based model for HBVs is presented in Section II. An analysis of different critical aspects in the design of HBVs is accomplished in Section III. The influence of temperature in HBV performance is analysed in section IV. Some conclusions are drawn in section V.

II. HBV physical device model

The harmonic balance method (HBM) is the most common technique for the design of large-signal nonlinear microwave circuits. The HBM depends critically on the accuracy of the nonlinear element model employed in the analysis. This model must be valid for a wide range of frequencies and embedding impedances. The electrical and RF performance characteristics of millimetre-wave and submillimeter-wave HBV diodes and frequency multiplier circuits investigated here are based on an accurate physical model, which combines drift-diffusion current transport [3] with thermionic and thermionic-field emission currents at the interfaces caused by material composition discontinuities [4].

The electrical performance of the HBV diodes is investigated with a one-dimensional (1-D) drift-diffusion formulation: The governing equations are Poisson's equation, and the carrier continuity equations for electrons and holes. The recombination rate is modelled by the Shockley-Read-

Manuscript received 21 April 2009. This work was supported in part by the Spanish National Research Programme under project TEC2005-07010-C02-01/TCM.

The authors are with the Signal, System, and Radioommunications of the Technical University of Madrid, ETSI Telecomunicación, Ciudad Universitaria s/n, 28040 Madrid (phone: +34 913367358, fax: +34 913367362, e-mail: jesus@gmr.ssr.upm.es).

Hall recombination, and the generation rate is restricted to impact ionization [3].

Our physics-based model incorporates accurate boundary and interface conditions. We impose Dirichlet's boundary conditions at metal contacts for Poisson's and carrier continuity equations [3]. On the other hand, thermionic and thermionic-field carrier transport at the barriers is imposed self-consistently at the different interfaces caused by material composition discontinuities [4].

Tunnelling transport through the barriers is significant especially for HBV diodes with high doping in the modulation layer. The time-independent Schrödinger's equation is solved using the transfer matrix approach [5] in order to calculate the transmission coefficient through the different barriers in the device.

Newton's method is used for the solution of the coupled system of equations obtained after the discretization of the partial differential equations through finite difference methods at the points of a nonuniform mesh.

Our physical model has been validated with measurements from several HBV diodes with different material compositions, modulated layer thicknesses, doping levels, and areas. The parameters for these diodes are provided in Table 1, and references [1], [6].

Table 1 HBV diode parameters

HBV Composition	Modulation layer		Barrier
	Doping (cm^{-3})	Length (nm)	Length (nm)
UVa-NRL-1174 [1] $Al_{0.7}Ga_{0.3}As/GaAs$	$8x10^{16}$	250	20
SHBV[6] $AlAs/In_{0.52}Al_{0.48}As/In_{0.53}Ga_{0.47}As$	10^{17}	300	5/3/5

A good agreement for I-V and C-V characteristics was presented in a previous contribution [7] for the diodes of Table 1.

III. Design of HBV Diodes

The first step in the design of a frequency multiplier is the optimisation of the active device. The nonlinearity used in HBVs working as a frequency tripler or quintupler is the capacitance. Therefore, the designer must maximise the capacitance swing for a given input power, while reducing the DC current consumption. The minimisation of the current will result in a reduction of the thermal problems and an improvement of the reliability of the circuit.

Figure 1 shows the influence of the Al content of the barrier on the I-V characteristic for a single barrier diode UVa-NRL-1174, Table 1. The higher the Al content is, the higher the discontinuity in the conduction band is, and, therefore, the current through the barrier diminishes. However, the C-V characteristic is not significantly affected by the variation of the Al content of the barrier.

A higher reduction of the current through the barrier can be obtained by using different material for the HBV. Figure 2 compares two SHBVs (single HBV) for the material systems described in Table 1. The conduction band discontinuity created by the heterostructure $AlAs/In_{0.52}Al_{0.48}As/In_{0.53}Ga_{0.47}As$ is higher than for the $Al_{0.7}Ga_{0.3}As/GaAs$ barrier. Therefore, the current through the barrier presents an additional reduction.

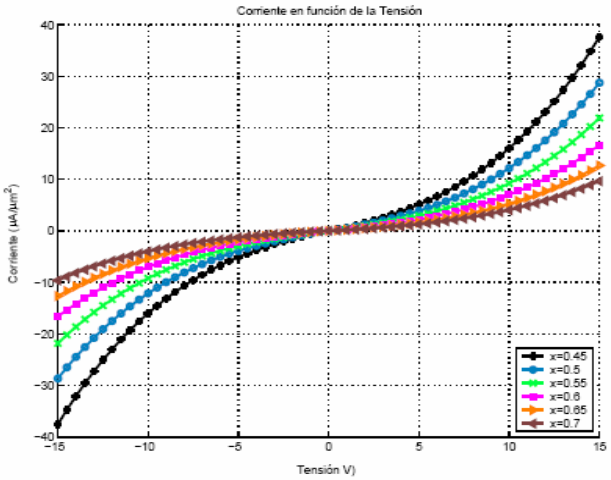

Figure 1.- I-V characteristic of a SHBV $Al_xGa_{1-x}As/GaAs$ as a function of the Al composition, Table 1.

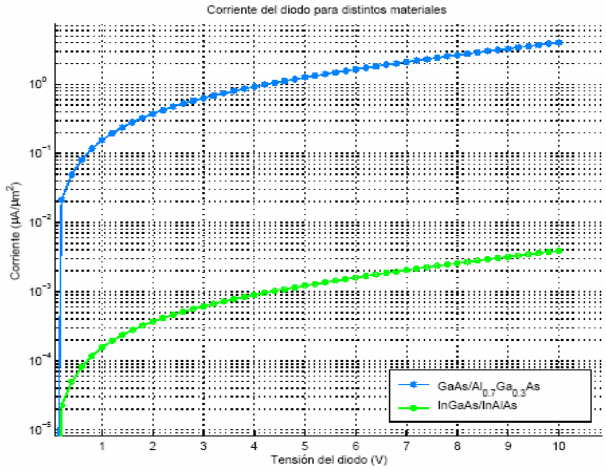

Figure 2.- I-V characteristics of a SHBV $Al_{0.7}Ga_{0.3}As/GaAs$ and a SHBV $AlAs/In_{0.52}Al_{0.48}As/In_{0.53}Ga_{0.47}As$, Table 1.

The second step consists of selecting the thickness of the modulation layer and the barrier. The thickness of the modulation layer must accommodate the maximum length of the depletion region for a given input power. If this rule is not accomplished, the capacitance swing is reduced, Figure 3. On the other hand, the thickness of the barrier must be thin enough to improve the capacitance swing, Figure 4, but thick enough to reduce the transmission probability for tunnelling transport through the barrier.

The final step is the selection the number of barriers taking into account the available input power. HBVs can stack several barriers in a single device easily in order to improve the power handling capability. Figure 5 and Figure 6 shows the I-V and C-V characteristics of the diode UVa-NRL-1174 [1] based on the material system $Al_{0.7}Ga_{0.3}As/GaAs$ as a function of the number of barriers. Both the current and the capacitance are inversely scaled as a function of the number of barriers.

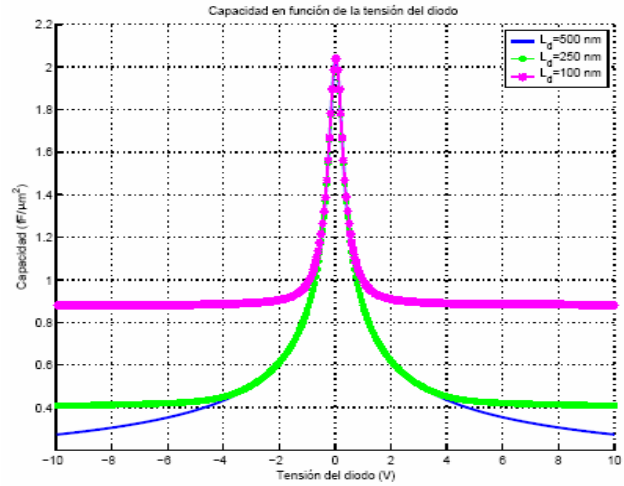

Figure 3.- C-V characteristic for the SHBV $Al_{0.7}Ga_{0.3}As/GaAs$ as a function of the modulation layer thickness. Other parameters as in Table 1.

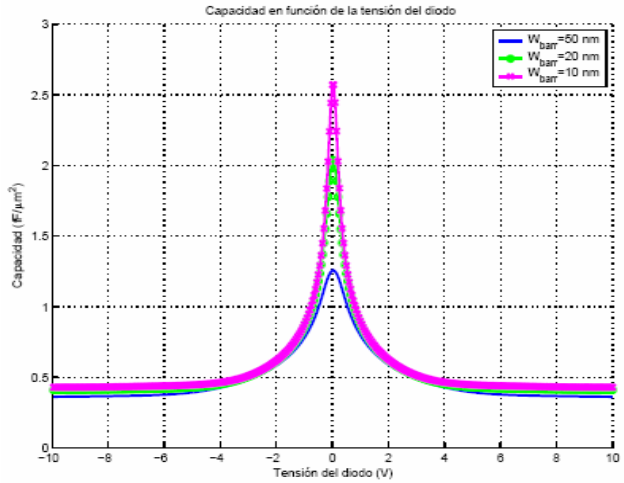

Figure 4.- C-V characteristic for the SHBV $Al_{0.7}Ga_{0.3}As/GaAs$ as a function of the barrier layer thickness. Other parameters as in Table 1.

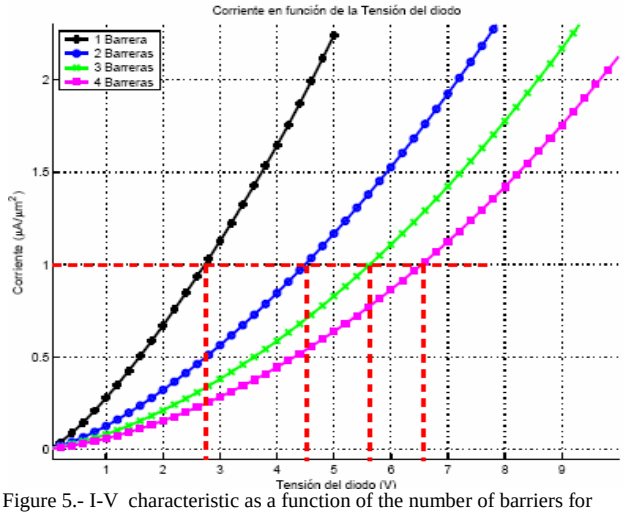

Figure 5.- I-V characteristic as a function of the number of barriers for $Al_{0.7}Ga_{0.3}As/GaAs$ UVa-NRL-1174 [1].

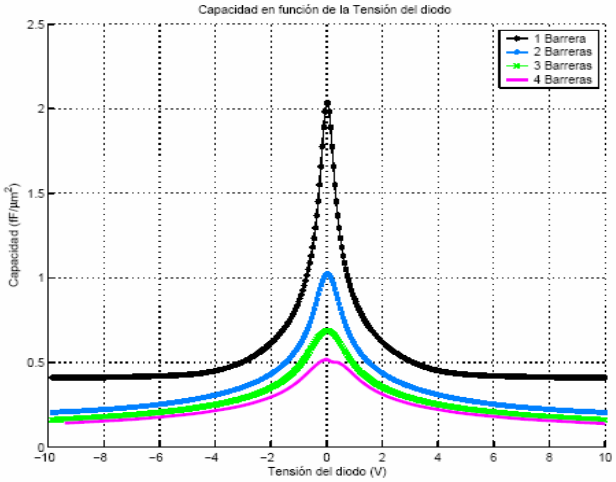

Figure 6.- C-V characteristic as a function of the number of barriers for $Al_{0.7}Ga_{0.3}As/GaAs$ UVa-NRL-1174 [1].

IV. Influence of Temperature in HBV Charcacteristics

Once the structure of the device is fixed, and before the optimisation of the embedding circuit which was presented in [7] following the approach described in [8] for Schottky diodes, it is important to analyse the impact of the temperature on the device performance. In fact, self-heating could be the limiting mechanism for frequency multiplication if a proper thermal design is not carried out [9]. Figure 7 and Figure 8 present the degradation of the diode characteristics as a function of ambient temperature. I-V characteristics are more affected because the thermionic emission current through the barrier is enhanced.

It has been demonstrated in [9], [10] that the increase in the temperature has a crucial responsibility on the decrease in the efficiency for HBV-based frequency multipliers, as it is shown in Figure 9 for a 3x100 GHz tripler designed with the $Al_{0.7}Ga_{0.3}As/GaAs$ SHBV described in table 1.

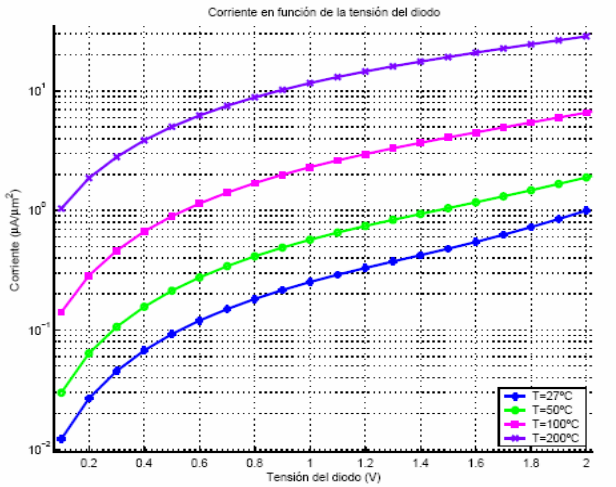

Figure 7.- I-V characteristic for the SHBV $Al_{0.7}Ga_{0.3}As/GaAs$ as a function ambient temperature. Other parameters as in Table 1.

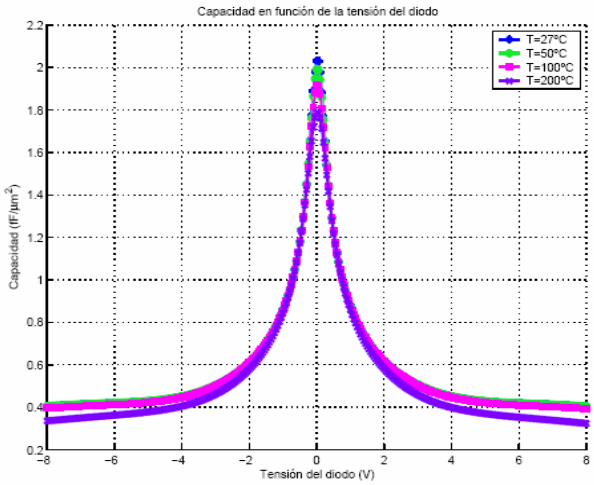

Figure 8.- C-V characteristic for the SHBV $Al_{0.7}Ga_{0.3}As/GaAs$ as a function ambient temperature. Other parameters as in Table 1.

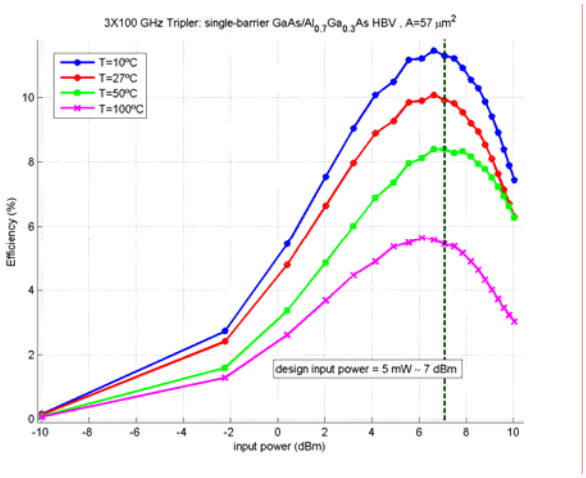

Figure 9.- Simulated efficiency versus input power for a SHBV-based 3x100 GHz frequency tripler as a function of room temperature. The SHBV is the $Al_{0.7}Ga_{0.3}As/GaAs$ diode described in Table1.

V. Conclusion

The flexibility of our CAD tool allows the joint design of the internal HBV structure and the external circuit. This tool offers the opportunity to perform an in-depth study of the impact of material system and device structure on the limiting transport mechanisms in HBVs and on HBV-based frequency multiplier performance.

References

[1] J.R. Jones, "CAD of millimeter wave frequency multipliers: An experimental and theoretical investigation of the heterostructure barrier varactor", *School of engineering and applied science*, *Ph. D. Thesis*, University of Virginia, January 1996.

[2] M. Ingvarson, "Modelling and design of high power HBV multipliers", *Ph. D. Thesis*, Göteborg, Suecia, 2004.

[3] S. Selberherr,"Analysis and simulation of semiconductor Devices", *Springer-Verlag*, Wien-New York, 1984.

[4] K. Horio and H. Yanai, "Numerical Modelling of Heterojunction including the Thermionic Emission Mechanism at the Heterojunction Interface", *IEEE Transaction on Electron Devices*, Vol. 37 No. 4, April 1990.

[5] W. W. Lui and M. Fukuma, "Exact Solution of the Schrodinger equation across an arbitrary one-dimensional piecewise-linear potential barrier", *Journal of Applied Physics*, Vol. 60, pp. 1555-1559, September 1986.

[6] E. Lheurette, P. Mounaix, P. Salzenstein, F. Mollot and D. Lippens, "High performance InP-Based Heterostructure Barrier Varactors in single and stack configuration", *IEEE Electronic Letters*, Vol. 32, No. 15, pp. 1417-1418, 1996.

[7] V. Bernaldo, J. Grajal, J. V. Siles, "Design of heterostructure barrier varactor frequency multipliers at millimeter-wave bands", 17th ISSTT, Paris, 2006.

[8] J.Grajal, V. Krozer, E. Gonz´alez, F. Maldonado and J. Gismero, "Modeling and design aspects of millimeter-wave and submillimeter-wave Schottky diode varactor frequency multipliers", *IEEE Transaction on Microwave Theory an Techniques*, vol. 48, no. 4, pp. 910-928, April 2000.

[9] J. Stake, L. Dillner, S. H. Jones, C. Mann, J. Thornton, J. R. Jones, W. L. Bishop and E. L. Kollberg, "Effects of Self-Heating on Planar Heterostructure Barrier Varactor Diodes", *IEEE Transactions on Electron Devices Letters*, Vol. 45, No. 11, pp. 2298-2303, Nov. 1998.

[10] M. Ingvarson, B. Alderman, A. O. Olsen, J. Vukusic and J. Stake, "Thermal Constraints for Heterostructure Barrier Varactors", *IEEE Electron Device Letters*, Vol. 25, No. 11, November 2004.

A new, simple method for fabricating high performance sub-mm focal plane arrays by direct machining using shaped drill bits.

J. Leech, G. Yassin, B.K. Tan, M. Tacon, P. Kittara, A. Jiralucksanawong and S. Wangsuya

***Abstract*—Large focal–plane arrays consisting of tens, hundreds or thousands of elements will dominate the next generation of sub–mm mapping instruments. While "CCD–style" filled–aperture bolometer arrays, such as SCUBA–2, are suitable for some mapping applications, heterodyne and sub–mm CMB polarisation mapping receivers, such as HARP–B and Clover, continue to consist of close packed arrays of feedhorns. Such feedhorn arrays are popular since they offer the high aperture efficiencies, low sidelobes, low stray light sensitivities and low–cross polarisations required for many astronomical applications. The problem of fabricating large numbers of high quality feeds at a low cost is becoming increasingly acute, and the cost of horn array fabrication is rapidly becoming a large fraction of the total instrument cost.**

In previous work, we have described novel multi–flare angled smooth–walled horns designed using a genetic algorithm. These horns have one or two flare–angle discontinuities and promise to be much easier to machine than corrugated horns at sub–mm wavelengths and yet offer similar radiation patterns. We have previously measured very good beam patterns for electroformed prototypes of these horns across a 17% bandwidth at 230 GHz.

In this paper, we describe our fabrication process for these horns by direct machining into a block of aluminium using shaped drill bits. This is a new fabrication technique and is very rapid compared to the electroforming or direct machining of corrugated horns. We describe the construction of prototype 230 GHz horns using this technique and present experimentally measured beam patterns. We also present photographs of a split prototype horn and discuss the overall machining quality achieved.

***Index Terms*—Antenna array feeds, Genetic algorithms, Horn antennas, Reflector antenna feeds.**

I. Introduction

The ability to rapidly map large areas of the sky to a high sensitivity is of prime importance for many scientific goals at mm and sub–mm wavelengths [1], [2]. The scientific productivity of all–sky surveys, Galactic plane surveys, and cosmic microwave background mapping all increasingly depend on integrating larger numbers of individual feed horns into the telescope's focal plane. The next generation of telescopes will incorporate hundreds or thousands of horns feeding ultra–sensitive detectors into focal plane array receivers. Therefore, the ability to manufacture large numbers of high quality telescope feed horns rapidly, reliably and at a manageable cost is vitally important.

J. Leech, G. Yassin, B.K. Tan and M. Tacon are with the Astrophysics group, Department of Physics, University of Oxford, UK, (email: jxl@astro.ox.ac.uk).

P. Kittara, A. Jiralucksanawong, and S. Wangsuya are with Physics Department, Mahidol University, Bangkok, Thailand.

Traditional corrugated horns have many $\sim 1/4$ wavelength deep azimuthal grooves (corrugations) along their interiors. These are the usual choice for sub–mm telescope feed horns and give excellent beam patterns over bandwidths of up to 50%. Unfortunately, to obtain this performance, several corrugations per wavelength are required, so these horns become more difficult and expensive to fabricate at increasingly smaller wavelengths. For the next generation of large format focal–plane arrays, with many hundreds or thousands of such horns, the cost of the corrugated horns alone can be a significant fraction ($\sim 50\%$) of the entire cost of the complete receiver.

A much simpler horn design is the Potter horn [3],[4] which uses either a step or angular discontinuity to excite a combination of TE_{11} and TM_{11} modes to give a close to uniform plane polarised field at the horn aperture. In the far field, this results in sidelobe cancellation and low–cross polarisation in the horn radiation pattern. The size of the discontinuity is carefully chosen to excite the required amplitude ($\sim$16%) of the TM_{11} mode with respect to the incident TE_{11} mode. The length of the rest of the horn is then chosen to ensure that these two modes arrive at the aperture in phase. The conventional analytical analysis of Potter horns assumed only TE_{11} and TM_{11} modes propogate to the horn aperture. In reality, however, higher order modes will also be excited by the discontinuity, which can carry energy to the horn aperture. To successfully account for these modes, the numerical technique of modal matching[5] is commonly used to propogate these higher order modes to the horn aperture. This analysis method can be used to accurately calculate far–field patterns for lossless horns with a rectangular or cylindrical geometry.

While modal matching can calculate far–field patterns accurately given a horn geometry, predicting the horn geometry that will yield optimum performance over a required bandwidth is not straighforward. The performance depends in a complicated way on details of the excitation and phasing of modes higher than TE_{11} and TM_{11}. The design of a horn is thus well suited to numerical optimisation (minimisation) techniques, where the horn parameters are varied and the quality of the resulting beam pattern, calculated using modal matching, is evaluated using a suitable cost (or quality) function. We have previously reported [6] [7] our use of a genetic algorithm, followed by a simplex technique, to perform horn optimisation. We have had considerable success in designing horns with one flare angle discontinuity (2–section, Fig. 1(a)) and two flare angle

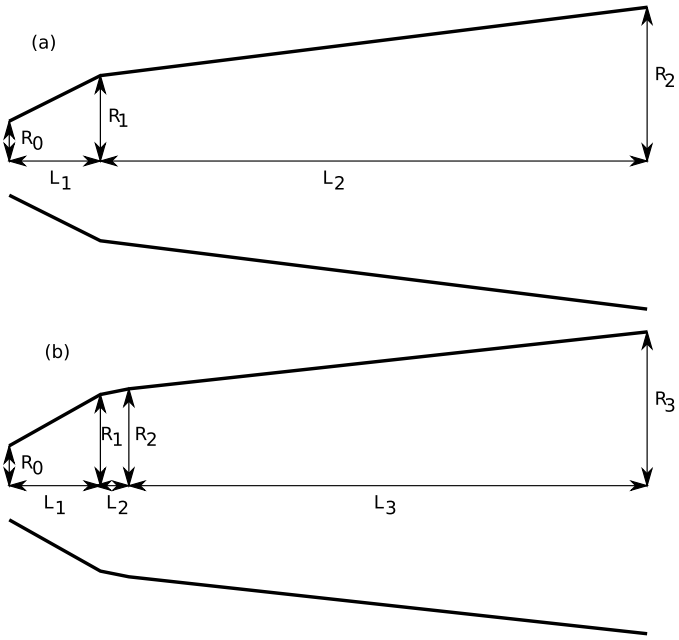

Fig. 1. A schematic of (a) a 2–section and (b) a 3–section smooth walled horn with one and two discontinuities in flare angle, respectively.

discontinuities (3–section, Fig. 1(b)). We have also constructed a prototype 3–section horn using traditional electroforming. The experimental beam pattern measurements of this horn showed good agreement with theory, validating our design procedure.

One attraction of the relatively simple geometries of these smooth–walled horns is the fact that they readily lend themselves to much simpler fabrication techniques compared to corrugated horns, which are usually made by electroforming. In this paper, we describe our fabrication of 3–section 230 GHz prototype horns by direct drilling into a block of aluminium. We have been developing this technique with the aim of rapidly contructing large arrays of horns by simply repeatedly drilling into a single plate of aluminium. We present photographs and measurements of the interiors of these horns, showing the overall surface quality and feature sharpness. Finally, we present experimental beam patterns for our prototype horns and outline our plans to constuct a 37 horn prototype array.

II. Horn design using a Genetic Algorithm

Genetic algorithms employ a "natural selection" process which is similar to biological evolution[8]. We begin by encoding the parameters which describe a certain horn design to form a "chromosome". We then construct a random set of horn designs and their corresponding chromosomes to form a population. We then evaluate a cost (or quality) function for each design to measure its fitness. Our cost function incorporates weighted measures of beam circularity and cross–polarisation, calculated using modal matching[5], across the required frequency band [6],[7]. The chromosomes forming the fittest half of the population are then randomly paired to form parents which produce offspring to form a new generation. When the offspring are generated, crossover and mutation are used to introduce variation into the next generation. The whole process is then repeated with the new population. After many iterations, this evolutionary process yields an increasingly fitter population, with the optimised design being the fittest individual. Once the position of the global cost function minimum has been approximately found using the genetic algorithm, the precise position of the minimum can be quickly found using a downhill simplex technique.

A careful choice of the cost function is important for efficient optmisation with the GA. Our cost function is chosen to maximise far–field beam circularity and minimise the peak cross–polar level. A Potter horn with good beam circularity and low cross–polarisation will also tend to exhibit low sidelobe levels and high beam efficiency, so we have not included the latter parameters explicity in the cost function. The return loss for smooth walled Potter horns is usually low and does not depend strongly on the horn profile, so we have not explicitly included this pararameter in the cost funcion. Our cost function, at single frequency f may be written as

$$\delta_f^2 = w_X \left[\sum_{P=-1}^{P=-30} \left(\frac{\sigma_P}{\sigma_P^{\rm av}} \right)^2 w_P \right] \qquad (1)$$

where P is the power level in dB, $w_P = 10^{P/15}$ is the weighting function for the beam circularity, w_X is the peak cross–polar power relative to main–beam peak power, σ_P is the difference between the E and H–plane beamwidths at power level P dB and $\sigma_P^{\rm av}$ is the mean E and H–plane beamwidths at power level P dB. We calculate our final cost function across bandwidth $\sigma_f = f_U - f_L$ centred at frequency f_0 via

$$\delta^2 = \sum_f \delta_f^2 w_f \qquad (2)$$

where $w_f = \exp(-(f-f_0)^2/2\sigma_f^2)$ is the frequency dependent weighting factor. While this cost function works well for our purposes, it should be emphasized that other cost functions can be easily incorporated into the design software, depending on the design requirements.

We have developed a fully automated suite of horn design software using a genetic algorithm for design synthesis and modal matching for pattern computation, and produced designs with excellent predicted patterns over a bandwidth of up to 20%. We have also successfully parallelized the code to run on multiple CPU Beowulf clusters using MPI messaging for communication between tasks. We are using this code to optimise designs with a larger number of discontinuities, and hope to produce designs with bandwidths of up to 50%.

III. Performance of an electroformed 230 GHz prototype horn

In order to verify the efficacy of the design technique described above, we had a prototype horn made commercially using traditional electroforming. This prototype horn was designed for a centre frequency of 230 GHz and had 3 conical sections (2–flare angle discontinuities, Fig. 1(a)). The dimensions for this horn are given in Table I. We chose

TABLE I
GEOMETRICAL PARAMETERS FOR THE 3–SECTION 230 GHZ DESIGN

Parameter	Length (mm)
R_0	0.62
R_1	1.486
R_2	1.812
R_3	3.652
L_1	1.479
L_2	1.212
L_3	24.0

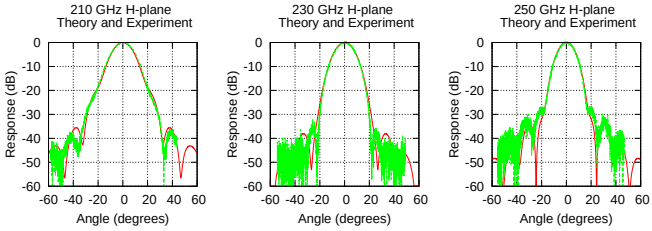

Fig. 2. A comparison with theoretical beam patterns calculated using modal matching and the experimentally measured H–plane beam patterns, for the electroformed prototype.

to fabricate this prototype using electroforming to enable a precise realisation of the horn design enabling verification the expected beam patterns in the absence of significant manufacturing errors. We have reported the experimentally measured the beam patterns of these horns previously [9][1] and we reproduce them here (Figs. 2 and 3). Agreement of the experimental beam patterns with theoretical expectation was seen to be very good, confirming the performance of our designs in the absence of significant manufacturing errors. The experimental copolar and crosspolar beam patterns (Fig. 4), show a low cross polarisation <-27 dB across the measured 17% fractional bandwidth.

IV. HORN FABRICATION BY DRILLING

By measuring the beam patterns for an electroformed prototype horn, we had a suitable benchmark with which to compare our horns manufactured using our experimental direct drilling

[1]This previous work also presents beam patterns measured for drilled horns – these should be disregarded as it was subsequently found that these horns were incorrectly fabricated with the correct 3–section horn aperture ($R_3 = 3.652$ mm) but with a tool for an older 2–section horn design.

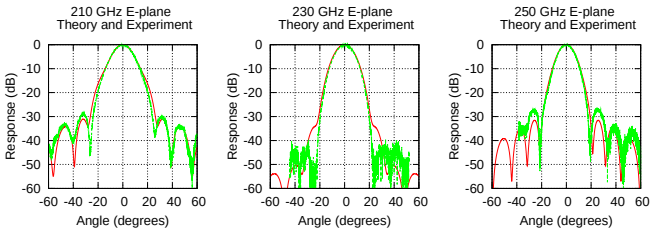

Fig. 3. A comparison with theoretical beam patterns calculated using modal matching and the experimentally measured E–plane beam patterns, for the electroformed prototype.

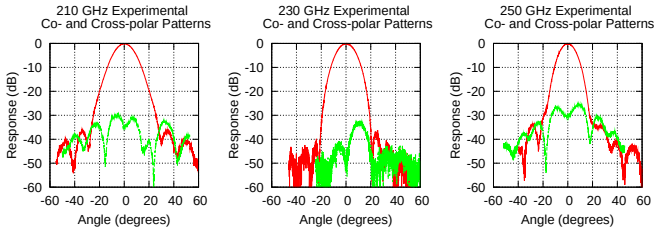

Fig. 4. Experimental co–polar and cross–polar beam patterns, measured for the electroformed prototype.

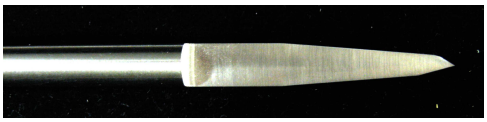

Fig. 5. The machine tool used for the fabrication of the drilled horn prototype.

technique. This method is much faster and less expensive than electroforming or split block machining, and should lend itself well to the fabrication of large focal plane arrays by repeated drilling into a single aluminium block.

To demonstrate the technique, we had a high–speed steel tool (Fig. 5) produced with the required horn profile for our 230 GHz 3–section horn described above (Table I). We first machined an accurate aluminium cuboid which was bolted into our milling machine. We used our shaped tool to drill into the front side of the block, forming the horn interior and then drilled a cylindrical waveguide into the rear of the block using a standard reamer of an appropriate size. A standard UG/387 (modified) flange was then drilled into the rear of the block, and the block finally turned down on a lathe to give the finished horn (Fig. 6).

We produced three prototype horns by direct drilling, splitting one of the horns in half using a milling machine while retaining the other two for beam pattern measurements. We then examined the split horn under a microscope to examine the machining tolerance and accuracy of the interior finish. As can be seen from Fig. 7, the interior surface quality is quite smooth, with surface machining marks no larger than $\sim 10\mu$m. The flare angle discontinuities are also seen to be sharp and well defined, which is important since the spectrum of higher order modes generated at these discontinuities is expected to depend strongly upon their sharpness.

We also used the microscope to measure the aperture radius of the horn, this was found to be 3.652 mm, within 0.005 mm of the specification. This indicates that the drill bit was inserted to the correct depth with a high positional accuracy. A close examination of the throat region in Fig. 7 indicates that there may have been a slight mismatch between the axis of the waveguide drill and the waveguide of the horn drill by around $\sim 50\mu$m. The expected effects of such non–axisymetric errors are hard to model using modal–matching, which usually assumes that each waveguide segment shares a common axis to enable the use of analytical expressions for the waveguide mode overlap integrals. We are currently determining the likely accuracy and systematic errors in our microscope measurements and investigating the possibility

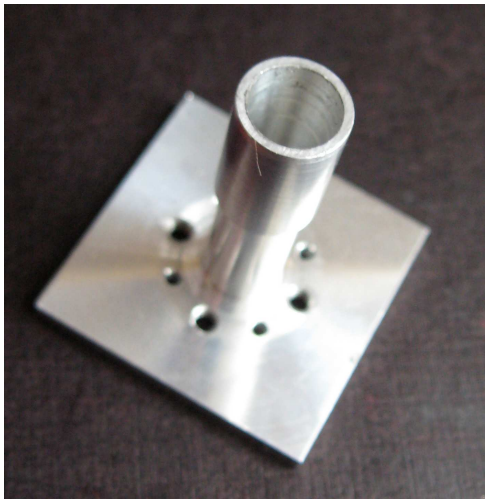

Fig. 6. The completed prototype drilled horn.

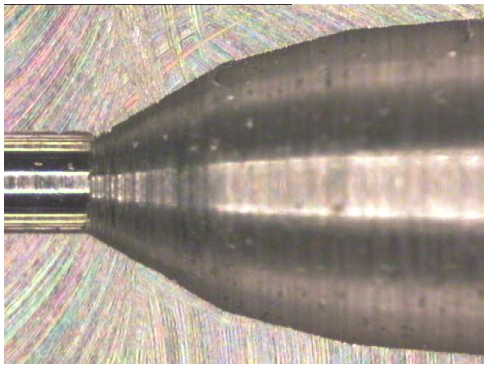

Fig. 7. The throat region one half of the split drilled horn.

of extending the usual modal matching technique to handle circular waveguide segments which have an offset axis.

V. Drilled Horn Beam Patterns

The far field radiation patterns for the drilled horns were measured directly in an anechoic chamber at the Rutherford Appleton Laboratory. We used an ABmm vector network analyser as a simple total power detector and rotated the horn under test with a motorised rotary table under computer control. Two identical prototype horns were used for transmission and reception, separated by 350 mm ($\sim 9D^2/\lambda$). We removed the effect of stray reflections and standing waves by careful positioning of Eccosorb RF absorber, and we were confident that we successfully eliminated stray power pickup to within the dynamic range of our measurements, which was around 50 dB.

Figures 8 and 9 show a comparison with the experimental and theoretical beam patterns in the H–plane and E–plane respectively, for the drilled horn prototype No. 1. Figures 10 and 11 show the corresponding patterns for drilled horn prototype No. 2. One notices immediately that the experimental beam patterns obtained from horn No. 1 and horn No. 2 are essentially identical, an important result which shows that the manufacturing tolerances between drilled horns on a large array are unlikely to be significantly different.

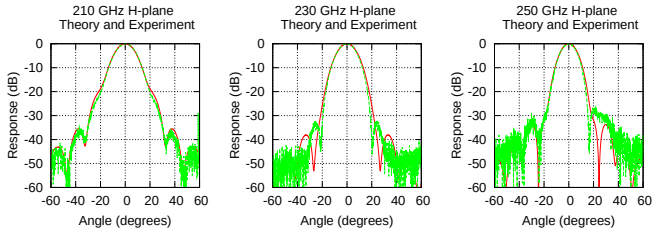

Fig. 8. A comparison with theoretical beam patterns calculated using modal matching and the experimentally measured H–plane beam patterns, for the drilled horn, prototype No.1.

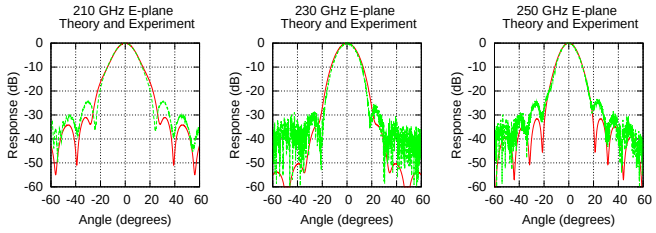

Fig. 9. A comparison with theoretical beam patterns calculated using modal matching and the experimentally measured E–plane beam patterns, for the drilled horn, prototype No. 1.

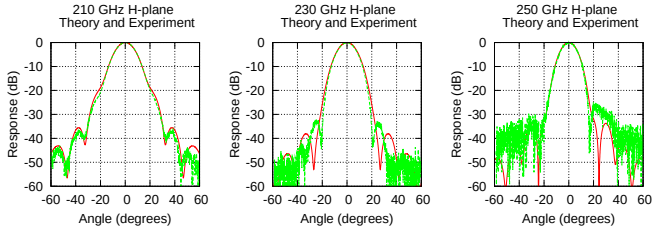

Fig. 10. A comparison with theoretical beam patterns calculated using modal matching and the experimentally measured H–plane beam patterns, for the drilled horn, prototype No. 2.

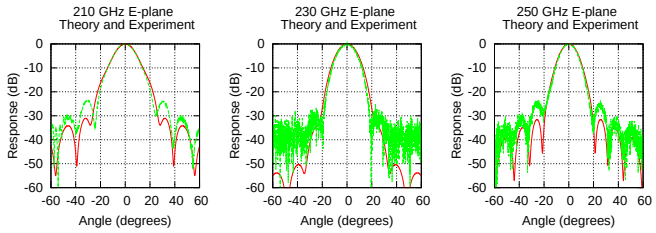

Fig. 11. A comparison with theoretical beam patterns calculated using modal matching and the experimentally measured E–plane beam patterns, for the drilled horn, prototype No. 2.

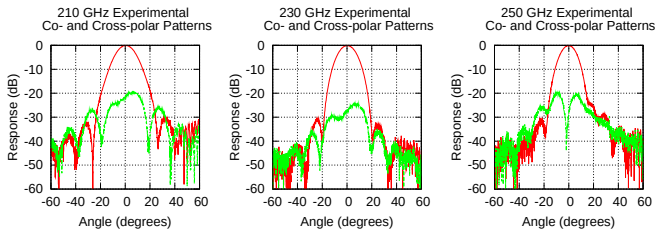

Fig. 12. Experimental co-polar and cross-polar beam patterns, measured for the drilled horn prototype No. 1.

Overall, the experimental beam patterns for the drilled horns show a good match to the theoretical expectations but this match is not quite as good as that found for the electroformed horns (Figs. 2 and 3). Nevertheless, the beam patterns show clean main beams, with none of the flattening of the beam at the centre of the patterns which often occurs when a horn becomes very overmoded. The positions of the sidelobes agree reasonably well with theory for the H–plane patterns, but are around +5 dB higher than expected in the E–plane patterns. Nevertheless, all sidelobes are below 25 dB across the measured fractional bandwidth of 17%. Beam circularity, as exhibited by the difference in main–beam width between the E and H–planes, is also very good over the band. An interesting feature is the fact that both the E and H–plane main–beam widths at 230 GHz are somewhat narrower than theory at 230 GHz, yet match theory quite well at 210 and 250 GHz. We also note that the first sidelobe in the H–plane at 250 GHz exhibits a slight asymmetry, with the right hand sidelobe being around 5 dB higher than the left for both prototype horns. The experimental co–polar and cross–polar beam patterns measured for the drilled horn prototype No. 1 are shown in Fig. 12. The cross polar levels are somewhat higher than measured for the electroformed prototype (Fig. 4), but remain below -20 dB across the measured fractional bandwidth of 17%.

VI. Conclusions and further work

We have demonstrated that one can make smooth–walled multi–flare angle feed horns with good performance by using a novel direct drilling technique. The beam circularity and symmetry of the horns' far–field patterns are good and sidelobe levels are below -25 dB across a fractional bandwidth of 17%. The beam patterns obtained from two prototype drilled horns are essentially identical, a result which is very promising for the development of this technique to construct repeatable large format focal plane arrays by repeated drilling.

The beam patterns for our prototype drilled horns have been shown to be not quite as good as those obtained when the same horn design is constructed using traditional electroforming. We plan to obtain a deeper understanding of this discrepancy by making precision measurements of the interiors of the horns' profiles microscopically and then modelling the recovered horn geometries using the modal matching technique, perhaps extending the technique to handle non–axial geometries.

In parallel with this effort we intend to construct and test a 37 horn focal plane array of horns by repeated drilling into a single plate of aluminium. Our result so far show that this technique promises the rapid construction of large high performance arrays at a fraction of the cost of an equivalent array of corrugated horns. We are currently pursing the commercialisation of both our horn design software and our fabrication techniques, in collaboration with Isis Innovation, the technology transfer company of the University of Oxford.[2]

[2]The horn designs disclosed in this paper are available for licensing. Please contact Isis Innovation Ltd, the to discuss commercialising this opportunity (innovation@isis.ox.ac.uk).

Acknowledgment

The authors would like to thank Henry Manju, Jeunne Treuttel, Peter Huggard and Matthew Oldfield for their assistance in setting up and using the ABmm Vector Network Analyser and 230 GHz antenna test range at the Rutherford Appleton Laboratories.

References

[1] H. Smith, J. Buckle, R. Hills, G. Bell, J. Richer, E. Curtis, S. Withington, J. Leech, R. Williamson, W. Dent, P. Hastings, R. Redman, B. Wooff, K. Yeung, P. Friberg, C. Walther, R. Kackley, T. Jenness, R. Tilanus, J. Dempsey, M. Kroug, T. Zijlstra, T. M. Klapwijk, 2008, "HARP: a submillimetre heterodyne array receiver operating on the James Clerk Maxwell Telescope", Society of Photo-Optical Instrumentation Engineers (SPIE) Conference Series, Vol 7020.

[2] C. E. North, B. R. Johnson, P. A. R. Ade, M. D. Audley, C. Baines, R. A. Battye, M. L. Brown, P. Cabella, P. G. Calisse, A. D. Challinor, W. D. Duncan, P. G. Ferreira, W. K. Gear, D. Glowacka, D. J. Goldie, P. K. Grimes, M. Halpern, V. Haynes, G. C. Hilton, K. D. Irwin, M. E. Jones, A. N. Lasenby, P. J. Leahy, J. Leech, B. Maffei, P. Mauskopf, S. J. Melhuish, D. O'Dea, S. M. Parsley, L. Piccirillo, G. Pisano, C. D. Reintsema, G. Savini, R. Sudiwala, D. Sutton, A. C. Taylor, G. Teleberg, D. Titterington, V. Tsaneva, C. Tucker, R. Watson, S. Withington, G. Yassin and J. Zhang, 2008, "Detecting the B-mode Polarisation of the CMB with Clover". Proceedings of the XXXXIIIrd Rencontres de Moriond "Cosmology".

[3] Potter P., 1963. "A new horn antenna with suppressed sidelobes and equal beamwidths". Microwave J., 6, 71–78.

[4] Pickett H., Hardy J. & Farhoomand J., 1984. "Characterisation of a dual mode horn for submillimetre wavelengths". IEEE Trans. Microwave Theory Tech., MTT32(8), 936–937.

[5] Olver A., Clarricoats P., Kishk A. & Shafai A., 1994. "Microwave horns and feeds". Bookcraft, Bath.

[6] Yassin, G., Kittara, P., Jiralucksanawong, A., Wangsuya, S., Leech, J. and Jones, M.E. "A high performance horn for large format focal plane arrays", Proc. of the 18th International. Symposium Space Terahertz Technology, Pasadena, USA, 2007.

[7] Kittara, P., Jiralucksanawong, A., Wangsuya, S., Leech, J. and Yassin, G., 2007 "The design of potter horns for THz applications using a genetic algorithm" International Journal of Infrared and Millimeter Waves (2007) 28: pp.1103-1114.

[8] Haupt R.L. and Haupt S.E. (1998). "Practical genetic algorithms". Wiley-Interscience Publication.

[9] Kittara, P., Leech, J., Yassin, G., Tan, B. K., Jiralucksanawong, A. and Wangsuya, S., 2008 "The fabrication and testing of novel smooth-walled feed horns for focal plane arrays" Proc. 19th International Symposium on Space Terahertz Technology.

P2B

High Performance Frequency Selective Surfaces for Passive Radiometry

R. Dickie[1], R. Cahill[1], H. S. Gamble[1], V. F. Fusco[1], P. G. Huggard[2*], M. Henry[2], M. L. Oldfield[2], P. Howard[3], Y. Munro[3], and P. de Maagt[4]

1 The Institute of Electronics, Communications and Information Technology
Queen's University Belfast, Northern Ireland Science Park, Queen's Road, Belfast BT3 9DT, UK
2 Space Science & Technology Department, STFC Rutherford Appleton Laboratory, Didcot, OX11 0QX, UK
3 EADS ASTRIUM, Earth Observation & Navigation Directorate, Anchorage Road,
Portsmouth PO3 5PU, UK
4 European Space Agency, Antenna and Submillimetre Wave Section,
PO Box 299, NL 2200 AG Noordwijk, The Netherlands
* Contact: peter.huggard@stfc.ac.uk, phone +44-1235-445245

***Abstract*— Two frequency selective surfaces (FSS), developed for spaceborne millimetre and sub-millimetre characterization of the Earth's atmosphere by passive radiometry, are described. Radiometry provides valuable information on the distribution and dynamics of molecules such as H_2O, NO_2 and NO_2, as well as information on atmospheric temperature and cloud water content. Given that radiometer's receivers usually share a common main antenna, FSS are critical frequency demultiplexing components and demands on their performance in terms of insertion loss and isolation of unwanted channels are stringent. The reported FSS have some common features: they have a very low insertion loss, operate for a range of angles of incidence around 45°, have near-identical behaviour for both TE and TM incident polarizations, and their performance is accurately modelled using Ansoft HFSS or CST Microwave Studio. Both structures have also satisfactorily passed preliminary space qualification trials.**

The first FSS, designed for a proposed millimetre wave meteorological instrument, operates in low pass mode to separate a transmitted channel at (31.40± 0.09) GHz from a reflection band between 50.2 and 55.7 GHz. It comprises of rectangular patterns of 1.6 mm diameter copper rings produced by photolithography on both sides of a 1.575 mm thick PTFE/glass dielectric sheet. The FSS was designed and optimised using HFSS. The FSS transmission loss at 31.4 GHz was measured as 0.3 dB, whereas reflection loss in the band centred on 53 GHz was found to be 0.2 dB or less.

The second FSS, destined for a limb sounding radiometer, operates at sub-millimetre wavelengths to separate the signal and image bands of a double sideband mixer. The filter consists of two identical, 30 mm diameter, 12.5 µm thick, optically flat, freestanding perforated metal screens separated by 450 µm. Each of the ≈5000 micromachined unit cells contains two nested, short circuited, rectangular loop slots and a rectangular dipole slot. Careful optimisation of the shapes of these elements, plus the interactions between the adjacent screens, allows nearly coincident spectral responses to be obtained for both polarisations. The FSS transmission was measured using an ABmm vector network analyser and a quasi-optical test bench. The insertion loss over the transmitted 316.5 - 325.5 GHz signal band was 0.6 dB or less: rejection ≥ 30 dB was achieved in the 349.5 - 358.5 GHz image band. Results are in excellent agreement with the CST predictions. Such a dual polarisation performance, with a band edge frequency ratio of 1.07, has not previously been reported.

The Ring-Centered Waveguide Flange for Submillimeter Wavelengths

A. R. Kerr and S. Srikanth

***Abstract* – The standard UG-387 waveguide flange (MIL-DTL-3922/67C) is not well suited for frequency bands above ~110 GHz. The proposed ring-centered flange has a precisely machined boss centered on the waveguide aperture and is aligned by a ring which centers the bosses of two mating flanges. The flange is compatible with the UG-387 type, allowing components with the new flange to be connected directly to older components without adapters. Like the UG-387 standard, it is sexless and the contact surfaces are not recessed, which facilitates cleaning and lapping to repair damage. The maximum misalignment between waveguides using the new flange should be < 0.001" (25 µm), corresponding to a worst-case return loss of 26 dB in the WR-1.9 band (400-600 GHz), or 16 dB in the WR-1.0 band (750-1100 GHz). A miniature version of the ring-centered flange is also proposed.**

***Index Terms* — Waveguide flanges, waveguide interfaces, waveguides, millimeter-wave, submillimeter-wave.**

I. Introduction

The MIL-DTL-3922/67C waveguide flange, commonly called "UG-387" or "750-round", shown in Fig. 1(a) is not well suited for frequency bands above ~110 GHz. The tolerances allow a misalignment between waveguides as large as 0.006", which can result in a return loss as low as 24 dB [1] at the upper end of the WR-10 band (75-110 GHz). Modified versions of the UG-387 flange, with tighter tolerances and smaller clearance between pins and pin holes, are in use for bands as high as WR-3 and beyond [2][3], but the practical limit of waveguide alignment using non-interfering pins appears to be about 0.0028" [3], which results in a return loss as low as 37 dB in WR-10 but only 19 dB in the WR-3 band (220-330 GHz) and 2 dB at the upper end of the WR-1.0 band (750-1100 GHz). This degree of misalignment is clearly unacceptable for many submillimeter applications.

A flange described by Lau and Denning [4] improved the alignment between waveguides by using a male flange with a boss and a mating female flange with a close fitting receptacle – Fig. 1(b).

Like the Lau-Denning design, the proposed ring-centered flange has a precisely machined boss centered on the waveguide aperture, but alignment is achieved by a ring which centers the bosses of two mating flanges – Fig. 1(c).

Manuscript received 19 April 2009.

A. R. Kerr and S. Srikanth are with the National Radio Astronomy Observatory, Charlottesville, VA 22903. Contact: akerr@nrao.edu.

The National Radio Astronomy Observatory is a facility of the National Science Foundation operated under cooperative agreement by Associated Universities, Inc.

2. Relative Merits

The alignment accuracy of the older UG-387 flange is determined by: (i) the clearance between the pins and the pin holes, (ii) the position of the pins and holes relative to the waveguide apertures, and (iii) the perpendicularity of the pins relative to the flange faces.

The Lau-Denning design does not rely on pins for alignment but on a boss and receptacle whose diameters need differ only by an amount sufficient to prevent jamming. The waveguide alignment accuracy depends largely on the precision with which the boss and receptacle can be centered on their waveguide apertures. The design has three shortcomings, however: it is not backward compatible with the UG-387 design, it is not sexless, and the contact surfaces are not accessible for lapping.

The ring-centered flange is compatible with the UG-387 type, allowing components with the new flange to be connected directly to older components without adapters. Like the UG-387 standard, it is sexless, and the contact surfaces are not recessed, which facilitates cleaning and lapping to repair damage. It also has an anti-cocking rim [5] which has been incorporated into many of the newer implementations of the UG-387 design. The maximum misalignment between waveguides using the new

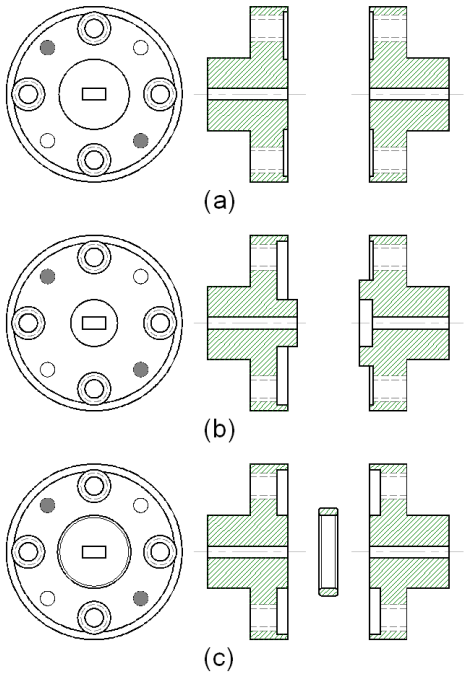

Fig. 1. (a) The standard MIL-DTL-3922/67C (or UG-387 or 750-round) flange. (b) The Lau-Denning flange. (c) The proposed ring-centered flange. Pins are omitted from the cross-sections for clarity.

flange should be <0.001" (25 µm), corresponding to a worst-case return loss of 26 dB in the WR-1.9 band (400-600 GHz), or 16 dB in the WR-1.0 band (750-1100 GHz).

2. Construction

The two most critical aspects of the ring-centered flange are: (i) the clearance between the coupling ring and the boss; and (ii) the alignment of the boss with the waveguide aperture. The coupling ring can be made from commercially available precision stainless steel shim bushing stock [6] which is available with outside diameter 0.3750" and inside diameter 0.3125" +0.0002/−0.0000. If the diameter of the boss is machined to 0.3125" +0.0000/−0.0002, the maximum misalignment of a pair of waveguides resulting from the tolerances of the ring and boss diameters is 0.0004" (10 µm).

The boss is machined on a CNC milling machine which has been centered on the waveguide aperture using an optical centering microscope fitted with a small video camera as shown in Fig. 2. The centering microscope is mounted in the spindle of the CNC milling machine and the flange positioned so the bottom right corner of the waveguide is centered in the cross-hairs. The machine coordinates (X_1, Y_1) are read. The centering microscope is then rotated 180° and the flange positioned so the top left corner of the waveguide is centered in the cross-hairs. The machine coordinates (X_2, Y_2) are read. The true center of the waveguide is (X_0, Y_0), where $X_0 = (X_1 + X_2)/2$ and $Y_0 = (Y_1 + Y_2)/2$. Rotating the centering microscope 180° between measurements eliminates any run-out in the spindle or offset in the microscope optics from the deduced center position (X_0, Y_0). The boss is machined, slightly over size initially, centered at (X_0, Y_0), and then reduced in diameter in small steps while a standard coupling ring is used as a gauge to determine the final diameter.

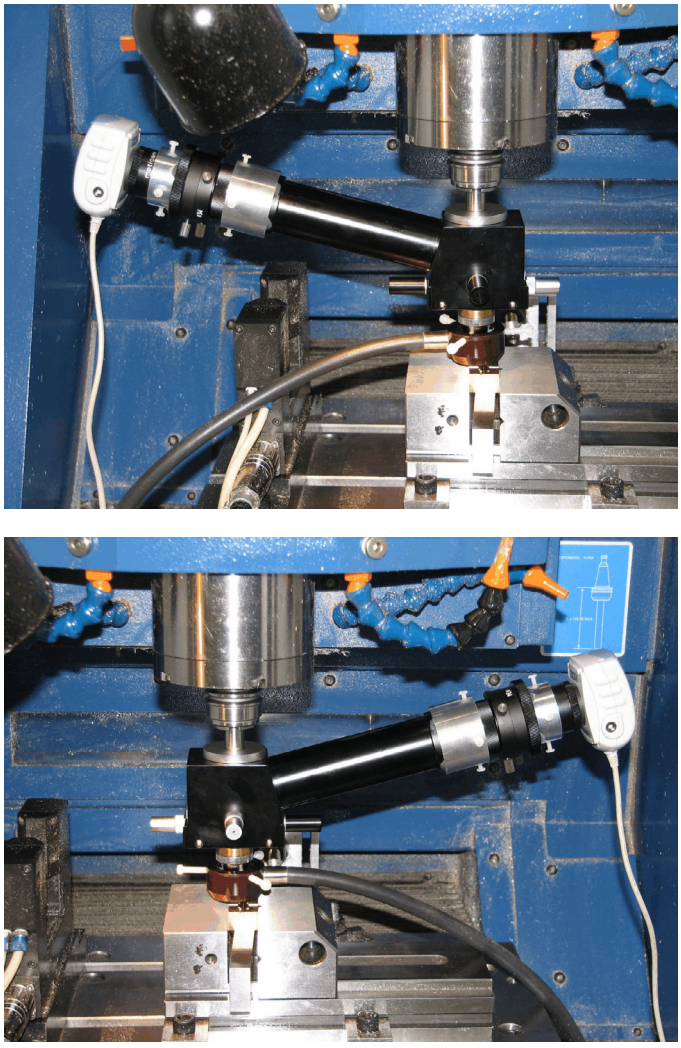

Fig. 2. Determining the center of the waveguide aperture using a centering microscope with video camera and ring illuminator. Top: Measuring the coordinates of the upper left corner of the waveguide. Bottom: Measuring the coordinates of the lower right corner of the waveguide.

Pins are required in the ring-centered flange only to prevent angular misalignment of the mating waveguides. To prevent the pins interfering with the centering function of the ring and bosses, oversize pin holes should be used. Holes of diameter 0.0670" with 0.0615"pins, as for the original MIL specification, would allow a maximum angular misalignment of 0.6° which has negligible effect (see next section).

3. Effects of Misalignment

The effects of lateral and rotational misalignment of waveguide flanges have been described in [1] where it was found that for rectangular waveguides of the usual 2:1 aspect ratio

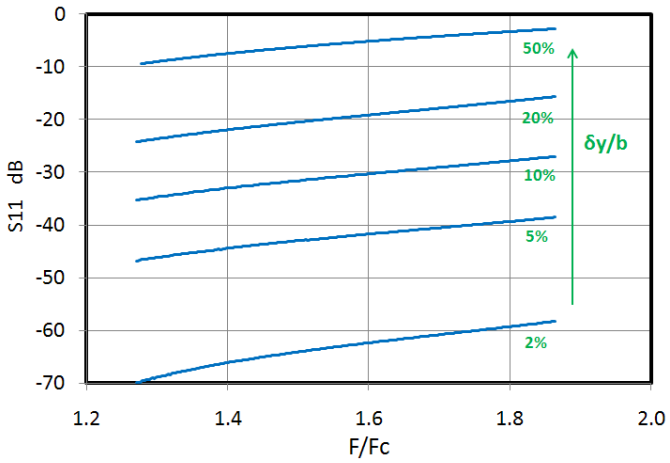

Fig. 3. Effect of a misalignment δy in the b direction as a function of frequency (simulated [7]).

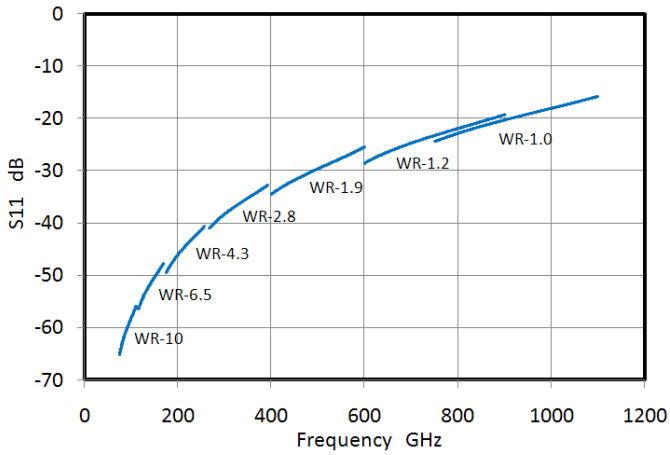

Fig. 4. Reflection at a waveguide joint with a 0.001" (25 µm) misalignment in the b direction, for several waveguide bands (simulated [7]).

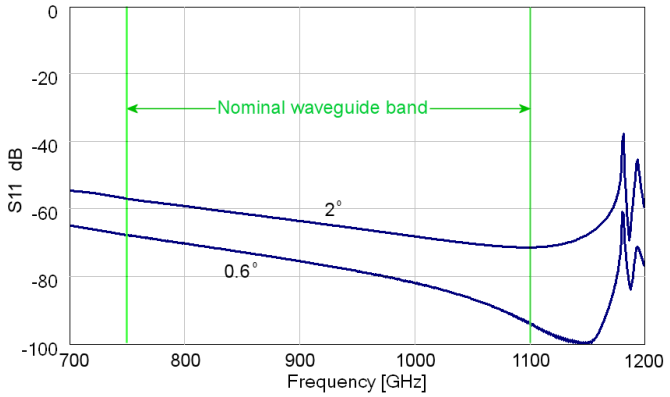

Fig. 5. The effect of angular misalignments of 0.6° and 2° at a waveguide joint. The results are independent of waveguide band (simulated [7]).

misalignment in the direction of the smaller dimension *b* is more serious than misalignment in the *a* direction or a diagonal misalignment. Fig. 3 shows the simulated [7] effect of a misalignment δy in the *b* direction as a function of frequency (normalized to the cutoff frequency). The expected maximum waveguide misalignment for a pair of ring-centered flanges is 0.001" (25 μm), and Fig. 4 shows the effect of such a misalignment in the *b*-direction in several waveguide bands.

The effect of a rotational misalignment at a pair of ring-centered flanges is independent of waveguide band and is shown in Fig. 5 for waveguides with a 0.6° rotation corresponding to the pin clearance in 0.067" holes, and a 2° rotation which would be clearly visible. Even with a 2° rotation the return loss is >56 dB across the band.

4. A Miniature Ring-Centered Flange

In some applications a flange smaller than the UG-387 type is desirable. The Grammer miniature flange [3] was developed at NRAO for use in the ALMA project. With an outer diameter of 0.500", it is sexless and has no screw or pin holes in the E-plane, a desirable characteristic for split-block waveguide components. A ring-centered version of the Grammer miniature flange is shown in Fig. 6. The coupling ring is made from commercial precision stainless steel shim bushing stock [6] with ID 0.4375" +0.0002/−0.0000 and 0.500" OD. As for the larger ring-centered flange, alignment between the waveguide apertures depends on the clearance between the ring and bosses and the alignment of the bosses with the waveguide apertures. A total misalignment < 0.001" (25 μm) should be possible.

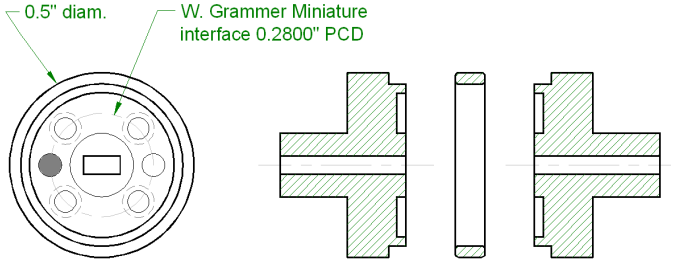

Fig. 6. The miniature ring-coupled flange based on the Grammer miniature flange. Pins omitted for clarity.

5. Conclusion

The proposed ring-centered flange offers a higher degree of precision than the older UG-387 type. Compared with the Lau-Denning design, the ring-coupled flange is inherently somewhat less precise because it has three mating parts as opposed to two in the Lau-Denning design.

We plan to make measurements of the reproducibility of waveguide joints using ring-centered flanges in the near future.

References

[1] A. R. Kerr, E. Wollack, and N. Horner, "Waveguide Flanges for ALMA Instrumentation," ALMA Memorandum 278, 9 Nov. 1999. http://www.alma.nrao.edu/memos/

[2] A. R. Kerr, L. Kozul and A. A. Marshall, "Recommendations for Flat and Anti-Cocking Waveguide Flanges," ALMA Memo 444, National Radio Astronomy Observatory, Charlottesville VA 22903, 6 Jan 2003. http://www.alma.nrao.edu/memos/

[3] J. L. Hesler, A. R. Kerr, W. Grammer, and E. Wollack, "Recommendations for Waveguide Interfaces to 1 THz," Proc. 18th International Symposium on Space Terahertz Technology, Pasadena, 21-23 March 2007, pp.100-103. http://www.gb.nrao.edu/electronics/edir/edir319.pdf

[4] Y. Lau and A. Denning, "An Innovative Waveguide Interface for Millimeter Wave and Submillimeter Wave Applications," 69th ARFTG Microwave Measurements Conf. Dig., Honolulu, HI, June 2007.

[5] See, *e.g.*, http://www.flann.com/Sales/FMI_Catalogue.pdf, p. 119.

[6] McMaster-Carr: http://www.mcmaster.com/#shaft-shim-bushings/=1ch1xv

[7] QuickWave-3D, QWED Sp. z o.o., 02-010 Warsaw, Poland. http://www.qwed.com.pl/qw_3d.html

Ideal Grid Generates Cross Polarization

B. Lazareff *Member IEEE*, S. Mahieu, and D. Geoffroy

***Abstract*—The ALMA Band 7 cartridge dual-polarization cold optics has been designed to meet a number of specifications, among which the level of cross polarization (initially <–20dB, now <–23dB). The initial design was based on the assumption that the coupling diagram from each of the two horns would be free from cross polarization (Xpol) just beyond the polarization diplexing grid, with the only contribution to Xpol comping from the final refocusing mirror.**

Initial measurements were showed levels of Xpol significantly worse than expected. This led (after some time) to the realization that an ideal grid can generate cross polarization, which can be brought down to a negligible level by a proper orientation of the grid.

The design has been modified accordingly, and the measurements indeed have shown a significant improvement, that allowed a tighter specification to be instated.

Optics, Polarization, Quasi-optics, Grid.

I. INTRODUCTION

THE ALMA Band 7 cartridge is a module of the ALMA front end, located in the Cassegrain focal plane of the telescope. It contains the tertiary optics and electronic components for a dual polarization and dual sideband receiver, covering the 275-373 GHz band, and delivering four 4-8 GHz IF bands. The transition between guided and open-space propagation is realized, for each of the two SIS mixers, by a corrugated horn.

The tertiary optics, that interface these two horns to the optics of the Cassegrain telescope, must meet a number of specifications, generally aimed at maximizing the efficiency of the system. It comprises, among other, a polarization diplexer consisting of a conducting grid.

One important specification is the level of cross polarization (Xpol), i.e; the coupling of one channel to the polarization orthogonal to its nominal state. In the present case, as is most frequent, the nominal polarization states are linear.

This contribution provides an account on how the Band 7 tertiary optics was initially designed, found to not meet the expected performance, how it was realized that the Xpol issue arose in the grid, and how that issue was resolved.

II. INITIAL DESIGN

As is customary when dealing with quasi-optical systems, we will describe the system from the horn outwards to the telescope, as if we were dealing with a transmitter.

The beam from each horn is refocused by an offset elliptical mirror (respectively M1 and M1R), with a deviation angle of 40°; that relatively large angle is not optimized for low Xpol.

In the next step, a wire grid recombines the two beams, respectively in transmission and reflection. With the chosen grid parameters (25μm diameter, 100μm pitch), the unwanted couplings, intrinsic to the grid, should be below 1%. Furthermore, the Xpol rejection of the grid combines with the intrinsic polarization purity of the scalar horns (even degraded by the first offset elliptical mirror), so that we expected the polarization purity just after beam recombination to be better than –30dB.

Accordingly, a driving consideration in the design of the Band 7 tertiary optics has been to minimize the Xpol induced by the final offset elliptical mirror (M2). This requires "slow" beams and a small angle of reflection. We designed for a *1/e* beam width (at the central frequency) w=13mm, an equivalent focal length f=77mm, and a reflection angle of 25° (i=12.5°). Accordingly, following equation 21 of [1], we expected an (integrated) cross polarization level of –34 dB.

Figure 1. The Band 7 cold optics. Mirrors M1 and M1R are at the top, partly hidden; horns at the back, circular grid in middle, mirror M2R bottom foreground.

Manuscript received 20 April 2009. This work was supported in part by the ALMA Band 7 cartridge production contract.

Authors are with the Institut de Radio Astronomie Millimétrique, 300 rue de la Piscine, 38406 St Martin d'Hères Cedex, France. Respective emails are lazareff[at]iram.fr, mahieu[at]iram.fr, geoffroy[at]iram.fr.

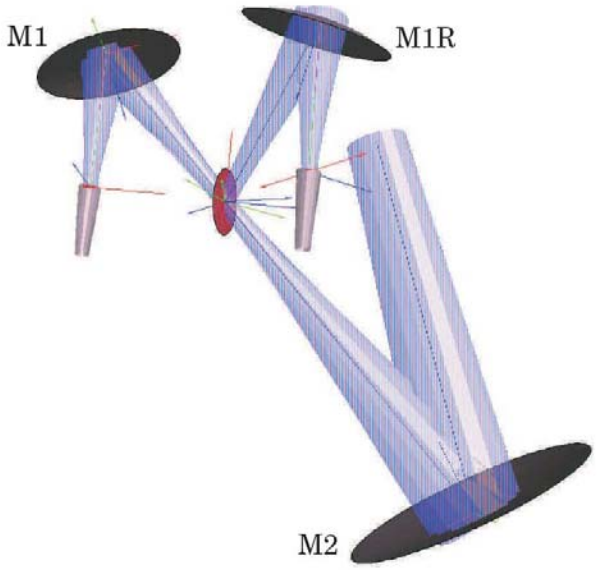

Figure 2. A schematic of the Band 7 tertiary optics. Reproduced from the design verification contracted by ESO to TICRA.

III. Initial Measurements

Initial measurements were disappointing. Not only did we not come close to the design value of –34 dB, but, more often than not, we failed to meet the contractual specification of -20 dB !

IV. Analysis

A. A matter of definitions

It is straightforward to show that a sheet that is a perfect conductor in one direction, and has zero conductivity in the orthogonal direction, acts a perfect polarization diplexer for a plane wave, under arbitrary oblique incidence, and for arbitrary orientation of the incident polarization with respect to the incidence plane. A wire grid is (with proper parameters) a close approximation to such an ideal diplexer.

However, in real-world systems, a quasi-optical beam has a finite transverse extent, typically in the range 5-50 wavelengths. As a result, its decomposition into plane waves (a straightforward Fourier transform) contains a spectrum of spatial directions, around the central direction, or chief ray, of the beam.

These directions can be thought of as spanning a region of the unit sphere. And the notions of co- and cross- polarization over a finite region of the sphere require a definition of "parallel" and perpendicular over that region. That question has no canonical answer.

That issue has been addressed in [2]. Ludwig proposes and analyzes three possible definitions of co- and cross-polarization over the sphere. Definition 3 has been generally adopted, because a) the two patterns (co- and cross-) transform into each other by a *global* rotation; b) it has a natural implementation in beam scanner hardware.

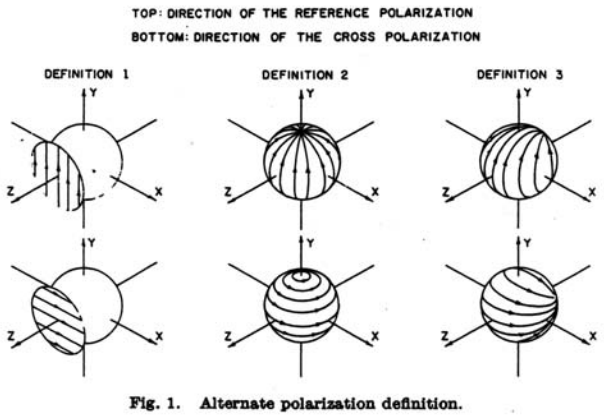

Figure 3. The three definitions of co- and cross-polarization according to Ludwig [2]. Picture worth thousand words.

But, if the definition of co- and cross-polarization over a finite angular extent is, to a degree, arbitrary, does it make sense to discuss the cross-polarization induced by an ideal grid? To help answer that question, we have evaluated the coupling between Cp and Xp belonging to different Ludwig definitions. This results in a 3x3 matrix of coupling maps. Along the diagonal, we have of course zero cross couplings between Cp and Xp belonging to the same definition; note that the matrix is *not* symmetrical. The strongest cross coupling is between Ludwig2 Cp and Ludwig1 Xp, shown on Figure 4. The 1/e angular extent of the intermediate beam (between M1 and M2) is ≈0.13rd, and at that radius, the cross-coupling is below –40dB. The Xpol level would be even lower if referred to the co-polarized beam on bore sight, rather than to its local value. The levels of Xpol that we will discuss in the next section are significantly higher, and therefore do not boil down to a matter of choice between Ludwig1/2/3.

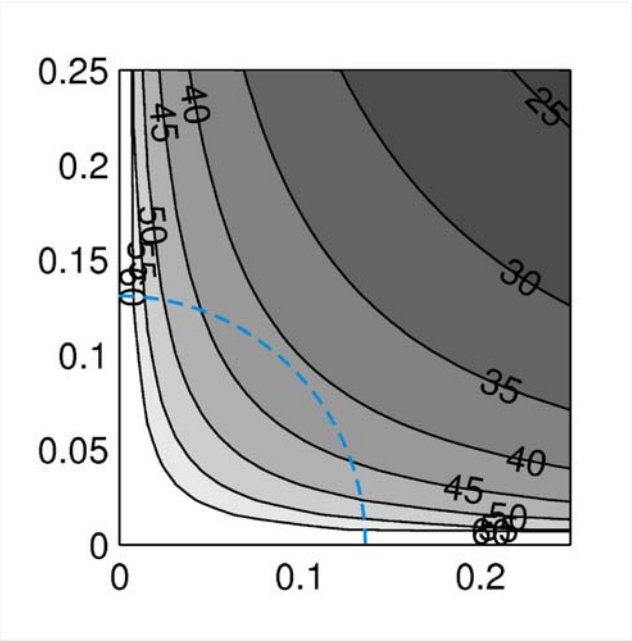

Figure 4. Isolation (dB) between Cp Ludwig2 and Xp Ludwig1. Coordinates are azimuth and elevation, in radians, with the origin at bore sight (chief ray). The 1/e angular radius of the Band 7 intermediate beam is shown (dotted blue). See text for discussion.

B. Cross polarization from an ideal grid

We have evaluated the cross polarization in the beam(s) emerging from the grid in the following way (transmitted beam):

a) Define the beam's waist size, and therefore its angular spectrum;
b) Along the direction of the chief ray, define Xpol as the projection of the grid wires onto the plane perpendicular to the chief ray, and Cpol perpendicular to the latter, in that same plane.
c) Set up a spherical coordinate system with polar origin along the chief ray; this defines, according to the Ludwig3 definition, the Xp and Cp vectors over the whole sphere.
d) Along any arbitrary direction, define the actual Xpol vector (as outlined above) and compute its coupling with the Ludwig3 definition of Cpol along the same direction.

With the grid in its original orientation, a maximum Xpol level of –23dB is obtained. See Figure 5. Note that Xp levels are referred to the *peak* Cp level. (We did not reach the –20dB specification, because of another, unrelated issue with birefringence in molded IR filters, that was addressed separately)

The dual-lobe pattern, provides evidence that the obtained Xp is unrelated to matters of definition (as discussed in the previous section), that are at a much lower level (<-40dB) and produce a four-lobe pattern.

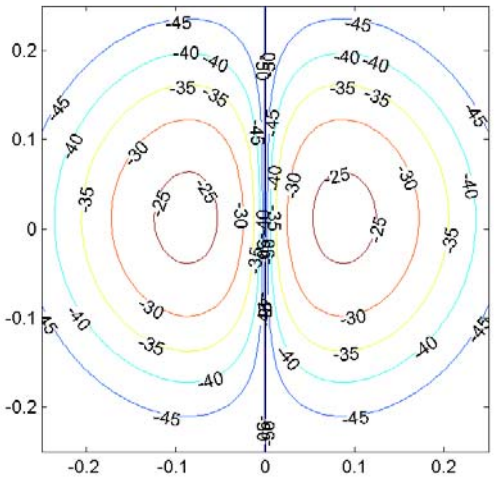

Figure 5. Xp levels in the intermediate beam after recombination by the grid, with grid in original orientation. Coordinates are radians

Following heuristic arguments, we determined that the Xp would be minimized with the grid oriented with its wires perpendicular to the beam's chief ray. This required turning the grid by 120.7° from its original position. Indeed, the same modeling calculation, for the new orientation, results in much lower Xp levels (and a 4-lobe pattern).

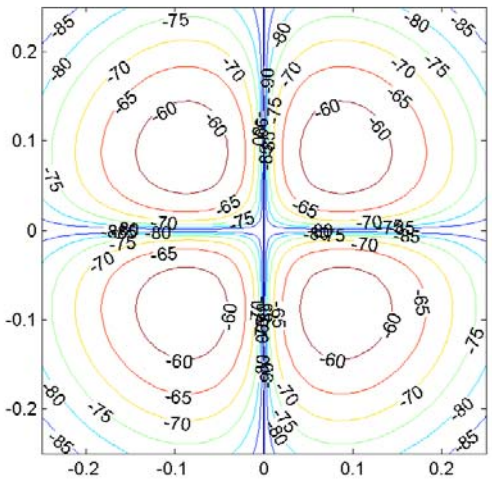

Figure 6. Same as previous, but with grid rotated 120.68° from its original position. The coordinate system is tied the Cp orientation, and therefore the figure does not reflect the change of Cp and Xp orientation.

V. Experimental Verification

We first show on Figure 7 the cross polarization measured for cartridge SN07, with the original grid orientation.

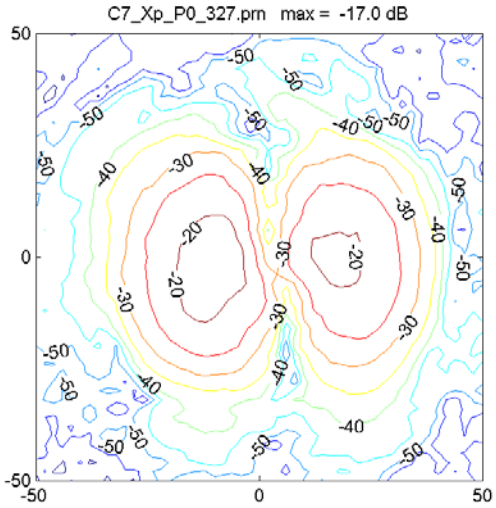

Figure 7. Level of Xp (relative to CP bore sight) measured for cartridge SN07, polarizarion channel 0, mid-band. Scan location is approximately 250mm past the Cassegrain plane. Coordinates are mm. Note similarity with Figure 5;

Implementing the modification required the following:

1. Changing the alignment pins to define the new grid orientation;
2. Adapting the mixers to the new polarization; this was achieved by integrating a 37° wave guide twist in the feed horns.
3. Adopting a new definition of the two polarization channels, as concerns the E-field orientation in the telescope frame; these were also rotated by 37°.

An example of the cross polarization performance of cartridge SN09 is shown on Figure 8. The Xp level is, in that particular instance, almost 7dB lower than previously.

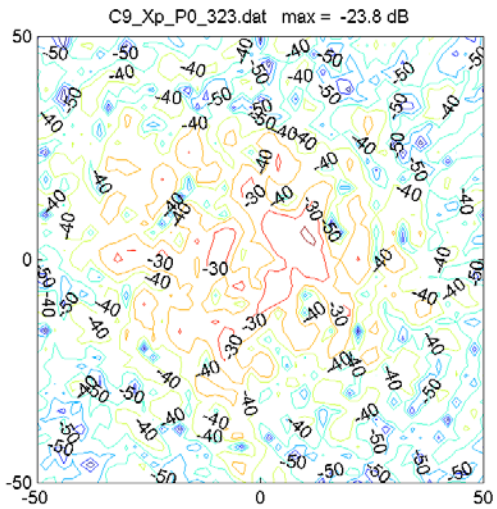

Figure 8. Same as previous, except Cartridge SN09, with modified grid orientation.

At present, a different metric is used by the ALMA project to characterize the cross-polarization: it is the integrated power over the telescope aperture. Because the Xp pattern (particularly after the modification) tends to have structure on smaller scale than the Cp pattern, that metric gives more favorable results. The nominal gain in the Xp performance, in that instance, is close to 8dB.

Table 1; Xp levels compared for cartridges SN07 (pre-modification) and SN09 (post-modification). The levels shown are based on the power integral over the pupil of the telescope.

	Xp level
C7 323 P0	-20.218
C7 323 P1	-20.155
C9 323 P0	-28.355
C9 323 P1	-28.814

VI. Re Inventing the Wheel

As most of the work described here had been completed, we became aware through IRAM colleagues of previous work [3] analyzing the same issue, with the conclusion that the wire grids should be perpendicular to the plane of incidence.

Acknowledgment

B. Lazareff thanks his IRAM colleagues C. Thum and D. Morris for mentioning the reference [3].

References

[1] J. A. Murphy, “Distortion of a simple Gaussian beam on reflection from off-axis ellipsoidal mirrors" International Journal of Infrared and Millimeter Waves, vol. 8, Sept. 1987, p. 1165-1187.

[2] A. C. Ludwig, "The definition of cross polarization" IEEE Transaction on Antennas and Propagation AP-21(1), 116-119, 1973..

[3] T. S. Chu, M. J. Gans, and W. E. Legg; "Quasi optical polarization diplexing of microwaves", The Bell System Technical Journal, 54, 10, 1975, pp1665-1680.

Some Experiments Concerning Resolution of 32 Sensors Passive 8 mm Wave Imaging System

A. Denisov, V.Gorishnyak, S.Kuzmin, V.Miklashevich, V.Obolonskv, V.Radzikhovsky, B.Shevchuk, B.Yshenko, V.Uliz'ko, J.Y.Son

***Abstract*—Passive 32-sensors imaging system operating in 8-mm waves band has been tested at SRC "Iceberg" over the last time. This system consists of the focal plane array connected with processor, quasi-optical antenna and scanning mechanism. The system provides the 120 x 16 degrees field-of-view, and displays the acquired image during 3 seconds.**

Sensitivity of the sensor in total power mode is better than 10 mK at integration time τ = 1 sec. It was necessary and interesting to evaluate some technical parameters, concerning the resolution on radio images. Some experiments performed by using the metal lists with sizes 1,25 m x 2,5 m and under the angles 25…70° to azimuth surrounded at the distance 500 m from passive imaging system.

***Index Terms* – Passive millimeter wave imaging systems, radiometer, resolution, sensitivity**

I. INTRODUCTION AND BACKGROUND

PASSIVE millimeter wave sensors provide the ability to see through fog, clouds, smoke and dust, drizzle, dry snow, smoke, and other obstacles makes the millimeter waves imaging systems the most efficient instrument to resolve a wide scope of problems which can't be solved with help of infrared and optic systems.

At the same time the absence of any active radiation as in radars can be used for the remote and invisible control of the neighborhood situation in case of enough small, middle and real distances. Reasonable to say this time there exists big boom in field of the design and production the various passive microwave systems [1, 2] for the finding the concealed objects under closing. Such devices have some the same technical task. Possibly it is necessary to remark that such systems for security will not find wide application according to short working distances, the presence of the special control chambers or the understanding about remote control.

In our opinion the real microwave remote systems for the security items will find the real wide application in case of the working distances not smaller than 10 meter (or more).

In this case it will be possible to provide some invisible control, don't think beforehand firstly about small size of system and to have enough safe distance. Naturally according to more big distance it will be necessary to use the receiving antenna with bigger diameter according to size of one pixel on the microwave image. At the same time reasonable to remove all unnecessary microwave losses before the sensors with best sensitivity and to use the radiometric scheme of the full power mode.

According to such preliminary analysis and our real current possibilities with 8 mm microwave components it was designed and produced the experimental system for the remote control of the neighborhood situation.

Manuscript received 19 April 2009. This work was supported in part by the joint scientific program between Ukraine and Republic of Korea

A. Denisov, V.Gorishnyak, S.Kuzmin, V.Miklashevich, V.Obolonskv, V.Radzikhovsky, B.Shevchuk, B.Yshenko, V.Uliz'ko are with the State Research Center of Superconductive Radioelectronics "Iceberg", Kiev, Ukraine, tel/fax: +(38-044)-526-54-54, e-mail:denisov@ukrpack.net

J.Y.Son is with the Hanyang and Daegu University, Kyungbuk(in Daegu), 712-714, Republic of Korea, Tel:. +(82-17)-232-57-91, e-mail: sjy5002@gmail.com)

II. RESULTS

The focal plane array is built on base of radiometric sensors [3,4], which are direct detection receivers with input low-noise amplifiers. The sensors operate in frequency band 33…38 GHz and have temperature sensitivity not worse than 10 mK/Hz$^{1/2}$ in total power mode. Small sizes of the sensors (14 x 14 x 80 mm) and stretched configuration provide its efficient packing into array. The array contains 32 sensors located in form of two vertical rows. Each row contains 16 sensors. The rows are shifted relative to each other in such way to form with antenna 32 beams, which will draw 32 strips during first scanning of array with antenna in horizontal direction and 64 strips after second (reverse) scan. The elevation angle of antenna with array changes at the end of the every horizontal scan on 120 °.

Multi-beams quasi-optical antenna consists of the main antenna and feeds located in focal plane of the main antenna. The prime-focus-fed parabolic reflector is used as main antenna. The reflector has diameter D = 900 mm providing the beam width near 0.6 degrees at 3 dB level. The focal length of antenna F = 990 mm, that satisfies to condition F/D $\geq$ 1 for multi-beams antennas.

As feeds the dielectric (ε = 2.1) rods antennas are used. This type of feed has smaller cross size compare with horn feeds that allow more compact to arrange the sensors in the array construction. Real construction has the sizes on Fig. 1.

Antenna with array is attached to the scanning mechanism; hitch provides the scanning of an antenna in the horizontal plane by angle ± 60°. At the end-points of each scan the calibration of the sensors is carried out. The calibration noise sources represent the quasi-optical wide aperture reference radiators which provide the calibration signals for the all

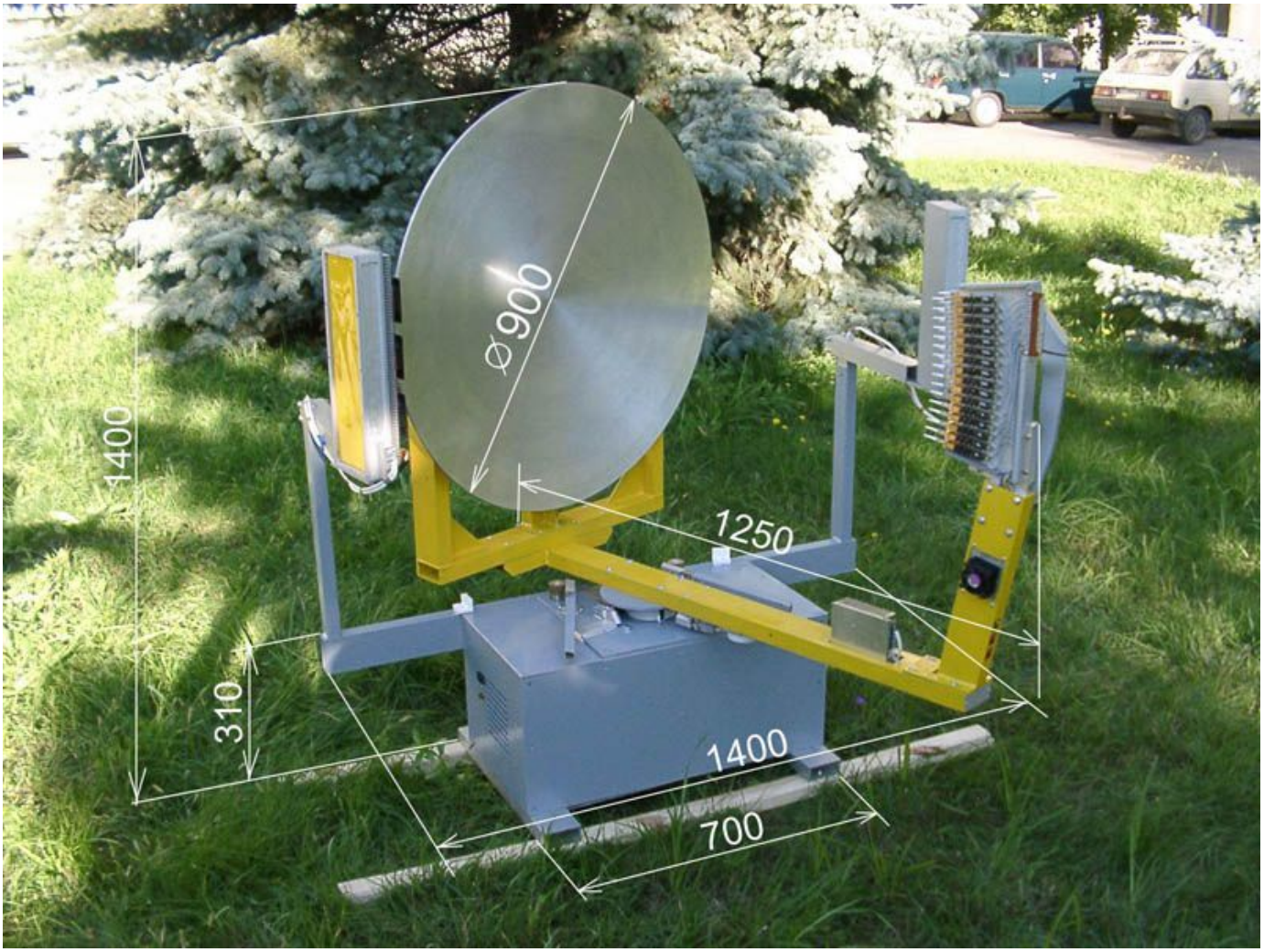

Fig.1 Passive 8 mm imaging system and her real sizes

receiving channels. The radio-absorbing material was used for the coating of the radiators. The standing-wave ratio of the quasi-optical reference source ("loading") does not exceed 1.15. Metallic plates inside of radiators is cooled till T_1 = 278 K (5 C) by means of the thermal-electric coolers or heated at T_2 = 323 K (50 C) with an accuracy ± 0,1 K with help of the electronic unit of the temperature stabilization. The calibration reference sources were mounted on the fixed section of the system in such way that at the beginning of the each antenna scan "cold" and "hot" reference overlaps all feeds in the calibration parts of the scanning sector.

During the scan, each beam draws the horizontal strip, and thus all observed scene find itself completely covered by beams. The scanning mechanism includes the optical sensor of the angle, which gives information about the antenna position in any time during the system operation. The reading of the signals is carried out through each 0.17 degree (1 pixel) in full angle of view in the horizontal plane 120 °.

The scanning mechanism is designed on the base of the usual asynchronous three-phase motor. The axis of the motor is mounted vertical. The antenna with array is mounted on the motor's axis.

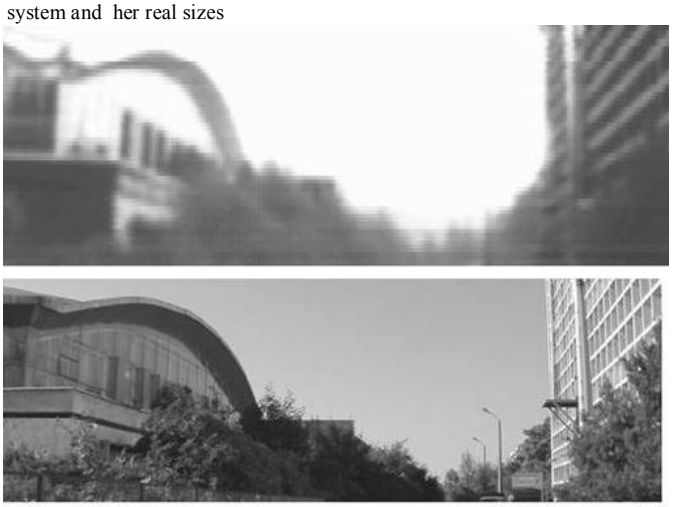

Fig.2 Buildings near the SRC "Iceberg" - 8 mm image and optical

Power applies to a motor from converter, which transforms a single-phase voltage (220 V) into three-phase pulse-duration voltage. The converter is controlled from the computer and provides switch-on and switch-off operations of the motor, the smooth stop and reverse. In order to facilitate a

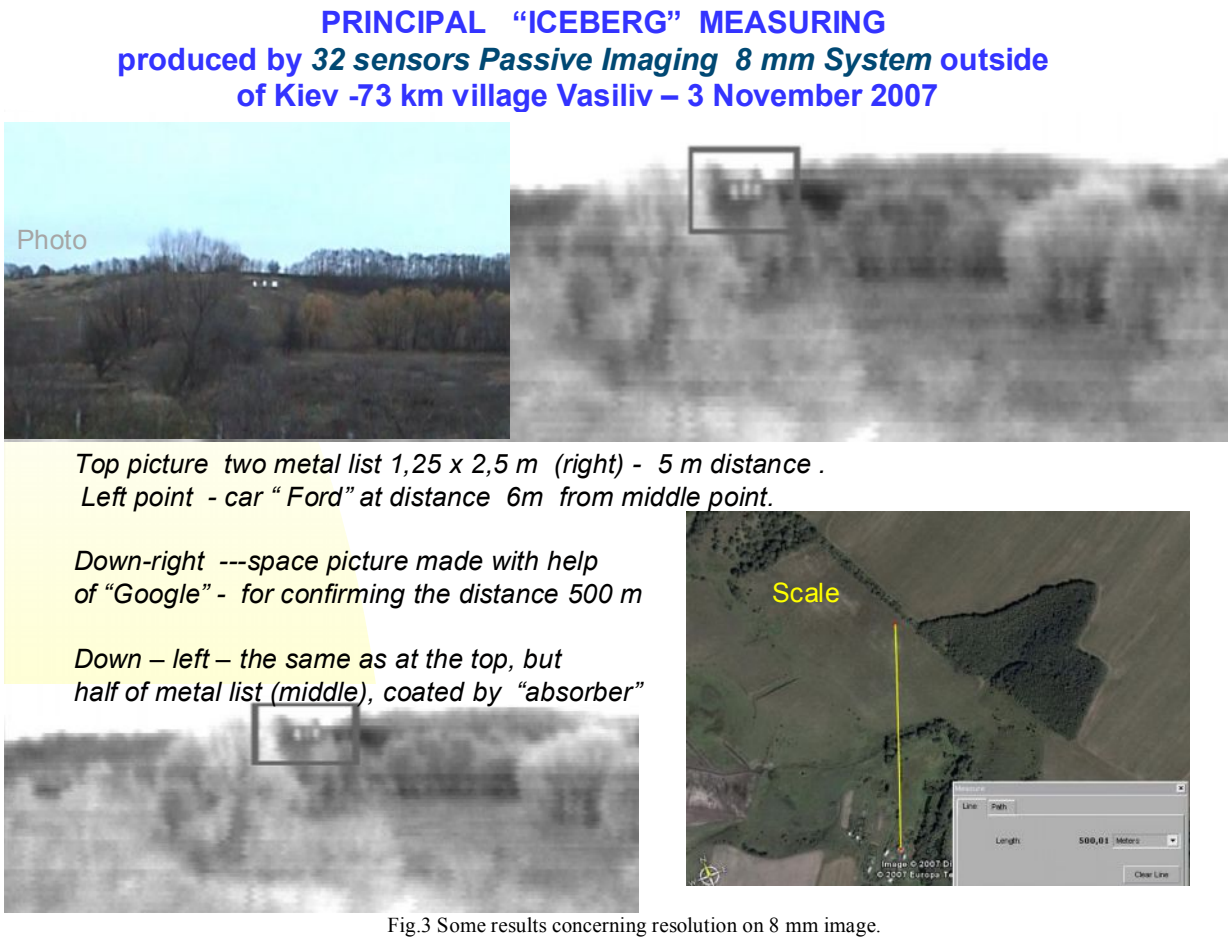

Fig.3 Some results concerning resolution on 8 mm image.

Fig.4 From the top of building. Optical and the same 8 mm images

load onto the motor at time of reverse the special springs are used. On practice the current is not going to the motor during the time of reverse.

Real 8 mm images cut off to the same size of optical image presented on fig.2…4. According to high sensitivity of sensors it was possible to register the some active radiation from some places of city (darkest places on Fig.4) where the retransmitted stations for mobile phone are surrounded – possibly it is the harmonics of main frequency. This technical possibility can be really used for the ecological and electromagnetic radiation dirty control.

It was interesting to evaluate some technical parameters, concerning the resolution on radio image which were evaluated with the help of metal lists with sizes 1,25 m X 2,5 m and the angles 25…70 ^{o} to azimuth surrounded at the distance 500 m from passive imaging system. This results presented on Fig.3. Reasonable to remark the theoretical evaluation the possibility to see the small size metal object under our technical conditions are poor than experimental one.

III. CONCLUSION

Passive 32-sensors imaging system operating in 8-mm waves band has been tested and provided the 120 ^{o} x 16 ^{o} field-of-view, and displays the acquired image during 3 seconds. This time there exists the technical decisions for the design the imaging system which can provide 360 ^{o} image at the same time in 8 and 3 mm wave bands.

REFERENCES

[1] J.M.Chamberlain "Developments in PMMW and THz imaging", Proc. of SPIE, vol.5619, pp.1-15, 2004

[2] http://www.brijot.com, http://www.sago.com, http://www.millivision.com, http:// www.thruvision.com, http://www.xytrans.com

[3] V.N.Radzikhovsky, V.P.Gorishniak, S.E.Kuzmin, B.M.Shevchuk, "16-channels millimeter-waves radiometric imaging system", MSMW'2001 . Symposium Proceedings. Kharkov, Ukraine, June 4-9, pp.

[4] V. Gorishnyak, A.Denisov, S.Kuzmin, V. Radzikhovsky, B.Shevchuk "8 mm Passive Ima ging System with 32 channels" , EurRAD , Amsterdam, Netherland, 2-14 October, 2004

A Single 30 cm Aperture Antenna Design for The Operation of 2 Widely Separated Frequency Bands for the Active Temperature, Ozone and Moisture Microwave Spectrometer (ATOMMS)

Sarmad. H. AlBanna, Chris Groppi, Chris Walker, Michael Schein, Steve Bell, Brian Wheelwright, Christian Drouet d'Aubigny, Abram Young, Dathon Golish, E. Robert Kursinski, Angel Otarola, Dale Ward, Kate Sammler, Willy Bertiger, Mark Miller, Herb Pickett

Abstract—***The Active Temperature Ozone and Moisture Microwave Spectrometer (ATOMMS) is an active aircraft to aircraft remote sensing occultation instrument that is designed to accurately measure the vertically resolved profiles of temperature, pressure, density, water and ozone content of the atmosphere. It uses a complimentary set of microwave transmitters and receivers in ~22 GHz and ~183 GHz water bands installed in each aircraft to measure the absorption of water and ozone as a function of altitude. Space constraints prevent the use of two separate antennas for each of these bands, so a single, dual frequency antenna system has been designed to simultaneously transmit and receive these two widely spaced frequency bands. This paper presents a detailed design of a HDPE anti-reflection grooved lens antenna that is illuminated by 2 separate, coaxially mounted feed horns for the two different frequency bands. We present the design, optimization and initial testing of the feed and lens system***.

***Index Terms*—Beam waist, Corrugated Feed Horn, Edge Taper,**

Manuscript received 26 May 2009.

Sarmad H. Albanna (Electrical Engineer & a PhD Graduate student the college of Optical Science University of Arizona Tucson AZ 85721 USA (520-626-0226; fax: 520-621-1632; e-mail: salbanna@as.arizona.edu)

C. Groppi (NSF Astronomy and Astrophysics Postdoctoral Fellow), M. Schein, B. Wheelwright and S. Bell are with Steward Observatory, University of Arizona, Tucson, AZ 85721 USA (520-626-1627; fax: 520-621-1532; e-mail: cgroppi@as.arizona.edu).

E.R. Kursinski, D. Ward, A. Otarola and K. Sammler are with the Department of Atmospheric Sciences, University of Arizona, Tucson AZ 85721.

Christian Drouet d'Aubigny Abe Young, and Dathon Golish are with TeraVision Inc, Tucson AZ.

W. Bertiger, M. Miller and H. Picket are with the NASA Jet Propulsion Laboratory, Pasadena, CA 90220 USA.

V. INTRODUCTION

The current water vapor and temperature remote sensing Earth systems do not provide accurate, complete, nor enough data sufficient to better understand and characterize our rapidly changing climate. Each present global observation system has its own measurements limitations. At the same time they all share their biased estimates of water vapor, oxygen, and O_3 distributions and densities. The current global observing system is not able to keep up with our rapidly changing climate, and its evolving climate processes.

According to the National Academy Reports [1], it is crucial to ensure the existence of a long-term more definite observing system of variables such as temperature, precipitation, humidity, pressure, clouds and turbulence. Such systems should be able to provide a 10-100 years scale of variability and change. These set of systems should also be able to break the ambiguity of wet and dry components, as is the case for the existing GPS Radio Occultation systems, via measuring of the absorption of water-vapor, reduce ionospheric sensitivity with the use of much higher frequencies, eliminate the need of using boundary conditions and weighting factors of middle atmosphere climatology, and profile other constituents such as O_3 via absorption. Reference [2] covers in details the global measuring systems that are operating today and their limitations. The ATOMMS instrument remote sensor will bring unique new capabilities in vertical resolution, accuracy, to the global observation measurement techniques [3].

ATOMMS is an active orbiting limb-viewing spectrometer that combines the strengths of both the GPS Radio Occultation and the NASA Microwave Limb Sounder (MLS) system. With ATOMMS, the atmosphere constituent's absorbing lines are actively probed in two different microwave bands (22 GHz and 183 GHz) where there are strong water absorbing lines. With the support from NASA and NSF, and some support

from JPL, the ATOMMS group at the University of Arizona has been developing the prototype ATOMMS instrument. A prototype proof of concept instrument will be flown in specially reengineered NASA WB-57 aircraft [4]. The noses of these aircrafts have been modified such that they can carry instrumentation for weather observation in their WAVE (WB-57F Ascent Video Experiment) gimbal system. The 3 beams from the microwave transmitting and receiving bands will enter and exit the gimbal through a microwave transparent radome that will replace the front skin and optical window of the WAVE System. C. Groppi in this proceeding [5], provides a very good description of the WAVE system, the pointing operations when used for ATOMMS, a detailed description of the overall operation of the ATOMMS instrument, system architecture, electronic design and the live data recording system. Figure (2) shows one of the fully assembled ATOMMS instrument (ATOMMS A) that carries 2 microwave transmitting bands 13 GHz, and a 22 GHz band which consists of 8 fixed tones about 1 GHz wide and separated by 1 GHz spacing, as well as a receiving band at 183 GHz that includes 2 tunable tones. The second ATOMMS instrument (ATOMMS B) carries the complimentary receiver and transmitters for ATOMMS A. The 13 GHz system is a dual transmit receive system included in both instruments and is used for calibration, referencing and to provide relative phase measurement in the lower troposphere where 183 GHz signal doesn't penetrate. A detailed link budget has been developed for all the bands to simulate and or calculate the power levels at every point in the system using realistic antenna parameters and estimated losses. The specifications of all the microwave components have been derived using the link budget. Table 1 shows some of the link budget obtained parameters for the 200 GHz and 22 GHz band transmissions.

In an active sounding system such as ATOMMS, a vertical profile of the air index of refraction is obtained from the vertical profile of bending angle by means of an Abel transform [6]. The bending angle is derived from the atmospheric Doppler frequency that gets computed from the difference between the measured Doppler shift and the Doppler shift that could have been observed in the absence of the atmospheric along the signal's path.

Table 1: ATOMMS Link Budget

Symbol	Quantity description	Values
$L_{path\_200GHz\ (dB)}$ (100 km)	Free space path loss	177.5 dB for 200 GHz band 160 dB for 22 GHz band
G_{Tx}, G_{Rx}	Transmitting or Receiving antenna Gain	$G_{Rx/Tx\text{-}200GHz}$=50 dB $G_{Rx/Tx\text{-}22GHz}$=34 dB
SNR	Receiver Signal to noise ratio	$SNR_{200\ GHz}$=36.7 dB (400 KHz Bandwidth SNR_{22GHz}= 55.3 dB (50 KHz Bandwidth)

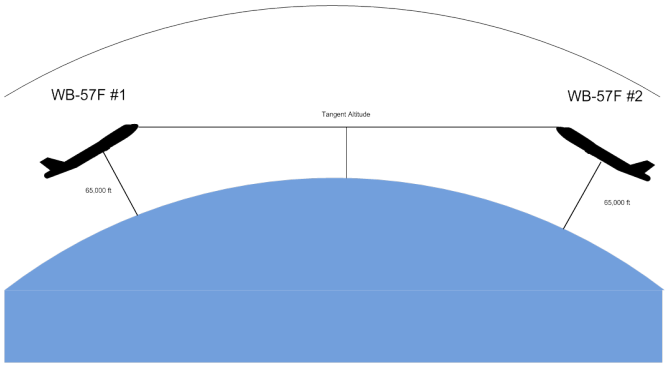

Figure 1 Aircraft to aircraft simplified occultation geometry

All the received tone's amplitudes and frequencies are derived from post processing, and by using a complete retrieval system that is under development we will be able to determine within ~100 m resolution the densities of water vapor, O_3 and the index of refraction at these higher resolution altitudes.

One of the biggest challenges of the ATOMMS prototype is antenna pointing. In order to achieve high SNR with low transmitted power, directional antennas are needed. This paper focuses on the quasi-optics subsystems and lens antenna design that plays the important role in focusing and collimating the transmitting and receiving beams.

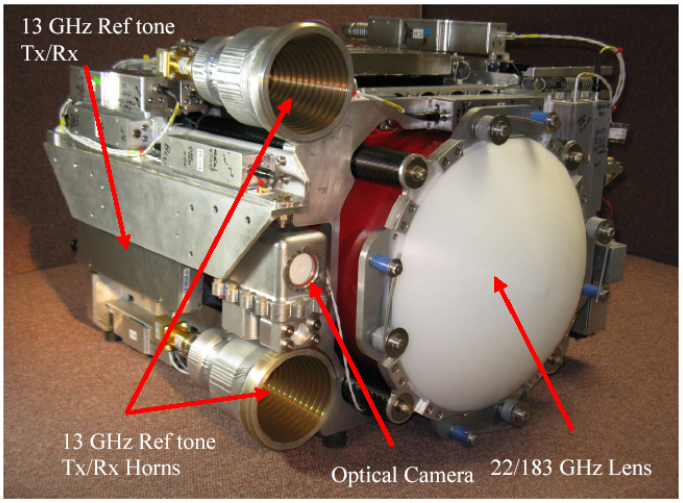

Figure 2 The ATOMMS instrument showing the 30 cm Antenna Lens and the 13 GHz TX and RX feed-horns.

VI. ATOMMS QUASIOPTICS SUBSYSTEM

The goal of the quasioptics subsystem is to produce two coaxial collimated beams using a single lens antenna. The performance was optimized for the 200 GHz such that the 22 GHz system didn't suffer from too much losses. The limited space inside the gimbal system put some constraint on the design options for the quasioptics. For example, it would have been easier to design the system such that the 22 GHz and the 200 GHz had their own separate feed and antenna, or to use reflective based antennas. In our case we employed the configuration shown in Figure (3) where the 2 feed-horns (FHs) are coaxially placed, separated by the total length of the 200 GHz FH and the polarizer that is attached to it. The FHs

are designed to symmetrically illuminate their beams into a single common refractive lens antenna. This configuration causes an obscuration of the 22 GHz beam by the 200 GHz FH and the plastic spider that holds it. The impact on the system performance will be addressed in a future section. The maximum allowed space for a lens to fit in that small geometry is about 40 cm. However, as a first step in the design, a lens of diameter D= 30 cm was chosen, since it is a standard size commonly used in the past, especially in the satellite industry. Free space Gaussian beam propagation theory has been used to analyze the beam propagation entering or existing the FHs and the lens antenna assembly. Since we illuminate the lens symmetrically, conical FHs are used with corrugations to minimize the VSWR. Corrugated conical FHs generate a balanced hybrid mode (HE11) if they are sufficiently large such that $2\pi a/\lambda > 1$, where a is the largest dimension of the source of radiation which is estimated to be 1.7cm for the case of this design. The HE11 modes have field distributions that are azimuthally symmetric and are uniformly polarized. The axial symmetry of the field distribution provides an excellent coupling to the lowest Gauss-Laguerre beam mode (m=0). A maximum power coupling ratio $|c_o|^2$ of 98% of the fundamental mode of Gaussian beam and HE11 mode can be achieved if beam radius w is equal to 0.644a of, where a here is the diameter of the FH. Some of the design guidelines used in this paper have been well researched and well established in the literature, such as the coupling of Gaussian beam into the radiating elements is well covered in chapter 7 in [7].

The following sections will show the steps taken for the design of the on-axis Gaussian beam parameters for the 22 and 200 GHz bands. Once that is done the specifications for the FH are chosen, basic type of antenna choice is made with estimated losses associated with it. We used ray tracing with (Zemax) in order to optimize the spot size at focus.

A. 200 GHz Quasi-optics system

One of the 200 GHz science requirements is to meet a pointing accuracy between the two aircraft of 0.5°. Roughly speaking that forces the diameter of the lens antenna to be 15 cm. Since we are using a 30 cm diameter lens, the 200 GHz FH is used to illuminate the lens with very large edge taper producing a beam size roughly equivalent to uniformly illuminating a 15 cm lens. Using $G_{193.5G}=20\log(\pi D/\lambda)$ with D=15cm, and $G_{193.5G}$=49.66 dB, the 1-D HPBW is determined from (1) [8]:

$$G_{193.5G} \sim 30'000/(\phi_x.\phi_y) \quad (1)$$

$\phi_x=\phi_y=0.57^o$ for symmetrical antenna illumination.
The 1-D edge taper (T_e) defines the normalized E-field at the antenna with respect to its aperture radius [9].

$$T_e\,(\text{dB}) = [\phi\,(\text{in rad})/(\lambda/D) - 1.02]/0.0135 \quad (2)$$

From equation (2), T_e is found to be 67 dB. From the T_e we determine all the parameters of the Gaussian beam propagation at the lens, and propagating the beam backward to the FH to determine the beam waist w_o. The beam radius at the antenna aperture is easily calculated also from [9].

$$\alpha = 0.115 * T_e\,(\text{dB}) = (r_a/w_a)^2 \quad (3)$$

For 1-D, w_a= 5.4 cm**,** and selecting an initial distance from the FH to the back surface of the antenna to be $z_{193.5G}$=12.1"= 30.73 cm, we can solve for w_o, and then for z_0 using (4) and (5):

$$z_o = \pi w_o^2/\lambda_{193.5G} \quad (4)$$

$$w(z)^2 = w_o^2[1+(z/z_0)^2] \quad (5)$$

$$R_{193.5G} = Z_{193.5G}\,(1+(\pi w_{o\_193.5G}^2/(\lambda_{193.5G} Z_{193.5G})^2) \quad (6)$$

$$\theta_o \cong 1.18\frac{\lambda}{\pi\omega_o} \quad (7)$$

Where z=0 plane is defined to be z_o a distance away from the aperture of the FH.

z_o = confocal distance (Rayleigh length)=14.9 mm.
w_o= beam waist=2.701mm (where the E- field is at maximum) and the wave front is flat (or plane) and the on-axis phase shift ϕ_o is 0.
$R_{193.5G}$ =31.46 cm at the back surface of the lens (at z = $z_{193.5G}$= 30.734 cm away from the 200 GHz FH.
$\theta_o \cong 12.4^o$ is the far-field divergence angle.
In most quasi-optics system designs it is important to address the location of the phase center of the beam with respect to the FH aperture Δpc (offset of the phase center relative to the beam waist) [7]

$$\Delta pc = -\frac{(\pi\omega_o^2/\lambda)^2}{z} \quad (8)$$

$$z = \frac{R_h}{1+[\lambda R_h/\pi(0.644a)^2]^2} \quad (9)$$

R_h is the slant length of the FH. Δ_{pc} becomes more important if higher modes of the Gaussian beams are included in the design. The calculated value for Δ_{pc} was ~ 1.11 cm.

Typically the E-field that excites the waveguide feeding into the FH is linearly polarized, however in order to minimize the losses due to the relative orientation between the 2 aircrafts while in the air, we chose to have a circular polarizer to be placed between the waveguide and the FH, the output then is RHC (Right Hand Circular) for one of the instrument and LHC (Left Hand Circular) on the other one. Adding the polarizer makes the total length of the assembly to be 6.06 cm, which causes the 22 GHz band FH to be placed at least 6.06 cm behind the 200 GHz FH. Since the transmitted and the received power through the 22 GHz system are considerably higher than those of the 200 GHz system, it was important to make sure that the lens antenna was designed to have maximum gain and minimum losses at the 200 GHz center band. Consequently, the 22 GHz signal will see more losses, both due to the FH blockage and due to the defocusing of the lens. However as mentioned earlier, these losses can be mitigated by increasing the transmitter power.

The output beam waist (w_{out}) and the distance from the system output plane to the output beam waist are calculated using Gaussian beam transformation method. Since $z_{in}=f=30.73cm$ (the beam waist is located at the front focal plane), $z_{out}=f$ (output beam waist (image waist) is found to be at the back focal plane of the lens with w_{out}=5.37 cm. This is very different from the imaging in geometric optics, since we expect placing a source at the front focal plane would produce and image at infinity. The Gaussian beam will behave much more like a spherical wave if z_o/z approaches 0, or $z>>z_o$. As a result the output divergence angle is found to be close to 0.5°, and the output beam is for the most part is collimated. Also $z_{o\_200Gout}$=5.89 m with system magnification at maximum M_{max}=20.

B. 22 GHz Quasi-optics system

As a first step, in the evaluation of 22 GHz quasi–optic system design, we used CST microwave to simulate a simplified version of the system. Here, we were interested in examining the quality of the 22 GHz beam pattern in the far-field region when the spider and the 200 GHz FH obscuration are placed 6.06 cm in front of the 22 GHz feed. In order to simplify and shorten the simulation, a smooth walled FH model was used rather than corrugated horn such as the one that is used in the actual system. The spider was added (without the 200 GHz FH), Microwave absorbers [MODEL ECCOSORB MFS-124] will be added in the real system to minimize reflections inside the 22 GHz beam path in particular, and reduce unwanted reflections in general. The dimensions of the 22 GHz FH were estimated for 22.5 GHz excitation. Figure (3) shows the simplified geometry used without including the 183 GHz FH.

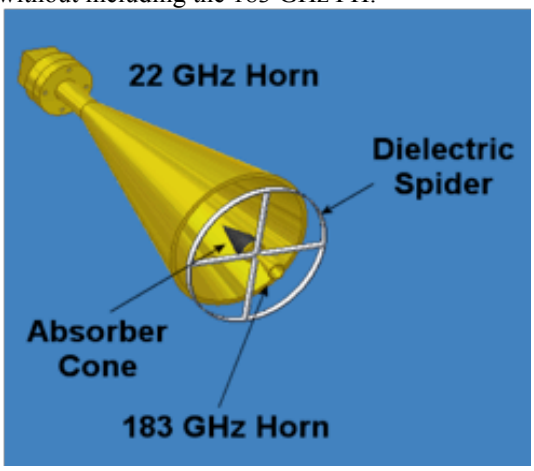

Figure 3: The simplified quasi-optics system diagram showing both the 22GHz & 200 GHz FHs, 30 cm lens antenna, a dielectric spider and absorber cone.

Figure (4) shows the 22 GHz FH E and H-plane beam patterns, at the spider legs and 45° away from spider legs. The dotted and solid lines represent the orthogonal polarization patterns (E & H-planes). While the 22 GHz beam pattern is degraded by the presence of the spider and the central blockage, the overall system performance is still very good, thanks to the amount of transmitted power at 22 GHz (~100 mW per tone). The Gaussian beam propagation calculation for the 200 GHz system was repeated here for the 22 GHz with a few differences. Assuming 0.55 aperture efficiency, the gain of the circular lens antenna at the middle of the 22 GHz band is 34 dB using (10).

$$G \approx 10 \log [0.55(\pi D/\lambda)^2] \quad (10)$$

Using, the same Gaussian propagation equations for one dimension we find that for the 22 GHz beam, $\phi_x=\phi_y=3.304^o$, T_e= 20.5 dB, w_a= 9.99 cm at the antenna back surface. At z_{22G}=36.79 cm (30.73+6.06cm) away from the lens, $w_{o\text{-}22G}$ =1.58 cm, $z_{o\text{-}22G}$= 5.9 cm, and the radius of curvature at the back surface of the lens is R_{22GHz} =36.92 cm, $\theta_o \cong 18.2^o$.

C. Lens selection and Zemax simulation

The distance between the 2 aircrafts is very large (from 20 km to 1000 Km). With this configuration modeled as having a point source at a vey large distance such that received waves behave like plane waves ($R_{in}\sim\infty$). We use a single lens to focus the incoming beam to a smallest spot possible at the 200 GHz FH aperture. Using the thin lens equation below:

$$1/R_{out\_200GHz} = 1/R_{in\_200GHz} + 1/f_{200GHz} \quad (11)$$

$R_{out\_200G}=f_{200G}$=30.79 cm. Since we are interested in a simple, low-cost design, low absorption loss, therefore the smallest central thickness is desired. However, at the same time the material of the lens needs to be hard, mechanically stable, relatively inexpensive for higher altitude environment, cheap and easy to machine. At first two materials were considered, Rexolite (n=1.59 @ 200 GHz), and HDPE [8] (n=1.529). Rexolite was found to have high losses (close to 4.8 dB for a center thickness t_c =6.5 cm), therefore HDPE (High Density Polyethylene) was chosen as the basis of the lens design. The estimated absorption losses of < 1 dB for the same t_c. At first our model used values of index of refraction found in the literature [10]. We were then able to use empirical values based on an in-house index of refraction measurement of samples of the actual material the lens was fabricated from. Using Time Domain Spectroscopy (TDS) techniques for 30 samples the average measured n at 193.5GHz was=1.520 with maximum sample-to-sample measuring error of 0.092%.

The empirically obtained index of refraction was used to improve the Zemax lens design parameters. Spherical-plano shaped lenses were avoided for this application as they tend to be thicker (t_c=10.85 cm) compared to hyperbolic-plano lens designs. In a first step we optimized the lens design for the 200 GHz beam only without including the 22.5 GHz beam. The optimization criteria chosen were: First, to achieve the smallest focused spot size, and second, to achieve the lowest optical path difference (OPD) with respect to the chief ray in the y direction (the x- directions results are identical), all this while keeping the thickness as small as possible, and therefore minimizing transmission loss. . The optimized spot size, and the OPD are shown in figure (5) top and bottom, respectively. Previously, the estimated aperture diameter of the 200 GHz FH was 11.36 mm.

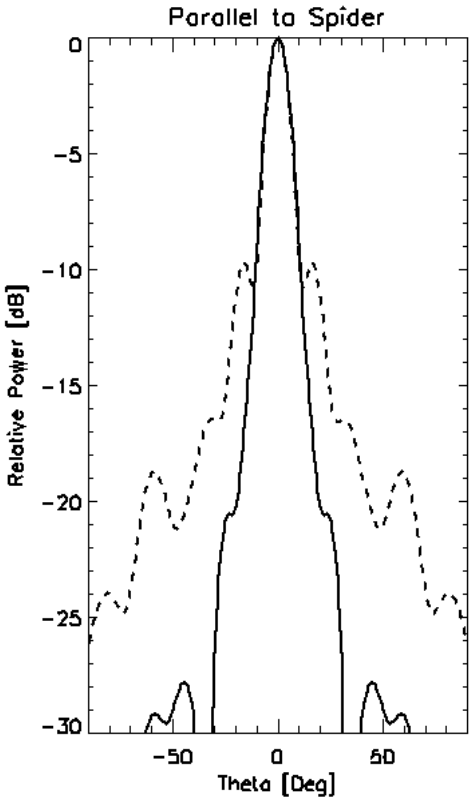

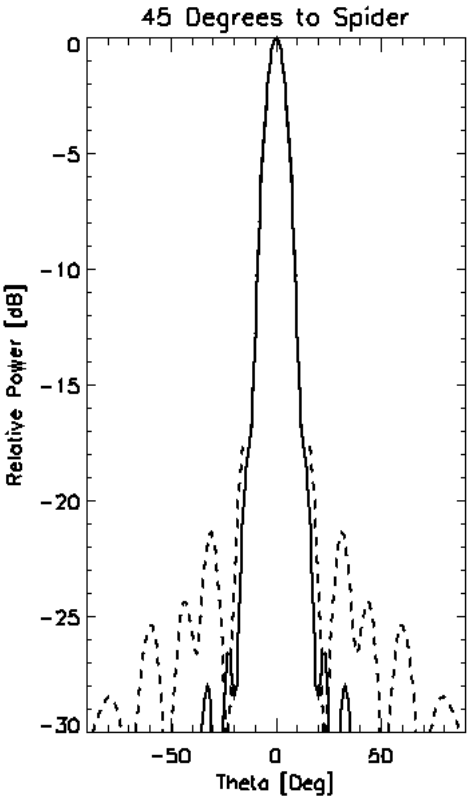

Figure 4: E & H-field beam pattern (solid and dotted line respectively), with respect to the angle θ, with θ=0 (top) (parallel to the dielectric spider), and 45° tilt away from it (bottom).

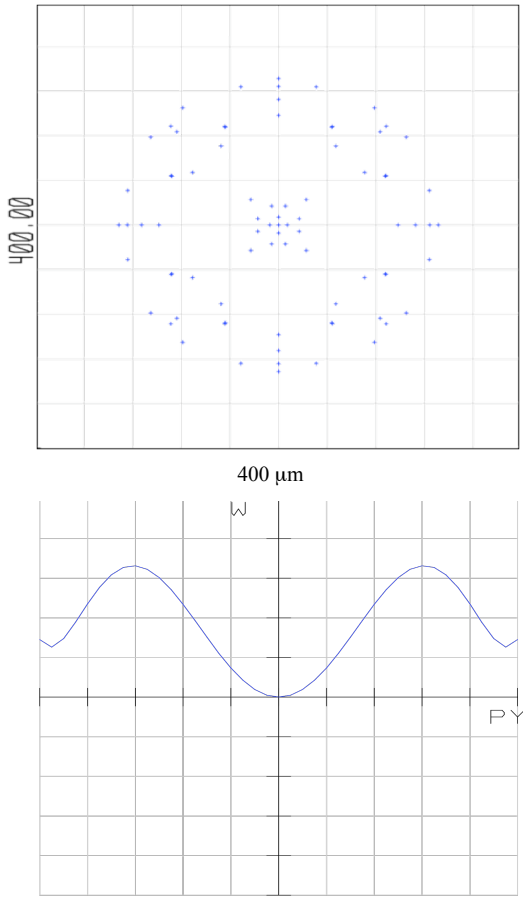

Figure 5**:** The spot size in in μm at the 200 GHz FH aperture (top), 40 μm/div and the optical path difference (bottom) with respect to chief ray in waves at the wavelength of 0.155 cm.

The design and manufacturing of the FHs were done by Quinstar microwave after providing them with required Gaussian beam paramteres. A spot size of ~260μm is well centered within the 10.58 mm diameter of the FH. The optimum value of the central thickness of the lens was 7.5 cm. The first Zemax optimization for the 200 GHz beam caused the incoming 22 GHz beam to be focused at ~ 5.3 cm to the right of the 22 GHz FH aperture, which caused the 22 GHz system to operate in a defocused mode. The antenna gain reduction due to the defocus can easily be calculated using (12) in [9].

$$\varepsilon_a(\delta) = \frac{\varepsilon_a(0)}{1 + (\delta / z_o)} \tag{12}$$

Where $\varepsilon_a(\delta)$ is the antenna efficiency for a Gaussian illuminated beam with a defocusing distance of δ=5.3cm, and $\varepsilon_a(0)$ is the antenna efficiency when the Gaussian beam is in focus. The defocusing losses becomes 10 log $(\varepsilon_a(\delta)/\varepsilon_a(0))$ which results to about 2.3 dB gain reduction. As mentioned earlier, the losses in the 22.5 GHz system are easily compensated by the provided extra gain provided through various attenuators placed in the 200 GHz microwave chain. The resulting defocused beam radius centered at the edge of the 22 GHz FH is obtained to be w_{22Gnew}= 2.24 cm, indicating

a growth of only 6.5 mm from its $w_{o\ 22G}$ location. After a sequence of design optimization in Zemax, the resulting lens surface produced fits exactly polynomial of the 10th degree.

III. Loss Calculation & measurments

Since the goal of this design is to balance the performance of the 200 GHz system with that of the 22 GHz system, we designed and produced an AR-layer in the two lens surfaces to reduce reflections of the 200 GHz transmitted and received beams. Our approach has well been established and has been used for many years in radio astronomy [11]. The method involves machining circular grooves in the two surfaces such that the resulting surfaces acts like a matching layer with an effective index of refraction n_{eff}, such that $n_{eff} \sim n^{1/2}$. This procedure provides better matching impedance to free space resulting in a reduction of reflection loss. For frequencies up to 400 GHz, grooving the surfaces with circular grooves is done via micro machining with a CNC milling. This method creates a well-defined topologies with depth $d=\lambda/4n^{1/2}$ depth and pitch values, and a filling factor that determines the value of the n_{eff}. In [12] and [13] 1-D structures have been investigated and used in the past such as rectangular, multi-step, or sine wave-grooves, and 2-D structures are also known with structures like rectangles and holes. 1-D structures are more likely to be polarization dependent and might be birefringent than 2-D structures. The design selections for the groove's specific pitch, depth and filling factor were done by studying examples in the listed literature as well as by using the program "SCATTER " written by R. Padman [14]. Reflection losses for a single surface dielectric material can be expressed for normal incident as in (13):

$$L_{Ref}(dB) = 10\log\left(\frac{(n-1)^2}{(n+1)^2}\right) \qquad (13)$$

Calculating L_{Ref} show that for n=1.52, $L_{Ref\_ungrooved}$ =-13.7 dB, however for a grooved surface with estimated $n_{eff}= n^{1/2}$=1.23, $L_{Ref\_grooved}$= -19.7 dB. The above calculation ignores the effect of variation of index of refraction with frequency, which will have small impact on the calculated reflection. The effect of the second surface reflectance is also small compared to the material loss for a center thickness of d=7.6 cm. In order to count for the 2nd surface reflection, we reduced and suitably parameterized eq (59) in [15] for normal incident in air media ($n_1=n_3=1$), which resulted in $L_{Ref\_2surf\_ungrooved} \cong$-14 dB, and $L_{Ref\_2surf\_grooved}$ = -19.75 dB. From the reported values of loss tangent tan(δ) for dielectric materials, its found to be ≅ 4e-4 for HDPE. The resulting material attenuation loss for a 7.6 cm thick is found to be -0.85 dB at 183 GHz and -0.94 dB at 203 GHz, which is much larger than the extra loss added due to the 2nd surface reflection. The result of the averaged through transmission and material loss of simulating two grooved surfaces sandwiching the lens material using program "SCATTER " with thickness of 6.4 cm is shown in Figure (6).

The total transmission T_{total}, where $T_{total} = T_{surface1or2}^2 + A$ (the material loss =-0.85 dB) is found to be -0.92 dB at 183 GHz. Therefore $T_{surface1or2}$ is found to be 0.992. The reflection of a single grooved surface based on R=1-T is then ≅ -20.9 dB. Repeating the same calculations for f=203 GHz results in a single surface reflection -19.34 dB. The simulation and the earlier calculations above are in a very good agreement showing approximately an average reduction in reflection of about ≅ 6 dB. The concentric lines of grooves were applied to the center of the two surfaces of the lens up to r=15 cm, since the main lobe of the 200 GHz beam will be centered on that area. Comparative reflection measurement was performed using a THz Time Domain Spectroscopy (THz-TDS) system. In THz-TDS ultra short pulses are generated that last only a few picoseconds. Each pulse creates broadband radiation from 0.05 to 2 THz. At the receiver the E-field of the terahertz pulse is sampled and digitized. A delayed femtosecond optical pulse gates the receiving dipole antenna "ON" through an identical LT-GaAs semiconductor. By repeating this procedure and varying the delay of the gating laser pulse, it is possible to scan the THz pulse and construct its E-field as a function of time with 0.1picosecond resolution over a 1 nanosecond time period. Subsequently, a Fourier transform is used to extract the frequency spectrum from the time-domain data. THz TDS was used to measure the reflection of the grooved lens surfaces as shown in Figure (7).

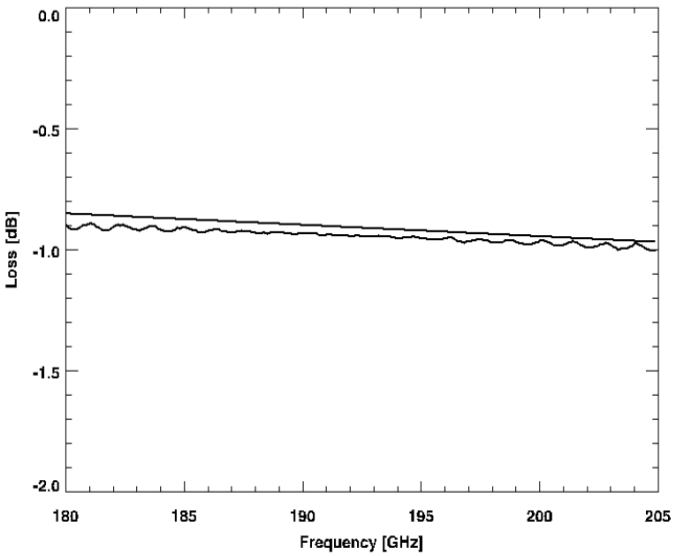

Figure 6: Reflection and absorption losses versus frequency for a grooved HDPE lens with n=1.52. The straight line is just the material losses, and the Fabry-Perot reflection line is material losses plus reflection losses, simulated using program "SCATTER " written by R. Padman [13].

The linearly polarized in the x-direction THz E-field beam is propagated through the Polarization Beam Splitter (PBS), and a Quarter Wave Plate (QWP) that changes the Polarization from linear to circular. As the beam reflects back from the lens surface, the incident circularly polarized beam changes its handedness. By the time it pass through the QWP in the second pass, it become linearly polarized in the same plane as the wires of the PBS such that it reflects into the THz Rx. In this experiment the QWP used was centered at ≅ 350 GHz, which will make the polarization more elliptical rather than linear, which could introduce some coupling and or cross polarization losses into the receiver. The results of the reflection measurements are shown in Figure (8). The red curve represents the reflection coefficient of the grooved surface and the blue for the un-grooved surface. Since the

majority of the incident beam will be transmitted through the lens in the case of grooved and the un-grooved surfaces, the measurement of the reflected beam in this case is clearly dominated by the 1st surface reflection (-13.7 dB) since adding the material and 2nd surface reflection will give (-13.6 dB). At 183 GHz we see a difference of ≅ 8 dB and 9 dB at 203 GHz between the grooved and un-grooved data plots, which is 2 to 3 dB higher than what was predicted in the simulation and calculations. Understanding fully the reasons of the differences between the calculated and measured values for both the grooved and un-grooved surfaces are not totally resolved nor concluded in this paper, and will continue to be a topic of an on going study in our group. However, it is our understanding that the factors that contribute to these differences could range anywhere between losses due to beam alignment errors, beam proper coupling, cross polarization and stigmatism losses. For example, it is highly likely that difference of ≅ 4.3 dB observed between the calculated and the measured reflection in the un-grooved surface case could be related to the rise of polarization losses at the receiver. Since the QWP used is not centered at 200 GHz it will result in producing an elliptically polarized beam incident on the surface of the lens, which could cause polarization losses at the receiver after passing through the rest of system.

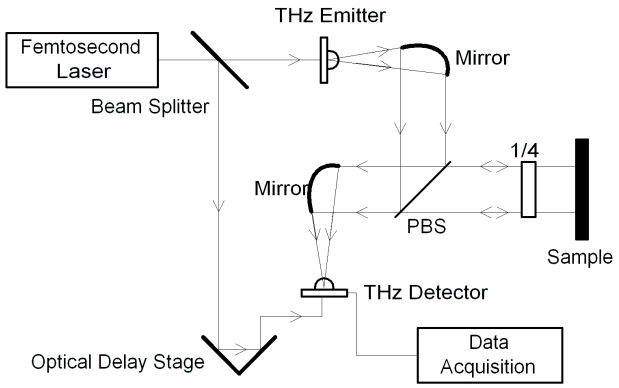

Figure 7: THz Pulse TDS reflection measurments setup diagram of the grooved and un-grooved surfaces of the HDPE lens.

Another example will be the observed difference of ≅6 to 7.2 dB between the calculated and measured values of reflection in the case of the grooved surface could be due to the cross polarization losses and stigmatism. The latter loss factors might be present when a polarized wave is incident on a material with effectively an anisotropic surface. This situation is highly likely to occur since the index of refraction of the grooved surface exhibits a variation in the x-and y-directions due to the grooves, which that might not be symmetric. Cross polarization and stigmatism losses produced could both be in the order of 0.2% of the reflected beam which calculated to be ≅ (-7.8 dB), as has been shown in J. Lamb analysis and simulation work in [16]. A much more comprehensive analysis for these previously discussed topics may be carried

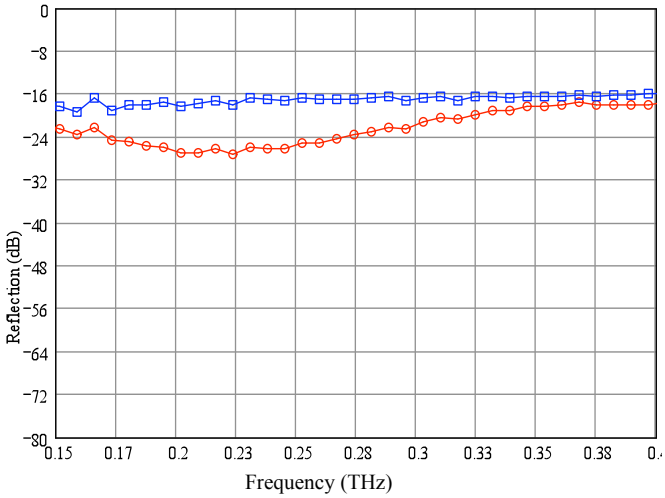

Figure 8: THz TDS reflected E-field measurements for the grooved (red) lens flat surface and un-grooved (blue) flat surface with respect to frequency (THz). Reflected losses for the un-grooved surface at both 183 GHz and 203 GHz is ≅ -18 dB, while at the grooved surface the total losses are -26 dB at 183 GHz and -27.2 dB at 203 GHz.

out in future publications. It is important to also mention that the design for a large bandwidth AR dielectric coating and optimized for selective frequencies using the grooving technique is extremely hard to make especially as the frequency of interest increases. Our initial design specifications for the groove's depth such that the grooves will induce the maximum matching to air in the middle of the 200 GHz band ≅ 193.5 GHz. The resulting desired groove depth was found to be 0.314 mm, however the measured grooves depth in the delivered HDPE lens that is under test was 0.264 mm exceeding the tolerance of ±0.025mm. The difference between the preselected and measured depths caused a shift of ≅ 36.5 GHz in the minimum observed reflection from the grooved surface as shown in Figure 8, where at 230 GHz the reflection is at minimum of -28 dB. However, from the overall quasi-optics system design point of view, a minimum of a 6 dB reduction in the reflection across the desired 200 GHz band has been met, and is considered very acceptable.

IV. FUTURE WORK

From the quasi-optics modeling and design point of view, it will be very useful to remodel in much more details the 200 GHz FH and spider assembly to look at its effect on the blockage of the 22 GHz far-field pattern using CTS. Also with the help of Zemax, a suite of simulations of the system tolerance will be very helpful in order to determine the impact of any mechanical deviations and environmental variations to the optics performance. From the testing point of view, it will be very useful to measure the phase center of the two beams, so that final optimization of the beam coupling is possible. System end-to-end far field lab bench optics measurement is needed to characterize the performance of the entire link. This will be followed by a comprehensive instrument-to-instrument test with the instruments transmitting from roof top to roof top between two high building across the university campus After

final adjustment on all fronts of the system, ATOMMS will be ready to be tested in a radio occultation configuration with the systems installed in the gimbal sections of the two NASA WB57-F aircrafts as explained in the introduction to this work.

V. Conclusion

This paper describes the ATOMMS instrument quasi-optical system design and provides some of the preliminary testing made so far. The design of the ATOMMS instrument can be found in another paper in this volume [5]. Once fully built and tested, the ATOMMS instrument promises to revolutionize the way of doing atmospheric science measurement and will add increased accuracy, resolution and coverage in the sounding of the Earth's atmosphere. An important aspect not covered in this work is the relevance of atmospheric turbulence in the propagation of microwaves through the atmosphere. This in fact is an error source that ATOMMS researchers have been investigating with dedication [17]. We have also covered the procedure used in designing both the 22 GHz and the 200 GHz TX/RX optics system by means of employing Gaussian beam propagation, and geometric optics. The goal was to make the coupling of the 200 GHz & the 22 GHz beams into their perspective feed horns as high as possible, and to minimize both reflections back to the transmit FHs and losses. This paper included the reflection measurements, and the effect of anti-reflection coating the surface of the lens by adding concentric grooves, which resulted in a reduction in the reflection of 6 dB. As we have mentioned before, considerable work is still needed to verify the performance of the lens, understanding further the extra losses seen in the measurement.

Acknowledgements

I am very thankful to all the people who at any level have helped and added so much in their very special talented way into the making of the 1st one of a kind ATOMMS instrument. ATOMMS is supported by the NSF Major Research Instrumentation Program under award # ATM-0723239.

References

[1] Cicerone, Ralph J., et al., *Climate Change Science: An Analysis of Some Key Questions* National Research Council, 2001, National Academy Press, pp 23-24

[2] http://www.atmo.arizona.edu/personalpages/kursinsk/papers/ATOMMS_051605_corrected.pdf.

[3] E. R. Kursinski, E. R., et al., "The Active temperature, ozone and moisture microwave spectrometer (ATOMMS)", in ECMWF/EUMETSAT GRAS SAF Workshop Proceedings, The pplications of GPS Radio Occultation Measurements. S. Healy Ed. 2008.

[4] http://www.nasa.gov/returntoflight/launch/wb57_chasejets.html.

[5] C. Groppi, E. R. Kursinski, D. Ward, Angel Otarola, Kate Sammler, Michael Schein, S. Al Banna, B. Wheelwright, S. Bell, W. Bertiger, M. Miller, H. Pickett "ATOMMS: the Active Temperature, Ozone and Moisture Microwave Spectrometer" Proceedings of the International Symposium on Space Terahertz Technology, in press, 2009.

[6] G. Fjeldbo, A. J. Kliore, and V. R. Eshleman (1971), 'The neutral atmosphere of Venus studied with the Mariner V radio occultation experiments", *The Astronomical Journal*, 76(2), 123-140.

[7] P. F. Goldsmith, *QuasiOptics Systems,* NewYork, IEEE Press, John Wiley & Sons, 1998 pp157-176.

[8] Constantine A. Balanis, *Antenna Theory: Analysis and Design*, New York, NY, John Wiley & Sons,1997, 2nd Edition, p60.

[9] P. F. Goldsmith, *QuasiOptics Systems,* NewYork, NY, IEEE Press, John Wiley & Sons, 1998 pp129-139.

[10] A. Sengupta, A. Bandyopadhyay, B.F. Bowden, J.A. Harrington and J.F. Federici, Characterization of Olefin copolymers using terahertz spectroscopy" The Institution of Engineering and Technology 2006, 13October2006. Electronics Letters online no: 20063148 1

[11] G. A. Ediss & T. GlobusÜ, "60 to 450 GHz Transmission and Reflection Measurements of Grooved and Un-grooved HDPE Plates", ALMA Memo No. 347, National Radio Astronomy Observatory Charlottesville, VA 22903 ÜDept of EE, University of Virginia.

[12] D. Raguin, G. Morris, "Analysis of anti-reflection-structured surfaces with continuous one-dimensional surface profiles", Applied Optics 32 (14) (1993) 2581–2598.

[13] D. Raguin, G. Morris, Anti-reflection structured surfaces for the infrared spectral region, Applied Optics 32 (7) (1993)

[14] Nancyjane Bailey and A. R. Kerr, Electronics Division Technical Note No. 155 PROGRAM "SCATTER" FOR THE ANALYSIS OF DIELECTRIC MATCHING LAYERS, 12 September 1989. http://www.gb.nrao.edu/electronics/edtn/edtn155.pdf

[15] Born and Wolf, *Principles of Optics,* London, UK, 4th edition1970, PERGAMON PRESS S.A.R.L, P61

[16] J.Lamb, "Cross-Polarization and Astigmatism in Mathcing grooves." International Journal of Infrared and Millimeter Waves Vol.17, No. 12, 1996.

[17] Otarola, A.C., The effects of turbulence in an absorbing atmosphere on the propagation of microwave signals used in an active sounding system. Ph.D. dissertation, The University of Arizona, United States -- Arizona. ProQuest Digital Dissertations @ University of Arizona database. (Publication No. AAT 3336701) 2008.

P3A

Toward THz Single Photon Detection with a Superconducting Nanobolometer

D. F. Santavicca[1], B. Reulet[2], B. S. Karasik[3], S. V. Pereverzev[3], D. Olaya[4], M. E. Gershenson[4], L. Frunzio[1], and D. E. Prober[1*]

1 Department of Applied Physics, Yale University, New Haven, CT 06511
2 Laboratoire de Physique des Solids, Universite Paris-Sud, 91405 Orsay
3 Jet Propulsion Lab, Pasadena, CA 91109
4 Department of Physics, Rutgers University, Piscataway, NJ 08854
* Contact: daniel.prober@yale.edu, phone 203-432-4280

***Abstract*—Testing a single-photon-sensitive THz detector poses significant technical challenges, especially for a bolometric detector. The challenge is the very low background required over a frequency range dc to several THz. In addition, the thermal conductance due to *photons* must be made less than that due to phonons. To enable device optimization prior to developing a full THz test system, we propose an alternative testing technique that is much easier to implement. A short microwave pulse with a total energy equal to a single THz photon is coupled to the detector. The microwave coupling can be precisely calibrated, and the detector can be well isolated from background IR photons. We call this microwave test pulse a faux photon, or *fauxton*. We use a 20 GHz source with a pulse width of 200 ns. The pulse width is much shorter than the thermal time constant of the detector (~5 μs). The energy of the fauxton can be changed simply by adjusting the amplitude of the microwave source, equivalent to adjusting the THz single-photon frequency. The detector response is determined from the change in the power reflection coefficient measured with a 1.3 GHz CW probe. This readout technique is well suited to frequency-domain multiplexing of a multi-pixel detector array.**

The detector consists of a superconducting Ti nanobridge 4 μm long, 0.4 μm wide, and 70 nm thick with a critical temperature (T_c) of 300 mK. The nanobridge spans thick Nb contacts, which have a higher T_c and hence create Andreev barriers that block the outdiffusion of hot electrons from the nanobridge. The resulting bolometer is phonon-cooled, with a thermal conductance proportional to T^3 at low temperature. Minimizing both the thermal conductance and the operating temperature is essential for achieving high sensitivity. Current micron-size Ti bolometer devices can clearly resolve mid-IR fauxtons with a device-limited sensitivity. Sufficient sensitivity to detect single THz photons can be achieved by scaling down the active device volume or by reducing T_c.

A New Laboratory for Terahertz Photonics

J. Castillo, *Student Member IEEE*, C. Barrientos, V. H. Calle, L. Pallanca, F. P. Mena, E. A. Michael*

***Abstract*—We are currently setting up a new photonics laboratory at the Electrical Engineering Department of the University of Chile. We describe the planned research in this laboratory, which will be devoted to the application of terahertz photonics in radioastronomical instrumentation and will be two-fold:**

First, the distribution of ultra-stable terahertz phase references through long fiber links will be investigated while participating in the current testing and commissioning of the central photonic local oscillator system of ALMA. This would include investigation of sources of phase drifts, the impact of polarization mode dispersion (PMD) to the ultimate phase instability of a fiber link, and new line-length correction schemes to include PMD correction. For this we acknowledge the support from the ALMA project (Backend-LO-group at NRAO Charlottesville and ALMA AIV Santiago).

Second, more efficient continuous-wave photonic near-infrared mixers as terahertz sources will be investigated within international collaborations with the motivation to develop a universal photonic local oscillator for astronomical submillimeter/terahertz receiver systems. Continuing previous own work, new concepts of vertically illuminated traveling-wave (TW) photomixers will be investigated. Miniaturization of the TW-optics for fiber-pigtail integration, device simulation/modeling and optical/terahertz testing will be done within our lab, whereas device fabrication at the facilities of a collaboration partner. Here we greatly appreciate possibilities for collaborations with J. Stake, Chalmers Technical University and J. Campbell, University of Charlottesville.

***Index Terms*— heterodyne detection, high-speed optical techniques, optoelectronics, microwave oscillators, microwave photonics, millimetre wave generation, optical transmitters, optical fibers, photodetectors, Interferometry.**

I. INTRODUCTION

The laboratory introduced here is devoted to the application of photonics in astronomical instrumentation and will be two-fold: First, the ultra-phase-stable distribution of terahertz reference signals through long fiber links will be investigated along a cooperation with the ALMA project for commissioning the central photonic local oscillator of ALMA (PLO). [1] Second, more efficient terahertz sources based on photonic near-infrared mixers will be investigated within international collaborations for use as universal local oscillators in astronomical submillimeter/terahertz receiver systems[2]. This new laboratory dedicated to research on photonic terahertz-sources and on terahertz reference fiber links is being set up at the Electrical engineering department..

Manuscript received 20 April 2009. J. Castillo, C. Barrientos, V. H. Calle, L. Pallanca, F. P. Mena, and E. A. Michael are with the Electrical Engineering Department, Univesidad de Chile, Santiago, 7790829 Chile (* contact e-mail: emichael@ing.uchile.cl).

II. TERAHERTZ PHASE REFERENCE FIBER LINKS

Polarization mode dispersion (PMD) is a phenomenon caused by birefringence of the fiber, which means that the light velocity is dependent on the state of polarization (SOP). There are two orthogonal principal states of polarization (PSP, see fig. 1, generally could be any elliptical polarization), in which the velocity is maximal or minimal.

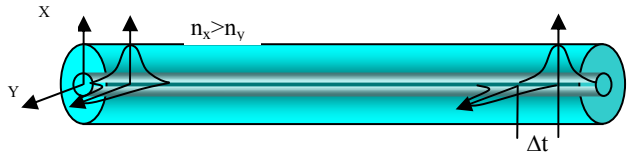

Fig. 1. Effect of PMD in the time of flight of pulse traveling through a fiber, depending on the polarization of the light relative to the PSP of the fiber.

This effect can produce instability of the state of polarization at the input of the photomixer, adding the requirement of polarization independency of this device. If this requirement is not fulfilled by the photomixers, PMD causes larger instability of the phase and power of the RF beat note at the output of the photomixer. [3]

All of this adds risks to the ALMA PLO system, so it is important to quantify these effects on the final on-site performance.

Fig. 2 shows the setup proposed to the ALMA integration and verification team (AIV). The objective of it is to measure the PMD behavior of the system and its effect on the phase stability of the system, and Fig. 3 shows the proposed setup to evaluate the polarization stability of the PLO signal.

Other research projects within this line of research are: 1.) a new optical delay modulator scheme for the line length corrector system (LLC) of ALMA (Fig. 4), based on free-space optics in a length-controlled multipass-cell instead of a fiber-stretcher, and therefore avoids any polarization activity. 2.) a new holographic type of n-way beam splitter, to replace the current beam splitter in the fiber distribution scheme of the ALMA Photonic LO (PLO), see Fig. 5. The goal is to reduce a big risk of ALMA: Because these beamsplitters are outside the phase correction loops for the individual fibers to the antennas, the measured uncontrollable polarization-to-phase coupling effects of the commercial n-way splitters available up to now will cause an increasing degradation of the resolution performance of ALMA towards higher frequencies.

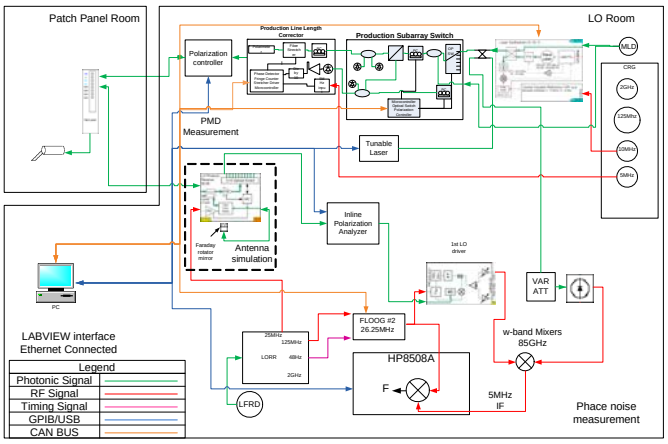

Fig. 2. this figure shows the proposed setup. to make the evaluation of the phase stability measurement of the ALMA LO photonic distribution system, and its dependency on PMD.

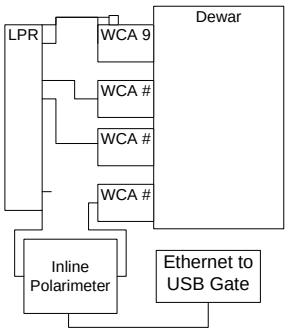

Fig. 3. Setup proposed to evaluate the polarization stability of the ALMA LO photonic distribution system.

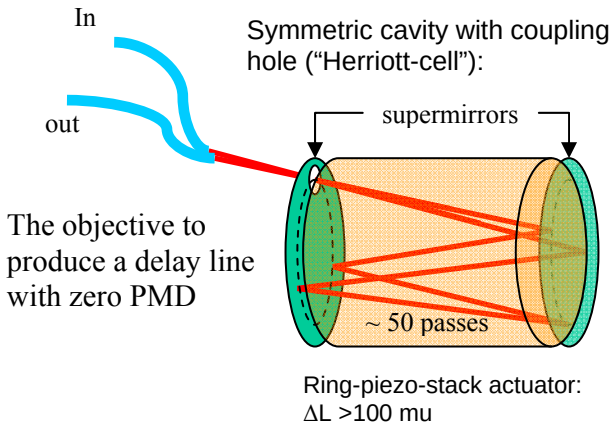

Fig. 4. New optical delay modulator schemes

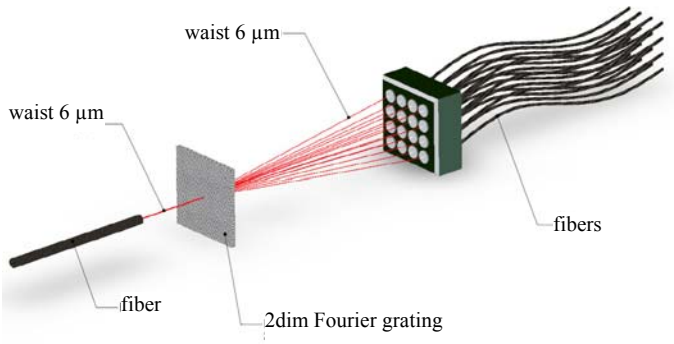

Fig. 5. Holographic n-Way splitter

III. PHOTONIC TERAHERTZ SOURCE: OPTICAL HETERODYNING

The second line of research is devoted to the development of more efficient continuous-wave photonic near-infrared traveling-wave photomixers as terahertz sources. This will be investigated within international collaborations with the motivation to develop a universal photonic local oscillator for astronomical submillimeter/terahertz receiver systems. After design and simulation, the devices will be fabricated through these collaborations and finally characterized optically in our photonics lab, where we have a photomixer test bank, as shown in the

Fig. 6 left, which has been used during recent work to develop vertically pumped traveling-wave (TW) planar structures based on LT-GaAs [4][5] (see Fig. 7).

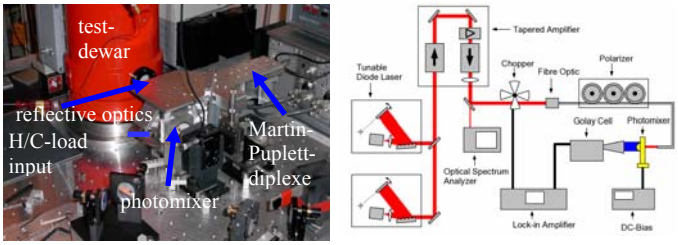

Fig. 6. left: Photonic local oscillator test setup for TW-photomixers; right: Fiber-based test setup for lumped-element photomixers

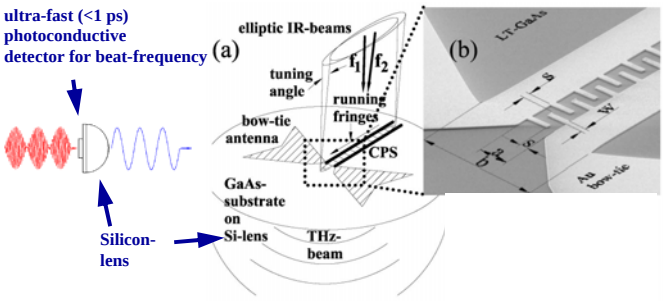

Fig. 7. Planar travelling-wave (TW) structures based on LT-GaAs (operational wavelength 0.780 µm): (a) Velocity-match of IR interference fringes to the THz-wave by a tuning-angle between the two heterodyned IR beams; (b) planar structure with inner part of bow-tie antenna.

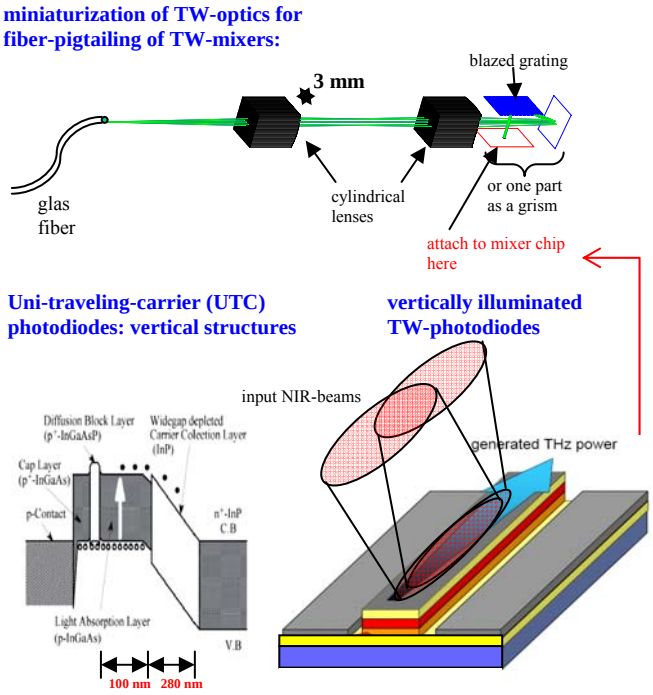

Fig. 8. top: Miniaturized optics for vertical illumination of traveling-wave photodiodes; bottom: scheme of proposed work on vertically illuminated uni-traveling-carrier (UTC) photodiodes implemented in a traveling-wave structure.

ACKNOWLEDGMENTS

This work was supported in part by the ALMA-CONICYT Fund, under Grant 31080020. and Fondecyt under Grant 1090306.

REFERENCES

[1] J. Cliche y B. Shillue, "Precision timing control for radioastronomy: maintaining femtosecond synchronization in the Atacama Large Millimeter Array," *Control Systems Magazine, IEEE*, vol. 26, 2006, pages 19-26.

[2] E.A. Michael, "Travelling-wave photonic mixers for increased continuous-wave power beyond 1 THz," *Semiconductor Science and Technology*, vol. 20, 2005, pages. S164-S177.

[3] P. Shen, N. Gomes, P. Davies, y W. Shillue, "Polarization Mode Noise in Ultra-low Drift Phase Reference Distribution System over a Fiber Network," *Microwave Photonics, 2005. MWP 2005. International Topical Meeting on*, 2005, pages 297-300.

[4] E.A. Michael, I.C. Mayorga, R. Gusten, A. Dewald, y R. Schieder, "Terahertz continuous-wave large-area traveling-wave photomixers on high-energy low-dose ion-implanted GaAs," *Applied Physics Letters*, vol. 90, Abr. 2007, pages 171109-3.

[5] E.A. Michael, B. Vowinkel, R. Schieder, M. Mikulics, M. Marso, y P. Kordos, "Large-area traveling-wave photonic mixers for increased continuous terahertz power," *Applied Physics Letters*, vol. 86, Mar. 2005, pages 111120-3.

IMPLEMENTATION OF A TWO-TEMPERATURE CALIBRATION LOAD UNIT FOR THE SUBMILLIMETER ARRAY

C. Edward Tong, D. Cosmo Papa, Steve Leiker, Robert Wilson, Scott Paine,
Rob Christensen, and Ray Blundell

***Abstract*—A calibration load unit has been constructed and implemented for the Submillimeter Array (SMA). This unit incorporates an ambient load and a heated load, in addition to a waveplate assembly. The unit is installed inside the SMA antenna cabin near the compact image plane along the SMA beam waveguide. The loads are constructed from a matrix of 9 RAM tiles with a clear aperture diameter of 75 mm. The heated load is heated through the copper plate on which the RAM tiles are mounted, and the temperature of the plate is servo controlled. A 3 μm thick mylar window is used to reduce the effects of convection cooling. Both loads can slide in and out of the signal beam under computer control. The target temperatures of the ambient and heated loads are 15 and 55 degrees C respectively. An *in-situ* calibration procedure has been developed to calibrate the radiation temperature of the heated load. The procedure includes a modulated noise injection technique to remove any non-linearity of the receivers.**

***Index Terms*—Submillimeter wave receivers, superconductor-insulator-superconductor mixer, calibration**

I. INTRODUCTION

RECEIVER calibration in the laboratory is usually carried out using an ambient and a liquid nitrogen-cooled load in a Y-factor measurement. However, for routine operation in a radio telescope, a cryogenic temperature load is not always available. For a radio interferometer, such as the Submillimeter Array (SMA), where operators are responsible for tuning and optimizing many receivers at the same time, a two-temperature calibration unit is very valuable. The SMA has, thus far, been operating with the use of a single ambient temperature calibration load. The receiver output in response to the ambient load and the sky provides an approximate measure of the double-side-band system noise temperature. Receiver noise temperature is estimated with knowledge of the atmospheric opacity at the observing frequency, provided by the 225 GHz tipping radiometer or by sky dips. The actual flux from astronomical objects is determined by observing calibrators (objects with known radio flux) either at the end of an observation track or interlaced in the track.

Manuscript received 20 April 2009.

C. Edward Tong, D. Cosmo Papa, Steve Leiker, Robert Wilson, Scott Paine, Rob Christensen and Ray Blundell are all with the Harvard-Smithsonian Center for Astrophysics, Cambridge, MA 02138 USA (e-mail: etong@cfa.harvard.edu).

A two-temperature calibration unit is desirable since it provides a direct measure of the receiver noise temperature, allowing direct receiver optimization, and it is also a useful tool in precise flux measurements. This is particularly important in the observation of bright objects, such as planets, for which there is relatively large swing of receiver output power when the antennas are switched from on source to off source. In addition, the use of a two-temperature calibration unit can diagnose spectral baseline issues. A flat baseline will be instrumental in the current effort at the SMA to use atmospheric ozone lines for atmospheric phase correction [1].

In this paper, we describe the construction of the two-temperature calibration loads recently installed in the SMA. A calibration procedure has been developed. We also discuss calibration uncertainties.

II. CONSTRUCTION OF THE CALIBRATION UNIT

The calibration unit is installed near an intermediate beam waist in the SMA beam waveguide [2]. The required load size is therefore very small; we have used a clear aperture of 75 mm diameter but only the central 25 mm part of the load is nominally illuminated by the receiver. The load position corresponds to a pupil plane of the telescope such that all the receivers see the same geometrical area of the load. The three fold size margin of the loads should eliminate any diffraction or truncation effects.

Fig. 1 is a photo of the entire calibration load assembly. It consists of 3 sub-assemblies. In order from the receiver towards the sky, there is a rotatable quarter-wave-plate unit for circular to linear polarization transformation, followed by the heated load assembly, and finally the ambient load assembly. Each of the sub-assemblies is mounted on a linear actuator and can slide into the receiver beam independently under computer control. Typical travel time into or out of the beam is about 0.5 second.

Both the ambient and heated loads are made from a square matrix of 3x3 Thomas Keating RAM tiles (25 mm x 25 mm each) [3, 4]. The interlocking tiles are set on a copper plate. In the case of the heated load, each tile is attached to the plate with a nut through its back stub. In addition, four springs provide further contact force pushing the 4 corner pieces against the copper plate. A flat heater is cemented to the back of the copper plate. An electronic and computer interface allows the temperature of the copper plate to be kept constant. Testing in an environmental chamber showed that the tiles

could withstand prolonged days of heating to above 100° C. In order to maintain a reasonable safety margin and because of gain compression issue, the maximum set point of the heated load is limited to below 65 ° C. A small temperature sensor (Analog Device 590) is inserted into a small side hole in one of the tiles to more directly measure the tile temperature which is typically a few degrees below that of the copper plate. Finally, a thin mylar window is used in the heated load to reduce air convection.

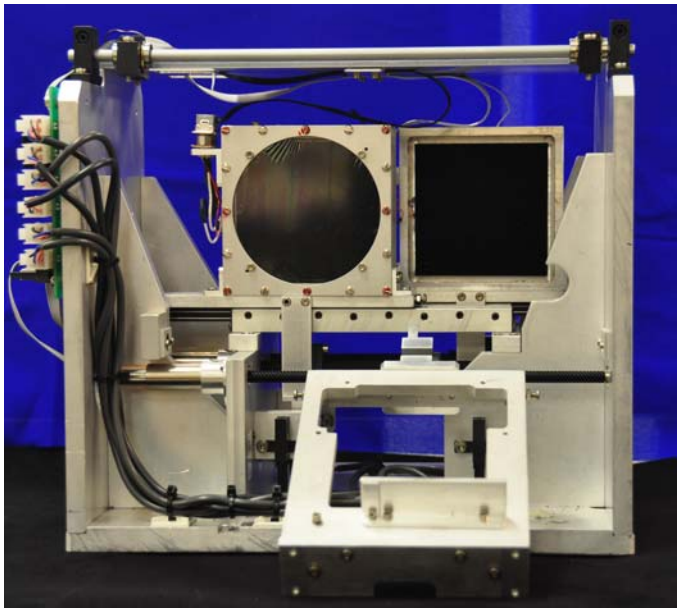

Fig. 1. Front view of the SMA calibration load assembly (taken from the receiver side). In this photo, the rotatable quarter-wave plate module has been removed and its carrier is flipped down to allow a better view of the heated and ambient loads. All 3 sub-assemblies are mounted on carriers that can be translated horizontally into or out of the signal beam. Note that the heated load is equipped with a 75 mm diameter window, which is absent in the ambient load.

III. Return Loss of the Heated Load

We have studied the input return loss of the loads by measuring the output power spectra of the receiver with an FFT spectrometer. Since the SIS receiver is generally not well matched, standing waves will be present if the return losses of the loads are not small enough. Standing waves in the beam waveguide lead to baseline ripples in the receiver IF output spectrum. Because the SMA operates in double-side-band (DSB) mode, the amplitude of the baseline ripples depends on whether the standing waves associated with the two sidebands are in constructive or destructive interference, which in turn depends on the Local Oscillator (LO) frequency. Since the optical path between the loads and the receiver is about 3.3 meters, a 45 MHz periodic ripple is observed in the output power spectra. The magnitude of the standing waves can be studied and accessed by tuning the LO frequency over a cycle of the baseline ripple pattern to find its maximum amplitude as observed in the DSB IF output spectrum.

By taking the ratio of the receiver power spectrum with the hot load in the signal beam to that of the ambient load, which is equivalent to taking spectral Y factor measurements, we can compare the return losses of different load configurations. It is found that the heated load is generally poorer in return loss, primarily due to its window. We have tried different window materials, and our final choice is a 3 μm thick mylar film, which is both electrically thin even for our highest operating frequency and is effective in reducing convection cooling of the front surface of the heated load.

In an effort to further improve the performance of the loads, we have determined empirically that a rotation of 3 degrees about a vertical axis can further reduce the baseline ripples.

IV. Load Calibration Procedure

Since the ambient load is in thermal equilibrium with the environment, we can assume that its radiation temperature is that of the ambient temperature. A commercial grade precision temperature sensor, with calibration traceable to NIST standard, is mounted on the ambient load to provide accurate temperature measurements.

For the heated load, its radiation temperature is determined from the receiver responses to a liquid nitrogen cooled load and an ambient load. Since the SIS receiver is unlikely to be perfectly linear, a two-step calibration procedure is employed. First, its approximate temperature is determined by assuming that the receiver is perfectly linear. Then any gain compression of the receiver is measured using an injected modulated signal method [5], from which the correct load temperature is derived.

A. Linear Calibration

For a linear receiver, the radiation temperature of the heated load is given by:

$$T_{hot} = T_{amb} + \frac{(P_{hot} - P_{amb})}{(P_{amb} - P_{cold})}(T_{amb} - T_{cold}) \qquad (1)$$

where P_{hot}, P_{amb} and P_{cold} are the receiver output power in response to heated, ambient and cold loads respectively, and T_{hot}, T_{amb} and T_{cold} are their physical temperatures respectively. The above equation gives accurate result if the receiver gain is stable. In the presence of gain fluctuations, the result T_{hot} would exhibit statistical variations.

The SMA cryostat currently operates without any temperature stabilization scheme. The 4 K stage exhibits temperature fluctuations of about 20 mK over a 60 – 80 second cycle, with more irregular temperature spikes occurring every 5 – 10 cycles. Thus, the measurement of P_{hot}, P_{amb} and P_{cold} should be performed as quickly as possible to minimize the effects of receiver gain fluctuations induced by cryogenic temperature changes. In our measurement setup, we are able to cycle through the three temperature loads in 7 seconds. A series of measurement cycles are performed and the derived value of T_{hot} exhibits a standard deviation of about 0.25 K.

B. Linearity Calibration

In the second phase of calibration, the linearity of the receiver is probed by injecting a modulated signal into the LO unit [5]. This method was adapted from an approach proposed by Kerr *et al* [6]. In the present procedure, instead of injecting a CW signal, a noise source is employed, which eliminates the effects of standing wave associated with any particular

frequency. The band-limited injected noise is up-converted by the frequency multiplier in the LO unit, providing a very low level double-side-band AM modulation to the LO. This modulation is down-converted by the single-ended SIS mixer. The 1 kHz modulation can then be recovered using a power detector at the receiver output using a lock-in amplifier. The strength of the injected noise source is adjusted so that the detected modulation power represents ~1% of the total power at the receiver output when the receiver input is terminated by an ambient load. This same technique is used to study the linearity of THz Hot-Electron Bolometer mixer [7].

For small deviation from linearity, we model the receiver output power as:

$$P_{out}(T_{load}) = P_0 + mT_{load} - \alpha T_{load}^2 \quad (2)$$

The voltage measured by the lock-in amplifier, U, is proportional to the slope of the above equation. Note that for a linear receiver, the lock-in amplifier should register the same voltage irrespective of the load temperature. In the presence of gain compression, it is clear that the lcok-in voltage corresponding to the cold load, U_{cold} , should be bigger than that corresponding to the ambient load, U_{amb}. Let R_{amb} be the ratio U_{amb} / U_{cold} .

$$R_{amb} = \frac{U_{amb}}{U_{cold}} = \frac{m - 2\alpha T_{amb}}{m - 2\alpha T_{cold}} \approx 1 - 2\frac{\alpha}{m}(T_{amb} - T_{cold}) \quad (3)$$

Using the data from the first and second step of the measurement procedure, the coefficients in equation (2) can be solved, and P_{hot} can be mapped to T_{hot}. Since the lock-in amplifier has a very high dynamic range, the value of R_{amb} can, in principle, be determined fairly accurately. Accuracy is limited by receiver gain fluctuations. In our measurements, the standard deviation for R_{amb} is between 0.4 – 0.8 %. The receiver gain compression is expected to increase with temperature. We have, therefore measured the value of the ratio $R_{hot} = U_{hot}/U_{cold}$.

V. Results and Discussion

As of April 2009, three complete calibration units have been installed in the SMA. The SMA antenna cabin is maintained at a temperature of about 15° C. Initially, we have set the copper plate in the heated loads to 65 ° C. We found that such an arrangement caused the ambient load to be heated above the ambient temperature of the cabin because of its proximity to the heated load. Subsequently, we have reduced the copper plate servo temperature to 55 ° C. This reduces the heating effect of the heated load on the ambient load. At this set point, the temperature sensor buried inside the RAM of the heated load registers temperatures of between 50 ° and 52 ° C, indicating a few degrees drop between the copper plate and the RAM material.

The equivalent radiation temperature of the heated load, calibrated by the above procedure, is a few degrees below that indicated by the temperature sensor inside the heated load RAM. Clearly, the radiation temperature is related to the surface temperature of the RAM which is an insulating material. Table 1 gives the calibration data for one of the heated load measured with the SMA 200 GHz receiver [8]. For this data set, the copper plate of the heated load was 65 ° C.

It is noted from Table 1 that the SMA 200 GHz receivers have non-negligible gain compression for an ambient input load, which increases with decreasing frequency (or decreasing width of photon step) [9]. The calibration procedure appears to be successful in removing this effect because the final calibrated temperature shows little frequency dependence. Clearly, the successful application of the calibration load depends on a knowledge of the amount of gain compression of the receiver in normal operation. The measured values of R_{hot} is only slightly smaller than that of R_{amb} showing that gain compression is not significantly different between the ambient and heated loads.

The same procedure has been used in the 300 GHz receiver. For this frequency range, the values of R_{amb} and R_{hot} are somewhat higher: between 0.92 and 0.97, corresponding to gain compression below 5% with the ambient load. Therefore, the temperature correction needed to account for deviation from linearity is smaller. However, the calibrated temperature shows some weak frequency dependence. It is believed that this is a result of the poorer match of the receiver, especially near the band edges. Further investigation is being pursued.

VI. Conclusion

A two-temperature calibration load unit has been designed and is being installed in the Submillimeter Array. The assembly consists of an ambient (15 ° C) and a heated load with low return loss in the submillimeter band. The heated load offers a radiation temperature ~50 ° C. Both loads can be moved into the intermediate beam waist of the SMA beam waveguide in ~0.5 seconds. An *in-situ* calibration procedure has been developed to determine accurately the equivalent radiation temperature of the heated load. Using the modulated injection noise technique, the calibration procedure takes the gain compression of the SIS receiver into account. This calibration unit will be used in receiver optimization and calibration, allowing a more accurate measurement of sub-millimeter flux.

TABLE I Calibration Data of Heated Load Installed in SMA using SMA-200 GHz Receiver

LO Freq. (GHz)	Calibrated Ambient Temp (C)	Heated Load sensor Temp (C)	T_{hot} assuming linear receiver (from eq. (1))	Ratio of Lock-in voltages		Final Calibrated Temperature T_{cal} (C)	Percentage of gain compression @ T_{amb}
				R_{amb}	R_{hot}		
215	14.01	59.0	52.45 ± 0.25	0.881 ± 0.004	0.877 ± 0.009	55.4 ± 0.3	8%
225	14.54	59.1	53.10 ± 0.13	0.911 ± 0.005	0.907 ± 0.008	55.2 ± 0.2	6%
235	14.34	59.0	53.83 ± 0.34	0.940 ± 0.008	0.937 ± 0.011	55.2 ± 0.4	4%

REFERENCES

[1] S. Paine, "Atmospheric phase correction for Submillimeter astronomy using stratospheric ozone line emission," in XXIX URSI General Assembly, Chicago, IL, Aug. 2008.

[2] S. Paine, D. C. Papa, R. L. Leombruno, X. Zhang, and R. Blundell, "Beam waveguide and receiver optics for the SMA," in *Proc. 5th Int. Symp. Space THz Tech.,* pp. 811–823, Ann Arbor, MI, May 1994.

[3] Thomas Keating Ltd., UK. Website: http://www.terahertz.co.uk

[4] A. Lonnqvist, A. Tamminen, J. Mallat, and A.V. Raisanen, "Monostatic reflectivity measurement of radar absorbing materials at 310 GHz," *IEEE Trans. Microwave Theory &Tech.,* vol. 54, pp. 3486-3491, Sept. 2006.

[5] C.-Y. E. Tong, A. Hedden, and R. Blundell, "Gain expansion and compression of SIS mixers," *IEEE Trans. Appl. Superconductivity.*, to appear in June 2009.

[6] A. R. Kerr, J. Effland, S.-K. Pan, G. Lauria, A.W. Lichtenberger, and R. Groves "Measurement of gain compression in SIS mixer receivers" in *Proc. 14th Int. Symp. Space THz Tech.,* pp. 22-24, Ventana Canyon, AZ, April 2003. (Also in ALMA memo 460.1: http://www.alma.nrao.edu/memos).

[7] Y. Lobanov, C.E. Tong, R. Blundell and G. Gol'tsman, "A study of direct detection effect on the linearity of hot electron bolometer mixers," *these proceedings.*

[8] R. Blundell, C.-Y. E. Tong, D.C. Papa, R. L. Leombruno, X. Zhang, S. Paine, J.A. Stern, H.G. LeDuc, and B. Bumble, "A wideband fixed-tuned SIS receiver for 200 GHz operation," *IEEE Trans. Microwave Theory & Tech.,* vol. 43, pp. 933-937, Apr. 1995.

[9] M. J. Feldman, and L. R. D'Addario, "Saturation of the SIS direct detector and the SIS mixers," *IEEE Trans. Magnetics,* vol. 23, pp. 1254-1258, Mar. 1987.

ALMA Band 9 Cartridge Automated Test System

J. Barkhof, B. D. Jackson, A. M. Baryshev, and R. Hesper

***Abstract*— The Atacama Large Millimeter/Sub-millimeter Array (ALMA) requires 73 state-of-the-art receivers for the 602-720 GHz range – the ALMA Band 9 cartridges. 65 cartridges are due between 2009 and 2012, with each undergoing thorough acceptance testing to verify its operation and performance prior to delivery. This is enabled by an automated test system developed during the project's pre-production phase in 2004-2008. The core of this system are a single-cartridge test cryostat, a dual-channel intermediate frequency signal processor, a phase-and-amplitude near-field test system, and script-based measurement and control software that enables automated cartridge tuning and unattended execution of time-consuming tests. Two test systems are operated in parallel to allow a delivery rate of at least 2 cartridges per month to be achieved.**

***Index Terms*—submillimeter wave receivers, automatic test equipment, superconductor-insulator-superconductor mixers, radio astronomy**

I. INTRODUCTION

THE Atacama Large Millimeter / Sub-millimeter Array project is a collaboration between Europe, North America, Asia, and Chile, to build an aperture synthesis telescope of at least 66 antennas at 5000 m altitude in Chile [1]. When complete, ALMA will observe in 10 frequency bands between 30 and 950 GHz, with a maximum baseline of up to 14 km, offering unprecedented sensitivity and spatial resolution at millimeter and sub-millimeter wavelengths. As the highest frequency band in the baseline project, the 602-720 GHz Band 9 receivers (see Fig. 1) will provide the observatory's highest spatial resolutions and probe higher temperatures to complement observations in the lower-frequency bands in the baseline project (between 84 and 500 GHz).

ALMA's aggressive integration and commissioning plans call for the delivery of up to two Band 9 cartridges per month to the Front End Integration Centers during the coming years. Prior to delivery, each of these cartridges will be thoroughly tested to ensure that the project's performance and interface requirements are met. Included in the list of properties that are to be tested are: heterodyne sensitivity and cartridge output power as a function of local oscillator (LO) frequency and intermediate frequency (IF), aperture and polarization efficiency, output power and signal path phase stability, and gain compression.

In order to realize these critical tests in a timely and reliable manner, a semi-automated test system has been developed for the Band 9 cartridges. Core elements of this test system include a cryo-cooled single-cartridge test cryostat (developed at NAOJ, Japan) [2], an ALMA Band 9 room-temperature LO [3] and cartridge bias electronics (both developed at NRAO, USA), a dual-channel IF processor, and a near-field phase-and-amplitude test system. These and other elements of the

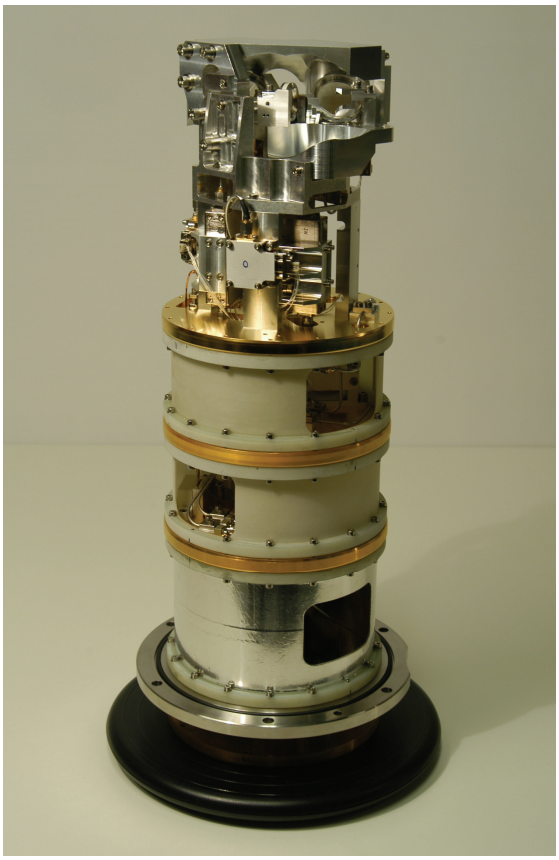

Fig. 1 – An ALMA Band 9 cold cartridge (i.e. not including the cartridge's warm electronics units). The cartridge is roughly 50 cm tall and 20 cm in diameter.

Manuscript received 20 April 2009. This work was financed by the European Organisation for Astronomical Research in the Southern Hemisphere under contract number 16173/ESO/07/14997/YWE.

J. Barkhof, A. M. Baryshev, and R. Hesper are with the Kapteyn Astronomical Institute, University of Groningen, Landleven 12, 9747 AD Groningen, The Netherlands.

J. Barkhof, B. D. Jackson, A. M. Baryshev, and R. Hesper are with Netherlands Research School for Astronomy (NOVA), Niels Bohrweg 2, 2333 CA Leiden, The Netherlands.

B. D. Jackson and A. M. Baryshev are with the SRON Netherlands Institute for Space Research, Landleven 12, 9747 AD Groningen, The Netherlands (corresponding author phone: +31-50-363-8935; fax: +31-50-363-4033; e-mail: B.D.Jackson@sron.nl).

test system are combined and controlled by script-based control software that enables automated optimization of the mixer and LO bias parameters and unattended execution of time consuming tests such as amplitude and phase stability tests and near-field beam-pattern measurements.

II. Cartridge Technical Requirements

The Band 9 cartridge is a double side-band, dual-polarization SIS receiver with state-of-the-art performance, including low noise, high optical efficiency, wide IF and RF bandwidth, and high output power and phase stability. The mechanical design of the cartridge is driven by the design of the blank cartridge body (a cylinder 17 cm in diameter and 28 cm tall, with plates at each of the temperature levels: 300, 110, 15, and 4 K) and the 20 cm of space available above the 4 K plate. Fig. 1 contains a photograph of the cryogenic portion of the Band 9 cartridge. Additional details regarding the cartridge design and production can be found in [4,5].

Table 1 summarizes the main performance requirements for the Band 9 cartridge. Effectively, these also specify the test system that is used for cartridge acceptance testing, as every cartridge is tested to verify compliance with each of these requirements.

TABLE 1 Main Performance Requirements

Property	Required Performance
mixer configuration	linearly polarized, double side-band
RF bandwidth	614-708 GHz (LO) 602-720 GHz (signal)
IF)bandwidth	4-12 GHz
total power receiver noise temperature	< 169 K over 80% of the LO range < 250 K over 100% of the LO range
total power output power	-32 dBm < P_{out} < -22 dBm
output power variations	< 7 dB p-p over 4-12 GHz IF band < 5 dB p-p within 2 GHz sub-bands of the IF band
output power Allen variance	< 4 x 10^{-7} for 0.05-100 s delay < 3 x 10^{-6} for 300 s delay
signal path phase stability	7.1 fs for 20-300 s delay
aperture efficiency	80% for an ideal / unblocked telescope
polarization efficiency	> 97.5%
beam squint	polarization beam co-alignment better than 10% of FWHM

III. Cartridge Test System Design and Sample Test Results

A. System Design

The Band 9 cartridge test system was developed in parallel with the development of the cartridge design and the production of the first 8 cartridges. Design verification and acceptance tests of the first cartridge in 2005-2006 were used to demonstrate all of the required tests, while acceptance tests of the remainder of the first 8 units were used to further refine and streamline the test equipment and test procedures.

The test system is built up around 4 main components:

- a single-cartridge test cryostat developed by the National Astronomical Observatory of Japan [2];
- a dual-channel IF processor that includes 4-12 GHz band-pass filters, two amplification stages, computer-controlled YIG filters to sample the 4-12 GHz IF band at ~ 50 MHz resolution, and switches that select measurements in total-power or narrow-band mode;
- a phase-and-amplitude near-field system that includes a superlattice harmonic generator [6] as a tunable 602-720 GHz signal source, a 3-D scanning stage mounted on top of the cartridge test cryostat, and a phase-detection system; and
- measurement and control software that is used to operate (and optimize) the cartridge bias and control all associated test equipment.

Additional important components include a hot-cold chopper for heterodyne sensitivity testing with 77 and 295 K blackbody loads, a rotatable polarizing grid for cross-polarization measurements, and a 373 K heated load that is used for linearity testing. Both the hot-cold load and the polarizer are computer-controlled to facilitate automated measurements.

Fig. 2 includes a photograph of the cartridge test system configured for cross-polarization tests – the rotatable polarizer in the cartridge beam between the cryostat window and the hot-cold load allows the receiver sensitivity to be measured as a function of source polarization.

Fig. 2 – The Band 9 cartridge test system configured for polarization efficiency measurements, with a rotating polarizing grid placed between the receiver and the hot-cold load (both computer-controlled).

B. Monitor and Control Software Design

The cartridge and cartridge test system are operated via custom-built control software written in LabWindows. This software is designed to allow cartridge tests to be performed reliably and efficiently. Test execution generally requires manual intervention to reconfigure the test hardware and initialize some test parameters, but once initialized, time-consuming tests are performed with a minimum of operator intervention (such as refilling liquid nitrogen loads).

Key elements of the test system control software are:

- a script-based user interface that facilitates test standardization (acceptance tests are executed from standard scripts centrally stored in text files) and allows every test command to be logged;
- a "nested loop" functionality that allows complex measurements to be built up as multi-dimensional scans, both for standard tests (i.e. receiver sensitivity vs. LO and IF frequency) and one-time exploratory tests (i.e. output power stability as a function of SIS junction bias);
- semi-automated optimization of cartridge operating parameters (mixer magnet tuning and SIS junction bias voltage and pump level optimization); and
- a modular structure that aids in maintainability, and eases the incorporation of new test equipment and portability to ALMA partner institutes.

C. Semi-Automated SIS Mixer Tuning

Band 9 cartridge operation requires tuning of the SIS mixers' electromagnets and optimization of the (LO frequency dependent) SIS bias voltage and current.

The mixers' magnets are tuned after first demagnetizing the magnets (by applying a series of magnet currents of alternating sign and decreasing amplitude) and defluxing the junction (by applying a single pulse to the mixer's deflux heater, where a pulse is ~ 0.2 s in duration). Once the magnet has been demagnetized and defluxed, the mixer's zero-bias supercurrent is measured as a function of magnet current to locate the 2nd minimum in the Franhofer pattern. Due to hysteresis, the magnet current is always tuned starting from 0 mA, after demagnetizing and defluxing.

The optimum bias voltage and pumped current of the cartridge's SIS mixers are determined by a nested set of 1-dimensional scans of cartridge hot and cold output power as a function of LO power and SIS junction bias voltage. The optimum bias is found from the minimum noise temperature versus LO power and maximum output power versus SIS bias voltage. To facilitate exchange of local oscillators and simplify retuning for new LO frequencies, the optimum LO power is defined in terms of the resulting SIS bias current. Thus, optimization is performed for 13 LO frequencies between 614 and 710 GHz, and a frequency-independent optimum bias current is defined as the average of the 13 optimum currents. The SIS bias voltage remains LO frequency dependent. In operation, the optimum bias is obtained by tuning the LO power amplifier to obtain the required SIS bias current at the optimum SIS bias voltage.

D. Heterodyne Sensitivity Testing

Cartridge sensitivity acceptance tests are performed at a standard set of 13 LO frequencies between 614 and 710 GHz, at optimum bias for each LO frequency. Measurements are taken in narrow-band mode (at 40-50 MHz IF resolution over the full 4-12 GHz IF band), with total power results obtained by off-line integration of the narrow-band results.

For diagnostic purposes, and to characterize the Band 9 LO in terms of excess noise, sensitivity measurements can also be performed at finer LO spacing (typically 1 GHz), fully sampling the IF band at ~ 50 MHz resolution. These measurements are performed at a fixed (LO-independent) SIS bias voltage and pumping level (tuning the LO power at each frequency to obtain a defined SIS bias current).

Fig. 3 presents total power noise temperature data for 14 cartridges and sample narrow-band data of noise temperature versus LO and IF frequency for one polarization channel of one cartridge.

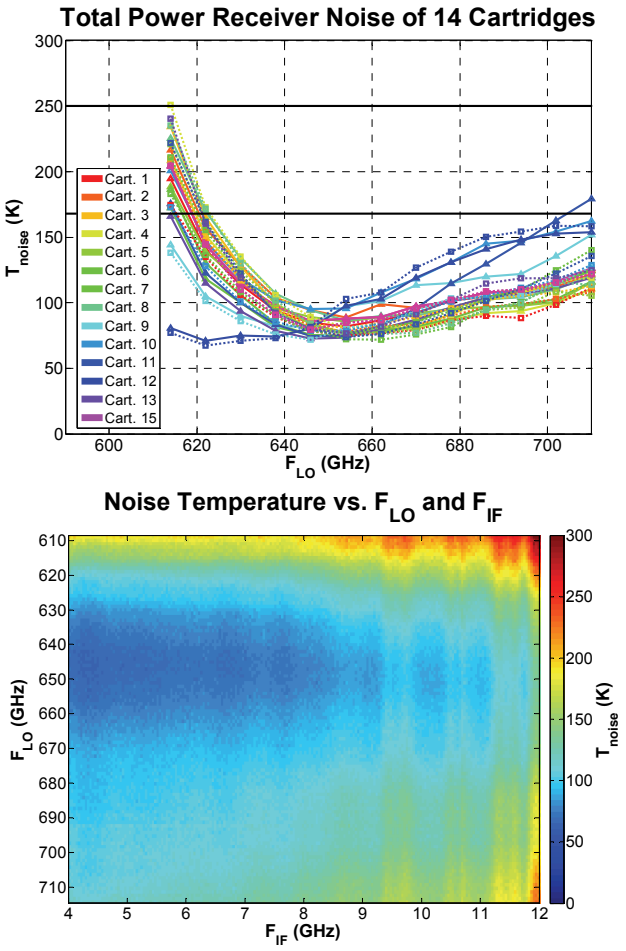

Fig. 3 – Sample receiver noise temperature test results. (top) Total power receiver noise for 14 cartridges at 13 LO frequencies, measured at optimum bias for each frequency. (bottom) Narrow-band receiver noise at 1 GHz LO spacing and 50 MHz IF spacing, for a fixed LO-independent mixer bias point. The automated control system allows this 2-D noise temperature scan to be completed in less than 1 hour.

E. Near-Field Testing

Near-field phase-sensitive tests are used for two purposes in

cartridge acceptance testing – phase-and-amplitude beam-pattern measurements and long-term phase drift measurements.

The basic elements of the near-field test system are:

- a signal source – a superlattice diode harmonic generator [6] driven by a microwave signal generator (SG1);
- a 2nd microwave signal generator (SG2) that replaces the YIG oscillator in the Band 9 LO;
- a microwave circuit that mixes harmonics of the outputs of SG1 and SG2 to create a reference signal;
- a phase detection system that uses a vector network analyzer to compare the amplitude and phase of the cartridge's response to the signal source with the reference signal; and
- a 3-D scanning stage that is mounted on the cartridge test cryostat, allowing the signal source to be scanned in a plane above the cryostat's optical window.

Beam-pattern measurements are performed at standard test frequencies across Band 9. Measurements are performed in two planes, separated by ¼-wavelength, to allow standing waves between the receiver and the probe to be removed [7]. The near-field data is Fourier transformed to the far-field and corrected for the far-field pattern of the corrugated probe horn. The angular size and position of the corrected far-field pattern are then compared with those of the antenna's secondary mirror. The far-field data is also analyzed to determine the receiver's aperture efficiency and phase center. Finally, the phase centers of the cartridge's two polarization beams are compared to determine their co-alignment in the focal plane. (The signal source's polarization is manually rotated to allow the cartridge's two polarization beams to be sampled.)

Fig. 4 shows the cartridge test system configured for near-field measurements. The off-axis mirror that normally focuses the cartridge beam into the hot-cold load (see Fig. 2) is removed and the 3-D scanning stage is mounted on the cryostat with the signal source above the cryostat window.

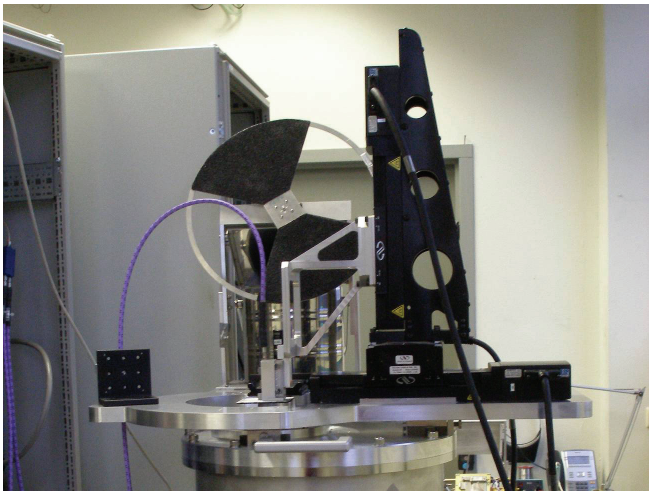

Fig. 4 – The Band 9 cartridge test system configured for near-field phase-and-amplitude beam-pattern measurements. A harmonic source is scanned in a plane directly above the cryostat window and can be rotated without disturbing its lateral alignment to allow the relative alignment of the cartridge's two polarization beams to be verified.

Fig. 5 presents sample near- and far-field data for one polarization of one Band 9 cartridge. The far-field amplitude plot includes an outline and marker indicating the angular size and position of the antenna's secondary mirror (which is nominally offset by 0.95° from the vertical). The data shown (with 201x201 points sampling a 40 mm x 40 mm scan region) is obtained in ~ 1 hour per frequency and polarization.

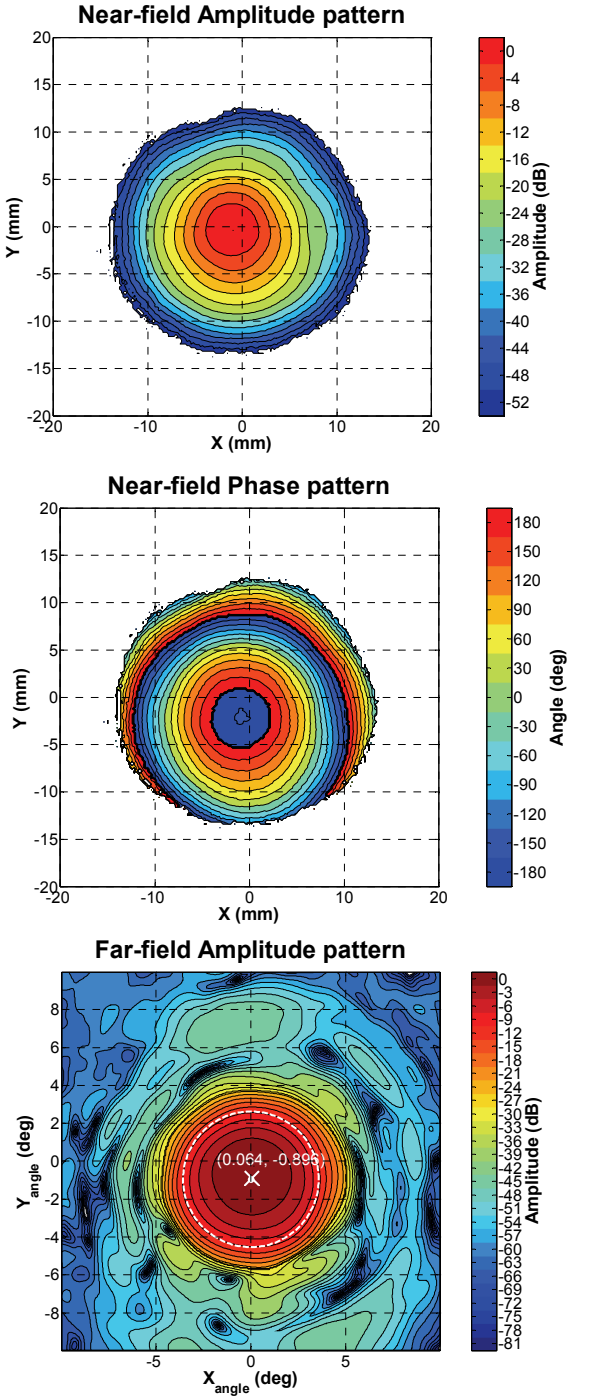

Fig. 5 – Antenna beam-pattern test results. (top and middle) near-field amplitude and phase patterns. (b) far-field amplitude pattern obtained from the measured near-field data (corrected for the far-field pattern of the corrugated probe horn).

F. Stability Testing

Two forms of stability test are performed on each cartridge – Allen variance measurements of the total power output power when observing a room-temperature blackbody, and phase drift measurements. Both measurements are performed for 3 standard frequencies and both cartridge polarizations.

Output power stability measurements are performed with 25 ms sampling for 60 min., allowing the cartridge's Allen variance to be verified for delays of 0.05 to 300 s. Fig. 6 (top) presents data for 15 cartridges at 670 GHz LO frequency.

Phase drift measurements are performed using the near-field test system with the source fixed in position at the center of the cartridge beam. The cartridge phase is sampled with ~ 0.1 s sampling over a 70 min. duration. The measured data is then integrated to create 10 s samples, which are statistically analyzed to determine the standard deviation in the data for delay times up to 5 min..

Fig. 6 (bottom) presents sample phase drift data for one polarization of one cartridge. Also included in this plot is the variation in the temperature of the phase lock loop (PLL) in the Band 9 LO. This is used as an indicator of variations in the ambient temperature during the measurement. As the data indicates, these long-term phase drift measurements are sensitive to drifts in the ambient temperature on the order of 0.5° over a 1 hour period. In general, the requirement that the maximum standard deviation of phase be less that 1.6° is met with margin in all cartridges.

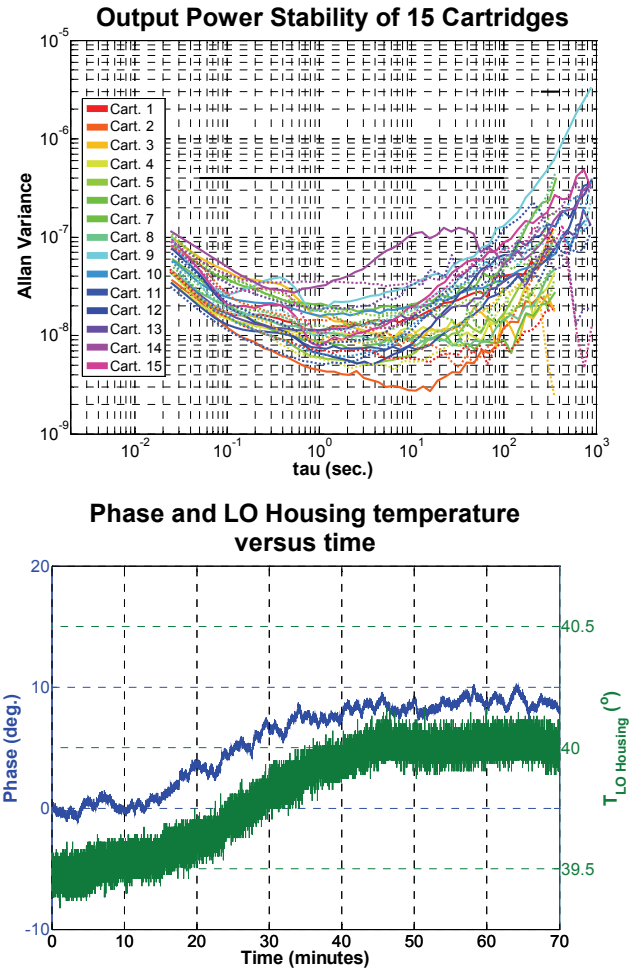

Fig. 6 – Receiver stability test results. (top) total power output power Allen variance of 15 cartridges at 670 GHz LO frequency. (bottom) signal path phase and LO housing temperature drift with time. Both stability tests are sensitive to the ambient environment. Optimal results are obtained from unattended overnight tests (3 frequencies can be tested in one night).

IV. Conclusion and Production Plans

An automated test system has been developed to allow each ALMA Band 9 cartridge to be thoroughly tested prior to delivery to the project. The system was fine-tuned while testing the first 8 cartridges between 2004 and 2008.

During the project's production phase, 65 cartridges are to be delivered to the project over 2009-2012, at a rate of up to 2 cartridges per month. Given a need for retesting and/or reworking of some cartridges, experience shows that the full acceptance test program can be completed in an average of 3 weeks. For this reason, a duplicate test system was built in 2008 – the use of two test systems in parallel is needed to allow the required delivery rate to be achieved.

Acknowledgment

The staff of the NOVA Band 9 group at the University of Groningen and SRON (M. Bekema, M. van den Bemt, G. Gerlofsma, M. de Haan, R. de Haan, R. Jager, A. Koops, J. Koops van het Jagt, P. Mena, J. Panman, and C. Pieters) are acknowledged for their continuing efforts to produce and test the Band 9 cartridges. W. Boland and E. van Dishoeck (NOVA), F. Helmich (SRON), and G. H. Tan (ESO) are acknowledged for their ongoing support of the Band 9 effort. R. Rivas is acknowledged for his contributions to the development of the cartridge test software. D.G. Paveliev is acknowledged for developing the superlattice harmonic generators used in the near-field test system.

References

[1] www.almaobservatory.org,

[2] Y. Sekimoto *et al.*, "Cartridge Test Cryostats for ALMA Front End," ALMA memo 455, 2003.

[3] E. Bryerton, M. Morgan, D. Thacker, and K. Saini, "Maximizing signal-to-noise ratio in local oscillator chains for sideband-separating single-ended mixers," *18th Intl. Symp. on Space Terahertz Technology*, Pasadena, CA, March 2007.

[4] R. Hesper *et al.*, "Design and development of a 600-720 GHz receiver cartridge for ALMA Band 9," *16th Int. Symp. On Space THz Technology*, ISSTT 2005, Chalmers University of Technology, Göteborg, Sweden, May 2-4, 2005.

[5] B.D. Jackson *et al.*, "Series production of state-of-the-art 602-720 GHz SIS receivers for Band 9 of ALMA," these proceedings.

[6] D. G. Paveliev *et al.*, "Short GaAs/AlAs superlattices as THz radiation sources," in Proc. of the 19th Int. Symp. On Space THz Technology, Groningen, 28-30 April 2008, pp. 319-328.

[7] A. Baryshev, M. Carter, W. Jellema, and R. Hesper, "Design and evaluation of ALMA band 9 quasioptical system," in: Proceedings of the 5th International Conference on Space Optics (ICSO 2004), 30 March - 2 April 2004, Toulouse, France. Ed.: B. Warmbein. ESA SP-554, Noordwijk, Netherlands: ESA Publications Division, ISBN 92-9092-865-4, 2004, p. 365 – 371.

A 380 GHz sub-harmonic mixer using MMIC foundry based Schottky diodes transferred onto quartz substrate

J. Treuttel, B. Thomas, A. Maestrini, H. Wang, B. Alderman, J.V. Siles, S.Davis, T.Narhi.

***Abstract*—In this paper, we report upon the development of a 380 GHz sub-harmonic mixer using foundry planar Schottky diodes. The device has been fabricated by the commercial foundry UMS (United Monolithic Semiconductors) using the BES process, and post-processed afterwards to transfer the GaAs circuit membranes onto a quartz substrate. The measurement of a single device has been done with a fast automatic Y factor test bench, with a resolution of 0.001 dB.**

***Index Terms*—Schottky diode, transferred substrate, sub-harmonic mixer, 380 GHz.**

I. Introduction

While visible and infrared observations from geostationary satellites are available for already three decades and provide only information on the top of the clouds, sub-millimeter wave radiometry offers new perspectives for the characterization of clouds and rain at global scale.

Indeed, recent theoretical studies on the atmospheric sounding capabilities of space borne sub-millimeter wavelengths have shown that cloud content, cloud profile, rain detection and quantification, as well as properties of ice particles, can be derived from brightness temperatures simultaneously measured at different frequencies above 100 GHz with multi-channel retrieval algorithms [1].

Sub-millimeter technology also offers the possibility to deploy a geostationary sensor that would monitor continuously the evolution of the clouds at an adequate spatial resolution. Schottky-diode-based radiometers are highly interesting because of their capabilities to work at ambient temperature and to operate with a fast response.

A MMIC sub-harmonic 380 GHz mixer could then be used to measure the radiometric signal in the 380 GHz H2O band required in the Geostationary Observatory for Microwave Atmospheric Sounding (GOMAS) mission [2]. Additionally MMIC technology based components are more reproducible and could bring the instrumentalists forward to build multi-pixel receivers [3] that would offer new scan strategy for Earth observations.

In this context, the European Space Agency ESA has initiated a programme to investigate the use of the GaAs foundry service from United Monolitic Semiconductor UMS and push forward the limitations of this service for frequencies up to 1 THz [4]. In order to enhance device performance, and particularly reduce dielectric constant and improve thermal conductivity, an amended way of post processing GaAs wafers has been explored [5]. We will report on the design and performance of a 380 GHz sub-harmonic mixer with integrated Schottky diodes fabricated using this process.

A. A high frequency MMIC industrial fabrication process

1) Purposes of development : Schottky diodes are generic components that are used in practically all non-cryogenic millimeter and submillimetre wave receivers in Earth observation and space science. MMIC technology applied to integrated Schottky structures has nevertheless not been conducted by industry at submillimeter ranges. This program consists in demonstrating that MMIC devices could be developped with existing industrial processes enhanced by a transfer substrate technique. The circuit presented this paper has been fabricated by UMS using an amended BES process.

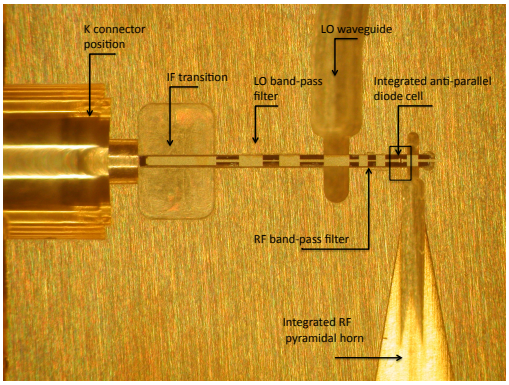

Fig. 1. Picture of the 380GHz mixer placed inside the lower half of the waveguide cavity.

Two fabrication runs have been planned to correct possible diode fabrication default of the first prototype run.

Manuscript received April 20, 2009. This work was supported by ESA program ESA AO/1-5084/06/NL/GLC.

J.Treuttel and H. Wang are with Observatoire de Paris, LERMA, 75014 Paris, FRANCE and STFC, Rutherford Appleton Laboratory, Didcot, OX11 0QX, UK. E-mail: jeanne.treuttel@obspm.fr

B.Thomas is with Rutherford Appleton Laboratory, Didcot, OX11 0QX and now with Jet Propulsion Laboratory, California Institute of Technology, Passadena CA 91109,USA.

A.Maestrini is with Observatoire de Paris, LERMA, 75014 Paris and Universite Pierre et Marie Curie Paris 6.

B.Alderman is with Rutherford Appleton Laboratory, Didcot, OX11 0QX.

J.V. Siles is with Universidad de Politecnica de Madrid, Ciudad Universitaria s/n, 28040 Madrid, Spain.

S.Davis is with University of Bath, Bath, BA2 7AY, UK.

T.Narhi is with ESA/ESTEC, Keplerlaan1, 2200 AG Noordwijk ZH, The Netherands.

2) Transferred substrate technique: A novel yet straightforward transferred substrate technique is described in detail in [5]. This technique does not involve high temperatures and/or high pressures operation, which is very important to avoid circuit degradation. In particular, an etchtop layer was introduced to facilitate membrane formation. This developement for MMIC devices allows the transfer of large surfaces of GaAs membranes (typically 0.7 x 0.7 cm2) onto a wide variety of host substrates. In the case of the circuit presented in this paper, quartz was used.

B. Mixer design

The circuit design of a 380 GHz fixed-tuned MMIC subharmonic mixer similar to [6] is presented hereafter. In particular, the sub-harmonic mixer features an anti-parallel pair of BES planar Schottky diodes integrated with the passive microstrip circuit onto a 4-um thick GaAs membrane.
The GaAs membrane is then transferred onto a 50-um thick quartz substrate using the transferred substrate technique. A gold beam-lead is formed at the RF end during the circuit fabrication, providing precise grounding of the diode pair at IF/DC frequencies. The LO/RF waveguides, the microstrip channel and the IF connector socket are milled into two split-waveguide metal blocks. The circuit placed inside the lower half of the waveguide cavity is shown in Fig.1.

The methodology used to design and optimize the mixer circuit uses a combination of linear/non-linear circuit simulations (Agilent ADS) and 3D electro-magnetic simulations with Ansoft and HFSS.

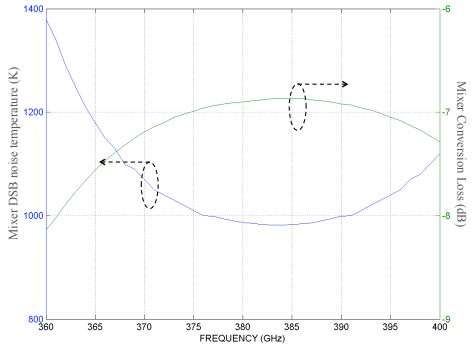

Fig. 2. Simulated conversion loss and mixer noise temperature in the 360-400 Ghz frequency band.

The electrical parameters of the BES Schottky diode model considered in the simulations are a series resistance Rs = 11 Ω, an intrinsic zero voltage junction capacitance of Cjo = 1.7 fF, a saturation current Isat = 50 fA, an ideality factor = 1.25 and a built-in potential Vbi = 0.8 V. Fig.2 shows the estimated DSB conversion losses of the mixer versus RF frequency. A local oscillation power of 2.5 mW is assumed during the simulations. An IF frequency of 1.5 GHz is chosen. The estimated DSB mixer noise temperature is bellow 1000 K around 380 GHz, and bellow 1200 K between 360 GHz and 400 GHz. The instantaneous RF/LO bandwidth is predicted to extend over a relative bandwidth of more than 10 percents.

C. First run results

I/V measurements of several anti-parallel pair of diodes have been performed at the Rutherford Appleton Laboratory(RAL) and show unsymmetrical diode characteristics. For example the serie resistance have been measured as Rs_{Diode1} = 19.88 Ω and Rs_{Diode2} = 40.4 Ω, the ideality factor as η_{Diode1} = 1.26 and η_{Diode2} = 1.39 and the saturation current as Is_{Diode1} = 1.55 e-14 A and Is_{Diode2} = 7.55 e-14 A. These first run I/V results affect the mixer predicted performance.
Preliminary measurements of the mixer noise temperature done at the Observatory of Paris (LERMA) are given in Fig.3. The mixer presents a double sideband noise temperature of 3667 K and 10.9 dB of conversion loss at 390 GHz. The experimented results are for one single device only and are a outcome of the first prototype farication run. Two others mixers are expected to be tested in the future for the second run.

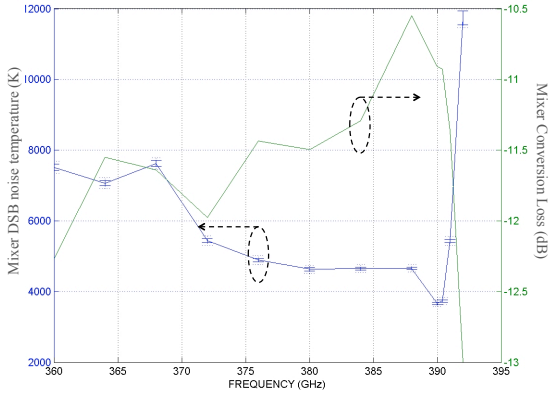

Fig. 3. Mixer characterisation results done at LERMA. Left-hand side curve: DSB mixer noise temperature(K), Right-hand side curve: conversion loss(dB). Worth case and quadratic errors bars are plotted for the DSB mixer noise temperature for load temperatures uncertainty of 0.5 (hot load) and 3 K (cold load).

D. LERMA mixer measurement set up

1) Measurement procedure: The G_{Mix} and T_{mix} are deduced from consecutive measurements of T_{Rec} and T_{IF} with an internal noise diode switched on and off as follow:

$$T_{IFon} = \frac{T_{hot} - Y_{IFon} * T_{cold}}{Y_{IFon} - 1} \quad (1a)$$

$$T_{IFoff} = \frac{T_{hot} - Y_{IFoff} * T_{cold}}{Y_{IFon} - 1} \quad (1b)$$

By substracting (1a) and (1a) and injecting it into the respective Friis formula, we deduce (2a) and (2b).

$$G_{mix} = \frac{T_{IFon} - T_{IFoff}}{T_{RECon} - T_{RECoff}} \quad (2a)$$

$$T_{mix} = T_{RECoff} - T_{IFoff} * \frac{T_{RECon} - T_{RECoff}}{T_{IFon} - T_{IFoff}} \quad (2b)$$

This straight forward operation allow us to deduce the gain of the chain with local and time related measurements.

2) Measurement error: The quadratic error of the measurement chain, i.e. mixer noise temperature ΔT_{Mix} and gain ΔG_{Mix} have been calculated from the uncertainty budget element taken as the measurement error $\Delta Y_{reading}$ and load temperature error ΔT_{cold}, ΔT_{hot} . Because the error depends on the different derivative value, the contribution on each parameter error will not be homogenous. We note that the final error is drastically depending on mixer absolute noise temperature and conversion loss. For this purpose we have descibed the uncertainty of the measurement for different mixer performance in table I. We take for the hot and cold load an error of respectively 4 % and 0.5 %.

T_{Mix}-G_{Mix}	$Y_{reading}$	Quadratic error (ΔT_{Mix}-ΔG_{Mix})
683K - 0.3717	0.115 %	1.32 % - 2.58 %
3667K - 0.0812	0.5 %	1.745 % - 4.18 %
11740K - 0.0501	1 %	3.32 % - 14.77 %

TABLE I
UNCERTAINTY OF THE OVERALL MEASUREMENT CHAIN FOR A GIVEN MIXER PEFORMANCE IN PERCENTAGE

For the presented mixer, we have a quadratic error of 1.32 % (64 K) for ΔT_{Mix} and 4.18 % (0.0034) for ΔG_{Mix} at 390 GHz. Two set of error bars, quadratic and worth case are plotted in Fig.3 for each frequency points.

3) Description of the test bench: The setup is mounted on top of an optical table and uses multiple opto-mechanical parts from Newport to firmly fix the mixer, the Local Oscillator (LO) chain and the Intermediate Frequency (IF) amplifier chain to the bench. The IF 2-4 GHz chain amplifies the output signal of the mixer with a gain of 77 dB. The power meter (N1912A and a fast power sensor Agilent E9325) is externally synchronized with a mechanical chopper used to present alternatively a blackbody at room temperature and a blackbody at 77 K in front of the mixer feed horn. Chopper frequency is set to 33 Hz.

4) IF chain: In addition to classical Y factor measurement chain, LERMA IF chain has an internal noise source that can be switched on and off to modify its noise factor.This feature is very useful since two independent Y-factor measurements are necessary to extract both the equivalent noise temperature of the mixer and its conversion losses. The IF chain is integrated on an aluminum box (see Fig.4).

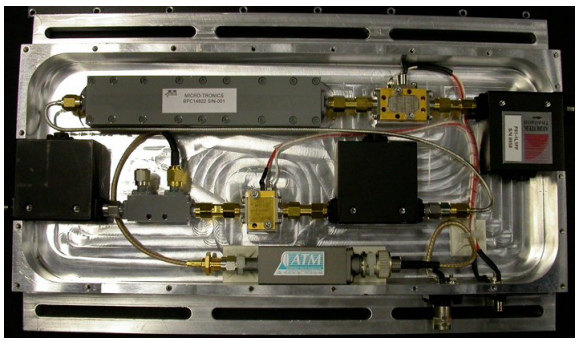

Fig. 4. 2-4 GHz IF chain with internal noise diode described in [7].

5) Power sensor and power meter setup: Our mixer bench uses an Agilent N1912A power meter and an Agilent E9325A peak power sensor for measuring the power delivered by the IF chain. Two time gates are defined on the N1912A power meter : one corresponds to the room temperature black body being totally in front of the mixer feed horn, the other corresponds to the 77 K black body being totally in front of the mixer feed horn. The Agilent E9325A peak power sensor is configured in normal mode and bandwidth is set to off. The power meter measures in Feed1 the average power of gate1 while feed2 records the average power of gate2. A combined measurement can be defined as Feed1/Feed2 which is the uncorrected value of the Y-factor. The power meter gives directly an uncorrected value of the Y-factor with a resolution of 0.001dB and a noise floor of 0.001 dB after video averaging over 256 periods.

6) Agilent E9325A peak power non-linearity corrections: As the Agilent E9325A power sensor has only 300kHz of bandwidth it is not calibrated for measuring white noise signals of several gigahertz of bandwidth. It is necessary to calibrate the power sensor against a sensor with unlimited bandwidth like the Agilent 8482A thermocouple sensor. Our calibration procedure is able to correct the Y-factor with an estimated remaining non-linearity error below 0.005 dB/dB. For white noise signals in the 2-4 GHz band and for powers ranging from -5 dBm to -1 dBm, the uncorrected Y factor is biased by a systematic error of +0.097 dB/dB. For power in the -10 dBm to -5 dBm, the uncorrected Y factor is biased by a systematic error of +0.093 dB/dB. Note that the non linearity of the E9325A sensor decreases if it is configured in average only mode but in this case time gating is not available.

II. CONCLUSION

A 380 GHz sub-harmonic mixer has been fabricated with a new transferred substrate process using MMIC industrial process and avoiding high pressure and temperature. The device shows performances affected by diode unexpected characteristics. Other devices fabrication and test are on-going for a second run expecting better diode performances. This first attempt to use UMS process at these frequencies is very promising for MMIC fabrication at industrial scale adding a simple transfer substrate process. We expect this technique to be developped in the future for multipixel Schottky receivers. The mixer has been tested with a Y factor mixer characterisation test bench built at LERMA observatory of Paris. The Y factor has a resolution of 0.001 dB and an estimated remaining non-linearity error below 0.005 dB/dB. The quadratic error is depending on absoulte mixer performance.

ACKNOWLEDGMENT

This work has been conducted with the ESA program ESA AO/1-5084/06/NL/GLC.

REFERENCES

[1] E. Defer, C. Prigent, F. Aires, J.R. Pardo , C.J. Walden, O.Z. Zanife , J.P. Chaboureau,and J.P. Pinty : *Development of precipitation retrievals at millimeter and sub-millimeter wavelengths for geostationary satellites*,JOURNAL OF GEOPHYSICAL RESEARCH, VOL. 113,April 23, 2008.

[2] B. Bizzari et al.: *GOMAS - Geostationary Observatory for Micro-wave Atmospheric Sounding, submitted to ESA in response to the call for ideas for the Next Earth Explorer Core Missions*

[3] H. Wang, A. Maestrini, B. Thomas, B. Alderman , G. Beaudin : *Development of a Two-Pixel Integrated Heterodyne Schottky Diode Receiver at 183GHz*, Proceedings of the 19th Int. Symp. on Space THz Technology, Groningen, the Netherlands, April 28-30, 2008.

[4] B. Alderman, H. Sanghera, B. Thomas, D. Matheson, A. Maestrini, H. Wang, J. Treuttel, J. V. Siles, S. Davies, T. Narhi : *Integrated Schottky Structures for Applications Above 100 GHz*, proceedings of the 38th European Microwave Conf., European Microwave Week, Amsterdam, October 27-31, 2008.

[5] B. Thomas,J. Treuttel,B. Alderman,D. Matheson,T. Narhi: *Application of substrate transfer to a 190 GHz frequency doubler and 380 GHz sub-harmomic mixer using MMIC foundry Schottky diodes*,SPIE Astronomical Instrumentation conference, Marseille , France, June 2008.

[6] B. Thomas,A. Maestrini and G. Beaudin: *A low noise fixed tuned 300-360 GHz sub-harmonic mixer using planar Schottky diodes*, IEEE Microwaves and Wireless Component Letters, p.865-867, vol.15,no.12, December 2005.

[7] http://lerma7.obspm.fr/ maestrini/

Conception and Fabrication of GaAs Schottky diodes for Mixers

Cecile Jung, Alain Maestrini, Antonella Cavanna, Ulf Gennser,
Isabelle Sagnes, Hui Wang, Yong Jin

***Abstract*—We report on the design and fabrication of Schottky diodes for millimeter and submillimeter wave mixers. The process for anti-parallel pairs of diodes with submicronic anode areas on 10/50µm thick GaAs substrates is presented and these diodes will be used in 183GHz and 330GHz mixer blocks.**
I(V) measurements have been performed and values of the ideality factor and the reverse saturation current have been determined.

***Index Terms*—GaAs Schottky diodes, Air-bridges, Millimeter and submillimeter waves mixers**

I. INTRODUCTION

Millimeter and submillimeter heterodyne observations will improve our understanding of the universe, the solar system and the Earth atmosphere. Schottky diodes are strategical components that can be used to build THz sources or mixers working at room temperature. A GaAs Schottky diode is one of the key elements for multipliers and mixers at THz frequencies since the diode can be extremely fast by reducing its size and also very efficient thanks to the low forward voltage drop[1].

II. FABRICATION TECHNOLOGY

The fabrication process presented below is based on electron beam lithography and conventional epitaxial layer designs. The starting material is a semi-insulating 500µm GaAs substrate with epitaxial layers grown by Metal-Organic Chemical Vapor Deposition (MOCVD) or Molecular Beam Epitaxy (MBE).

The layer structure consists of a first 400nm of AlGaAs etch-stop layer and a first GaAs 40µm membrane followed by a second 400nm of AlGaAs etch-stop layer and a second GaAs thick membrane.

The active parts of the substrates are as followed, 40nm AlGaAs etch-stop layer, an 800nm heavily doped $5x10^{18}$ cm^{-3} n^+ GaAs layer and a 100nm n type GaAs layer doped $1x10^{17}cm^{-3}$.

Manuscript received 20 April 2009. This work is partly supported and funded by the CNRS (Centre National de la Recherche Scientifique), the CNES (Centre National d'Etudes Spatiales) and Astrium.
C. Jung is with LPN (Laboratoire de Photonique et Nanostructures) – CNRS, route de Nozay, 91460 Marcoussis, France, and is associated with LERMA (Laboratoire d'Etude du Rayonnement et de la Matière en Astrophysique) - Observatoire de Paris, 77 avenue Denfert-Rochereau, 75014 Paris, France.
Email: cecile.jung@lpn.cnrs.fr
A. Maestrini and H. Wang are with LERMA – Observatoire de Paris.
A. Cavanna, U. Gennser, I. Sagnes and Y. Jin are with LPN - CNRS.

A. Device Processing

Two different structures for mixers, a 183GHz MMIC mixer (Fig 1-a) and a 330GHz circuit mixer (Fig 1-b) have been designed via CAD systems and fabricated using e-beam lithography.

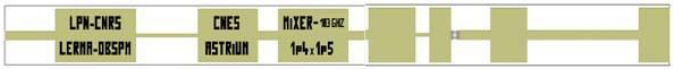

(a)

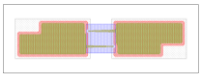

(b)

Fig 1: CAD captures of 183GHz MMIC mixer (a) and 330GHz circuit mixer (b).

A selective AlGaAs/GaAs wet etching is used to define the device mesas, the etch rate slows down sufficiently when the etch-stop layer is reached.
For the ohmic contacts, the n+ GaAs layer is recessed, Ni/Ge/Au metal films are successively evaporated and a rapid thermal annealing is performed.

For the air-bridges and Schottky anodes/connection pads, the process is as followed. Firstly, a square of resist is exposed and reflowed to form the support for the air-bridges.
The anodes are then fabricated using two layers of resists and the required profile is obtained by the combination of resist layer thicknesses, sensitivities and exposure doses.
Finally, Ti/Au metal film is evaporated to make the Schottky contacts and connection pads.

The diodes are then passivated using Si_3N_4 deposited by PECVD (Plasma Enhanced Chemical Vapor Deposition). To allow circuit integration, circuits are separated by a deep dry etching using ICP (Inductive Coupled Plasma) - RIE: 10µm etching for the 330GHz circuit and 50µm etching for the 183GHz MMIC.

Finally, the wafer is then mounted topside-down onto a carrier wafer by using wax. The semi-insulating GaAs substrate is thinned to the desired thickness (10µm or 50µm) using the same process as in [2].

Some scanning electron microscopy (SEM) pictures of the circuit and the diodes are shown in Fig 2 and Fig 3.

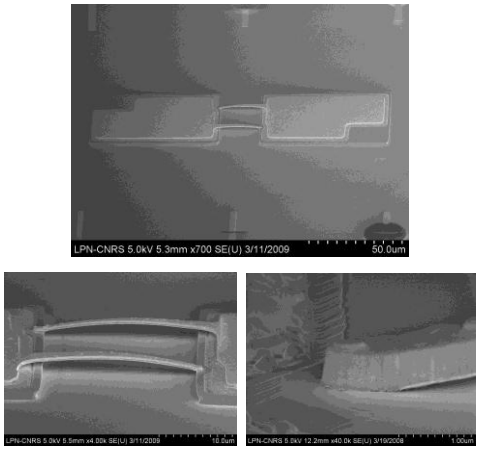

Fig 2: SEM pictures of the 330GHz circuit mixer

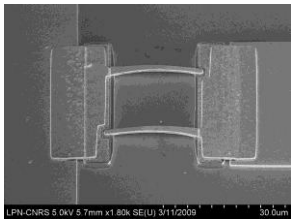

Fig 3: Close-up of the anti-parallel pair of Schottky anodes and air-bridges of the 183GHz MMIC mixer.

B. Devices DC Characteristics

Table 1 represents diode parameters fabricated at the LPN. All the diodes have the same finger length of 20µm. Electrical characteristics for each diode are deduced by standard I(V) measurements and reported in Table 2.

TABLE 1: FABRICATED DIODES PARAMETERS

Circuit Name	Diode #	Anode dimensions [µm x µm]
183 GHz	117M5	1.4 x 1.5
183 GHz	117M7	1.4 x 1.5
330GHz	117M8	0.8 x 1
330GHz	117M9	0.8 x 1
Best 1.10^{17}	117B2	5 x 7

TABLE 2: MEASURED DC PARAMETERS

Diode #	Ideality Factor n	Saturation current Is [A]	Series Resistance Rs [Ω]
117M5	1.165	$6.56\text{x}10^{-14}$	8.6
	1.178	$1.39\text{x}10^{-13}$	8.6
117M7	1.148	$2.25\text{x}10^{-13}$	5.71
	1.171	$8.18\text{x}10^{-14}$	7.11
117M8	1.097	$3.51\text{x}10^{-14}$	9.22
	1.125	$3.91\text{x}10^{-14}$	11.92
117M9	1.11	$6.13\text{x}10^{-14}$	10.47
	1.116	$6.54\text{x}10^{-14}$	11
117B2	1.08	$2.53\text{x}10^{-11}$	5.8

III. CIRCUIT INTEGRATION

183GHz MMIC Mixer: The completed testing structure consists of the circuit on a 50µm thick GaAs membrane, directly integrated onto the testing block pictured in Fig 4-a.

330GHz Mixer: The pair of anti parallel diodes, on a 10µm thick GaAs membrane is transferred topside down onto a 50µm thick quartz filter circuit substrate using epoxy [3]. A second quartz circuit completes the testing structures and the subharmonically 330GHz pumped mixer block is shown in Fig 4-b.

RF measurements will be performed at the Observatoire de Paris.

(a)

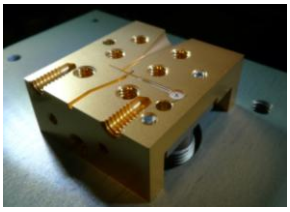

(b)

Fig 4: 183 GHz mixer bloc (a) and 330GHz mixer (b) bloc.

IV. CONCLUSION

Schottky diodes for mixers have been fabricated and their electrical parameters have been characterized. Since all fabrication steps are performed using e-beam lithography, our process allows further shrinking of the anode surface for higher frequencies mixers and multipliers.

RF Tests are in progress and results will be presented soon.

ACKNOWLEDGMENT

The authors wish to thank the MOCVD and MBE team of the LPN who grew the substrates and all the LPN clean room staff involves in this project. This work is partly supported and funded by the CNRS (Centre National de la Recherche Scientifique), the CNES (Centre National d'Etudes Spatiales) and Astrium in Toulouse.

REFERENCES

[1] I. Mehdi, S. C. Martin, R. J. Dengler, R. P. Smith and P. H. Siegel, "Fabrication and Performance of Planar Schottky Diodes with T-Gate-Like Anodes in 200-GHz Subharmonically Pumped Waveguide Mixers", IEEE Microwave and Guided wave letters, Vol. 6, No. 1, January 1996.

[2] S. Martin, B. Nakamura, A. Fung, P. Smith, J. Bruston, A. Maestrini, F. Maiwald, P. Siegel, E. Schlecht & I. Mehdi, "Fabrication of 200GHz to 2700GHz multipliers devices using GaAs and metal membranes", proceedings of the IEEE MTT-S, Vol.3, pp. 1641-1644, Phoenix, Arizona, May 20-25, 2001.

[3] B. Thomas, A. Maestrini, and G. Beaudin, "A Low-Noise Fixed-Tuned 300-360 GHz Sub-Harmonic Mixer using Planar Schottky Diodes", IEEE Microwave and Wireless Component Letters, Vol. 15, Issue 12, pp. 865 - 867, December 2005.

A Sideband-Separating Mixer Upgrade for ALMA Band 9

Ronald Hesper, Gerrit Gerlofsma, Patricio Mena, Marco Spaans, and Andrey Baryshev

***Abstract*—The ALMA band 9 (600–720 GHz) receiver cartridge, as currently being produced, features two single-ended (dual sideband) SIS mixers in orthogonal polarisations. In the case of spectral line observations in the presence of atmospheric backgound, the integration time to reach a certain desired signal to noise level can be reduced by about a factor of two by rejecting the unused sideband. A proof-of-concept sideband separating mixer has been successfully designed and produced over the past few years, the results of which have been presented earlier at this conference. At the time that the band 9 cartridge got its final form, however, this mixer was not yet ready for series production. Here, we present a design study that investigates the feasibility of upgrading the current ALMA band 9 cartridge to full dual-polarisation sideband separating capability, with minimal impact on the overall structure of the cartridge. The goal is to re-use as many of the parts and techniques of the existing cartridge as possible to provide a minimal-cost upgrade path, to be available in a couple of years.**

***Index Terms*—Sideband separating mixers, Submillimeter mixers, ALMA band 9**

I. INTRODUCTION

AT the time that the current ALMA band 9 receiver cartridge was made ready for large-scale series production, it was not feasible with the then-current state-of-the-art to equip it with anything more sophisticated than single-ended double-sideband (DSB) mixers. Now that the series production is well under way, it seems to be a good time to consider future alternatives. The most obvious candidate, since it promises an immediate improvement in the quality of observations, is replacing the double-sideband (DSB) mixers with sideband-separating (2SB) mixers.

In a DSB mixer, both the RF frequencies are detected that satisfy $\omega_{IFb} \leq (\omega_{RF} - \omega_{LO}) \leq \omega_{IFt}$ and $\omega_{IFb} \leq (\omega_{LO} - \omega_{RF}) \leq \omega_{IFt}$, with ω_{RF} and ω_{LO} respectively the antenna input and local oscillator frequencies, and ω_{IFt} and ω_{IFb} the top and bottom of the IF band. In other words, any signals that end up with negative frequencies during the downconversion process overlay those with positive frequencies. Especially for high frequency bands like band 9, this is a significant handicap because of the relatively high absorption (and therefore emission) of the atmosphere, even under the best of observing conditions. Removing the atmospheric noise from the image band can reduce the required observation time by a factor of the order of two, depending on the relative intensities of the spectral lines and the background.

Manuscript received 20 April 2009. This effort is supported by the European Community Framework Programme 7, Advanced Radio Astronomy in Europe, grant agreement no.: 227290, as well as by the NOVA3 program of NOVA, the Dutch Research School for Astronomy. A.M. Baryshev is supported by a personal NWO/STW VENI grant "Advanced Heterodyne Mixers for THz Applications".

R. Hesper, G. Gerlofsma and M.C. Spaans are with the Kapteyn Astronomical Institute, University of Groningen, Postbus 800, 9700 AV Groningen, The Netherlands.

F.P. Mena was with the SRON Netherlands Institute for Space Research and the Kapteyn Astronomical Institute, University of Groningen. Currently, he is with the Electrical Engineering Department, Universidad de Chile, Av. Tupper 2007, Santiago, Chile

A.M. Baryshev is with the SRON Netherlands Institute for Space Research, Postbus 800, 9700 AV Groningen, The Netherlands.

Contact: r.hesper@sron.nl, phone +31-50-363 4074

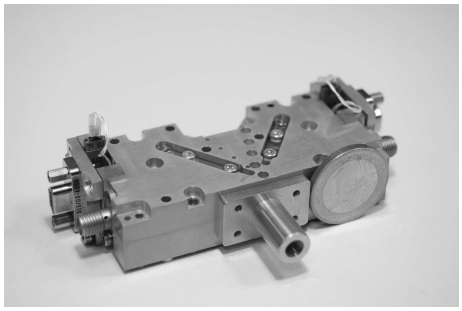

Fig. 1. Photograph of the original prototype 2SB mixer block.

The baseline of the design study presented here is a minimal-impact upgrade for the as-produced band 9 cartridges. This means that we try to reuse as many of the existing components (especially the expensive and long lead-time items). Also the per-cartridge effort to do the upgrade itself is intended to be minimized.

II. HISTORY

Several years ago, an effort was initiated to investigate the possibility to provide 2SB mixers for ALMA band 9 [1]. A design for a proof-of-concept mixer block was prepared [2], fabricated in several ways [3], [4] and characterized. A full account has been submitted for publication [5]. Here we will just summarize some key features and results.

The original 2SB mixer (Fig. 1) was a monolithic split-block design containing the RF hybrid, LO couplers, LO horn, matched loads, SIS junctions, magnet coils and magnet conductors for Josephson suppression and DC bias tees. The corrugated RF input horn is bolted as a separate component to the mixer block.

A conventional scheme is used for sideband-separation (shown in figure 2): a 90° RF input hybrid, -9dB LO couplers, two SIS mixers and a 90° IF output hybrid. The waveguide implementation of this scheme is shown in figure 3.

The most important results (noise temperature and separation efficiency) that were obtained with this mixer block are

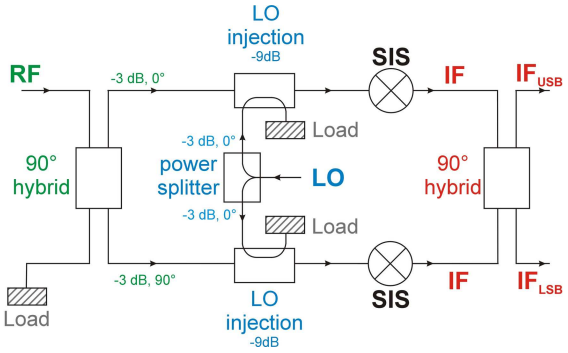

Fig. 2. The mixing scheme employed in both the original prototype and new design.

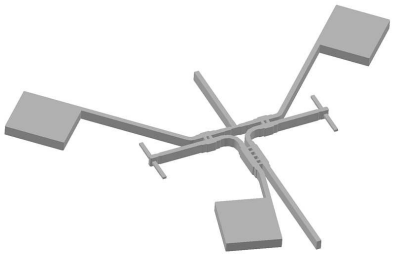

Fig. 3. The waveguide structure, shown in negative, of the RF part of the prototype 2SB mixer. The RF input is in the front, the LO input on the rear. The large square cavities contain the matched loads.

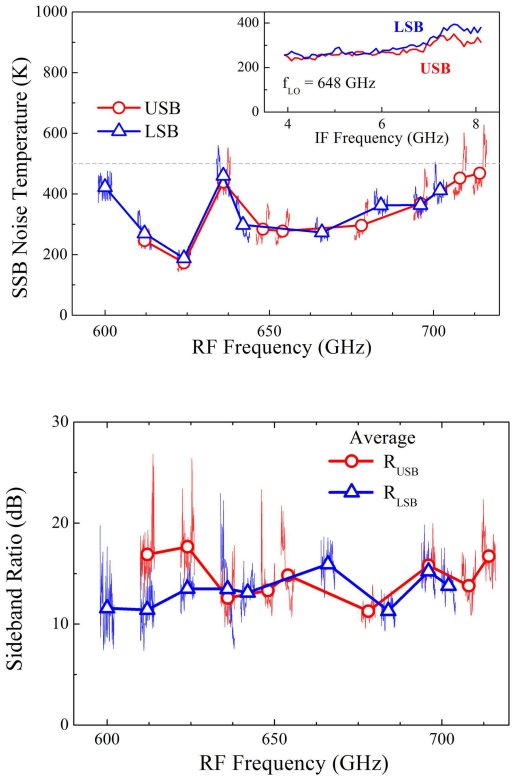

Fig. 4. The noise temperature and sideband-separation performance as obtained with the prototype mixer block. The ALMA requirements are 335K SSB noise temperature over 80% of the band, and 500K over the entire band; the separation should be better than 10dB.

shown in figure 4. As can be seen, even in its prototype state, the performance is already within ALMA specs for most of the frequency band.

III. Design Concept

One of the main lessons learned from the implementations of the original 2SB mixer block is the importance of a modular design, for several reasons. In the first place, because of the high complexity of the mixer block, involving machining on vastly different scales, it turned out to be very difficult to obtain blocks of satisfactory quality. Many times, in a late stage of production, small mistakes or accidents happened, ruining all the machining effort that had been put in already. In a more modular design, production is still critical, but the consequences of errors will be much more contained.

Another serious handicap that turned up in the monolithic design was the inability to replace mixer devices individually. To obtain a high sideband separation, not only the hybrids have to be of high quality, also the junctions (especially their gain) must be balanced as much as possible. Removal of a mixer device from the monolithic 2SB block involved dissolving the glue that held the device, and this turned out to be impossible without losing the other junction, which was only a couple of millimeters away. This made the matching of junctions a very laborious and time-consuming process. In the new design it will be possible to exchange the mixer devices independently.

Even a modular design of a mixer block does not automatically imply ease of assembly. Therefore, additional design criteria were defined, such as that a minimum number of components have to be removed to replace junctions, no wires have to be unsoldered, PCBs removed, etc.

Because this design study targets a minimal-impact upgrade of the currently produced receiver cartridges, compactness is an important issue. Especially the optics package, which in the production cartridges consists of two closely integrated blocks that contain all the mirror surfaces, is an expensive and critical part. The initial intention is to keep the current optics blocks, possibly with minor reworking. Other parts, like the optics mounting bracket (“cradle”) are easier and cheaper to manufacture again, and less effort shall be spent to try to reuse those.

Other expensive or long-lead time parts are the 4–12GHz cryogenic isolators and low-noise amplifiers. Whether these can be kept depends for a large part on the chosen IF configuration, which in turn is determined by the capabilities of the back-end and correlator, and, last but not least, the preferences of the observer community.

IV. Configurations

One of the requirements for any ALMA receiver cartridge is that the total bandwidth is 8 GHz. Currently all bands employing 2SB mixers output both upper and lower sidebands, both over a band of 4–8 GHz. Band 9 is the only production

band with DSB mixers, so there an IF band of 4–12 GHz is required to meet the total bandwidth specification.

When moving from a DSB to 2SB scheme, two different IF configurations can be envisioned.

- True 2SB, exporting both lower and upper sidebands, each over 4–8 GHz at the output of the cartridge.
- Effective SSB, terminating one of the sidebands in a 50 Ω load, exporting the other one over a 4–12 GHz IF band.

The SSB option has the advantage that expensive items like the IF isolators and cryogenic low-noise amplifiers (LNAs) can be reused, provided that the IF output hybrid of the 2SB mixer is of sufficient quality that a single isolator can be placed after it, instead of two in between the mixers and the IF hybrid.

In the case of the true 2SB option, new 4–8 Ghz isolators and LNAs have to be procured, which, although they are less expensive than their 4–12 GHz counterparts, still constitute quite an expense, especially since four of each are needed per cartridge. On the other hand, since 4–8 GHz components are easier to produce with high performance than 4–12 GHz components, the overall system noise temperature may be slightly better in the 2SB case.

Note that in the SSB case, it is still possible to choose which sideband is presented at the output, simply by reversing the bias of one of the mixers. It is therefore not necessary to extend the LO range to cover the entire 600–720 GHz RF band.

Sometimes, it can be an observational advantage to have two sidebands some distance apart, so two widely-spaced spectral lines can be observed at the same time, one in each sideband. On the other hand, if the lines are less than 8 GHz apart, the SSB option is more favorable. It should be clear that the final decision has to be made in close collaboration with the observing community.

There is of course a third possibility, which involves exporting both sidebands over 4–12 GHz. At the moment (to the best of our knowledge) neither the back-end nor the correlator can handle a total bandwidth of 16 GHz. However, if there is an opportunity to extend those systems in the future, a 4-12 GHz 2SB option can be considered. It might be feasable to make the design in such a way that the additional isolators and amplifiers can be retrofitted at a later stage.

V. Modular hybrid - mixer block

Since the current production of single-ended mixers for the ALMA band 9 cartridges involves testing and characterisation of many devices, it was decided to design the new 2SB mixer block around the standard band 9 junction holders (“backpieces”). These are compact, easy to mount on a standard horn for testing and matching, reusable, and, because of the high production volume, relatively cheap. The mounting and unmounting of mixer substrates is routinely done in-house. And, finally, since the junctions are in the same RF environment as the single-ended band 9 mixers, no new junction design is necessary; in fact, the 2SB mixer development effort benefits immediately from improvements and developments in the current production devices.

Figure 5 shows a cross-section through the proposed 2SB mixer. All parts are arranged around the central hybrid block.

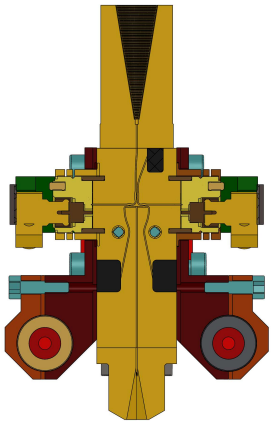

Fig. 5. Cross-section of the new 2SB mixer block. The RF input horn is at the top, the LO horn at the bottom. Left and right of the hybrid are two standard ALMA band 9 mixer backpieces, below them the magnet coils.

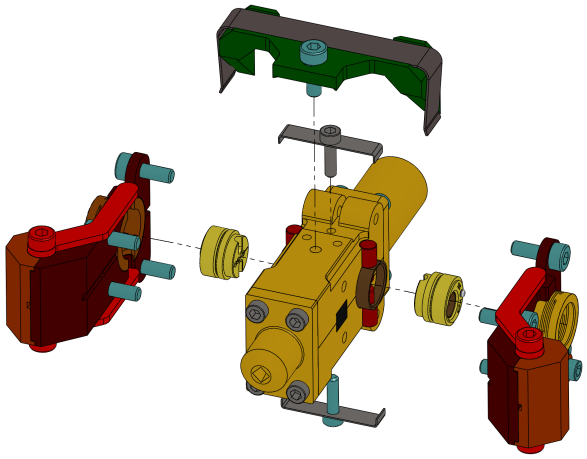

Fig. 6. Exploded view of the new 2SB mixer, showing the way it is disassembled to replace the mixer backpieces.

Two band 9 backpieces mate to the waveguides coming from the LO couplers. The alignment of the waveguides to the backshort cavity in the backpieces is done by a centering ring, a proven concept used in the single-ended band 9 mixers. It allows for easy exchange of the mixer devices without need of any special tools or even a microscope. The backpieces are held in place by spring-loaded retainer caps, also adapted from the DSB mixers. The magnet coils for the suppression of the Josephson current are integrated into the backpiece covers, together with the magnetic field conductors that guide the field

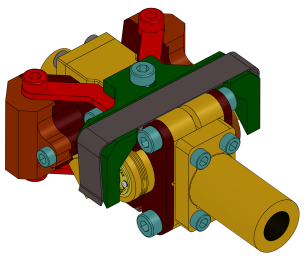

Fig. 7. The new design in its assembled state.

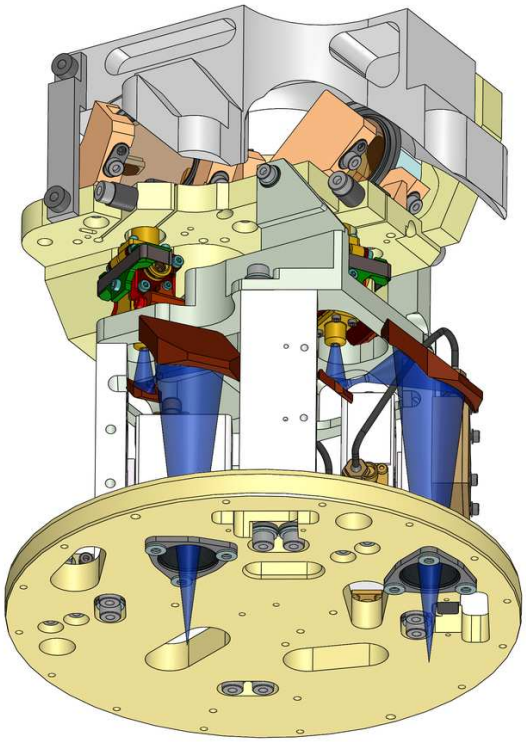

Fig. 8. The two 2SB mixers in place in the original optics assembly. The LO beams are diverted and refocussed onto the LO input horns.

to the junction. Figure 6 shows how the assembly is done. A few clips mounted on the top and bottom of the blocks provide pressure to the field conductors and the cable-mounted GPO IF connectors. The entire 2SB mixer block is shown in its assembled state in figure 7. A few auxiliary parts, like temperature sensors and DC connectors are not implemented yet, since their placement depends on space restrictions around the mixer, which have not been considered in detail yet.

VI. LO INSERTION

The LO insertion into the mixer block is mainly a geometrical problem. Two slow LO beams, one for each polarisation, are formed on the 90 K deck of the cartridge and pass upwards through the 12 K and 4 K decks. In the original DSB cartridge, they are then intercepted and horizontally focussed into the mixer horns by way of two 45° beamsplitters.

In the new design, the LO beams have to be diverted to axes diametrically opposite to the RF input horns. Because the optical pathlengths are now different from the original design, the beams have to be refocussed before they can couple to the LO horns in the mixer blocks. A design concept is shown in figure 8. Not worked out yet are the exact shapes of the mirrors and their mounting fixtures.

VII. IF HYBRID

One of the conclusions from the measurements on the original 2SB mixer block is that the sideband-separation performance was probably mainly limited by the quality of the IF output hybrid [5]. No commercial hybrids were found that would perform satisfactorily at 4K. An in-house effort involving a three-layer PCB to obtain a coolable 90° hybrid was somewhat successful performance-wise, but turned out to be a real challenge to produce even in a single copy.

Since the IF hybrid performance is of key importance to the 2SB mixer, especially in the 4–12 GHz case, we intend to construct a new hybrid, probably based on some form of interdigitated microstripline structure [6], made out of a superconducting film on a high-epsilon substrate, such as silicon. This should provide a compact and essentially lossless device. The technology to produce these, including the necessary bridges over the striplines is available in-house nowadays. The intention is to integrate the DC blocks, bias tee and eventual filter structures on the same substrate.

As an aside, a completely different solution (obviously out of the question for an ALMA cartridge upgrade) would be in the form of a real-time digital back-end performing the function of the IF hybrid, in which case it would even be possible to correct for rather large phase errors in the RF input hybrid.

VIII. OTHER IMPROVEMENTS

If it is decided that an upgrade of the produced cartridges is to go forward at a future date, it would of course be a good opportunity to look for other possible improvements. One of the most interesting ones would be an improvement of the cross-polarization performance, which leaves something to be desired in the current production cartridges. Since this would involve a major redesign of the entire optics package, we cannot speak about a minimal-impact upgrade anymore, and the cost would be substantially higher. We intend, in time, to present different options, with their estimated price-tags to the project, of course in close contact with the observing community. Actually, since most of these things will take several years to develop, about now would be the perfect time to start voicing ideas, suggestions and requests for future upgrades.

REFERENCES

[1] F.P. Mena, J.W. Kooi, A.M. Baryshev, C.F.J. Lodewijk and W. Wild, *Design of a side-band-separating heterodyne mixer for band 9 of ALMA*, 16th Intern. Symp. Space THz Technology, Göteborg, Sweden (2005)

[2] F.P. Mena, J.W. Kooi, A.M. Baryshev, C.F.J. Lodewijk, G. Gerlofsma and W. Wild, *Side-band-separating heterodyne mixer for band 9 of ALMA*, 17th Intern. Symp. Space THz Technology, Paris, France (2006)

[3] F.P. Mena, J.W. Kooi, A.M. Baryshev, C.F.J. Lodewijk, T.M. Klapwijk, R. Hesper and W. Wild, *Construction and Characterization of a Sideband-separating heterodyne mixer for band 9 of ALMA*, 18th Intern. Symp. Space THz Technology, Pasadena, California, USA (2007)

[4] F.P. Mena, J.W. Kooi, A.M. Baryshev, C.F.J. Lodewijk, T.M. Klapwijk, W. Wild, V. Desmaris, D. Meledin, A. Pavolotsky and V. Belitsky, *RF Performance of a 600–720 GHz Sideband-Separating Mixer with All-Copper Micromachined Waveguide Mixer Block*, 19th Intern. Symp. Space THz Technology, Groningen, The Netherlands (2008)

[5] F.P. Mena, J.W. Kooi, A.M. Baryshev, C.F.J. Lodewijk, R. Hesper, G. Gerlofsma, T.M. Klapwijk and W. Wild, *A Sideband-separating Heterodyne Receiver for the 600–720 GHz Band*, IEEE Trans. Microwave Theory Techn., submitted

[6] J. Lange, *Interdigitated stripline Quadrature Hybrid*, IEEE Trans. Microwave Theory Techn., Vol. 17, Pages 1150-1151 (1969)

P5B

Limits of image rejection of sideband-separating mixers

D. Maier[1*]
1 Institut de RadioAstronomie Millimétrique, St. Martin d'Hères, France
* Contact: maier@iram.fr, phone +33 4 76 82 49 16

***Abstract*—Nowadays many groups are working on sideband-separating mixers. The ALMA receivers e.g. will be equipped with 2SB mixers for band 3 to 8. And Band 9 is also working on a sideband-separating version. Initially the specification for the image rejection of the ALMA receivers was set to –10 dB. But since all groups had difficulties in achieving these values for all produced mixers, the specification had to be relaxed. It still seems to be difficult to explain, why it is a problem to achieve good image rejections with 2SB mixers. Simply summing up gain and phase imbalances of the different components and calculating the image rejection almost always results in better values than finally achieved in real mixers.**

We will examine in detail the influence of each component of the 2SB mixer on the achieved image rejection for the case of our ALMA Band 7 mixer. The measured results will be compared to theoretically derived values.

P5C

Shot-Noise Characteristics of NbN Superconducting Tunnel Junctions

Jing Li[1*], Xue-Song Cao[1], Masanori Takeda[2], Hiroshi Matsuo[3], Zhen Wang[2], and Sheng-Cai Shi[1]
1 Purple Mountain Observatory, CAS, Nanjing, JiangSu 210008, China
2 Kobe Advanced ICT Research Center, NiCT, Kobe, Hyogo 651-2492, Japan
3 National Astronomical Observatory of Japan, NINS, Mitaka, Tokyo 181-8588, Japan
* Contact: lijing@mail.pmo.ac.cn, phone +86-25-8333-2229

***Abstract*—An 0.5-THz superconductor-insulator-superconductor (SIS) mixer incorporating with all-NbN superconducting tunnel junctions has been developed and put into real astronomical applications [1]. Even with a measured receiver noise temperature down as low as five times the quantum limit ($5h\nu/k_B$), this NbN SIS mixer doesn't demonstrate reasonably good direct-detection behavior as conventional Nb SIS mixers. It is thought that the enhanced shot-noise due to the MAR (multiple Andreev reflection) effect [2] is considerably larger in direct detection than in heterodyne mixing. To better understand this difference, in this paper we mainly investigate the shot-noise characteristics of NbN superconducting tunnel junctions. Firstly, the power spectral density of the shot noise resulting from 0.5-THz NbN twin SIS junctions is measured with respect to the dc bias voltage by a low-frequency (~100 Hz) and high-frequency (a few GHz) method. The measured results are compared with simulated ones to understand how the shot noise is enhanced by the MAR effect. Secondly, the direct-detection and heterodyne mixing characteristics of the 0.5-THz NbN twin SIS junctions are measured and compared. Detailed experimental and simulation results will be presented.**

1. Jing Li, Masanori Takeda, Zhen Wang, Sheng-Cai Shi, and Ji Yang, Appl. Phys. Lett., vol. 92, 222504, June 2008.
2. P. Dieleman, H. G. Bukkems, T. M. Klapwijk, M. Schicke, and K. H. Gundlach, Phys. Rev. Lett., vol. 79, pp. 3486-3489, Nov. 1997.

Unilateral finline transition at THz frequencies

Boon Kok Tan and Ghassan Yassin

***Abstract*—We present a new type of waveguide to microstrip transition designs for a 700 GHz SIS mixer. The transition comprised a unilateral finline taper and the RF power from the finline slot is coupled through coplanar waveguide to microstrip using two radial stubs. This transition is significantly easier to design and fabricate than the conventional antipodal finline taper since the fins do not overlap at any stage. A key feature of this design is that it can be deposited on Silicon-on-Insulator resulting in a finline mixer chip on approximately 15 μm silicon substrate. This allows the mixer chip to be held in the E-plane of the waveguide without a supporting groove in the waveguide wall, avoiding the excitation of higher order modes. The chip is simply supported by gold leads deposited on the substrate. It should be emphasized that the employment of such substrate will also decrease the loss and allow finline mixers design to be extended to the THz region.**

***Index Terms*—finline transition, submillimeter wave mixers, slotline transition, coplanar waveguide transition, silicon-on-insulator technology**

I. Introduction

In previous publications we have reported the successful operation of SIS finline mixers in the frequency range 220-700 GHz [1]–[3]. These mixers have proven advantageous in providing broadband RF operation. The finline mixer chip is insensitive to mixer block machining tolerances, hence only requires basic block fabrication which becomes important at higher frequencies. The large chip area enables sophisticated planar circuit design to be elegantly integrated into a single detector chip.

The waveguide-to-microstrip taper we have so far employed an antipodal section with overlapping fins separated by a thin insulating layer ($\sim$ 400 nm). Although the fabrication of antipodal SIS mixers chip is certainly feasible, a lot of care is needed during processing in order to avoid narrow spikes that can potentially ac-short the chip, especially at the stage when the fins start to overlap [4]. Moreover, the complicated nature of the finline taper which comprises two dielectric layers and slightly overlaping superconducting fins makes it extremely difficult to compute or even model the electrical behaviour of the structure.

To overcome this difficulty, we have developed a new waveguide-to-planar circuit transition that does not employ an antipodal section [4]. Power is initially coupled from the waveguide using a unilateral finline taper as in the conventional design. The gap width is decreased to about 2 μm in order to decrease the impedance as much as possible while keeping the fabrication feasible with photo-lithography. At this stage, power is coupled to a coplanar waveguide (CPW) with the aid of two radial stubs as shown in figure 4.

Boon Kok Tan and Ghassan Yassin are with the Department of Physics (Astrophysics), University of Oxford, Denys Wilkinson Building, Keble Road, Oxfordshire, OX1 3RH. (phone: +44 (0)1865 273303; e-mail: tanbk@astro.ox.ac.uk; email:g.yassin1@physics.ox.ac.uk ; email: pxg@astro.ox.ac.uk).

Manuscript received 20 April 2009.

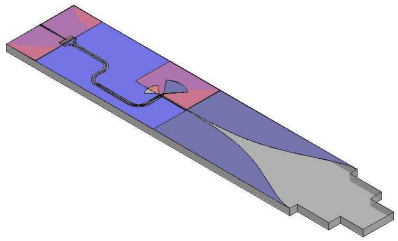

Fig. 1. Full finline chip design on a 15 μm silicon-on-insulator substrate.

A fundamental difficulty in realising the finline mixer design at THz frequencies is because the mixer chip is deposited on a quartz or silicon substrate which has a relatively high dielectric constant. This is because of the mismatch that the loaded waveguide presents to the incoming signal. Moreover, a groove of finite depth and height is needed in order to support the substrate in the E-plane of the waveguide. This can potentially excite higher order modes, hence limits the high frequency end of the mixer bandwidth. So far we were able to overcome this problem by using rectangular noches to match the loaded waveguide to free space and thin the substrate following device fabrication to avoid excitation of higher order modes within the band of operation. For example, at 220 GHz we needed to thin the quartz substrate to 180 μm while at 700 GHz we needed to thin it to less than 70 μm. At higher frequencies, even thinner quartz substrates are required which clearly becomes awkward if not impossible.

The introduction of the Silicon-on-Insulator (SOI) technology which has been reported in recent years overcomes all the difficulties explained above [5]. The ability to fabricate finline chips on extremely thin silicon substrate ($\sim$ 10 μm), will improve the performance of finline mixers, make them easier to design and fabricate, and more importantly extends their operation into the THz region. The very thin substrate presents light loading to the incoming waveguide signal, hence the notch structure may no longer needed and will prevent the excitation of higher order modes within a relatively large bandwidth. The mixer block design will become even simpler and will only consist of two halves of a rectangular waveguide. This is because the light chip will no longer need a deep groove in the waveguide wall but will now be supported by a few microns beam leads deposited on the chip and attached to the waveguide. The advantages of the above proposed idea

may be summarised as follows:

- The introduction of the new finline avoids the employment of an antipodal finline section which improves the performance of the mixer chip and makes it easier to fabricate and model.
- The employment of SOI allows the fabrication of the chip on a very thin substrate which improves the performance, broadbands the operation and extends it to the THz region.

In this paper, we present the design of a unilateral finline to microstrip transition at 700 GHz, deposited on a 15 μm Si substrate. The transition comprises a unilateral finline section, a slotline to coplanar waveguide section and a coplanar waveguide to microstrip transition, as shown in figure 1.

II. A NEW UNILATERAL FINLINE TO PLANAR CIRCUIT TRANSITION

The SIS finline mixers designed so far employed an antipodal finline section to realise the waveguide to microstrip transition. An important advantage of this design is that it provides an extremely wide band transition from the waveguide impedance to a low microstrip impedance, directly, without intermediate transformers. For example, assuming that the thickness of the isolating layer (SiO) that separates the fins is 400 nm and a microstrip width of 3 μm (which is easy to achieve using standard lithograpy), we obtain a characteristic impedance of 20 Ω, which is ideal for SIS junctions. As explained above however, the employment of an antipodal section presents difficulties in both fabrication and design, hence an alternative design is presented, which provides direct coupling of power from the unilateral finline to a planar circuit. The unilateral finline transition retains the advantages of the finline taper, outlined in the introduction, and yet is much easier to design and fabricate. The resulting transmission line is shorter and hence reduces the insertion loss and allows fabricating a larger number of devices on the same wafer.

Figure 2 shows an example of a unilateral finline taper, deposited on a 15 μm silicon-on-insulator substrate or on 60 μm of a quarts substrate. Power is coupled from the waveguide to the finline taper, which is tapered to the desired gap width gradually using a profile that gives the shortest possible taper [4]. A two-step notch is used on the substrate to match the impedance of the air-filled rectangular waveguide to the loaded waveguide, with broad band performance. Figure 3 shows the computed scattering paramaters of a unilateral finline taper deposited on both 15 μm silicon substrate and 60 μm quartz substrates, using Ansoft HFSS software package. It can be seen that for both the silicon and the quartz substrates, the return loss is less that 20 dB over 200 GHz which is sufficiently broad for many applications. In fact the bandwidth is mainly limited by the 2-stage notch component rather than the finline taper.

A. Slotline to coplanar waveguide transition

Planar circuits, in particular those that employ complex structure are usually fabricated in microstrip. This is because this structure provides a well defined frequency independent

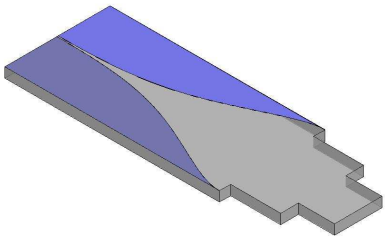

Fig. 2. Example of a unilateral finline taper deposited on a 15 μm silicon-on-insulator substrate.

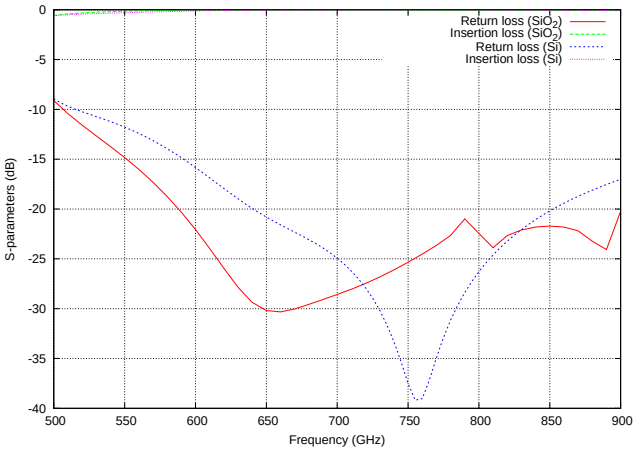

Fig. 3. Scattering parameters of the unilateral finline taper of 15 μm silicon-on-insulator substrate and 60 μm quartz substrate.

TEM fields confined between the strip and the ground plane. Moreover, manipulation of this structure has been thoroughly studied and realised in many applications. Making the transition from unilateral finline to microstrip directly however is not feasible in practice since the impedance of a slotline is much higher than that of a microstrip. For example, the impedance of a slotline of 2 μm gap on 15 μm silicon is about 60 Ω while the impedance of a 3 μm wide microstrip is about 20 Ω. Reducing the lateral dimension of the slot or the mirostrip further is not practical using standard lithography.

The impedance of the coplanar waveguide transition can easily be adjusted to match that of the unilateral finline, with dimensions that can easily be fabricated using photolithography. For example, a 60 Ω CPW can be realised with strip width of 2 μm and gap width of 2.5 μm.

Transition from unilateral finline to CPW is therefore first made. A short section of microstrip bridge is deposited across the slotline on a 425 nm insulator layer, terminated by a quarter wavelength shorted radial stub. The microstrip section is immediately stepped down after the bridge to form the central conductor of the coplanar waveguide. The slotline also is terminated by a radial stub which forms an RF short, as shown in figure 4. We would like to emphasise that since the length of the microstrip bridge is much shorter than a wavelength, the impedance seen by the slot is that of a CPW rather than a microstrip. We had simulate the performance

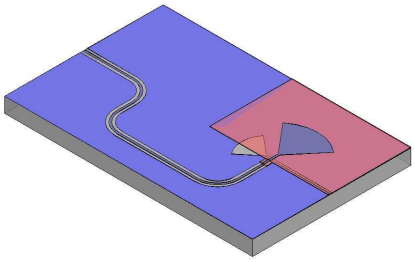

Fig. 4. Slotline to CPW transition via a short section of microstrip bridge. The ground plane, microstrip bridge and the central conductor of CPW is shown in blue, while the insulator layer is shown in pink.

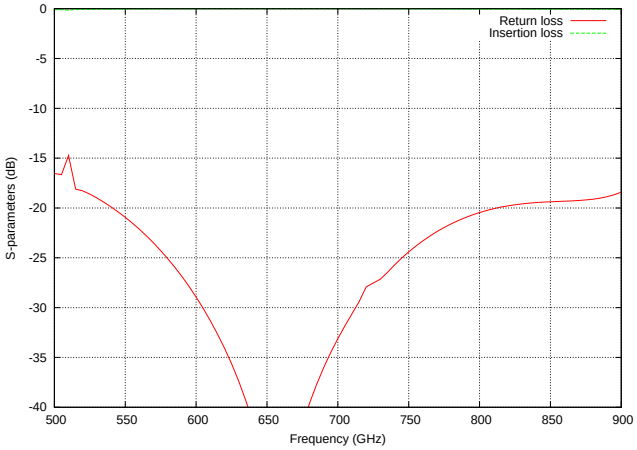

Fig. 5. Coupling efficiency of the transition deposited on a 15 μm silicon substrate.

of the transition using HFSS and the scattering parameters are shown in figure 5. The simulation shows very broad band behaviour at 700 GHz. The return loss is lower than -20 dB across a bandwidth of 350 GHz.

B. Coplanar waveguide to microstrip transition

We have already stated that complex mixer planar circuits such as tuning or sideband separating circuits can easily be realised in microstrip. Consequently, we have designed a three-steps CPW to microstrip transformer which is described in

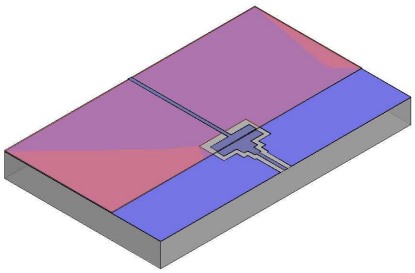

Fig. 6. CPW to microstrip transition via a 3-steps transformer. The ground plane and the microstrip is shown in blue while the insulator layer is shown in pink.

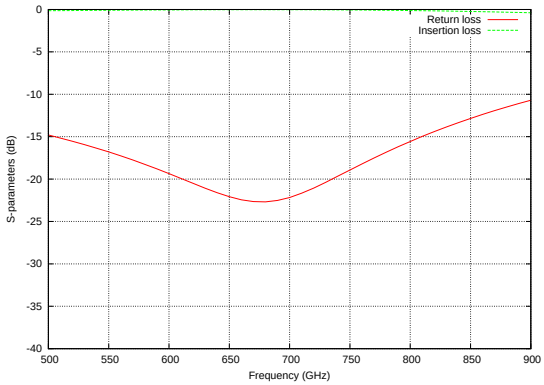

Fig. 7. Coupling efficiency of the CPW to microstrip transition on 15 μm silicon substrate.

Figure 6. The high impedance of the coplanar waveguide with narrow central conductor is slowly transformed to lower impedance coplanar waveguide by widening the central conductor to match the microstrip line impedance. The central conductor is then stepped up over the insulator layer to form the microstrip line. This stepping-up does not change the field configuration significantly as the thickness of the insulator layer is small compare to the width of the central conductor and the substrate thickness. Figure 7 shows the HFSS simulation of the transition. It can be seen that this simple transition design yields broadband operation although the return loss is typically -20 dB. This performance however can be easily improved by increasing the number of steps or tapering the transition.

III. Conclusion

We have presented a new type of waveguide to microstrip transition using unilateral finline deposited on a 15 μm silicon substrate for THz SIS mixers. The transition is deposited on a silicon-on-insulator substrate and hence greatly simplifies the mixer chip and block design and fabrication.

We are currently in the process of designing a back-to-back finline mixer using the above-described technology. The back-to-back design allows the feeding of the signal from one end and the LO from the other, thereby avoiding the employment of beam splitters. This will allow the mixer to be pumped with a much less powerful local oscillator, which can be useful for either the construction of focal plane arrays or the employment of photonic LOs. This, and the available large substrate area will allow elegant integration of sideband separating circuits on the mixer chip.

Acknowledgment

The authors would like to thank Chris North for the support on Finsynth script, and appreciates the useful discussions with Paul Grimes and Jamie Leech.

References

[1] G. Yassin, R. Padman, S. Withington, K. Jacobs, and S. Wulff, "A broad band antipodal finline mixer for astronomical imaging arrays," *Electron. Lett.*, vol. 33, pp. 498–500, 1997.

[2] G. Yassin, S. Withington, K. Jacobs, and S. Wulff, "A 350 ghz antipodal finline mixer," *IEEE Trans. Microw. Theory Tech.*, vol. 48, pp. 662–669, 2000.

[3] P. Kittara, G. Yassin, R. Padman, S. Withington, K. Jacobs, and S. Wulff, "A 700 ghz antipodal finline mixer fed by a pichett-potter horn reflector antenna," *EEE Trans. Microw. Theory Tech.*, vol. 52, pp. 2352–2360, 2004.

[4] G. Yassin, P. K. Grimes, O. G. King, and C. E. North, "Waveguide-to-planar circuit transition for millimetre-wave detectors," *Electron. Lett.*, vol. 44, no. 14, pp. 866–867, 2008.

[5] J. W. Kooi, "Advanced receivers for submillimeter and far infrared astronomy," Ph.D. dissertation, Rijksuniversiteit Groningen, Netherlands, 2008.

Superconducting SIS Mixers with Vertically Stacked Junctions

Ming-Jye Wang, Tse-Jun Chen, Chuang-Ping Chiu, Wei-Chun Lu, Jing Li, and Sheng-Cai Shi

***Abstract*—The SIS mixers with two vertically stacked junctions, VSJ, have been fabricated. Using standard Nb-technology, the Nb/Al-AlOx/Nb/Al-AlOx/Nb multilayer is deposited in a single vacuum process. The junction, near 1μm^2 in size, is defined by etching the top three layers (Nb/Al-AlOx/Nb) using ICP-RIE system. The receiver noise of mixers are measured in the 4K wet dewar. Wide bandwidth is demonstrated in VSJ mixers, which is consistent with the Fourier Transformation Spectroscopy, FTS, results. The numerical simulations demonstrate a similar behavior as experimental result, but shift to lower frequency. This discrepancy might result from some difference between the model and real device (mixer mount in particular).**

***Index Terms*—Fourier Transform Spectroscopy, receiver noise temperature, superconductor-insulator-superconductor mixers.**

I. INTRODUCTION

VERTICALLY stacked SIS junction (VSJ), with individual junctions connected in series but without introducing any additional connection wires, has been demonstrated as mixer operated at frequency above 100GHz [1-3]. The advantages of mixer with junctions in series are having a simple structure and an equivalent normal-state resistance of relatively large value, which makes impedance matching easier in mixer application. In addition, the dynamic range of VSJ mixer can improved by a factor of N^2 [4, 5], where N is the number of series SIS junctions. The design of junction in series could also improve the gain compression problem, especially in low frequency range. Furthermore, the photon-assisted quasi-particle tunneling in the stacked SIS junction becomes interesting if the thickness of middle Nb is rather thin. The tunneled quasi-particle might not re-condense to superconducting pairs in the middle layer of Nb before the second tunneling happened. Non-equilibrium phenomena might become important and modified the mixing result. Recently, THz radiation had been demonstrated in high temperature superconductor which has intrinsic stacked Josephson junctions [6]. However, the challenge is to fabricate junctions with identical parameters. For conventional type, the individual tunnel junction is fabricate at same growth condition and is connected with the adjacent junction by a Nb film. In this type, the superconducting critical current density, J_c, of junction should have good uniformity. However, the size of junction is dependent on the quality of photo-lithography process, especially for small junction. On the other hand, the VSJ type is easy to have identical junction size because of using the same PR pattern, but having same critical current density in both junctions might be the critical issue. In this paper, we would like to report the fabrication of VSJ mixers and their DC/RF characteristic results. A numerical simulation program based on quantum mixing theory with five ports model was performed to simulate the mixer performance.

Manuscript received 20 April 2009. This work was supported in part by the Institute of Astronomy and Astrophysics, Taiwan.

Ming-Jye Wang, Tse-Jun Chen, Chuang-Ping Chiu, and Wei-Chun Lu are with the Institute of Astronomy and Astrophysics, Academia Sinica, Taipei 106, Taiwan (Ming-Jye Wang, phone:+886-2-33652200 ext.708; fax: +886-2-23677849; e-mail: mingjye@asiaa.sinica.edu.tw).

Jing Li and Sheng-Cai Shi are with the Purple Mountain Observatory, NAOC, CAS, China (e-mail: scshi@mail.pmo.ac.cn).

II. DEVICE FABRICATION

The VSJ mixers are fabricated by conventional Nb-AlOx-Nb junction technology [7]. Two stacked junctions with structure of Nb/Al-AlOx/Nb/Al-AlOx/Nb are grown in situ without breaking the chamber vacuum. The fabricating procedures are shown in Figure 1. The thickness of middle Nb is 100nm to avoid the complication in simulation model. As mentioned above, the J_c and size of junctions are two important issues for VSJ mixer fabrication. Firstly, the tunneling barriers of two junctions should have same J_c. According to our previous study [8], the value of J_c is very sensitive to the wafer temperature. Therefore, during the growth procedure, wafers were well thermally anchored to a temperature control cooling stage. Another important issue is to keep the sizes of two stacked junctions same. Low processing pressure was performed to etch the Nb/Al-Ox/Nb trilayer in our ICP-RIE etching system. Designs for 400GHz frequency band mixers with regular single junction are used in the experiment. Therefore, the impedance matching was not optimized for reported VSJ mixers.

III. RESULTS AND DISCUSSIONS

A. DC characteristics

The DC I-V characteristics with various external magnetic fields are shown in the Figure 2. The supercurrent of junction can be suppressed by adjusting the external magnetic field. The inset shows the magnetic dependence of junction current biased at voltage of 0.1mV. A Fraunhofer-pattern-like magnetic field dependence of supercurrent was observed. The I-V curves with magnetic fields at different current minimum in I-B curve were also illustrated in the Figure 2. As the magnetic field increased, the gap structure is smoothened due the suppression of

superconducting proximity effect in Al layer near the tunnel barrier. All features of DC I-V characteristic show that our VSJ mixer behaves just like a mixer with single junction, indicating that these two stacked junctions have identical parameters. This result will simplify the simulation model during data analysis.

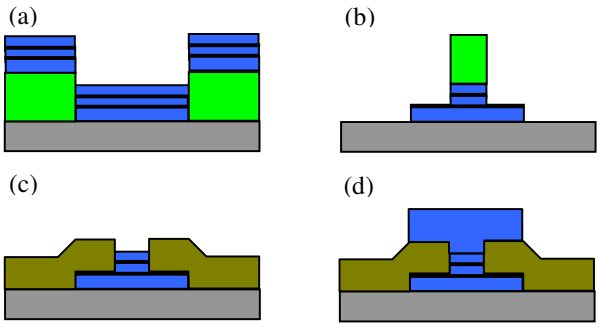

Fig. 1. The fabricating process of VSJ mixers. (a) The growth of double tunneling barrier structure, Nb/Al-AlOx/Nb/Al-AlOx/Nb. The respective thickness of base, middle, and top Nb is 200nm, 100nm, and 100nm. (b) The junction patterning by ICP-RIE system. SF_6 and Ar processing gases were used for Nb and Ar etching respectively. (c) 300nm thick SiO_2 deposition and lift-off. (d) The wiring Nb deposition (500nm).

B. Fourier Transform Spectroscopy Measurement

The Fourier transformation spectroscopy technique is an excellent tool to evaluate the RF response of a detector. VSJ mixer was mounted in a 400GHz mixer block designed for SMA receiver. The mixer block, then, was mounted on the cold plate of liquid helium dewar with optical window. The room temperature window was made of 23 μm thick mylar film. Two Zitex films were mounted at 77K and 4K stages respectively, in front of mixer block, to block the IR radiation. The VSJ mixers were biased at 4mV by a battery-based bias circuit. Our FTS system is model of FARIS-1, made by JASCO, Japan. The system has a light source with an equivalent black body temperature of 5000K. The scanning speed of movable roof mirror is set at 0.5mm/sec. The final output signal of VSJ mixer is averaged from 50 scan results. The transformed spectrum has a frequency resolution of 3.5GHz.

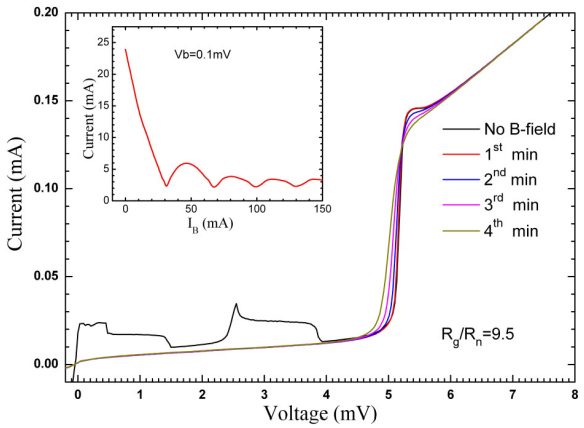

Fig. 2. The DC IV characteristics of VSJ mixer with external magnetic field. The inset shows the magnetic field dependence of supercurrent. The VSJ behaves just like a regular SIS tunneling junction.

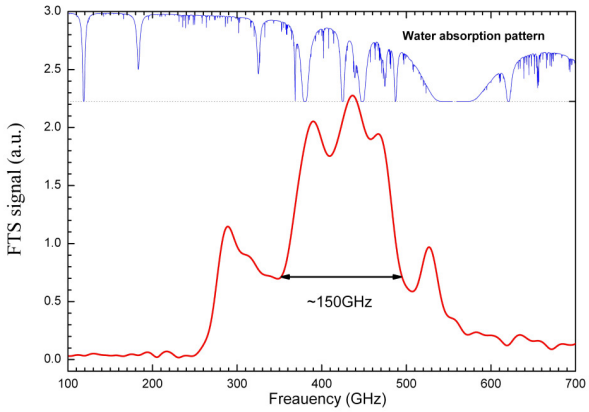

Fig. 3. The RF response of VSJ 400GHz mixer measured by Fourier transform spectroscopy system. Two strong suppressions near 330GHz and 500GHz are observed. The upper part of figure shows the absorption spectrum of water. The bandwidth of VSJ 400GHz mixer is more than 150GHz, and even can be expanded to 220GHz if the degradation near 330GHz can be improved.

The FTS response of VSJ 400GHz mixer are shown in Figure 3. A broad band response was observed from 270GHz to 540GHz. The lower frequency response is limited by the cut-off frequency of wave guide, 636μm×158μm. The upper frequency is limited by the tuning circuit of mixer chip. Two strong dips were observed near 330GHz and 500GHz. According to the water absorption spectrum, as shown in the upper part of Figure 2, the absorption lines are not coincident with the dip structure of FTS result. Therefore, we can exclude the absorption of water condensed on the window. We will discuss this issue later. The VSJ mixers can have a bandwidth larger than 150GHz if we defined the FWHM (full width at half maximum) as the bandwidth of RF response of a detector. The bandwidth can be even expanded to 220GHz if the degradation near 330GHz can be improved.

C. Receiver Noise Measurement

The VSJ 400GHz mixers were tested by typical hot/cold load method. The magnetic field is set at the 3rd minimum of I-B curve to suppress the superconducting pair tunneling. The RF and LO signals were coupled by a wire grid with a proper angle relative to the waveguide of mixer block to have enough LO pumping. The contribution from the loss of RF/LO coupler has been subtracted by standard procedures. The signal coupling efficiency was calculated by projecting the wire gird angle to waveguide plan. Then the corrected T_{rx} is obtained through the formula of $T_{rx} = T_{rx}' \times C - T_{amb} \times (1-C)$, where T_{rx}' is the uncorrected receiver noise temperature, C is the coupling efficiency of wire grid, T_{amb} is the ambient temperature. Two sets of LO source were used to cover wide frequency range (240GHz~500GHz).

Figure 4 shows a typical I-V and P_{IF}-V curves of VSJ mixer under optimum LO pumping. The nominal LO frequency is 288GHz. Very similar to a regular mixer, photon-assisted quasi-particle tunneling steps were observed clearly, except of doubling the voltage value. The doubled photon-assisted

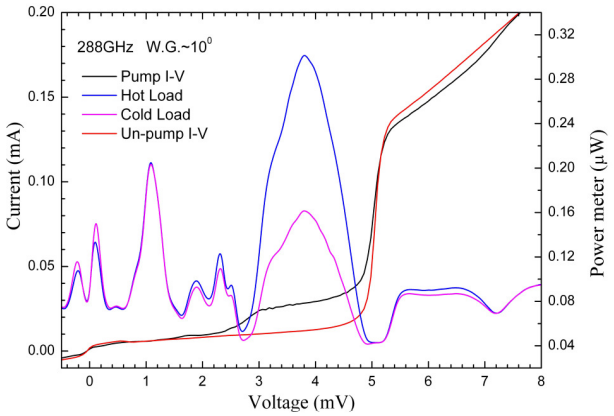

Fig. 4. The I-V and PIF-V curves of VSJ mixer with optimum LO pumping. The photon-assisted quasi-particle tunneling steps are observed clearly.

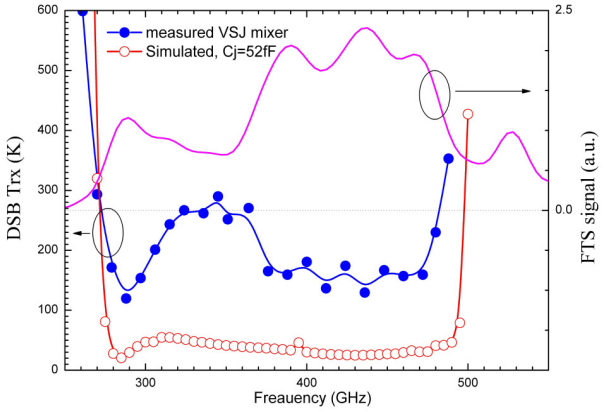

Fig. 5. The corrected receiver noise temperature of VSJ mixer, solid circles. The simulated mixer performance is also shown, open circles. The simulation result has similar feature as the experimental data, except of shifting the bump to lower frequency.

quasi-particle voltage steps provide the advantages of avoiding the gain compression effect and having a wider range of the optimum bias point.

The corrected receiver noise temperature, T_{rx}, of VSJ mixer was illustrated in the Figure 5, accompanying with the FTS result for comparison. The overall frequency dependence of T_{rx} is consistent with the FTS spectrum. T_{rx} becomes higher at the frequency with low FTS response. The value of T_{rx} of this VSJ mixer is about 150K in a wide frequency range of 270GHz to 480GHz, except of being a higher value of 250K near 340GHz. The receiver noise temperature is higher than that of the regular mixer designed for Taiwan receiver of SMA, ~80K. We attribute this difference to the RF mis-matching because the tuning structure of these VSJ mixers is identical to the regular mixers.

D. Numerical Simulation

On the numerical simulation, we treated a VSJ just like conventional junction arrays in series, with its equivalent normal-state resistance (i.e., measured R_n for the VSJ) twice that of individual junctions and its equivalent geometric capacitance half that of individual junctions. The voltage and current of its dc I-V curve was both reduced by a factor of two for simulation [9]. With the measured R_n (34Ω) and calibrated junction critical current density J_c (~10kA/cm^2), the junction area was estimated to be slightly larger than 1μm^2 in terms of the constant I_cR_n product, which was assumed to be 1.95mV. Thus the equivalent geometric capacitance was equal to 52fF by taking a specific capacitance of 90fF/ μm^2.

The mixing behavior of the measured VSJ was simulated by using the quantum theory of mixing [9] with a quasi-five port model [10]. The RF embedding impedance seen by the VSJ was obtained with the help of HFSS simulation and modeling for thin-film superconducting microstrip lines as integrated impedance transformers and tuning inductance, while the IF impedance was simply taken as 50Ω. During simulation, the dc bias voltage (as for a single junction) and reduced LO pumping level were both optimized for the receiver noise temperature at each frequency.

The simulated receiver noise temperature was shown in Figure 5, open circles. The simulated data has a bump, similar to experimental results but shifted to a lower frequency of 320GHz. It might be due to the discrepancy between model and real devices and also mixer block. However, the overall measured receiver noise temperature is much higher than the simulated result. Detailed breakdown of receiver noise sources is necessary to understand the reason of this large difference.

IV. Conclusion

We have fabricated 400GHz mixer with vertical stacked junction (VSJ) by using Nb-based technology. The VSJ behaves like a single barrier SIS junction, indicating the stacked two junctions have identical size and J_C. The FTS spectrum and receiver noise temperature demonstrate the VSJ mixer has a bandwidth larger than 110GHz, although the on chip tuning circuit is not designed for it. The VJS mixer has worse performance around 340GHz which might be attributed to large impedance mismatch. A numerical simulation was done to model the equivalent circuit of the stacked junctions. We have demonstrated the good consistency between measurement and simulation results. However, the receiver noise temperature is still much higher than the simulation result. Further works are needed to understand the reason of this difference.

Acknowledgment

The authors would like to thank Dr. Matsuo from NAOJ, Japan for his help on the bias circuit design for FTS system.

References

[1] V. Yu. Belitsky, "100GHz mixer vertically integrated (stacked) SIS junction array," *International J. Infrared and Millimeter waves*, vol.14, no.5, pp.949-957, 1993.

[2] K. H. Gundlach, "Double-barrier tunnel junctions for quasiparticle mixers," *J. Appl. Phys*., nol. 75, no. 8, pp.4097-4102, 1994.

[3] T. Lehnert, "Fabrication and Mixer performance of Nb/Al Bouble-Barrier Junctions," *IEEE Trans. Appl. Supercond.* Vol.5, no. 2, pp.2220-2223, 1995.

[4] S. Rudner, "Superconductor-insulator-superconductor mixing with arrays at millimeter-wave frequencies," *J. Appl. Phys.*, vol. 52, no.10, pp.6366-6376, 1981.
[5] D.G. Grete, "Performance of Arrays of SIS Junctions in Heterodyne Mixers," *IEEE Trans. MTT*, vol. MTT-35, no. 4, pp.435-440, 1987.
[6] L. Ozyuzer, "Emission of Coherent THz Radiation from Superconductors," *SCIENCE*, vol.318, pp.1291-1293, 2007.
[7] M.J. Wang, "Low noise Nb-based SIS mixer for sub-millimeter wave detection," *J. Phys. Chem. Soli,.* vol. 62 pp.1731-1736, 2001.
[8] M.J. Wang, "New Thickness Control Process of Oxide Barrier for Nb-based Tunnel Junctions," *IEEE Trans. Appl. Supercond*., vol.13, no.2, pp.1100-1103, 2003.
[9] J.R. Tucker, "Quantum detection at millimeter wavelengths," *Rev. Mod. Phys.*, vol.57, pp.1055-1113, 1985.
[10] A.R. Kerr, "Embedding Impedance Approximations in the Analysis of SIS Mixers," *IEEE Trans. MTT*. vol.41, no.4, pp.590-594, 1993.

Magnetic Field Dependence of the Microwave Properties of Proximity Effect Nb/Al Bilayers Close to the Gap-frequency

S. Zhu, T. Zijlstra, C. F. J. Lodewijk, A. Brettschneider, M. van den Bemt, B. D. Jackson, A. M. Baryshev, A. A. Golubov, and T. M. Klapwijk

Abstract— High critical current density tunnel barriers of AlN have two effects on the operation of niobium-based SIS mixers close to the upper frequency limit of superconducting niobium: 1. the bandwidth is no longer limited by the RC time constant of the tunnel-junction, but the physical processes in the superconductors at high frequencies; 2. the devices have smaller lateral dimensions in order to provide impedance matching given the low R_nA value, which requires the application of a higher magnetic field to quench the Josephson-effect through the Fraunhofer pattern. Consequently, under operating conditions the superconducting properties are no longer the equilibrium properties as realized by the fabrication conditions, but are deteriorated by the applied magnetic field. We report the measurements of I-V curves and Fourier transmission spectrum to determine and correlate the evolution of the superconducting properties in a high magnetic field. The results are compared with a calculation of the proximity effect based on the Keldysh Greens' function technique, leading to a magnetic field dependent density of states in the Al toplayer of the commonly used Nb-Al bilayer to fabricate tunnel barriers as well as forming one part of the superconducting stripline.

***Index Terms*— Fourier transmission spectrum, gap frequency, magnetic field, proximity effect**

I. Introduction

Superconductor-insulator-superconductor (SIS) mixers for the ALMA Band-9 project (frequency range from 602 to 720 GHz) have been realized using the recently developed AlN technology. The epitaxial crystalline nature of the AlN barriers of the SIS junctions makes the distribution of tunnel-transmissivities much more narrow leading to good quality tunnel-junctions with an achievable critical current density, J_c, of up to 400 kA/cm^2 [1], much larger than those reported for amorphous AlO_x barriers [2]. The most beneficial contribution of high J_c junctions is that a larger bandwidth can be achieved due to the lower R_nC_j time constant with R_n the normal state resistance and C_j the junction capacitance (provided the matching circuit is not limiting [3]). Because of the lower specific resistance, R_nA value, of the barrier, the junction area, A, should be smaller to provide the desired impedance matching.

In the junction fabrication, the AlN barrier is produced by depositing about 7-8 nm Al layer on a 200 nm Nb ground plane, followed by a nitridation of the Al layer in a nitrogen plasma for a fixed time to form an insulating barrier with a thickness of about 1 nm. The final structure of the SIS junction is Nb/Al/AlN/Nb and the corresponding tuning circuit is Nb/Al/AlN/SiO_x/Nb multilayer, as illustrated in Fig. 1. The thickness of SiO_x is 250 nm and top Nb 500 nm. Here the tuning circuit is, as usual, employed to match the antenna impedance with the SIS junction impedance.

From the point of view of applications the higher J_c and lower A of the junction mean also that a higher magnetic field has to be applied to suppress the Josephson current, which shows a Fraunhofer pattern with the magnetic field. As a consequence, the superconducting properties, especially for the Nb/Al ground plane, are no longer in the equilibrium state, but are deteriorated by the magnetic field. Technologically, it is of interest to investigate the influence of magnetic field on the electrodynamics of the tuning circuit in the SIS mixer. The superconductivity of the proximity-coupled Nb/Al bilayer is potentially dependent on the external field, in particular for frequencies close to the gap frequency.

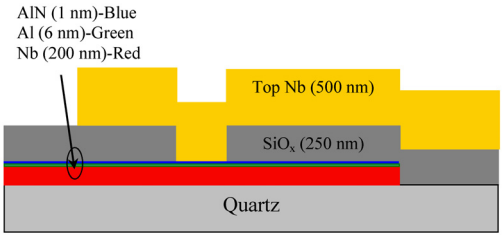

Fig. 1. Cross-section of the SIS junction and tuning circuit. Proximity effect can be directly observed in the I-V measurements of the junction. Transmission efficiency of the Nb/Al ground plane is correlated with the I-V curves and magnetic fields.

II. Proximity Effect Model

The proximity effect has been studied theoretically and

Manuscript received 20 April 2009. This work was supported in part by NanoImpuls, the Dutch Research School for Astronomy (NOVA), the Dutch Organization for Scientific Research (NWO), Radionet, and the European Southern Observatory (ESO).

S. Zhu, T. Zijlstra, C. F. J. Lodewijk, A. Brettschneider, and T. M. Klapwijk are with the Kavli Institute of Nanoscience, Faculty of Applied Sciences, Delft University of Technology, Lorentzweg 1, 2628 CJ Delft, The Netherlands (corresponding author to provide phone: 0031-15-2786113; e-mail: s.zhu@tudelft.nl).

M. van den Bemt, B. D. Jackson, A. M. Baryshev are with SRON National Institute for Space Research, 9747 AD Groningen, The Netherlands.

A. A. Golubov is with Faculty of Science & Technology, University of Twente, 7500 AE Enschede, The Netherlands.

experimentally in the past twenty years [4]-[6]. When a normal metal N is electrically in contact with a superconductor S, the properties of both S and N are altered. A model applicable to our samples has been developed by Golubov *et. al*. to deal with the proximity-coupled S/N bilayer in the dirty limit condition [4], also in the presence of a magnetic field. Considering the polycrystalline of Nb and Al layers deposited using the sputtering technique at room temperature, this dirty limit condition also holds for our samples.

The Usadel equations [7], describing the inhomogeneous state of a dirty superconductor in the weak-coupling limit, can be rewritten in a so-called θ-parameterized way [5]:

$$\xi^2 \frac{\partial^2}{\partial x^2}\theta(x) + j\varepsilon \sin[\theta(x)] + \Delta(x)\cos[\theta(x)] = 0, \tag{1a}$$

$$\Delta(x)\ln\frac{T}{Tc} + 2\frac{T}{T_C}\sum_{\omega_n}\left(\frac{\Delta(x)}{\omega_n} - \sin[\theta(x)]\right) = 0, \tag{1b}$$

where θ is a unique Green functions, ξ the coherence length, ε the quasi-particle energy, and $\omega_n=\pi T(2n+1)$ $(n=0,1,2,...)$ the Matsubara frequency. The quasi-particle density of state can be defined as

$$\frac{N(E)}{N(0)} = \mathrm{Re}[\cos(\theta)]. \tag{2}$$

For the proximity-coupled S/N bilayer, (1) can be used to describe the S and N layers, respectively, with the boundary conditions at the S-N interface:

$$\xi_S \frac{\partial}{\partial x}\theta_S(x) = \gamma\xi_N \frac{\partial}{\partial x}\theta_N(x), \gamma = \rho_S\xi_S / \rho_N\xi_N, \tag{3a}$$

$$\gamma_{BN}\xi_N \frac{\partial}{\partial x}\theta_N(x) = \sin[\theta_S(x) - \theta_N(x)], \gamma_{BN} = R_B / \rho_N\xi_N, \tag{3b}$$

as well as at the free surface of both S and N layers:

$$\frac{\partial}{\partial x}\theta(d_S) = 0, \tag{4a}$$

$$\frac{\partial}{\partial x}\theta(-d_N) = 0, \tag{4b}$$

where γ and γ_{BN} are the interface parameters describing the nature of the interface between the S and N layers, $\rho_{S,N}$ denote the normal state resistivities, R_B is the product of the resistance at S/N interface and its area, and $d_{S,N}$ the thickness of S and N layer, respectively. When a weak magnetic field is applied, an extra energy term related to the orbital effect can be added to the quasi-particle energy in (1a) as $\varepsilon+j\Gamma\cos[\theta(x)]$. Here, $\Gamma=(H\xi W/\Phi_0)^2\pi^{1/3}$ is the effective pair-breaking rate and H is the magnetic field, ξ the coherence length of S layer, W the thickness of bilayer, and Φ_0 the flux quantum [8].

To numerically solve (1), we set the interface parameters γ and γ_{BN} as 0.5 and 0.7, respectively, both of which have been experimentally determined by Zehnder *et.al.* for the Nb/Al SNINS junction with 200 nm Nb and 4 nm Al layers [6]. These values are also very close to the ones (γ=0.3 and γ_{BN} =1.0) reported by Dmitiriev *et. al.* without considering the film thickness [9]. The other input parameters, such as temperature and film thickness, can be set according to the details of the experiment.

Fig. 2 shows the calculated density of state at four typical positions, *i.e.*, the free surfaces and interfaces of Nb and Al layer, in two different magnetic fields. It can be observed that the curves for the density of states at these typical positions in the same field are almost identical except for a slight difference at the free surface position of the Nb layer when d_{Nb} (200 nm)>>d_{Al} (6 nm). This means that the very thin Al layer has similar superconducting properties as the thick Nb layer. As a rough, but reasonable, approximation, the Nb/Al bilayer can be treated as a single layer with uniform superconducting properties. For thicker films the properties become inhomogeneous [4]-[6].

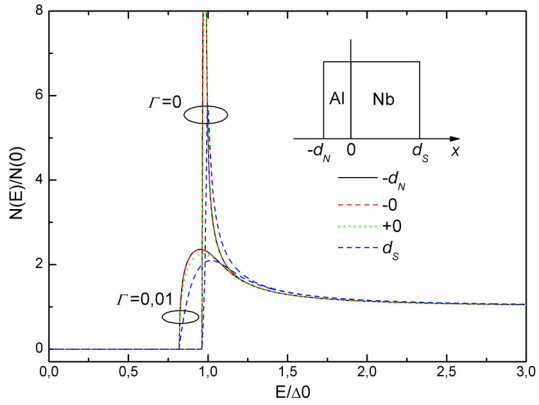

Fig. 2. Density of states at four typical positions inside the proximity-coupled Nb/Al bilayer. The thicknesses of Nb and Al layer are 200 nm and 6 nm, respectively. Δ0 is the calculated gap energy of bulk Nb superconductor, which is normalized to $\pi k_B T_{CS}$, T_{CS}=9.27 K. Γ is the pair-breaking rate defined in [8]. Inset shows the sketch of the Nb/Al bilayer.

III. Surface Impedance

The electromagnetic behavior of a uniform superconductor is described by the Mattis-Bardeen theory [10]. The application to a proximity-layer is usually done by assuming full Nb superconducting properties throughout the Al. It has been shown, at the low frequency of about 10 GHz, that only for thick enough Al (tens of nanometers) the surface impedance of the Nb/Al bilayers begins to deviate from those of bare Nb samples [11]. In our case, with the frequency close to the gap frequency of Nb (~680 GHz), it is likely that similar deviations will occur already for thinner Al layers.

In order to describe the microwave response of the Nb/Al bilayer, we use the reformulation of Mattis-Bardeen proposed by Nam. It is a more general theory that can be applied to the strong-coupling and to the impure superconductors [12]. We calculate the complex conductivity, $\sigma/\sigma_N=(\sigma_1-j\sigma_2)/\sigma_N$, of the proximity-coupled Nb/Al bilayer by assuming an uniform superconductivity in the bilayer.

Nam's equations for the complex conductivity calculation in the dirty limit read as [12]:

$$\frac{\sigma_1}{\sigma_N} = \frac{1}{\hbar\omega}\int_{\Delta-\hbar\omega}^{-\Delta} g_1(1,2)\tanh[\frac{1}{2k_BT}(\hbar\omega+E)]dE + \frac{1}{\hbar\omega}\int_{\Delta}^{\infty} g_1(1,2)\{\tanh[\frac{1}{2k_BT}(\hbar\omega+E)] - \tanh(\frac{1}{2k_BT}E)\}dE, \tag{5a}$$

$$\frac{\sigma_2}{\sigma_N} = \frac{1}{\hbar\omega}\int_{\Delta-\hbar\omega}^{\Delta} g_2(1,2)\tanh[\frac{1}{2k_BT}(\hbar\omega+E)]dE + \frac{1}{\hbar\omega}\int_{\Delta}^{\infty}\{g_2(1,2)\tanh[\frac{1}{2k_BT}(\hbar\omega+E)] + g_2(2,1)\tanh(\frac{1}{2k_BT}E)\}dE \tag{5b}$$

Here the functions $g_{1,2}$ are known as coherence factor and given

by:

$$g_1(1,2) = \mathrm{Re}[N(1)]\mathrm{Re}[N(2)] + \mathrm{Re}[P(1)]\mathrm{Re}[P(2)], \quad (6a)$$

$$g_2(1,2) = \mathrm{Im}[N(1)]\mathrm{Re}[N(2)] + \mathrm{Im}[P(1)]\mathrm{Re}[P(2)], \quad (6b)$$

where N and P denote the density of state and pairs as calculated from (1), and the arguments 1, 2 represent the quasi-particle energy of E and $E+\hbar\omega$. The gap energy, Δ, can be derived from the density of states as shown in Fig. 2 and the normal state conductivity, σ_N, as evaluated experimentally.

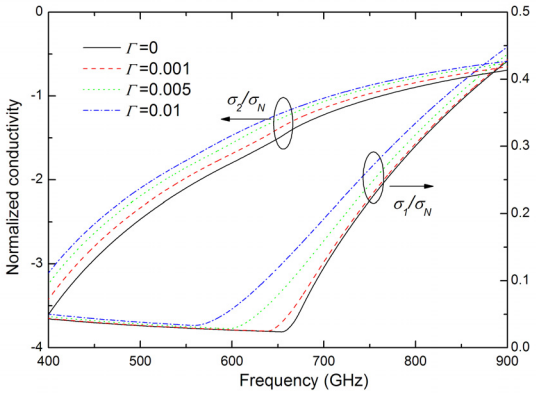

Fig. 3. Dependence of the complex conductivity on the frequency at different magnetic fields. The densities of state and pairs of surface of Al layer are used to calculate the complex conductivity.

Fig. 3 shows the calculated complex conductivity of the bilayer. It can be seen that the gap frequency of the Nb/Al bilayer is about 650 GHz and can be further suppressed by the magnetic field. The absolute value of the imaginary part of complex conductivity, which is related to the paired electrons, decreases, while the real part contributed by the quasi-particles increases when the magnetic field is increased, which indicates the pair-breaking role of the magnetic field.

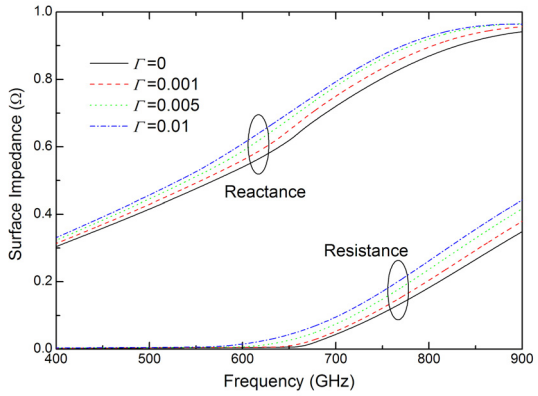

Fig. 4. Calculated surface impedance of the Nb/Al bilayer according to (7). The normal state conductivity σ_N is 1.0×10^7 *S/m*.

When the electric field penetration depth is long compared to the electron mean free path, a local equation can be assumed for the relation between the current density, J, and the electrical field, E, as $J=\sigma E$, where σ is the complex conductivity. If the thickness d of a conductor is not very much greater than the penetration depth, the field at one side of the conductor penetrates partially into the film. In this case, the normal skin effect surface impedance is found by solving Maxwell's equations in the local limit [13]:

$$Z_S = \sqrt{\frac{j\omega\mu_0}{\sigma}}\coth(d\sqrt{j\omega\mu_0\sigma}). \quad (7)$$

By substituting the calculated complex conductivity in (7), one can get the surface impedance of the Nb/Al bilayer as shown in Fig. 4. Here the normal state conductivity is set as $\sigma_N = 1.0\times10^7$ *S/m* and the thickness of the bilayer is 200 nm. Both the surface resistance and the reactance increase with magnetic field, which means that more losses will be introduced in the transmission line (tuning circuit). It can be expected that the Fourier transform spectrometer (FTS) response of the mixer would be depressed by the magnetic field, as discussed in a very similar situation, *i.e.*, the anodization process [3].

IV. I-V Curves and FTS Response in Magentic Field

I-V measurement can provide some important information about the quality of the superconducting films, although they do not directly provide the information about the quality of the materials forming the tuning circuit. It is well known that there is a characteristic "knee" structure in the I-V curves of a SNINS or SNIS junction, which can be explained in the framework of the proximity-effect theory [4]. We have measured the DC I-V curves of the SIS mixer at 4.2 K in different magnetic fields. The magnetic field is generated by a superconducting magnet-coil, and its value is determined from the applied coil current, I_m.

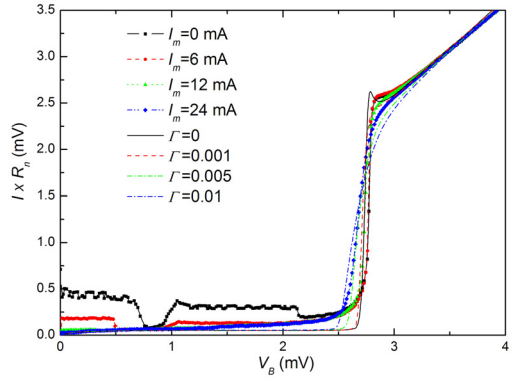

Fig. 5. Measured (symbols) and calculated (lines) I-V curves of the SIS junction at different magnetic fields. The product of I and R_n is used to represents the tunnel current. The measured value of R_n is 18 Ω. The calculation shows a lower V_g than the measurements.

As shown in Fig. 5, the Josephson current is suppressed by the magnetic field, while the gap voltage and the sharp non-linearity at the gap get also depressed at sufficiently high magnetic fields. Using the calculated density of states at the free surface of Al layer, we compare the measured I-V curves with the calculated ones. It is seen that the calculations are qualitatively in agreement with the measurements, *i.e.*, the "knee" structure disappears and the gap voltage is reduced while the nonlinearity at the gap weakens. The Josephson current is not included in the calculation. It also should be mentioned that the calculated V_g, for the given set of parameters, is smaller than the one determined from the measurements. The measured V_g can be up to 2.77 mV, while the calculated result is only 2.74 mV for the Nb bulk and 2.64 mV for the Nb/Al bilayer.

The multi-section Nb/Al/AlN/SiO_2/Nb microstripline is used to tune out the junction capacitance and transfer the RF signal

from the probe point to the junction. The transmission efficiency of the microstripline is evaluated using a FTS setup by measuring the changes in the DC current produced by the incoming radiation at a bias voltage of 2.0 mV. The SIS device is mounted in a waveguide backpiece and the FTS setup is operated in air, which leads to water vapor absorption at the edges of the band.

The FTS data are taken at 4.2 K as shown in Fig. 6. A good FTS response is obtained over the full desired band (602-720 GHz). The minima in the response at 560 and 750 GHz are due to the absorption of water vapor in the atmosphere. The magnetic field is applied to suppress the Josephson current during the measurement. It is observed that the FTS response decreases with the increase of the magnetic field when the frequency is between 630 and 730 GHz. We suggest that, since the magnetic field has less influence on the top Nb wire, it should result from the deteriorated superconductivity of the Nb/Al ground plane. As discussed in section III, when the magnetic field is applied, the bilayer shows a lower gap energy and a higher surface impedance at frequencies higher than the gap frequency. Based on the transmission line theory [14], the lower gap energy means a lower frequency cut-off and higher surface resistance leads to increased losses in the tuning circuit, *i.e.*, smaller transmission efficiencies.

We have calculated the transmission efficiencies and the results are shown in Fig. 6. The fitting parameters are: $R_nA=9.8\ \Omega.\mu m^2$, $C_j=60\ fF/\mu m^2$, $\sigma_N=0.9\times10^7\ S/m$, and dielectric constant of SiO_x $\varepsilon=4.8$. The complex conductivity of the top Nb layer is calculated using the Mattis-Bardeen equations [10], and the V_g of top Nb layer is 2.8 mV. The 80% absorption of the atmosphere is also considered in the calculation. It is seen that the calculated FTS decreases with the increase of the magnetic field, but less dramatically than the measured result. The reason of this difference in sensitivity should be further explored.

We also like to argue that this calculation is justified in the case that the Pippard coherence length is much larger than the penetration depth. For a more detailed description of the Nb-based superconducting microstripline above the gap frequency, the full Mattis-Bardeen, or Nam, theory could be used, as pointed out by Pöpel [15].

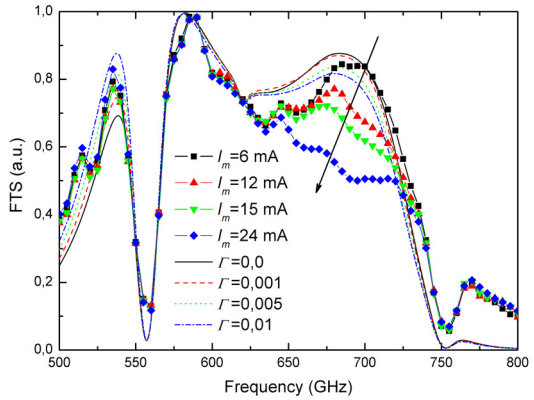

Fig. 6. Measured (symbols) and calculated (lines) FTS response of the SIS mixer with different magnetic fields. Each curve has been normalized to its max value. The calculation shows less sensitivity to the variation of magnetic field compared to the measurement.

V. Conclusion

We have analyzed the influence of the magnetic field on the transmission efficiency of a Nb/Al/AlN/SiO_x/Nb tuning circuit of the SIS mixer for the ALMA Band-9 project. Both the calculations and the measurements clearly indicate a significant deterioration of the FTS response with the applied magnetic field when frequency is close to the gap frequency of the proximity-coupled Nb/Al bilayer. This deterioration can be qualitatively described by the proximity theory of S/N bilayer and the electrodynamics of inhomogeneous superconductor.

The observed magnetic field dependence of the FTS response also exists in the SIS mixers with AlO_x barrier. However, due to the relatively low J_c and large A, the magnetic field used to suppress the Josephson current is small and this behavior can usually be ignored. To avoid the depression of FTS response in magnetic field, we suggest that a light anodization-step could be used to make the metallic Al layer into insulating AlO_x layer in the tuning circuit.

References

[1] T. Zijlstra, C. F. J. Lodewijk, N. Vercruyssen, F. D. Tichelaar, D. N. Loudkov, and T. M. Klapwijk, "Epitaxial aluminium nitride tunnel barriers grown by nitridation with a plasma source," Appl. Phys. Lett., vol 91, Dec. 2007, pp. 233102-1-3.

[2] R. E. Miller, W. H. Mallison, A. W. Kleinsasser, K. A. Delin, and E. M. Macedo, "Niobium trilayer Josephson tunnel junctions with ultrahigh critical current densities," Appl. Phys. Lett., vol 63, Sep. 1993, pp. 1423-1425.

[3] C. F. J. Lodewijk, T. Zijlstra, S. Zhu, F. P. Mena, A. M. Baryshev, and T. M. Klapwijk, "Bandwidth limitations of Nb/AlN/Nb SIS mixers around 700 GHz," IEEE Trans. Appl. Supercond., to be published.

[4] A. A. Golubov, E. P. Houwman, J. G. Gijsbertsen, V. M. Krasnov, J. Flokstra, H. Rogalla, and M. Yu. Kupriyanov, "Proximity effect in superconductor-insulator-superconductor Josephson tunnel junctions: theory and experiment," Phys. Rev. B, vol 51, Jan. 1995, pp. 1073-1089.

[5] G. Brammertz, A. A. Golubov, A. Peacock, P. Verhoeve, D. J. Goldie, R. Venn, "Modelling the energy gap in transition metal/aluminium bilayers," Physica C: Superconductivity, vol 350, Feb. 2001, pp. 227-236.

[6] A. Zehnder, Ph. Lerch, S. P. Zhao, Th. Nussbaumer, E. C. Kirk, and H. R. Ott, "Proximity effects in Nb/Al-AlO_x-Al/Nb superconducting tunnel junctions," Phys. Rev. B, vol 59, Apr. 1999, pp. 8875-8886.

[7] K. D. Usadel, "Gerneralized diffusion equation for superconducting alloys," Phys. Rev. Lett., vol 25, Aug. 1970, pp. 507-509.

[8] W. Belzig, C. Bruder, and Gerd Schön, "Local density of states in a dirty normal metal connected to a superconductor," Phys. Rev. B, vol 54, Oct. 1996, pp. 9443-9448.

[9] P. N. Dmitiriev, A. B. Ermakov, A. G. Kovalenko, V. P. Koshelets, N. N. Iosad, A. A. Golubov, M. Yu. Kupriyanov, "Niobium tunnel junctions with multi-layered electrodes," IEEE Trans. Appl. Supercond., vol 9, Jun. 1999, pp. 3970-3973.

[10] D. C. Mattis and J. Bardeen, "Theory of the anomalous skin effect in normal and superconducting metals," Phys. Rev., vol 111, Jul. 1958, pp. 412-417.

[11] M. S. Pambianchi, S. N. Mao, and S. M. Anlage, "Microwave surface impedance of proximity-coupled Nb/Al bilayer films," Phys. Rev. B, vol 52, Aug. 1995, pp. 4477-4480.

[12] S. B. Nam, "Theory of electromagnetic properties of superconducting and normal systems," Phys. Rev., vol 156, Apr. 1967, pp. 470-486.

[13] R. L. Kautz, "Picosecond pulses on superconducting stripelines," J. Appl. Phys., vol 49, Jan. 1978, pp. 308-314.

[14] G. de Lange, J. J. Kuipers, T. M. Klapwijk, R. A. Panhuyzen, H. van de Stadt, and M. W. M. de Graauw, "Superconducting resonator circuits at frequencies above the gap frequency," J. Appl. Phys., vol 77, Feb. 1995, pp 1795-1804.

[15] R. Pöpel, "Surface impedance and reflectivity of superconductors", J. Appl. Phys., vol 66, Dec. 1989, pp. 5950-5957.

Measurement of electron-phonon interaction time of Niobium using heating effect in SIS tunnel junction

Boon Kok Tan, Ghassan Yassin, Phichet Kittara and Jamie Leech

***Abstract*—The heating of SIS tunnel junctions by local oscillator (LO) power and bias voltage is well known and has been reported previously. In this paper, we present a novel method for recovering the heating parameters from the experimental pumped I-V curves of an SIS device at 700 GHz, together with the coupled LO power and the embedding impedance. Since this is obtained without assuming a particular power law between LO power and junction temperature, we will be able to find τ_{eph}, the electron-phonon interaction time of the superconducting material at various bath temperatures. We would deduce a power law that describes the dependence of the heat flow equation on temperature.**

***Index Terms*—Superconductor-insulator-superconductor devices, electron-phonon interaction time, heat flow, power law.**

I. Introduction

NIOBIUM based superconductor-insulator-superconductor (SIS) tunnel junctions are currently the most promising heterodyne mixers for submillimetre radio astronomy below $\sim$ 1 THz. The performance and characteristic of an SIS mixer near its energy gap is itself an interesting subject to study. Here radiation near the energy gap is strong enough to break the Cooper pairs. A strong dependency of gap voltage on the local oscillator (LO) pumping level can clearly be observed when the mixer is operating in this frequency range. This is commonly related to the heating effects taking place in the device [1], [2]. The implication of the effect on mixer performance is worth studying since accurate determination of the energy gap is central to the performance characteristic of the mixer. In this paper, we present a simple model for studying the heating effects in SIS tunnel junctions near the energy gap, and demonstrate that the electron-phonon interaction time, τ_{eph}, of the superconducting material can be directly recovered from the dc pumped I-V curves of an SIS device.

II. Method of Analysis

Our SIS device consists of a Nb-AlO_x-Nb junction, sandwiched between the Nb wiring layers and ground plane deposited on quartz substrate across a microstrip line. The junction area is typically 1μm $\times$ 1μm with the Nb thickness about 200 nm. The I-V curves measured at different pump levels are shown in Figure 1 and the gap depression with increasing pump level is clearly noted, which is typically in the $\sim$ 0.1 mV range. The critical temperature of Nb used throughout this paper is assumed to be 9.3 K. The measured curves used in our calculations were obtained using a niobium finline mixer in the frequency range of 650-720 GHz. The Josephson current is suppressed by magnetic field during measurement.

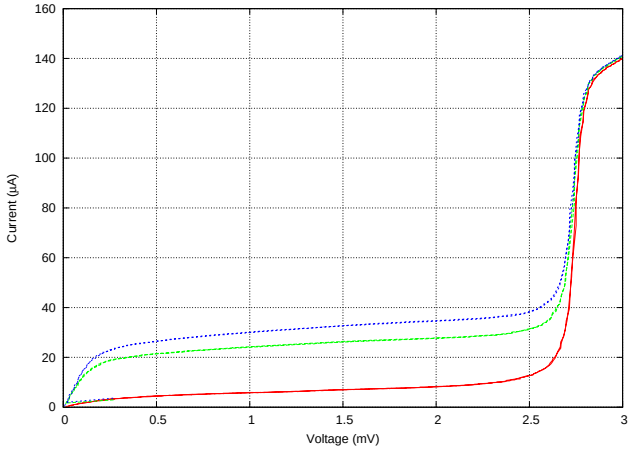

Fig. 1. The measured I-V curve for different LO pump levels.

Although the heating effect by RF signals for hot electron bolometer (HEB) has been widely studied, there is relatively limited information reported on similar effects in SIS junctions. Leone et. al. [3] has previously reported electron heating of a niobium SIS mixer, using Niobium Titanium Nitrate (NbTiN) stripline with Nb-Al-AlO_x-Nb junction. They explained that the mechanism responsible for the heating is the energy gap discontinuity at Nb/NbTiN interface. We, however, believe the heating effect in SIS mixers can result from different mechanisms, although there are some similarities to HEB.

As the photon excites quasiparticles to tunnel through the junction barrier, power is dissipated in the junction. In steady state, this power is transfered by thermal conduction through the superconducting ground film to the substrate. For simplicity, we assume that the entire junction is essentially at the same temperature. The heat transfer from the junction to the bath can be described phenomenologically using an effective heat transfer coefficient, α, which may be written as

$$P_{total} = \alpha(T_e)wlt(T_e^n - T_b^n) \quad (1)$$

Boon Kok Tan, Ghassan Yassin and Jamie Leech are with the Department of Physics (Astrophysics), University of Oxford, Denys Wilkinson Building, Keble Road, Oxfordshire, OX1 3RH. (phone: +44 (0)1865 273303; e-mail: tanbk@astro.ox.ac.uk; email: g.yassin1@physics.ox.ac.uk; email: jxl@astro.ox.ac.uk).

Phichet Kittara is with Physics Department, Faculty of Science, Mahidol University Bangkok, Bangkok 10400 Thailand. (phone: +66(0)96996479; email: peaw@yahoo.com).

Manuscript received 20 April 2009.

where P_{total} is the total power coupled the junction, T_e is the effective electron temperature (junction temperature), T_b is the bath temperature, wlt is the junction volume and n is an index which depends on the model used for heat transfer. Equation 1 is a rather general equation to describe the heat transfer process. The heat transfer coefficient $\alpha(T_e)$, is a temperature dependent parameter defined as

$$\alpha(T_e) = \frac{C_e}{nT_e^{n-1}\tau_{eph}} \tag{2}$$

where C_e is the electron heat capacity and τ_{eph} is the electron-phonon interaction time. In order to incorporate the temperature dependence effect of the heat capacity into the final equation, the low temperature limit heat capacity equation is used to calculate C_e [4].

$$C_e = \frac{2N(\xi_F)\Delta^2}{T_e} \exp\frac{-\Delta}{k_B T_e} \tag{3}$$

Recovery of the embedding parameters, including coupled LO power and embedding impedance, are obtained by matching the measured IV-curves with theoretical models based on Werthamer [5] and BCS theory [6]. We have used CalTech's SuperMix package for this purpose. In recovering the embedding impedance, we have assumed that the heating effect is negligible, which is a reasonable assumption, since we are working with the narrow range of the first photon step. From the BCS equations, the DC and RF power dissipated in the junction at each bias point are given by,

$$P_{rf} = \sum_{n=-\infty}^{n=+\infty} \frac{n\hbar\omega}{e} J_n^2(eV_{LO}/\hbar\omega) I_{dc}(V + n\hbar\omega/e) \tag{4}$$

$$P_{dc} = V_{bias} \times I_{dc} \tag{5}$$

where J_n is the n^{th} order Bessel function of the first kind and V_{LO} the voltage across the junction associated with the LO power, which is calculated from the recovered LO power from SuperMix. V_{bias} is the bias voltage and I_{dc} is given by the standard BCS unpumped I-V relation

$$I_{dc} = \frac{1}{eR_n}\int_{-\infty}^{\infty} N(\xi)N(\xi - eV)[f(\xi - eV) - f(\xi)]d\xi \tag{6}$$

where R_n is the junction normal state resistance, $f(\xi)$ is the Fermi-Dirac distribution function and $N(\xi)$ describes the density of states. Note that both functions, $f(\xi)$ and $N(\xi)$, are explicit functions of the voltage-dependence electron temperature, in our case,

$$N(\xi) = \frac{\xi}{\sqrt{\xi^2 - \Delta^2(T_e)}} \tag{7}$$

$$f(\xi) = \frac{1}{\exp\frac{\xi}{k_B T_e} + 1}. \tag{8}$$

We start with an initial guess of τ_{eph} and index n, and use equation 5 and equation 4 to give P_{total} into equation 1. By substituting equation 2 and equation 3 in equation 1, we can then solve for T_e. The new gap voltage Δ is then numerically re-computed using the standard temperature dependent expression,

$$\frac{1}{N(\xi_F)V} = \int_0^{\hbar\omega_c} \frac{\tanh(\frac{1}{2k_B T_e}\sqrt{\xi^2 + \Delta^2})}{\sqrt{\xi^2 + \Delta^2}} d\xi \tag{9}$$

where $N(\xi_F)$ is the density of states at Fermi level, V is the attractive potential, and $\hbar\omega_c$ is the Debye frequency. It should be noted that the above equation gives a specific value of Δ at a certain electron temperature, where in reality the I-V curve near the transition is rounded.

Since all the junction parameters found using SuperMix are normalized to the gap voltage, the theoretical current calculated using the previously recovered LO power and embedding impedance, is simply the product of the normalized current from SuperMix and the gap current given as V_{gap}^2/R_n. This entire process is repeated throughout the whole range of bias voltages. The generated I-V curve is then compared to the measured curve, and the parameters are optimized until both theoretical and measured curves are matched.

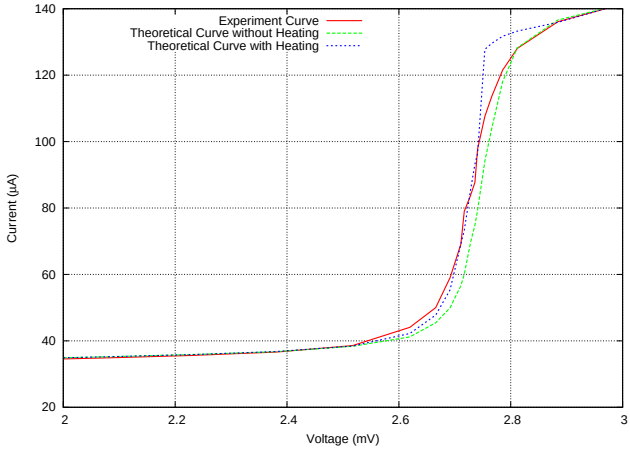

Fig. 2. The matching of simulated I-V curves with and without the heating effect with the experimental I-V curve.

III. Result and Discussion

Figure 2 shows the I-V response of our SIS junction using the highest pumping level curve shown in figure 1. Also in the figure we show the theoretical I-V curves calculated using embedding parameters recovered by the SuperMix model with and without the heating effect. The curve with heating is simulated using the value of τ_{eph} = 7.8 ns and index $n = 4$. The glitch in the heated curve near the knee of the gap voltage is probably due to the electron temperature being calculated without the rounding of the gap voltage in BCS equation, as noted previously. This can potentially be corrected by incorporating the imaginary lifetime-broadening parameter in the density of states equation [7], [8]. Unfortunately, the value of this parameter for Nb is difficult to obtain from the literature. This sudden step change is also seen in figure 3, where T_e, gap voltage and power across the junction are plotted as a function of bias voltage.

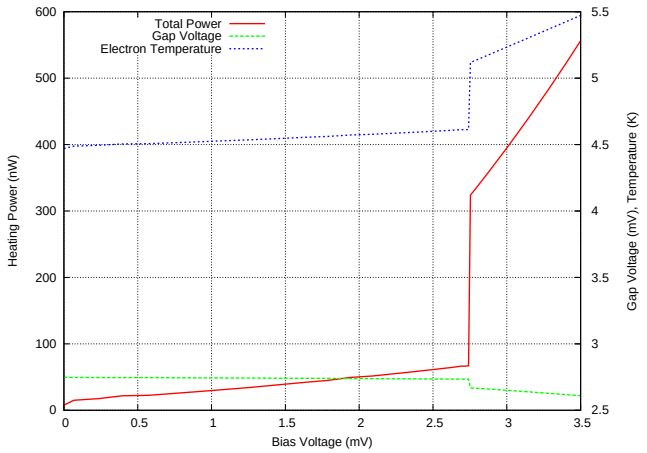

Fig. 3. The heating power coupled to the junction as a function of bias voltage. Shown together are the junction temperature and the gap voltage change corresponding to the bias voltage.

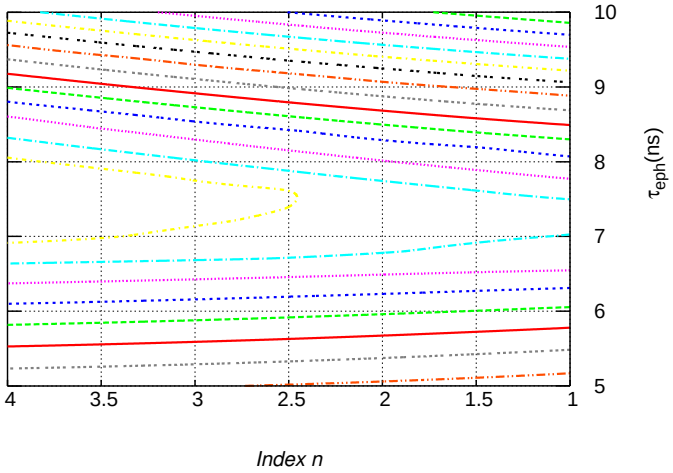

Fig. 4. Contour of the error surface with different guess value of τ_{eph} and index n.

Figure 4 shows the error surface contour of different guess value of n and τ_{eph}. It is clear from the figure that the change in n had little effect on the error surface. In other words, the index n is not as significant as τ_{eph}. This can easily be explained if we assume the difference between T_e and T_b is small compared to T_e and T_b. The term $(T_e^n - T_b^n)/nT_e^{n-1}$ can then be approximated as $T_e - T_b$ without index n in the final equation.

It should be noted that heating parameters can also be recovered solely from the unpumped I-V curve. A procedure similar to the one described above can be employed, with the junction model replaced by a modified temperature dependence polynomial equation. The results obtained in this method can be compared with those obtained using the pumped I-V curve to give better constrains on the heating parameters recovered.

IV. Conclusion

We present a simple model for measuring parameter of a superconductor by recovering the change in the electron temperature from the experimentally pumped I-V curve. Our results also show that the heat transfer equation does not depend significantly on the index n.

References

[1] B. Leone, B. D. Jackson, J. R. Gao, and T. M. Klapwijk, "Geometric heat trapping in niobium superconductor-insulator-superconductor mixers due to niobium titanium nitride leads," *Applied Physics Letters*, vol. 76, no. 6, pp. 780–782, 2000.

[2] P. Dieleman, T. M. Klapwijk, S. Kovtonyuk, and H. van de Stadt, "Direct current heating in superconductorinsulatorsuperconductor tunnel devices for thz mixing applications," *Applied Physics Letters*, vol. 69, no. 3, p. 418, 1996.

[3] B. Leone, J. R. Gao, T. M. Klapwijk, B. D. Jackson, and W. M. L. amd G. de Lange, "Hot electron effect in terahertz hybrid devices," *IEEE Transactions on Applied Superconductivity*, vol. 11, no. 1, pp. 649–652, 2001.

[4] T. V. Duzer and C. W. Turner, *Principles of superconductive devices and circuits*. New York, Oxford: Elsevier, 1981.

[5] N. R. Werthamer, "Nonlinear self-coupling of josephson radiation in superconducting tunnel junctions," *Physical Review*, vol. 147, pp. 255–263, 1966.

[6] J. Bardeen, L. Cooper, and J. Schrieffer, "Theory of superconductivity," *Physical Review*, vol. 108, no. 5, pp. 1175–1204, 1957.

[7] R. C. Dynes, V. Narayanamurti, and J. P. Garno, "Direct measurement of quasiparticle-lifetime broadening in a strong-coupled superconductor," *Phys. Rev. Lett.*, vol. 41, no. 21, pp. 1509–1512, 1978.

[8] B. Mitrovi and L. A. Rozema, "On the correct formula for the lifetime broadened superconducting density of states," *Journal Physics: Condense Matter*, vol. 20, pp. 15 215–15 218, 2008.

Submillimeter-wave Emitted by small parallel Josephson junction arrays

F. Boussaha, A. Féret, M. Salez, C. Chaumont, B. Lecomte, J-M. Krieg and L. Lapierre

***Abstract*— We report the first heterodyne measurements of microwave radiation emitted by a parallel Josephson junction array at submm-wave frequencies. The array consists of 5 small Nb-based Josephson junctions non-evenly distributed in a superconductive microstrip and designed for RF coupling in the 480-640 GHz range. The microwave radiation was detected using a SIS-mixer spectrometer optimized in the same range. We observed submillimeter-wave emission when the array was biased on certain Josephson steps, at the fundamental frequency of 493 GHz and 2nd harmonic frequency of 242 GHz. This strongly suggests that such non-uniform junction arrays optimized for RF-coupling, in spite of their strongly discretized nature, can host fluxon-induced resonances, which one can use in several areas of submillimeter-wave technology and superconductive digital electronics.**

***Index Terms*—Josephson junction array, Submillimeter waves, fundamental radiation, harmonic radiation.**

I. INTRODUCTION

SIS (Superconductor-Insulator-Superconductor) junction is widely used in the submillimeter waves detection ranging particularly from 0.3 to 1.5 THz [1-2]. It became a standard and inescapable component thanks to its high sensitivity, able to approach the limited quantum. [3-4] have successfully demonstrated the ability of the parallel quasiparticule tunnel SIS junction arrays to produce low noise frequency mixer in wide bandwidth. In this case, the mixer is optimized by considering the Josephson current completely suppressed when a sufficient external magnetic field is applied perpendicularly to the plan of the array. Conversely, when the complex Josephson current is considered, this same parallel Josephson junction array is potentially able to generate radiations at millimeter and submillimeter waves range. In deed, as in long Josephson junction (LJJ), resonances appear in the *I-V* curve at non-zero voltage values when an external magnetic field is applied [5]. The corresponding frequency is obtained by $f=2eV_{array}/h$. A fundamental issue is to know the ability of the parallel junction array to produce a real and usable submillimeter signals. In this paper, we report the first measurement results of parallel junction radiation in the submm-wave range using the heterodyne technique.

Manuscript received 20 April 2009. This work is supported by the French Space Agency CNES. Paper titles should be written in uppercase and lowercase letters, not all uppercase. Avoid writing long formulas with subscripts in the title; short formulas that identify the elements are fine (e.g., "Nd–Fe–B"). Do not write "(Invited)" in the title. Full names of authors are preferred in the author field, but are not required. Put a space between authors' initials.

F. Boussaha, A. Féret, M. Salez, B. Lecomte and J-M. Krieg are with LERMA Department – Paris Observatory, 77 avenue Denfert-Rochereau 75014 Paris - France (corresponding author to provide phone: +33-1-40512381; fax: +33-1-40512232; e-mail: faouzi.boussaha@obspm.fr).

C. Chaumont is with GEPI Department Paris Observatory, 77 avenue Denfert-Rochereau 75014 Paris - France

P. Lapierre is with CNES - BP 2220, 18 avenue Edward Belin, 31401 Toulouse Cedex 4 - France.

II. CIRCUIT

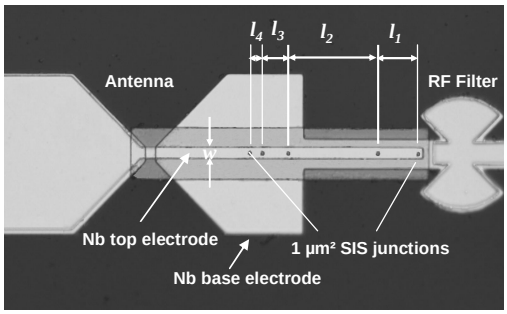

Fig. 1. Photograph of parallel Josephson junction array integrated with bowtie antenna and RF choke filter. The circuit is constituted of 5 Nb/Al-AlO_x/Nb identical junctions of l_jxw_j=1x1 µm² embedded in superconductive Nb/SiO/Nb stripline of width w=5 µm. The lengths separating the junctions are l_1 = 20 µm, l_2 = 42, l_3 = 12 µm and l_4=6 µm. Nb/Al-AlO_x/Nb is made up of 200 nm Nb-base-electrode, 10 nm Al and 400 nm Nb-top- electrode. The thickness of the SiO layer is 250 nm.

We investigated non-uniform parallel junction arrays whose number and spacing between the junctions have been optimized only in order to achieve broadband submillimeter-wave heterodyne quasiparticle SIS mixers [3-4]. As is shown in figure 1, the circuits defined on 50µm-thick fused quartz substrate are made up of 5 Nb/Al-AlO_x/Nb identical junctions of l_jxw_j=1x1 µm² embedded in superconductive Nb/SiO/Nb stripline of width w=5 µm and length l=80 µm. The spacing between junctions, allowing to tune out the tunnel barrier capacitance at desired frequencies, were optimized for best RF coupling in 480-640 GHz allowing well detection, but also well emission, of submillimeter-wave signals in that range. The circuit is placed in a waveguide mount providing purely real, near-constant 50 Ω source impedance over the whole band of 480-640 GHz, with no mechanical tuner [5]. The fabrication process is detailed in [6].

III. MEASUREMENTS AND RESULTS

The measurements were performed using the setup bench shown in figure 3. Two identical mixer blocks optimized at 480-640 GHz frequency range were employed, each in its own liquid helium cryostat, respectively hosting the junction array

used as a submm-wave source, and a twin-junction as the SIS mixer [6]. The mixer output signal at intermediate frequency (IF) is fed through an isolator and a cryogenic HEMT preamplifier at 4-8 GHz, then measured using a power-meter and spectrum analyzer.

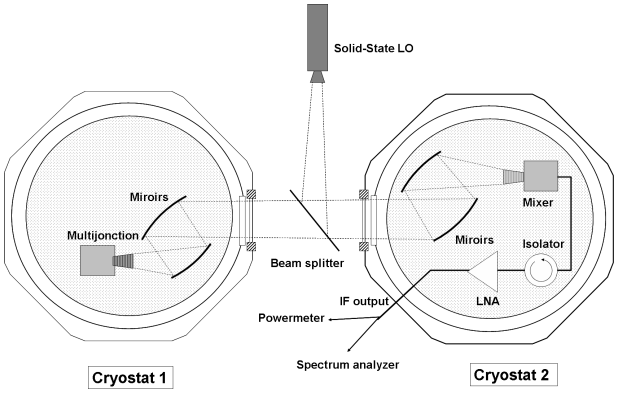

Fig. 2. Setup bench to characterize resonances observed in 5 Nb/Al-AlO_x/Nb junction array IV curve. Cryostat 1 and cryostat 2 contain respectively the junction array operating as submillimeter wave generator and the twin-junction as mixer.

The Josephson currents are entirely suppressed in the twin-junction and must be finely controlled in the junction array by a magnetic field generated by NbTi superconductive wire coiled around a cryoperm core. On its quasioptical path, the RF signals from the junction array must pass through a 13-µm mylar beam splitter, and twice across a 25-µm mylar window at room temperature, a 250-µm Zitex infrared filter at 77K, and a pair of cold elliptical mirrors at 4.2K. A 385-550 GHz solid-state local oscillator (LO), combining a Gunn source and a Schottky frequency-multiplier, was used to pump the SIS twin-junction mixer.

Figure 3 displays resonances appearing in the *I-V* curve of the array whose current density is 10 kA/cm² for different values of applied external magnetic field, measured at 4.2 K. Three Josephson resonances emerged at V_{array} ~ 0.5 mV, 0.84 mV and 1.02 mV when the magnetic field ranges from 60 to 83 Gauss. The corresponding fundamental frequencies ($f = 2eV_{array}/h$) are ~ 242, 406.5 and 493.6 GHz.

To determine which Josephson resonances, i.e. which frequencies could be measured with our setup, we characterized the RF coupling bandwidths of both the emitter (junction array) and the detector (twin-junction), by Fourier Transform Spectrometry technique (FTS). The instantaneous frequency response of the twin junction mixer and the junction array are respectively 410-640 GHz and 430-630 GHz frequency range [4]. The table 1 that summarizes the available frequencies shows that in this case only the fundamental of the third resonance and the 2nd harmonic of the first resonance can be measured.

Heterodyne measurements

First, the circuit was voltage-biased on the third resonance at V_{array} = 1.01 ± 0.005 mV then 1 ± 0.005 mV mV (voltages correspond to the maximum current where we expect maximum output power, before escaping to another state that is either the next resonance or the gap voltage). The respective frequencies are $f_{array} \approx 488.2 \pm 2.42$ GHz GHz and 483.4 ± 2.42 GHz, whereas the solid-state LO was tuned at f_{LO} = 493.8 GHz. The external magnetic field of 87 Gauss was applied. The twin-junction mixer is biased at 1.9 mV where it is most sensitive. The IF power spectrum measured across the 4-8 GHz frequency range is shown in figure 4.

TABLE 1 VOLTAGES AND CORRESPONDING FREQUENCIES GENERATED BY THE 5 PARALLEL JOSEPHSON JUNCTION ARRAY

N	V (mV)	FUNDAMENTAL (GHz)	HARMONIC 2 (GHz)
1	0.5	242	**484**
2	0.84	406.5	813
3	1.02	**493.6**	987.2

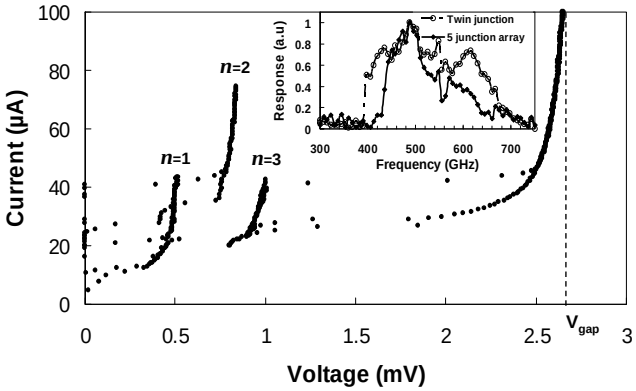

Fig. 3. *I-V* characteristic of the parallel Josephson junction array measured at T = 4.2 K. Three resonances appear when weak external magnetic field is applied. The insert shows the rf bandwidths of both the array and the SIS receiver (twin junction) measured by FTS technique (Fourier Transform Spectrometry).

Results

Reproducible spectral structure is obtained only in the presence of the resonance (ON). The change of the bias voltage value from 1.01 ± 0.005 mV (488.2 ± 2.42 GHz) to 1 ± 0.005 mV (483.4 ± 2.42 GHz) led the shift of the spectral structure position from f_{IF} ~ 4.3 GHz to f_{IF} ~ 7 GHz confirming the spectral structure to be a beat product at $f_{IF} = |f_{LO} - f_{array}|$.

Using the first resonance, similar measurements were performed. The junction array was current-biased at 0.5 ± 0.005 mV corresponding to 483.5 ± 2.5 GHz with 60 Gauss of applied magnetic field. Similar spectral structures were obtained as shown in figure 5. The solid-state LO was first tuned at 490.1 then at 491.5 and 493.1 GHz. The position of the structure shifted accordingly. When the array was biased on the second resonance, all frequencies of which (fundamental and harmonics) are completely outside of rf bandwidths, no beat signal was detected. In all detection, the IF signal was broad with a Full Width at Half Maximum

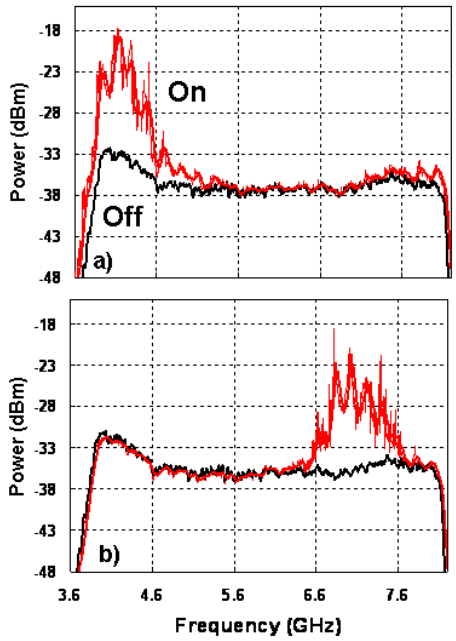

Fig. 4. IF power spectrum measured across the IF band of 4-8 GHz. The junction array is biased on the third resonance at a) 1.01 ± 0.005 mV then b) 1 ± 0.005 mV. The solid-state LO is tuned at 494 GHz.

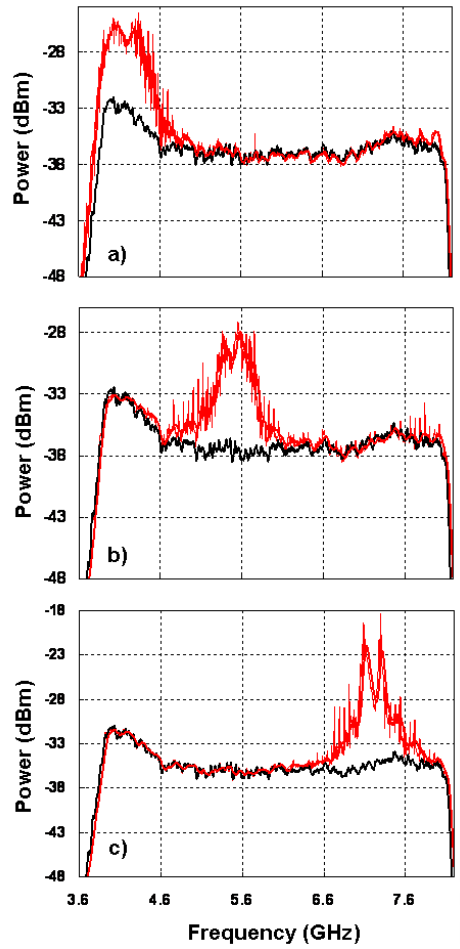

Fig. 5. IF power spectrum measured across the IF band of 4-8 GHz. The array is biased at 0.5 ± 0.005 mV corresponding to 483.5 ± 2.5 GHz. The solid-state LO is first tuned at a) 490.1 then at b) 491.5 and c) 493.1 GHz.

(FWHM) ~ 200 – 300 GHz. This is probably due to the instability of our voltage-bias: narrower IF signal by ~ 20 % using the more stable current-bias mode, was obtained. In addition, the LO source was not phase locked, nor was the array magnetically shielded. With the use of a phase lock loop, a very stable current-bias and the array magnetically shielded, the linewidth can be greatly reduced. We also noted the presence of 200 MHz noise signal probably caused by one of the measurement instruments.

The radiation reported here is probably generated by dynamic fluxons and the observed resonances as Fiske steps. Under the influence of the magnetic field, fluxons propagate unidirectionally and synchronized to cavity mode standing waves. *Further details are given in* [7].

IV. Conclusion

We investigate a non-uniform array of small Nb/AlO_x/Nb Josephson junctions with ~ 10 kA/cm² of current density operating as submm signals generator. Using the heterodyne technique, the measurements indicate with no ambiguity that SIS junction array can generate submm-wave signals at its fundamental and harmonic frequencies. They open the way to on-chip integration of heterodyne receivers with the digital processing unit. They could be used as local oscillator instead of a LJJ (Long Josephson Junction), suitable to deliver higher output power with larger bandwidth. Indeed, LJJ has an impedance often < 1Ω while the small junction array can present several tens of ohms. Moreover, non-uniform arrays can be designed to provide very wide coupling bandwidths.

Acknowledgment

The authors would like to thanks G. Beaudin, P. Encrenaz, and M. Perault for their continued support. The circuits and the mixer blocks were optimized by Y. Delorme and F. Dauplay. The parallel junction arrays is sponsored by the Centre National d'Etudes Spatiales (CNES) and the Institut National des Sciences de l'Univers (INSU).

References

[1] J. Zmuidzinas and P. L. Richards," Superconducting detectors and mixers for millimeter and submillimeter astrophysics", Proceedings of The IEEE, Vol.92, no. 10, pp.1597-1616, 2004.

[2] A. Karpov, D. Miller, F. Rice, J.A. Stern, B. Bumble, H.G. LeDuc, and J. Zmuidzinas "Low noise 1 THz-1.4 THz mixers using Nb/Al-AlN/NbTiN SIS Junctions ", IEEE trans. App. Superconductivity, Vol. 17, no. 2, June 2007.

[3] S.-C. Shi, T. Noguchi, J. Inatani, Y. Irimajiri, and T. Saito, 1998, "Experimental results of SIS mixers with distributed junction arrays", Proc. 9th International Symposium on Space Terahertz Tech. 223, 1998

[4] M. Salez, Y. delorme, M.-H. Chung, F. Dauplay, "Simulated Performance of multi-junction parallel array SIS mixers for ultra broadland submillimeter-wave applications ", Proc. 11th International Symposium on Space Terahertz Technology, Ann Arbor, MI, May 1-3, 2000.

[5] M. Salez, Y. Delorme, I. Péron, B. Lecomte, F. Dauplay, F. Boussaha, J. Spatazza, A. Féret, J.-M. Krieg, and K. Schuster, "A 30% bandwidth tunerless SIS mixer of quantum-limited sensitivity for Herschel/HIFI band 1", in Proceedings of SPIE Conference on Telescopes and Astronomical Instrumentation, Hawaii, 2002, vol. 4855, p. 402.

[6] Boussaha F.; Salez M.; Delorme Y.; Féret A.; Lecomte B.; Westerberg K.; Chaubet M. "Submillimeter mixers based on superconductive parallel junction arrays" SPIE; *1st Int.Symp. Microtechnologies for the New Millennium 2003*; Maspalomas; Canary Islands; Spain ; 19-20 mai 2003.

[7] F. Boussaha, M. Salez, A. Féret, B. Lecomte, C. Chaumont, M. Chaubet, F. dauplay, Y. Delorme and J-M. Krieg "Harmonic and Subharmonic Submm-

Wave emitted by Parallel Josephson Junction Arrays" J. Appl. Phys, Vol. 105, Issue 7, April 2009.

A Study of Direct Detection Effect on the Linearity of Hot Electron Bolometer Mixers

Yury V. Lobanov, Cheuk-yu E. Tong, Raymond Blundell, and Gregory N. Gol'tsman

Abstract— **We have performed a study of how direct detection affects the linearity and hence the calibration of an HEB mixer. Two types of waveguide HEB devices have been used: a 0.8 THz HEB mixer and a 1.0 THz HEB mixer which is ~5 times smaller than the former. Two independent experimental approaches were used. In the ΔG/G method, the conversion gain of the HEB mixer is first measured as a function of the bias current for a number of bias voltages. At each bias setting, we carefully measure the change in the operating current when the input loads are switched. From the measured data, we can derive the expected difference in gain between the hot and cold loads. In the second method (injection method [1]), the linearity of the HEB mixer is independently measured by injecting a modulated signal for different input load temperatures. The results of both approaches confirm that there is gain compression in the operation of HEB mixers. Based on the results of our measurements, we discuss the impact of direct detection effects on the operation of HEB mixers.**

Index Terms—**hot electron bolometer mixers, direct detection effect, conversion gain linearity.**

I. INTRODUCTION

SUPERCONDUCTING Hot Electron Bolometer (HEB) mixers have recently become the focus of active research in instrumentation for radio astronomy in the THz frequency band. Not only do HEB mixers exhibit good sensitivity in the THz regime (~10 times the quantum limit) [2]-[4], their Local Oscillator (LO) power requirements are low. This lends itself to operation with solid state sources. Earlier work on HEB mixers was mostly concentrated on noise performance and IF bandwidth. Now there is growing interest to study the direct detection response of HEB mixers and its effect on the linearity of its heterodyne response [2], [5]-[8].

It is well known that the bias current of an HEB mixer changes when its input port is switched between hot and cold loads. This phenomenon is commonly referred to as direct detection effect. Although HEB mixers are used mainly in heterodyne receivers, a direct detection response is always present because the incident black body radiation coming from the input load heats the electrons in the HEB element in the same way as the applied LO power. Given that the conversion gain of an HEB mixer is a function of its bias current, it is clear that the mixer gain will be different when its input port is switched between two very different temperatures. This non-linear behavior affects the accuracy of receiver calibration which in turn dictates the scientific usefulness of the receiver.

In this paper, we present our study of the linearity of HEB mixers. We demonstrate that the true noise temperature of an HEB mixer is lower than that computed from *linear Y-factor* measurements due to calibration error caused by direct detection effect.

In our experiments, we employ waveguide HEB mixers designed for 0.8 and 1.0 THz. These mixers were fabricated in the processing lab in Moscow State Pedagogical University. The details of the fabrication process and HEB characteristics have been reported elsewhere [3], [9]-[11]. For our waveguide HEB mixers, the superconducting NbN film (3.5 nm thick) is deposited on crystalline quartz substrate with an MgO buffer layer. Two different device sizes were used in our investigation, which helps us understand the impact of device volume on mixer linearity.

II. DIRECT DETECTION EFFECT

A. Mixer bias current

The direct detection response of an HEB mixer can readily be observed as a shift of bias current as the input load is switched between two very different temperatures. In Fig. 1a, an unpumped current – voltage characteristic (I-V curve) for an HEB mixer is displayed, together with an optimally pumped I-V curve. The latter is shown in greater detail in Fig. 1b from which we note that the pumped curve obtained with a cold (77 K) input load is different from that obtained with an ambient (295 K) input load. The bias current changes by ~ 0.1-0.4 μA near the low noise operating region marked in Fig. 1a as the input loads are switched between ambient and liquid nitrogen temperature, and $\Delta I/\Delta T_{input}$ is negative.

Manuscript received 20 April 2009.

Y. V. Lobanov, C. E. Tong, and R. Blundell are with the Harvard-Smithsonian Center for Astrophysics, Cambridge, MA 02138, USA (phone: 1-617-495-7189; e-mail: ylobanov@cfa.harvard.edu).

G. N. Gol'tsman is with the Department of Physics and Information Technology, Moscow State Pedagogical University, Moscow, 119992 Russia, (e-mail: goltsman@rplab.ru).

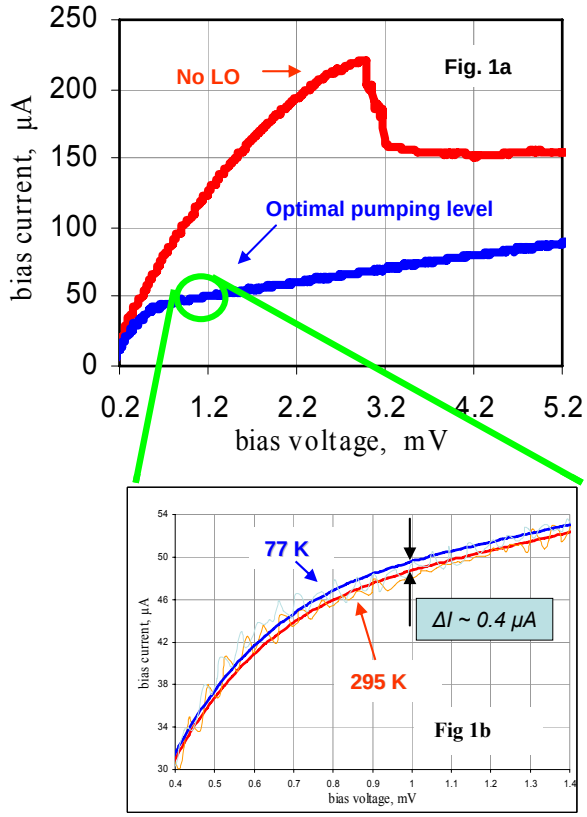

Fig. 1. Unpumped and optimally pumped I – V curves for the 0.8 THz HEB mixer under investigation. The low noise operating region is marked with a green circle (1a). Details of the I-V curves around the low noise region, show the mixer's response to different temperature input loads (1b).

In mathematical terms, the bias current in an HEB mixer, I_b, for an applied bias voltage, V_b, and applied local oscillator power, P_{LO}, can be written:

$$I_b = f(V_b, P_{LO}, P_{ext}) = I_{op}(V_b, P_{LO}) - S_I(V_b, P_{LO}) \cdot P_{ext} \qquad (1)$$

In this equation, P_{ext} is the incident signal power coming from a load placed at the receiver input and I_{op} is the nominal operating current set by the applied bias voltage and LO power in the absence of signal power. The second term of this equation represents the direct detection response of the mixer; S_I is the current responsivity of the mixer which is a function of the electron temperature in the HEB element and which in turn depends on the applied LO power P_{LO} and DC bias. Clearly, S_I increases with decreasing mixer volume because there are fewer electrons in the device. For our devices, S_I is estimated to be of the order of 100 A/W. The external incident signal power P_{ext} is given by

$$P_{ext} = k \cdot B_{Rx} \cdot T_{in}, \qquad (2)$$

where k is Boltzmann's constant, B_{Rx} is the receiver input bandwidth, and T_{in} is the input load temperature. In our experiment, B_{Rx} is around 0.3 THz and 0.5 THz for the 0.8 THz and 1.0 THz devices respectively. When we switch from an ambient to a liquid nitrogen cooled load, we have

$$\Delta P_{ext} = k \cdot B_{Rx} \cdot (T_{amb} - T_{cold}) \approx 1nW.$$

This is not negligible when compared to the absorbed LO power. Thus, it is clear that the direct detection effect induced change in bias current, ΔI_b, will affect the operation of the mixer.

B. Mixer output power

The output power P_{out} of an HEB receiver can be written as:

$$P_{out} = 2 \cdot k \cdot B_{IF} \cdot G_R \cdot (T_{in} + T_{Rx}), \qquad (3)$$

where B_{IF} is the IF bandwidth, G_R is the mixer conversion gain and T_{Rx} is the receiver noise temperature.

It is well known that the conversion gain of an HEB mixer operating near its optimal low noise region is a monotonically increasing function of the bias current (hence, a monotonically decreasing function of LO power) [12]. This effect is illustrated schematically in Fig.2.

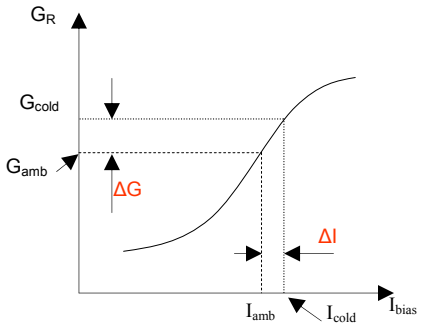

Fig. 2. Illustration of the dependence of mixer conversion gain as a function of the mixer bias current.

As a result of the bias current shift, the conversion gain for the cold input load is higher than that for the ambient load by ΔG. In terms of the measured Y-factor Y^{meas}, we have the following expression:

$$Y^{meas} = \frac{P_{out}^{amb}}{P_{out}^{cold}} = \frac{G_R^{amb} \cdot (T_{amb} + T_{Rx})}{G_R^{cold} \cdot (T_{cold} + T_{Rx})}. \qquad (4)$$

Since G_R^{cold} is larger, the measured Y-factor is expected to be reduced for larger values of direct detection induced bias current shift.

III. Experimental Methods

We have two different methods to evaluate the deviation from linearity caused by direct detection effect: the *ΔG/G method* and an *injected signal method*. In addition, two different types of devices have been used in our investigation.

A. Device type

Table I shows the parameters of the two different types of devices used in our study. Although the HEB elements were fabricated at different times, they are expected to have similar

film thickness of about 3.5 nm. From Table I we note that the 1.0 THz device is about 5 times smaller than the 0.8 THz device. Therefore, we expect it to demonstrate more pronounced direct detection effects.

TABLE I HEB MIXERS CHARACTERISTICS

Frequency, THz	Chip size, mm × μm × μm	Active element area, μm × μm	Room resis-tance, Ohm	Critical current, μA
0.8	2 × 126 × 30	0.12 × 1.5	55	218
1.0	1.5 × 90 × 23	0.065 × 0.5	90	103

B. ΔG/G method

Using the substitution $G_R^{amb} = G_R^{cold} - \Delta G$ and writing G instead of G_R^{cold}, (4) can be rewritten:

$$Y^{meas} = Y^{linear} \cdot (1 - \frac{\Delta G}{G}), \qquad (5)$$

where Y^{linear} is the Y-factor corresponding to the mixer exhibiting no direct detection effect.

In this method, (5) is used to derive the error in Y-factor measurements due to direct detection effects. In order to obtain the value of $\Delta G/G$, the following steps are taken. First, the relative receiver conversion gain G is estimated by making use of equation (3),

$$P_{out}^{amb} - P_{out}^{cold} = 2 \cdot k \cdot B_{IF} \cdot G \cdot [(T_{amb} - T_{cold}) - \frac{\Delta G}{G} \cdot (T_{amb} + T_{Rx})]. \qquad (6)$$

If $\Delta G/G < 0.02$, the term $(T_{amb}+T_{Rx})\cdot\Delta G/G$ is less than a few percents of $(T_{amb} - T_{cold})$ for $T_{Rx} \sim 500$ K. By neglecting the second term in (6), we can write down an approximate expression for the normalized receiver gain G_n:

$$G_n = \frac{P_{oout}^{amb} - P_{out}^{cold}}{2 \cdot k \cdot B_{IF} (T_{amb} - T_{cold}).} \qquad (7)$$

G_n is readily measured as a function of bias current for a given bias voltage. The experimental data set $G_n(I_b)$ is then fitted with a second order polynomial:

$$G(I) = a \cdot I_b^2 + b \cdot I_b + c \qquad (8)$$

In Fig. 3. we plot one set of measured data of $G_n(I_b)$ against I_b together with the quadratic fit. Once the dependence of G on I_b is derived, ΔG is calculated as follows:

$$\Delta G = \frac{dG_n}{dI} \cdot \Delta I = (2 \cdot a \cdot I_b + b) \cdot \Delta I, \qquad (9)$$

The quantity ΔI is simply the difference between bias current under different load conditions: $\Delta I = I_b^{cold} - I_b^{amb}$ and was measured simultaneously with the gain measurement.

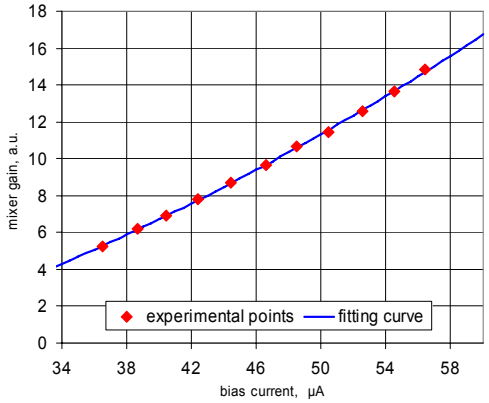

Fig. 3. Mixer normalized gain vs. mixer bias current: experimental data and for using (8).

In principle, the value of ΔG obtained from (9) can be fed back into (6) to increase the accuracy of the derived value of $\Delta G/G$. However, we have not used an iterative approach in our study as $\Delta G/G$ is small.

The experimental set up for the $\Delta G/G$ method is the standard receiver Y-factor measurement set up (Fig. 4). In our cryostat, an isolator is used between the HEB mixer and the cold HEMT amplifier. It has been shown that the isolator helps mitigate unwanted effect caused by a mismatch between mixer and IF amplifier. This subject was not part of our study but has been covered by other researches, e.g. [6], [8]. The output IF signal from the cryostat is further amplified and filtered with a 2.7 GHz – 3.1 GHz bandpass filter. Finally, the IF output power is measured with a calibrated Agilent power meter. A computer controlled robotic arm carrying the ambient load, made from a square matrix of 3×3 Thomas Keating RAM tiles (25 mm square tile) [13], can swing periodically into the signal beam which is normally terminated by a 77 K cold load. ΔI and ΔG are measured simultaneously each time the loads are switched.

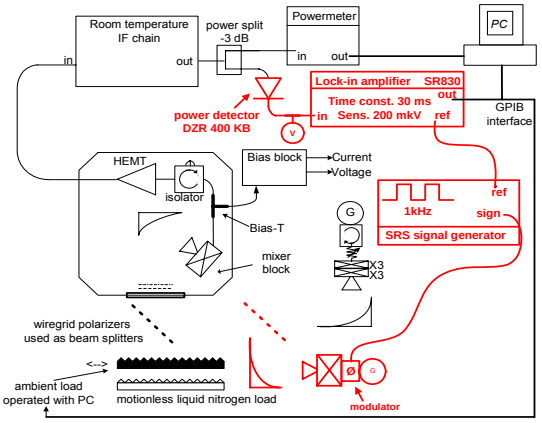

Fig. 4. Elements needed for the injected signal method (Lock-in amplifier, Power detector, SRS signal generator and modulated RF source) are shown in red. The room temperature IF chain consists of a cascade of amplifiers with a 2.7-3.1 GHz bandpass filter. The LO frequency is 0.810 THz.

C. Injected signal method

By injecting a weak signal at the receiver input port and recovery the same signal at the output port, we can derive the differential response of the receiver under its nominal operating conditions. This method has successfully been implemented for SIS mixer calibration [1], [14], [15]. Non-linear mixer conversion gain response can easily be observed by comparing the magnitudes of the injected signal at the receiver output under different input load temperatures with equal injected signals.

Referring to Fig. 4, an additional modulated RF signal source is coupled to the LO beam using an additional wire grid polarizer. The additional Gunn oscillator is modulated by a 1 kHz square wave (ON/OFF modulation) before driving a frequency multiplier to generate modulated radiation at 0.813 THz.

At the receiver output, the modulated signal is picked up by a power detector DZR 400 KB [16] followed by a lock-in amplifier. The detector is operated well-below saturation. A calibration procedure [1], [6] performed by injecting test signal into IF chain thru directional coupler does not show any deviation from linearity so long as detector voltage remains less than 4 mV. The voltage registered by the lock-in amplifier is set to be ~ 1% of the DC voltage measured by the detector.

The principle of the measurement is illustrated schematically in Fig. 5.

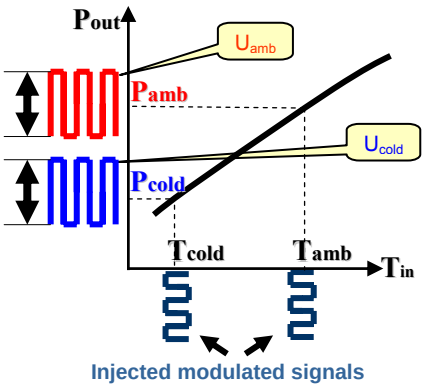

Fig. 5. Schematic representation of mixer output power vs. input load temperature. Modulated injected signals generate input power switching and the modulation created at the output depends on the slope of the P-T curve for a given input load temperature. U_{amb} and U_{cold} are voltages measured by the lock-in amplifier following for the power detector.

Let U_{amb} and U_{cold} be the voltages measured by the lock-in amplifier when the receiver is terminated by an ambient and a cold load respectively. For a perfectly linear mixer, U_{amb} and U_{cold} should be equal. In the presence of gain compression, U_{amb} and U_{cold} are no longer equal and any observed difference between them can be used to derive the mixer's gain non-linearity.

For small deviations from linearity ($\Delta G/G < 0.02$) the receiver output power as a function of input temperature can be written:

$$P(T_{in}) = P_0 + mT_{in} - \alpha T_{in}^2, \qquad (10)$$

for some coefficients m and α. Since the lock-in amplifier measures the differential changes of output power, the ratio between U_{amb} and U_{cold} is proportional to the slope of the $P(T)$ curves in (10) for $T = T_{amb}$ and T_{cold} respectively. This ratio, R, can be written down as:

$$R = \frac{U_{amb}}{U_{cold}} = \frac{\left.\frac{dP}{dT_{in}}\right|_{T_{amb}}}{\left.\frac{dP}{dT_{in}}\right|_{T_{cold}}} = \frac{m - 2\alpha T_{amb}}{m - 2\alpha T_{cold}}. \qquad (11)$$

Note that the quadratic term in (10) represents the mixer's deviation from linearity as a result of the mixer's direct detection response. The output power from a perfectly linear mixer would only contain the constant and linear terms: $P(T_{in}) = P_0 + mT_{in}$. The theoretical Y-factor for such a perfectly linear mixer with no direct detection effect Y^{linear} can be written:

$$Y^{linear} = \frac{P_0 + mT_{amb}}{P_0 + mT_{cold}} \qquad (12)$$

where the coefficients P_0 and m are solved from (11) and (10) for T_{amb} and T_{cold}.

IV. Experimental Results And Discussion

In the *ΔG/G method*, we measure values of ΔI_b for the 0.8 THz device ranging from 0.1 μA – 0.4 μA depending on the nominal bias current. In order to compare the significance of this bias current shift, ΔI_b has to be normalized by the nominal bias current I_b. Fig. 6 gives a plot of $\Delta I_b/I_b$ as a function of bias current.

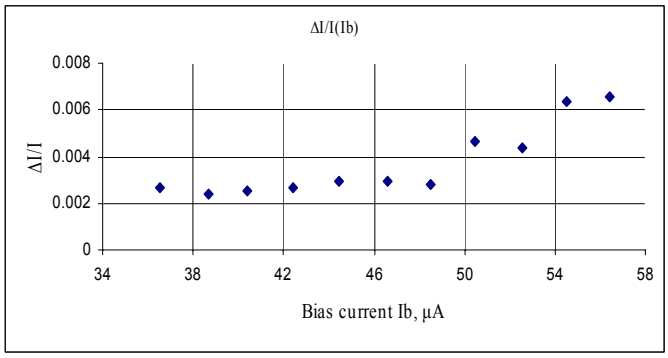

Fig. 6. $\Delta I_b/I_b$ vs. I_b for 0.8 THz receiver.

We note that the bias current shift caused by the direct detection effect is larger at higher bias current, where LO power is lower and conversion gain is higher. For the 1.0 THz device $\Delta I_b/I_b$ lies in this range of 0.4% – 0.8% versus 0.2% - 0.6% for the 0.8 THz device. The slightly higher value for the 1.0 THz device is most likely a result of its smaller size.

Compared with quasioptical HEB mixers which were studied in [2], [5], [6], [8], [10], [11] the value of $\Delta I_b/I_b$ registered by our waveguide HEB mixer tends to be smaller by about an order of magnitude. This difference is probably because of difference in input bandwidth which is usually much wider for quasioptical mixers.

For both 0.8 THz and 1.0 THz devices, the value of $\Delta G/G$ is less than 0.02. This verifies the validity of the approximate expression for receiver gain given by (7). As expected, $\Delta G/G$ is also larger in the case of the 1.0 THz mixer by a factor of 2-3.

In the *injected signal method,* the ratio of lock-in voltages lies between 1.008 and 1.014 for the 0.8 THz device and between 1.035 and 1.050 for the 1.0 THz device.

Receiver noise temperature is measured at the optimal operating voltage bias for the given HEB mixer (that is 1.0 mV for 0.8 THz receiver and 0.5 mV for 1.0 THz receiver) as a function of bias current I_b. First, Y-factor and bias current change ΔI_b are measured for each bias point and, then a modulated injection signal is introduced, U_{amb} and U_{cold} are measured. All measured values are statistically analyzed for experimental errors and measurement uncertainties. After that, corrected Y-factors determined by both methods by (5) and (12) are computed. The results for the 0.8 THz HEB mixer are given in Fig. 7. From the figure, the injection method yields a smaller correction to the measured Y-factor. Correction given by the *ΔG/G method* is larger and is more sensitive to the value of the bias current. In fact, the required correction is close to the accuracy of our Y-factor measurement, which is limited by receiver instability.

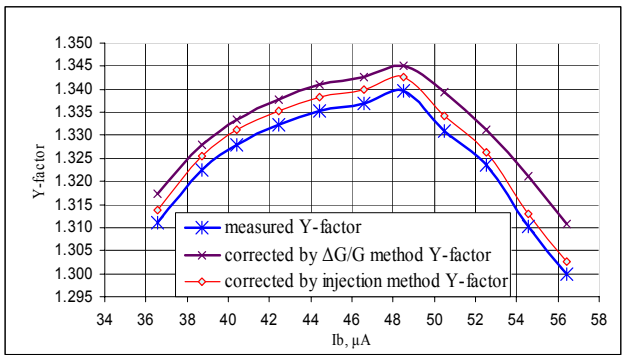

Fig. 7. Measured and corrected Y-factor vs. bias current I_b.

The results of our measurements in terms of receiver noise temperature are summarized in Table II for both 0.8 THz and 1.0 THz devices. Comparing the two methods, the percentage correction in noise temperature given by the injection method appears to show less scattering. This may be attributed to the larger error in the measurement of ΔI_b, resulting from receiver instability and noise in our measurement system. Both methods confirm that the use of smaller devices would lead to larger correction in the experimental Y-factor using ambient load.

TABLE II CORRECTED AND UNCORRECTED NOISE TEMPERATURE

Frequency, THz	Bias current, μA	Measured noise temperature, K	*ΔG/G method*		*Injection method*	
			Corrected noise temperature, K	Correction in %	Corrected noise temperature, K	Correction in %
0.8	36.5	624	610	2.23	618	0.98
	42.4	579	568	1.80	573	0.97
	48.5	565	555	1.73	559	0.99
	54.5	626	602	3.81	620	0.98
1.0	27.3	702	652	7.23	681	3.00
	28.1	723	680	5.94	692	4.26
	29.2	721	691	4.05	688	4.57

V. CONCLUSION

Direct detection response of the waveguide HEB mixers was observed experimentally and has been studied with both theoretical considerations and experiments. Two independent experimental methods were adopted for precise HEB mixer based receiver calibration which takes into account direct detection response of the HEB mixer.

Our experimental data demonstrate that direct detection effects produce calibration error which is less than 10% for receiver noise temperature calibration and less than 1% for receiver gain calibration.

As predicted, the smaller device volume is, the stronger is the observed direct detection effect. Clearly, when an HEB mixer is chosen for a certain task that requires very tight calibration standard, it may be necessary to employ either devices with larger volume or calibration load with a lower physical temperature instead of an ambient one. Alternatively, the use of our experimental methods can also allow a partial removal of the nonlinearity effect caused by gain compression.

ACKNOWLEDGMENT

The authors would like to thank technological group in the Moscow State Pedagogical University for device fabrication and Steve Leiker for robotic load design and fabrication.

REFERENCES

[1] C.-Y. E. Tong, A. Hedden, and R. Blundell, "Gain expansion and compression of SIS mixers," *IEEE Trans. Appl. Superconductivity.*, to appear in June 2009.

[2] J. Baselmans *et al*., "NbN hot electron bolometer mixer: sensitivity, LO power, direct detection and stability," IEEE trans. On Appl. Superc., 15, 2, 2005.

[3] G. Gol'tsman, "Hot electron bolometric mixers: new terahertz technology," Infrared Phys. and Techn., v. 40, pp. 199-206, 1999.

[4] A. D. Semenov, G. N. Gol'tsman, and R. Sobolewski, "Hot-electron effect in superconductors and its applications for radiation sensors," *Supercond. Sci. Technol.*, vol. 15, pp. R1–R16, 2002.

[5] J. Baselmans *et al.,* "Direct detection effect in small volume hot electron bolometer mixers," Appl. Phys. Lett., 86, 2005.

[6] J. Baselmans *et al.*, "Influence of the direct response on the heterodyne sensitivity of hot electron bolometer mixers," J. of Appl. Phys., 100, 2006.

[7] W. Ganzevles, "Direct response of microstrip line coupled Nb THz hot-electron-bolometer mixers," Appl. Phys. Lett., V.79, no15, 2001.

[8] S. Cherednichenko, V. Drakinskiy, E. Kollberg, I. Angelov, "The direct detection effect in the hot electron bolometer mixer sensitivity calibration," IEEE Trans. On Microw. Theory and Techniques, v.55, no.3, March, 2007.

[9] D. Meledin, D. Marrone, C.-Y. E. Tong, H. Gibson *et all.*, "A 1-THz superconducting hot electron bolometer receiver for astronomical observations," *IEEE Trans. On Microwave Theory and Techniques,* v. 52, No. 10, Oct. 2004.

[10] M. Hajenius, "Terahertz heterodyne mixing with a hot electron bolometer and a quantum cascade laser," 2006.

[11] J. Kooi, "Advanced receivers for submillimeter and far infrared astronomy," 2008.

[12] P Burke *et al.*, "Mixing and noise in diffusion and phonon cooled superconducting hot electron bolometers," J. of Appl. Phys., V.85, No3, Febr., 1999.

[13] Thomas Keating Ltd., UK. Website: http://www.terahertz.co.uk

[14] C.E. Tong, D. Papa, S. Leiker, B. Wilson, S. Paine, R. Christensen, and R. Blundell, "Implementation of a two-temperature calibration load unit for the submillimeter array," these proceedings.

[15] A. Kerr, J. Effland, S. Pan, G. Lauria, A. Lichtenberger, R. Groves, "Measurement of gain compression in SIS mixer receivers" in *Proc. 14th Int. Symp. Space THz Tech.,* pp. 22-24, Ventana Canyon, AZ, April 2003. (Also in ALMA memo 460.1: http://www.alma.nrao.edu/memos).

[16] http://www.herotek.com

P7B

Multiplexing of Hot-Electron Nanobolometers Using Microwave SQUIDs

B.S. Karasik *, P.K. Day, and J.H. Kawamura
Jet Propulsion Laboratory, California Institute of Technology, Pasadena, CA 91109
* Contact: boris.s.karasik@jpl.nasa.gov, phone +1-818-393-4438

***Abstract*—We will present the first data demonstrating multiplexed operation of the titanium (Ti) hot-electron nanobolometers at ~ 0.4 K. Nanobolometers are very promising for meeting the most demanding sensitivity requirements for THz spectroscopy in space [1]. At the same time, they have a short time constant (~ μs at 400 mK) that makes impossible application of time-domain or audio-frequency domain multiplexing schemes commonly use for leg-isolated (slow) superconducting bolometers.**

A novel solution pursued in this work is called MSQUID and uses dc SQUIDs coupled to X-band microresonators [2]. SQUIDs are very low-noise, low power dissipating superconducting devices commonly used for readout of superconducting bolometers. Their input bandwidth is limited by inductive coupling to the bolometer and does not exceed ~1 MHz that is suitable for one hot-electron detector pixel. At the same time, the SQUIDs themselves are very fast and can operate at many GHz. This gives a way to implement a multiplexed readout for nanobolometers by measuring a change of the Q-factor of an X-band coplanar waveguide (CPW) resonator coupled to the SQUID. The detected radiation causes a change of the current through the bolometer and through the input coil of the SQUID. This causes a change of the magnetic flux through the SQUID loop, which changes the SQUID impedance and introduces damping in a coupled resonator. Each SQUID in the array is coupled to its individual resonator. The unique resonator frequency (resonator length) provides microwave frequency encoding for each pixel. The number of channels (pixels) per one MSQUID depends on the Q-factor of the resonators and can be about several 100s. At the same time, all MSQUIDS require just 2 pairs of wires for biasing and flux modulation and two microwave cables for passing the probe signal through the resonators. The output of many (~100) MSQUIDs can be also multiplexed thus leading to a possibility to read a 10,000-pixel array using this approach. The type of the multiplexor was inspired by the Microwave Kinetic Inductance Detector (MKID) [3] and has the same advantages (large bandwidth, many pixels).

We are setting up a demo-array consisting of 4 hot-electron nanobolometers with the noise equivalent power NEP ~ 10^{-17} W/Hz$^{1/2}$ at 400 mK connected to a 4-element MSQUID chip. The entire system will operate in a He3 dewar with the optical access. We plan to demonstrate the complete recovery of the detector noise after demultiplexing and also the simultaneous detection of NIR single photons in all 4 channels. The latter is important since the nanobolometers are seen as potential THz calorimeters for on-chip FIR spectroscopy. The follow-up work will address larger scale fully integrated array of more sensitive nanobolometers hybridized with a matching MSQUID chip.

[1] J.Wei et al., *Nature Nanotechnology* 3, 496 (2008)
[2] I.Hahn et al., *J. Low Temp. Phys*. 151, 934 (2008)
[3] P.K.Day et al., *Nature* 425, 817 (2003)

Performance Investigation of a Quasi-Optical NbN HEB Mixer at Submillimeter Wavelength

W. Miao, Y. Delorme, A. Feret, R. Lefevre, L. Benoit, F. Dauplay, J.M. Krieg, G. Beaudin, W. Zhang, Y. Ren, and S.C. Shi.

***Abstract*—In this paper, the performance of a quasi-optical phonon-cooled NbN superconducting hot electron bolometer (HEB) mixer is thoroughly investigated. The variation of the receiver noise temperature and the conversion gain around 600 GHz with respect to DC bias voltage and LO pumping level has been measured. The lowest receiver noise temperature is 750 K and reduced to about 250 K after correcting the quasi-optical losses before the HEB mixer. We compared the measured results with the predictions according to one dimensional distributed hot spot model. A reasonable match between theoretical model and experiment is observed. In addition, the direct response of the HEB mixer (integrated with a log-periodic spiral antenna) is measured by using Fourier Transform Spectrometer (FTS). The stability of the receiver is also investigated by means of Allan variance time measurements performed with an intermediate frequency (IF) bandwidth of 40 MHz.**

***Index Terms*—NbN HEB mixer, noise temperature, conversion gain, frequency dependent response, stability.**

I. INTRODUCTION

EXPLORING the terahertz (THz) frequency range is crucial for astronomy since a wealth of spectral lines from molecules providing important information of planet and star formation fall into this range [1]. Detectors of high sensitivity and good stability are necessary to observe efficiently these spectral lines since the astronomical signals are generally very weak. Among all detectors available today, superconducting hot electron bolometer (HEB) mixers [2] have been proved to be the most competitive devices of coherent detection in the THz frequency range. Space or ground based projects such as TREND [3] and HIFI [4] have selected superconducting HEB mixers. In this paper, we have thoroughly investigated the DC characteristics and the noise performance around 600 GHz of a quasi-optical NbN superconducting HEB mixer through experiments and modeling. The receiver stability is also studied by measuring the Allan variance time at the LO frequency of 600 GHz.

Manuscript received 17 April 2009. This work was supported in part by CNES (Centre National d'Etudes Spatiales) under contract No. RS06/SU-0002-041 and the National Natural Science Foundation of China under contract Nos. 10673033, 10621303, and 10778602.

W. Miao, Y. Delorme, A. Feret, R. Lefevre, L. Benoit, F. Dauplay, J.M. Krieg and G. Beaudin are with LERMA, Observatoire de Pairs, France (phone: 33-01-40-51-20-60; e-mail: wei.miao@obspm.fr).

W. Zhang, Y. Ren and S.C. Shi are with Purple Mountain Observatory, NAOC, CAS, China.

II. HEB MIXER AND EXPERIMENTAL SETUP FOR HETERODYNE MEASUREMENT

The quasi-optical phonon-cooled NbN superconducting HEB mixer was fabricated in Moscow State Pedagogical University (MSPU). The HEB mixer itself is indeed a microbridge made up of an extremely thin superconducting NbN film deposited on a thick silicon substrate by DC reactive magnetron sputtering. The superconducting NbN microbridge is 0.15 μm long, 2.4 μm wide and 3.5 nm thick and is placed between the feed point of a log-periodic spiral antenna which couples RF and LO signals to the HEB mixer.

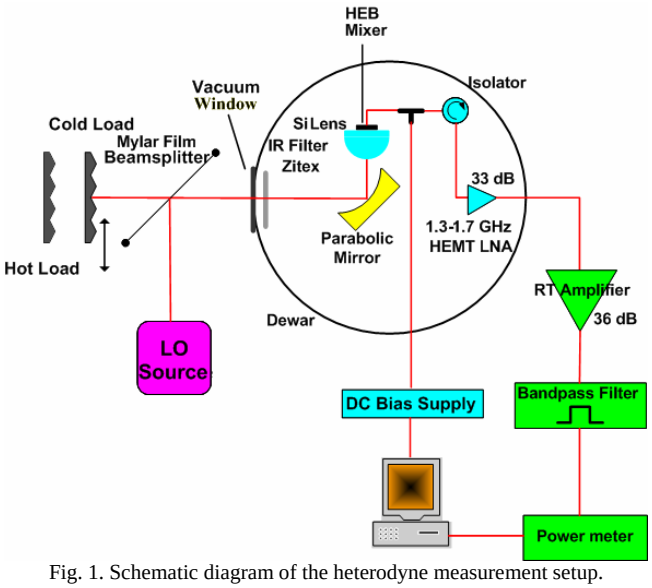

Fig. 1. Schematic diagram of the heterodyne measurement setup.

Heterodyne characterization of the quasi-optical superconducting HEB mixer was performed at frequencies near 600 GHz. The experimental setup is shown in Fig. 1. The HEB device was glued on the centre of a silicon hyper-hemispherical lens with a diameter of 12.7 mm, and then mounted in a copper mixer block fixed on the 4-K cold plate of the cryostat. The 600 GHz LO source is provided by a solid state source (Gunn oscillator and frequency multiplier). The LO and RF (hot or cold blackbody) signals are combined by a beamsplitter made of a 25 μm thick Mylar film, and then transmitted into the cryostat through a vacuum window (25 μm thick Mylar film) and an IR filter (Zitex G110). For signal focusing, a parabolic reflection mirror is situated in front of the mixer block on the plate of the cryostat. The HEB mixer's IF output signal is

connected to a 0.1-10 GHz bias-tee, a 1.3-1.7 GHz cooled low noise HEMT amplifier (of 33 dB gain and 5 K noise temperature), a 36 dB gain room temperature amplifier, a 1.5± 0.02 GHz YIG bandpass filter, and finally detected by a power meter.

III. Experiment and Analysis

A. Current-voltage characteristics

We first measured the current-voltage characteristics of the HEB mixer for different LO pumping levels, as shown in Fig. 2. The critical current of this HEB device is about 80 μA. Fig. 2 also shows the current-voltage characteristics calculated by one dimensional distributed hot spot model [5], which is based on solving a heat balance equation for electron temperature along the superconducting microbridge. In this model, we adopted the measured temperature dependent resistance of the HEB device instead of a Fermi form assumption [6] to determine the resistance of the device. The effect of bias current on the critical temperature of the HEB is also taken into account as expressed by equation (1) [7]:

$$T_c(I_0) = (1-(I_0/I_c)^{1/\gamma})T_c(0) \quad (1)$$

where I_0 and I_c are respectively the bias and the critical current of the device at $T=0$ K. γ is the exponent of the temperature dependence of the superconductor band gap and is estimated to be 0.8 for our HEB according to the measurement of the temperature dependent resistance at several bias currents, as shown in Fig. 3.

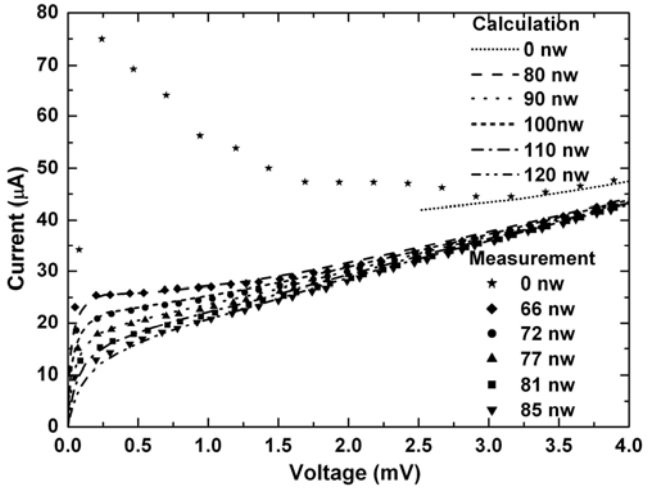

Fig. 2 I(V) curves of the HEB mixer for different LO heating powers.

According to Fig. 2, it is clear that the computed current-voltage characteristics are in good agreement with the measured ones over the whole bias range. Note that the measured LO power is determined by the isothermal technique. We attribute the difference between the predicted and measured LO power absorbed by the microbridge to imperfections of the isothermal technique, which is based on a lumped element model and is not capable of distinguishing the DC bias heating efficiency from that of LO power.

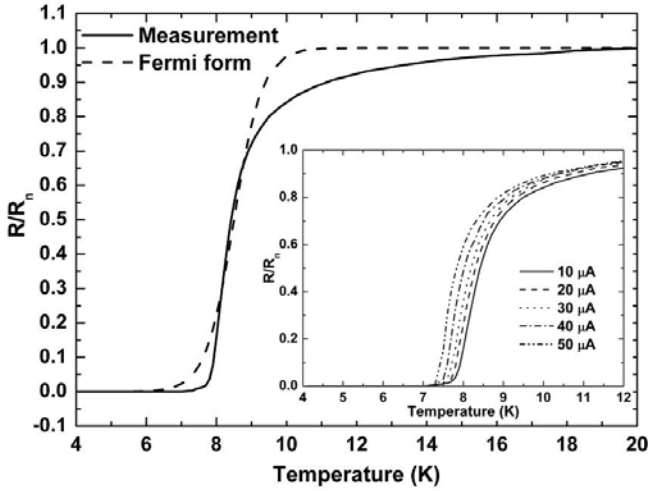

Fig. 3 R-T (resistance-temperature) curve of the NbN HEB mixer. The inset shows the effect of bias current on R-T curve.

B. Noise temperature and conversion gain

The receiver noise temperature T_{rx} of the HEB mixer was obtained from conventional Y-factor measurement using a room-temperature (295 K) and a cold (77 K) blackbody as input signal source. Fig. 4 shows the measured DSB receiver noise temperature at the optimal LO pumping level (66 nw) over the whole bias range of interest. Biased at 0.8 mV and 26 μA, the HEB mixer demonstrates a lowest DSB receiver noise temperature of 750 K. After correcting the noise contributions of the quasi-optical components, we found that the lowest noise temperature was reduced to 250 K. The conversion gain G_{mixer} of the same mixer was characterized by U-factor method. The U factor is defined as the ratio of the IF output powers at the operating bias and the zero dc bias without LO pumping, and is given by

$$U = \frac{P_{295}}{P_{sc}} = \frac{2(T_{295}+T_{rx})}{(T_{bath}+T_{if})} G_{total} \quad (2)$$

where T_{295} and T_{bath} are the effective radiation temperatures determined from their own physical temperatures by the Callen-Welton formulation, T_{if} is the equivalent input noise temperature of the IF chain (assumed to be 10 K), and G_{total} is the total conversion gain of the receiver. By reducing the contributions of the quasi-optical components (- 3.8 dB in our case) from G_{total}, the conversion gain of the NbN HEB mixer can be obtained. We compared the measured results with the predictions by one dimensional distributed hot spot model, and found that predicted conversion gains are about 3.5 dB higher than the measured ones (inset of Fig. 5) while similar trend is observed. This result implies that the hot spot model would have overestimated the IF current ΔI produced by incident signals and there would be some still unknown intrinsic losses of the HEB mixer or unconsidered losses in the IF circuit [8]. Here we introduced a tuning factor of 0.65 to the IF current ΔI in the hot spot model, and the computed conversion gains are found in better agreement with the measurements over the whole bias range (see Fig. 5).

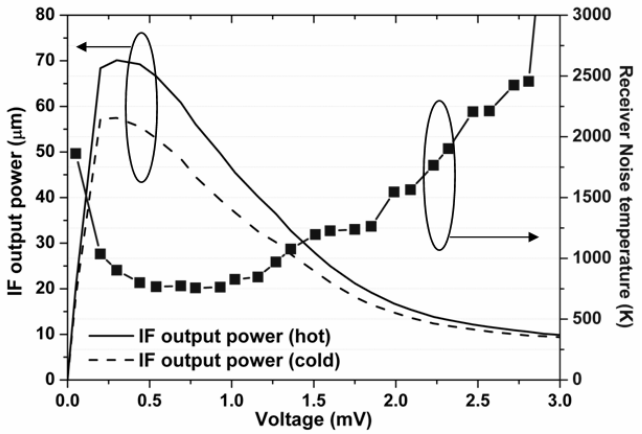

Fig. 4 Measured IF output powers responding to the hot and cold load (left axis) as well as the DSB receiver noise temperature (right axis) at the optimal LO pumping level for different bias voltages.

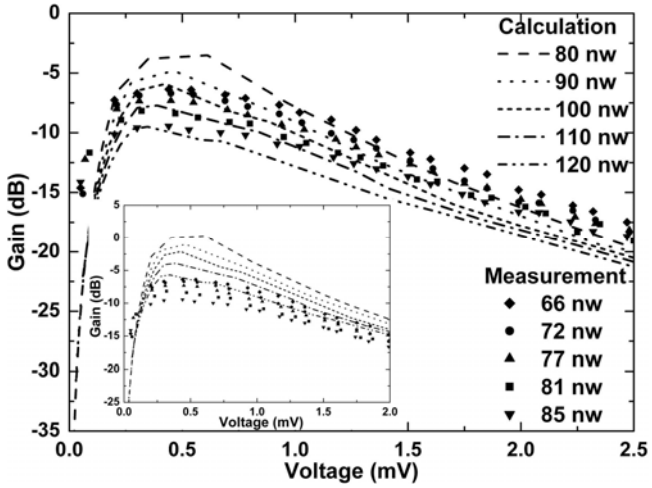

Fig. 5 Conversion gains of the HEB mixer for different bias voltages and LO pumping levels. The inset shows the calculated conversion gains without applying the tuning factor of 0.65.

C. Direct response

To get the direct response of the quasi-optical HEB mixer, Fourier Transform Spectrometer (FTS) measurement is performed when the HEB mixer is heated to its resistive state. The FTS measurement system consists of a Michelson interferometer with a chopped Hg lamp providing broadband THz radiation. The cryostat is placed in front of the FTS output and the biased signal of the HEB is connected to a lock-in amplifier that was synchronized with the chopper. The FTS system is operated in a step and integration mode. Performing the Fourier transform on the measured interferogram would give us the frequency spectrum. In this measurement, the maximum span and the minimum step size of the movable mirror was chosen to be 15 mm and 50 μm, which gives a frequency resolution of 10 GHz and a frequency range of 1.5 THz, respectively. Fig. 6 shows the normalized spectrum response of the mixer. We find that the direct response of the HEB mixer is in the frequency range from 200 to 1000 GHz. For frequencies higher that 1000 GHz, the response of the HEB mixer becomes weak due to the strong absorption by water (dash line in Fig. 6) although the log-periodic spiral antenna (originally designed for the 850 GHz band) should operate in that frequency region.

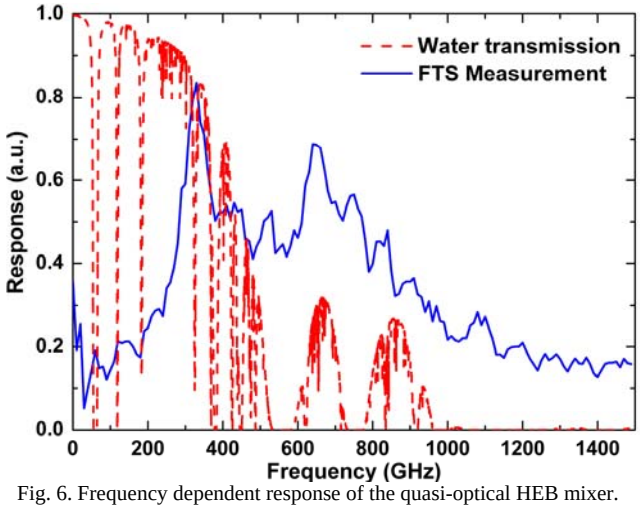

Fig. 6. Frequency dependent response of the quasi-optical HEB mixer.

D. Stability

One of the important parameters for heterodyne receivers is the receiver stability. A general method to determine the receiver stability is to measure so called Allan variance as a function of integration time. In order to obtain the Allan variance plot, we sampled the IF output power of the HEB mixer at the rate of 100 readings per second. Note that the IF output power of the HEB mixer is filtered by a YIG filter with a 40 MHz bandwidth centered at 1.5 GHz. According to the well known radiometer equation [9], the effective bandwidth determines the contribution of the white noise, and consequently determines the Allan variance time. Fig. 7 shows the Allan variance plot of the HEB mixer. In this case, the HEB mixer was biased at its optimum operating point and the IF output power used to obtain the Allan variance plot has been divided by its mean value. According to Fig. 7, the minimum Allan variance is on the order of 10^{-6} and the Allan variance time is about 0.3 s, which is close to published results [10].

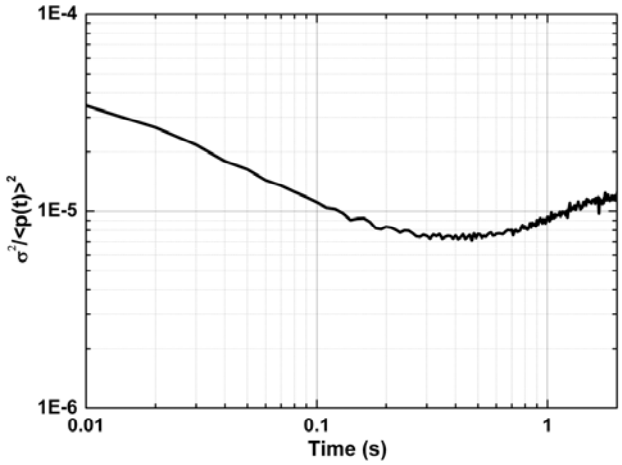

Fig. 7. Allan variance of the quasi-optical HEB mixer when it was biased at its optimum operating point.

IV. Conclusion

We have thoroughly investigated the performance of a quasi-optical phonon-cooled NbN superconducting HEB mixer. The measured lowest DSB receiver noise temperature is 750 K at 600 GHz, and down to 250 K after correcting the noise contributions of the quasi-optical components. Compared to the predictions by hot spot modeling, a good agreement has been observed with respect to current-voltage characteristics and conversion gains of the HEB mixer. In addition, the direct response of the HEB mixer has been investigated by means of FTS measurement and is found to be in the frequency range from 200 to 1000 GHz. The stability of the HEB mixer has also been studied and the Allan variance time is about 0.3 s.

Acknowledgment

W. M. would like to thank French Embassy in China for the funding of the joint French-Chinese PhD program.

References

[1] P.H. Siegel, "Terahertz technology," *IEEE Transactions on Microwave Theory and Techniques*, Vol. 50, No. 3, pp. 910-928, March 2002.

[2] E.M. Gershenzon, G.N. Gol'tsman, I.G. Gogidze, A.I. Eliantev, B.S. Karasik, and A.D. Semenov, "Millimeter and submillimeter range mixer based on electron heating of superconducting films in the resistive state," *Soviet Physics Superconductivity*, Vol. 3, pp. 1582-1597, 1990.

[3] E. Gerecht, S. Yngvesson, J. Nicholson, Y. Zhuang, F. Rodriguez, X. Zhao, D.Z. Gu, R. Zannoni, M.J. Coulombe, J.C. Dickinson, T.M. Goyette, J. Waldman, C.E. Groppi, A.S. Hedden, D. Golish, C.K. Walker, A.A. Antony, C. Martin, and A. Lane, "TREND: a low noise terahertz receiver user instrument for AST/RO at the south pole," *Proceedings of the SPIE*, Vol. 4855, pp. 574-582, 2003.

[4] S. Cherednichenko, M. Kroug, H. Merkel, P. Khosropanah, A. Adam, E. Kollberg, D. Loudkov, G. Gol'tsman, B. Voronov, H.Richter, and H.W. Hubbers, "1.6 THz heterodyne receiver for the far infrared space telescope," *Physics C: Superconductivity*, Vol. 372, pp. 427-431, 2002.

[5] P. Khosropanah, H.F. Merkel, K.S. Yngvesson, A. Adam, S. Cherednichenko, and E.L. Kollberg, "A distributed device model for phonon-cooled HEB mixers predicting IV characteristics, gain, noise and IF bandwidth," *in Proc. of 11th International Symposium on Space Terahertz Technology*, Ann Arbor, Michigan, pp. 474-488, 2000.

[6] R. Barends, M. Hajenius, J.R. Gao, and T.M. Klapwijk, "Direct correspondence between HEB current-voltage characteristics and the current-dependent resistive transition," *in Proc. of 16th International Symposium on Space Terahertz Technology*, Gothenburg, Sweden, pp. 416-419, 2005.

[7] H.F. Merkel, "A hot spot model for HEB mixers including Andreev reflection," *in Proc. of 16th International Symposium on Space Terahertz Technology*, Gothenburg, Sweden, pp. 404-415, 2005.

[8] D.W. Floet, "Hotspot mixing in THz niobium superconducting hot electron bolometer mixers." PhD thesis, 2001.

[9] J.D. Kraus, "Radio astronomy," 2nd edition, Powell, OH: Cygnus-Quasar Books, 1986.

[10] J.W. Kooi, J.J.A. Baselmans, A. Baryshev, R. Schieder, M. Hajenius, J.R.Gao, T.M. Klapwijk, B. Voronov, G. Gol'tsman, "Stability of heterodyne terahertz receivers," *Journal of Applied Physics*, Vol. 100, No. 6, pp. 064904, 2006.

Low Noise Terahertz Receivers Based on Superconducting NbN Hot Electron Bolometers

J. Chen, *Senior Member, IEEE,* L. Kang, M. Liang, J. P. Wang, and P. H. Wu*, *Senior Member, IEEE*

***Abstract*—Low noise terahertz (THz) receivers based on superconducting niobium nitride (NbN) hot electron bolometer (HEB) mixers have been designed, fabricated and measured for applications in astronomy and cosmology. The NbN HEB mixer consists of a planar antenna and an NbN bridge connecting across the antenna's inner terminals on high-resistivity Si substrates. Double sideband (DSB) receiver noise temperatures of 698 K at 0.65 THz, 904 K at 1.6 THz, 1026 K at 2.5 THz and 1386 K at 3.1 THz have been obtained at 4.2 K without corrections and using changeable input local oscillation (LO) power to eliminate the affects of direct detection and instability of the LO power. The excess quantum noise factor β of about 4 has been estimated using a quantum noise model.**

***Index Terms*—hot electron bolometers (HEBs), quasi-optical superconducting heterodyne mixer, terahertz (THz), receiver noise temperature.**

I. Introduction

LOW noise receivers working at terahertz (THz) frequencies are very important for many applications and basic researches [1]. Due to the lack of high quality amplifiers at such high frequencies, the front end of a THz receiver is usually a mixer whose noise and conversion performances play the key role in determining the quality of the whole system. Below 1.4 THz, Superconductor-Insulator-Superconductor (SIS) mixers exhibit noise temperatures quite close to the quantum limit $T_Q=hf/k_B$ (where h is the Planck constant, k_B is the Boltzmann constant and f is the operating frequency) [2, 3], while for operating frequencies higher than 1.4 THz, superconducting Hot Electron Bolometer (HEB) heterodyne mixers have higher sensitivity and require less local oscillation (LO) power [4-9]. Typically an HEB mixer consists of two parts, a bolometer for mixing the signal with the LO and a planar antenna for coupling both of them into it. It can be expected that superconducting HEB mixers will be used widely at THz waveband in the near future. Here, the fabrication and properties of low noise receivers based on niobium nitride (NbN) HEB mixers at THz frequency band are reported.

Manuscript received 20 April 2009. This work was supported in part by the National Natural Science Foundation of China (NSFC) under Grants 10778602, 60721063, the National Basic Research Program of China (973 Program) under Grants 2006CB601006, 2007CB310404 and National High-tech R&D Programmer of China under Grant 2006AA12Z120.

J. Chen, L. Kang, M. Liang, J. P. Wang, P. H. Wu, are with the Research Institute of Superconductor Electronics (RISE), Department of Electronic Science & Engineering, and National Laboratory of Nanjing Microstructures, Nanjing University, Nanjing 210093, P. R. China (*corresponding author to provide phone: 86-25-83594540; fax: 86-25-83686680; e-mail: phwu@nju.edu.cn).

II. Experiments and Results

We use NbN films to make the devices. The films should be thin enough to increase the gain bandwidth of the receivers but remarkable suppression of *Tc* always accompanies reduction of film thickness when films are about or less than Bardeen-Cooper-Schrieffer (BCS) coherence length ξ_0。Thus the fabrication of such films is crucial. Here the superconducting NbN film is deposited by DC magnetron sputtering on high-resistivity (> 5 kΩcm) Si substrate in $Ar+N_2$ gas mixture with the substrate kept at room temperature (RT) [10]. Fig. 1 shows an atomic force microscopy (AFM) image of a 4.5-nm thick NbN film sample on Si substrate. A root-mean-square (RMS) roughness of about 0.42 nm is obtained over an area of 5 μm squared, indicating that the film is of high quality with rather smooth surface. And the excellent interlayer growth between the film and the substrate can be confirmed by the transmission electron microscopy (TEM) observations. T_c of about 9 K and critical current density (J_c) of about 1.5×10^6 A/cm^2 at 4.2 K have been obtained for such ultra-thin films. When the small bridge made of the ultra-thin superconducting film is irradiated with THz photons, the electrons inside will be heated up (so called hot electrons) and the energy will subsequently relax to the substrate through the electron-phonon interaction [4,5].

The NbN HEB mixer consists of a complementary logarithmic-spiral antenna made of gold and an NbN film (bridge) connecting across the antenna's inner terminals. The outer diameter of the antenna should be larger than $\lambda_{0max}/4$ and inner diameter be smaller than $\lambda_{0min}/20$, where λ_{0max} and λ_{0min} are the maximum and minimum wavelengths in the free space respectively [11]. During the fabrication, NbN thin film is first deposited. It is then covered by photoresist. Two square

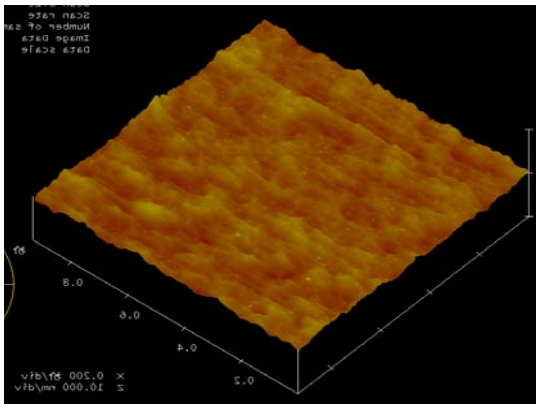

Fig. 1. AFM imaging of a 4.5-nm thick NbN film on Si substrate.

openings are positioned on the photoresist through which an additional NbN layer about 10 nm thick is deposited after a 10 s argon ion etching. Finally gold is deposited. The two square openings, with a preset distance between each other, are used to help maintain the desirable length of the bridge while the additional NbN is used as a buffer so that the superconductivity of the bridge underneath will not be seriously degraded by the gold contact [8]. The superconducting NbN HEB bridge is fabricated by electron-beam (EB) lithography, while the gold antenna defined by photolithography on Si substrate.

The NbN HEB mixer used in the experiments to be reported here is 3.5-4 nm thick, 3-4 μm wide and 0.4 μm long. Its T_c is about 8 K and ΔT_c is about 1.3 K. The normal resistance at RT R_{300} (about 150 Ω) is 2 times higher than the calculated impedance of the log-spiral antenna (about 75 Ω). In general, the RF impedance of the HEB mixer is approximately equal to R_{300}, which is frequency independent. Thus there is some mismatch between the quasi-optical superconducting HEB mixer and the log-spiral antenna, leaving much room for further improvements of our receivers.

With the quasi-optical NbN HEB as its mixer and operating at THz waveband, the receiver's double sideband (DSB) noise temperature (T_N) is measured by the Y-factor method using the equivalent temperatures of the blackbody loads at 300 and 77 K according to the Callen-Welton definition [12]. The loads are placed about 30 cm from the cryostat As shown in Fig. 2, an optically pumped far-infrared gas laser (FIRL100 from Edinburgh Instruments Ltd., with output power of about several milliwatts and linear polarization at 1.6, 2.5 and 3.1 THz) or a Gunn oscillator with its multipliers at 0.65 THz is used as the LO source. Although a THz band-pass (BP) filter at 4.2 K with about 10% bandwidth, made by Virginia Diodes, Inc. (VDI), is tried to eliminate the direct detection effect, it looks not enough for this purpose. So a wire grid is used to change the LO power for noise temperature measurements, which is not influence by the direct detection effect and instability of LO power [9]. To reduce the environment noise in our lab, an RF shielding room houses all the equipments except the laser which is too big to go into it.

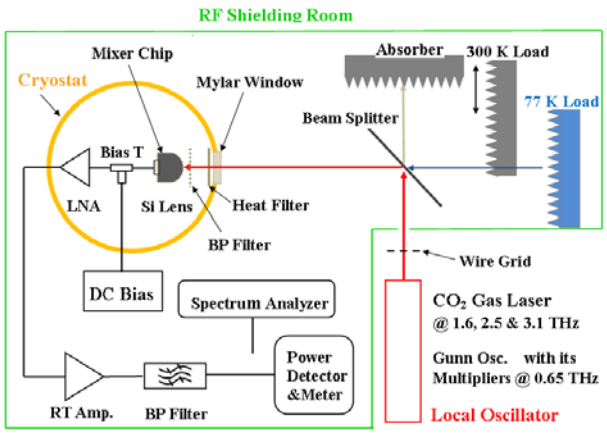

Fig. 2. Schematics of the measurement system. 36-μm and 15-μm thick Mylar films are used as the window and beam splitter. A wire grid is used to change LO power for noise temperature measurements, which is not influence by the direct detection effect and instability of LO power.

The distance between the laser and the cryostat is about 70 cm, and thus only about 2% of the laser's output power can reach the window of the cryostat at 2.5 THz and a humidity of 30%. The radiation is focused onto the antenna-coupled HEB mixer using a Si hyper-hemispherical lens (12 mm in diameter) which has no anti-reflection (AR) coating or an AR coating layer on its surface (see Fig. 2). A cryogenic low noise amplifier (LNA; noise temperature ~ 12 K, gain ~ 30 dB, frequency range of 1.3-1.7 GHz) working at ~ 15 K together with two other ordinary RT amplifiers are used to amplify the intermediate frequency (IF) signal of the mixers. No additional isolator is used between the mixer and the LNA, but a bias tee is used there. An IF filter with the center frequency of 1.5 GHz and bandwidth of 100 MHz is used between the IF amplifier and the microwave power meter or RF detector. The beam splitter and the cryostat window are Mylar films, a thickness of 15-μm for the former and 36-μm for the latter from the considerations that the losses of the LO power caused by them should be as little as possible and that mechanically they should be robust enough. With the beam splitter at 45 degrees to the incidence and the window normal to the incidence, the optical losses at 2.5 THz are calculated to be about 0.05 dB for the window and 1.2 dB for the beam splitter.

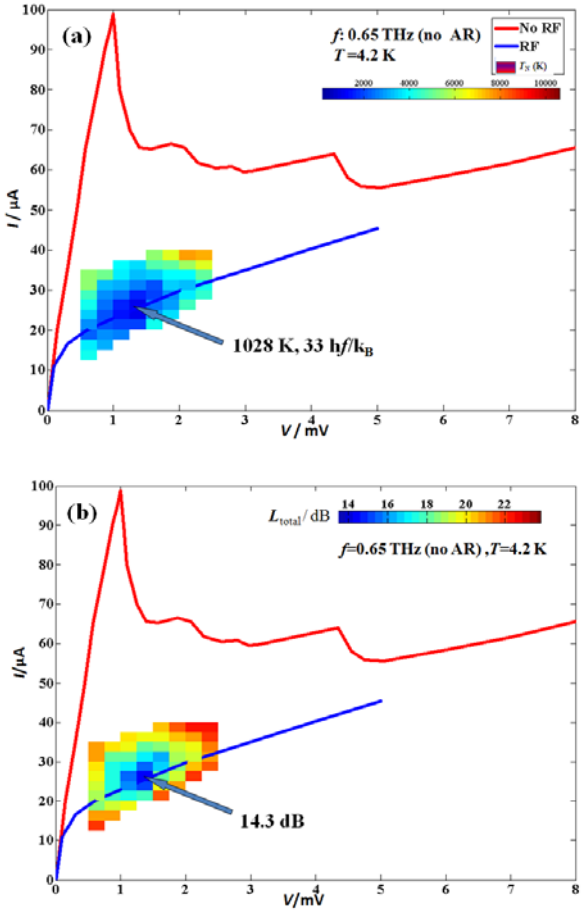

Fig. 3. *I-V* curves without and with optimized LO power, as well as DSB noise temperature (a) and conversion loss (b) as a function of bias voltage for the receiver with a Si lens without AR coating at 0.65 THz. 36-μm and 15-μm thick Mylar films are used as the window and beam splitter, respectively.

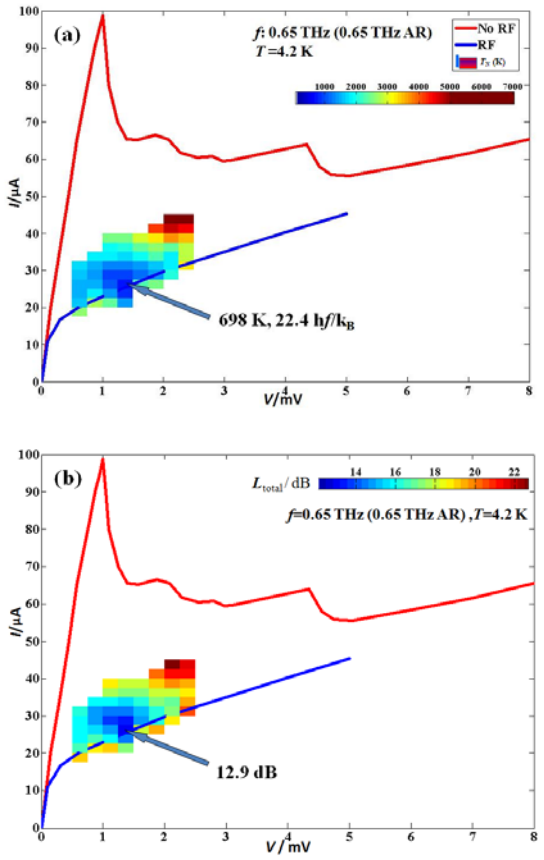

Fig. 4. *I-V* curves without and with optimized LO power, as well as noise temperatures (a) and conversion loss (b) as a function of bias voltage for the receiver with a Si lens with 70-μm thick AR coating layer at 0.65 THz. 36-μm and 15-μm thick Mylar films are used as the window and beam splitter, respectively.

The unpumped (without LO) and optimally pumped (with LO at 0.65 THz) current-voltage (*I-V*) curves of an NbN HEB mixer working at 4.2 K and without the AR coating on Si lens are shown in Fig. 3 (a), together with the DSB receiver noise temperatures (T_N) measured as a function of the dc bias voltages along the pumped *I-V* curve. As the *I-V* curves are measured using two-probe method, a contact resistance of about 10 Ω is evident in the *I-V* curve, which should be improved in near future by the *in-situ* method [13]. The uncorrected T_N reaches a lowest value of 1026 K. As the operating frequency is 0.65 THz, this value is about 33 times of the quantum limit T_Q. T_N increases considerably while the dc bias is shifted away from the optimum bias point. Using the isothermal method [14], the absorbed LO power of about 130 nW is estimated. The conversion loss L_{total} of the HEB mixer was characterized using U-factor method [15]. The calculated L_{total} for different bias voltages and LO pumping levels around optimized condition are shown in Fig. 5 (b). A lowest value of 14.3 dB has been obtained.

When there is no AR coating on the lens, the loss incurred by it is approximately 30% of the total loss. To reduce the loss and thus improve the noise performance of the receiver at some frequencies, Parylene C has been chosen as the material for AR coating on the Si lens [16, 17]. A refractive index *n* of 1.65 is determined at RT using a femtosecond (fs) laser driven

Table I Lowest receiver noise temperatures and conversion loss at different frequencies for different AR coating conditions.

AR conditions \ *f*	0.65 THz	1.6 THz	2.5 THz	3.1 THz
No AR	1028 K 33 hf/k_B 14.3 dB	1165 K 15.2 hf/k_B 14.3 dB	1396 K 11.6 hf/k_B 14.7 dB	1734 K 11.7 hf/k_B 16.4 dB
AR @ 2.5 THz	1278 K 41 hf/k_B 17.7 dB	904 K 11.8 hf/k_B 13 dB	1026 K 8.5 hf/k_B 12 dB	1401 K 9.4 hf/k_B 12.9 dB
AR @ 0.65 THz	698 K 22.4 hf/k_B 12.9 dB	1057 K 13.8 hf/k_B 13.5 dB	1462 K 12.2 hf/k_B 15.2 dB	1386 K 9.3 hf/k_B 12.8 dB

THz time-domain spectroscopy (TDS) system [18]. The thicknesses of the AR coating layers are 18.5 μm at 2.5 THz and 70 μm at 0.65 THz. The results are shown in Fig. 4 for a receiver with AR coating at 0.65 THz. The lowest T_N is about 698 K, which is about $22.4T_Q$ and 32% improvement over the case without coating. Also, lowest L_{total} becomes to be 12.9 dB.

In order to quantify the effect of the quantum noise to the receiver noise, lowest T_N and L_{total} of different receivers with same HEB mixer chip and different AR coating conditions are characterized at different frequencies in details. The results are summarized in Table I. The lowest T_N of 698 K at 0.65 THz, 904 K at 1.6 THz, 1026 K at 2.5 THz and 1386 K at 3.1 THz have been measured at 4.2 K without corrections. Using a quantum noise theory [19] as well as the frequency dependences of the beam splitter, optical window and AR coating layers, the excess quantum noise factor β of about 4 can been estimated as shown in Fig. 5.

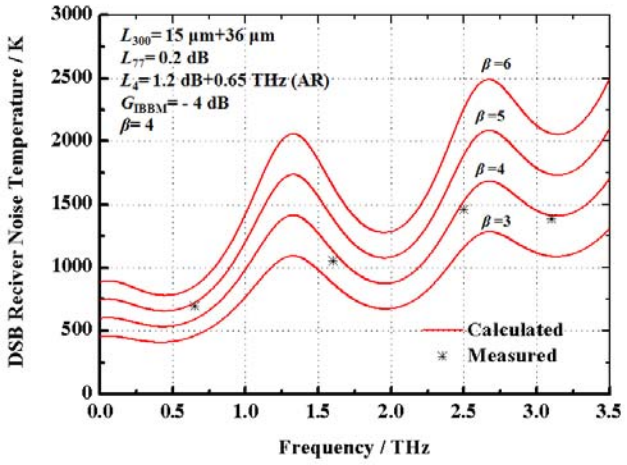

Fig. 5. Frequency dependence of lowest receiver noise temperatures for a Parylene C AR coating on Si lens with thickness of 70-μm (@ 0.65 THz). β=3,4,5,6 were assumed for calculations and best fit is obtained for β=4.

III. Conclusions

The receiver performances of the quasi-optical superconducting NbN HEB mixers have been investigated at frequencies from 0.65 THz to 3.1 THz. The lowest DSB receiver noise temperature measured at 2.5 THz is 1026 K, which is about 8.5 T_Q, without any corrections. Also, the excess quantum noise factor β of about 4 has been estimated using a quantum noise model.

Acknowledgment

We thank Drs. W. Zhang, L. Jiang, S. C. Shi, and Prof. G. N. Gol'tsman for their helpful discussions.

References

[1] P. H. Siegel, "Terahertz Technology", IEEE Trans. on Microwave Theory and Tech., **MTT-50**, 910-928, (2002)

[2] J. Kawamura, J. Chen, D. Miller, et al., "Low-noise submillimeter-wave NbTiN superconducting tunnel junction mixers", Appl. Phys. Lett., **75** (25), 4013-4015, (1999).

[3] A. Karpov, D. Miller, F. Rice, J. A. Stern, B. Bumble, H. G. LeDuc, and J. Zmuidzinas, "Low-noise 1THz -1.4 THz mixers using Nb/Al-AlN/NbTiN SIS junctions", IEEE Trans. on Appl. Supercond., **17**(2), 343-346, (2007).

[4] A. D. Semenov, G. N. Gol'tsman, and R. Sobolewski, "Hot-electron effect in superconductors and its applications for radiation sensors", Supercond. Sci. Technol., **15**, R1-R16, (2002).

[5] A. D. Semenov, H. Richter, H. W. Hübers, et al., "Terahertz performance of integrated lens antennas with a hot-electron bolometer", IEEE Trans. on Microwave Theory and Tech., **55**, 239-247, (2007).

[6] H. Richter, A. D. Semenov, S. G. Pavlov, et al., "Terahertz heterodyne receiver with quantum cascade laser and hot electron bolometer mixer in a pulse tube cooler", Appl. Phys. Lett., **93**, 141108, (2008).

[7] S. Cherednichenko, V. Drakinskiy, T. Berg, P. Khosropanah and E. Kollberg, "Hot-electron bolometer terahertz mixers for the Herschel Space Observatory", Rev. Sci. Instruments, **79**, 034501, (2008).

[8] J. J. A. Baselmans, M. Hajenius, J. R. Gao, et al., "Double of sensitivity and bandwidth in phonon cooled hot electron bolometer mixers", Appl. Phys. Lett., **84** (11), 1958-1960, (2004).

[9] J. J. A. Baselmans, A. Baryshev, S. F. Reker, et al., "Direct detection effect in small volume hot electron bolometer mixers", Appl. Phys. Lett., **86**, 163503, (2005).

[10] P. H. Wu, L. Kang, Y. Chen, et al., "Fabrication and characterization of NbN/AlN/NbN junction on MgO(001) and AlN/NbN bilayer on MgO(111) substrates", IEEE Trans. on Appl. Supercond., **15** (2), 209-211, (2005)

[11] J. D. Dyson, "The equiangular spiral antenna", IRE Trans. Antennas Propag., **AP-7**, 181-187, (1959).

[12] A. R. Kerr, "Suggestions for Revised Definitions of Noise Quantities, Including Quantum Effects", IEEE Trans. on Microwave Theory and Tech., **47**, 325-329, (1999).

[13] S. A. Ryabchun, I. V. Tretyakov, M. I. Finkel, et al., "Fabrication and charaterisation of NbN HEB mixers with in situ gold contacts", Proc. of 19th International Symposium on Space Terahertz Technology, 62-67, (2008).

[14] H. Ekstrom, B. S. Karasik, E. L. Kollberg, and K. S. Yngvesson, " Coversion gain and noise of niobium superconducting hot-electron-mixers", IEEE Trans. on Microwave Theory and Tech., **43**, 938-947, (1995).

[15] S. Cherednichenko, M. Kroug, H. Merkel, et al., "1.6 THz heterodyne receiver for the far infrared space telescope", Physica C, **372-376**, 427-431, (2002).

[16] A. J. Gatesman, J. Waldman, M. Ji, C. Musante, and S. Yngvesson, "An anti-reflection coating for silicon optics at terahertz frequencies", IEEE Microwave and Guided Wave Lett., **10** (7), 264-266, (2000).

[17] H. W. Hubers, J. Schubert, A. Krabbe, et al., "Parylene anti-reflection coating of a quasi-optical hot-electron-bolometric mixer at terahertz frequencies", Infrared Phys. & Tech., **42**, 41-47, (2001).

[18] T. D. Dorney, R. G. Baraniuk and D. M. Mittleman, "Material parameter estimation with terahertz time-domain spectroscopy", J. Opt. Soc. Am. A, **18**, 1562-1570, (2001).

[19] E. L Kollberg and K. S. Yngvesson, "Quantum-noise theory for terahertz hot electron bolometer mixers", IEEE Trans. Microwave Theory & Tech., 54, 2077-2089, (2006).

P7E

A room temperature Nb_5N_6 microbolometer for detecting 100 GHz radiation

L.Kang[1*] , P.H.Wu[1], X.H.Lu[1], J.Chen[1], Q.J.Yao[2], and S.C.Shi[2]

1 Research Institute of Superconductor Electronics (RISE), Department of Electronic Science and Engineering, Nanjing University, Nanjing 210093 ,China.

2 Purple Mountain Observatory, NAOC, CAS, Nanjing, China

* Contact: kanglin@nju.edu.cn, phone +86-25-8359 2933

The work was Supported in part by the National Basic Research Programme of China under Grant No 2006CB601006 and 2007CB310404, National High-tech R&D Programme of China under Grant No 2006AA12Z120.

***Abstract*—Based on Nb_5N_6 thin film microbolometers, detectors have been designed, fabricated and characterized for detecting 100 GHz signals at room temperature. Such a detector typically consists of two parts, a Nb_5N_6 thin film microbolometer for detecting the radiation and an Al planar bow-tie antenna with a center frequency of 100 GHz for coupling the radiation from free space to the microbolometer.**

Using radio frequency (RF) magnetron sputtering, at a high pressure of gas mixture of 2Pa (N_2:Ar, 4:1), 100 nm thick Nb_5N_6 film is grown on a high resistance Si (100) substrate with a SiO_2 layer 100nm thick. The resistance vs temperature relationship of the Nb_5N_6 thin film is of semiconductor type with a negative temperature coefficient of resistance of about 0.6 – 0.7 % and a sheet resistance $R_\square$ of about 500 Ω at room temperature. The root mean square (rms) surface roughness of Nb5N6 thin film with a thickness of 100 nm is 0.45 nm over an area of 2μm×2μm.

Bearing in mind that the sheet resistance $R_\square$ of Nb_5N_6 thin film is about 500 Ω and considering that the impedance of the planar metallic antenna should be matched to that of the Nb_5N_6 microbolometer, the impedance of the bow-tie antenna is designed by Ansoft HFSS to be 800 Ω, corresponding to the microbolometer sizes of 3μm ×1.5μm. The detector based on Nb_5N_6 microbolometer is fabricated using lithography and reaction ion etching.

The high frequency response of the detector is characterized by a quasi-optical system. The electrical responsivity S_E of the detector can be evaluated from the I – V curve using Jones' expression

$$S_e = (Z - R)/2IR \qquad (V/W)$$

where Z = dV/dI and R are the resistances of the bolometer with and without 100 GHz irradiation respectively. At room temperature, the electrical responsivity of the detector is about 400 volts per watt at a bias of 0.4 mA and a modulation frequency of 200 Hz.

To evaluate the electrical noise equivalent power (NEP) we first measure the noise voltage spectrum of the detector and then divide it by the responsivity. Using a low noise preamplifier, the noise voltage is measured to be about 7 nV/ $Hz^{1/2}$ at a frequency of 1 KHz. Thus the NEP is as low as 2×10^{-11} W/$Hz^{1/2}$. If we correct the result by taking into account the contribution of the noise of the preamplifier, which is 4 nV/ $Hz^{1/2}$, even lower NEP can be obtained. The response time of the detector is less than 50 μs. It is good enough for many practical applications.

Such detectors based on Nb_5N_6 microbolometers and fabricated on Si substrates offer tremendous opportunities in making Si-based hybrid integration circuits, which can be used in detecting and imaging arrays at terahertz frequencies.

P7F

A Dual-Polarization TES Bolometer Detector for CMB B-pol Measurements

V. Yefremenko[1], G. Wang[1], A. Datesman[1], L. Bleem[2,3], J. McMahon[2,4], C. Chang[2,4], J. Pearson[1], G. Shustakova[1,5], A. Crites[2,6], T. Downes[2,3], J. Mehl[2], S. Meyer[2,3,4,6], J. Carlstrom[2,3,4,6], and V. Novosad[1*]

1 Materials Science Division, Argonne National Laboratory, Argonne, IL 60439

2 Kavli Institute for Cosmological Physics, University of Chicago, Chicago, IL 60637

3 Department of Physics, University of Chicago, Chicago, IL 60637

4 Enrico Fermi Institute, University of Chicago, Chicago, IL 60637

5 B. Verkin Institute for Low Temperature Physics & Engineering, Kharkov, Ukraine

6 Department of Astronomy and Astrophysics, University of Chicago, Chicago, IL 60637

* Contact: novosad@anl.gov, phone/fax +1-630-252-5507/7777

The submitted work has been created by UChicago Argonne, LLC, Operator of Argonne National Laboratory ("Argonne"). Argonne, a U.S. Department of Energy Office of Science laboratory, is operated under Contract No. DE-AC02-06CH11357.

***Abstract*— Investigation of the Cosmic Microwave Background (CMB) has provided strong constraints on the composition, geometry, and history of the universe. The CMB polarization signal represents the next frontier of cosmological discovery. The existence of B-modes in the CMB polarization signal, expected at the level of 10–100 nK, will indicate the presence of gravitational waves in the primordial universe and reveal the energy scale of inflation. Superconducting Transition Edge Sensor (TES) bolometer detectors operating in the millimeter-wavelength range offer the sensitivity required to investigate the CMB B-mode signal.**

We have developed a polarization sensitive TES bolometer detector for deployment in a kilo-pixel array for observations of CMB polarization. Each pixel is assembled from two dies. Each die consists of a proximity-effect Mo/Au bilayer TES and a single dipole absorber, suspended on a thin strip of silicon nitride. Two dies offset by 90 degrees and mounted face to face with a spacing of ~10 μm create a dual-polarization assembly. The assemblies are mounted in single-mode round waveguide with a quarter-wave backshort, which permits the radiation pattern to be defined by a corrugated feedhorn.

This report reviews our design, the status of this technology, and our development effort. A variety of approaches to achieve the required low values of the thermal conductance to bath, G, were examined. Both diffusive and radiative or ballistic heat transport were observed in silicon nitride membranes at temperatures ~500 mK. The target G of 200 pW/K was achieved using physically viable strip configurations only tens of microns wide by millimeters in length. Characterization of prototypes, including measurements of the detection bandwidth, RF bandwidth cross-polarization, noise, and detector stability is discussed. Initial results indicate an optical bandwidth exceeding 200 Hz and cross-polarization at the level of 2%, with background-limited noise suitable for ground-based observations.

P7G

Highly sensitive NbN hot electron bolometer mixer at 5.25 THz

W. Zhang[1,3], P. Khosropanah[1], T. Aggarwal[1,2], J.R. Gao[1,2*], T.M. Klapwijk[2], W. Miao[3], and S.C. Shi[3],

[1]*SRON Netherlands Institute for Space Research, Utrecht/Groningen, The Netherlands*
[2]*Kavli Institute of Nanoscience, Delft University of Technology, Delft, The Netherlands*
[3]*Purple Mountain Observatory, National Astronomical Observatories of China, Chinese Academy of Sciences, China*
*Contact: J.R.Gao@tudelft.nl, Phone: +31-15-278 1370

***Abstract*—We report noise measurements of a NbN hot electron bolometer (HEB) heterodyne receiver at super-THz frequencies and demonstrate a DSB receiver noise temperature (T_{rec}) of 1140 K at 5.25 THz, which is directly measured (no any corrections) and is 4.5×hν/k. The measured T_{rec} versus current for the optimal voltage is given in figure 1 and a 2D receiver noise temperature plot in figure 2.**

Our experiment is motivated by: a) demonstration of a sensitive HEB mixer for the observation of the fine-structure line of neutral atomic oxygen (OI) at 4.7 THz; b) establishing experimentally the ultimate sensitivity of an NbN HEB mixer at the high-end of THz frequency range.

The HEB mixer used consists of a 0.2 □m-long and 2 □m-wide NbN bolometer [1] and a tight winding spiral antenna with an inner diameter of 6.6 □m. Based on the HFSS simulation for the antenna, a high radiation power coupling efficiency between antenna and HEB up to 6 THz is expected.

The measurement setup is similar to the one in ref. [2] (all built in vacuum). In details, the optics between hot/cold load and the HEB consists of a Si lens coated with Parylene C designed for 4.25 THz, a QMC metal-mesh low-pass filter, and 3 μm thick beam splitter. As local oscillator, we use an optically pumped FIR ring gas laser.

[1] The NbN film on Si is standard, produced at Moscow State Pedagogical University, Moscow, Russia.
[2] P. Khosropanah, J.R. Gao, W.M. Laauwen, M. Hajenius and T.M. Klapwijk, "Low noise NbN hot-electron bolometer mixer at 4.3 THz," *Appl. Phys. Lett.*, **91**, 221111 (2007).

Improved Multi-octave 3 dB IF Hybrid for Radio Astronomy Cryogenic Receivers

Inmaculada Malo, Juan Daniel Gallego, *Member, IEEE*, Carmen Diez, Isaac López-Fernández and Cesar Briso

***Abstract*—Modern mm and sub-mm ultra low noise receivers used for Radio Astronomy have evolved to provide very wide instantaneous bandwidth. Some of the configurations used in present cryogenic front-ends, like sideband separating mixers and balanced amplifiers, need 90º 3 dB hybrids at the IF, typically in the 4-12 GHz band. There are commercially available devices covering this band with good ambient temperature characteristics, but poor cryogenic performance. We describe the design, construction and measurement of a multioctave stripline hybrid for the 4-12 GHz band specially conceived to perform reliably when cooled to 15 K. The coupling and reflection show very little temperature dependence.**

A balanced cryogenic amplifier was assembled with two 3 dB hybrid units and available amplifiers (~4.5 K noise temperature) designed and built in-house for ALMA. This device is critically compared with a single ended amplifier and with an amplifier with an input isolator. The latter is the typical arrangement of the IF of radio astronomy receivers. The balanced option shows an advantage of 2.8 K in noise with less sensitivity to input mismatches.

***Index Terms*—Balanced amplifier, cryogenic receivers, hybrid coupler, low noise.**

I. Introduction

A classical problem of millimeter and submillimeter radio astronomy receivers is how to match the mixer to the IF amplifier. The trend on the past decade has been to increase the instantaneous IF bandwidth as required for the achievement of new and more ambitious scientific goals, taking advantage of the continuous evolution of the analog and digital backends. For the HERSCHEL ESA mission, which will be launched this year, it was decided to set the value of the instantaneous IF bandwidth at 4 GHz. Later, for the development of ALMA[1], now in construction, it was decided to use even a wider 8 GHz instantaneous IF in the 4-12 GHz band. The wide fractional bandwidths involved imposed an important challenge in both sides, mixers and IF amplifiers. For the low noise amplifier (LNA) side, it soon became clear that obtaining simultaneously low reflection and noise in very wide bands was not an easy task. In the case of a traditional receiver, the mixer and the IF amplifier are different modules, sometimes cooled at different physical temperatures and connected by coaxial cables. If no action is taken, the ripple in noise and gain caused by the reflections at both sides of an electrically long cable is an important issue which may deteriorate the overall sensitivity. One approach, followed by some groups [1], [2] has been to eliminate the connecting cable by integrating the amplifier and the mixer. This solution, although very successful in some cases, has some practical difficulties, and has not been universally adopted. The other common approach has been to use wideband cryogenic ferrite isolators between the mixer and the LNA. There are now commercial cryogenic isolators available for the 4-8 GHz and 4-12 GHz bands, developed by the needs of HERSCHEL and ALMA projects, which have become a common building block in modern receivers. The performance obtained with the isolators is quite good in terms of reflection and isolation, but not as good in terms of insertion loss, particularly in the case of the 4-12 GHz band. The effect of the loss is especially painful, since part of the effort employed in obtaining very low noise state of the art devices is lost in the passive component. The motivation of the present work was to explore the possibilities of a balanced amplifier as an alternative to the isolator, with the idea of reducing the noise while keeping a good input reflection. Balanced amplifiers have been used for many applications since their introduction more than forty years ago, but not many have been reported for practical cryogenic applications [3].

The first thing needed for demonstrating the balanced amplifier is a suitable wideband cryogenic 90º 3 dB hybrid. Such a device may have other applications in radio astronomy receivers, like for example for the IF port in a 2SB image rejection receiver. There are some commercial devices available for the 4-12 GHz band which can be cooled, but the results obtained in our experiments showed degradation of their cryogenic performance. Furthermore, commercial units are not conceived to survive the aggressive thermal cycles from ambient to cryogenic temperature. Due to these limitations, it was decided to develop and build hybrids specially suited for cryogenic operation, improving the performance and reliability. The prototypes developed were used for the demonstration of a balanced amplifier and for the

Manuscript received 19 April 2009. This work was supported in part by the European Community Framework Programme 7, Advanced Radio Astronomy in Europe, grant agreement no.: 227290

I. Malo, J. D. Gallego, C. Diez and I. López-Fernández are with the Centro Astronómico de Yebes, Observatorio Astronómico Nacional, Guadalajara, Spain (phone: +34 949290311; fax: +34 949 200063; e-mail: i.malo@oan.es).

C. Briso is with the Universidad Politécnica de Madrid, Escuela de Telecomunicación, Madrid, Spain.

[1] Atacama Large Millimetre Array, a future radio astronomical interferometer now in construction in Chile.

comparison of the performance obtained with the classical amplifier isolator combination.

II. Hybrid Coupler Design and Fabrication

The simplest way to build a directional coupler of strong coupling is to use coupled transmission lines manufactured in stripline technology. The proposed 4-12 GHz hybrid design is focused in an offset broadside coupled stripline structure, using Mylar as a dielectric separation layer (see Fig. 1). To get the required bandwidth it is necessary to use three sections of λ/4 coupled lines [4], so the coupling has a contained ripple across the band.

The design has been done using the 2.5D EM tool Momentum (from HP EESOF ADS). The dielectric constant of the substrates is ε_r=2.94, with a thickness of 508 µm (20 mils), while the separation film is 23 µm thick, with ε_r=3. The critical dimensions of the hybrid are located in the central λ/4 section (see Fig. 1). This section has the narrowest line widths (w_2=159 µm) and an offset between the coupled lines (in the initial design) of wo_2=50 µm. This offset is essential for tuning the coupling factor.

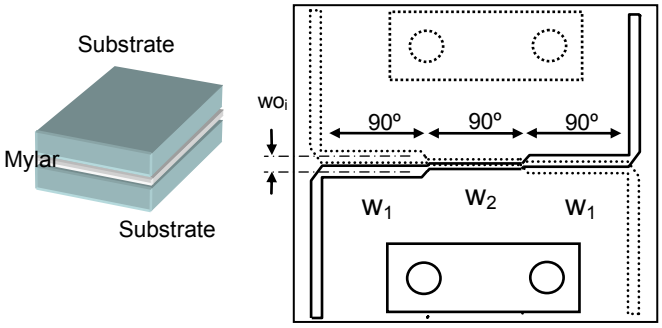

Fig. 1. Schematic of the three λ/4 sections hybrid coupler. The structure (substrates plus Mylar separator) is 21.4 × 16 × 1.073 mm. Mylar film is 23 µm thick.

The hybrid must operate at 15 K without degradation; therefore all the materials used in the fabrication process must have high thermal stability. The substrate selected is RT/Duroid[2] ® 6002, which has been previously used in other cryogenic designs, even for space applications, and whose performance and stability are well demonstrated. The thermal coefficient of the dielectric, as given by the manufacturer, is +12 ppm/ºC and the thermal expansion coefficient is 16 ppm/ºC (x,y axis) and 24 ppm/ºC (z axis). The cupper metallization covers one side only and is 0.5 oz/ft^2 thick.

The coupling factor is strongly affected by the distance between substrates. To keep this separation stable when cooling the structure, the chassis of the coupler has been built in aluminum alloy, whose thermal expansion coefficient (23 ppm/ºC at 25ºC) almost perfectly matches the z axis coefficient of the substrate. Mylar is chosen as separation layer because its dielectric constant is very similar to that of the Duroid, and it has higher rigidity and superior thermal stability (0.17 ppm/ºC) than other similar polymers [5].

The whole circuit has been manufactured using a laser milling machine (LPKF[3] ProtoLaser 200). Its resolution is better than needed and it allows etching and cutting the substrate in the same operation making the alignment of the coupled lines very accurate. Fig. 2 shows one half of the built coupler with the aluminum chassis and connectors.

An important practical problem is the reliability of the contact between the substrates and the input/output connectors. Commercial hybrids use standard SMA connectors directly soldered to the substrates. The mechanical stress produced by the variation of temperature from 300 K to 15 K can easily lead to failures in the solder joints after repeated cycles. To minimize this risk we have used connectors with sliding central pin (R.125.410.000 made by RADIALL[4]) which let slight shifts of the central pin alleviating the mechanical stress.

Another problem found was the electrical discontinuity between the coaxial connector and the stripline. The discontinuity was tuned out to obtain a -22 dB of return loss by means of an inductive gap between the flange and the substrate.

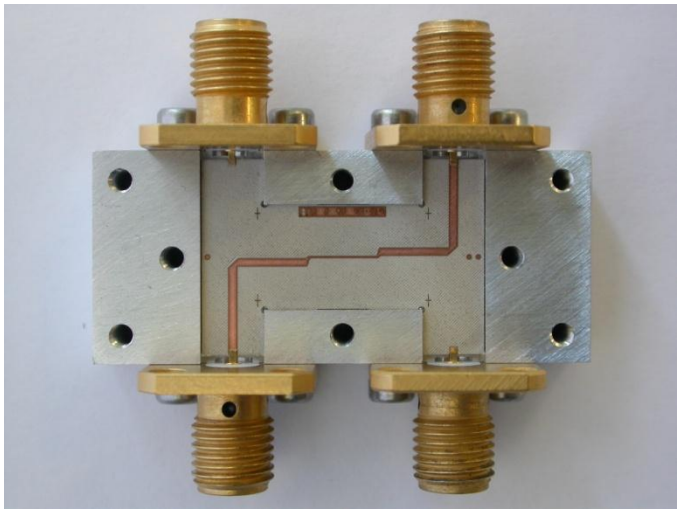

Fig. 2. Assembled coupler (one half shown). Mylar sheet and upper half of the stripline substrates are removed.

III. Hybrid Coupler Measurements and Results

Measurements at 300 K agree with Momentum simulations: return loss was better than -22 dB and the directivity was higher than 20 dB. Only the coupling factor was 0.15 dB lower than expected probably due to manufacturing tolerances of the Mylar sheet thickness (which is 20% as specified by the supplier). To compensate the reduction of the coupling factor, the offset of the central lines, wo_2, was reduced from 50 µm to 0 µm. With this modification the desired coupling factor was achieved.

The measurements were made using a cryostat calibrated at 300 K and at 15 K with SOLT standards, and the results are compared in Fig. 3. Almost no degradation in performance is observed when cooled. At 15 K the measured worst case

[2] Rogers Corporation Advanced Circuit Materials Division, Chandler, AZ 85226, USA.

[3] LPKF Laser & Electronics AG, Garbsen 30827, Germany.

[4] RADIALL SA, 93116 Rosny Sous Bois, France.

amplitude unbalance is ±0.3 dB and phase unbalance is ±2º, in the 4-12 GHz band. Table I compares this results with the best commercial hybrid available, tested in the same setup.

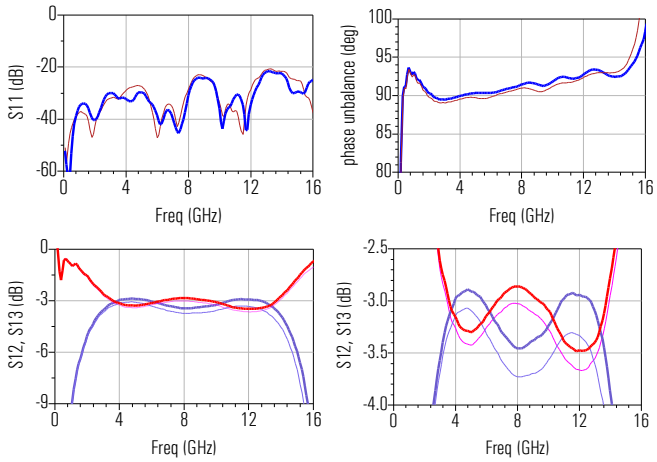

Fig. 3. Measurements of the hybrid at 15 K (thick lines) and 300 K (thin lines). Note the almost invariable behavior with temperature due to the careful selection of components and technologies.

TABLE I COMPARISON WITH COMMERCIAL UNITS

Measurement @ 15 K, 4-12 GHz	CAY design (average of 3 hybrids)	Best commercial unit
Return loss	<-22 dB	<-19 dB
Amplitude unbalance	±0.3 dB	±0.9 dB
Phase unbalance	±2º	±3º

The key of the high thermal stability of the hybrid is the careful selection of materials, as stated in section II. The aluminum chassis and substrate material have matched thermal expansion coefficient in the z axis, therefore they shrink approximately by the same amount when cooled and hence the distance between coupled lines remains almost constant with temperature.

The overall dissipative loss introduced by the hybrid has been estimated by calculating the equivalent insertion loss, L_{eq}, defined by:

$$L_{eq} = 10 \cdot \log_{10} \left(|s_{11}|^2 + |s_{12}|^2 + |s_{13}|^2 + |s_{14}|^2 \right) \quad (1)$$

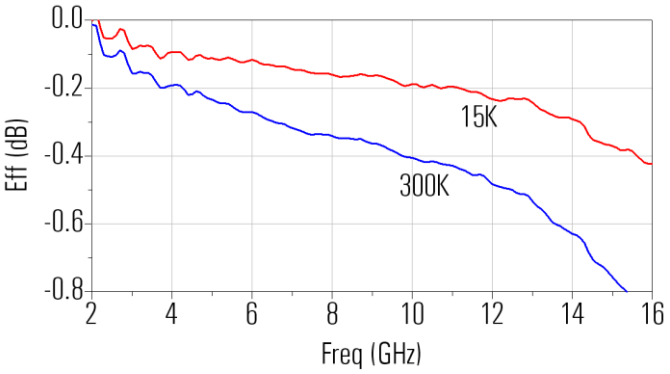

Fig. 4. Equivalent insertion loss obtained with (1) from measurements of the S parameters of the hybrid coupler.

The dissipative loss at 15K, shown in Fig. 4, is better than 0.2 dB in the 4-12 GHz band. This value is much lower than the typical insertion loss of a cryogenic isolator in the same band.

IV. REALIZATION AND MEASUREMENT OF A 4-12 GHZ BALANCED AMPLIFIER

State-of-the-art cryogenic low noise amplifiers in the 4-12 GHz band have been designed and built in our labs for the IF of band 9 of ALMA front-ends [6]. Some pre-production units are available at our premises and two of them, randomly chosen, were used together with two 90º hybrid coupler prototypes of the type described here, to assemble a balanced amplifier. A picture of one of the ALMA amplifiers is shown in Fig. 5. The balanced amplifier can be seen in Fig. 6, and a schematic is depicted in Fig. 7.

The amplifiers used incorporate InP NGST [7] devices and have an average noise temperature around 4.5 K with 34 dB of gain and -4 dB and -15 dB of input and output return loss (worst case) respectively. Note that the poor input reflection is due to the compromise made in optimizing the performance, with emphasis in the noise, for a very wide band. To avoid the mismatch between the SIS mixers and the IF amplifiers in ALMA receivers, it was decided to use them in combination with PAMTECH[5] cryogenic isolators.

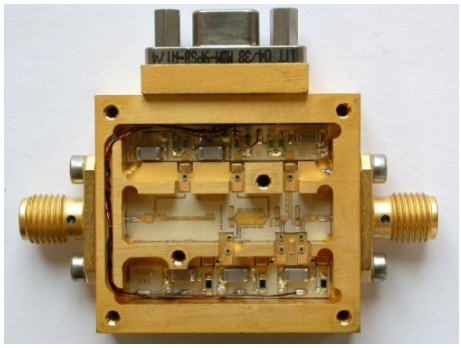

Fig. 5. ALMA band 9 4-12 GHz production cryogenic amplifier.

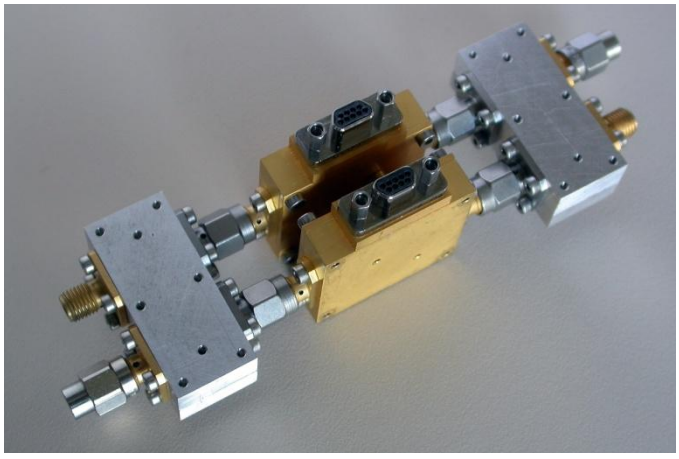

Fig. 6. Prototype 4-12 GHz cryogenic balanced amplifier made up of two 3 dB hybrids as described here and two ALMA-type amplifiers.

[5] Cryogenic isolator of the type currently used in ALMA receivers made by PAMTECH (Passive Microwave Technology, Camarillo CA 93012 USA).

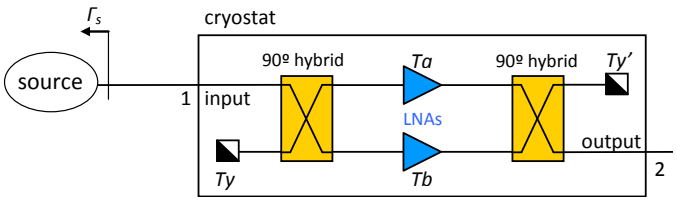

Fig. 7. Schematic of a balanced amplifier.

Fig. 8 presents the experimental setup inside the cryostat. Noise and gain were measured using he cold attenuator method, with an estimated absolute accuracy of ±1.4 K (3σ), and repeatability one order of magnitude better [8]. This method allows good accuracy even for amplifiers with high input reflection, and can be implemented with commercially available equipment (Agilent N8975A).

Fig. 9 shows the results of the three configurations. The first stage bias was optimized for low noise in all cases, while the bias of the second and third stages of both amplifiers in the balanced configuration was chosen to minimize the unbalance and thus optimize the overall noise as stated in section VI. B. Note the clear advantage in noise temperature (2.8 K in average) of the balanced amplifier over the cryogenic isolator due to the lower loss of the hybrid. The input return loss (worst case in the band) for both configurations is better than -15 dB whereas for the amplifiers is only about -4 dB.

V. Noise Performance for a Mismatched Input Termination

The practical advantage of the balanced amplifier over an amplifier with the best commercial available cryogenic input isolator has been demonstrated by measurements with a matched input termination, in the previous section. However, in a real receiver, the input impedance seen by the amplifier may be quite far from the matched condition. In the case of an SIS mixer, for example, the impedance presented at the IF output port depends on many factors, including the LO frequency, and typically sweeps a wide range of complex values across de IF band. The theoretical calculation of the noise parameters of an amplifier with an isolator at the input is possible without knowing the detailed noise parameters of the amplifier [9]. However, for the balanced amplifier, the complete information of noise parameters of the amplifier and its input reflection coefficient is needed in order to estimate the noise parameters of the combination [10]. As accurate measurements of noise with mismatched input terminations were not possible in our cryogenic measurement system, a model was used to predict the behavior under different circumstances. The three configurations (stand-alone, input isolator and balanced amplifier) were simulated at 15 K for a range of input impedances.

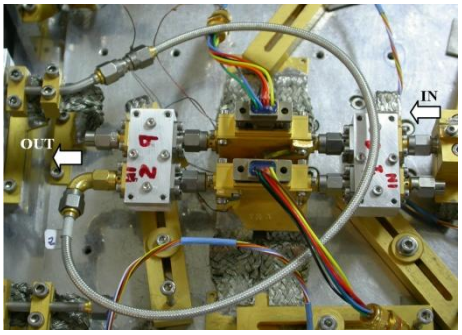

Fig. 8. Balanced amplifier inside the measurement cryostat.

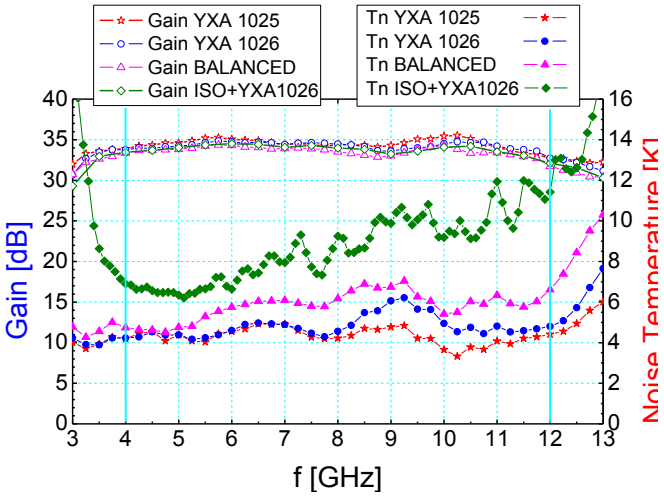

Fig. 9. Comparison of the noise temperature and gain for a balanced amplifier, amplifier with an input isolator and the individual amplifiers. Measurements were taken at 15 K.

Fig. 10 shows the results obtained for three different values of a pure real input termination connected by a length (10 cm) of 50 Ohm ideal line to the input of each configuration. To avoid confusion with other effects, the simulation was performed with a realistic model of the amplifier [6] but with ideal isolator and 3 dB hybrids (without loss). The length of 50 Ohm line was included to easily visualize the ripple pattern appearing in the case of the single ended amplifier caused by multiple reflections. Note that this ripple is totally eliminated, as expected, by the other configurations. The most interesting feature visible in Fig. 10 is that the balanced amplifier and the input isolator configurations are not totally equivalent; being the balanced the one showing lower noise under mismatched conditions. This is due to the lower value of the noise parameter R_n for the balanced amplifier at 15 K. Note that the prediction of this model assumes all the components cooled to the same physical temperature of 15 K. The situation may be the opposite, for example, if the termination of the isolator is cooled to a physical temperature below approximately 7 K.

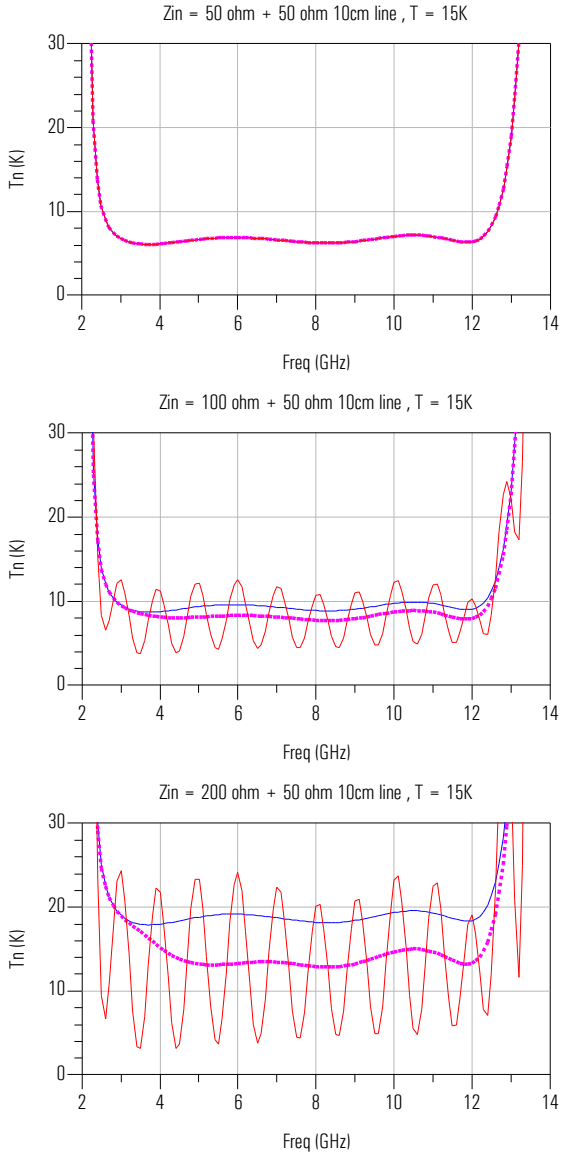

Fig. 10. Simulations at 15 K of the impact in noise temperature of the variation of the input load (50-200 ohm) placed after an ideal 10 cm line. Single-ended amplifier is in red, balanced amplifier is in magenta, amplifier with input isolator is in blue. The hybrid and isolator are assumed ideal.

VI. Disadvantages of a Balanced Configuration

A balanced configuration has an obvious drawback: its inherent complexity, needing two couplers and two amplifiers. This usually reflects also in an increased cost. Another consequence which may be significant for some applications is the higher power dissipation. There are other potential weaknesses which will be analyzed below, like the sensitivity of noise to amplifier gain and/or phase unbalance, or the variation of the output reflection with the input load.

A. Effects of amplifier gain and phase unbalance

In an ideal balanced amplifier the two branches are identical. In practice, however, some phase and gain unbalance is always present with the consequence of degradation of the performance.

In terms of noise temperature, the main effect is that the thermal noise from the termination of the input hybrid does not null at the output, causing an increment in the noise of the system. It can be shown that, for an ideal but not perfectly balanced amplifier, the noise temperature can be expressed as:

$$T_n(\Delta g, \Delta p_g) = \frac{T_y \cdot (1+\Delta g^2 - 2\Delta g \cdot \cos\Delta p_g) + 2T_a + 2T_b \cdot \Delta g^2}{1+\Delta g^2 + 2\Delta g \cdot \cos\Delta p_g} \quad (2)$$

where Δg is the module gain unbalance (g_a / g_b), Δp_g is the phase gain unbalance ($p_{gb} - p_{ga}$ in radians), T_a and T_b are the noise temperatures of the individual amplifiers and T_y is the physical temperature of the termination of the input hybrid.

Fig. 11 shows plots of the noise temperature as a function of the gain and phase unbalance. In case of equal phase, the noise temperature increases relatively fast as we depart from the balanced situation, but it is bounded: for a perfect balance, T_n is the average noise temperature of the component amplifiers, and at worst, it is always lower than the sum of the noise temperatures of both amplifiers plus the physical temperature of the hybrid. The sensitivity of the noise temperature to a small phase unbalance is lower than in the case of a gain unbalance, but it is not bounded.

In our case, the prototype hybrids, as explained in section III, exhibit a very good repetitivity, with ±0.3 dB amplitude unbalance and ±2º phase unbalance, so the impact in noise in the balanced structure can be neglected. In practice lots of amplifiers with the same type of devices and following the same design and manufacturing procedures use to have a relatively small dispersion in phase and gain. For example, the mass production units of band 9 ALMA IF preamplifiers, despite the intensive tuning needed in some cases, show a maximum gain and phase excursion of 3 dB and 22º respectively (for a total of 50 samples). This translates for a worst case combination in an increment of ~1.9 K in noise at the most unfavorable frequency point according to (2). However, in some cases it may be advisable to improve the balance of the amplifier.

A simple and effective way of doing it is to adjust the bias of the last stages of the amplifiers (keeping fits stage bias values compliant with the low noise specifications). This method is illustrated in Fig. 12, which shows the variation of the noise temperature of the balanced structure with the bias settings of stages 2 and 3 of one of the amplifiers. For the particular case of the amplifiers randomly chosen for our balanced structure, the unbalance was negligible, so only 0.2 K of improvement (over a T_n of 6 K) was achieved experimentally by tuning the bias.

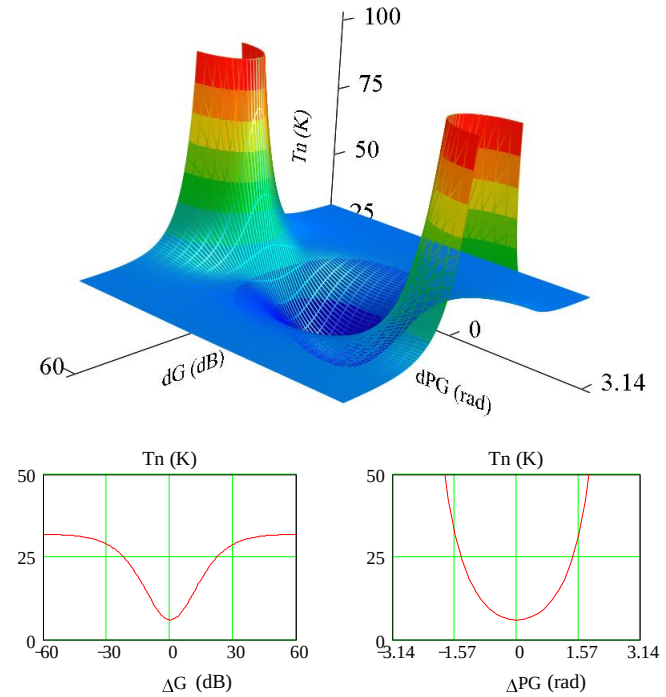

Fig. 11. Noise temperature for a balanced amplifier with amplifier temperatures $T_a=T_b=6$ *K* and physical temperature T_y *=15 K* according to (2). On the top, T_n vs Δg (in dB) and Δp_g. On the bottom, two sections of the 3D figure, T_n vs. Δg when Δp_g *=0* (on the left) and T_n vs. Δp_g when Δg =0 (on the right). The sensitivity to small changes is higher for the gain unbalance.

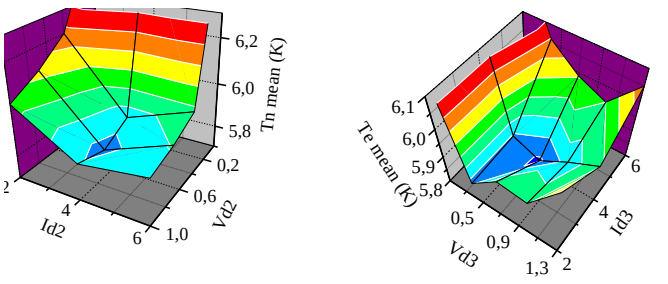

Fig. 12. Measurements of noise temperature of the balanced amplifier for different bias settings in stages 2 and 3. It is possible to improve the balance of the structure by changing slightly the gain of the individual amplifier and thus, optimize the noise temperature.

B. Effects of input load on output return loss

Another difference between balanced amplifiers and amplifiers with input isolator is that the output return loss of the input isolator is insensitive to changes in the input load. This was experimentally tested at room temperature by placing a sliding short at the input of the different configurations. The results varying the length of the short are shown in Fig. 13. Stand-alone and balanced structures display a similar dispersion of the S_{22} plots, whereas the isolated amplifier exhibits an almost invariable behavior. Still the results of the balanced amplifier are better in all cases due to the superior output reflection of the hybrids respect to the stand-alone amplifier.

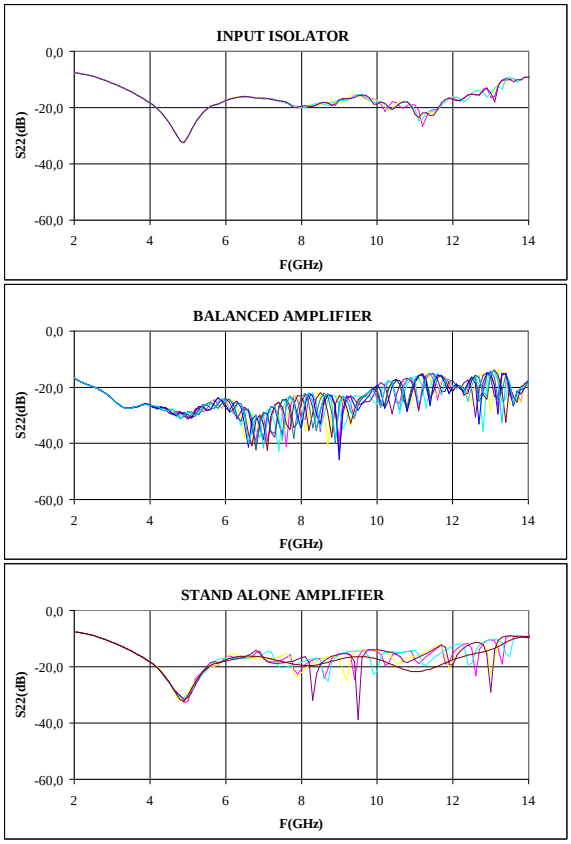

Fig. 13. Measurements of output reflection for different lengths of a sliding short-circuit at the input in the three amplifier structures. Note that the balanced amplifier is not immune to this change in input loading, but nevertheless its return losses are still always better than the stand-alone amplifier.

VII. Conclusion

A cryogenic 3 dB 90º hybrid optimized for cryogenic applications has been designed built and characterized. The result is a reliable unit, ease to assemble, repeatable and with very stable performance from ambient temperature to 15 K. The goal of obtaining lower insertion loss than in a commercial cryogenic isolator from the same band has been achieved. A cryogenic balanced amplifier using two randomly chosen standard ALMA production amplifiers has been assembled and tested to verify its advantage, obtaining an improvement of 33% in noise temperature respect to the input isolator configuration. Furthermore, the noise temperature of a balanced amplifier measured at 15 K is less sensitive to input mismatches. In addition, the effect of the gain unbalance between the component amplifiers, and its effect in increasing the noise of the balanced configuration has been estimated. Despite the fact of the additional complexity and power dissipation, the demonstration balanced amplifier shows a clear advantage in performance respect to the traditional isolator and amplifier configuration.

Acknowledgment

The authors wish to thank R. García-Nogal for his help in manufacturing the prototypes used in this work.

REFERENCES

[1] S. Padin, D. P. Woody, J. A. Stern, H. G. LeDuc, R. Blundell, C.-E. E. Tong and M. Pospieszalski, "An Integrated SIS Mixer and HEMT IF Amplifier," *IEEE Trans, Microwave Theory Tech.*, vol. 44, pp. 987-990, June 1996.

[2] E. F. Lauria, A. R. Kerr, M. W. Pospieszalski, S.-K. Pan, J. E. Effland and A. W. Lichtenberger, "A 200-300 GHz SIS Mixer-Preamplifier with 8 GHz IF Bandwidth," *MTT-S Int. Microwave Symp. Dig.*, pp. 1645-1648, June 2001.

[3] S. Padin, G. Ortiz, "A cooled 1-2 GHz balanced HEMT Amplifier," *IEEE Trans. Microwave Theory Tech.*, vol. 39, pp. 1239-1243, July 1991.

[4] J. K. Shimizu, E. M. T. Jones, "Coupled-Transmission-Line Directional Couplers", *IRE Trans. Microwave Theory Tech.*, vol. 6, pp. 403-410, October 1958.

[5] N. Honingh, M.Justen, Private Communications of AMSTAR project, KOSMA, 2007.

[6] I. López-Fernández, J. D. Gallego, C. Diez, A. Barcia, "Development of Cryogenic IF Low Noise 4-12 GHz Amplifiers for ALMA Radio Astronomy Receivers," *2006 IEEE MTT-S Int. Microwave Symp. Dig*, pp. 1907-1910, 2006.

[7] R. Lai et al, "0.1 µm InGaAs/InAlAs/InP HEMT Production Process for High Performance and High Volume MMW Applications." *1999 GaAs MANTECH.*

[8] J. D. Gallego, I. López-Fernández, "Definition of measurements of performance of X band cryogenic amplifiers," *Technical Note ESA/CAY-01 TN01*, July 2000.

[9] M. W. Pospieszalski, "On the noise parameters of isolator and receiver with isolator at the input," *IEEE Trans. Microwave Theory Tech.*, vol. 34, pp. 451-453, April 1986.

[10] A. R. Kerr, "On the noise properties of balanced amplifiers," *IEEE Microwave Guided Wave Lett.*, vol. 8, pp. 390-392, November 1998.

Analysis, Simulation and Design of Cryogenic Systems for ALMA Band 5 Prototype Cartridge

M. Strandberg, I. Lapkin, V. Belitsky, A. Pavolotsky, and S.-E. Ferm

***Abstract*—The ALMA frontend is designed for ten separate receivers channels covering 30-960 GHz range; the receiver accommodates these receiver channels as pluggable, fully electrically autonomous cartridges. These cartridges share the same cryogenic cooler. ALMA Band 5 cartridge is a dual-polarization heterodyne receiver employing 2SB SIS mixers with IF band 4-8 GHz and covers the frequency 163-211 GHz. The prototype for the ALMA Band 5 cartridge development is carried out by Group for Advanced Receiver Development (GARD) in Gothenburg, Sweden with the aim to provide six Band 5 cartridges for ALMA Project. The first prototype cartridge is currently being assembled. ALMA Band 5 cartridge is the lowest frequency channel in the ALMA receiver that employs all cold optics and thus has the biggest rim of the mirrors amongst other ALMA bands placed on the 4K cartridge plate. The size of the optics and its supporting brackets puts severe constrains on the design of the receiver. Another important issue of the Band 5 cartridge design, as well as other ALMA cartridges, is a very tight thermal budget. In this report, we present analysis and simulation results for the thermal and mechanical design of the ALMA Band 5 cartridge that has been carried out using different FEM software packages such as CFDesign and ANSYS. We compare simulation results obtained with these software and the analytical calculations. For the mechanical design, the major focus was put on the cartridge and the optics support structure deformation with cooling.**

***Index Terms*— ALMA frontend, receiver cartridge, cryogenics, mechanical stress, thermal contraction.**

I. INTRODUCTION

ALMA, the Atacama Large Millimeter/submillimeter Array [1], is an international collaboration between Europe, Japan and North America in cooperation with Chile. ALAM is located at Llano de Chajnantor in the Atacama Desert in northern Chile, 5000 meters above sea level. The array will consist of 50 moveable antennas of 12 meter in diameter and twelve 7-meters diameter antennas. The ALMA receivers will cover the range from 30 GHz and 960 GHz there ALMA Band 5 receiver cartridge is designed for a frequency range of 163-211 GHz. The prototype cartridge is currently being assembled at GARD's facilities with an intension to supply the ALMA project with six Band 5 cartridges. The basic cartridge structure is built upon a modular approach where the base plate has an operating temperature of 300K followed by 110K, 15K and 4K stages. These are separated by G10 fiberglass tubes for thermal insulation. The blank cartridge structure is designed and manufactured within the ALMA project by Rutherford Appleton Laboratories (RAL).

The major challenge for the cryogenic and mechanical design of the ALMA Band 5 cartridge is the thermal contraction that the structure experience under cooling to these cryogenic temperatures. The optics, which is located at the top of the cartridge, experiences the same thermal contraction and deformation.

Manuscript received 20 April 2009. This work is funded by EU Framework Program 6 (FP6) in its part of infrastructure enhancement under contract no. 515906.

Magnus Strandberg, I. Lapkin , V. Belitsky , A. Pavolotsky and S.-E Ferm are with the Group for Advanced Receiver Development (GARD), Chalmers University of Technology, S-412 96 Gothenburg, Sweden, (corresponding author M. Strandberg; phone: +46 31 7725653; fax: +46 31 7721801; e-mail: magnus.strandberg@chalmers.se)

D. Henke is currently with the NRC Herzberg Institute of Astrophysics, (NRC-HIA), 5071 West Saanich Road, Victoria, British Columbia, Canada V9E 2E7

II. THERMAL DEFORMATION

We consider deformation of the ALMA Band 5 cartridge as an effect of its cooling down to 4 Kelvin. This gives different degree of the thermal contraction inside the cartridge due to difference in thermal expansion coefficient of the materials. Therefore the internal cartridge parts, such as IF-cables and LO-waveguides, must include some margins to avoid excessive mechanical stress and are shaped with bends for this purpose.

The thermal stages of the Band 5 cartridge are made off different materials such as stainless steel as the bottom, 300 K, aluminum at the 110K stage and copper at both 15K and 4K stages. The optics structure is built of aluminum alloys (EN7075 and ALCA5), because of added weight limitation and good mechanical properties of the aluminum. This allows meeting the 2 kg limit of the added mass at cold stages [2]. The chosen aluminum alloys have reasonable thermal conductivity at cryogenic temperatures and provide cooling of the mixer assembly.

A. Thermal deformation of cartridge and waveguides

Thermal deformation is given by the equation

$$d = L \cdot \int_{T_1}^{T_2} \alpha(T) \cdot dT \qquad (1)$$

where α is the instantaneous coefficient of the thermal

expansion and L is the length of the object under consideration. The simulation program ANSYS is using a similar approach though with some modification.
ANSYS is using secant or average thermal coefficient of expansion (CTE). The thermal strain has the following formula;

$$\varepsilon^{th} = \alpha^{se}(T) * (T - T_{ref}) \quad (2)$$

where $\alpha^{se}(T)$ is temperature-dependent secant coefficient of thermal expansion and T_{ref} is the temperature at which thermal strain is zero [3]. The CTE data is often available from the material vendor in units of instantaneous CTE. For that, it was needed to be converted to secant form and converted to effective thermal coefficient of expansion. Fig 1 shows the difference between the instantaneous, secant and effective CTE.

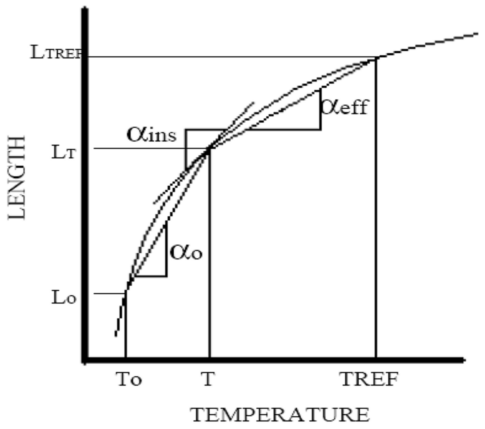

Fig. 1. Instantaneous (α_{ins}), Secant (α_0) and effective (α_{eff}) CTE [4]

The thermal deformation of the cartridge body and the LO waveguides is given in Fig 2.

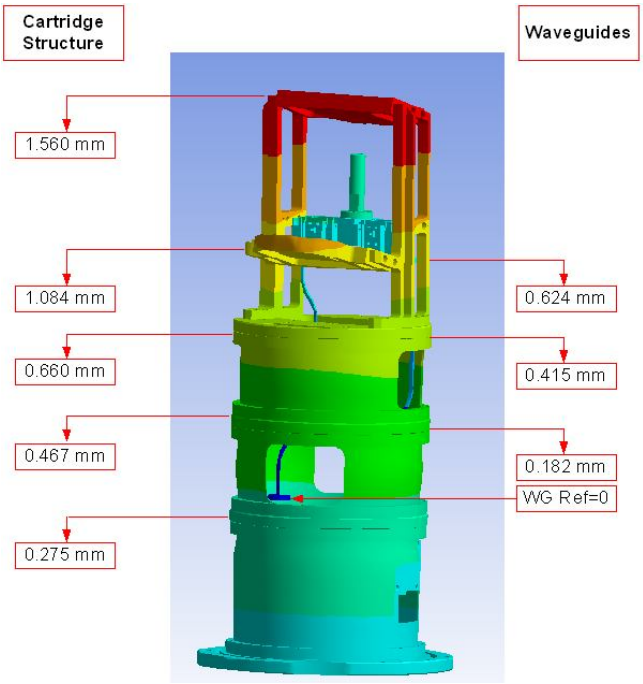

Fig 2. The cartridge structure and LO waveguides thermal deformation.

The simulation using ANSYS gives the cartridge body deformation of 0.660 mm, Fig.2, which is close to the deformation reported for Band 4 by National Astronomical Observatory of Japan (NAOJ), where the obtained deformation value of the cartridge structure is 0.5 mm against the 300 K base plate [5]. Overall Band 5 cartridge linear contraction including the optics is 1.56 mm and is quite consistent with the analytically (with simplification assumptions on the analyzed geometry) calculated value of 1.408 mm.

B. Thermal deformation of the optics structure

The thermal deformation of the optics was investigated with current design employing the guiding pins of Ø 1.5 and Ø4 mm and M4 screws attaching optics support brackets to the 4K plate, Fig 3.

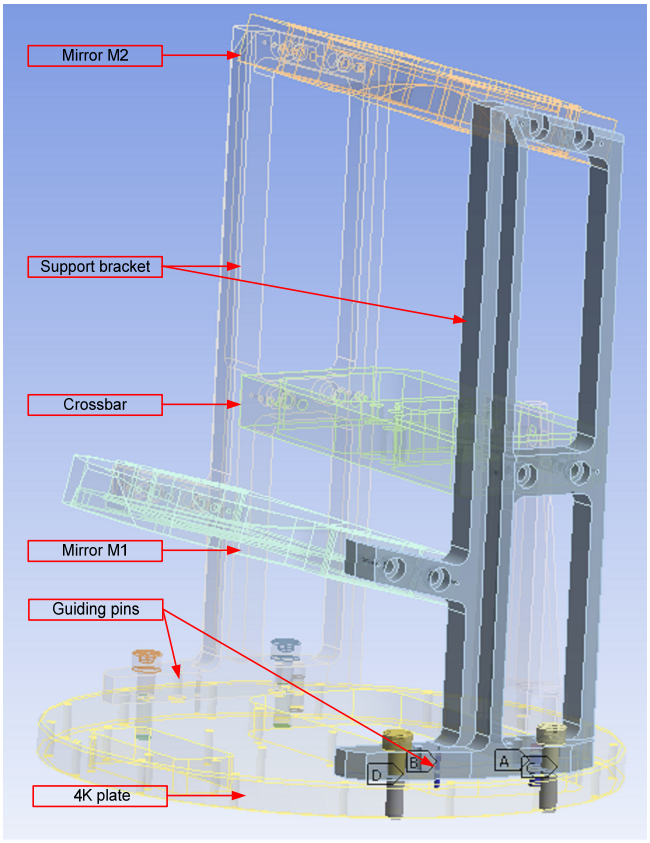

Fig 3. The optics structure with screws and pins attached to the 4K plate.

The major interest for this simulation was concerning the pins and screws deformation under cooling down to 4K as the cartridge 4K plate is made off copper whereas the Band 5 optics employs aluminum allows. The idea was to find out if the pins and screws could hold the optics structure at the required position with respect to the 4K plate. The obtained deformation shows a maximum displacement of the screw and pins of 5-10 micrometer whereas the optics thermal contraction has a maximum of 0.8 mm vertically and 0.3 mm in direction parallel to the 4 K plate. The thermal contraction was taken into account by applying scaling coefficient to the

nominal optics design.

III. COMPARISSON BETWEEN ANSYS AND CFDESIGN RESULTS

The study of the ALMA band 5 designs was carried out via comparative simulation using the two different specialized software packages, ANSYS [6] and CFDesign [7]. Both employ finite element method (FEM) and can be integrated with Inventor CAD software [8]. Comparison of the both packages was made by simulation of the same model structure, e.g., for the heat flow through UT-085B stainless steel coaxial cables and WR-10 stainless steel waveguide. The coaxial cable was simulated as a 3-layer structure (stainless steel, teflon, brass). The temperature dependence of the physical properties was implemented into the simulation as well. Fig 4 shows the deviation for the simulated heat flow through UT-085B-SS between different pairs of temperature ports: 300K and 110K, 110K and 15K, 15K and 4K. Optimization routine for the length as a compromise between RF losses and heat flow was provided for every temperature stage. The zero level represents analytically calculated value whereas the patterned lines show deviation of the simulated values obtained from simulations by ANSYS and CFDesign.

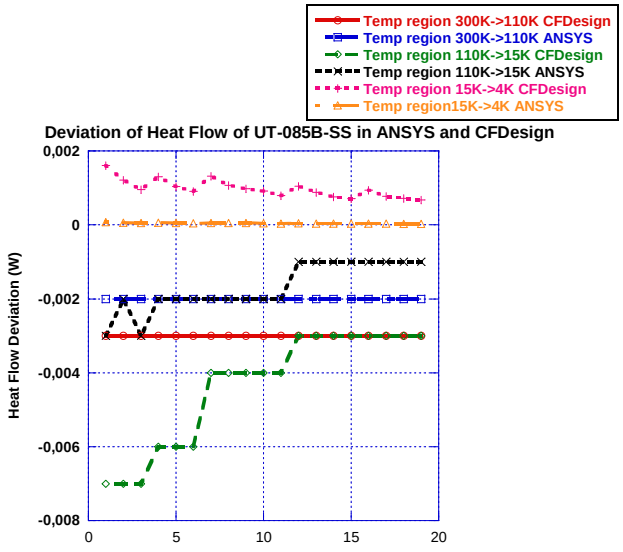

Fig 4. Heat Flow variation of coaxial cable UT-085B-SS with ANSYS and CFDesign compared with analyical values

The numbers along the x-axis correspond to the various cable lengths that were studied.

TABLE 1. DEVIATION OF HEAT FLOW POWER OF UT-085B-SS WITH SIMULATED VALUES IN ANSYS AND CFDESIGN SUBTRACTED WITH ANALYTICALLY OBTAINED VALUES.

Simulation packages	**Temperatures 300K->110K**	**Temperatures 110K->15K**	**Temperatures 115->4K**
ANSYS Heat Flow Variation (mW)	2	1-3	0.03-0.07
CFDesign Heat Flow Variation (mW)	3	3-7	1

The results of the simulations presented in the TABLE 1 show that ANSYS simulations apparently provide a better fit with the theoretical values giving ANSYS a clear advantage over CFDesign for the simulation of the thermal flow. Nevertheless it should be noted that CFDesign has the advantage of the using of a polynomial interpolation for the material thermal conductivity while ANSYS only has the option for piecewise linear interpolation.

The result is presented in Fig 5a, b and TABLE 2 show the simulation results for the waveguides, following the same approach.

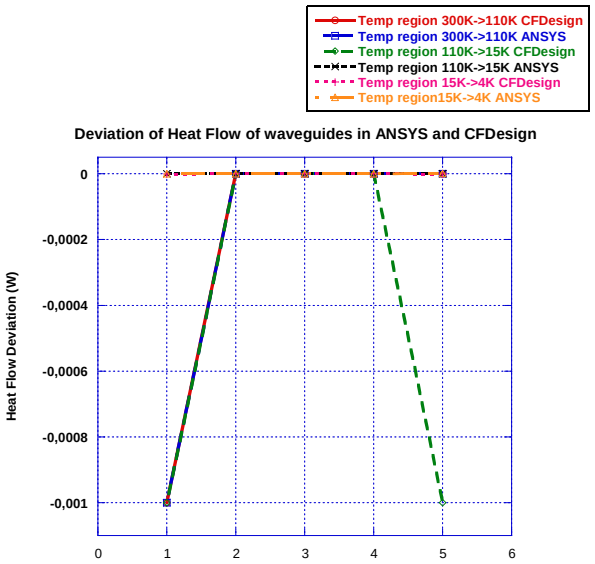

Fig 5a. Heat flow variation of waveguides with ANSYS and CFDesign compared with analytically obtained values.

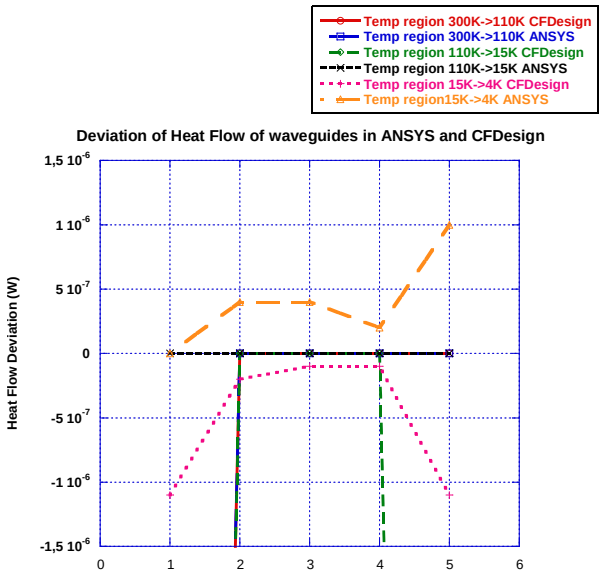

Fig 5b. Heat flow variation of waveguides with ANSYS and CFDesign compared with analytically obtained values (zoomed in)

For the waveguides, no major difference has been observed

between the simulation programs. This might be because the waveguides do consist of the single material, *i.e.*, stainless steel. Consequently, no errors could be accumulated due to the heat flow passing through different materials, as in the case of the coaxial cables UT-085B-SS.

TABLE 2. DEVIATION OF HEAT FLOW POWER OF WAVEGUIDES WITH SIMULATED VALUES IN ANSYS AND CFDESIGN SUBTRACTED WITH ANALYTICALLY OBTAINED VALUES

Simulation packages	**Temperatures 300K->110K**	**Temperatures 110K->15K**	**Temperatures 15->4K**
ANSYS Heat Flow Variation (mW)	1	0	Max 0.001
CFDesign Heat Flow Variation (mW)	1	1	Max 0.001

IV. CONCLUSION

ALMA Band 5 cartridge and its optical structure have been simulated for thermal deformation caused by cooling down to 4K. Comparison with ALMA Band 4 data shows good agreement for the vertical contraction of the cartridge body of 0.66 mm.. Both tested software packages ANSYS and CFDesign shows acceptable results whereas ANSYS gives more accurate result in comparison with the analytical values, with the CFDesign having an advantage of more convenient material properties setting.

ACKNOWLEDGMENT

The authors would like to thank Dr. S. Asayama, NAOJ for providing the data for Band 4 cartridge. Authors acknowledge Darren Erickson, NRC-HIA for his support for analytical issue of the coaxial cable UT-085B-SS. Anders Jansson, ANSYS and Martin Orphanides, Validus Engineering are greatly acknowledged by the authors for their support of the software packages ANSYS and CFDesign. We would like to thank Erik Sundin, Mathias Fredrixon, Doug Henke, GARD, and Ricardo Finger, DAS, for helpful discussions.

REFERENCES

[1] Official ALMA web-site, *http://www.almaobservatory.org*/
[2] H. Rudolf and G.H. Tan, "Band 5 Cartridge Technical Specifications-FEND-40.02.05.00-001-A-SPE",available from ALMA Project documentation server.
[3] Theory Reference for ANSYS and ANSYS Workbench Release 11.0.
[4] Bill Bulat, CSI ANSYS Tip of the Week, Effective Thermal Coefficient of Expansion in ANSYS, *http://ansys.net/tips/week4-effective_cte.pdf*
[5] Dr. S. Asayama, NAOJ, private communication
[6] ANSYS simulation software from ANSYS Inc, *www.ansys.com*
[7] CFDesign simulation softwafe from Blue Ridge Numerics Inc, *http://www.cfdesign.com/*
[8] Autodesk Inventor 3D software; from AutoDesck Inc., *http://www.autodesk.com/*

Design of a Heterodyne Receiver for Band 1 of ALMA

N. Reyes, P. Zorzi, F. P. Mena, C. Granet, E. Michael, L. Bronfman, and J. May

***Abstract*—Here we present the design of a receiver that will cover the frequency range from 31 to 45 GHz. The receiver will use a horn and a lens to couple the incoming radiation into the waveguide structure. Then, an orthomode transducer will split the signal in two polarizations. Each one of them is then amplified and down converted using the upper sideband mixing scheme. The results of the electromagnetic modeling of every component are also presented here. We also discuss how the components will be implemented.**

***Index Terms*—Millimeter wave receiver, HEMT, USB mixing.**

I. INTRODUCTION

The Atacama Large Millimeter Array (ALMA) is the largest radio astronomical array ever constructed. Every one of its constituent antennas will cover the spectroscopic window allowed by the atmospheric transmission at the construction site with ten different bands. Despite being declared as a high scientific priority by the ALMA Scientific Advisory Committee, band 1 (31.3−45 GHz) was not selected for construction during the initial phase of the project [ref.]. However, Universidad de Chile has recently started a program for the construction of a prototype receiver for band 1 of ALMA. In this paper we present the design of the proposed receiver and the results of the electromagnetic modeling of several of its parts.

II. RECEIVER DESIGN

The schematics of the receiver we are proposing is presented in Figure 1. The incoming signal is brought to a horn via a lens. Two different corrugated versions have been studied, a conventional conical horn and an optimized spline-profile horn. The first results with the optimized horn demonstrate an improved performance (Sec. III.A). After the horn, the signal is divided in its linear polarization components using an orthomode transducer (OMT). We have scaled up the OMT introduced to ALMA by Asayama [1] (Sec. III.B). Each polarization branch is first amplified and then down-converted independently. For amplification, we will use high electron mobility transistors (HEMT). In a first stage, we plan to test commercial chips that will be integrated at our laboratories. The design of the packaging is also presented (Sec. III.C). Given the frequency coverage of this band and the availability of the LO signal, an upper sideband mixing scheme has been selected. A high pass-band filter that cancels out the lower sideband is, therefore, needed. We have designed a multiple stage waveguide filter with a cut-off frequency of 30 GHz and a rejection of the image signal better than 20dB (Sec. III.D). Finally, the down-conversion and amplification of the intermediate signal is planned to be done with commercial components.

III. MODELING AND PROPOSED CONSTRUCTION METHODS

A. Optics and Horn

A bi-hyperbolic lens will refocus the ALMA Cassegrain antenna sub-reflector beam focus into a corrugated horn located inside the cryocooled receiver. This device will also act as a vacuum window of the receiver. The optimal lens design was carried out using a fundamental gaussian beam mode analysis [2]. We used high density polyethylene (HDPE) in our lens design which has a dielectric constant of 2.3. The final optimized lens design is 19.4 cm in diameter, 5.09 cm thick at the centre of the lens, and has a focal length of 18.8 cm. Both sides of the lens will be machine with rectangular grooves around the lens centre to form an anti-reflection layer that will minimize reflection losses [3].

We have analyzed two different corrugated horns, a standard conical horn, designed according to [4], and an optimized spline-profile horn. We used Ansoft HFSS 11 [5] to optimize the former and to check the performances of both horns. In Fig.2, the radiation patterns at 38 GHz and the profile dimensions of both corrugated horns are presented. It can be noted that the performance of the spline-profile horn in terms of size, first side lobe location, and cross-polar level are much better than the conical design. However, the thickness of the wall between corrugations in spline-profile horn design is much smaller than the same dimension in the other horn and, therefore, could present more challenges when constructed using milling techniques.

Manuscript received 20 April 2009. This work is supported by the Chilean Center of Excellence in Astrophysics and Associated Technologies (PFB 06).

N. Reyes, P. Zorzi, F. P. Mena, and E. Michael are with the Electrical Engineering Department, Universidad de Chile, Av. Tupper 2007, Santiago, Chile (corresponding author: +56-2-6784888; fax: +56-2-695 3881; e-mail: pmena@ing.uchile.cl).

C. Granet is with BAE Systems Australia Ltd, 40-52 Talavera Road, North Ryde 2113, Australia, Santiago, Chile.

L. Bronfman, and J. May are with the Astronomy Department, Universidad de Chile, Camino El Observatorio 1515, Santiago, Chile.

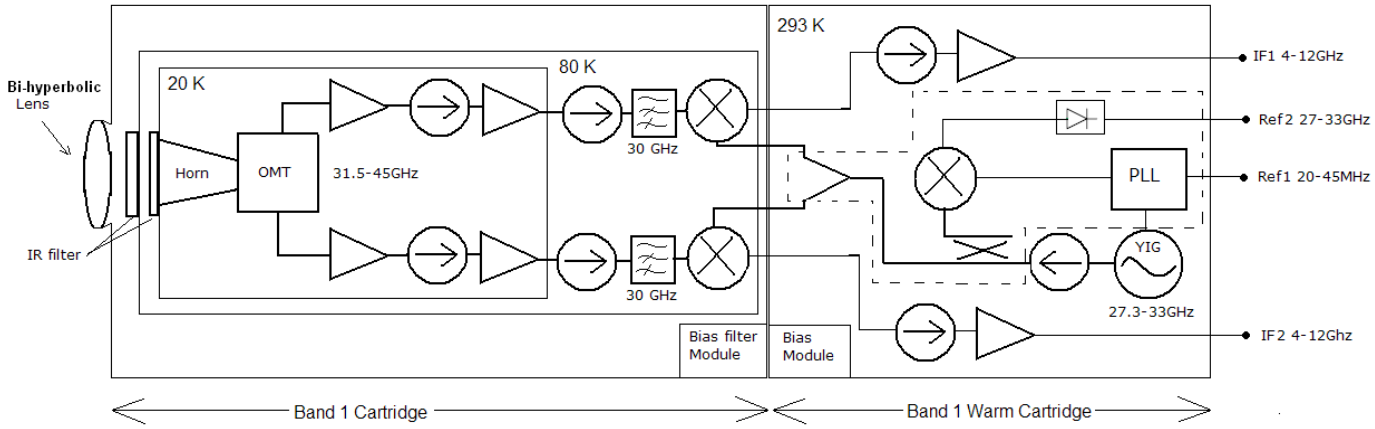

Fig. 1. Layout of the receiver for band 1 of ALMA. The incoming RF signal is coupled with the horn via a lens (Sec. III-A). The signal is then divided in its polarization components in an OMT (Sec. III-B). Then, each polarization signal is amplified in two consecutive HEMT's at 20 K (Sec. III-C). Finally, the amplified signals are filtered to suppress the lower sideband and mixed in separate Schottky diodes (Sec. III-D). Dashes lines represent the LO block developed by NRAO.

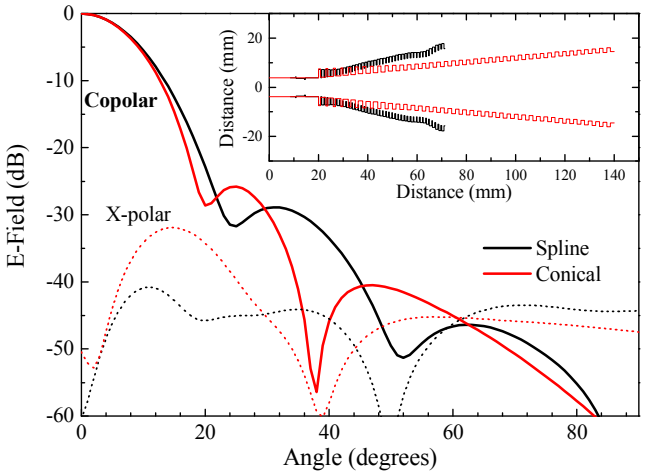

Fig. 2. Radiation patterns at 38 GHz of the spline and conical corrugated horns whose profiles are shown in the inset.

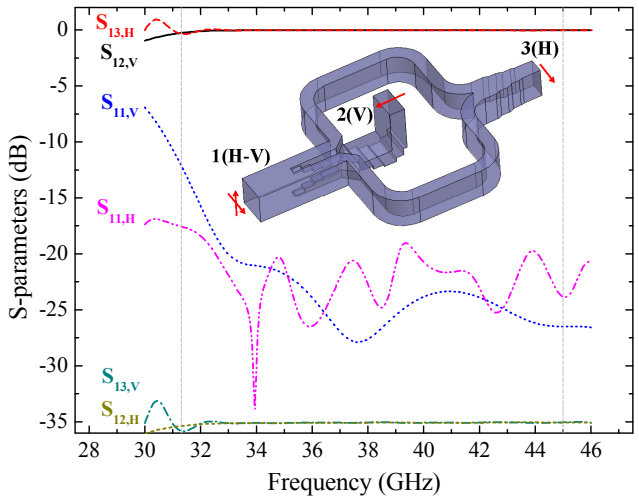

Fig. 3. Calculated S-parameters of the proposed orthomode transducer shown in the inset. The inset also shows the port numbers and the polarizations that each of them carries, H (horizontal) or V (vertical). Vertical dashed lines show the band-1 frequency range.

B. Orthomode Transducer

A "Dual Ridged" OMT has been adopted [1]. A preliminary model is illustrated in the inset of Fig. 3 and its main dimensions are presented in Table 2. This model was also optimized using Ansoft HFSS. The simulated S-parameters of this model are shown in the main panel of Fig. 3. We can note that this OMT should work properly between the 33 to 45 GHz range. Some further optimization work, especially at lower frequencies, is needed to cover the entire bandwidth properly.

TABLE 1 MAIN DIMENSIONS OF THE ORTHOMODE TRANSDUCER (INSET OF FIG. 3)

Parameter	Dimensions (mm)
Input square waveguide	5.69 × 5.69
Output rectangular waveguide	5.69 × 2.845
Distance between ports 1 and 3	54.0
Distance between lateral waveguides	34.0

C. Amplification

The strategy proposed for the band 1 receiver is to amplify the RF signal by 30 or 40 dB to allow the use of a commercial Schottky mixer at either 80 K or at ambient temperature. This amplification signal will be done by a HEMT amplifier.

As a first stage we will test low noise amplifiers from Hittite (ALH376). This MMIC have a noise figure of 2.2dB and 20 dB of amplification at room temperature. The chip will be integrated at our laboratory. We have defined that the input and output of the amplification block will be WR22 waveguides. The coupling of the signal into the MMIC will be done by a waveguide-to-microstrip transition where we have compared rectangular [6] and radial probes [7]. We have found that radial probes have better response than the rectangular ones as shown in Figure 5.

D. Filter for Lower-Sideband Suppression and Down Conversion

A high pass filter cancels out the lower sideband signal before the down-conversion. For band 1 case we need a filter with a cut-off frequency of 30 GHz, with the pass-band at 31-45 GHZ and a rejection band of more than 20dB at frequencies lower than 29 GHz.

To design the filter we have followed [8] and [9]. We simulated the filter as a cascaded transmission lines with each section having physical dimensions a_i and c_i, a propagation constant β_i and impedance Z_{0i}. (see inset of Fig. 4). The dimensions a_i and c_i where optimized to have a filter with a maximum rejection at the sideband and a maximum transmission at the RF frequency. After the optimization process a three stage filter was selected. The dimensions are shown in Table 2. The performance of the filter was checked using a full electro-magnetic simulator (HFSS). The attenuation of the filter in the rejection band is more than 18dB. The transmission is better than 99% over the whole pass band. The results are summarized in Figure 4. If better response is needed, a higher order filter could be used.

Using this filter the sideband rejection ratio of the receiver is better than 20dB in 99% of the LO configurations. The worst case is a rejection ratio of 18.5 dB where the LO is at 33 GHz and we are observing an RF of 37 GHz.

Since the noise is dominated by the amplifier we can use a Schottky mixer at either 80 K or room temperature for the down-conversion without a penalty in noise. We are planning to use a commercial balanced mixer from Quinstar. The main problem that we see in this solution is the relative high LO power required by this device. Other mixers have to be studied to reduce the LO power requirements.

TABLE 2 DIMENSIONS OF THE WAVEGUIDE FILTER (INSET OF FIG. 4)

Parameter	Dimensions (mm)
$a1$, $a7$	5.69
$a2$, $a6$	5.41
$a3$, $a5$	5.27
$a4$	4.99

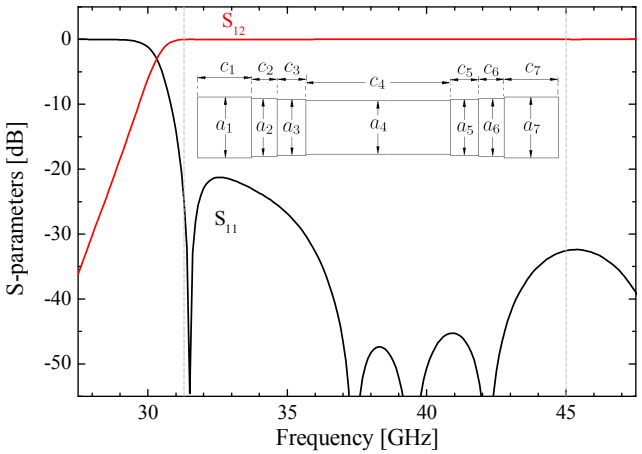

Fig. 4. S-parameters of the waveguide filter shown in the inset. In the frequency range of interest (vertical dashed lines), the transmission is better than –0.05 dB and the reflection lower than –20 dB.

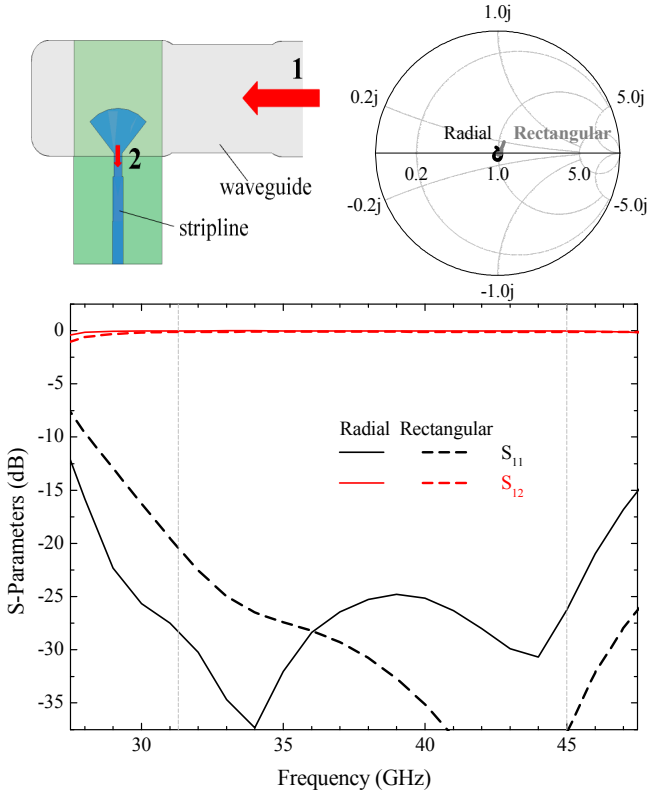

Fig. 5. *Top panel*: Waveguide-to-stripline transition that will be used to package the HEMT chips for amplification. The transition shown here (left) uses a radial probe to couple the incoming radiation into the stripline. When compared with the more traditional rectangular probe, the simulation results plotted in the Smith chart (right) show that a better coupling is obtained with the radial probe. *Bottom panel*: S-parameters of waveguide-to-stripline transitions using rectangular and radial probes, respectively.

IV. CONCLUSIONS

We have presented here the design of a receiver covering the 31−43-GHz band. This is the first step towards the construction of a prototype receiver for band 1 of ALMA. Once constructed, it will contribute importantly to the state of the art of the largest radio telescope array in the world. Moreover, in possession of this band, ALMA would be in the capability of performing very-large-base interferometry with other facilities around the world.

ACKNOWLEDGMENT

We would like to thank C. Jarufe and E. Guerrero for their help in simulating the different parts of the receiver that is proposed here.

REFERENCES

[1] S. Asayama, "Double-ridged Orthomode Transducer for ALMA Band 4 receiver," NAOJ internal MEMO, 2007.

[2] J. W. Lamb, "Miscellaneous data on materials for millimeter and submillimeter optics," Int. J. Infrared Millim. Waves, vol. 17, no. 12, pp. 1997–2034, Dec. 1996.

[3] J.W. Lamb, "Cross-polarization and astigmatism in matching grooves," Int. J. Infrared Millim. Waves, vol. 17, no. 12, pp. 2159–2165, Dec. 1996.

[4] C. Granet and G. L. James, "Design of Corrugated Horns: A Primer," IEEE Antennas and Propagation Magazine, Vol. 47, No. 2, April 2005.

[5] High Frequency Structure Simulator (HFSS), version 11, Ansoft Corporation, Pittsburgh, PA, USA.

[6] Yoke-Choy Leong, Weinreb, S., "Full Band Waveguide-to-Microstrip Probe Transition," Microwave Symposium Digest, 1999 IEEE MTT-S International Volume 4, Page(s):1435 -1438

[7] J. Kooi et al., "A full-height waveguide to thin-film microstrip transition with exceptional RF bandwidth and coupling efficiency," Int. J. Infrared Millimeter Waves, vol. 24, no. 3,pp. 261 - 284, Mar. 2003.

[8] Pozar, "Microwave Engineering" John Wiley & Sons, Second edition 1998

[9] LIU A_-Shyi , WU Ruey-Beei and LB Yi-Cheng, "A compact design of W-band high-pass waveguide filter using genetic algorithms and full-wave finite element analysis," IEICE transactions on electronics ISSN 0916-8524 ,2005, vol. 88, no8, pp. 1764-1771.

GREAT: ready for early science aboard SOFIA

S. Heyminck, R. Güsten, U.U. Graf, J. Stutzki, P. Hartogh, H.-W. Hübers, O. Ricken, B. Klein et al.

***Abstract*— GREAT, the German REceiver for Astronomy at THz frequencies, has successfully passed its pre-shipment acceptance review conducted by DLR and NASA on December 4-5, 2008. Shipment to DAOF/Palmdale, home of the SOFIA observatory, has been released; airworthiness was stated by NASA. Since, due to schedule slips on the SOFIA project level, first science flights with GREAT were delayed to mid 2010.**

Here we present GREAT's short science flight configuration: two heterodyne channels will be operated simultaneously in the frequency ranges of 1.25-1.50 and 1.82-1.91 THz, respectively, driven by solid-state type local oscillator systems, and supported by a wide suite of back-ends. The receiver was extensively tested for about 6 month in the MPIfR labs, showing performances compliant with specifications.

This short science configuration will be available to the interested SOFIA user communities in collaboration with the GREAT PI team during SOFIA's upcoming Basic Science flights.

***Index Terms*— airborne astronomy; heterodyne receiver; high resolution spectroscopy; SOFIA**

I. Introduction

GREAT[1][2] is a highly modular principal investigator heterodyne instrument designed for use aboard the SOFIA[3] airborne observatory. The instrument is developed and funded by a consortium of four German research institutions.

Main goal of the design was to provide best possible performance within the boundaries drawn by the observatory and the airworthiness requirements.

In total four independent heterodyne channels are under development for the instrument. Two out of these can be operated simultaneously during one observing flight. The channels being developed so far target at, e.g., high-J CO-transitions, ionized carbon (at ~1.9 THz), deuterated molecular hydrogen HD (~2.7 THz), and atomic oxygen (~4.7 THz).

For the first flight configuration GREAT will be equipped with the both so called low-frequency channels L#1 and L#2. L#1 operates from 1.25 to 1.52 THz while L#2 ranges from 1.82 to 1.92 THz.

Manuscript received 20 April 2009.

S. Heyminck, R. Güsten and B. Klein are with the Max-Planck-Institut für Radioastronomie, Bonn, Germany

U.U. Graf and J. Stutzki are with KOSMA, Universität zu Köln, Germany

P. Hartogh is with the Max-Planck-Institut für Sonnenforschung, Katlenburg-Lindau, Germany

H.-W. Hübers is with the Deutsches Zentrum für Luft- und Raumfahrt e.V., Institut für Planetenforschung , Berlin, Germany

Send correspondence to S. Heyminck; E-mail: heyminck@mpifr-bonn.mpg.de.

II. System description

GREAT consists of a main structure housing an electronics rack, two cryostat mounts, two optics compartments, two LO-mounts and a calibration unit. The telescope signal is either split by polarization or by frequency (dichroic mirror) to feed two independent heterodyne receiver channels for simultaneous operation. The cryostats are liquid Nitrogen and liquid Helium cooled wet dewars providing the 4.2 K operation temperature of the mixer-devices. The hold time is well above 20 hrs, which is far more than the expected flight duration of SOFIA (< 14 hrs). The calibration unit consists of two black-body radiators, one placed in a small liquid Nitrogen cooled dewar and one at ambient temperature. Switching between the two loads and the sky is done by a remote controlled mirror.

As heterodyne mixing elements in both first flight channels and in the 2.7 THz channel HEB-mixers made by KOSMA are used[4]. They show excellent noise performance and stabilities. Currently their IF-bandwidth is limited to about 600 MHz (by the isolator), but we hope to overcome this limitation with the next generation of KOSMA mixers expected to be operational within this year. The 4.7 THz channel will be equipped with HEB-mixers developed by DLR-PF[5].

The optics[6] of each channel is placed on an optical bench, which can be reproducibly mounted to the main structures optics compartment. This, together with easily exchangeable cryostats and LO-systems makes possible to reconfigure the system even between two flights of a SOFIA flight series, e.g. to change the RF-frequency channel.

The frontend is fully remote controllable via Ethernet. A VME-type computer provides all necessary control signals. In addition the system can be operated fully manual even when the computer is switched off. Together with a partly redundant electronics system this improves reliability of the system during flight, even in case of a device or software malfunction.

GREAT uses a two-stage IF-system which can provide signals for three different backend-types. The simultaneous use of the 8-channel AAOS[7] system, two CTSs[8], and a two channel fast Fourier transform spectrometer[9] is possible. The array-AOS, with the second stage of the IF-processor provides a total bandwidth of 4 GHz at 1 MHz spectral resolution per frequency channel. The CTS can simultaneously analyze a 220 MHz wide part of the band at approx. 45 kHz resolution. The free to configure FFTS-chains offers up to 1.8 GHz instantaneous bandwidth at 255 kHz resolution each. A higher resolution mode with correspondingly lower bandwidth can easily be configured by software (750 MHz with 53 kHz). The FFTS operates with the first IF-stage only, reducing complexity at the backend-side.

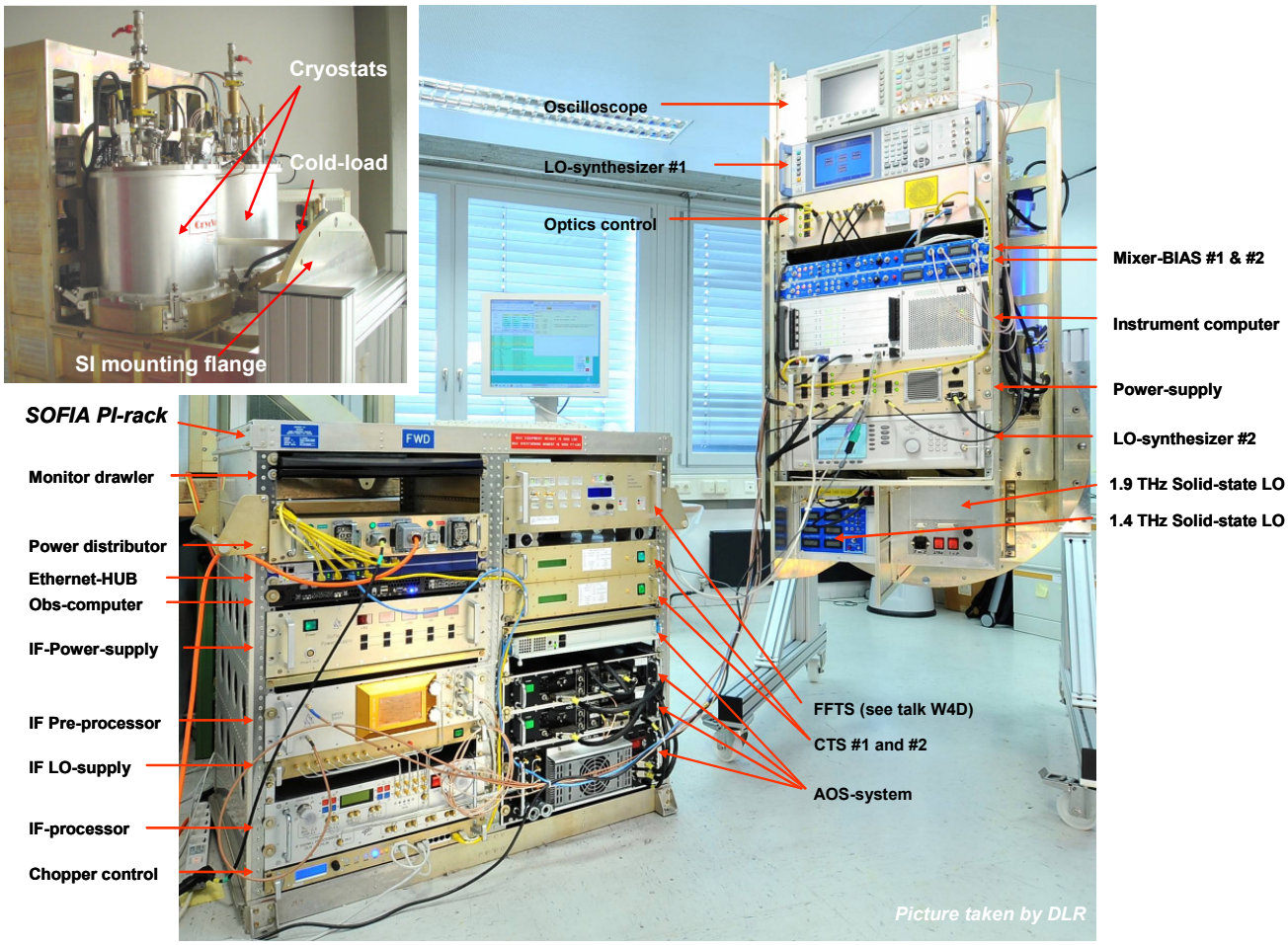

Fig. 1. GREAT in its early science flight configuration, equipped with channels L#1 and the L#2. All components are flight hardware including the airworthy wiring.

Table 1. GREAT performance data as measured during the lab-tests.

Channel	LO-coverage (using VDI solid-state chains)	spectr. Allan-variance minimum time	DSB noise-temperature	beam-shape
L#1: 1.4 THz	**Chain 1:** 1.25 – 1.40 THz (with a gap at 1.28 THz) **Chain 2:** 1.42 – 1.52 THz	>100 s TP Allan times are in the order of >30 s.	< 1800K (measured with wrong leveling of the IF)	expected waist-position and opening angle
L#2: 1.9 THz	1.81 – 1.905THz (with a gap at 1.88 THz)	>90 s TP Allan times are in the order of >15 s.	< 1300K best measured value at 1821GHz was 1150K.	expected waist-position and opening angle

III. Performance

During extensive AIV tests prior to the pre-shipment review both low-frequency channels have been characterized in detail. All minor problems that appear when operating new technologies for the first time were addressed and solved. Table 1 summarizes the basic performance numbers.

IV. Conclusion

GREAT meets all design requirements and is ready for shipment. All auxiliary equipment, as the transportation cart and shipping boxes, is ready to go. Ongoing development is concentrated to improve the IF-bandwidth of the both low-frequency HEB channels and to complete the mid-frequency channel at 2.7 THz within this year.

References

[1] R. Güsten, P. Hartogh, H.-W. Hübers, U.U. Graf, K. Jakobs, H.-P. Röser, F. Schäfer, R.T. Schieder, R. Stark, J. Stutzki, P. van der Wal, A. Wunsch, „GREAT: the first-generation German heterodyne receiver for SOFIA“, Proceedings of the SPIE, Volume 4014, pp. 23-30, 2000.

[2] S. Heyminck, R. Güsten, P. Hartogh, H.-W. Hübers, J. Stutzki, U.U. Graf, “GREAT: a first light instrument for SOFIA”, Proceedings of the SPIE, Volume 7014, pp. 701410-701410-7, 2008

[3] E. Becklin, “SOFIA: Stratospheric Observatory for Infrared Astronomy,” in IAU Symposium, D. C. Lis, G. A. Blake, and E. Herbst, eds., 231, p. 9, Aug. 2005.

[4] P.P. Munoz, S. Bedorf, M. Brandt, T. Tils, C.E. Honingh, and K.Jacobs, “Fabrication and characterization of phonon-cooled hot-electron bolometers on freestanding 2-µm silicon nitride membranes for THz applications”, in Millimeter and Submillimeter Detectors for Astronomy II. Edited by Jonas Zmuidzinas, Wayne S. Holland and Stafford Withington Proceedings of the SPIE, Volume 5498, pp. 834-841, 2004

[5] A. D. Semenov, H. Richter, H.-W. Hübers, B. Günther, A. Smirnov, K. Smirnov, K. I'lin, and M. Siegel, "Terahertz performance of planar antennas coupled to a hot electron bolometer," IEEE Trans. Microwave Theory and Technol., vol. 55, pp. 239-247, 2007.

[6] A. Wagner-Genter, U.U. Graf, M. Phillipp and J. Stutzki, „GREAT optics", Proceedings of the SPIE, Volume 5498, pp. 464-472, 2004.

[7] J. Horn, O. Siebertz, F. Schmülling, C. Kunz, R. Schieder, and G. Winnewisser, "A 4×1 GHz Array Acousto–Optical Spectrometer," Exper. Astron. 9, 1999.

[8] G. Villanueva and P. Hartogh, "The high resolution chirp transform spectrometer for the SOFIA–GREAT instrument," Experimental Astronomy 18(15), pp. 77–91, 2005.

[9] B. Klein, S. D. Phillip, I. Krämer, C. Kasemann, R. Güsten, K. M. Menten, „The APEX digital Fast Fourier Transform Spectrometer", A&A, Volume 454, pp. L29-L32, 2006

P8F

Microwave kinetic inductance detector (MKID) camera testing for submillimeter astronomy

N.G. Czakon[1*], P.K. Day[2], J.-S. Gao[1], J. Glenn[3], S. Golwala[1], H. LeDuc[2], P.R. Maloney[3], B. Mazin[4], D. Moore[1], O. Noroozian[1],H. T. Nguyen[2], J. Sayers[1], J. Schlaerth[3], J. E. Vaillancourt[1], A. Vayonakis[1], and J. Zmuidzinas[1]

*1 California Institute of Technology *, Pasadena, CA 91125*
2 Jet Propulsion Laboratory, Pasadena, CA 91109
3 University of Colorado, Boulder, CO 80309
4 University of California, Santa Barbara, CA 93106
* Contact:czakon@caltech.edu, phone +1(626)3954246

***Abstract*—State-of-the-art incoherent submm- and mm-wave detectors regularly achieve background limited performance. The only means to increase sensitivity further is to increase focal plane pixel counts. Microwave kinetic inductance detectors (MKIDs) provide a cost-effective, easily scalable means to produce fully lithographic background-limited kilopixel focal planes. We are constructing a MKID-based camera for the Caltech Submillimeter Observatory with 576 spatial pixels each simultaneously sensitive in 4 bands at 750, 850, 1100, and 1300 microns. Each spatial pixel consists of an octave-bandwidth phased-array slot-dipole antenna to define the radiation pattern. The antenna output is coupled to four independent MKIDs via parallel photolithographic band-defining filters corresponding to the four bands. The full focal plane will consist of 16 tiles of 36 spatial pixels each. Each tile will use a single coplanar waveguide to couple the 144 quarter-wave microwave resonators to a single cryogenic amplifier.**

The novelty of MKIDs has required us to develop new techniques for detector characterization. To determine optical loading, measurements of lifetime were made by coupling energy into the resonators both optically and by driving the third harmonic of the resonator. The two techniques yield equivalent lifetime measurements with values in the few microsecond range under optical loading. Optical loading has also been determined using internal Q measurements, which range between 15,000 and 30,000 for our resonators. Quasiparticle lifetime and resonator Qs have been measured for detector bath temperatures between 200 mK and 400 mK. Spectral bandpasses have been measured for the 850 and 1300 micron bands using a Fourier transform spectrometer. Additionally, beam maps have been taken and we have found that they conform to expectations. The same device design has been characterized on both sapphire and silicon substrates.

First-astronomical light was obtained with these devices in 2007 and a second engineering run is planned for mid-2009. The full camera will be commissioned at the CSO during 2010 and will become a facility instrument. We report on the status of the cryogenics, optics, detector design, and electronic readout system of the final camera.

P8G

Radiometer MMIC

A. Emrich[1*], T. Pellikka[1] and S.E. Gunnarsson[2]
*1 Omnisys Instrument AB *, Västra Frölunda, Sweden*
2 Chalmers University of Technology
* Contact: ae@omnisys.se, phone +46 31 7343401

***Abstract*—There are several radiometer instruments covering 10-1000 GHz planned and projected over the next 10-15 years. There exist MMIC based front-end solutions up to 60-90 GHz today but for frequencies above 100 GHz, Schottky mixers have been preferred in most cases. Omnisys has now through a development project under the GHz Center at Chalmers University of Technology, financed partly under an ESA GSTP contract, developed heterodyne radiometer MMIC's for the 118 and 183 GHz bands using "Fraunhofer Institute for Applied Solid State Physics" 100nm mHEMT process. Radiometer components such as LNA's, mixers and frequency multipliers have been development as well as integrated radiometer MMIC's. Test results will be presented for components as well as for the first iteration of the integrated radiometer MMIC's.**

The 118 GHz LNA measurements show a gain of more than 20 dB over 80-135 GHz with NF of 2.5-3 dB. For the 183 GHz LNA, the gain is > 17 dB over 130-210 GHz with a NF 5 dB for frequencies below 185 GHz going up to 6.5 at 195 GHz. Both the 118GHz and 183GHz mixers are single ended resistive mixers for a broadband response with good conversion loss. The measured values are about 6dB for the 118GHz design and about 10dB for the 183GHz design. The usable bandwidth for both RF and LO is at least +-20GHz. For the system design we have also developed multiplier chains for both frequency bands. As LO chain for the 118GHz we have an X4-multiplier that with the output power amplifier is delivering +6dBm output power at saturation. For the 183GHz receiver we have an X6 multiplier also with an output power amplifier, delivering at least +4dBm.

STEAMR Receiver Chain

Peter Sobis, Anders Emrich and Magnus Hjorth

Abstract— **We report on the development of the STEAMR radiometer system, including the front-end receivers, LO multipliers and the back-end spectrometer system. STEAMR constitutes the submillimeter wave limbsounder on board PREMIER, one of three ESA Earth Explorer Core missions that have entered a feasibility study phase. The STEAMR instrument is based on a linear array of 14 heterodyne receivers operating in the 320 GHz to 360 GHz band processing over 260 GHz of instantaneous IF bandwidth. Thereto, eight of the fourteen receivers are to be sideband separating (2SB) and a novel waveguide based topology with integrated LNA's has been developed.**
An overview of the receiver system is presented together with a conceptual design optimized to meet the scientific goals of the instrument. Preliminary results on critical receiver components such as front-end mixers, LO chains and the back end spectrometer are presented and different alternatives for realization are discussed.

***Index Terms*—Radiometer Systems, Submillimeter wave circuits, Submillimeter wave mixers, Submillimeter wave receivers, Submillimeter wave waveguides**

I. Introduction

The STEAMR (Stratosphere Troposphere Exchange And Climate Monitor Radiometer) instrument is a part of the ESA PREMIER mission [1] with the overall goal to observe atmospheric composition for a better understanding of the chemical and climate interaction. The mission has its provenance from earlier IR emission sounders (MIPAS Envisat, 2002, HiRDLS and TES Aura, 2004) and millimetre wave limb emission sounders (SMR Odin, 2001 and MLS Aura, 2004), with the main objective to provide vertically (1-2 km) and horizontally (30-50 km) well resolved information on the distribution of UT-LS constituents such as water vapor, ozone and carbon monoxide on the global scale by using the 320-360 GHz range.
PREMIER was recently selected as one of three Earth Explorer Core missions that now have entered a feasibility study phase with the goal to be launched in 2016. Omnisys Instruments AB is currently under contract for the development of the STEAMR receiver electronics including front-ends, back-ends, control and power interface electronics. The Swedish Space Corporation (www.ssc.se) is the prime contractor and is responsible for the instrument design concept and final integration of the subsystems.

Limb sounding provides vertical resolution and allows for the detection of key trace gases which are too tenuous to be detectable thru the shorter path lengths of nadir observations. The limb sounding geometry also has a better contrast (S/N ratio) as the cold space rather than the warm earth is used as a background. The STEAMR millimeter wave limb sounder will together with two infrared instruments, an InfraRed Limb Sounder and an Infrared Cloud Imager, fly in the MetOp satellite sun-synchronous orbit (with a reference altitude of 817 km) in a rearward limb-viewing configuration of the UT-LS range, see figure 1. This will make it possible for co-registration of the MetOp nadir observations and PREMIER limb soundings and will produce unique data on the atmospheric chemistry and climate processes.

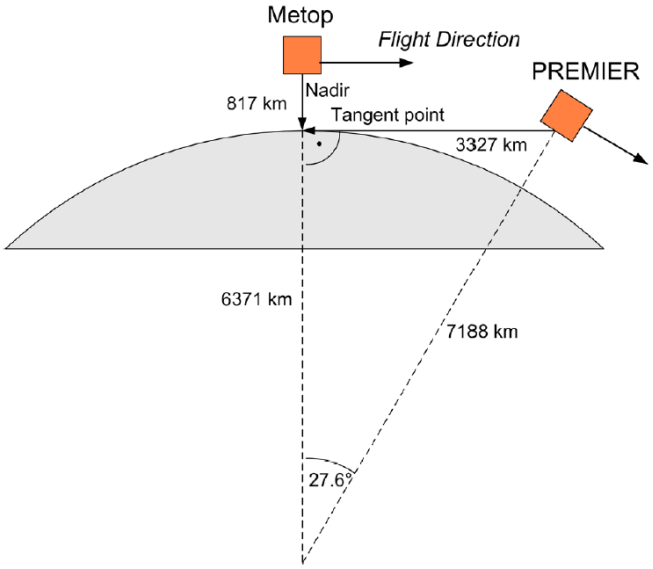

Figure 1. Observation geometry of the Metop and PREMIER satellites [1].

The STEAMR measurement concept is based on tomographic multibeam limb sounding using heterodyne Schottky diode detectors, where 14 predefined tangent heights will be observed simultaneously utilizing a staring view configuration with 7 beams for each polarization, see figure 2. A linear fixed array of 14 heterodyne receivers is used instead of 1-2 single channels being scanned in altitude, thus providing an order of magnitude improvement in sensitivity and simplification in parts of the optics. The instrument integration time will be around 2.5 s per measurement producing highly resolved spectral data with a spatial vertical resolution of about 1.5 km.

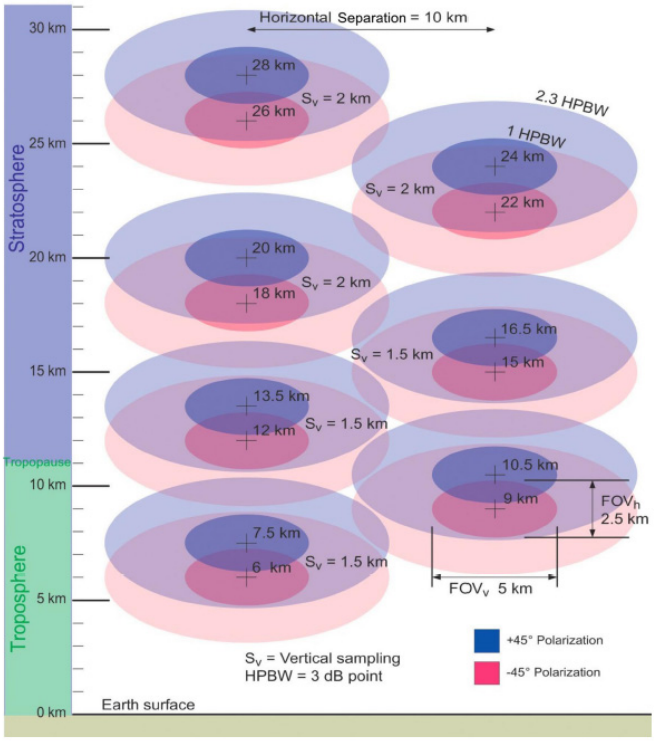

Figure 2. Staring view concept of the STEAMR satellite [1].

II. Receiver System

STEAMR will use receivers operating at a fixed LO frequency of about 170 GHz covering the 320-360 GHz range with a T_{rec} of less than 2000 K DSB. The receivers will be divided into blocks of 3-4 elements employing DSB or sideband separating (2SB) functionality depending on the specific altitude coverage. The effect of line broadening at lower altitudes is the driving factor that motivates the use of sideband separating (2SB) receivers, see figure 3 for a schematic overview of the system.

The focal plane unit beam array concept will be adopted from the Compact Heterodyne Array Receiver Module (CHARM), developed at the KOSMA observatory in Köln, Germany, employing a 9 pixel array of 345 GHz SIS mixers. The horns within each receiver block are tightly spaced, about 20-25 mm distance from each other, and a six-mirror antenna system will be used with a main reflector measuring 1.6m by 0.8m adopting a Ritchey-Chretien telescope (RCT) design.

Back-end units consisting of a autocorrelator spectrometer with a total of 12 GHz of bandwidth and 20 MHz resolution will be used. This is achieved using wideband IQ mixers dividing the IF into four 3 GHz wide channels processed by state of the art single autocorrelator ASIC chips from Omnisys Instruments, with more than 6 GHz of bandwidth.

A. Front-End Subsystem

The front-end subsystem will use a subharmonic (x2) Schottky diode mixer [2], where the current baseline is to use a design employing an inverted suspended hybrid topology [3]. The mixer consists of a 75um thick fuzed quartz circuit, on which an anti-parallel diode chip is mounted in a flip-chip fashion. The mixer circuit is then mounted using silver epoxy in a micromachined E-plane splitblock containing an IF LNA chip. Waveguide flange interfaces are used for the LO and RF signal interconnects and a coaxial interface is used for the IF output, see figure 4.

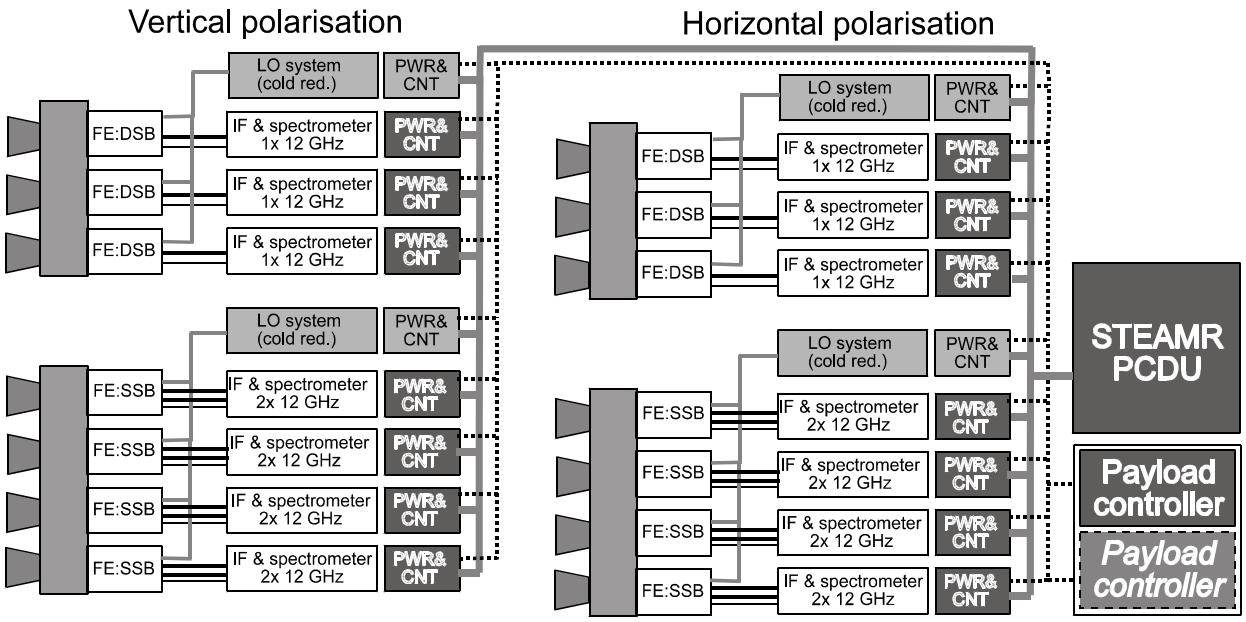

Figure 3. Schematic overview of the STEAMR receiver system.

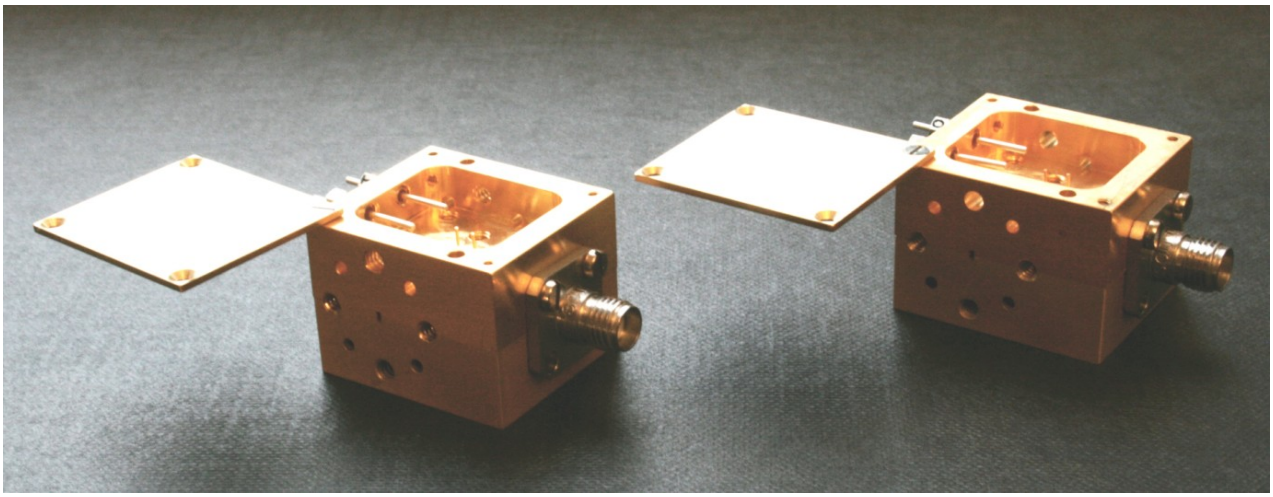

Figure 4. Photo of the mixer with integrated LNA assembly.

1) Subharmonic Sideband Separating Mixers

Based on the subharmonic mixer architecture with an integrated LNA, two sideband separating (2SB) mixer topologies have been considered. A series of different waveguide hybrid designs have been manufactured in order to evaluate the two concepts. Preliminary results are showing an advantage of using 90 degree hybrids for the LO and RF to a matched Y-junction for the RF and 45/135 degree hybrid for the LO feeding [3]. The reason is that branch guide couplers (90 degree hybrids) have isolated ports resulting in less ripple in the image rejection response and a lower SWR at the inputs as a larger amount of the reflected power is terminated in the isolated port.

The downside of using hybrids with isolated outputs is that the RF termination will radiate noise into the system increasing the receiver noise temperature. In figure 5 the modular 2SB receiver prototype can be seen and a drawing of a proposed integrated prototype sideband separating mixer module is presented in figure 6.

2) Mixer with Integrated LNA

An estimate based on obtained results from the mixer configured with a custom 1-12 GHz LNA (50 K noise temp.) developed at Chalmers University of Technology, and on the results of the newly developed mixer modules containing an integrated AMMC-6220 LNA (175 K noise temp.) from Agilent, is showing that a receiver noise temperature of less

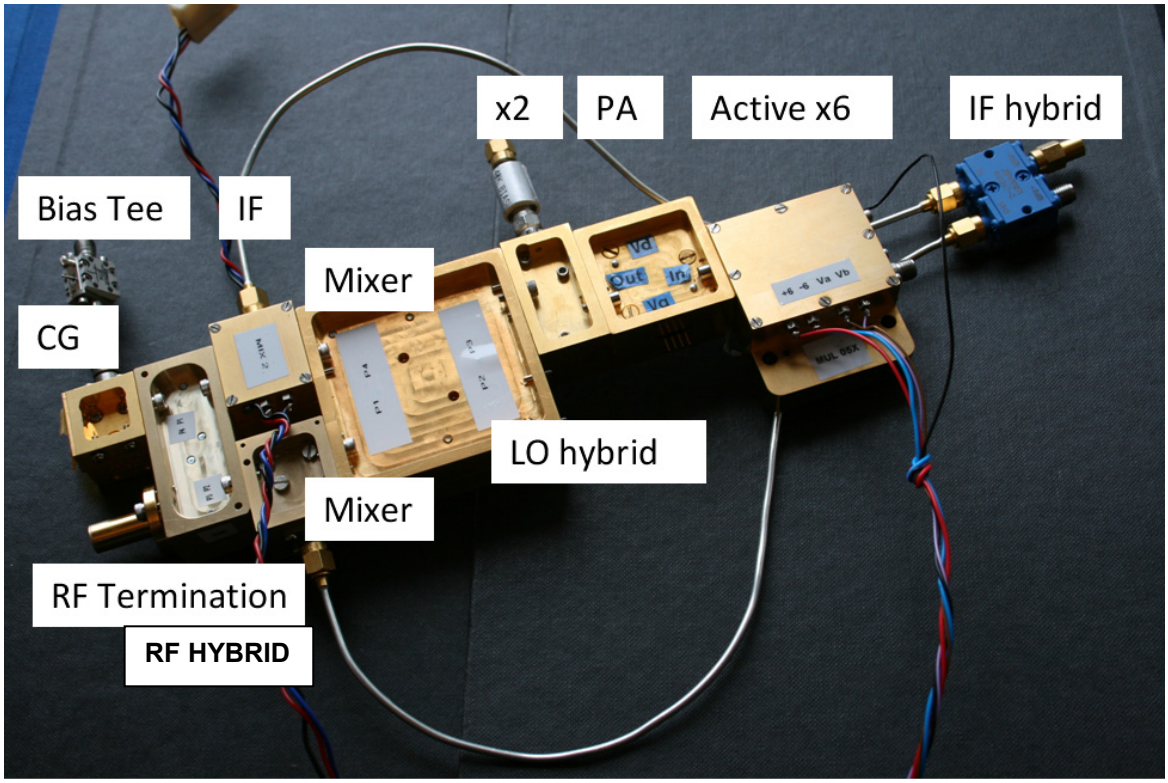

Figure 5. Modular prototype sideband separating (2SB) receiver.

then 1800 K (DSB) covering 20 GHz of IF bandwidth is realistic, see figure 7. In the estimate calculation a total mixer conversion loss of 8 dB and average difference in LNA noise of 120 K has been assumed.

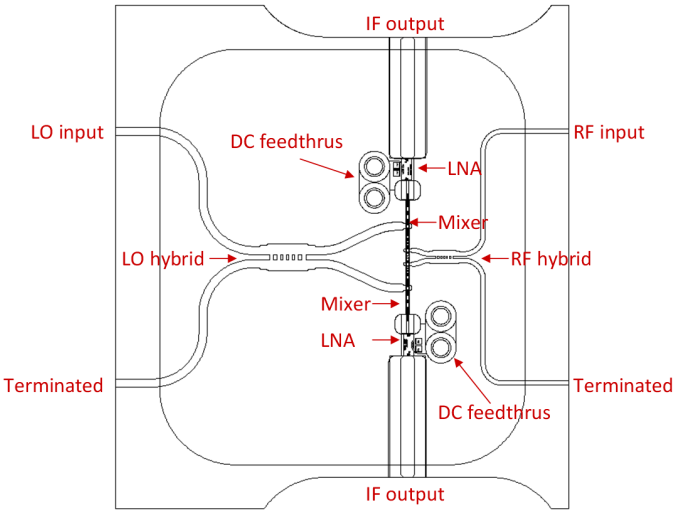

Figure 6. 2D-drawing of the proposed integrated prototype sideband separating (2SB) mixer module.

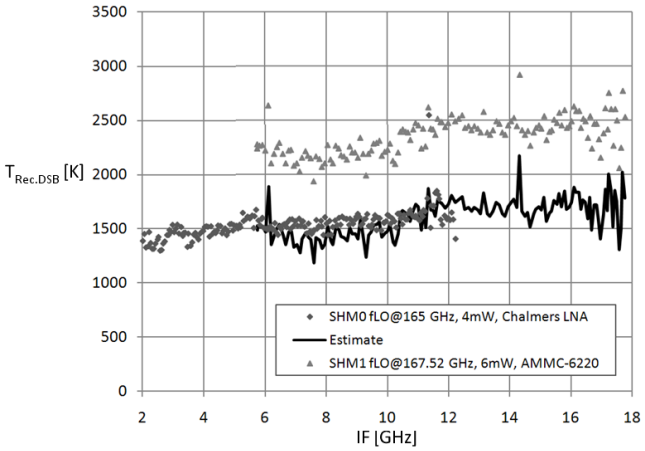

Figure 7. Measured receiver noise temperature and noise estimate based on simulated performance of a custom 6-18 GHz LNA design.

III. Local Oscillator System

Three different LO solutions are being considered in this project, two high power alternatives able to pump 2-4 mixers and one low power alternative able to pump only one mixer. Even though it today is possible to produce output power levels that could cover the LO need of 10 mixers or more, this is not wanted from a reliability perspective.

The first high power alternative consists of a Schottky doubler D166 from VDI, driven by an active W-band multiplier module that was developed for the ALMA WVR. This LO chain can, in its current state deliver up to 12 mW of output power consuming less then 2 W of DC power. The other alternative is a high power module based on a HBV quintupler developed by Wasa Millimeter Wave [4]. The quintupler module is not much larger then a waveguide flange and the first prototype module is capable of producing output powers of around 16 mW with a 3 dB bandwidth of about 4%. The third low power alternative is a single MMIC chip solution from Fraunhofer IAF using GaAs Metamorphic HEMT technology. The design has been developed in cooperation with Herbert Zirath's group at Chalmers University of Technology, see figure 8. The power amplifier is showing a measured output power of 6 dBm in compression broadband and consumes about 0.5 W of DC power. An extra stage would probably increase its' power handling capabilities.

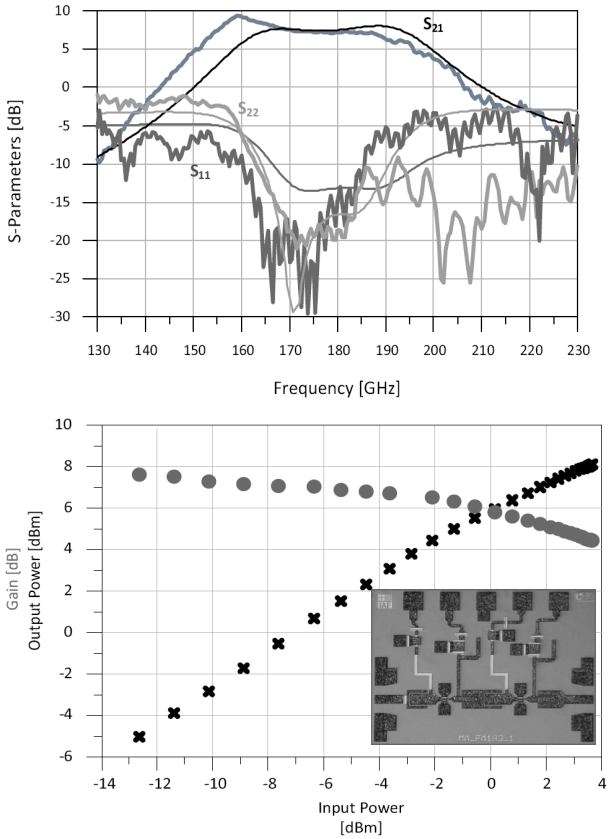

Figure 8. Measured performance of the Chalmers developed power amplifier MMIC chip using the Fraunhofer IAF mhemt process.

IV. Back-End Subsystem

The back-end subsystem will encompass a chain of intermediate broadband amplifiers and a duplex filter stage leading to the IQ-mixers modules. The IQ-outputs with around 3 GHz of bandwidth are processed by ASIC custom designed correlator chips, see figure 9 for a block diagram.

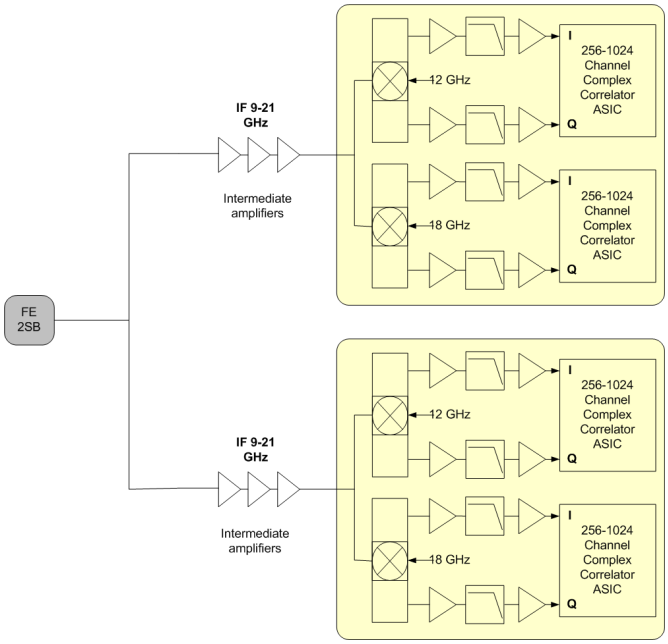

Figure 9. Back-End spectrometer block diagram.

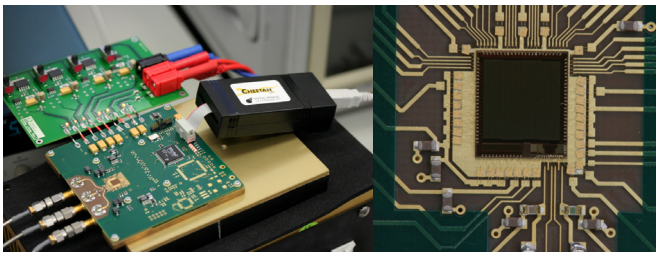

Figure 10. Test board for correlator ASIC(left). Close-up on ASIC (right)

A. Autocorrelator unit

A full-custom ASIC using the IBM 7WL process (0.18 um BiCMOS technology) has been developed, featuring both 3-level digitiser and a digital autocorrelator, see figure 10. One single chip is capable of processing more than 6 GHz of RF bandwidth with 250 channel resolution, while dissipating slightly over one Watt of power, see figure 11 for test results of power consumption for different modes of operation.

B. Initial test

An initial test of the front-end prototype and back-end breadboard combined has been made, and a test signal in the 320-360 GHz range (generated by a comb generator) was successfully captured by the spectrometer. See figure 12 for test setup and results.

V. Conclusions

A concept for realizing the instrument has been developed. Initial breadboarding results of critical receiver components such as mixers, LNA's and backend processing are pointing to that fundamental instrumental specifications can be met. The project has moved from a concept study phase to a prototype phase and the work will now be intensified to further develop and integrate the subsystems and to narrow down the number of options for realization.

Sample clock frequency	**Power consumption when running, total (mW)**			
	256 ch (1 bank)	512 ch (2 banks)	768ch (3 banks)	1024ch (4 banks)
1 GHz	479	567	645	724
2 GHz	582	742	896	1036
3 GHz	710	985	1253	1474
4 GHz	751	1037	1312	1560
5 GHz	917	1365	1792	2158
6 GHz	1041	1534	2698	3233
7 GHz	1271	1888	2926	3520
8 GHz	1332	2401		
9 GHz	1822			

Figure 11. Total correlator power consumption in different operating modes.

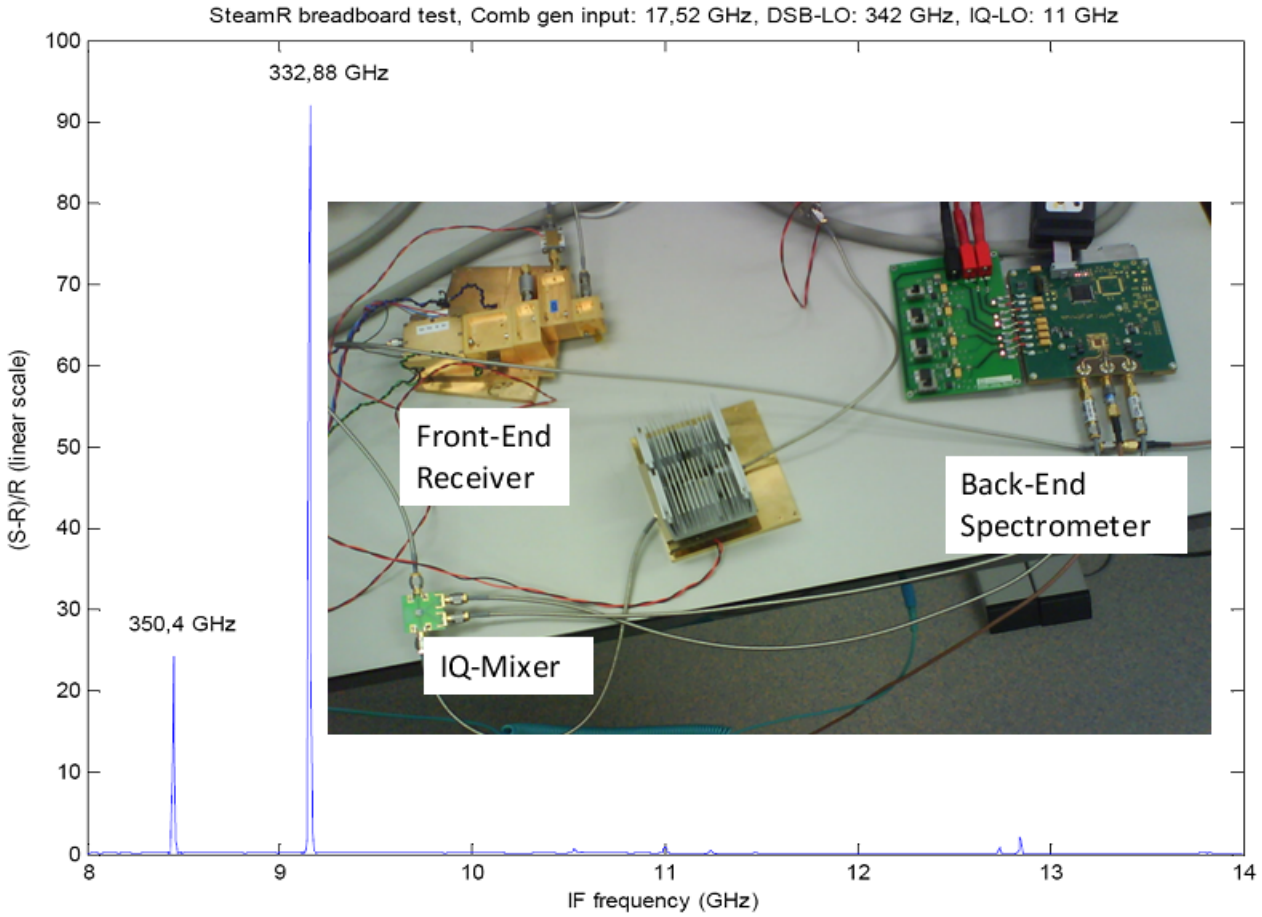

Figure 12. Test results from a prototype receiver setup consisting of the front-end and spectrometer back-end units, successfully transmitting and capturing the spectrum of a RF CW signal running the correlator chip with 6 GHz of bandwidth.

VI. Acknowledgments

We wish to thank Morteza Abbasi with the Microwave Electronics Laboratory at Chalmers University of Technology (MC2) for providing us with the measured data on the developed MMIC amplifier. Thanks to Niklas Wadefalk also at Chalmers University of Technology (MC2) for providing the LNA. We would also like to thank Victor Belitsky with the Group of Advanced Receiver Development at Chalmers University of Technology, for helpful discussions regarding sideband separation topologies.

VII. References

[1] ESA SP-1313/5 Candidate Earth Explorer Core Missions – Reports for Assessment: PREMIER – Process Exploration through Measurements of Infrared and millimetre-wave Emitted Radiation, 2008, ISBN 978-92-9221-406-7, ISSN 0379-6566

[2] M. Cohn, J. Degenford and B. Newman, "Harmonic mixing with an antiparallel diode pair", *IEEE Trans. Microw. Theory Tech., vol MTT-23*, no. 8, pp. 667-673, Aug. 1975.

[3] P. Sobis, J. Stake and A. Emrich, "A 170 GHz 45 degree Hybrid for Submillimeter Wave Sideband Separating Subharmonic Mixers" *Microwave and Wireless Components Letters*, IEEE, vol. 18, NO. 10, pp. 680-682, Oct. 2008.

[4] J. Stake, T. Bryllert, A. O. Olsen and J. Vukusic, , "Heterostructure Barrier Varactor Quintuplers for Terahertz Applications" *Proc. of the 3rd European Microwave Integrated Circuits Conf.*, 2008.

P8I

A Multi-beam 2SB Receiver for Millimeter-wave Radio Astronomy

W.L. Shan[1*], J. Yang[1], S.C. Shi[1], Q.J. Yao[1], Y.X. Zuo[1], S.H. Chen[1], A.Q. Cao[1], Z.H. Lin[1], W.Y. Duan[1], J.Q.Zhong[1,2], Z.Q. Li[1,2], and L. Liu[1,2]

1 Purple Mountain Observatory, Chinese Academy of Sciences, Nanjing 210008, China

2 Graduate School, Chinese Academy of Sciences, Beijing 100039, China

* Contact: shawn@mwlab.pmo.ac.cn, phone +86-25-8333 2229

***Abstract*—A 3x3 multi-beam receiver is being developed for Delingha millimeter telescope, the major open facility for millimeter-wave radio observation in China, aiming to significantly enhance the mapping capability in millimeter-wave line observation. The receiver employs sensitive SIS mixers, working over 85-116GHz frequency range. Sideband separation (2SB) scheme is adopted to enable high-precision calibration procedure and to reduce the idle sideband noise especially when the atmosphere transparency is not good in some seasons. The SIS mixers were designed to have nearly constant dynamic resistance and uniform conversion gain, allowing stable bias and direct connection of the SIS mixer and the cryogenic low noise amplifier without an IF isolator. Besides, low noise and stable digital SIS bias circuit has been designed to operate the SIS mixer efficiently. The nine 2SB mixers are driven by a single LO signal source. Two stages of cascaded power dividers realized by 6-branch line directional couplers distribute the LO signal with good isolation between paths. The LO is generated by a frequency synthesizer followed by an amplifier-multiplier module providing output put power not less than 10mW across the RF band. The IF band is centered at 2.64GHz and bandwidth 1GHz allowing simultaneously observing three CO lines ($C^{18}O$, ^{13}CO and ^{12}CO), which has been proved to be an efficient observation mode in probing a broad range of gas density. The nine pixels yield 18 independent IF outputs. Each of them is processed by a digital FFT spectrometer with 200MHz-1GHz reconfigurable bandwidth and 16384 channels, which has obvious merits over the present analog AOS system to form a compact and reliable backend system for focal array receiver. The whole multi-beam receiver system will be demonstrated in lab by the end of 2009.**

P8J

CASIMIR – Caltech Airborne Submillimeter Interstellar Medium Investigations Receiver

D. Miller[1], M. L. Edgar[1*], A. Karpov[1], S. Lin[1], S. J. E. Radford[1], F. Rice[1], M. Emprechtinger[1], J. Zmuidzinas[1], and A. I. Harris[2]

1 California Institute of Technology, Pasadena, CA 91125*

2 University of Maryland, College Park, MD 20742

* Contact: mick@submm.caltech.edu, phone (626) 395 3740

***Abstract*— CASIMIR is a multiband, far-infared and submillimeter, high resolution, heterodyne spectrometer under development for SOFIA. It is a first generation, PI class instrument, designed for detailed, high sensitivity observations of warm (100 K) interstellar gas, both in galactic sources and in external galaxies. CASIMIR will have unprecedented sensitivity by combining the 2.5-meter SOFIA mirror with state-of-the-art superconducting mixers. These planar mixers are quasi-optically coupled to the telescope beam using twin-slot antennas, and silicon hyperhemisphere lenses with Parylene antireflection coatings. Ongoing mixer developments point to DSB noise temperature improvements of 3 *hv/k* at frequencies below 1 THz, and 6 *hv/k* above 1 THz. All CASIMIR bands use advanced Superconductor-Insulator-Superconductor (SIS) mixers fabricated with Nb/AlN/NbTiN junctions in the JPL Micro Devices Lab. Five bands are under development: 550 GHz, 750 GHz, 1000 GHz, 1250 GHz, and 1400 GHz. Observing time is maximized by having four bands available on each flight. Tunerless solid-state local oscillators are mounted on the outside of the cryostats, with injection to the mixers via mirrors and cryogenically-cooled mylar beamsplitters. The optics box supporting the two cryostats is open to the telescope cavity and contains the relay optics and calibration systems. Besides the cryostat pressure and IR-block windows, all optics are reflective and can accommodate the entire 8' telescope field of view. Bias electronics and warm IF amplifiers are mounted on the cryostats, while electronics racks contain the backend spectrometer, control electronics, and power supplies. The entire instrument is about 1.5 m long, 1 m diameter, and weighs about 550 kg. CASIMIR embodies a versatile and modular design, able to incorporate future major advances in detector, LO and spectrometer technology.**

CASIMIR will enable the study of fundamental rotational transitions of many significant hydrides and other molecules, which can provide critical tests of our understanding of interstellar chemical networks and reactions. CASIMIR will aid in understanding the chemistry of oxygen in interstellar clouds, with observations of key species, such as O, O_2, H_2O, H_2O^+, and OH. The H_2D^+ ion is of particular interest, as it is the deuterated version of H_3^+, which is believed to be responsible for driving much of the chemistry of molecular clouds. CASIMIR will allow the study of the abundance and distribution of interstellar water, which plays an important role in the energy balance of molecular clouds; nine rotational transitions of the rare $H_2{}^{18}O$ istopomer can be detected, including several lines near the ground state.